MITNE-172

GAS-COOLED FAST BREEDER REACTOR FUEL ELEMENT THERMAL-HYDRAULIC INVESTIGATIONS

Final Report

by

Thomas E. Eaton

David D. Lanning

Neil E. Todreas

August, 1975

DEPARTMENT OF NUCLEAR ENGINEERING
MASSACHUSETTS INSTITUTE OF TECHNOLOGY
138 Albany Street
Cambridge, Massachusetts 02139

Prepared for the

General Atomic Company
P.O. Box 81608
San Diego, California 92138

MITNE - 172

GAS-COOLED FAST BREEDER REACTOR
FUEL ELEMENT THERMAL-HYDRAULIC INVESTIGATIONS

Final Report

by

Thomas E. Eaton

David D. Lanning

Neil E. Todreas

Department of Nuclear Engineering
Massachusetts Institute of Technology
138 Albany Street
Cambridge, Massachusetts 02139

August, 1975

Prepared for the

General Atomic Company
P.O. Box 81608
San Diego, California 92138

ABSTRACT

GAS-COOLED FAST BREEDER REACTOR
FUEL ELEMENT THERMAL-HYDRAULIC INVESTIGATIONS

by
Thomas E. Eaton

Experimental and analytical work was performed to determine the influence of rod surface roughening on the thermal-hydraulic behavior of rod array type, nuclear fuel elements. Experimental data was obtained using a grid-spaced, 37-rod hexagonal test section with both a smooth and a rough rod array. The rods were 0.331 inch (8.41 mm) diameter with a pitch/diameter of 1.30. The roughened surface used trapezoidal ribs 6-mils (0.15 mm) high with a rib pitch/height of 12.

Velocity profiles taken at the flow exit plane indicated that, when comparing the rough array results with the smooth, the gap velocities were lower, the peak-to-average velocities were higher, and the peripheral subchannel velocities were higher. Axial static pressure profiles were used to determine rod array friction factors and grid loss coefficients. The friction factor results were in agreement with predictions using tube data. The friction factor multipliers were strongly Reynolds number dependent and grid losses were apparently 10% higher in the rough rod array. Detailed pressure profiles were taken in the axial vicinity of the grid spacers.

Coolant mixing data using a salt solution tracer was obtained for smooth and rough arrays. Flow scattering at the spacers was responsible for most of the smooth array tracer dispersion. In the rough array, turbulent interchange was considerably higher. The grid-spaced, rough array, dimensionless mixing coefficient was estimated to be 0.020 ± 0.005. Flow scattering at the grids prevented the determination of geometry and Reynolds number effects, as well as, the smooth array mixing coefficient.

By neglecting coolant mixing and radial pressure gradients, an equation was developed to determine the flow rate in the subchannels of a nuclear fuel element with roughened surfaces and gas-cooling. Relative subchannel flow rates were influenced by flow regime, fuel element geometry, fuel rod surface roughening, Reynolds number and coolant property variations. Two simple models were discussed which estimate the "equivalent friction factor" in partially roughened flow passages.

Computational results obtained using the RUFHYD code showed that fuel element thermal-hydraulics are influenced by both rod array design parameters and operating conditions. Calculational results included axial subchannel flow distributions, optimum subchannel design estimates, and peripheral subchannel flow sensitivities to changes in rod-to-wall gap.

Thesis Supervisors: David D. Lanning, Professor of Nuclear Engineering; Neil E. Todreas, Professor of Nuclear Engineering.

TABLE OF CONTENTS

TABLE OF CONTENTS (Continued)

TABLE OF CONTENTS (Continued)

TABLE OF CONTENTS (Concluded)

LIST OF FIGURES

LIST OF FIGURES (Continued)

LIST OF FIGURES (Continued)

LIST OF FIGURES (Continued)

LIST OF TABLES

LIST OF TABLES (Concluded)

ACKNOWLEDGEMENTS

The author would like to express his gratitude to Professor David D. Lanning and to Professor Neil E. Todreas for supervising this research project. The financial support of the project by the Gas-Cooled Fast Breeder Reactor Group of the General Atomic Company is also gratefully acknowledged.

Special thanks go to Professor Neil E. Todreas, who is also supervisor of the M.I.T. "Coolant Mixing in LMFBR Rod Bundles" Project (supported by the U.S. Energy Reasearch and Development Agency, formerly the U.S. Atomic Energy Commission, under Contract AT(11-1)-2245), for permitting the use of his Mixing Project hydraulic and instrumentation facilities by the author for the experimental program reported herein. The use of these facilities reduced considerably the funding and time required to perform the experimental program of this project. The author is also grateful to Mr. Alan S. Hanson and Lt. Carl Oosterman (USN) of the M.I.T. Nuclear Engineering Department for their assistance and cooperation regarding the use of Mixing Project hydraulic and instrumentation facilities.

Mr. H. Bob Barra, Mr. Donald Bash, Mr. Fred Johnson and Mr. J.A. "Tiny" Caloggero, employees of the M.I.T.

Mechanical Engineering Department are thanked for their assistance with the construction, operation and maintenance of the experimental facility used for this work.

The author would like to express his gratitude to the U.S. Atomic Energy Commission for the financial support received during the period September 1970, through August 1973, as a U.S.A.E.C. Fellow. During the latter part of the appointment, work was initiated on this project.

The author would like to express his most sincere gratitude to Mr. P.B. Bon for his patient, understanding instruction without which this work might not have been possible.

Mrs. Shirley Okun is gratefully acknowledged for the preparation of the majority of the final draft.

The author is grateful to the following personnel of the General Atomic Company for their assistance with this project: A.F. Weinberg, J.B. Dee, H.J. Snyder, Jr., J.A. Larrimore, W.I. Thompson, G. Melese-d'Hospital, J.T. Ream, J. Goodman, and T.L. Ward. The assistance of G. Markoćzy of the Swiss Federal Insitute for Reactor Reasearch is acknowledged also.

Finally, it has been necessary for the author to invest a considerable amount of his personal time and financial assets in order to ascertain the completion of this project.

CHAPTER I

SUMMARY AND CONCLUSIONS

1.1 Gas-Cooled Nuclear Fuel Elements

The Gas-Cooled Fast Breeder Reactor (GCFR) uses rod array-type nuclear fuel elements with a triangular rod lattice, a 0.389 inch rod-to-rod pitch and a 0.285 inch rod diameter (pitch/diameter = 1.36). The hexagonal element contains 271 fuel rods and uses helium pressurized to 1290 psia as a coolant. This report deals principally with the development of a thermal-hydraulic analysis method for roughened, gas-cooled nuclear fuel elements and with comparative hydraulic experiments on rod arrays with both smooth and artificially roughened rod surfaces.

1.1.1 Characteristics of Gas-Cooled Fuel Elements

Gas-cooling is characterized by a low coolant density, low convective heat transfer coefficients, and a pressurized coolant. Further, the density, dynamic viscosity, and thermal conductivity of the coolant are dependent on both pressure and temperature. Because of the low forced convection heat transfer coefficients, it is advantageous to artificially roughen the heated surfaces of the fuel element over part of the active core length.

Through a boundary layer tripping mechanism, not an extended area (fin) effect, roughened surfaces improve the thermal-hydraulic performance of the fuel element.

1.1.2 Roughened Surfaces to Augment Convective Heat Transfer

A roughened surface design is specified by six geometrical parameters; A. Rib height, B. Rib-to-rib pitch, C. Rib width, D. Rib geometry, E. Roughened length, and F. Rib helix angle. By far the more important geometrical parameter is the rib height, and typical optimums range from 0.002 to 0.006 inches. The next most important parameter is the rib-to-rib pitch for which the optimum ranges from 7 to 12 rib heights. Fabrication tolerances for the above two parameters may be more significant than the combined effects of rib, width, geometry and helix angle. Helical rib roughening may offer a small improvement in performance over transvers rib, but further investigation is required.

Inherently, the ratio of the roughened surface-to-smooth surface friction factors f_x increases faster than the ratio of the roughened surface-to-smooth surface Stanton numbers St_x. The experimental data in the literature may be approximately related by (see Norris [N1]):

$$St_x = f_x^{0.55} \qquad \text{(Eq. 1.1)}$$

TABLE 1.1

EXPERIMENTAL ROD ARRAY AND GCFR FUEL ELEMENT PARAMETERS

	EXPERIMENT	GCFR
Rod Diameter - Outside Diameter (Smooth), Over Ribs (Rough)	0.331 (8.41)	0.285 (7.24)
Rod Root Diameter - Roughened Region	0.319 (8.10)	0.273 (6.93)
Rod-to-Rod Pitch -	0.430 (10.9)	0.369 (9.88)
Rod Pitch-to-Diameter Ratio -	1.30	1.36
Rod-to-Wall Gap -	0.065 (1.65), Nominal	0.043 (1.22), Nominal
Number of Rods -	37	271
Rod Array Shape - (Overall)	Hexagonal	Hexagonal
Rod Array Lattice	Triangular (Equilateral)	Triangular (Equilateral)
Rod Length	60.0 (1525)	39.2 (996), Active Core
Roughened Length -	30.0 (762), Downstream End	29.4 (747)[a] Downstream End
Roughened Surface Rib Height, e -	0.006 (0.152)	0.006 (0.152)
Roughened Surface Rib Pitch, p -	0.072 (1.83) p/e = 12	0.072 (1.83) p/e = 12
Roughened Surface Rib Helix Angle -	12.7° Single Start Helical Rib	0.0° Transverse Rib
Roughened Surface Rib Width, w -	0.018 (0.457) w/e = 3	0.018 (0.457) w/e = 3
Roughened Surface Rib Geometry -	Trapezoidal[b]	Trapezoidal[b]
Relative Surface Roughness, e/d_e -	0.025	0.021
Equivalent Hydraulic Diameter (Bundle Average) -	0.238 (6.05)	0.284 (7.21)
Flow Duct Width (Across Flats)	2.70 (68.6)	6.44 (164.)
Spacer Type -	AGATHE Grid (Similar to GCFR)	Grid
Spacer Grid Axial Separation -	7-3/4 (197) Nominal	10. (254) Nominal

* Dimensions given are in inches (millimeters)

a 3/4 of active core length on the downstream end.

b See Figure 4.1 , same as General Atomic Co. Drwg. No. 5001-15, 30 April 1973.

Using tube data, it was shown that the friction factor multiplier for fully developed roughened surface flow, i.e.,

$$Re > \frac{(d_e/e)}{0.005\sqrt{f_r}} \quad , \qquad \text{(Eq. 1.2)}$$

varies as follows with Reynolds number and relative roughness d_e/e:

$$f_x = \frac{7.18\ Re^{0.20}}{[\ln(d_e/e) + 1.31]^2} \quad . \qquad \text{(Eq. 1.3)}$$

Much of the experimental data in the literature on roughened surface behavior was obtained using a roughened rod contained within a smooth tube. Considerable difficulty has arisen and still persists concerning the isolation of the effects of the roughened surface from that of the experimental geometry - a mandatory requirement for data reduction. In nuclear fuel element thermal-hydraulic analysis, a similar problem arises in attempting to determine the behavior of a roughened surface in the partially roughened peripheral subchannels.

1.1.3 Radiative Transfer in GCFR Fuel Elements

Because the coolant is transparent and the film temperature rise is characteristically high, the role of radiative heat transfer in the GCFR fuel element was of interest. Using a simplified model for the complex radiative

transfer phenomenon, the radiative transfer in the GCFR fuel element was conservatively determined to be less than 0.5% of the convective heat transfer. The maximum radiative transfer was less than 2000 BTU/hr-ft^2 and occurred between the fuel rods and the unheated duct wall at the end of the smooth rod section. The metal surface temperatures were changed less than 2°F by radiative transfer effects, and it was concluded that radiative transfer was insignificant in the GCFR fuel elements during normal operating conditions.

1.1.4 Fuel Rod Spacer Design

Two alternative fuel rod spacer designs were considered to determine the merits of each, i.e., the reference design grid-type spacer and the alternative design twisted-tape spacer. Twisted-tape spacers are formed by twisting a thin metal strip of the appropriate width with an axial pitch of typically 4 to 9 inches and placing this device within the subchannels of the rod array to maintain rod array geometry and prevent fuel rod vibrations. Two twisted-tape spacer designs were considered: the one twisted-tape per fuel rod design (every other interior subchannel) and the one twisted-tape per interior subchannel design.

Twisted-tape spacers offered advantages of reduced cost, simple fabrication, simple fuel element assembly, and possibly, improved coolant mixing when compared to the grid

spacers. The one twisted-tape per fuel rod design offered the lowest core pressure loss, but flow calculations using the model discussed in section 1.2 indicated severe maldistributions of flow between taped and bare interior subchannels. In turbulent flow, the ratio of bare-to-taped interior subchannel flows was typically 1.62 in the smooth core section and 1.33 in the rough; in laminar flow, the ratio was 3.7. Because of the maldistributions of flow, the one twisted-tape per fuel rod design was not considered a feasible design. The grid spacer was recommended over the one twisted-tape per subchannel design because it had a slightly lower total core pressure loss, offered positive fuel rod positioning, and required less metal in the active core region. Further, both spacer designs could be expected to increase the coolant mixing in the spaced rod array compared to the bare rod array.

1.2 A Simplified Thermal-Hydraulic Analysis of Gas-Cooled, Roughened Nuclear Fuel Elements

A Simplified equation for determining the coolant flow in various types of subchannels in a rod array-type fuel element was developed by extending the method of Sangster [S1]. The derivation assumed tht radial pressure gradients and interchannel coolant mixing were negligible. The flow in area i with respect to area j , i.e., X_{ij}, was given by

$$X_{ij} = \frac{W_i}{W_j} = \left(\frac{A_i}{A_j}\right)\left(\frac{d_{ei}}{d_{ej}}\right)^{\left(\frac{1+m}{2-m}\right)} \left(\frac{\rho_i}{\rho_j}\right)^{\left(\frac{1}{2-m}\right)} \left(\frac{\mu_j}{\mu_i}\right)^{\left(\frac{m}{2-m}\right)} \left(\frac{f_{xj}}{f_{xi}}\right)^{\left(\frac{1}{2-m}\right)} \quad \text{.(Eq. 1.4)}$$

Subchannel Geometry Effect

Coolant Property Variation Effect

Roughened Surface Effect

The variables are defined in the nomenclature. The flow split equation included the effect of fuel rod surface roughening in addition to the commonly considered effects of subchannel geometry and coolant property variations.

1.2.1 Factors Influencing Subchannel Flow Rates

The fraction of the total fuel element flow which passes through given subchannel type was seen to be determined by both fuel element design and reactor operating conditions! The fuel element design options influencing subchannel flows included fuel rod pitch, fuel rod diameter, rod-to-wall gap, wall design, corner design and surface roughening. Reactor operating conditions influencing subchannel flows were coolant flow rate, flow regime, radial power gradients and power-to-flow ratio. The flow regime influence appeared through the nature of the friction factor, i.e., the Reynolds number dependence; the power-to-flow ratio and radial power gradient influences were apparent through the coolant property effects. The coolant flow rate

influences are the consequence of the Reynolds number dependence of the friction factor multipliers.

The equations developed formed the basis of a small computer code , RUFHYD, which was employed to do the thermal-hydraulic analysis of a typical GCFR Demonstration Plant fuel element. GCFR fuel element geometry details are given in Table 1.1. Flow regime, surface roughening and duct wall design most significantly influenced subchannel flow, e.g., Figure 1.1. Coolant property variations, i.e., changes in dynamic viscosity and density with temperature, were responsible for small axial variations in local subchannel flows which became increasingly important if the geometry of peripheral and corner subchannels varied from the thermal-hydraulic optimum.

1.2.2 Equivalent Friction Factor Multipliers in Partially Roughened Subchannels

Since it is not beneficial to roughen the unheated flow duct which surrounds the rod array, an important problem was the determination of the "equivalent friction factor" of subchannels with partially roughened perimeters. Two simple models were proposed and used throughout this work: the "perimeter-weighted, average resistance model" and the "perimeter-weighted parallel resistance model."

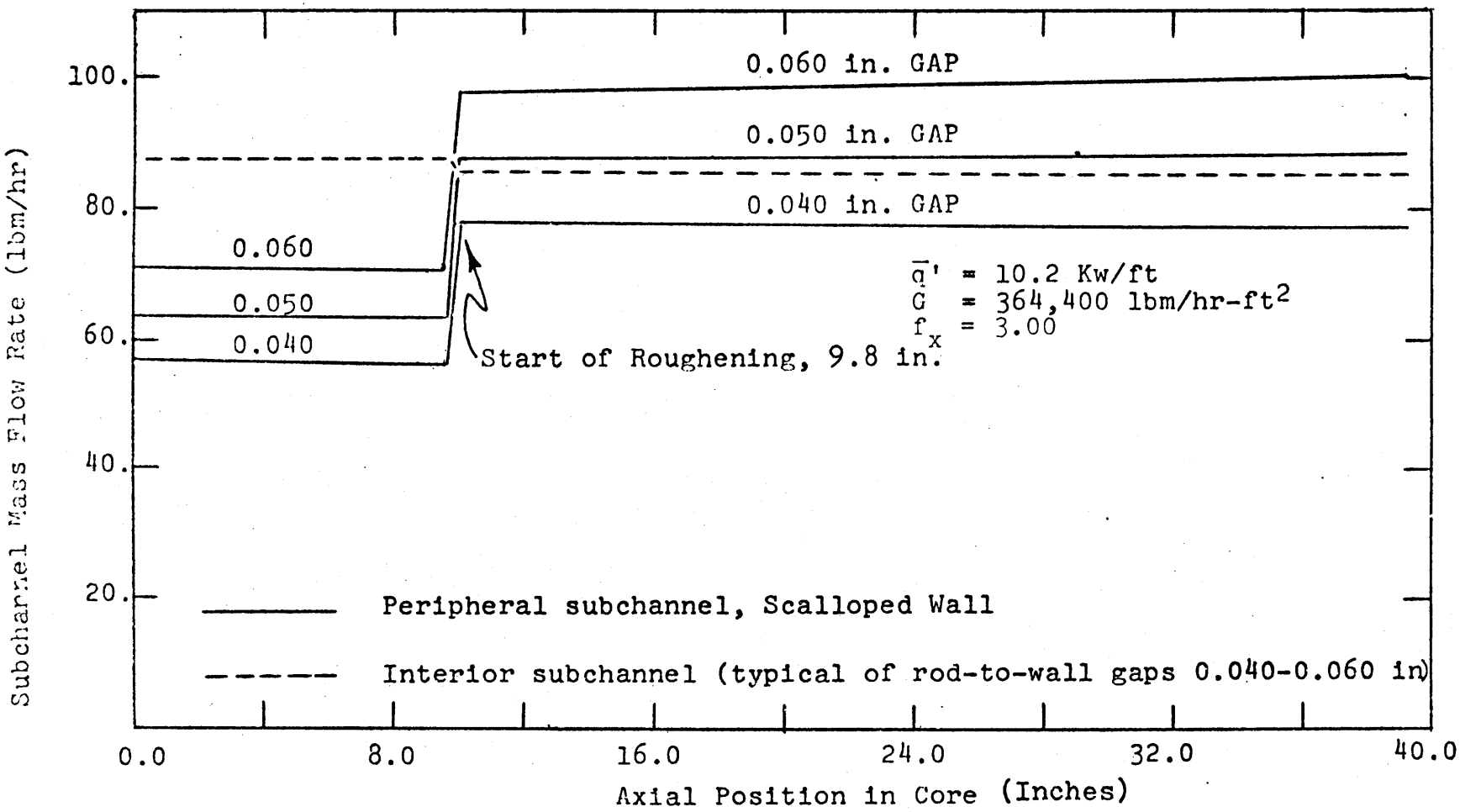

FIGURE 1.1- TYPICAL SUBCHANNEL FLOW RATES, CENTRAL FUEL ELEMENT

The models used the fraction of the wetted perimeter that was roughened and the experimentally determined, roughened surface friction factor multiplier to analytically estimate the "equivalent friction factor multiplier" for partially roughened subchannels. It is believed that the perimeter-weighted parallel resistance model offers a reasonable estimate of the friction factor multiplier of a partially roughened subchannel.

1.2.3 Optimum Peripheral Subchannel Design

It was possible to establish the optimum rod-to-wall gap for the various peripheral and corner subchannel designs. The criterion used for this optimum gap selection was that the outlet temperatures from all subchannel types be the same, i.e., that the ratio of flow between subchannel types be equal to the ratio of heated perimeters. Results obtained from this technique are summarized in Table 1.2. It is important to note that the optimum rod-to-wall gap is influenced by flow regime, wall design, rod array geometry, surface roughening, and coolant flow rate. The optimum rod-to-wall gap was different for the smooth and rough sections of the fuel element; it was different for corner and peripheral subchannels, and it changed with coolant flow conditions, e.g., Figure 1.2.

TABLE 1.2¢

SUMMARY OF OPTIMUM ROD-TO-WALL GAPS+

Subchannel Type	Laminar	Turbulent	
Surface	NA	Smooth	Rough*
Peripheral			
Scalloped Wall $	0.128 (3.25)	0.083 (2.11)	0.048 (1.22)
			(0.062)# 1.57
Flat Wall	0.070 (1.78)	0.050 (1.27)	0.030 (0.762)
Corner			
Sharp Corner	0.097 (2.46)	0.075 (1.91)	0.059 (1.50)
Rounded Corner	0.098 (2.49)	0.081 (2.06)	0.067 (1.70)

+ Differences in convection coefficients between subchannel types have been neglected, Rod-to-Wall gaps are given in inches (millimeters).

* Based on Perimeter Weighted, Parallel Resistance Model for the equivalent friction factor, # (Average Model), $f_x = 3.00$.

$ The Scallop Design was triangular in shape with a Base Width = Rod Diameter and Height = Rod-to-Wall Gap.

¢ Additional details are given in reference [E1].

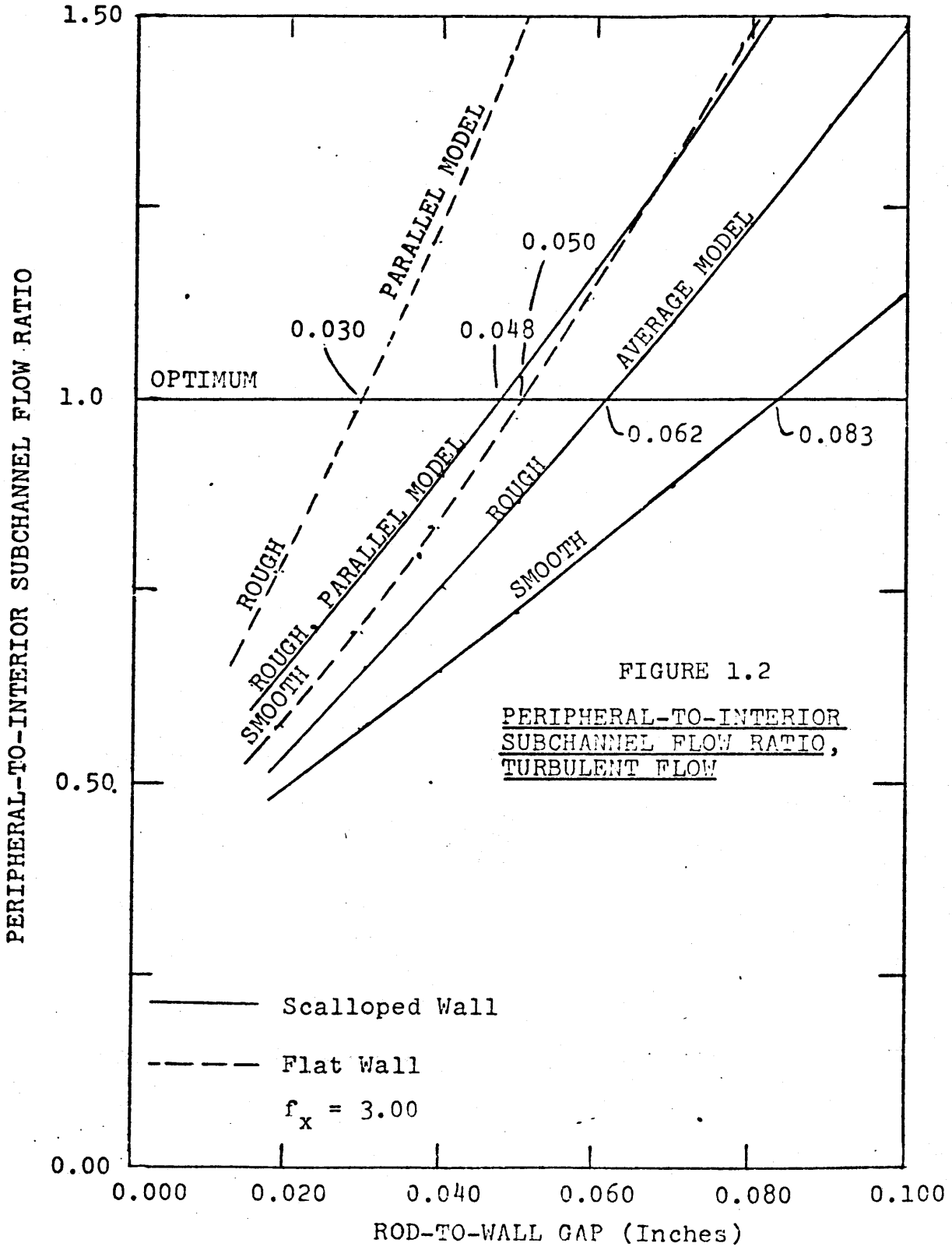

FIGURE 1.2

PERIPHERAL-TO-INTERIOR SUBCHANNEL FLOW RATIO, TURBULENT FLOW

1.2.4 Operating Requirements for Gas-Cooled, Roughened Fuel Elements

If the optimum operating conditions used for the fuel element design were to be commensurate with the normal, full power, reactor centerline power and flow conditions, then it will be necessary to adjust fuel element orificing to allow for flow rate, power-to-flow ratio and radial power gradient effects when shuffling (or rotating) fuel elements. During laminar flow conditions, it will be necessary to adjust the power-to-flow ratio to accommodate the loss of convective heat transfer augmentation characteristic of laminar flow, as well as, the non-optimum laminar flow fuel element geometry. These operating procedures will be required to prevent operating the fuel rod cladding beyond the design limit.

1.2.5 Peripheral Subchannel Flow Sensitivity to Changes in Rod-to-Wall Gap

Finite differences were used with RUFHYD computational results to determine the sensitivity of peripheral and corner subchannel flows to changes in the rod-to-wall gap, e.g., Figure 1.3. The flow sensitivity was influenced by fuel element design and operating conditions and decreased with increases in rod-to-wall gap; it was influenced by the wall shape; it was less in turbulent

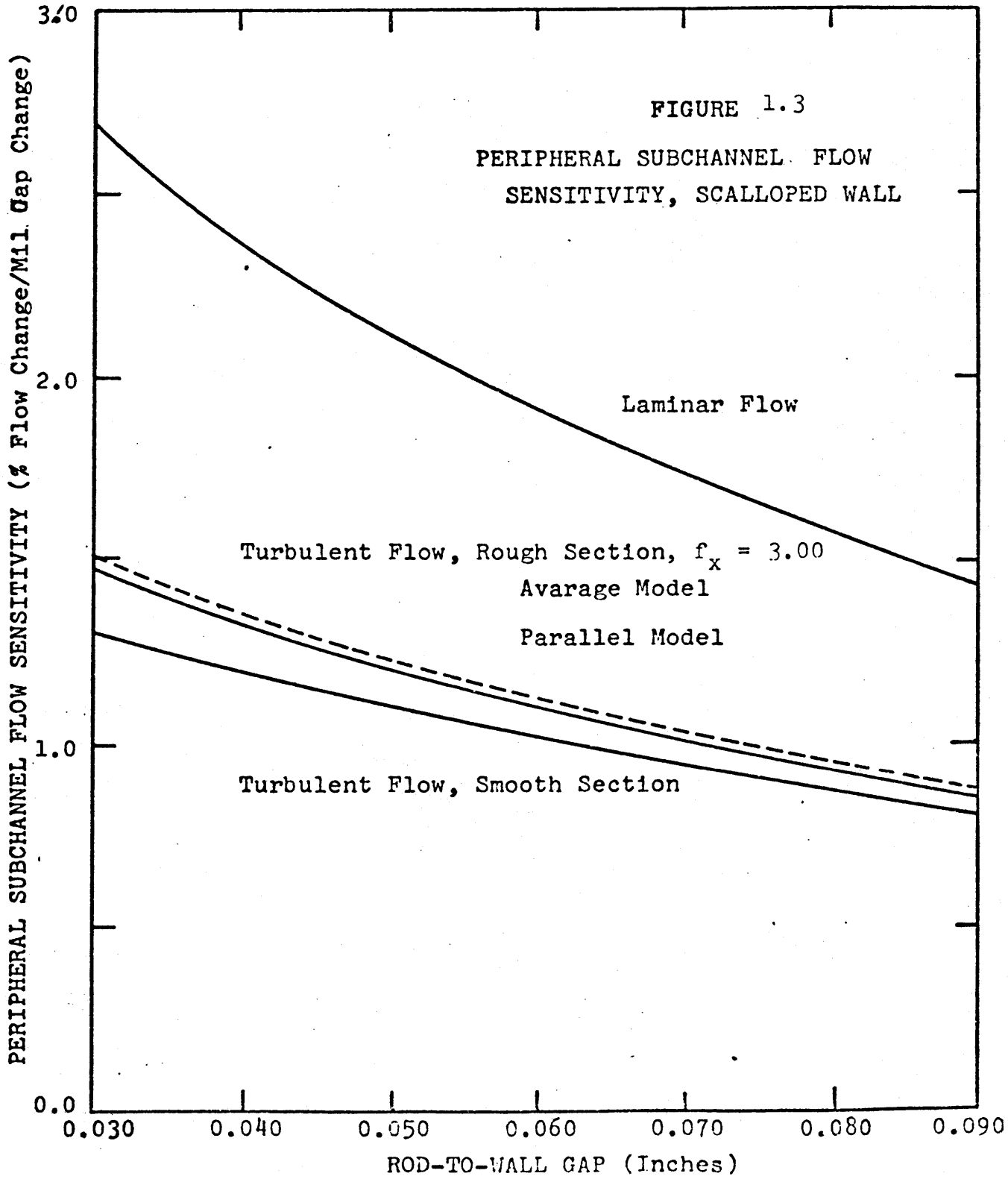
3.0
2.0
1.0
0.0
PERIPHERAL SUBCHANNEL FLOW SENSITIVITY (% Flow Change/Mil Gap Change)
FIGURE 1.3
PERIPHERAL SUBCHANNEL FLOW
SENSITIVITY, SCALLOPED WALL
Laminar Flow
Turbulent Flow, Rough Section, f_x = 3.00
Avarage Model
Parallel Model
Turbulent Flow, Smooth Section
0.030
0.040
0.050
0.060
0.070
0.080
0.090
ROD-TO-WALL GAP (Inches)

flow than laminar flow; it was less in the smooth rod region than in the roughened region, and it was less in the peripheral than the corner type subchannels.

1.2.6 Fuel Element Design Recommendations

The sharp corner design and the scalloped peripheral design offer the best thermal-hydraulic performance. The sharp corner design offered more flow area than the rounded corner design; the sharp corner design was preferred because the corner subchannel was undercooled. Further, the optimum rod-to-wall gap for the sharp corner design was closer to that of the peripheral subchannel.

The scalloped peripheral subchannel offered several advantages over the flat wall design. As noted by Markoczy [M2], the scalloped peripheral subchannel reduces hot-spot factors by reducing circumferential variations of the convection coefficient on fuel rods adjacent to the duct wall. The scallop design results in peripheral subchannel flows which are less sensitive to variations in the rod-to-wall gap as compared to the flat wall design. By varying the geometry of the scallop, the hydraulic design of the peripheral subchannel is more flexible (with flat walls only the rod-to-wall gap may be changed); the optimum

rod-to-wall gap for scalloped peripheral subchannels (when compared to the optimum gap for a flat wall) is closer to the optimum for the corner subchannel. The scallops serve as stiffeners on the spacer hanger shroud (reference design) and thus reduce any flow induced vibrations and distortions of the shroud.

1.3 Experimental Results

Comparative experiments to determine velocity profiles, rod array friction factors, spacer grid loss coefficients, and interchannel coolant mixing behavior were performed using a 37-rod hexagonal rod bundle with both a smooth and an artificially roughened rod array. Details are given in Figure 1.4 and Table 1.1. A concentric tube arrangement was used to measure static pressure and to inject salt solution tracer for the axial pressure profile and coolant mixing experiments, respectively, at any axial location in the downstream thirty inches of the rod array. In this arrangement, an inner tube was free to move in the axial direction. The outer tube was slotted such that a tube through the wall of the inner tube was exposed to the subchannel.

1.3.1 Rod Array Velocity Profiles at the Exit Plane

Velocity profiles were measured in interior and peripheral subchannels at the rod array exit plane using

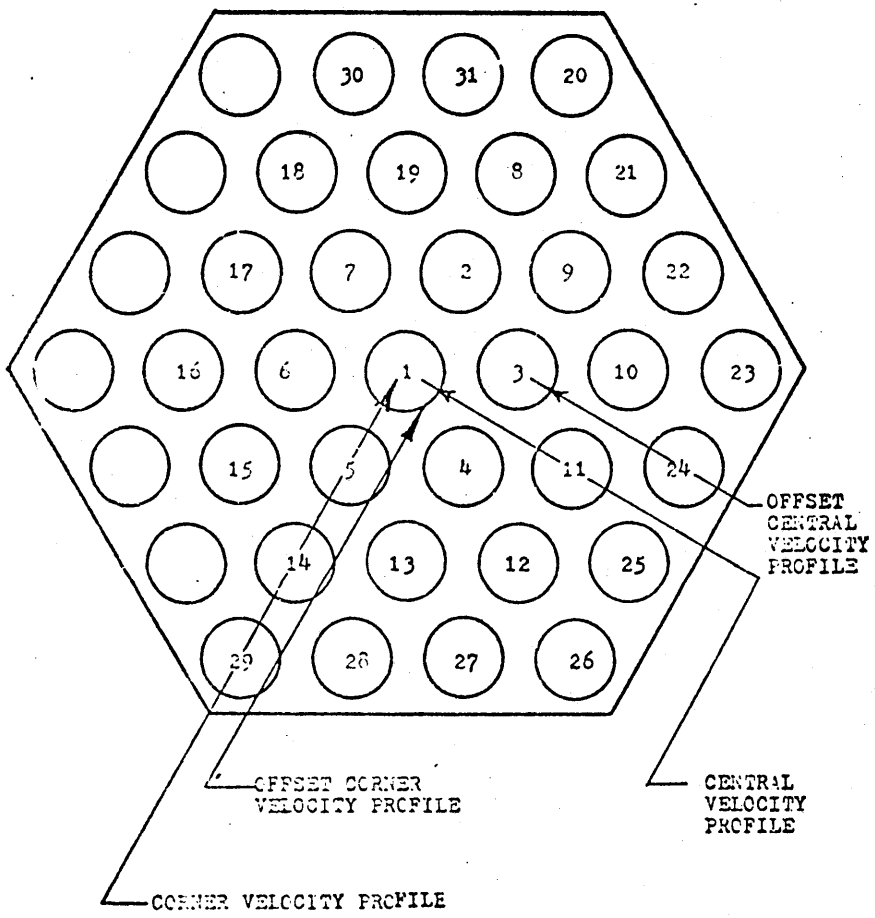

ROD IDENTIFICATION NUMBERS AND VELOCITY PROFILE LOCATIONS.

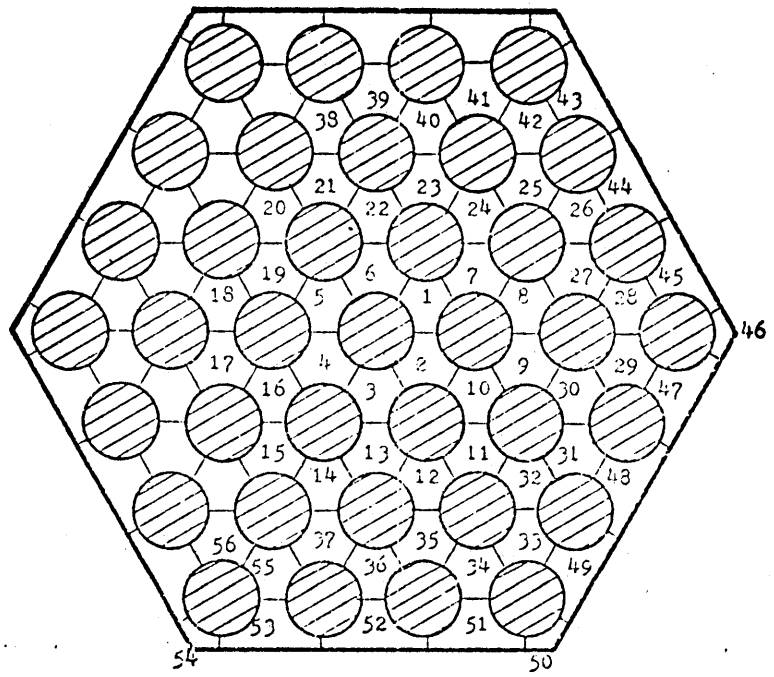

SUBCHANNEL IDENTIFICATION NUMBERS

FIGURE 1.4

SUBCHANNEL AND ROD IDENTIFICATION NUMBERS, VELOCITY PROFILE LOCATIONS

a pitot tube. Two one-dimensional traverses are reported here: the central and the offset central profiles (see Figure 1.4 for details). Results of the offset central profiles are shown in Figures 1.5 and 1.6 for the smooth and rough rod arrays, respectively. Similar results for the central velocity profiles are shown in Figures 1.7 and 1.8.

The following behavior of the fluid velocity in the rough rod array compared to the smooth rod array was noted: (A) the velocity gradients at the smooth duct wall were larger, (B) the peak subchannel velocities were higher, (C) the fluid velocities at flow constrictions, i.e., rod-to-rod or rod-to-wall gaps, were lower, (D) the peak-to-average velocities were higher, (E) the peripheral and corner subchannel velocities were higher, (F) the differences in behavior between rough and smooth arrays increased with Reynolds number and (G) the corner subchannel velocity increased faster than flow rate due to coolant mixing effects.

Average flow velocities for the various subchannel types were determined from the velocity profile data using an area weighting scheme. The results of this procedure are shown in Table 1.3 along with the respective values calculated using the RUFHYD code. Because of the partially roughened perimeter, the peripheral subchannels had higher

FIGURE 1.5

OFFSET CENTRAL VELOCITY PROFILE, SMOOTH ROD ARRAY

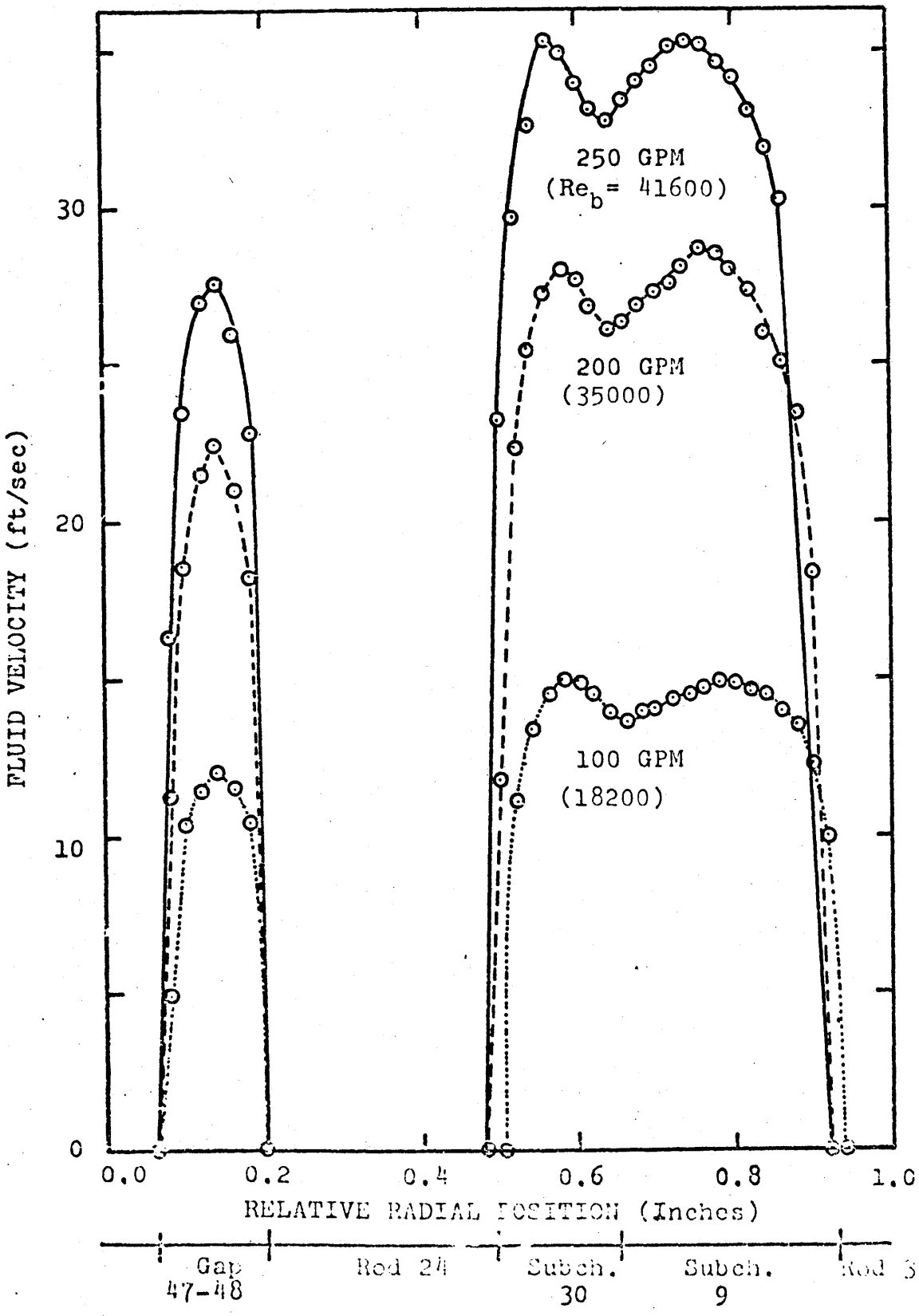

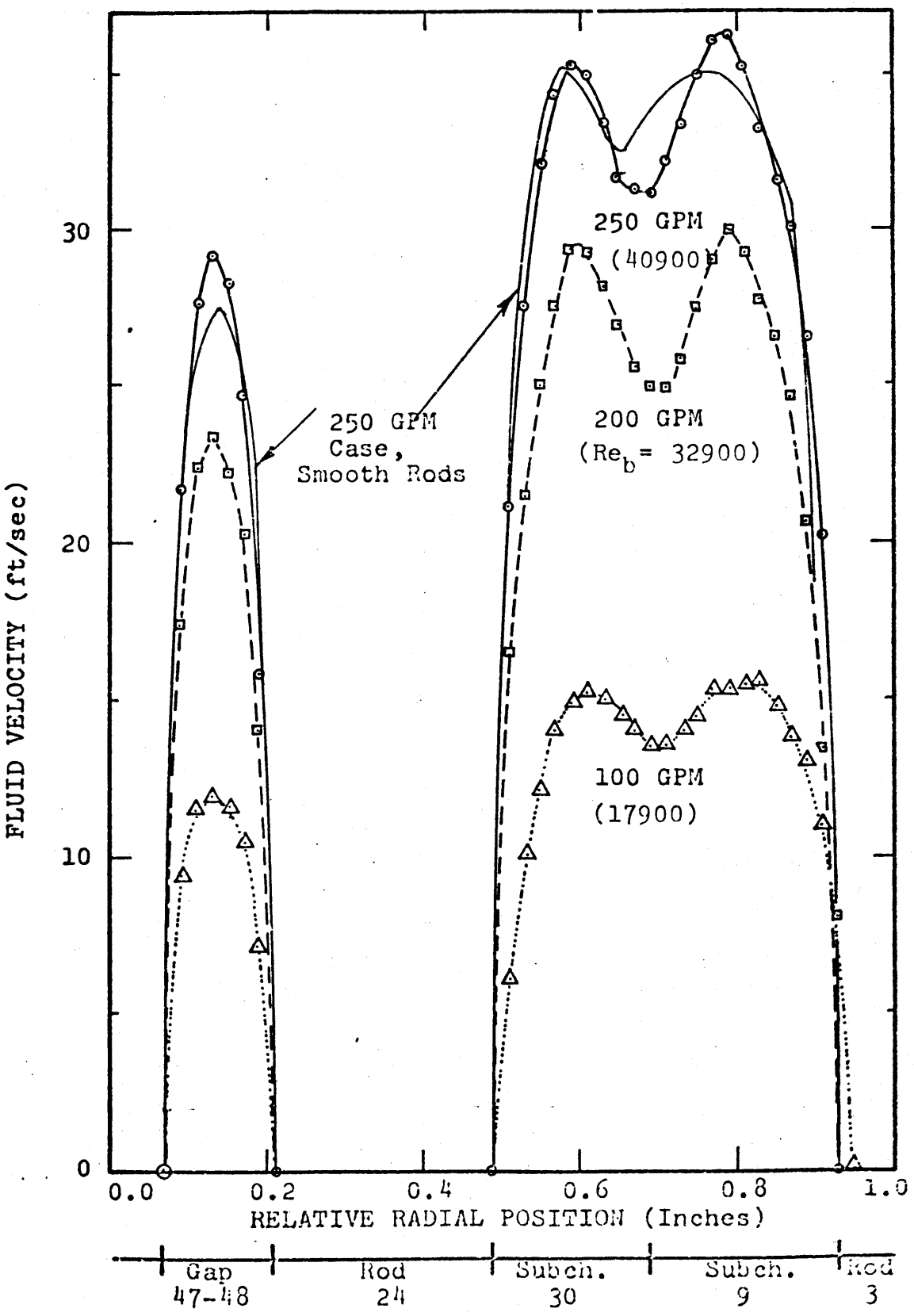

FIGURE 1.6

OFFSET CENTRAL VELOCITY PROFILE, ROUGH ROD ARRAY

FIGURE 1.7

CENTRAL VELOCITY PROFILE, SMOOTH ROD ARRAY

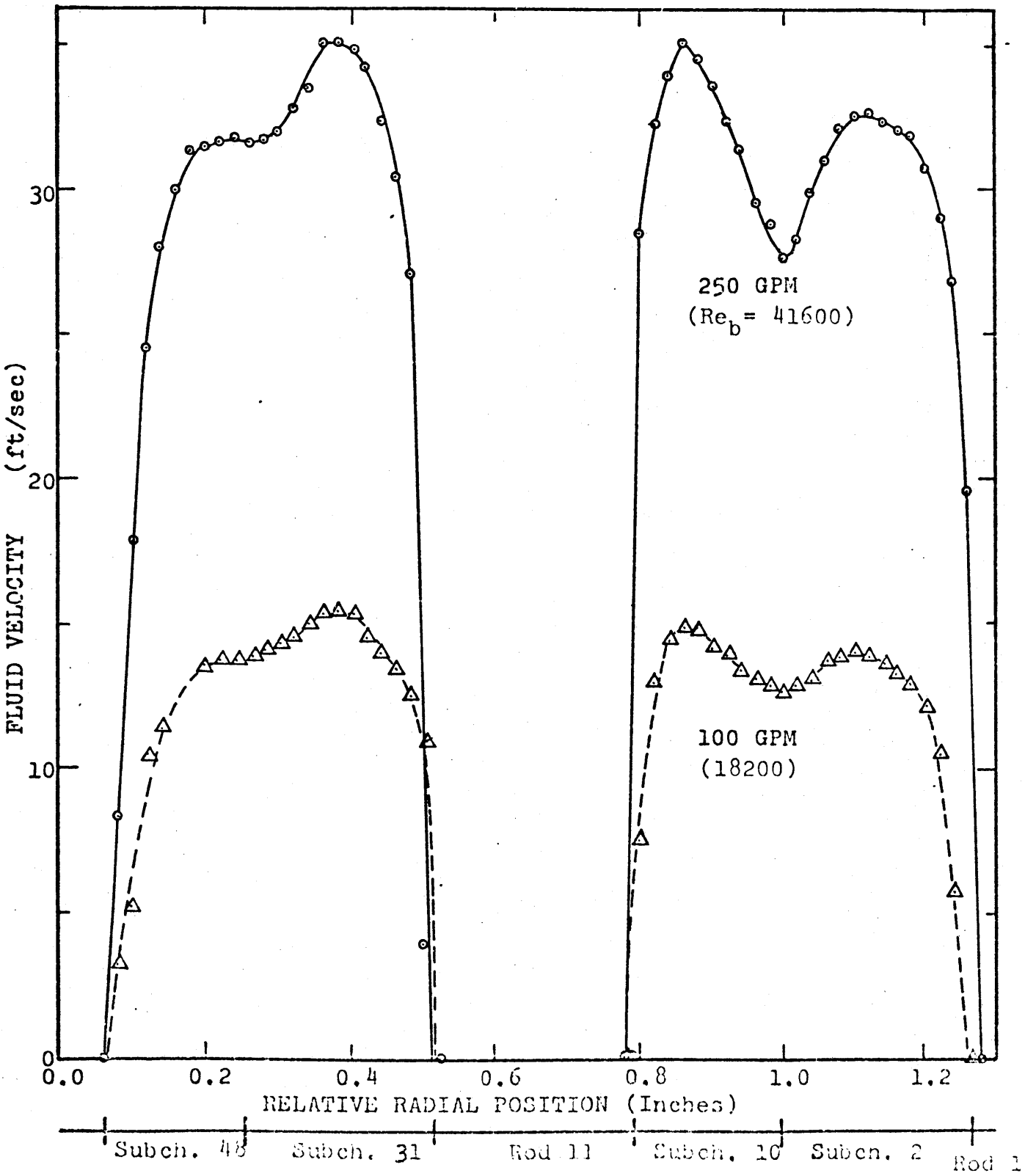

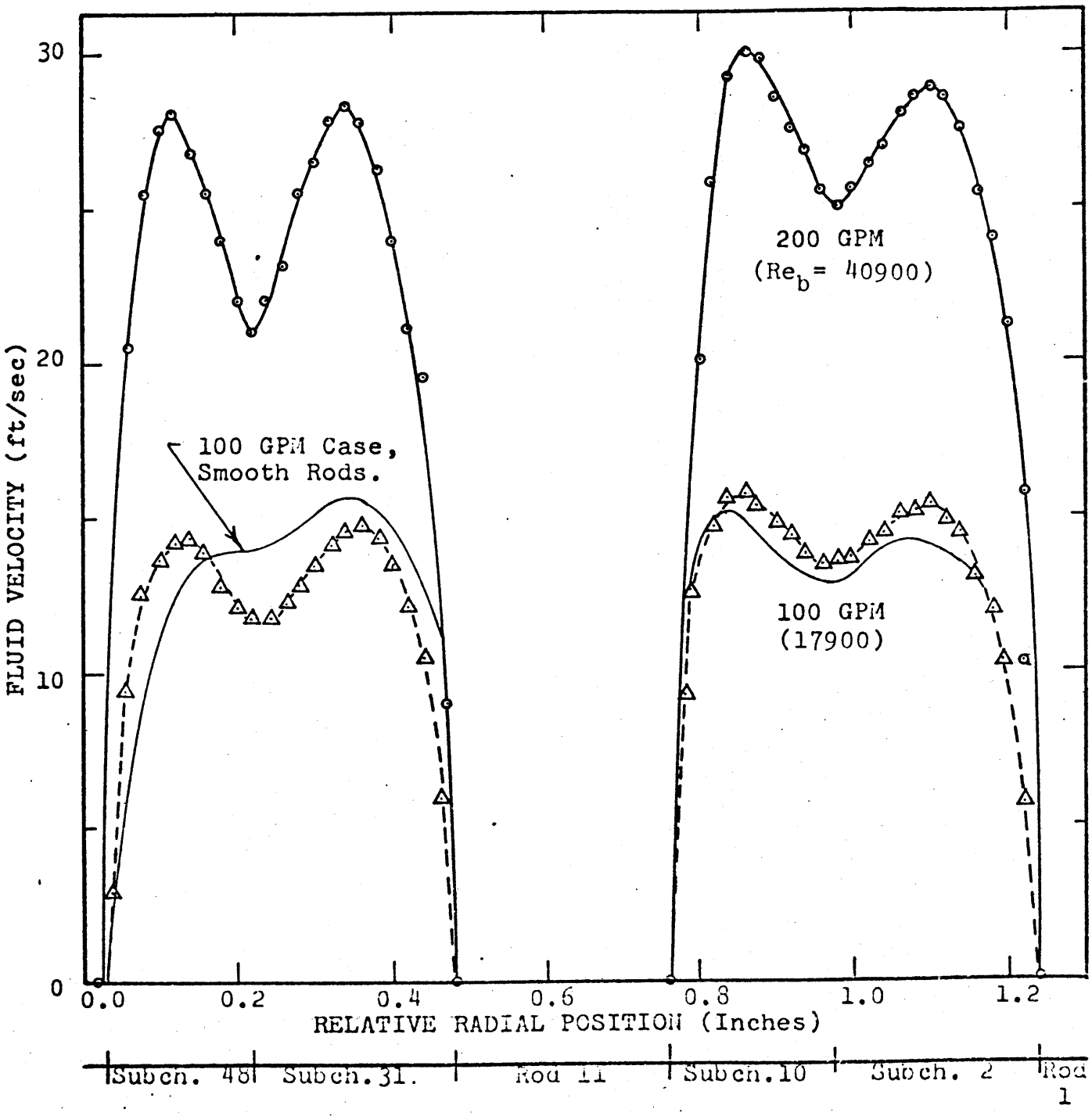

FIGURE 1.8

CENTRAL VELOCITY PROFILE, ROUGH ROD ARRAY

TABLE 1.3

AVERAGE VELOCITY IN THE VARIOUS SUBCHANNEL TYPES

Rod Surface	Smooth				Rough			
Source	Experimental (51°F)		Analytical		Experimental (47°F)		Analytical$	
Bundle Flow: Subchannel Type	Velocity* (ft/sec)	Flow Split Factor (X_{1b})	Velocity (ft/sec)	Flow Split Factor (X_{1b})	Velocity (ft/sec)	Flow Split Factor (X_{1b})	Velocity (ft/sec)	Flow Split Factor (X_{1b})
Bundle Flow (GPM)	115		100		113		100	
Interior - 1	13.6	0.0138	12.2	0.0141	13.1	0.0136	11.6	0.0133
Peripheral - 2	11.3	0.0139	8.7	0.0123	11.7	0.0148	10.2	0.0143
Corner - 3	4.8	0.0018	7.4	0.0031	4.7	0.0018	8.8	0.0037
Bundle Flow (GPM)	221		200		208		200	
Interior - 1	26.2	0.0140	24.4	0.0141	24.2	0.0135	22.8	0.0131
Peripheral - 2	(21.3)	(0.0138)	17.5	0.0123	21.5	0.0146	21.1	0.0149
Corner - 3	11.5	0.0022	14.8	0.0031	10.9	0.0022	18.3	0.0039
Bundle Flow	263		250		258		250	
Interior - 1	31.4	0.0138	30.5	0.0141	29.9	0.0134	28.3	0.0131
Peripheral - 2	25.1	0.0135	21.8	0.0123	26.7	0.0146	26.7	0.0151
Corner - 3	(14.4)	0.0023	18.5	0.0031	13.7	0.0022	23.2	0.0039

$ Rough Bundle analysis was done using $f_x = 0.24\ Re_1^{0.21}$ with the perimeter-weighted, parallel resistance model for the equivalent friction factor.

*Numbers in parenthesis indicate non-experimental values obtained by extrapolation or interpolation of available experimental data.

flow fractions in the rough array than in the smooth. The analytical methods predicted interior-to-peripheral subchannel flow ratios which were higher in the smooth rod array and lower in the rough rod array than was experimentally observed. These differences may be explained by the neglection of interchannel coolant mixing in the analytical model.

1.3.2 Rod Array Axial Pressure Profiles

Axial profiles of the local static pressure were measured in the smooth and rough rod arrays. Profiles were taken in an interior and a peripheral subchannel for total bundle flows of 50 to 250 GPM. A typical axial pressure profile is illustrated in Figure 1.9; the linear decrease in static pressure is due to friction losses in the rod array. The three sharp decreases in pressure are due to losses at the spacer grids. From the slope of the friction pressure loss lines, it was possible to determine the friction factor; from the offset between parallel lines, it was possible to determine the grid loss coefficient, i.e., the pressure losses due to the presence of the grid in the rod array.

A detailed plot of the static pressure profile in the vicinity of a spacer grid is shown in Figure 1.10. The rapid decrease in static pressure was caused by flow

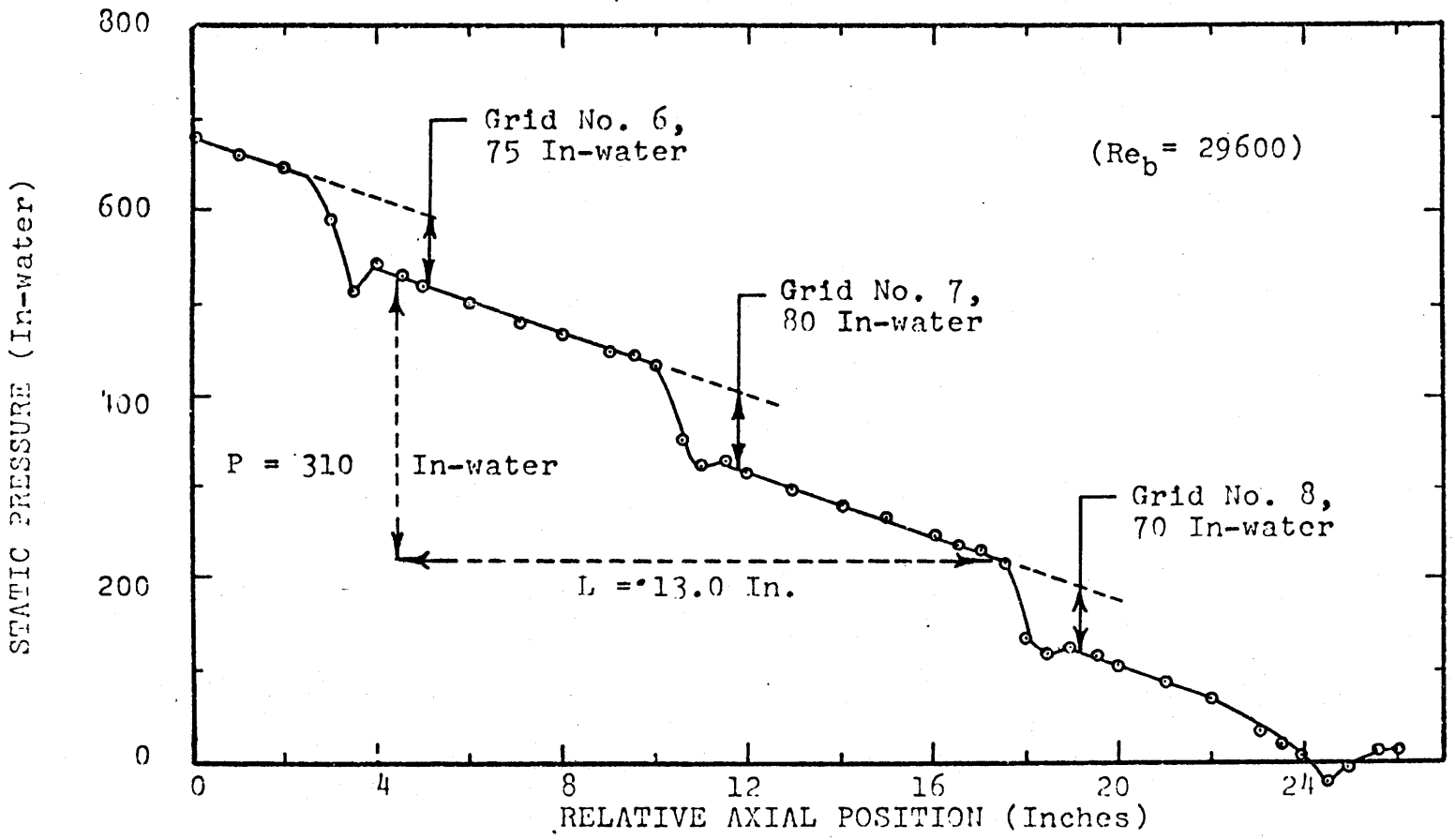

FIGURE 1.9

ROUGH ROD ARRAY, AXIAL PRESSURE PROFILE: INTERIOR SUBCHANNEL, 200 GPM

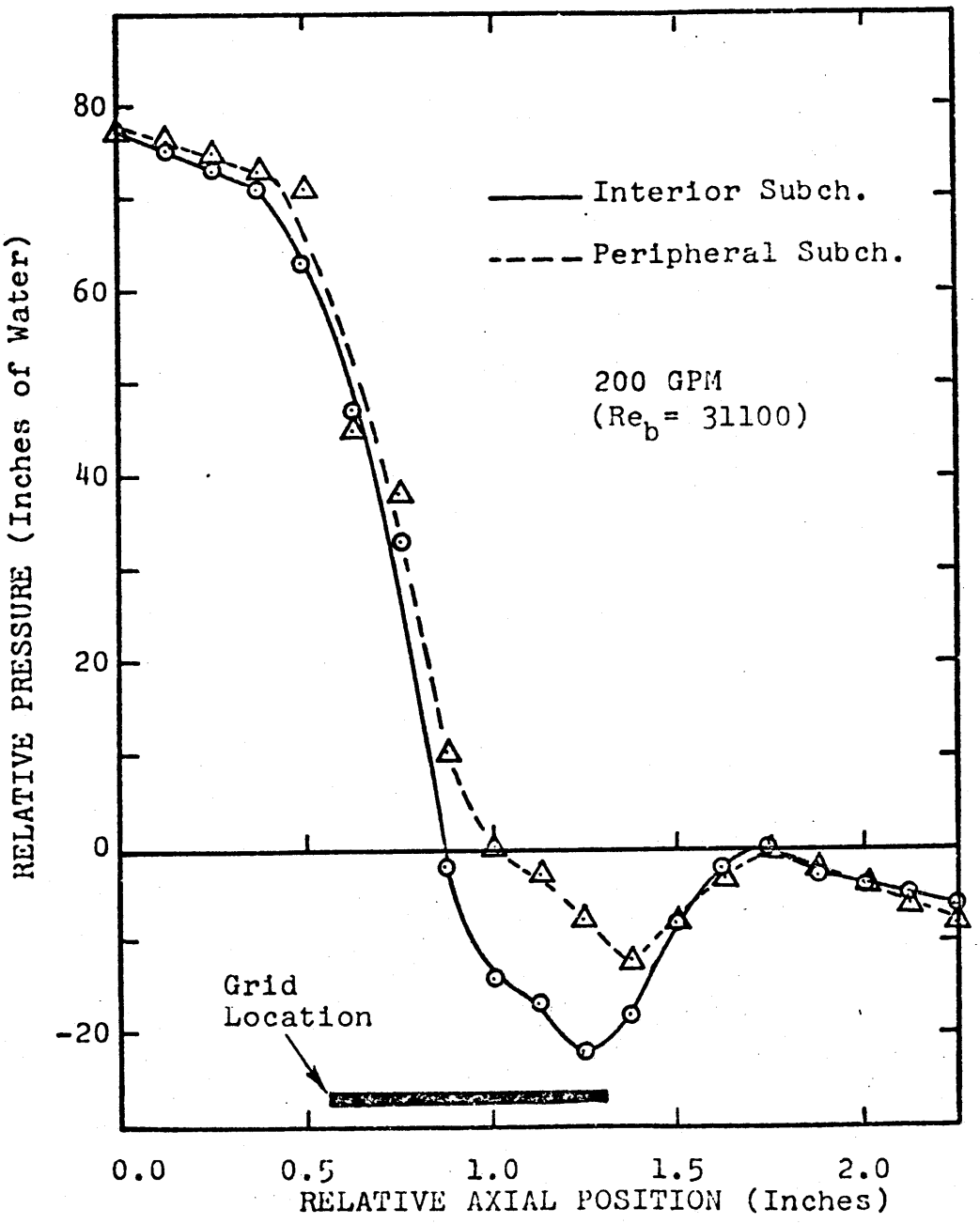

FIGURE 1.10

AXIAL PRESSURE PROFILE, SPACER NO. 8,
SMOOTH ROD ARRAY

acceleration (24% of the flow area was blocked by the grid), and entrance losses, as well as, increased friction losses within the grid. As the flow exited from the grid, part of the dynamic head was recovered during flow deceleration.

In the process of reducing the pressure profile data, it was necessary to specify the average velocity, as well as,the flow area of interest. The data was reduced using both experimentally determined and analytically calculated average velocities. Also, the data was considered as applying to both the subchannel in which it was measured and to the overall rod array.

1.3.3 Friction Factor Results

Using the pressure loss per unit length data from the static pressure profiles, the friction factor was determined from

$$f = \frac{\Delta P_f \, d_e}{L \, P_d} \qquad \text{(Eq. 1.5)}$$

The friction factors were compared with analytical predictions. The smooth surface friction factor was estimated by the Blasius equation:

$$f_s = 0.316 \, Re^{-0.25} \qquad \text{(Eq. 1.6)}$$

The roughened surface friction factor was estimeated using an equation developed from Moody chart [M1] data:

$$f_r = 0.076\ Re^{-0.04} \qquad \text{(Eq. 1.7)}$$

The equivalent friction factors in partially roughened flow passages were calculated using the perimeter-weighted parallel and average equivalent friction factor models.

The subchannel and rod bundle average friction factors determined using analytical flow data are shown in Figures 1.11 and 1.12, respectively. The friction factors for the subchannel types and the overall rod bundle which were determined using experimental flow data are shown in Figures 1.13 and 1.14, respectively.

The friction factor results agreed best with the predicted values at Reynolds numbers greater than 15,000. Because the experimental average velocities were higher than those calculated, the friction factors determined from measured velocities were lower than those determined from calculated velocities.

Typical experimental uncertainties have been illustrated with the results. Because the problem of determining the flow split was avoided by using bundle average velocity and hydraulic diameter, the most accurate experimental results were those for the bundle or rod array average flow data.

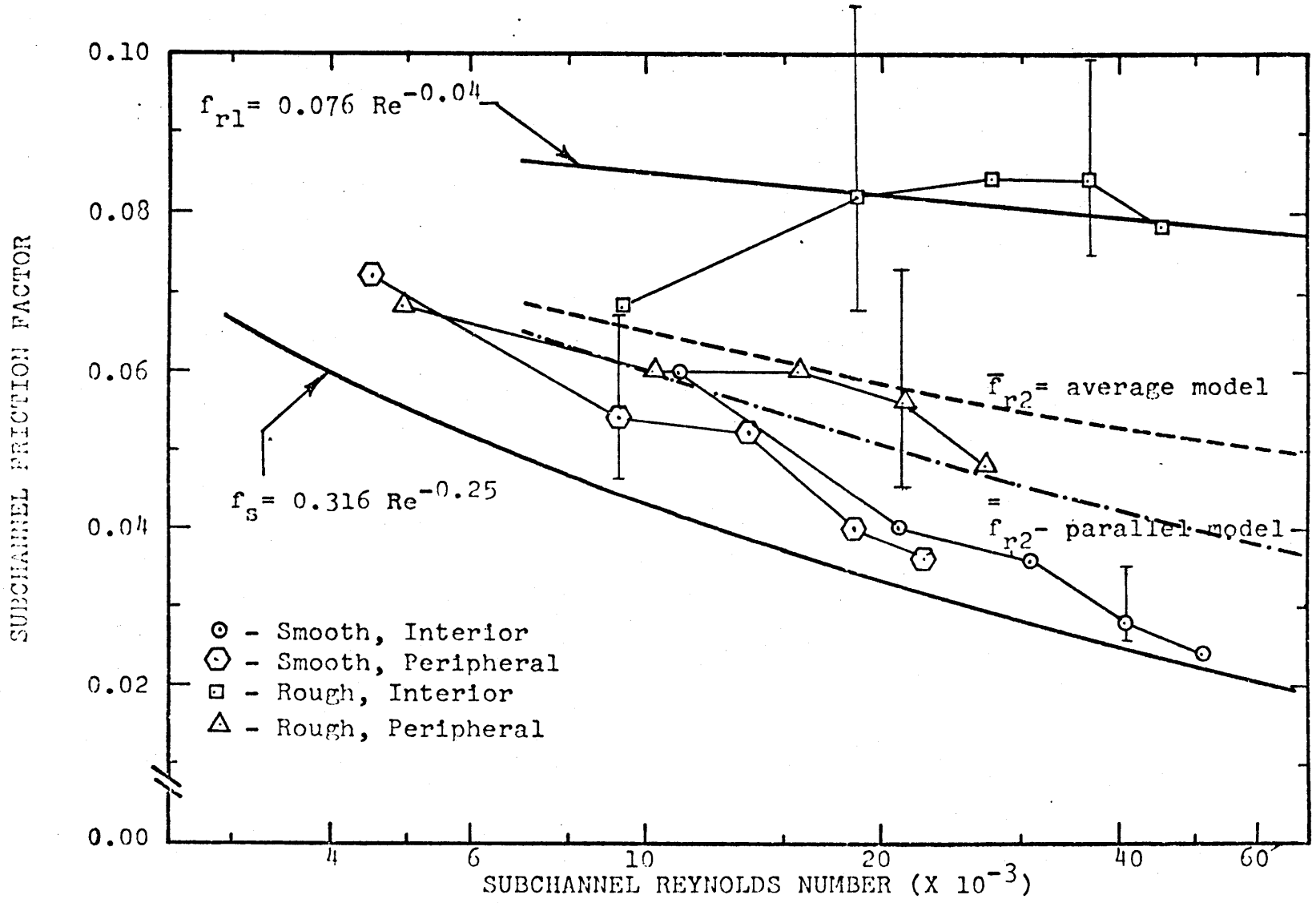

FIGURE 1.11

ANALYTICALLY DETERMINED SUBCHANNEL FRICTION FACTORS

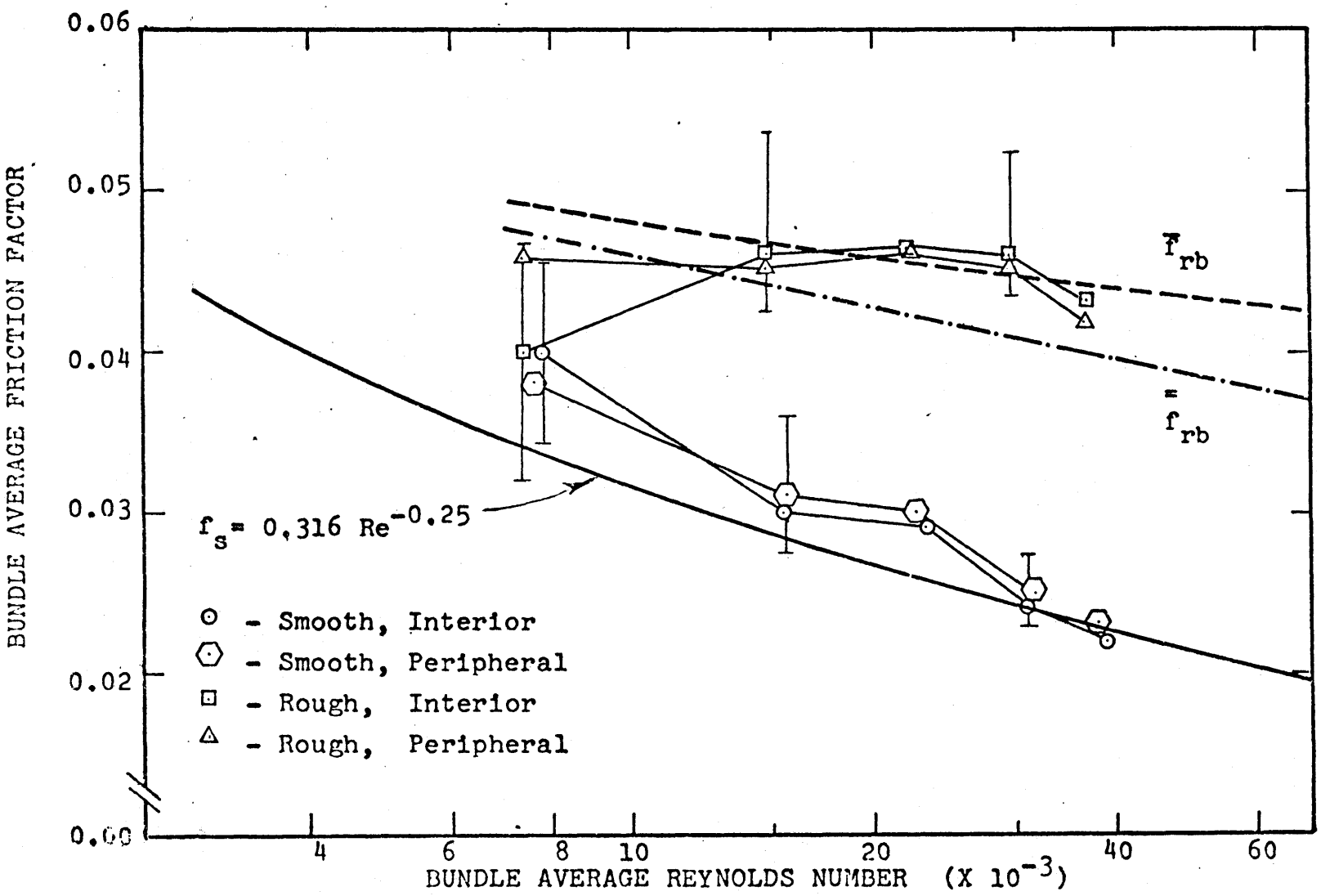

FIGURE 1.12

ANALYTICALLY DETERMINED ROD ARRAY FRICTION FACTORS

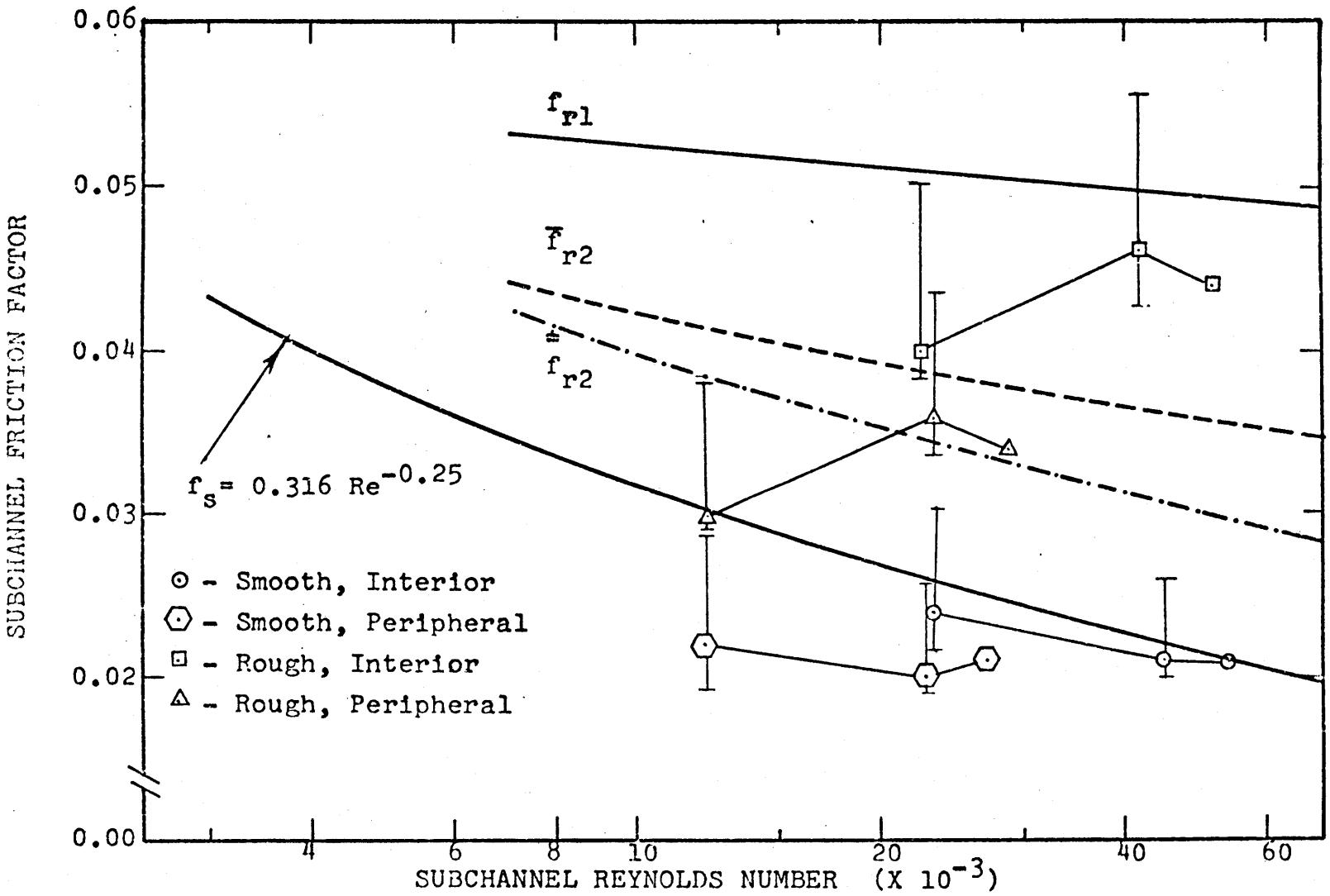

FIGURE 1.13

EXPERIMENTALLY DETERMINED SUBCHANNEL FRICTION FACTORS

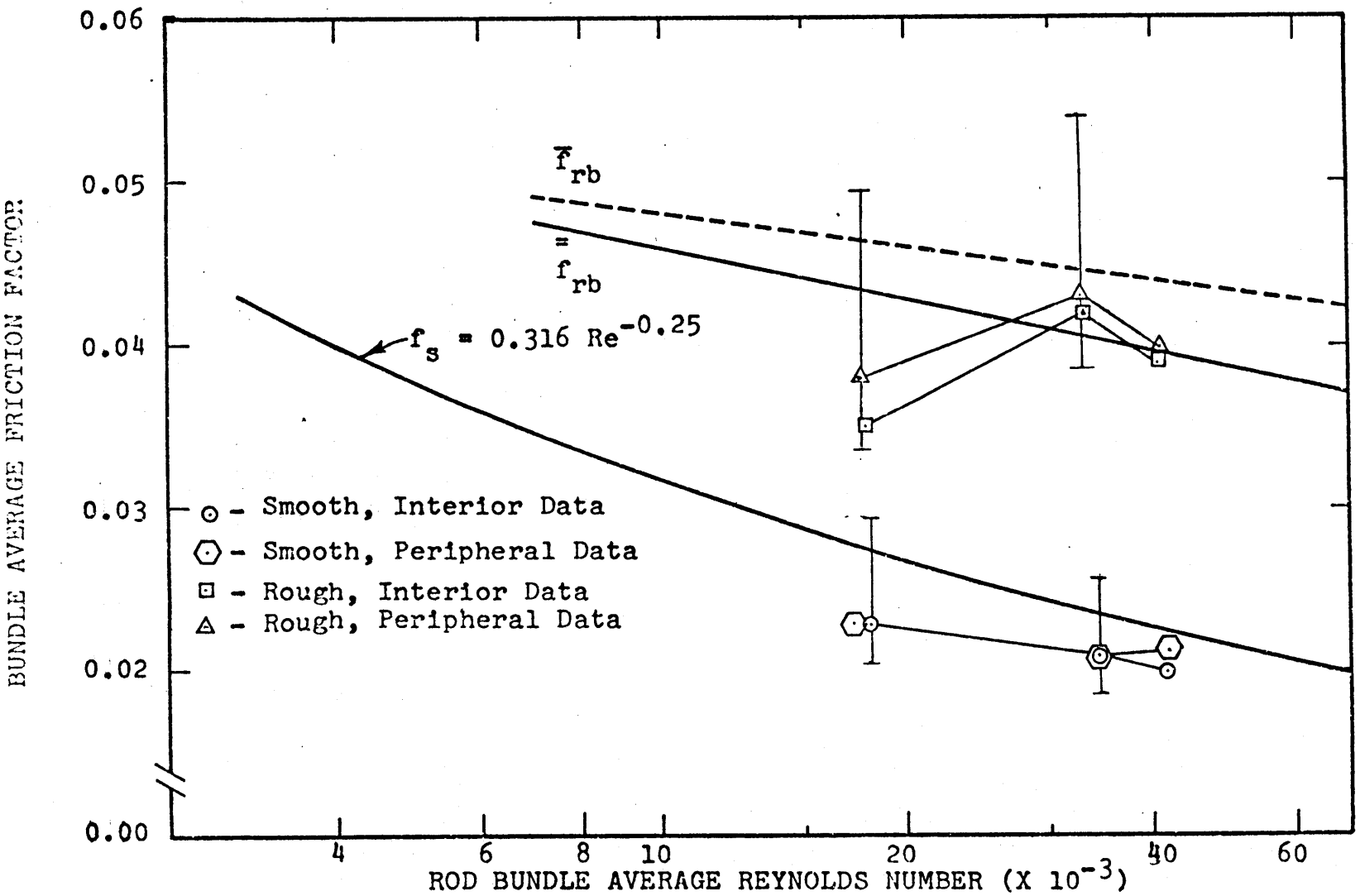

FIGURE 1.14

EXPERIMENTALLY DETERMINED ROD BUNDLE AVERAGE FRICTION FACTORS

1.3.4 Friction Factor Multiplier Results

By dividing the friction factor for a specified flow case and flow area in the rough rod array by the synomonous friction factor in the smooth array, the friction factor multiplier was determined. The results were compared with analytical predictions; for the friction factor multiplier in the Reynolds number range of interest, the following correlation was used:

$$f_x = 0.24\ Re^{0.21} \qquad \text{(Eq. 1.8)}$$

This equation was developed from data from the Moody chart [M1] for a relative roughness of 0.020. The equivalent friction factor multiplier in partially roughened flow passages was estimated using the perimeter-weighted parallel and average resistance models.

The friction factor multipliers determined using the calculated flow data are shown in Figure 1.15; those calculated using measured flow data are shown in Figure 1.16. Although the data follows the trend of the predicted multipliers, roughened surface flow development may have been occurring at Reynolds numbers below 15,000. A definite conclusion is not possible because of experimental uncertainties.

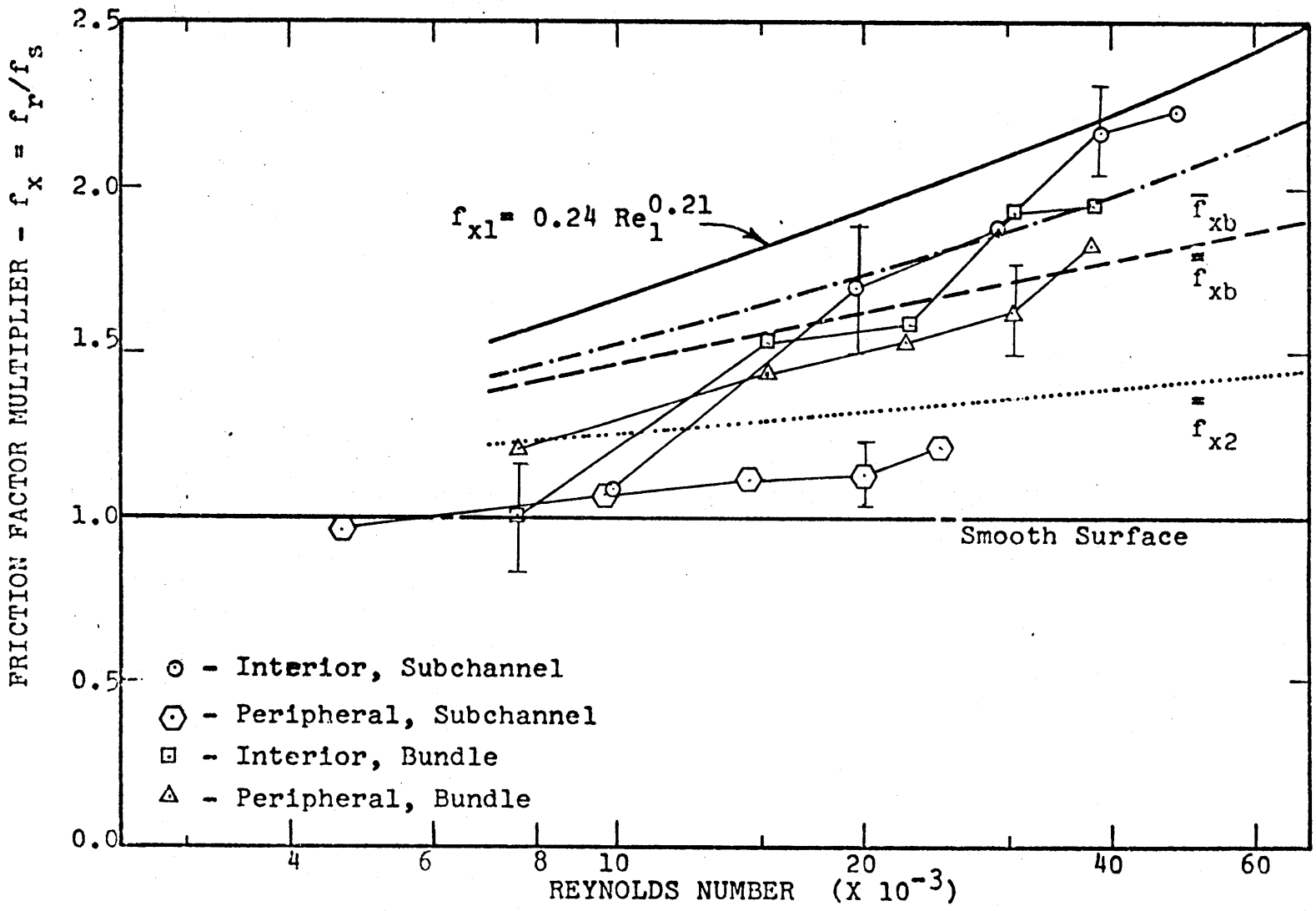

FIGURE 1.15

ANALYTICALLY DETERMINED SUBCHANNEL AND ROD BUNDLE FRICTION FACTOR MULTIPLIERS

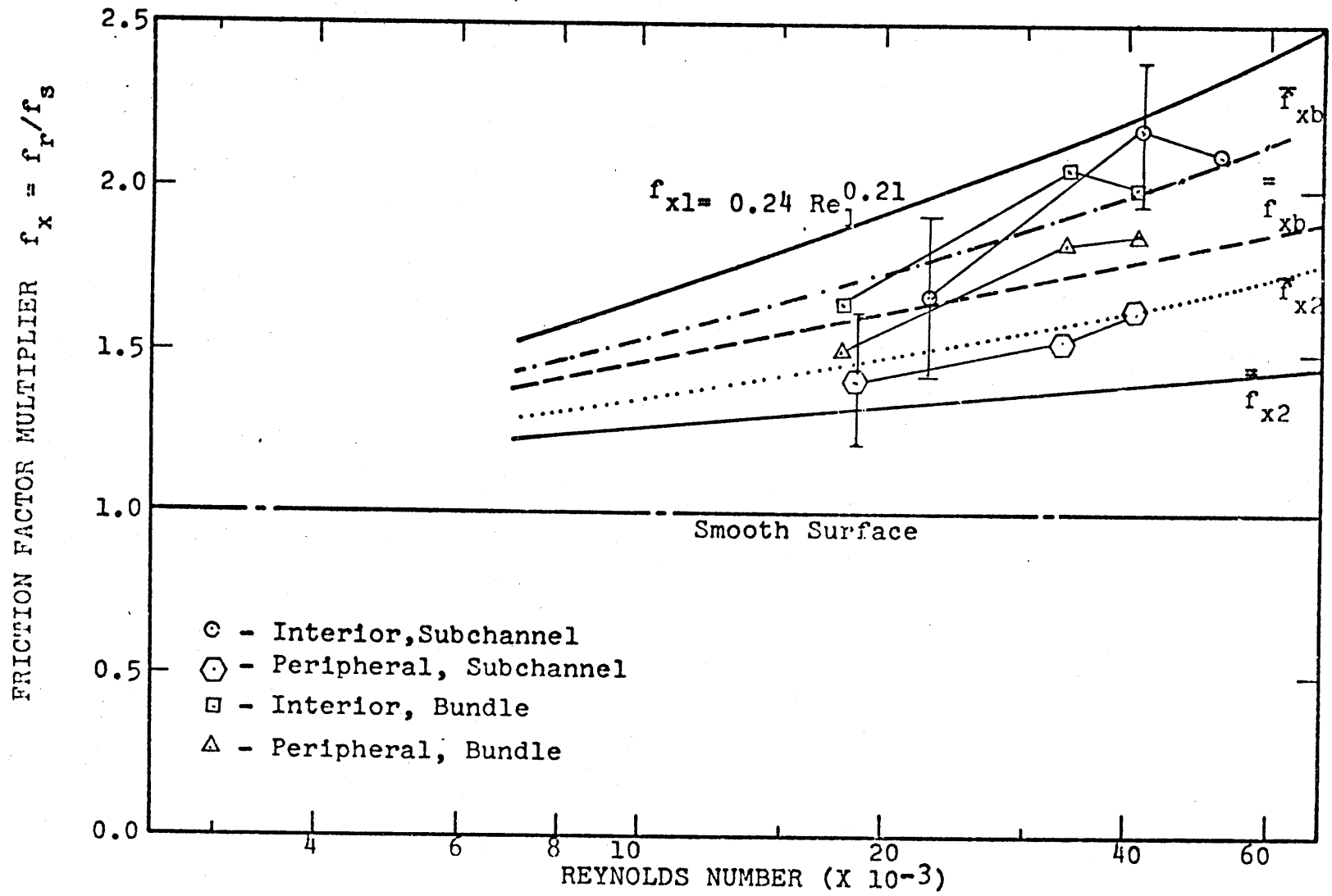

FIGURE 1.16- EXPERIMENTALLY DETERMINED SUBCHANNEL AND ROD BUNDLE FRICTION FACTOR MULTIPLIERS

1.3.5 Spacer Grid Loss Coefficients

Using the increase in pressure loss caused by the spacer grid, i.e., the distance between parallel lines in Figure 1.9, the spacer grid loss coefficients were determined from

$$\overline{K_{gi}} = \frac{\overline{\Delta P_g}}{P_{di}} = \frac{\overline{\Delta P_g}}{\frac{\rho \overline{V_i}^2}{2g_c}} \qquad \text{(Eq. 1.9)}$$

where the average velocity (dynamic head) is characteristic of either the measurement subchannel or the overall rod array and is determined either experimentially or analytically.

The average, subchannel and rod bundle spacer loss coefficients which were determined using calculated flow data are shown in Figures 1.17 and 1.18, respectively. The loss coefficients fall between two correlations for grid spacers, i.e., Buettiker [B1] and de Stordeur [S2]. Below Reynolds numbers of 20,000, the loss coefficients were notably larger than Buettiker's correlation. Although experimental uncertainties prevented a definite conclusion, the data indicated that the spacer loss coefficient was about 10% higher than in the smooth bundle.

The experimentally determined, average, subchannel and rod bundle spacer loss coefficients are shown in Figures 1.19 and 1.20, respectively.

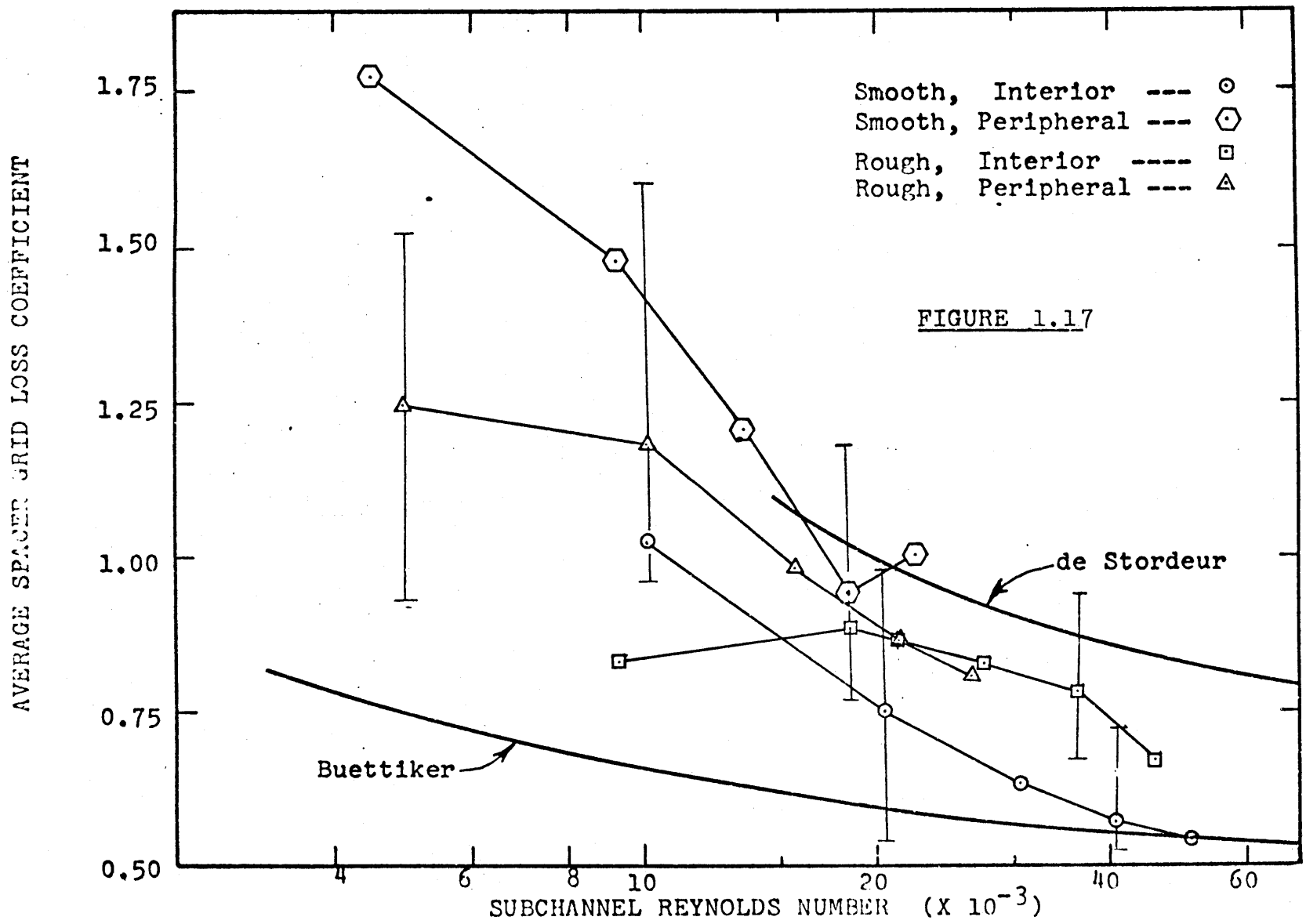

FIGURE 1.17

ANALYTICALLY DETERMINED SUBCHANNEL AVERAGE, SPACER GRID LOSS COEFFICIENTS

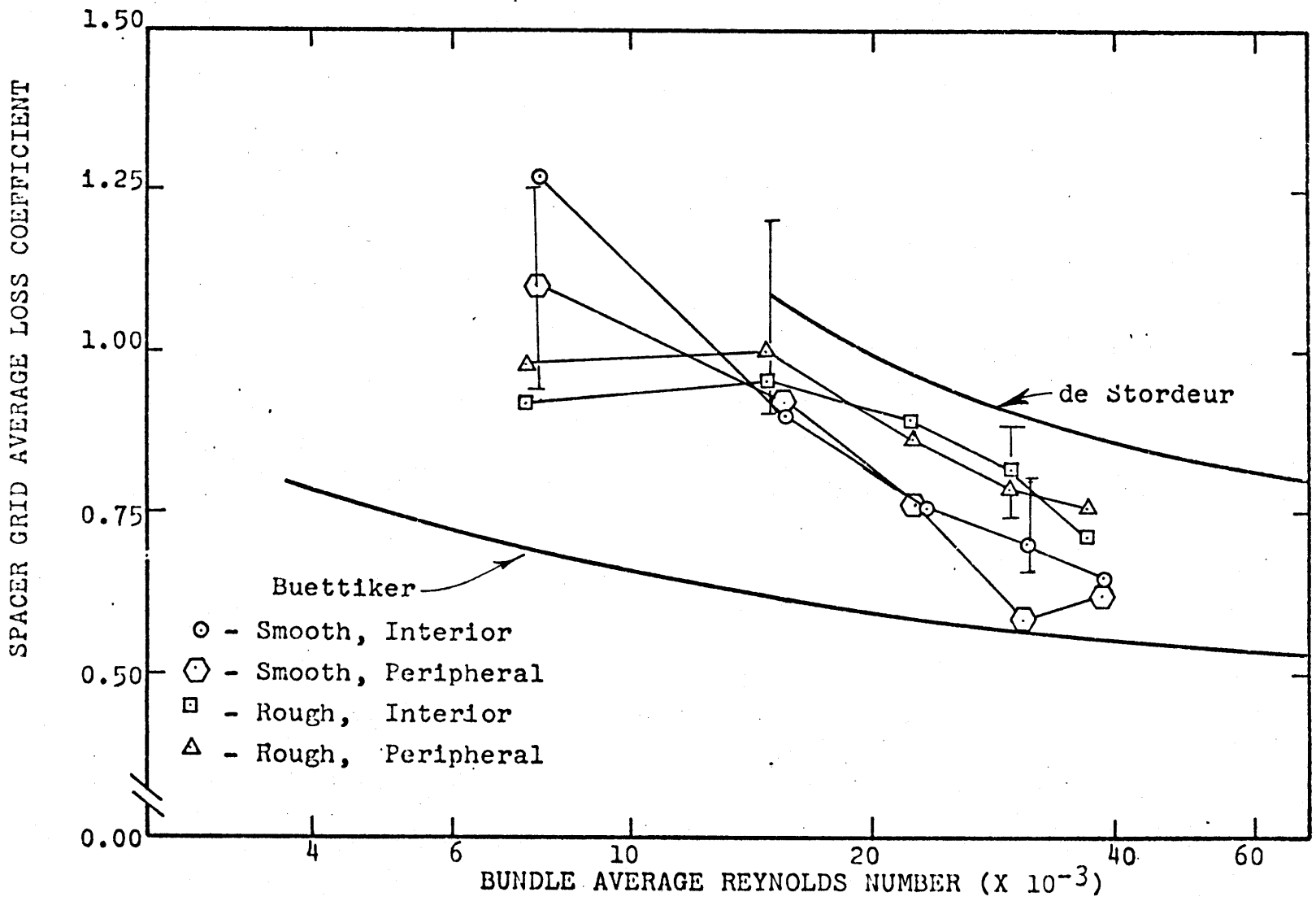

FIGURE 1.18

ANALYTICALLY DETERMINED ROD BUNDLE AVERAGE, SPACER GRID LOSS COEFFICIENTS

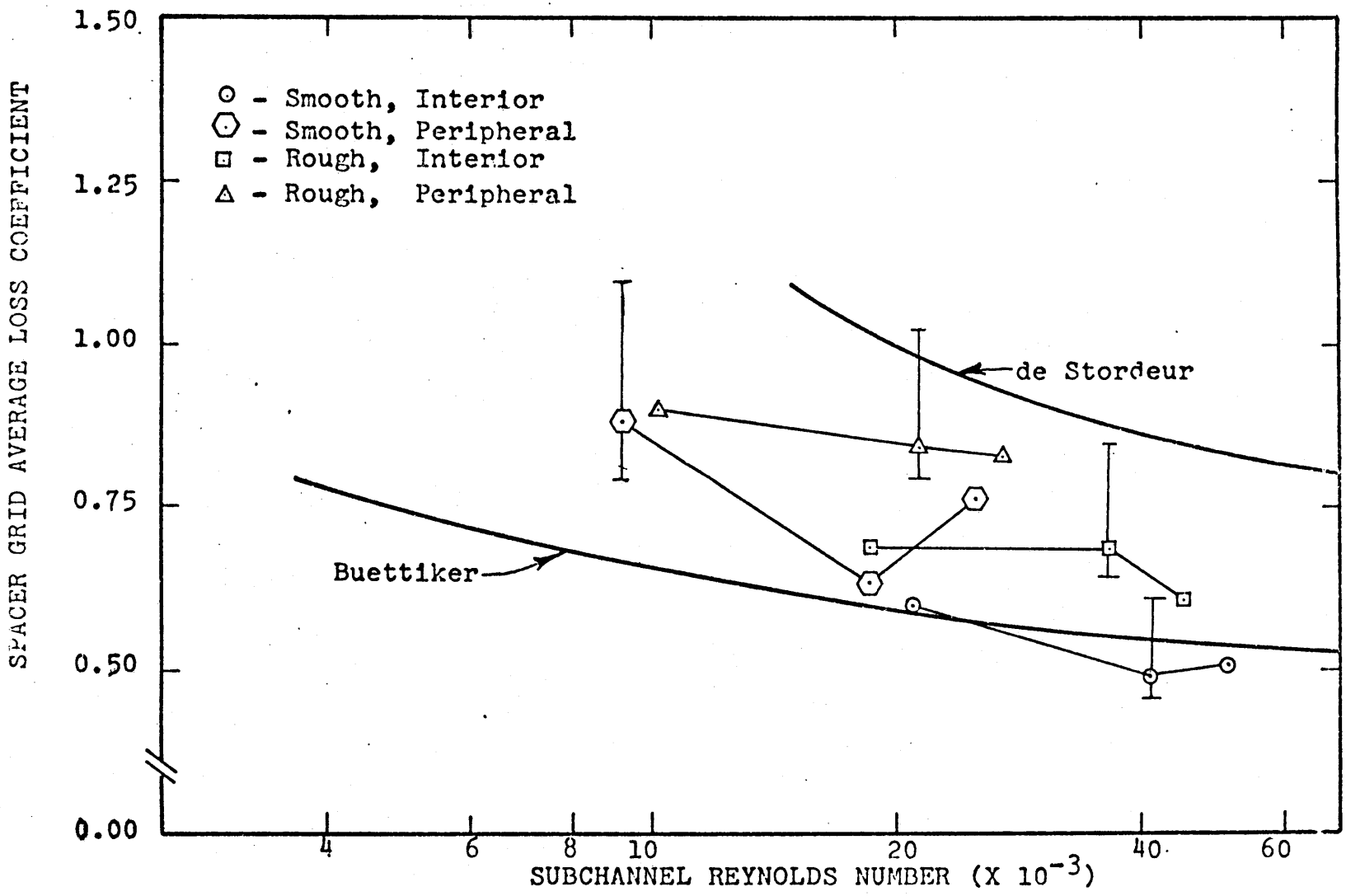

FIGURE 1.19

EXPERIMENTALLY DETERMINED AVERAGE, SUBCHANNEL SPACER GRID LOSS COEFFICIENTS

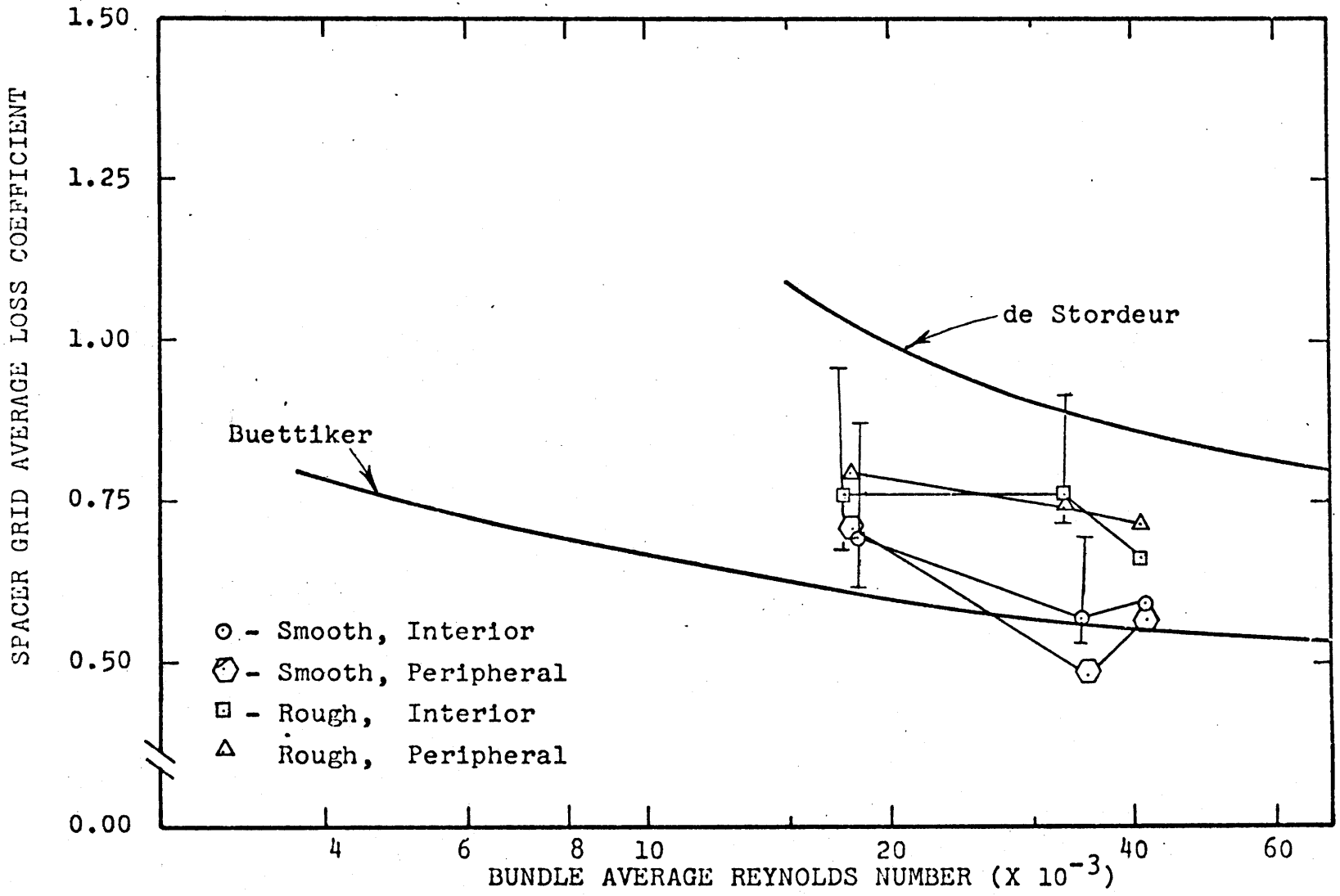

FIGURE 1.20

EXPERIMENTALLY DETERMINED ROD BUNDLE AVERAGE, SPACER GRID LOSS COEFFICIENT

1.3.6 Interchannel Coolant Mixing Results

In order to determine the coolant mixing behavior of both smooth and rough rod arrays, a salt solution tracer was injected into the flow of both an interior and a peripheral type subchannel; this tracer was than dispersed transversely by coolant mixing mechanisms, e.g., turbulent interchange and flow scattering (by spacer grids), as the flow axially traversed the test section.

A primary concern was that the tracer injection rate should equal the tracer detection rate. This tracer "mass balancing" showed that the tracer detection rate in the smooth rod array was only about 65% of that injected; in the rough array, the tracer detection rate was nearly equal to that injected. These balance results applied only at injector-detector separations greater than eight inches. In both smooth and rough cases, there was little tracer detection with the injection downstream of spacer grid no. 8.

The failure of the experimental data to meet the mass balance criterion was the result of inherent instrumentation design limitations; whenever the tracer injected was not uniformly mixed, the detectors could not properly measure the concentration of tracer.

Typical tracer dispersion patterns in the smooth rod array with interior subchannel injection and 200 GPM main

main flow are shown in Figures 1.21 through 1.23. Only subchannels with significant tracer concentrations were shown. In all cases, the majority of the tracer was diverted from the injection subchannel no. 1) to a contiguous subchannel (no. 2) by flow scattering at grid no. 8.

Typical results of tracer dispersion in the rough rod array are shown in Figures 1.24 through 1.26 for the case of interior subchannel injection and 200 GPM main flow. Details of the tracer dispersion in the vicinity of spacer grid no. 6 for interior injection and 100 GPM flow are shown in Figures 1.27 through 1.29. Although the grids introduce a strong perturbation into the tracer dispersion in the vicinity of the grid, the perturbations are damped out within three inches of the grids (about 12 hydraulic diameters).

Typical results of tracer dispersion in the rough rod array are shown in Figures 1.30 through 1.32 for the case of peripheral subchannel injection with a main flow of 150 GPM.

In all of the tracer mixing results, tracer dispersion was strongly influenced by flow scattering at the grid spacers; this was particularly true in the smooth rod array where turbulent interchange mixing was less than in the rough array. That the turbulent interchange mixing was higher in the rough array than in the smooth was

FIGURE 1.21

CASE SI-5: MASS BALANCE VERSUS INJECTOR TRAVEL

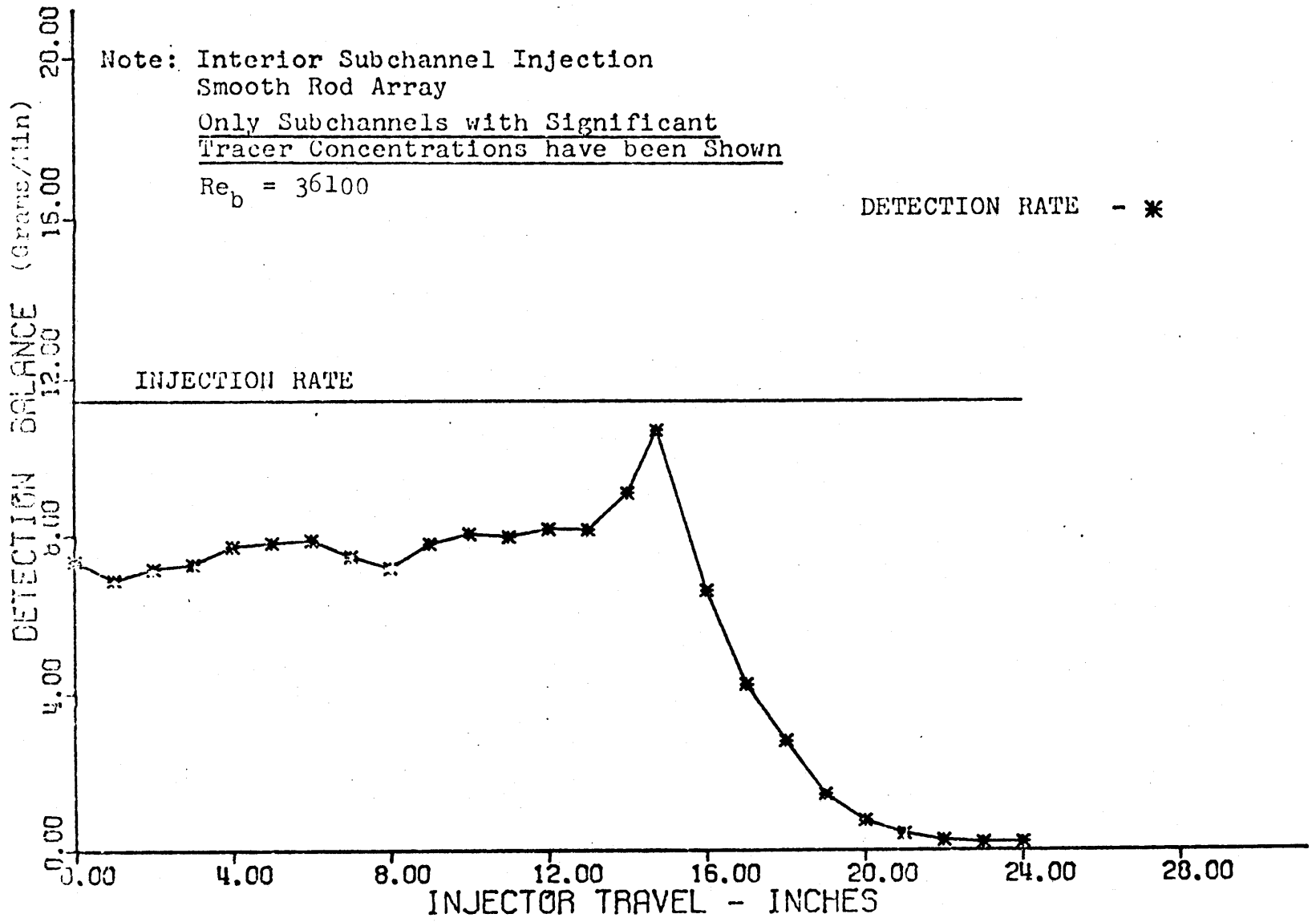

FIGURE 1.22

CASE SI-5: AXIAL TRACER CONCENTRATRATION, SUBCHANNELS 2, 1, 3, 4

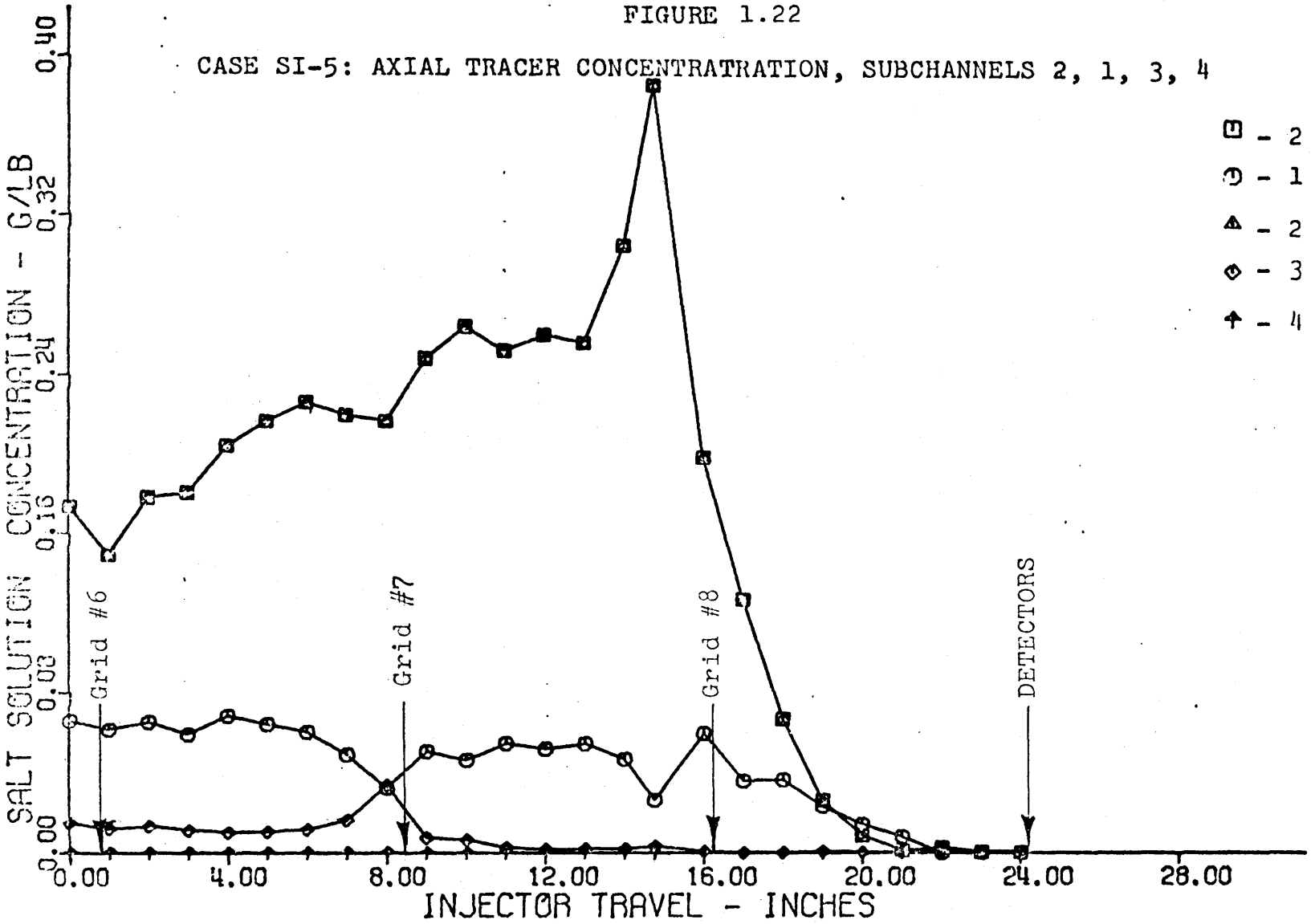

FIGURE 1.23

CASE SI-5: AXIAL TRACER CONCENTRATIONS, SUBCHANNELS 2, 5, 6, 7, 8

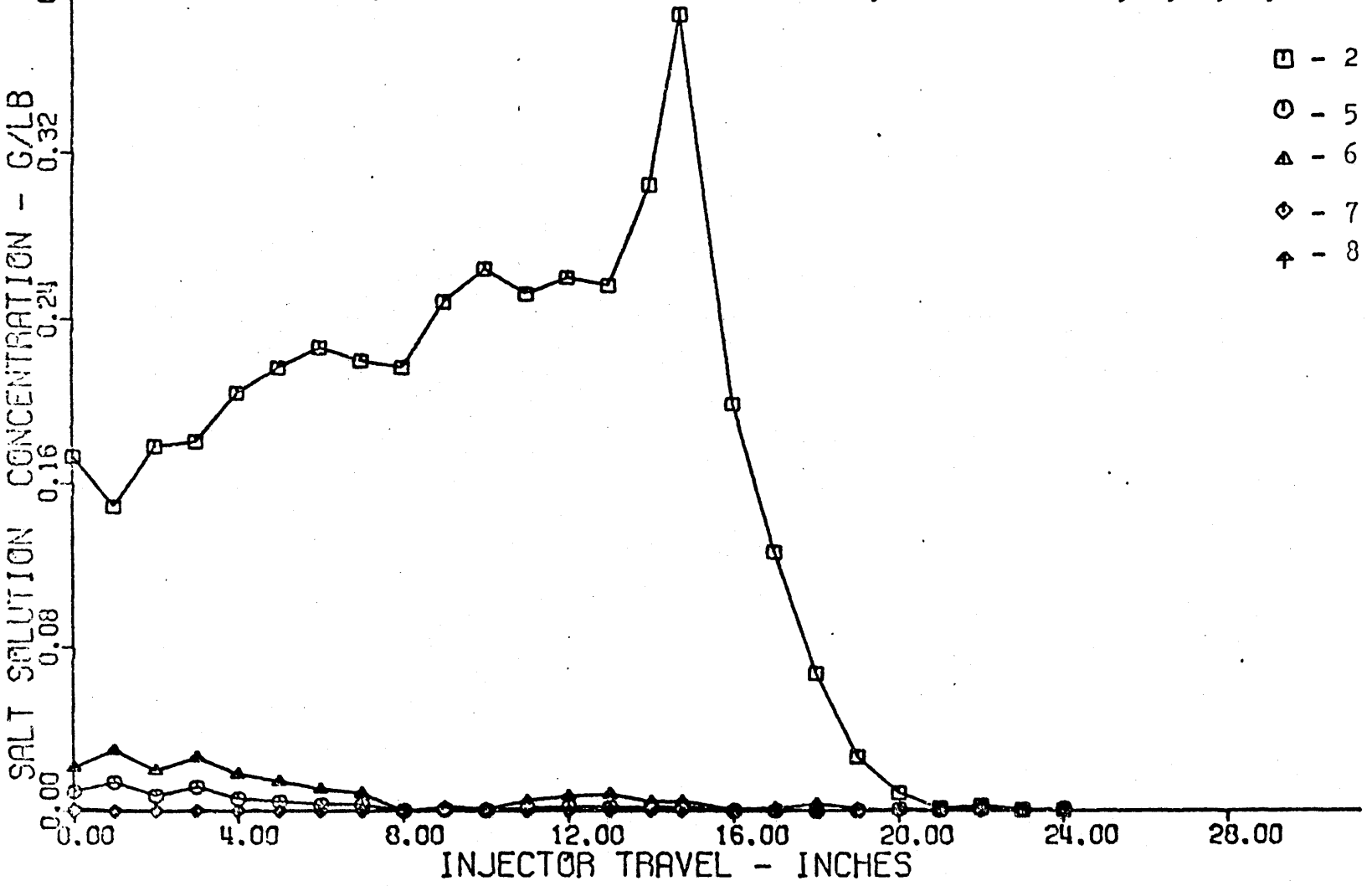

FIGURE 1.24

CASE RI-5: MASS BALANCE VERSUS INJECTOR TRAVEL

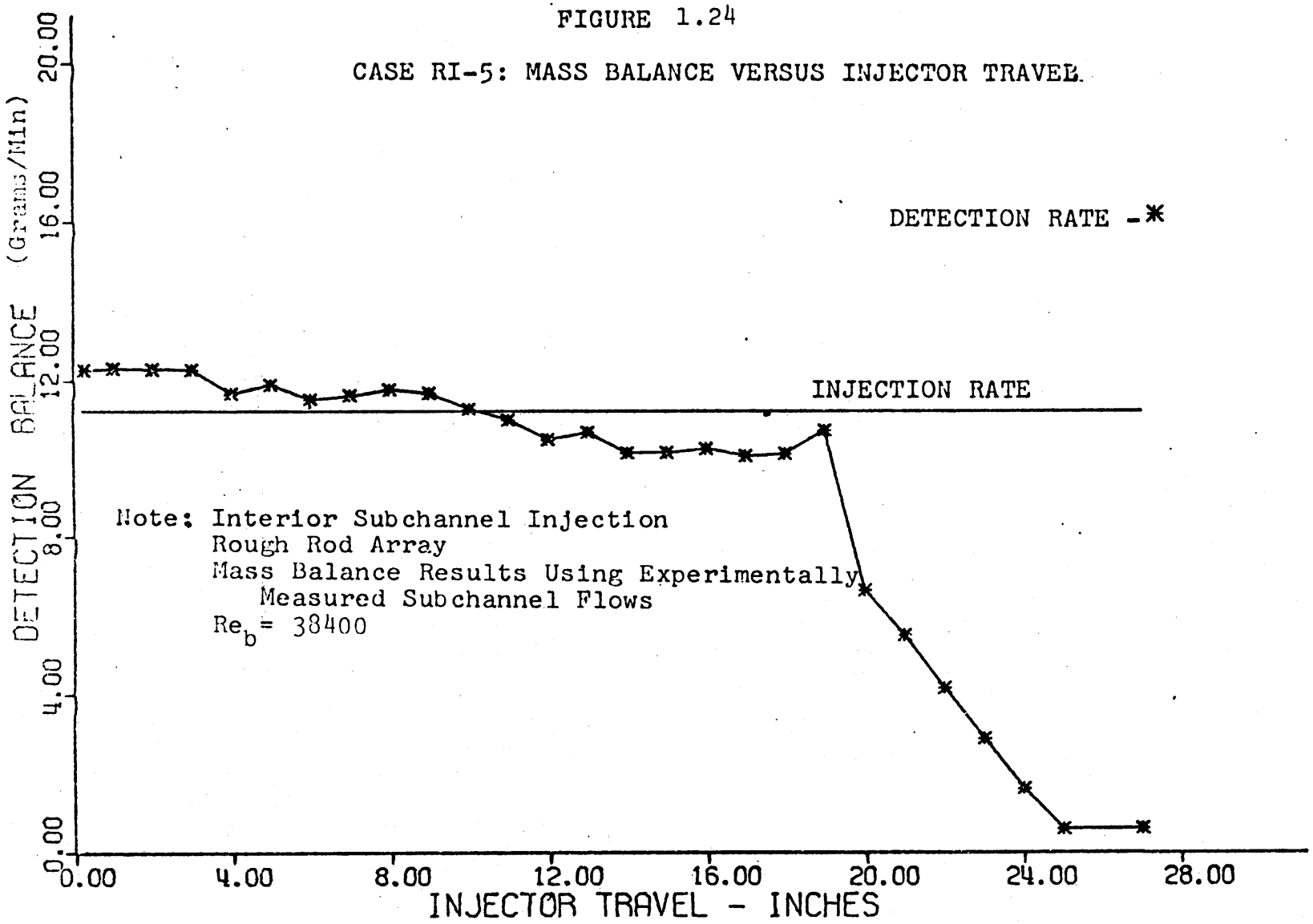

FIGURE 1.25

CASE RI-5: AXIAL TRACER CONCENTRATION, SUBCHANNELS 2, 1, 3, 4

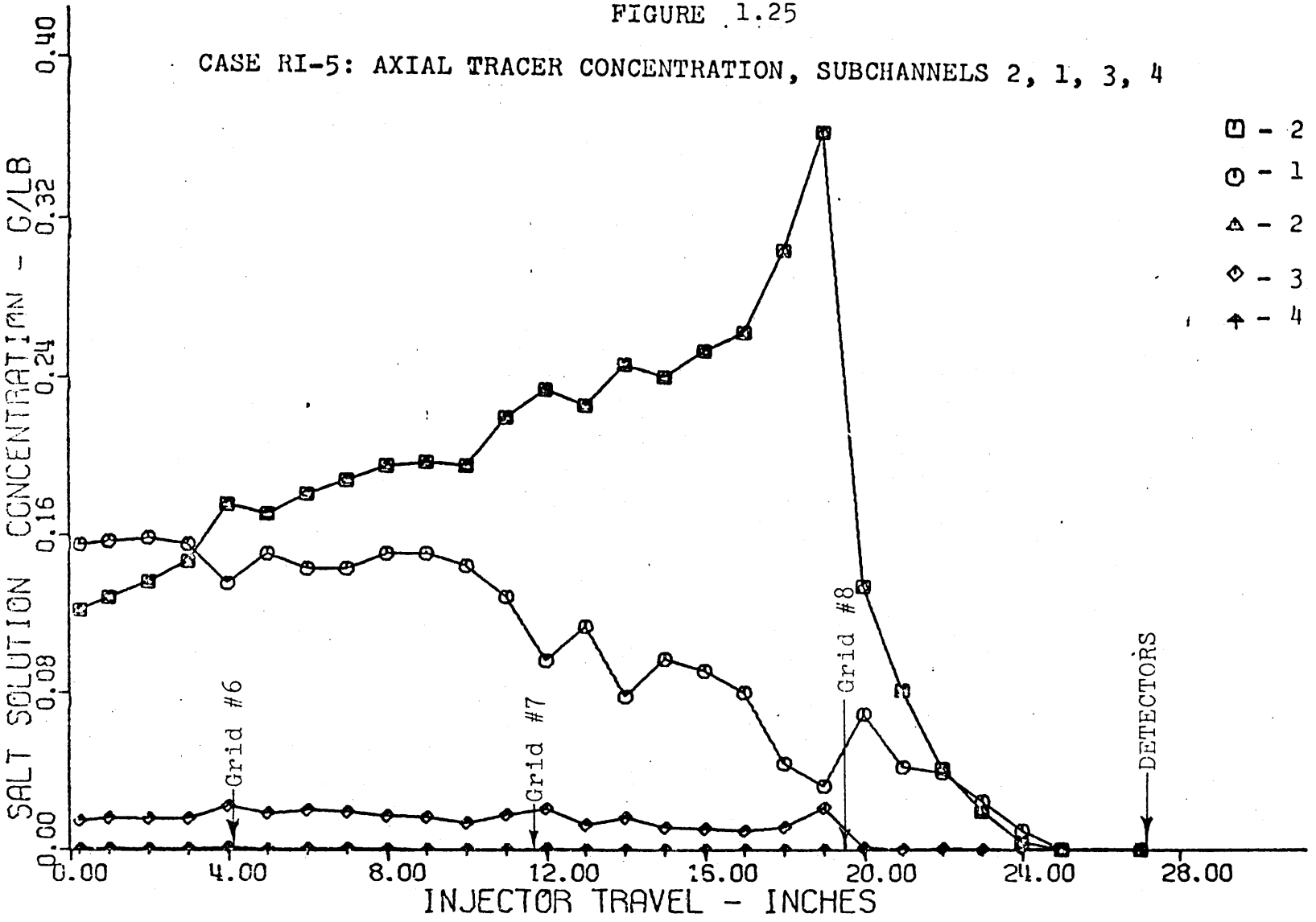

FIGURE 1.26

CASE RI-5: AXIAL TRACER CONCENTRATIONS, SUBCHANNELS 2, 5, 6, 7, 8

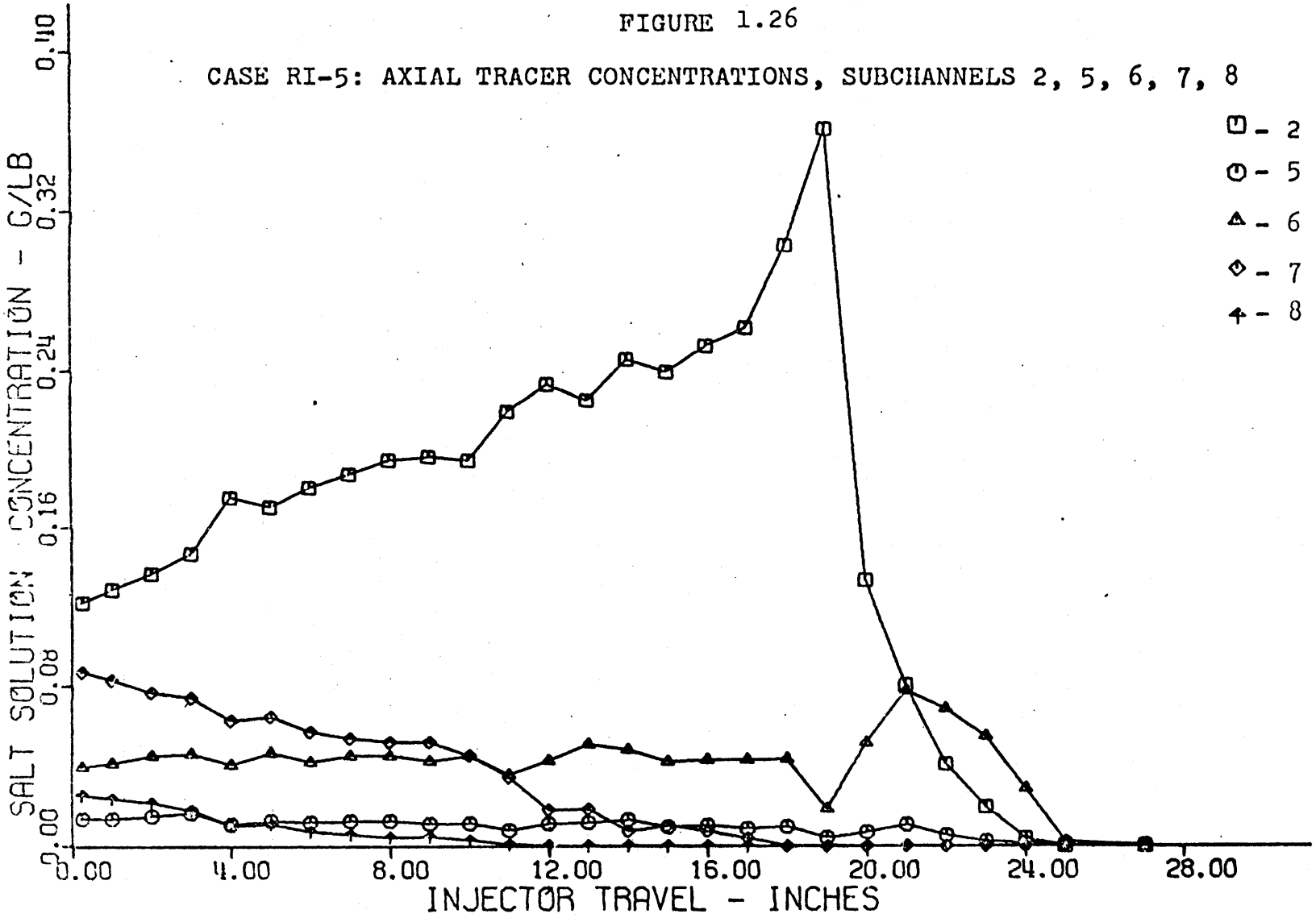

FIGURE 1.27

CASE RI-7: MASS BALANCE VERSUS INJECTOR TRAVEL

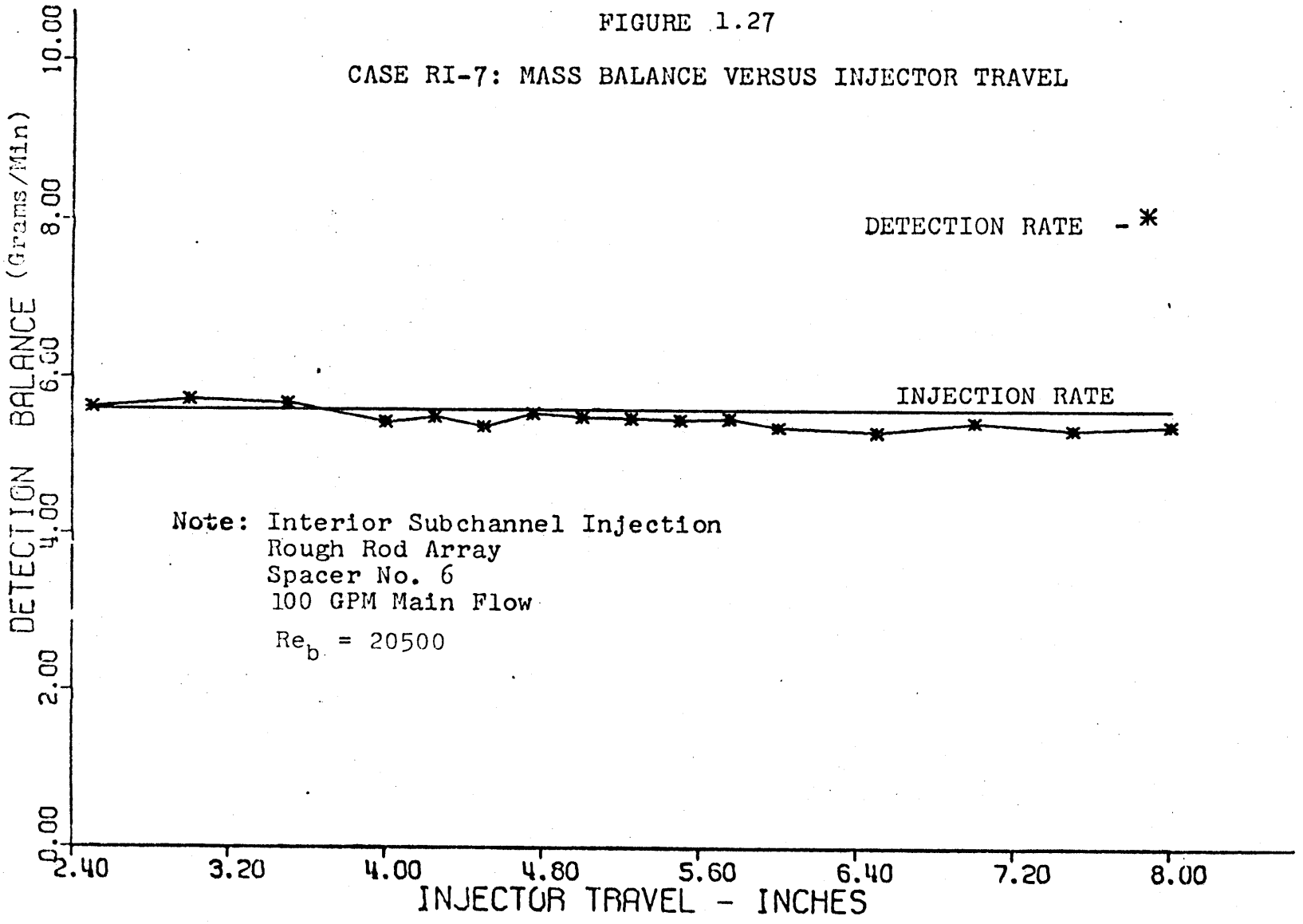

FIGURE 1.28

CASE RI-7: AXIAL TRACER CONCENTRATION, SUBCHANNELS 2, 1, 3, 4

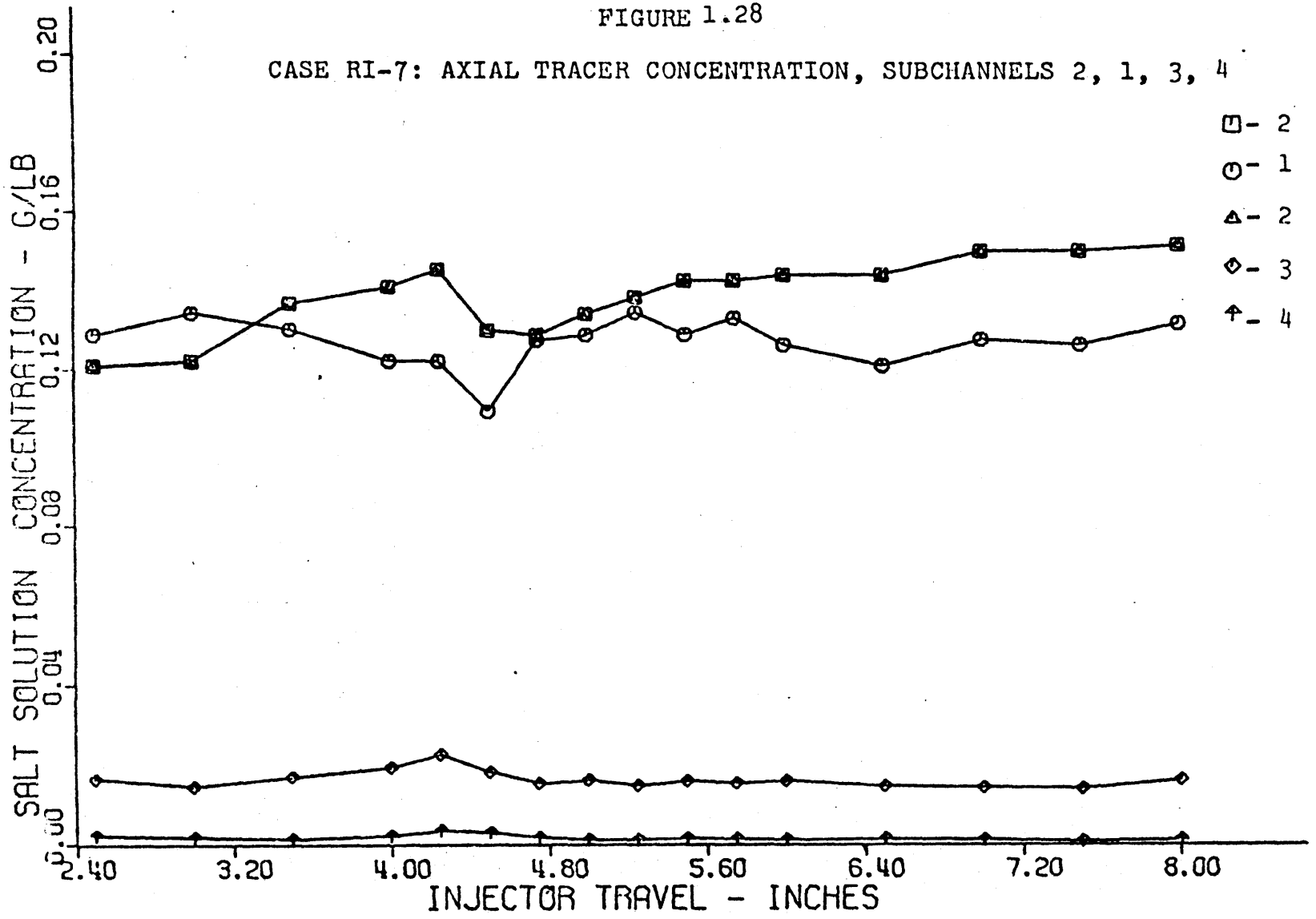

FIGURE 1.29

CASE RI-7: AXIAL TRACER CONCENTRATIONS: SUBCHANNELS 2, 5, 6, 7, 8

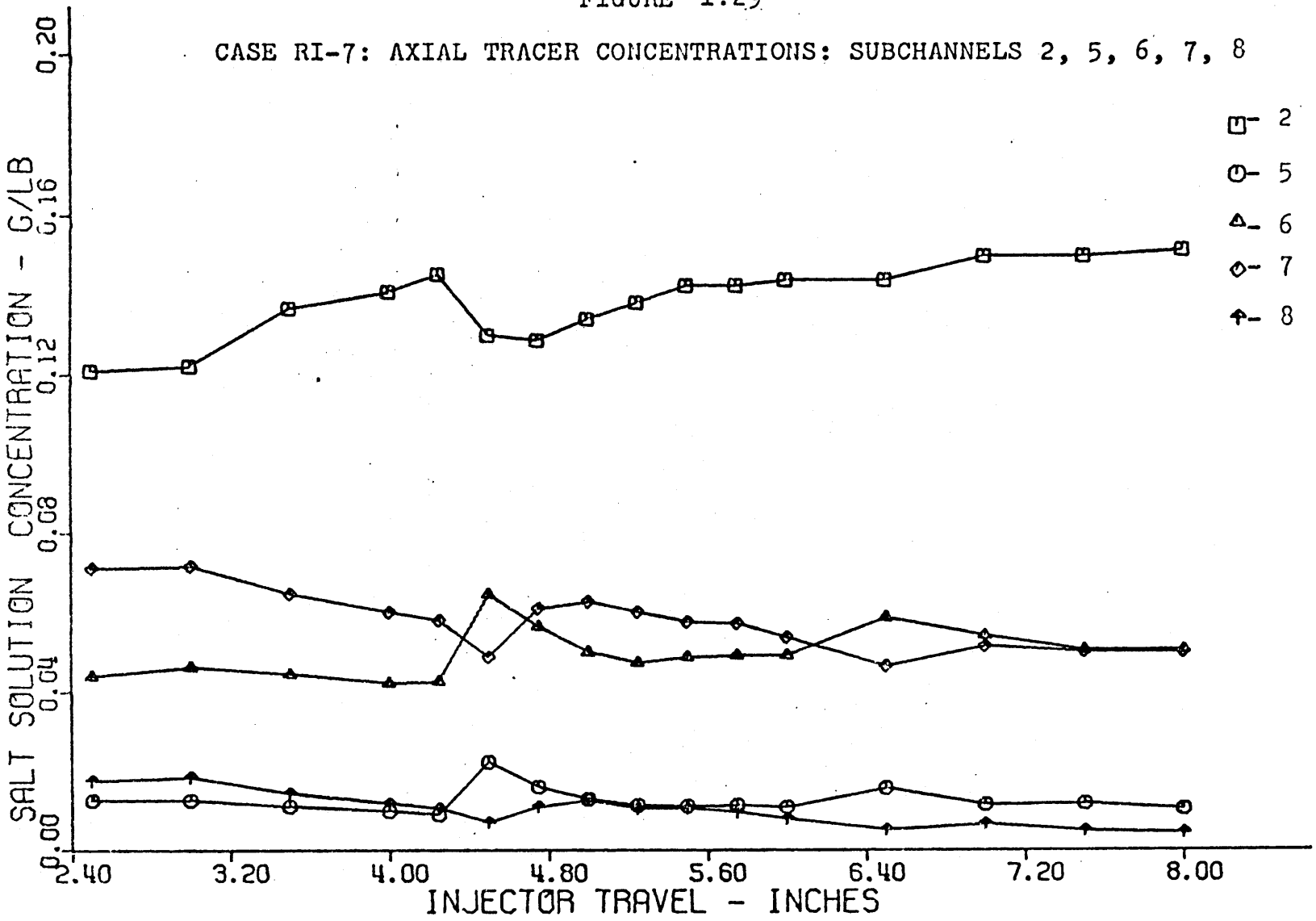

FIGURE 1.30

CASE RP-4: MASS BALANCE VERSUS INJECTOR TRAVEL

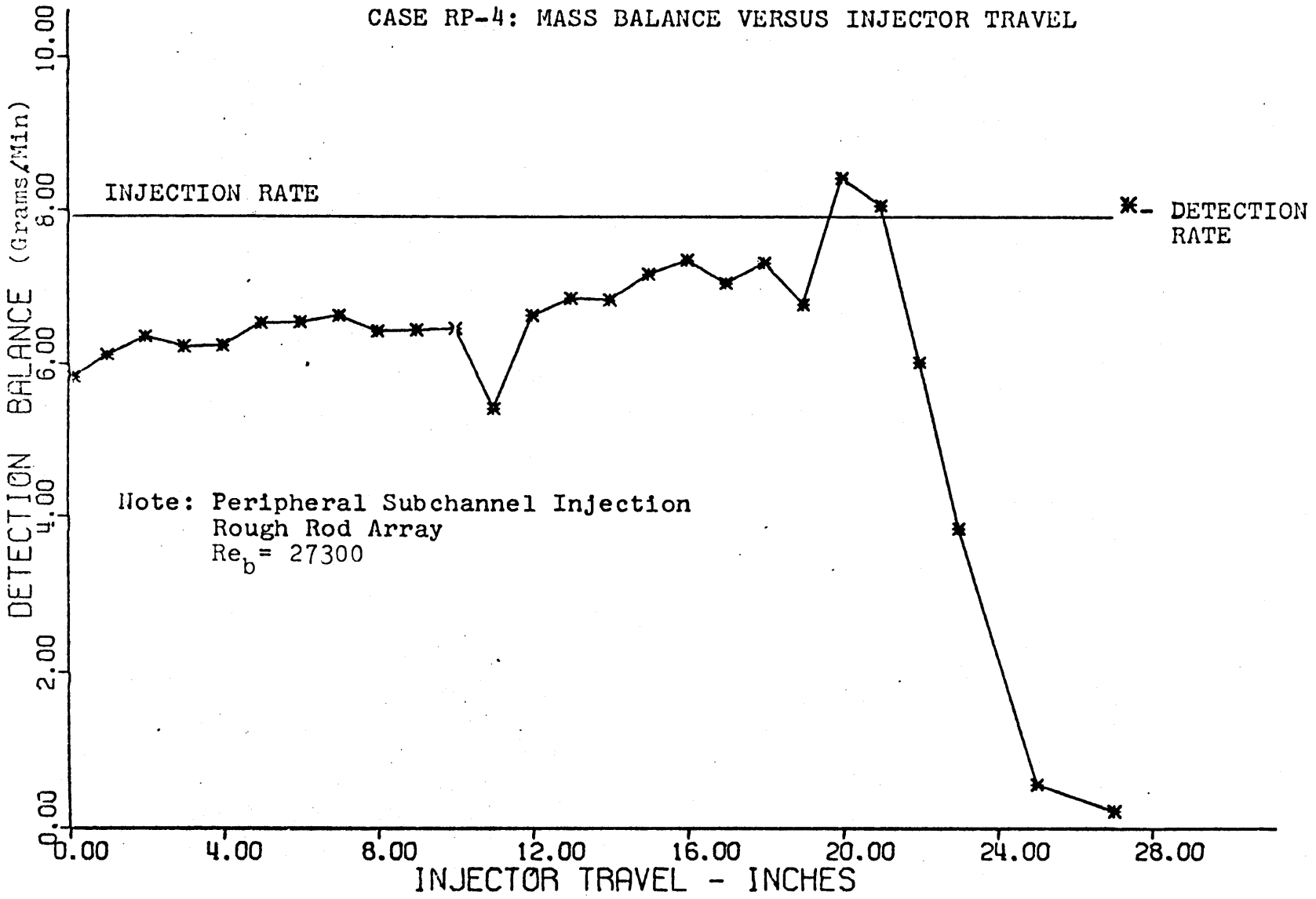

FIGURE 1.31

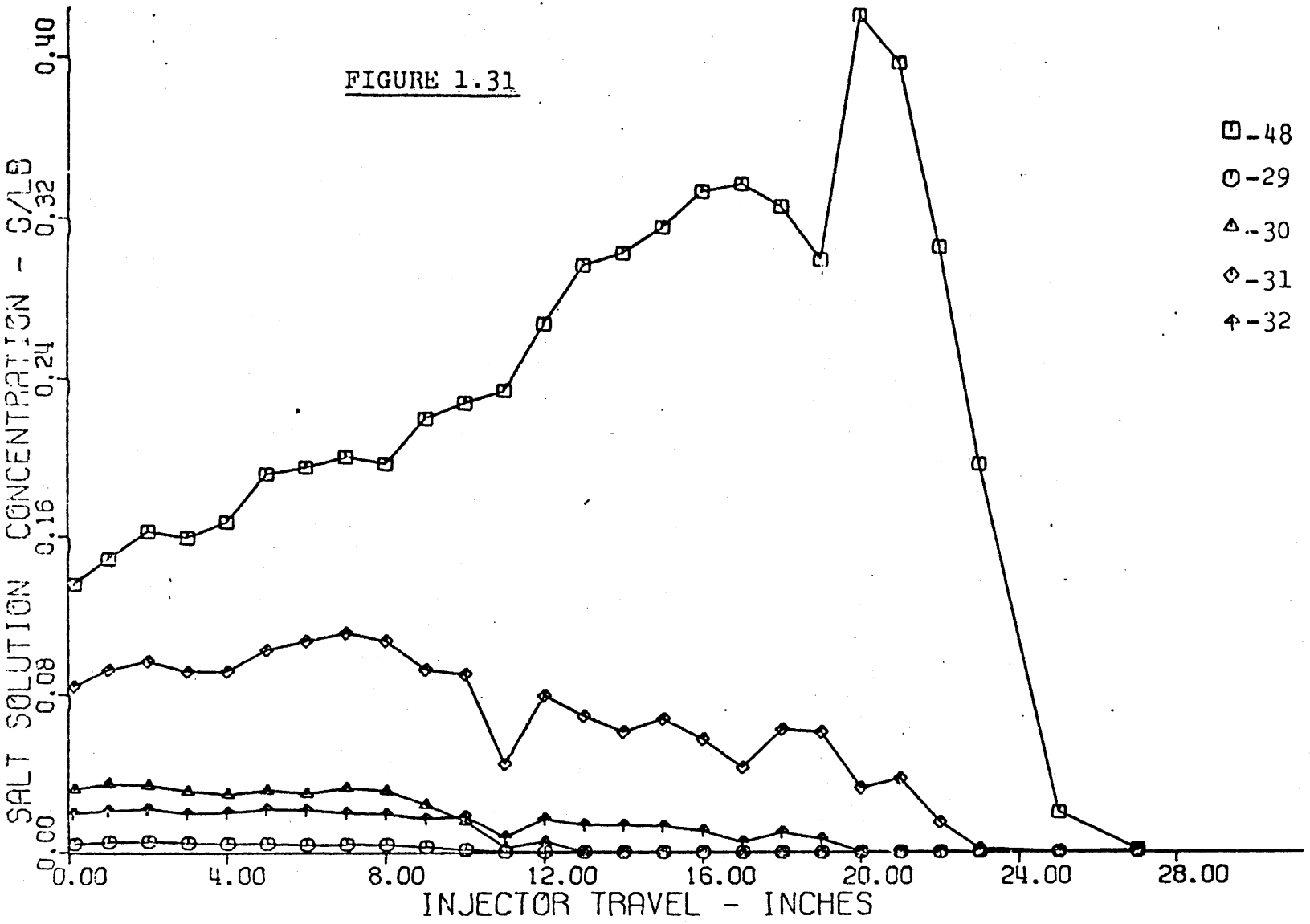

CASE RP-4: AXIAL TRACER CONCENTRATION, SUBCHANNELS 48, 29, 30, 31, 32.

FIGURE 1.32

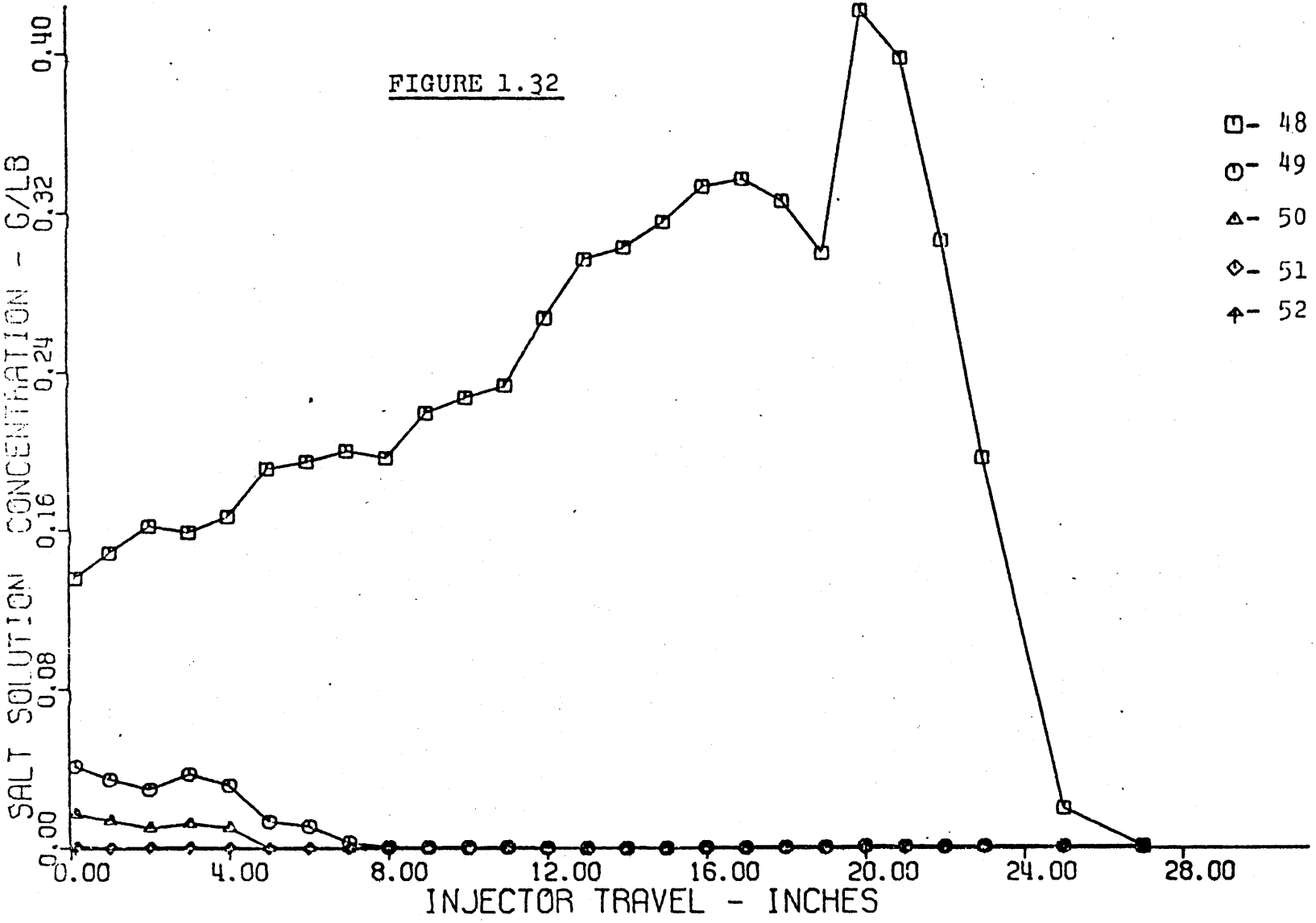

CASE RP-4: AXIAL TRACER CONCENTRATION, SUBCHANNELS 48, 49, 50, 51, 52.

evidenced by the observations that the tracer was more widely dispersed transversely in the rough array and that the tracer detection rates were in better agreement with the injection rates.

1.3.7 Quantitative Assessment of the Dimensionless Mixing Coefficient

In order to quantitatively assess the coolant mixing coefficient in the grid spaced rod array using the salt tracer data, it was necessary to have a long distance of tracer dispersion unperturbed by grid scattering and well removed from the region of the detectors. In the smooth rod array, the turbulent interchange mixing was so low that it was impossible to quantitize the mixing coefficient using the axial tracer dispersion patterns. This was because the flow scattering at the grids dominated the tracer dispersion and the tracer was not well mixed within the array.

Because the turbulent interchange mixing in the rough rod array was considerably higher than in the smooth array, it was possible to estimate the turbulent mixing coefficient in the grid spaced, rough rod array to be 0.020 ± 0.005. The error in this coefficient was large because flow scattering effects at the spacer grids was significant. Grid flow scattering also prevented the resolution of the effects of subchannel type (geometry) and Reynolds number on the mixing coefficient.

Chapter II

THE THERMAL-HYDRAULICS OF GAS-COOLED FAST BREEDER REACTOR FUEL ELEMENTS

2.1 Introduction

The Gas-Cooled Fast Breeder Reactor (GCFR) is being developed as an alternative to the Liquid Metal-Cooled Fast Breeder Reactor (LMFBR). For further information on the merits of the alternative designs the reader is referred to various review articles, e.g., references [D1], [E4]. The research work at hand is concerned with investigating various aspects of the thermal-hydraulic behavior of gas-cooled, roughened, rod array-type, nuclear fuel elements typical of the present GCFR design.

This report deals principally with the development of a thermal-hydraulic analysis method for roughened, gas-cooled nuclear fuel elements and with comparative hydraulic experiments on smooth and rough rod arrays. The thermal-hydraulic analysis is discussed in detail in Chapter 3; a simplified method is used to determine the flow in various subchannel types. Chapter 4 gives a description of the experimental program and facilities while the experimental results are given in Chapter 5. The comparative hydraulic

experiments include rod array and spacer grid axial pressure profiles, rod array outlet velocity profiles, and inter-channel coolant mixing data. Finally, in Chapter 6, recommendations are made for future work along with recommendations for the design of the GCFR fuel element.

The balance of this chapter will be used to discuss the GCFR fuel element design, to introduce the thermal-hydrualic behavior of roughened, gas-cooled fuel elements, to briefly review the literature concerning roughened surfaces, and to compare grid spacers with twisted-tape spacers.

2.1.1 A General Description of the GCFR Fuel Element

The present GCFR fuel element design consists of a hexagonal assembly of 271 fuel rods arranged in a triangular lattice array and enclosed in a hexagonal duct. The fuel rod diameter is 0.285 inches (7.24 mm), the rod-to-rod pitch is 0.389 inches (9.88 mm), and the rod-to-wall gap is 0.050 inches-nominal (1.27 mm). Grid spacers located every 10 inches (25.4 cm) (typical) are used to maintain rod array geometry. The coolant is helium pressurized to 1290 psia-nominal (89 bar). The active core is 39.55 inches in length (101 cm) with surface roughening over the upstream 75% of the core axial length

to improve forced convection heat transfer. Figure 3.1 shows the two types of GCFR fuel elements and identifies the four subchannel types used in thermal-hydraulic analysis. A cross section of the roughened surface rib design is shown in Figure 4.3. Details of the GCFR fuel element are given in Table 2.1 which were taken as the reference design for this work. Complete information regarding the GCFR fuel element may be found in reference [G3].

2.1.2 Thermal-Hydraulic Characteristics of GCFR Fuel Elements

The characteristics of gas cooling responsible for differences between gas-cooled and liquid-cooled fuel elements are low coolant density, low convective heat transfer coefficients, coolant transparency, as well as the temperature and pressure dependent nature of density, dynamic viscosity, and thermal conductivity.

Of course, the density of helium is directly proportional to pressure and inversely proportional to temperature. For an economically feasible gas-cooled reactor design, the coolant must be pressurized so as to increase the gas density. The coolant density decreases markedly in axially traversing the core due to the temperature rise/ The helium density in the GCFR is typically 0.35 lbm/ft^3 versus typically 50. lbm/ft^3 in a sodium cooled reactor.

TABLE 2.1

CHARACTERISTICS OF THE GAS-COOLED FAST BREEDER REACTOR (GCFR) FUEL ELEMENT [G3]

Fuel Rod Diameter, Hot, in. (mm)	0.285 (7.24)[1]
Rod-to-Rod Pitch, Hot, in. (mm)	0.389 (9.88)
Pitch-to-Diameter Ratio	1.36
Clad Wall Thickness, in. (mm)	0.019 (0.48)
Cladding Material	316-SS
Active Core Length, in. (cm)	39.6 (101)
Number of Fuel Rod	271
Rod-to-Rod Gap, in. (mm)	0.104 (2.64)
Rod-to-Wall Gap, in. (mm)	0.050 (1.27)
Peripheral Subchannel Design	Scalloped
Corner Subchannel Design	Annulus
Blanket Length, Top & Bottom, in. (cm)	17.7 (45.0)
Fuel Rod Spacer Design	Grid
Fuel Rod Lattice	Triangular (Equilateral)
Inside Hex Box Across Flats, Hot, in (cm)	6.49 (16.5)
Coolant Flow Area (Nominal), $in.^2$	19.2 (124 cm^2)
Reactor Coolant	Helium
Coolant Inlet Temperature, °F (°C)	613 (322)
Coolant Outlet Temperature, °F (°C)	1022 (550)
Hot-Spot Clad Temperature (Mid-Clad), °F (°C)	1260 (682)
Coolant Inlet Pressure, psia (bar)	1,305 (90)
Fuel Element Cross Section Shape	Hexagonal
Maximum Linear Power, KW/ft	12.5
Radial Maximum-to-Average Power Ratio	1.25
Axial Maximum-to-Average Power Ratio	1.21
Average Core Heat Flux, BTU/hr-ft^2	340,000
Maximum Core Heat Flux, BTU/hr-ft^2	510,000
Coolant Mass Velocity, lbm/hr-ft^2*	371,500
Fraction of Active Core Length Roughened	0.75
Length of Roughened Surface, in. (cm)	29.7 (75.4)
Length of Roughening	Downstream End

TABLE 2.1 (continued)

Roughened Surface	
Friction Factor Multiplier	3.0
Roughened Surface Convection	
Coefficient Multipler	2.0
Roughened Surface Geometrical Parameters:	
Rib height, e, in (mm)	0.006 (0.15)
Rib Pitch, p, in (mm), p/e = 12	0.072 (1.8)
Rib Width, w, in (mm), w/e = 3	0.018 (0.46)
Rib Cross Section	Trapezoidal
Leading Edges	Rounded
Rib Helix Angle	0.0° (Transverse Rib)
Relative Roughness, e/d_e:	
Interior Subchannel	0.020
Peripheral Subchannel	0.036
Corner Subchannel	0.056
Fuel Element Average	0.022
Average Reynolds Number*	102,100
Fuel Element Flow Rate, lbm/sec*	14.0
Fuel Element Mass Velocity, lbm/ft^2-hr*	364,400
Coolant Flow Area, in^2 (cm^2):	
Interior Subchannel	0.03363 (0.217)
Peripheral Subchannel	0.03586 (0.231)
Corner Subchannel	0.00877 (0.057)
Fuel Element Total	19.2 (124.)
Wetted Perimeter, in (cm):	
Interior Subchannel	0.4477 (1.137)
Peripheral Subchannel	0.8537 (2.168)
Corner Subchannel	0.3246 (0.824)
Fuel Element Total	265.6 (675)
Heated Perimeter, in (cm):	
Interior Subchannel	0.4477 (1.137)
Peripheral Subchannel	0.4477 (1.137)
Corner Subchannel	0.1492 (0.379)
Fuel Element Total	242.6 (616)
Equivalent Hydraulic Diameter, in. (cm)	
Interior Subchannel	0.3006 (0.764)
Peripheral Subchannel	0.1680 (0.427)
Corner Subchannel	0.1081 (0.275)
Fuel Element Total	0.2761 (0.701)
Flow Area/Heated Perimeter, in. (cm):	
Interior Subchannel	0.0751 (0.191)
Peripheral Subchannel	0.0801 (0.203)
Corner Subchannel	0.0588 (0.149)
Fuel Element Total	0.0791 (0.201)
Maximum Mid-Clad (Hot Spot) Temperature, °F (°C)	1292 (700)

1 Dimensions in Inches (Millimeters), unless noted otherwise.
* Refers to the Maximum Powered Fuel Element.

The operating density of the gaseous coolant is so low that natural convection heat removal is negligible; this requires that forced convection heat removal be maintained whenever significant thermal power is produced in the GCFR core.

The temperature and pressure dependence of helium density and dynamic viscosity could lead to what may be referred to as "an adverse coolant property feedback on subchannel flow." In cases where subchannels are overcooled and undercooled, differences in the axial changes of the coolant density and dynamic viscosity will cause the undercooled subchannels to become increasingly undercooled as flow is diverted to the overcooled subchannels. For fuel elements operating with non-optimum flow distributions or with radial power gradients, the distribution of flow worsens, i.e., flow is diverted from undercooled to overcooled regions, as the coolant traverses the reactor core axially. Further details on the effect of "coolant property feedback" on the flow distribution in gas-cooled fuel elements may be found in section 3.4. It is important to recognize that any change which causes redistribution of flow within a fuel element, i.e., the coolant mass flow split, will be influenced by the coolant property feedback effect. Items influencing the distribution of coolant flow within the fuel element include: (A) fuel

element rod array geometry, (B) flow regime, (C) surface roughening, (D) power-to-flow ratio, and (E) radial power gradients.

Because of the low forced convection heat transfer coefficients characteristic of a gas flow, it is advantageous to roughen the fuel rod (heated) surfaces over part of the active core. Through a boundary layer tripping mechanism (other than an extended area or fin effect), roughened surfaces provide a beneficial doubling (approximate) of the convection coefficient with the penalty of a tripling (approximate) of the friction factor. Because the heat removal per unit pumping power is proportional to the Stanton number cubed divided by the friction factor St^3/f, surface roughening gives improved thermal-hydraulic performance of the fuel element.

Surface roughening is beneficial only on the heated surfaces of the fuel element. For this reason, the unheated perimeter of the fuel element is not roughened. However, since only part of the perimeter of peripheral and corner subchannels is roughened, the "equivalent friction factor" of such subchannels is difficult to determine. The equivalent friction factor of peripheral subchannels is less than that of interior subchannels when only the rod surfaces are roughened. If the design of the peripheral subchannel

is the same along the entire length of the fuel element, then the coolant flow in a peripheral subchannel with respect to that in an interior subchannel will be higher in the roughened region than in the smooth region.

Thermal-hydraulic analysis of roughened, gas-cooled fuel elements is complicated further by the dependence of roughened surface behavior on relative roughness (hydraulic diameter/rib height) and Reynolds number. The Reynolds number dependence of roughened surface performance depends on the relative roughness. At high Reynolds numbers, the friction factor of a given roughened surface becomes independent of Reynolds number and depends only on the relative roughness. At low Reynolds numbers, i.e., in laminar flow, the friction factor depends only on Reynolds number and is independent of relative roughness.

Because the relative roughness (hydraulic diameter) and the Reynolds number varies with subchannel type, the friction factor and Stanton number of a given roughened surface design may be expected to vary with subchannel type. Further information on roughened surface behavior may be found in section 2.2 and in Appendix 1.

2.1.3 Radiative Transfer in the GCFR Fuel Element

With helium cooling and a rod array type fuel

element design, radiative transfer may be of interest because:

A) helium is a transparent cooling media,

B) the fuel rod film temperature rise is characteristically high,

C) the fuel element duct and flow shroud temperatures must be known accurately in the mechanical design of the reactor fuel element, and

D) the fuel element outlet coolant temperature is high enough so that radiative transfer can occur between the heated rods and the flow shroud.

Although radiative transfer occurs between fuel rods, it is expected to be most significant between the fuel rods and the unheated (except for gamma heating) peripheral flow boundary, particularly in the region near the core outlet.

In simplest terms, radiative transfer from a surface may be determined by $q'' = Q/A = \sigma \varepsilon T^4$. For the GCFR fuel element the analysis of the radiative transfer is complicated by several factors, e.g., (A) the helium coolant is a participating medium, which interacts with the radiative transfer between surfaces by absorbing and re-emitting radiation, (B) radiative transfer is influenced by the complex surface geometries, and (C) the rod and wall temperatures are strongly influenced by convective heat transfer.

In order to evaluate the role of radiative transfer in

GCFR fuel element thermal-hydraulics, the effect of combined radiation and convection in peripheral subchannels was estimated with a small computer code called WALRAD [E5] (WALl RADiative Transfer). Only peripheral subchannels were considered because the most significant radiative transfer occurs between the heated rods and the unheated flow shroud. A simplified radiative transfer model was utilized to deal with the extremely complex phenomenon actually occurring. Nevertheless, with the assumptions stated below, it was possible to assess the significance radiative transfer in the GCFR fuel element:

A) No coolant participation,

B) No axial radiative transfer,

C) No gamma ray energy transport,

D) Constant surface emissivities,

E) Infinite parallel plate geometry,

F) Uniform plate temperature,

G) Convective transfer based on RUFHYD calculations (see Chapter 3).

The WALRAD code has shown the following results for a GCFR fuel element near the core center with a normal power-to-flow ratio, i.e.,

turbulent flow,

average linear power = 10.2 kw/ft,

fuel element mass velocity = 364,400 lbm/hr-ft^2 :

A) the maximum radiation/convection heat transfer is less than 0.5% (average = 0.25%),

B) the maximum radiative transfer occurs at the end of the smooth rod surface,

C) the maximum radiative transfer is less than 2000 BTU/hr-ft^2 (average $\sim$ 1100 BTU/hr-ft^2),

D) the rod surface cools less than 2°F (0.6°F average) and the wall surface warms less than 2°F (0.9°F average) when radiative transfer is considered,

E) radiative transfer is insensitive to variations in the rod-to-wall gap.

Based on these findings and the fact that the assumptions are conservative, radiative heat transfer is insignificant in the GCFR fuel elements during normal operating conditions.

2.2 Surface Roughening to Augment Forced Convection Heat Transfer

The use of surface roughening in GCFR fuel elements results in an increase in the amount of thermal energy which can be removed from a given heated surface area per unit coolant circulating or pumping power. The economic incentive for surface roughening is reduced fuel element fabrication costs due to the use of increased fuel rod diameters permitted by roughening.

A large body of literature exists on the use of surface roughening to augment forced convection heat transfer. The reader is referred to symposiums and review articles as sources of information on this topic [B1, B2, B4, H4, M4, N1, W1, W2]. A listing of over two-hundred references on the subject may be found in reference [E6].

The purpose of this section shall be to provide a brief review of the use of surface roughening to augment forced convection heat transfer but not to give an exhausting review of the literature.

2.2.1 Roughened Surface Geometrical Parameters

A roughened surface design is specified by six (6) geometrical parameters. Where practical, these parameters are normally presented in dimensionless form as discussed below:

A) Rib Height or the ratio of the rib height to hydraulic diameter - e/d_e ,

B) Rib Pitch or the ratio of the rib pitch to rib height - p/e ,

C) Rib width or the ratio of the rib width to rib height - w/e ,

D) Rib Geometry or rib shape,

E) Roughened Length or the ratio of the roughened length to hydraulic diameter - L_r / d_e and

F) Rib Helix Angle - α

The transverse rib is a special case of the helical rib with the rib helix angle equal to zero. The helical rib axial pitch p is related to the helix angle by

$$p = \frac{d_r}{N_s} \cdot \text{Tan} \quad \alpha \qquad \text{(Eq. 2.1)}$$

where d_r is the rod diameter and N_s is the number of rib starts. The axial pitch or lead length l of a specific rib is simply

$$l = N_s p \quad . \qquad \text{(Eq. 2.2)}$$

Of all the design parameters by far the most important are the relative roughness (rib height-to-equivalent diameter ratio, e/d_e) and the rib pitch-to-rib height ratio (p/e); relative roughness is the more important of the two primary parameters. The combined influence of the remaining design parameters, i.e., rib width-to-rib height ratio (w/e), rib cross section geometry, rib helix angle (α) and roughened length, is probably much less than that of either primary design parameter, e/d_e or p/e. Indeed, the mechanical tolerance on the rib height e may be more influential on

roughening surface performance than any of the secondary effects.

2.2.2 A Discussion of Surface Roughened, Turbulent Convective Heat Transfer

The main advantage of using roughened surfaces is the increase in the convective heat transfer coefficient caused by a "boundary layer tripping" mechanism. The ribs of the roughened surface disrupt the development of the viscous sublayer thus causing the fluid velocity gradient near the wall to be larger than in the case of a smooth surface. Thus, boundary layer tripping causes an augmentation of convective heat transfer similar to that in the developing region in the entrance of a flow channel. The main disadvantage of using surface roughening is the increase is the friction factor which always accompanies increases in the convection coefficient.

Estimating Roughened Surface Performance

It is customary to relate the heat transfer performance of the roughened surface to that of the smooth surface via the Stanton number multiplier which is given by

$$St_x = St_r/St_s \qquad \text{(Eq. 2.3)}$$

where the r and s subscripts refer to the rough and smooth

regions, respectively. The friction factors are simialrly related by the friction factor multiplier

$$f_x = f_r/f_s \qquad \text{(Eq. 2.4)}$$

An extensive volume of data exists in the literature which has been used to correlate the roughened surface performance, i.e., the relationship between Stanton number multiplier and friction factor multiplier. Norris [N1] has shown that the bulk of the data for Nusselt number multiplier Nu_x versus friction factor multiplier f_x falls between two correlations

$$Nu_x = f_x^{0.63} \qquad \text{(Eq. 2.5)}$$

and

$$Nu_x = f_x^{0.50} \; . \qquad \text{(Eq. 2.6)}$$

Since

$$St = \frac{Nu}{Re\ Pr} = \frac{h}{\rho V C_p} \; , \qquad \text{(Eq. 2.7)}$$

equations 2.5 and 2.6 may be rewritten as (assuming Re_r = = Re_s and $Pr_r = Pr_s$)

$$St_x = f_x^{0.63} \qquad \text{(Eq. 2.8)}$$

$$St_x = f_x^{0.50} \qquad \text{(Eq. 2.9)}$$

because the comparative data for rough and smooth surfaces is normally taken with identical flow conditions, i.e., the fluid (Prandtl Number), the flow channel and flow velocity (Reynolds Number) are identical between tests. Melese-d'Hospital [M4] has recommended the following equation:

$$f_x = \frac{St_x^3}{1.0 + 5/3\ (St_x - 1.0)} \qquad \text{(Eq. 2.10)}$$

The three quations above have been plotted in Figure 2.1; additional numerical details may be found in [E7]. These roughening surface performance equations are not recommended with values of $f_x > 4.0$ because experiments have shown that the Stanton number multiplier cannot be increased further once it has reached a value of about 2.5 [N1, S3].

For purposes of the preliminary design of the GCFR fuel element, a roughened surface Stanton number multiplier of 2.0 and a friction factor multiplier of 3.0 have been used [G3]. This performance was selected because it was felt, this roughened surface behavior could be obtained with a reasonable degree of confidence. More recent work by Lewis [L1], indicates that, due to errors in data transformation, the Stanton number multiplier should be revised to approximately 1.8 for a friction factor multiplier of 3.0 (See also section 2.2.4)

Appendix 1 gives further insight into the behavior of roughened surfaces while section 2.1.2 discusses roughened

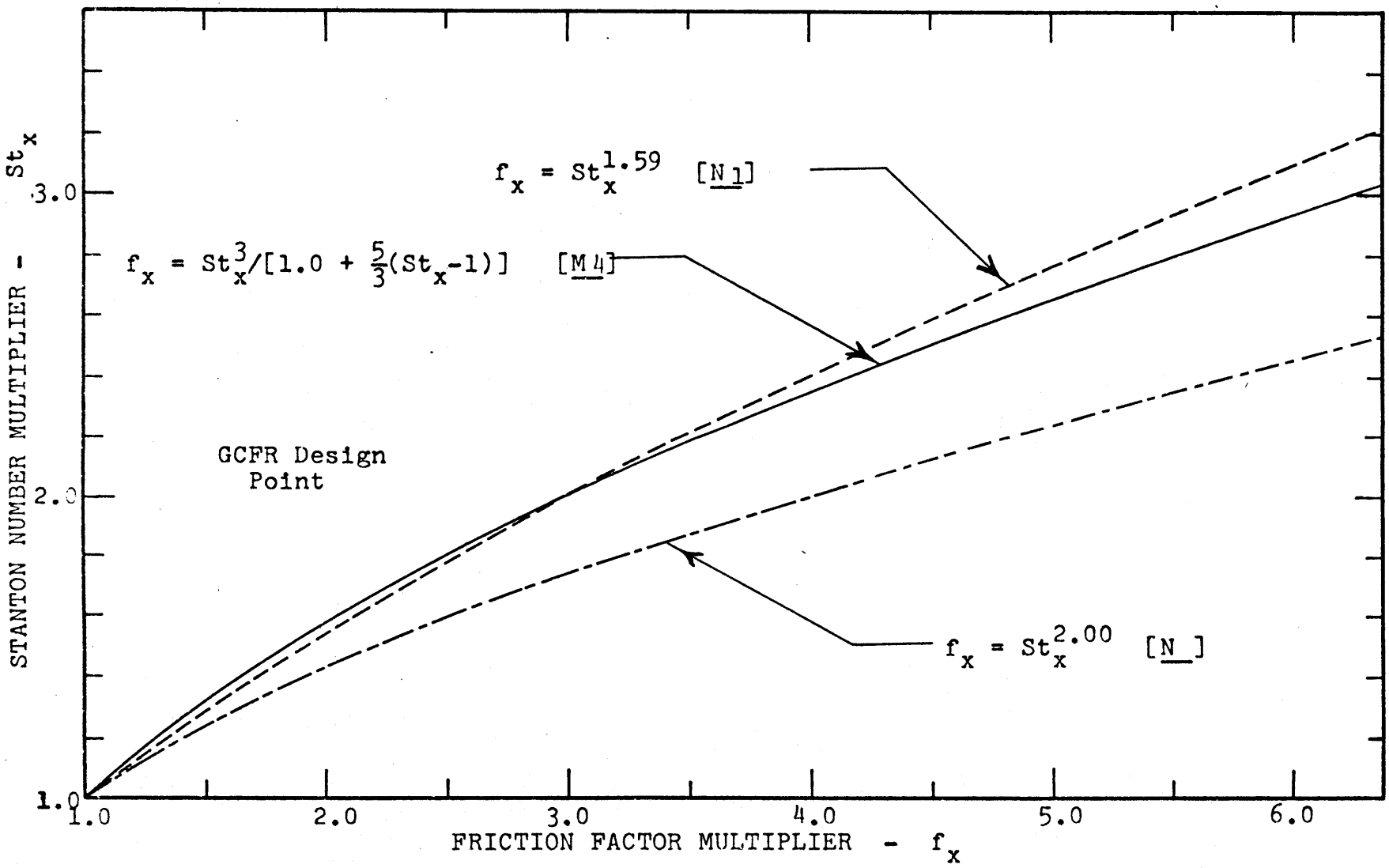

FIGURE 2.1 - CORRELATIONS FOR PREDICTING THE ROUGHENED SURFACE FRICTION FACTOR MULTIPLIER FROM THE STANTON NUMBER MULTIPLIER

surface behavior of interest in the roughened nuclear fuel elements.

Optimum Roughened Surface Geometry

As was noted earlier, the design of a roughened surface requires the specification of six geometrical parameters. Needless-to-say, a seemingly infinite number of combinations of surface roughening geometries can be conceived. The determination of the "optimum geometry" has been the subject of much activity (mainly experimental); however, at this time no specific optimums have been identified. Two obvious observations can be useful in the initial consideration of optimum roughness geometry: A) as the number of roughened surface ribs is increased from the optimum number, the surface will behave increasingly more like a smooth surface, and B) similarly, if the number of ribs is decreased from the optimum, the surface will behave increasingly more like a smooth surface. The axial rib pitch has been shown to have an optimum in the range of rib pitch-to-rib height ratio p/e of 7 to 12. [W1, M5, K1].

The most important geometric parameter in roughened surface design is the height of the rib e. If the rib height is too low, the roughened surface acts more like a smooth surface because it is too low to "trip" the viscous boundary layer. If the rib height is too high, then the rib penetrates through to the

main flow field. Even though the heat transfer improvement saturates when the rib height is approximately the same as the boundary layer thickness, the form drag of the rib increases rapidly as the rib penetrates into the main stream. This is why Stanton number multipliers are limited to less than about 3.0, while friction factor multipliers may exceed 6.0. (see also section 2.2.2).

The width of the roughened surface rib has a small influence on the performance of the surface. Loss of performance is possible chiefly when the rib is too wide. Although the top of the rib is in an area of highly promoted heat transfer [W1, T1, K2], using a wide rib requires the use of a larger rib pitch for the same tripping effect on the boundary layer development. The optimum rib width-to-rib height ratio appears to be between 1.0 and 2.0. It should be noted that because of the large axial variation of the convection coefficient in the region of the rib, the thermal conductivity of the fuel rod cladding material influences the optimum rib width-to-height ratio (as well as the optimum rib geometry) [M6, B5].

The actual roughening rib cross section geometry has been varied widely in the various experiments on roughened surfaces, cf., literature cited in [E6]. The rectangular rib is the most common and has given satisfactory performance. Tang [T1],

recommends a ramp follower behind the rib in order to eliminate the stagnation flow behind the rib. Rounding-off the sharp edges, particularly the leading edges of the rib cross section, has been found to slightly reduce the friction factor of the roughened surface with little or no loss in heat transfer improvement [W1].

2.2.3 Helical Rib Roughened Surface Design

Roughening ribs may be formed on the rod surface either as transverse rings around the rod or by helically twisting around the rod. Considerable interest was generated in the helical rib by Mantle [M7, M8, M9]. The primary advantage cited for the helical rib was that, because the roughening ribs formed an angle with the axial flow, helical roughening would promote interchannel coolant mixing through the generation of secondary flows. Further, by judicious location of fuel rods with clockwise and counter-clockwise ribs, it was estimated that the helical roughening would offer "a large improvement in heat transfer performance" [M8].

Mantle assessed the secondary flow due to helical ribs by optimistically assuming that the flow below the rib height would move with a transverse velocity component such that the angle of the velocity vector would equal the rib helix angle. The flow in the region bounded by the ribs was evaluated assuming

the axial pressure loss of the rib-contained flow equalled that of the main flow. This method neglected flow reattachment between the ribs and vortex flow behind the ribs, but Mantle's secondary flow predictions did agree with those observed with helically ribbed surface roughening experiments in annular channels [M10]. The results of helically ribbed experiments showed a significant improvement in fuel element heat transfer performance [M9]. However, enthusiasm for the helical rib roughening was markedly reduced after reevaluation of full scale, rod array experiments with helical ribs. Gatehouse, et. al, reported "...a secondary flow significantly lower than measured in single-pin tests" [G4].

Other work on helical (multi-start) rib surface roughening was reported by White and Wilkie [W3]; after studying helical roughened surfaces with rib helix angles from 3° and 63°, they concluded that helical rib roughening was advantageous over transverse rib roughening because: "The results show that Stanton number and friction factor fall off with increasing helix angle but since the friction falls off more rapidly, there is generally a gain in thermal performance." The White and Wilkie work [W3] showed the optimum helical rib roughening thermal performance to occur in the range of helix angles between 30° and 40°. Mantle [M10] predicted the optimum helix angle to be 37°.

It might be noted that single rod, annular channel measurements of secondary flow by Hudina [H5] showed no measurable secondary flow from a helically ribbed surface formed by photo-etching (chemical-milling).

The use of a helically ribbed roughened surface instead of a transverse rib appears to offer a potential improvement in thermal-hydraulic performance, but the literature to date is inconclusive. To completely resolve the performance advantage of helical rib roughening, further experimental evaluation is required. Nevertheless, there is a possibility of improved performance.

In addition to the details of the roughened surface rib geometry and spacing, it is also necessary to specify the total length of the heated surface to be roughened. In the beginning of the heated region of a rod-array type nuclear fuel element, the coolant temperature is low enough so that it is not necessary to increase the convection coefficient in order to keep the clad material below the design temperature limit. With this, it is only necessary to roughen the downstream three-quarters (approximate) of the total heated length. Roughening the active core over only part of its length has the advantage of a lower fuel element pressure drop than with total roughening.

2.2.4 Experimental Data Transformation

The transformation of experimental data taken in a given geometry for use with another geometry has been a difficulty for all roughened surface investigations. The fundamental problem has been one of isolating roughened surface thermal-hydraulic behavior from geometry. The problem has been compounded by gross differences in flow channel geometry and by the presence of both smooth and roughened surfaces on the flow passage boundary. Frequently, roughened surface performance has been experimentally assessed in an annular flow channel formed by a smooth tube enclosing a roughened rod; the advantage of this geometry is that it permits rapid, inexpensive performance testing of numerous roughened surface designs. The data taken in such geometries must be transformed for use in roughened, rod-array type, nuclear fuel elements. The transformation is complicated both by differences in geometry and by differences in the relative amount and location of smooth wetted perimeter.

The thermal-hydraulic phenomenon referred to above are extremely complex in nature and will not be discussed in detail here. The reader is referred to the literature cited below for further information.

The most frequently cited early work on roughened surface data transformation was by Hall[H6]. Hall

attempted to isolate the Stanton number and friction factor of the roughened surface from those of the flow passage. Subsequent work has been performed by Rapier [R1], Wilke [W4], Kjellström [K3], and others. Nevertheless, more recent work by Maubach [M5], Lewis [L1, L2] and Klein [K4], for example, has advanced the technique of data transformation notably. Lewis [L2] and Maubach [M5] have advanced the analysis of roughened surface thermal-hydraulics in a manner which deals with the problems of geometry and partially roughened perimeters.

2.3 Fuel Rod Spacer Design

Fuel rod spacers perform the important tasks of maintaining rod array geometry and preventing fuel rod vibrations. Although there are numerous designs for fuel rod spacers, only the grid-type spacer assembly design and the twisted-tape spacer design have been considered here. In the following discussion concerning fuel rod spacers, consideration is given to the seven general topics in nuclear reactor design: A. Thermal-Hydraulic, B. Thermodynamic, C. Nuclear, D. Structural, E. Economic, F. Chemical and G. Metallurgical.

2.3.1 A Comparison of Grid and Twisted-Tape Fuel Rod Spacers

The grid-type spacer is the design currently planned for use in the GCFR; the grid spacer

provides positive fuel rod positioning by enclosing the rod within a hexagonal cell of the grid. Three "dimples" extending from the cell walls (located 120° apart) position the rod centerline within a 0.007 inch (0.18 mm) diameter circle at the center of the grid cell. Seven mils (0.007 in.) diametral clearance is allowed to permit free axial motion of the fuel rod. (The AGATHE spacer grid assembly, shown in Figure 4.1, is similar in appearance to the GCFR spacer.)

An alternative fuel rod spacer design of interest here is the twisted-tape spacer. In this design, a thin metal strip, typically 0.17 inches wide by 0.010 inches thick, (0.43 mm × 0.25 mm, respectively) twisted with an axial pitch of 4.0 to 9.0 inches (10 to 23 cm), is placed in the flow subchannels between the rods in order to maintain rod array geometry. Two schemes are possible using twisted-tape spacing devices: A) the one twisted-tape per interior subchannel design and B) the one twisted-tape per fuel rod design. Regardless of the scheme, it is necessary to have a twisted-tape in every peripheral subchannel (types 2 and 4, Figure 3.1). In general, the peripheral subchannel tape will be of a different effective diameter, i.e., width, than the interior subchannel tape; further, it is not necessary to have twisted-tapes in the corner subchannels (type 3, Figure 3.1).

The three fuel rod spacer schemes discussed above are illustrated in Figure 2.2.

Although the grid spacer is the GCFR reference design, the twisted-tape spacer was of interest because of advantages in fabrication and fuel element assembly, and particularly because of potential improvement of interchannel coolant mixing.

Initial estimates of coolant mixing in twisted-tape spaced rod arrays by Bernath were very encouraging [B3]. This estimate assumed that all flow contained within the area swept by the spiral tape would be forced out of the subchannel of interest. It is more reasonable to assume that part of the subchannel flow swirls with the tape but does not flow out of the subchannel. The twisted tape can be expected to increase the turbulent interchange within the subchannel because more flow drag surface is added. Also the tape does help to "stir" the flow within the subchannel.

An assessment by Markoczy showed that the coolant mixing performance of twisted-tape spaced rod arrays had been "definitely overestimated," by Bernath and that the mixing for the tapespaced array might not be any better than that of the grid spaced array. Coolant mixing experiments on the twisted-tape spaced rod arrays would be required in order to determine the mixing performance of the alternative spacer designs.

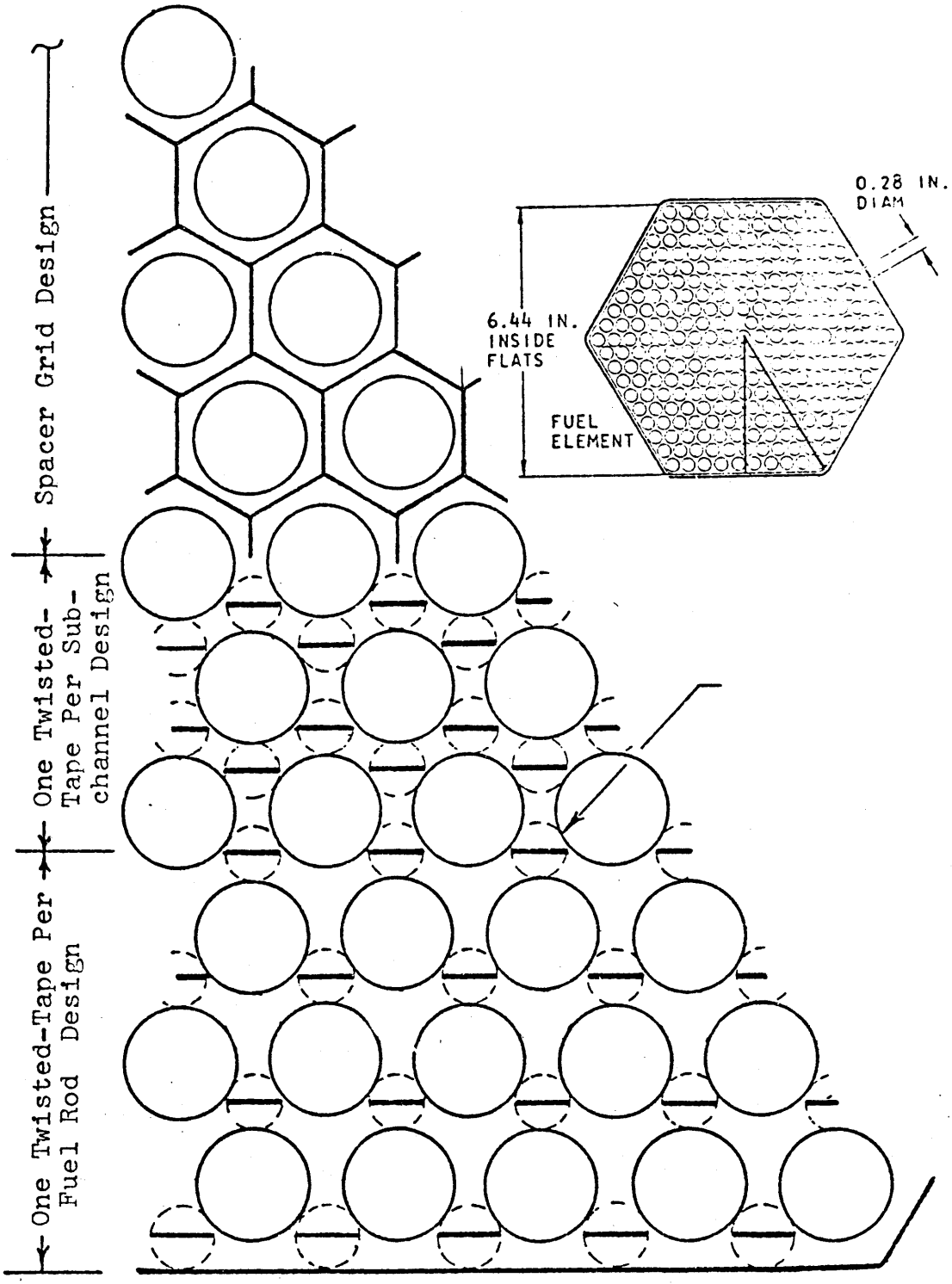

FIGURE 2.2 - FUEL ROD SPACER DESIGNS

Pressure losses due to fuel rod spacers are an important consideration because a change in spacer pressure losses will cause changes in the entire primary coolant system, principally in the power requrements of the primary system circulators. A thermal-hydraulic analysis using RUFHYD (discussed in Chapter 3) has shown that the spacer pressure losses are lowest for the one twisted-tape per fuel rod design and highest for the one tape per subchannel design. Even though the grid spacer had an intermediate pressure loss, it was considered to have the best thermal-hydraulic performance of the three designsconsidered due to high hot-spot factors caused by maldistribution of flow in the one tape per fuel rod design. The flow maldistribution was due to the lower hydraulic diameter, i.e., higher wetted perimeter or increased skin friction, of tape-bearing interior subchannels. The same wetted perimeter effect is responsible for high pressure losses in the one tape per subchannel design. Quantitative details are given in Table 2.2.

Qualitative considerations of the spacer designs have been given in Table 2.3 along with those already noted. Further information regarding the thermal-hydraulic behavior of twisted-tape spacers may be found in the following references: [B6, B2, G2, P1].

Table 2.2

A Comparison of Grid-Type and Twisted-Tape Fuel Rod Spacer Designs

Spacer Type	Grid	Twisted Tape	Twisted Tape
Description	See Fig. 2.2 and Fig. 4.1, also GA-10298 [G3]: Fig. 3.3-9.	One tape per fuel rod design; see Fig. 2.2.	One tape per subchannel design; see Figure 2.2.
	Grid members 0.010 in. thick, 0.75 in. wide.	Interior subchannel twisted-tape 0.010 in. thick, 0.164 in. wide (effective diameter). Peripheral subchannel twisted tape 0.010 in. thick, 0.163 wide (effective diameter).	Interior subchannel twisted-tape 0.010 in. thick, 0.164 in. wide (effective diamter). Peripheral subchannel twisted tape 0.010 in. thick, 0.163 wide (effective diameter).
Interior Subchannel:			
Flow Area (in^2)	0.0336	Bare: 0.0336 Taped: 0.0320	0.0320
Wetted Perimeter (in.)	0.448	Bare: 0.448 Taped: 0.796	0.796
Heated Perimeter (in.)	0.448	Bare: 0.448 Taped: 0.448	0.448

(Table 2. continued)

Hydraulic Diameter (in.)	0.300	Bare: 0.300 Taped: 0.161	0.161
Peripheral Subchannel: Flow area[a] (in^2)	0.0359	0.0414	0.0414
Wetted Perimeter (in.)	0.854	1.183	1.183
Heated Perimeter (in.)	0.448	0.448	0.448
Hydraulic Diameter (in.)	0.168	0.140	0.140
Wall Design	Scalloped	Flat	Flat
Core Pressure Loss (psi)*	21.[b]	12.1	24.1
Subchannel Flow Rates (lbm/hr):*[c]			
Smooth-Interior	89.7	Bare: 108.[g] Taped: 66.8	83.4
Peripheral	64.6	79.6	98.6

(Table 2.2 continued)

Rough -			
Interior	87.6	Bare: 96.7 Taped: 72.6	82.4
Peripheral	85.1	107.	109.
Subchannel Convection Coefficients *cd (BTU/hr-ft^2-°F):			
Smooth -			
Interior	1347	Bare: 1560 Taped: 1250	1500.
Peripheral	1106	1210	1430.
Rough -			
Interior	2507	Bare: 2710 Taped: 2540	2600
Peripheral	2614	2900	2710
Spacer Metal in active core:[f]			
Volume (in.^{3})	7.17[e]	23.3	34.9
Weight (lbm)	2.0	6.6	9.8
Total Metal in Active Core:[f]			
Volume (in.^{3})	273.	281.	292.
Weight (lbm)	76.5	78.7	81.9

(Table 2.2 continued)

* - Based on core central fuel element with mass velocity - 371,500 lb/hr-ft^2, inlet pressure = 1250 psia, inlet temperature = 600°F. In the roughened region, flows calculations were based on the parallel model for evaluating the equivalent friction factor and on theoretical correlation for the friction factor multiplier, i.e., $f_x = 0.26\ Re^{+0.20}$.

a.- Based on a rod-to-wall gap = 0.050 in.

b.- Includes spacer grid pressure losses of 7.0 psi total for four grids with a grid loss coefficient of 0.55.

c.- Flows are given for the center of the axial region, i.e., smooth or rough.

d.- Stanton number multiplier based on theoretical correlation, $St_x = 0.45\ Re^{+0.12}$, see Appendix 1.

e.- Includes only the weight of the "egg-crate" section; the spacer hanger is not included.

f.- Fuel element component weights (active core region): Hexagonal Duct - 24.9 lbm, Fuel Rod Cladding (0.019 in. wall) - 47.2 lbm, Spacer Hanger (Grid spacers only) - 2.4.

g.- Maldistribution of subchannel flows were considerably worse in the laminar flow regime, e.g. bare interior subchannel flow = 1.44 lbm/hr vs. taped interior subchannel flow = 0.39 lbm/hr.

(Table 2.2 concluded)

Table 2.3

A Comparison of Advantages and Disadvantages of Grid and Twisted-Tape Fuel Rod Spacers

Grid Spacers

Advantages:

- Positive Positioning of Fuel Rods
- Less Pressure Loss than the One Twisted-Tape Per Subchannel Design
- Less Flow Maldistribution than the One Twisted-Tape Per Fuel Rod Design
- Average Coolant Outlet Temperature is Higher than One Tape Per Fuel Rod Design
- Less Metal in the Active Core Region
- Spacer Functions are Independent of Fuel Element Duct Distortions

Disadvantages:

- More Pressure Loss than the One Twisted-Tape Per Fuel Rod Design
- Fuel Element Assembly is Difficult: Limited Roughened Surface Damage May Occur During Assembly.
- Fabrication Complicated
- More Difficult to Control Spacer Metallurgical Properties

Twisted-Tape Spacers

Advantages:

- Simplified Fuel Element Assembly
- Reduced Cost

(Table 2.3 continued)

Potential for Improvement of Interchannel Coolant Mixing

Less Pressure Loss with One Twisted-Tape Per Fuel Rod Scheme

Simple Fabrication

Disadvantages:

Uncertain Fuel Rod Positioning Due to a Complex Mechanical Interaction Between Fuel Rods, Twisted-Tapes, and Fuel Element Duct; the One Tape Per Fuel Rod Design has More Uncertainty than the One Tape Per Subchannel Design

One Twisted-Tape Per Interior Subchannel Design has More Pressure Loss than Either Grid Spacers or One Tape Per Fuel Rod Design.

Development Work is Required

One Twisted-Tape Per Fuel Rod has High Hot-Spot Factors Due to Flow Maldistribution Between Taped and Untaped Interior Subchannels.

One Twisted-Tape Per Fuel Rod has Lower Average Coolant Outlet Temperature Due to Flow Maldistribution Hot Spots.

More Metal in Active Core Region

(Table 2.3 concluded)

CHAPTER III

THERMAL-HYDRAULIC ANALYSIS OF GAS-COOLED ROUGHENED NUCLEAR FUEL ELEMENTS

In this Chapter the "flow-split analysis" is discussed, i.e., the division of the total assembly coolant flow among the various unit flow areas (subchannels), for fuel elements using gaseous coolants. Of particular interest are the effects of surface roughening, fluid property variations, flow regime, fuel element geometry, and radial power gradients on the division of flow within fuel elements typical of a GCFR. These fuel elements use helium pressurized to 1250 psia (84.8 bar) as a cooling media. The GCFR surface roughening design accomplishes (nominally) a doubling of the Stanton number while the friction factor is tripled.

A simplified method for determining the "flow split" of a roughened, gas-cooled rod array is presented in this Chapter. This analytical technique neglects flow development and coolant mixing. Calculational results were obtained by using the RUFHYD code and are presented in abbreviated form. Chapter 3 is a shortened version of reference [E1]. Section 3.7 discusses the requirements for modifying an existing code COBRA-3C to do the detailed thermal-hydraulic analysis of roughened, gas-

cooled nuclear fuel elements. The experimental data required to verify the computational methods is discussed in Chapter 6.

3.1 Flow Split Analysis of Rod Array Fuel Elements

The overall flow channel of a rod array type, nuclear fuel element may be divided into numerous unit flow areas called subchannels; see Figure 3.1 for an illustration of subchannels typical of GCFR fuel elements. Using such an approach, the local hydraulics of the fuel element may be determined as outlined below by extending the work reported by Sangster [S1].

Let all of the subchannels of a given type be identified as type i; each subchannel type has associated with it a flow area A_i, heated perimeter P_{hi}, wetted perimeter P_{wi}, equivalent hydraulic diameter de_i, coolant flow W_i, Reynolds number Re_i, coolant density ρ_i, coolant velocity V_i, and Darcy friction factor f_i. In the coolant flow channel (fuel element) there are a total of N_i subchannels of the same type i.

The total flow rate of coolant in the fuel element W_b is the sum of the flow in all the subchannels:

$$W_b = \sum_{i=1}^{n} N_1 W_1 = N_1 W_1 + \sum_{i=2}^{n} N_i W_i \qquad \text{(Eq. 3.1)}$$

FIGURE 3.1

GCFR FUEL ELEMENT

SUBCHANNEL TYPES

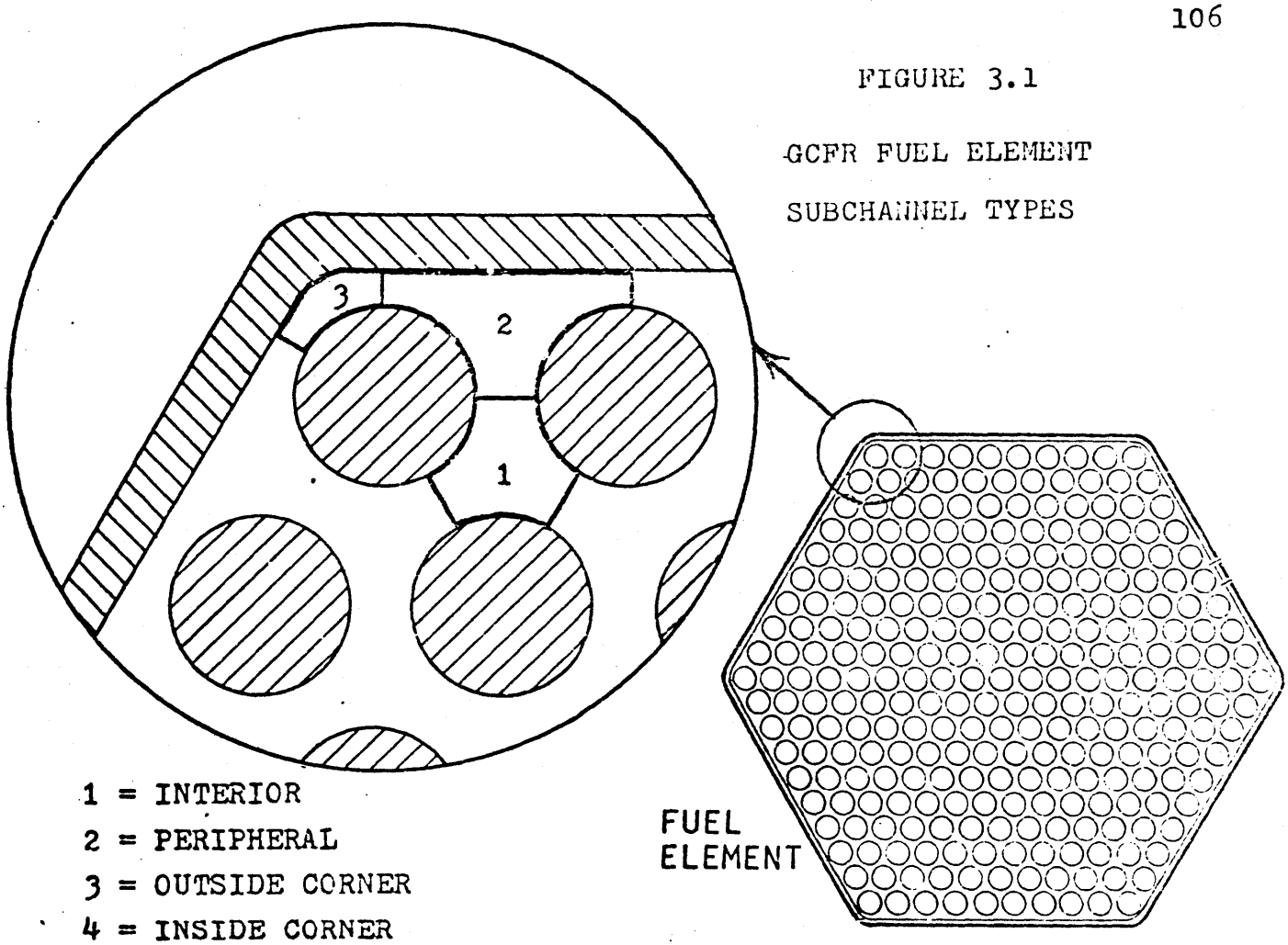

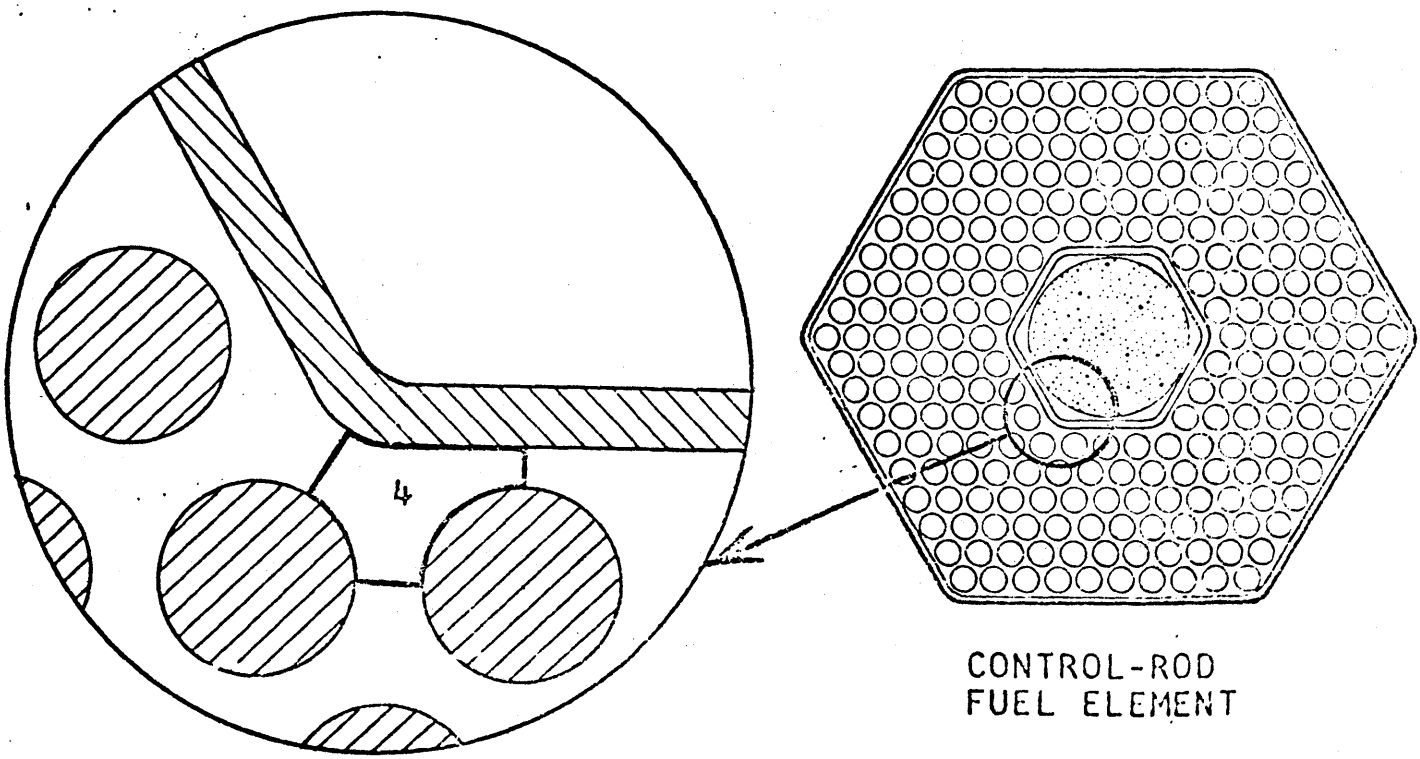

where n is the number of different subchannel types and i = 1 refers to an interior type subchannel. The pressure losses per unit length $\Delta P/L$ will be

$$\frac{\Delta P_i}{L} = \frac{f_i}{de_i} \frac{\rho_i V_i^2}{2g_c} = \frac{f_i}{de_i} \frac{W_i}{A_i} \frac{1}{2g_c \rho_i} \qquad \text{(Eq. 3.2)}$$

If one neglects radial pressure gradients and interchannel coolant mixing, then Equation 3.2 holds for all subchannel types, so

$$\frac{f_1}{de_1} \frac{W_1^2}{A_1^2} \frac{1}{2g_c \rho_1} = \frac{f_i}{de_i} \frac{W_i^2}{A_i^2} \frac{1}{2g_c \rho_i} \qquad \text{(Eq. 3.2A)}$$

Assume that the Darcy friction factor for the subchannels may be correlated to Reynolds nunber in the same manner as for smooth tubes:

$$f_i = \frac{C_i}{Re_i^m} \qquad \text{(Eq. 3.3)}$$

C is the correlation coefficient, and m is the Reynolds number exponent; both C and m depend on the flow regime. Note Equation 3.1 may be rewritten as

$$\frac{W_1}{W_b} = \frac{1}{N_1 + \sum_{i=2}^{n} N_i \frac{W_i}{W_1}} = X_{1b} \qquad \text{(Eq. 3.4)}$$

Substituting for f_i and rearranging Equation 3.2A,

$$\frac{W_i^2}{W_1^2} = \frac{de_i}{de_1} \frac{A_i}{A_1^2} \frac{\rho_i}{\rho_1} \frac{Re_i^m}{Re_1^m} \frac{C_1}{C_i}$$

Since

$$Re_i = \frac{\rho_i V_i d_{e_i}}{\mu_i} = \frac{W_i d_{e_i}}{\mu_i A_i} \qquad \text{(Eq. 3.5)}$$

$$\left[\frac{W_i}{W_1}\right]^{2-m} = \left[\frac{d_{e_i}}{de_1}\right]^{1+m} \left[\frac{A_i}{A_1}\right]^{2-m} \frac{\rho_i}{\rho_1} \left[\frac{\mu_1}{\mu_i}\right]^m \frac{C_1}{C_i} \qquad \text{(Eq. 3.6)}$$

$$X_{il} = \frac{W_i}{W_1} = \left[\frac{de_i}{de_1}\right]^{\frac{1+m}{2-m}} \frac{A_i}{A_1} \left[\frac{\rho_i}{\rho_1}\right]^{\frac{1}{2-m}} \left[\frac{\mu_1}{\mu_i}\right]^{\frac{m}{2-m}} \left[\frac{C_1}{C_i}\right]^{\frac{1}{2-m}} \qquad \text{(Eq. 3.7)}$$

Given the coolant temperature and pressure, the total fuel element flow, the flow geometry, the friction factor correlation, and the number of subchannels for each subchannel type, the flow of subchannel i relative to subchannel 1, X_{il}, may be calculated using Equation 3.7. It should be noted that this method assumes the coolant density and viscosity, i.e., the coolant temperature and pressure, are the same in all subchannels of the same type; this implies a uniform power distribution.

Next, Equation 3.4 may be used to determine the coolant flow in a subchannel of type 1 relative to the

total bundle coolant flow rate X_{lb}. Subsequently, the flow in a subchannel of type i may be related to the total bundle flow by

$$W_i = W_b X_{lb} X_{il} \qquad \text{(Eq. 3.8)}$$

At this point, the assumptions used to arrive at the main flow split equation, Eq. 3.7, should be summarized. The assumptions, although restrictive, do permit the development of the conveniently simple expression relating flow in one subchannel type to that in another subchannel type. Table 3.1 lists a summary of the assumptions required for the development of Eq. 3.7.

When roughened surfaces are used, it is customary to relate the friction factor of the roughened surface f_{ri} to that of the smooth surface f_{si} through a friction factor multiplier f_{xi}:

$$f_{xi} = f_{ri}/f_{si} \qquad \text{(Eq. 3.9)}$$

$$f_{ri} = f_{xi} f_{si} = \frac{C_{xi}}{Re_i^m} = \frac{f_{xi} C_i}{Re_i^m} \qquad \text{(Eq. 3.9A)}$$

where

$$C_{xi} = f_{xi} C_i \qquad \text{(Eq. 3.9B)}$$

TABLE 3.1

ASSUMPTIONS USED TO SIMPLIFY THE HYDRAULIC ANALYSIS OF THE FUEL ELEMENT

A. No Radial Pressure Gradients,

B. Fully Developed Flow,

C. No Interchannel Coolant Mixing,

D. Uniform Radial Power Distribution, i.e., All Subchannels of the Same Type Have the Same Temperature

E. All Subchannel Types Have the Same Friction Factor Correlation,

F. All Subchannels of the Same Type Have the Same Geometry,

G. Ideal Rod Array Geometry, i.e., No Mechanical Tolerances or Distortions.

With this, Equation 3.7 becomes

$$X_{i1} = \frac{W_i}{W_1} = \left[\frac{de_i}{de_1}\right]^{\left(\frac{1+m}{2-m}\right)} \frac{A_i}{A_1} \left[\frac{\rho_i}{\rho_1}\right]^{\left(\frac{1}{2-m}\right)} \left[\frac{\mu_1}{\mu_i}\right]^{\left(\frac{m}{2-m}\right)} \left[\frac{f_{x1}}{f_{xi}}\right]^{\left(\frac{1}{2-m}\right)}$$

(Eq. 3.10)

Noting

$$d_{e_i} = \frac{4A_i}{P_{wi}} \qquad \text{(Eq. 3.11)}$$

Equation 3.10 becomes, in general notation,

$$X_{ij} = \frac{W_i}{W_j}$$

$$= \left[\frac{P_{wj}}{P_{wi}}\right]^{\left(\frac{1+m}{2-m}\right)} \left[\frac{A_i}{A_j}\right]^{\left(\frac{3}{2-m}\right)} \left[\frac{\rho_i}{\rho_j}\right]^{\left(\frac{1}{2-m}\right)} \left[\frac{\mu_j}{\mu_i}\right]^{\left(\frac{m}{2-m}\right)} \left[\frac{f_{xj}}{f_{xi}}\right]^{\left(\frac{1}{2-m}\right)}$$

(Eq. 3.12)

More discussion of the friction factor multipliers f_{xi} will be given in the next section. It is interesting to note at this point that the relationship between flows of different subchannel types is dependent on (according to the method herein presented) subchannel geometry,

coolant properties, surface roughening, and flow regime (m, from the friction factor correlation, depends on the flow regime). Equation 3.12 shall be referred to as the "main flow split equation", for it determines how the total fuel element flow is split-up among all of the subchannel flow areas.

3.1.1. The Equivalent Friction Factor in Partially Roughened Subchannels

The determination of the equivalent friction factor for subchannels with flow boundaries which are partially roughened (roughened surfaces typically have friction factors three times those of smooth surfaces) is an important task in fuel element thermal-hydraulic analysis. This determination is straight-forward in the case where all of the wetted perimeter is roughened, e.g., interior subchannels; it is simply the friction factor multiplier for the roughened surface. However, when not all of the wetted perimeter is roughened, as in the case of peripheral and corner subchannels, the evaluation of the equivalent subchannel friction factor multipler is not a simple matter.

Although sophisticated methods for evaluating the equivalent friction factors are being developed [L2, M5], such methods are not convenient for a simplified analysis. In order to provide a simple method to

accommodate partially roughened flow channels in the hydraulic analysis discussed earlier, two models are described here with the admonition that they are crude approximations of a very complicated hydraulic phenomenon; these two equivalent friction factor models are the "perimeter-weighted, average resistance model" and the "perimeter weighted, parallel resistance model." For the perimeter weighting in each model, the wetted perimeter of a surface P_{wj} which formed the flow boundary of a subchannel was multipled times the term in the equivalent resistance equation that contained the friction factor multiplier of that surface f_{xj}. Only heated surfaces are assumed to be roughened.

The perimeter-weighted, average model for approximating the equivalent subchannel friction factor multiplier $\bar{f}_{xi}$ is fully described by its name and given by

$$\bar{f}_{xi} = \frac{\sum_{j=1}^{ns} f_{xj} \cdot P_j}{\sum_{j=1}^{ns} P_j} = \frac{\sum_{j=1}^{ns} f_{xj} \cdot P_j}{P_{wi}} \qquad \text{(Eq. 3.13)}$$

where ns is the number of surfaces bounding the subchannel.

The perimeter-weighted, parallel resistance model treats the friction factor multipliers divided by the wetted perimeter for each surface as a resistance in

parallel with the other surfaces. The equivalent friction factor multiplier for this model $\bar{\bar{f}}_{xi}$ is given by

$$\bar{\bar{f}}_{xi} = \frac{P_{wi}}{\sum_{j=1}^{ns} \frac{P_{wj}}{f_{xj}}} \qquad \text{(Eq. 3.14)}$$

It is felt that the "perimeter-weighted, parallel resistance model" is the more realistic of the two models. When the fraction of the perimeter roughened decreases, as may be seen in Figure 3.2 and Table 3.2, the parallel resistance model decreases the equivalent friction factor faster than the average resistance model; this faster reduction is in agreement with the expected behavior of partially roughened flow channels (qualitatively) as discussed in the next paragraph.

In a partially roughened subchannel, the drag (friction factor) is much higher on the rough surfaces; in order to equalize this drag force on the smooth surface, the flow velocity gradient on the smooth wall must become steeper. The resulting hydraulic differences in a partially roughened subchannel compared to either a totally smooth or fully roughened subchannel are as follows:

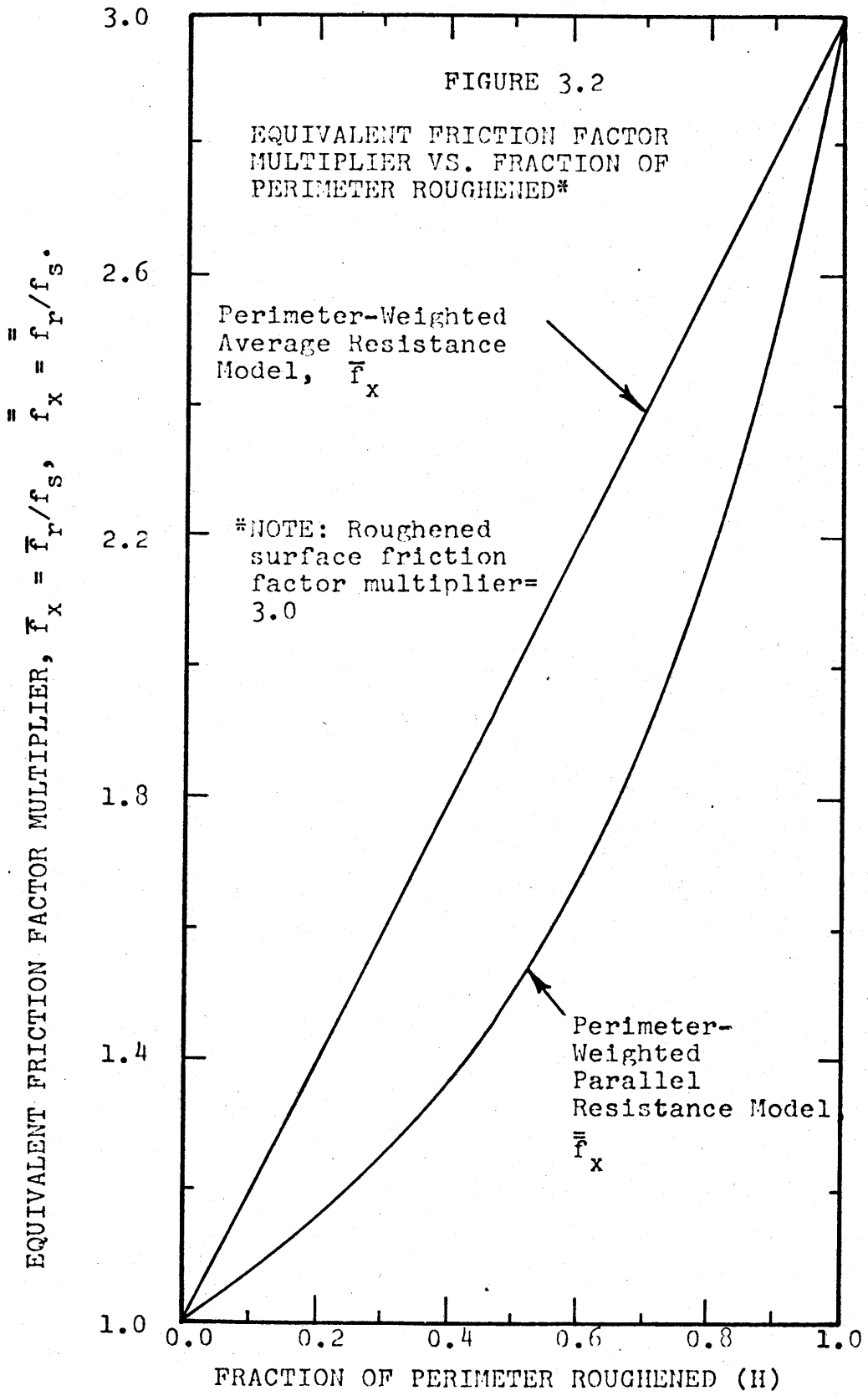

FIGURE 3.2

EQUIVALENT FRICTION FACTOR MULTIPLIER VS. FRACTION OF PERIMETER ROUGHENED*

TABLE 3.2

APPLICATION OF EQUIVALENT FRICTION FACTOR

MODELS TO PARTIALLY ROUGHENED SUBCHANNELS

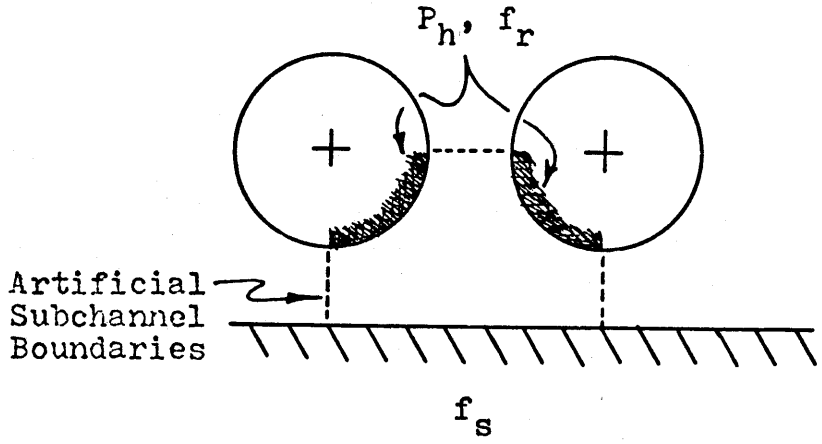

Typical Partially Roughened Subchannel Geometry

A. <u>The Perimeter-Weighted Average Resistance Model</u>

$$\bar{f}_{ri} = \sum_{j=1}^{ns} \frac{P_j f_{xj}}{P_j} = \frac{(P_{wi} - P_{hi})\, f_s + P_{hi} f_r}{P_{wi}}$$

$$= (1 - H_i) + H_i f_x = 1 + H_i(f_x - 1)$$

where $H = P_h/P_w$, $f_x = f_r/f_s$, i.e., H is the ratio of heated (roughened) perimeter-to-total perimeter for a subchannel.

TABLE 3.2
(Concluded)

B. The Perimeter-Weighted Parallel Resistance Model

$$\bar{\bar{f}}_{xi} = \frac{P_{wi}}{\sum_{j=1}^{ns} \frac{P_{wj}}{f_{xj}}} = \frac{f_x}{(1 - H_i)f_x + H_i}$$

C. Numerical Results of Equivalent Friction Factor Multiplier Models *

$H = P_h/P_w$	Average Model, $\bar{f}_x$	Parallel Model, $\bar{\bar{f}}_x$
0.0	1.000	1.000
0.1	1.200	1.071
0.2	1.400	1.154
0.3	1.600	1.250
0.4	1.800	1.364
0.5	2.000	1.500
0.6	2.200	1.667
0.7	2.400	1.875
0.8	2.600	2.143
0.9	2.800	2.500
1.0	3.000	3.000

* Based on a Roughened Surface Friciton Factor Multiplier f_x of 3.00.

A) velocity profile at the smooth wall(s) is steeper, i.e., the smooth wall velocity gradient is higher,

B) the velocity profile at the rough wall(s) is not as steep,

C) the flow and the maximum velocity location shifts toward the smooth surface.

These changes may be used to conclude that the friction factor of a smooth surface plays a greater role in determining the equivalent friction factor of a partially roughened subchannel than it does in a totally smooth subchannel. Also, the friction factor of a rough surface plays a smaller role in determining the equivalent friction factor of a partially roughened subchannel than it does in a fully roughened subchannel. For these reasons, the parallel resistance model, where the current flow in one resistance influences the current in the other resistances, better models the equivalent friction factor. That is, the electrical analogy of a parallel resistance model has a constant voltage across each resistance which corresponds in the flow case to a constant pressure drop along each surface. This model is better than the perimeter weighted, average resistance model which implies a constant current through each

resistance and is analagous to a constant flow along each surface (independent of the pressure drop).

The simplified models presented above offer an estimate to the equivalent friction factor in flow channels with partially roughened perimeters. Nevertheless, the hydraulic complications in this type of problem, such as increasing smooth wall shear stress, non-symmetric channel geometry, zero-shear surface displacements, decreasing rough wall shear stress, etc., are difficult to accommodate.

For a typical GCFR fuel element, i.e., rod diameter = 0.285 in (7.24 mm), rod-to-rod pitch = 0.389 in (9.88 mm), rod-to-wall gap = 0.050 in (1.27 mm), and roughening surface friction factor multiplier = 3.0, examples of the use of the above models are shown in Table 3.3.

3.2 A Summary of the Main Flow Split Equation

With the equivalent friction factor discussed, the main flow split equation may now be summarized. The various factors influencing the flow ratio between subchannel types are given in Table 3.4 while the equations for determining these ratios have been summarized in Table 3.5.

The flow split is influenced by the flow regime through the Reynolds number exponent m of the friction

Table 3.3

EQUIVALENT FRICTION FACTOR MULTIPLIERS FOR THE GCFR DEMO FUEL ELEMENTS[a]

Subchannel Type	i	A_i	$\frac{P_{hi}}{P_{wi}} = H_i$	d_{ei}	j	f_{xj}	P_j	$\overline{f}_{xi}$[b]	$\underline{f}_{xi}$[c]
Interior	1	0.03363	$\frac{0.4477}{0.4477}$ = 1.000	0.3005	1 2 3	3.0 3.0 3.0	0.1492 0.1492 0.1492	3.000	3.000
Peripheral (Scalloped Wall)	2	0.03586	$\frac{0.4477}{0.8537}$ = 0.524	0.1680	1 2 3	3.0 3.0 1.0	0.2239 0.2239 0.389	2.049	1.538
120° Corner (Annulus Design)	3	0.00877	$\frac{0.1492}{0.3246}$ = 0.460	0.1081	1 2	3.0 1.0	0.1492 0.1754	1.919	1.442
1/2 of 240° Corner	4	0.03048	$\frac{0.3731}{0.6680}$ = 0.559	0.1825	1 2 3	3.0 3.0 1.0	0.2239 0.1492 0.2949	2.117	1.593

Notes: a. Fuel Element Geometrical Data Typical of the GCFR Demo Plant Design (G1, GA-10298), Fuel Rod Diameter = 0.285 in., Rod-to-rod pitch = 0.389 in., Rod to wall Gap = 0.050 in., Roughened Surface Friction Factor Multiplier $f_x = 3.0$

b. Perimeter-Weighted, Average Resistance, Friction Factor Equivalent Model: $\overline{f}_{xi} = 1.0 + H_i (f_x - 1.0)$

c. Perimeter-Weighted, Parallel Resistance, Friction Factor Equivalent Model: $\underline{f}_{xi} = f_x/[H_i + f_x(1.0 - H_i)]$

TABLE 3.4

SUBCHANNEL FLOW SPLIT PARAMETERS IN ROUGHENED ROD ARRAYS USING A GASEOUS COOLANT

A. FLOW REGIME*
   1. Turbulent
   2. Laminar
   3. Transition

B. ROD ARRAY GEOMETRY +
   1. Fuel Rod Diameter
   2. Rod-to-Rod Pitch
   3. Rod-to-Wall Gap
   4. Wall Design (see Figure 3)

C. FUEL ROD SURFACE ROUGHENING+
   1. Completely Smooth
   2. Completely Roughened
   3. Partially Roughened
   4. Roughened Surface Friction Factor Multiplier*

D. COOLANT PHYSICAL PROPERTIES*
   1. Density (Compressibility)
   2. Dynamic Viscosity
   3. Power-to-Flow Ratio
   4. Radial Power Gradients

* OPERATING CONDITIONS

\+ FUEL ELEMENT DESIGN OPTIONS

TABLE 3.5

A SUMMARY OF SUBCHANNEL FLOW RATIO EQUATIONS

X_{ij} = The ratio of the flow rate in a subchannel of type i to the flow rate in a subchannel of type j

In terms of Subchannel Hydraulic Diameter:

$$X_{ij} = \frac{W_i}{W_j} = \left(\frac{A_i}{A_j}\right)\left(\frac{d_{ei}}{d_{ej}}\right)^{\frac{1+m}{2-m}} \left(\frac{\rho_i}{\rho_j}\right)^{\frac{1}{2-m}} \left(\frac{\mu_j}{\mu_i}\right)^{\frac{m}{2-m}} \left(\frac{f_{xj}}{f_{xi}}\right)^{\frac{1}{2-m}} \qquad \text{(Eq. 10)}$$

Subchannel Geometry Effect	Coolant Property Variation Effect	Equivalent Roughening Surface Friction Multiplier Effect

In terms of Subchannel Wetted Perimeter:

$$X_{ij} = \left(\frac{P_{wj}}{P_{wi}}\right)^{\frac{1+m}{2-m}} \left(\frac{A_i}{A_j}\right)^{\frac{3}{2-m}} \left(\frac{\rho_i}{\rho_j}\right)^{\frac{1}{2-m}} \left(\frac{\mu_j}{\mu_i}\right)^{\frac{m}{2-m}} \left(\frac{f_{xj}}{f_{xi}}\right)^{\frac{1}{2-m}} \qquad \text{(Eq. 12)}$$

Geometry	Coolant Properties	Roughening

where:

d_e = subchannel equivalent hydraulic diameter

A = subchannel flow area

P_w = subchannel wetted perimeter

W = subchannel coolant flow rate

ρ = subchannel coolant density

μ = subchannel coolant dynamic viscosity

f_x = subchannel equivalent roughened surface friction factor multiplier

(page 2 of 2) TABLE 3.5 (Concluded)

m = Reynolds number exponent in the smooth surface friction factor correlation:

$$f = C/Re^{m}.$$

For turbulent flow m = + 0.20 (+0.20 is recommended over +0.25 which applies for low Reynolds number, turbulent flows). For laminar flow m = + 1.0

Note: $W_t = N_j W_j + \Sigma_i N_i W_i$, thus

$$\frac{W_j}{W_t} = \frac{1}{N_j + \Sigma_i N_i \frac{W_i}{W_j}} = \frac{1}{N_j + \Sigma_i N_i X_{ij}} = X_{jt}$$

where:

W_t = total rod array flow rate

N_j = total number of subchannels of type j in the rod array

VALUES OF FLOW SPLIT EQUATION EXPONENTS

Flow Regime	m	$\frac{1+m}{2-m}$	$\frac{3}{2-m}$	$\frac{1}{2-m}$	$\frac{m}{2-m}$
Turbulent	+0.20*	0.667	1.667	0.555	0.111
	+0.25	0.714	1.714	0.577	0.143
Laminar	+1.00	2.0	3.0	1.0	1.0

* Recommended for Re > 30,000

factor correlation; m is either +0.20 or + 0.25 for turbulent flow and is 1.0 for laminar flow. (Assuming smooth tube correlations apply to the subchannels.) The fuel rod diameter, rod-to-rod pitch, rod-to-wall gap, and wall design (see Figure 3.3) are the geometrical parameters influencing the flow split. Furthermore, the rod-to-wall gap and wall design are the variables of most interest for the work at hand; the rod array parameters (fuel rod pitch and diameter) have been assumed fixed. Fuel rod surface roughening influences the flow split in turbulent flow, and the equivalent friction factor model used influences the result even further in the case of partially roughened subchannels. Finally, coolant density and dynamic viscosity influence the flow split because they change markedly as the coolant temperature increases in traversing the active core region. The degree of property variations are in turn influenced by the power-to-flow ratio and radial power gradients.

Table 3.5 summarizes the main flow split equation given by Eqs. 3.10 and 3.12. The values of the exponent groups have been included in Table 3.5 and show the changes in the significance of the various terms in the flow split equation with changes in flow regime. The

FIGURE 3.3

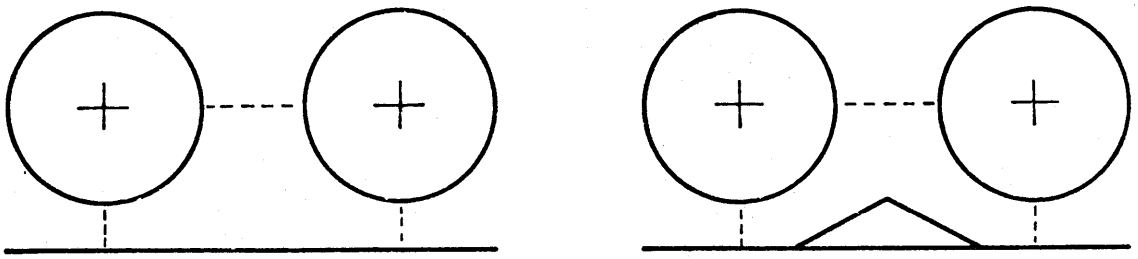

Flat Wall

Scalloped Wall*

PERIPHERAL SUBCHANNEL DESIGN

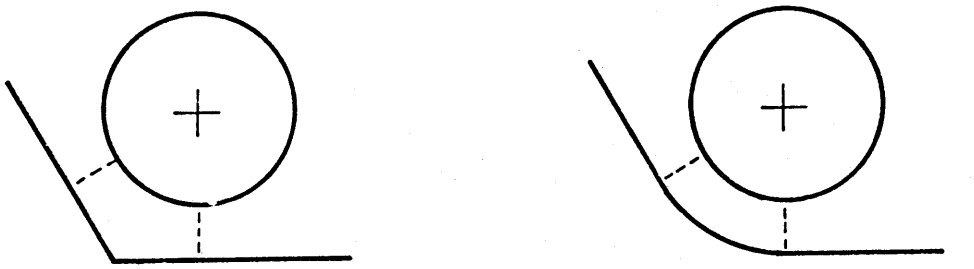

Sharp Corner

Rounded Corner
(Annulus Section)

CORNER SUBCHANNEL DESIGN

* For this work the scallop is assumed to have a base width equal to the rod diameter and a height equal to the rod-to-wall gap.

viscosity term becomes much more significant in laminar flow as does the wetted perimeter term (but to a lesser degree). Nevertheless, all of the exponent groups increase markedly with transition of flow from turbulent to laminar.

3.3 Optimum Design of Peripheral Subchannels

Given that the power profile of the fuel element is uniform, in order to achieve an equal core outlet temperature for all subchannels, the coolant flow rates in the various subchannel types should be approximately proportional to the subchannel heated perimeters, i.e.,

$$\frac{W_i}{W_j} = \frac{P_{Hi}}{P_{Hj}} \qquad \text{(Eq. 3.15)}$$

Substituting Eq. 3.15 into Eq. 3.12 gives an equation for the area ratio of the various subchannel types which result in a uniform fuel element outlet temperature:

$$\frac{A_i}{A_j} = \frac{\left(\frac{P_{hi}}{P_{hj}}\right)^{\frac{2-m}{3}}}{\left(\frac{P_{wj}}{P_{wi}}\right)^{\frac{1+m}{3}} \left(\frac{f_{xj}}{f_{xi}}\right)^{\frac{1}{3}} \left(\frac{\rho_i}{\rho_j}\right)^{\frac{1}{3}} \left(\frac{\mu_j}{\mu_i}\right)^{\frac{m}{3}}} \qquad \text{(Eq. 3.16)}$$

This peripheral or corner subchannel design criteria is influenced by rod array geometry, coolant properties, surface roughening, flow regime, and power-to-flow ratio.

The use of the constant coolant outlet temperature criteria for establishing the flow area for different subchannel types will lead to a near optimum design for peripheral subchannels where the design variables are the rod-to-wall gap and the scallop shape. This criterion does fail to give the exact optimum, however, because no treatment is given for differences in the convection coefficient between subchannel types. A better optimum fuel element thermal performance criteria would give equal mid-clad hot spot temperatures. A treatment which uses the hot spot temperature criterion in the optimum peripheral subchannel goemetry model is left to future work.

3.4 Fluid Property Variation Effects

In general, with axial cooling used in fast reactor fuel elements, the coolant traversing the core on the side of the fuel element closest to the core will be heated more than on the opposite side of the fuel element because of the inherent radial power gradient. Coolant mixing mechanisms that are effective in reducing transverse temperature differences between adjacent subchannels have

no effect at distances more than a few rod pitches.

In the presence of radial power gradients, fluid property effects are responsible for a net diversion of flow from the hotter to the cooler side of a gas-cooled fuel element. The flow diversion progressively worsens as the coolant axially traverses the core because the diversion of flow from hotter regions leads to further increases in under-cooling of the hotter side as well as increases in over-cooling of the cooler side; this effect, noted by Markoczy [M2], may be referred to as the "coolant property feedback" on the flow. This phenomenon is a consequence of the temperature dependence of the density and dynamic viscosity of gaseous coolants.

In addition to the other factors influencing the subchannel flow (and therefore the subchannel temperature and pressure), i.e., the flow regime, rod array geometry and fuel rod surface roughening, the magnitude of the coolant property effect is influenced also by the radial power gradient and the power-to-flow ratio.

The flow difference between subchannels of the same type located on opposite sides of a fuel element may be estimated by using Equation 3.12. Because the geometry and roughening are identical in this case, the ratio of flow in a hot subchannel to that of a cold subchannel X_{hc} may be estimated by:

$$X_{hc} = \left(\frac{\rho_h}{\rho_c}\right)^{\left(\frac{1}{2-m}\right)} \left(\frac{\mu_c}{\mu_h}\right)^{\left(\frac{m}{2-m}\right)} \qquad \text{(Eq. 3.17)}$$

This equation is directly influenced by only coolant properties and flow regime.

For the case at hand, assume that the temperature difference between opposite corners of the fuel element is 200°F (111°C), further, take the coolant properties at 1100°F (593°C) and 900°F (482°C). The hot subchannel-to-cold subchannel flow ratio in turbulent flow (m = +0.2) is found to be 0.92 with 90% of the flow reduction on the hot side due to the density ratio term. For the same temperature conditions in laminar flow, the ratio is 0.80 with only 60% of the hot side flow reduction due to the density ratio term. In laminar flow, the dynamic viscosity ratio term is more significant than in turbulent flow, and the combined effects of both density and viscosity are noticeably larger than in turbulent flow.

3.5 The RUFHYD Code

The equations developed earlier were programmed into a computer code called RUFHYD (a code for the hydraulic analysis of roughened, rod array-type nuclear fuel assemblies). RUFHYD results are restricted by all of the assumptions noted in Table 3.1. The primary function

of RUFHYD is to calculate the fuel element flow split, i.e., the division of total fuel element flow among the various subchannels. All of the effects noted earlier are included, see Table 3.3.

Once the subchannel flow has been calculated, the following subchannel information is determined: average coolant velocity, temperature, density, viscosity, Reynolds number, convection coefficient and film temperature rise. Subroutines are included to calculate geometrical data for the subchannel types of interest, the properties of helium as a function of temperature and pressure, and the equivalent friction factor using either the perimeter weighted-average or parallel resistance model. A subroutine is also available to calculate fuel rod vibrations using several empirical correlations.

The calculations are done at equally spaced axial locations from the core inlet to the core outlet. The calculations may be repeated for various fuel element designs, e.g., standard or control-type fuel elements. Although the rod array parameteres may be varied, the primary subchannel geometry parameteres of interest are the rod-to-wall gap and the shape of the peripheral and corner subchannel walls, i.e., either a scalloped or flat for the peripheral subchannel and either a sharp

corner or rounded corner (annulus section) for the corner subchannel, see Figure 3.3. The scalloped wall design is desirable because it reduces the circumferential variation of the convective heat transfer coefficient on the surface of peripheral fuel rods [M2] and because it introduces flexibility into the design of peripheral subchannels. (Both rod-to-wall gap and scallop design may be varied to determine the peripheral subchannel flow area and equivalent diameter.) The sharp corner design is of interest because it provides more flow area for the corner subchannel (approximately 25% more area).

3.6 Calculational Results

The results computed using the RUFHYD code to be reported herein are listed in Table 3.6. Also listed in the table are the parameters of interest in reporting the results. Table 3.7 gives details of the calculation variables used for the results.

It is significant to note that the thermal-hydraulics of a gas-cooled, roughened nuclear fuel element are strongly influenced by both

A. Fuel Element Design Parameters and

B. Fuel Element Operating Conditions:

the latter influence being due to the use of a gaseous coolant.

TABLE 3.6

RUFHYD CALCULATIONS*

A. Interior and Peripheral Subchannel Flow Versus Axial Position in the Active Core

B. Peripheral-to-Interior Subchannel Flow Ratio Versus Rod-to-Wall Gap

C. Optimum Peripheral Subchannel Rod-to-Wall Gap

D. Peripheral Subchannel Flow Sensitivity to Rod-to-Wall Gap

CALCULATIONAL VARIABLES

A.
A. Axial Position in Active Core

B. Rod-to-Wall Gap

C. Wall (Flow Shroud) Design

D. Corner Design

E. Surface Roughening

F. Equivalent Friction Factor Model

G. Total Fuel Element Flow (Flow Regime)

H. Average Linear Power (Power-to-Flow Ratio)

* Further details regarding peripheral and corner subchannel flow behavior may be found in reference [El]

TABLE 3.7

CALCULATIONAL VARIABLE DETAILS[$]

Active Core Height = 39.2 in (99.6 cm)
Fuel Rod Diameter = 0.285 in (7.24 mm)
Rod-to-Rod Pitch = 0.389 in (9.88 mm)
Pitch-to-Diameter Ratio = 1.365
Rod-to-Rod Gap = 0.104 in (2.64 mm)
Rod-to-Wall Gap - Variable:

a. Turbulent Flow, 0.020-0.100 in (0.508-2.54 mm),
b. Laminar Flow, 0.040-0.200 in (1.02-5.08 mm)

Peripheral Subchannel Design - Variable Wall Shape:

a. Scalloped Wall,
b. Flat Wall

Scallop Design - Triangular Shape:

Base Width = Rod Diameter

Height = Rod-to-Wall Gap

Corner Subchannel Design - Variable:

a. Annular Overall Shape,
b. Sharp 120° Corner Shape

Spacer Design - NO SPACER EFFECTS INCLUDED

Friction Factor Correlation Reynolds Number Exponent, i.e., $f = C/Re^m$:

Turbulent Flow - m = +0.20
Laminar Flow - m = +1.00

Surface Roughening Performance+ -

Friction Factor Multiplier = 3.0, Constant
Stanton Number Multiplier = 2.0, Constant

Equivalent Friction Factor Model -

a. Perimeter Weighted, Average Resistance Model,
b. Perimeter Weighted, Parallel Resistance Model

Length of Surface Roughening - 29.4 in (74.7 cm), Downstream End, 3/4 of Active Core Height

TABLE 3.7 (Concluded)

Helium Property Calculations - Via Varadi Correlations, EIR TM-IN 410 [V1]

Helium Coolant Inlet Temperature - 600°F (316°C)

Helium Coolant Inlet Pressure - 1250 psia (84.8 bar)

Helium Flow Velocity, Turbulent Flow - 364,400 lbm/hr-ft^2 *

Laminar Flow - 3,644 lbm/hr-ft^2

* Power/Flow typical of core central fuel element
Axial Power Shape - Chopped Cosine

$ RUFHYD results are not influenced by the number of fuel rods in the fuel element with the mass velocity constant.

+ Surface roughening effects do not occur in laminar flow, cf. any Moody friction factor chart for commercial pipe.

3.6.1 Peripheral Subchannel Flow Results

The axial behavior of the coolant flow rate in the various subchannel types is strongly influenced by (A) Subchannel Type, (B) Flow Regime, (C) Fuel Rod Surface Roughening, (D) Equivalent Friction Factor Model, (E) Rod-to-Wall Gap, (F) Wall Design. The effects of coolant properties (power-to-flow ratio and radial power gradients) are the smaller of the effects under normal operating conditions.

Figure 3.4 shows the axial behavior of the interior and peripheral subchannel flow rates in a standard GCFR fuel element positioned near the core center. The fuel element power/flow is typical of full power operation (turbulent flow). The effect of the start of surface roughening has a strong influence on the flow in the peripheral subchannels (recall that RUFHYD assumes fully developed flow). The peripheral subchannel flow changes because the wetted perimeter of these subchannels is only partially roughened while that of the interior subchannel is totally roughened, see Table 3.3 and Section 3.2. With the onset of roughening, the relative change of resistance in the interior subchannels is higher than that in the peripheral subchannels so that the flow around the bundle periphery increases. Note also that the rod-to-wall gap size also influencesthe peripheral subchannel

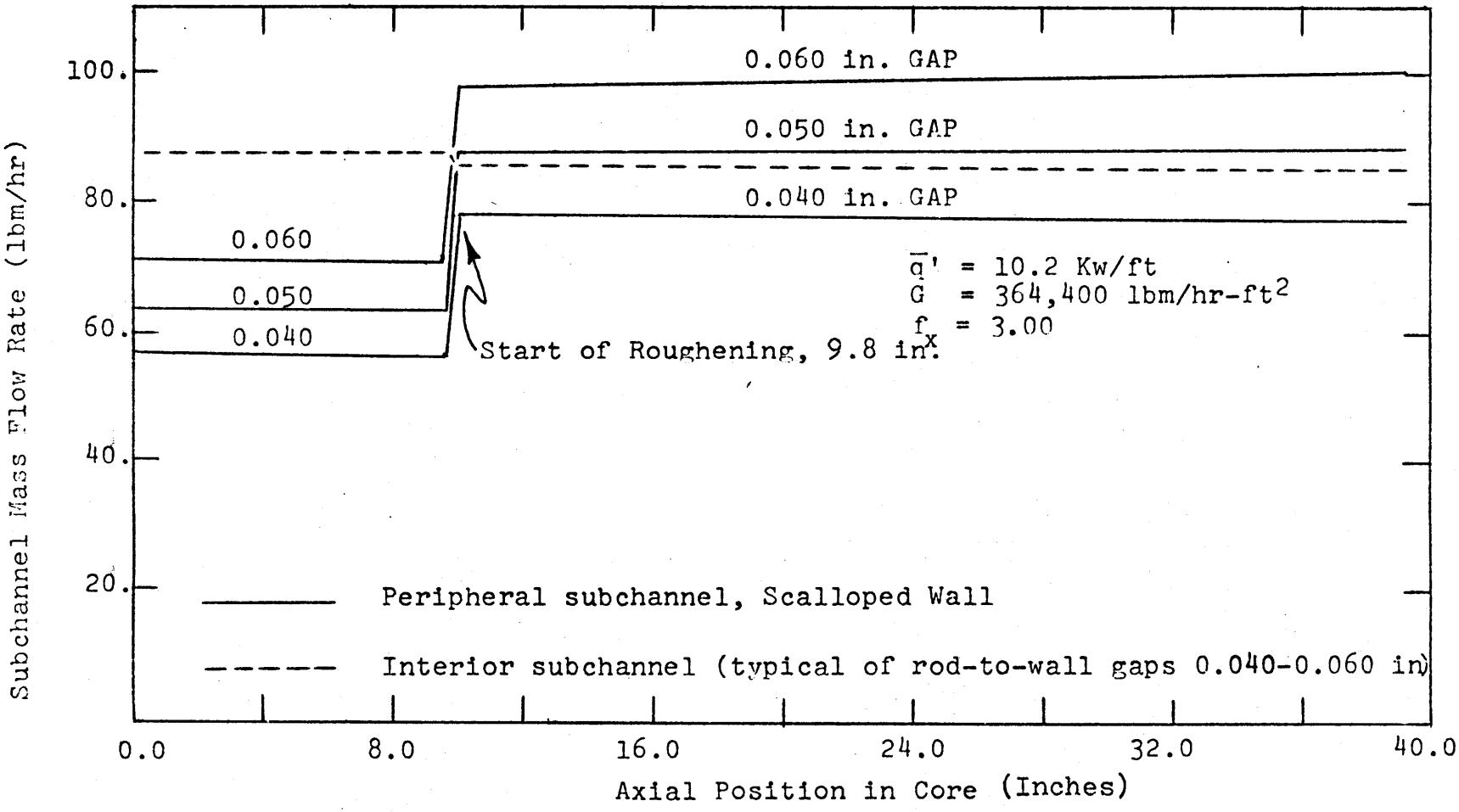

FIGURE 3.4- TYPICAL SUBCHANNEL FLOW RATES, CENTRAL FUEL ELEMENT

flow. The changes in interior subchannel flow due to the start of roughening and due to changes in rod-to-wall gap is much smaller than in the peripheral subchannels because there are about 10 times as many interior subchannels as peripheral.

Because heated perimeters of the interior and peripheral subchannels are the same, they should have approximately the same flow rate in the optimum thermal-hydraulic condition. From Figure 3.4 the optimum gap is seen to be 0.048 in. (1.22 mm), nominal. However, in order to achieve optimum thermal-hydraulic performance, the rod-to-wall gap must be different in the smooth rod surface region than in the roughened rod region; this results because the walls of the peripheral (and corner) subchannel is not heated and therefore not roughened.

Roughening unheated surfaces is an unnecessary consumption of circulator power. The overall GCFR fuel element, roughened region equivalent friction factor multiplier is 2.59 using the parallel model and 2.84 using the average model. In any event, roughening the flow boundary, i.e., the unheated walls, would lead to an equivalent friction factor multiplier of 3.00 and to an increase in coolant pumping power.

The small axial variations of all subchannel flows

is due to the effects of coolant property variations.

Figure 3.5 shows the influence of equivalent friction factor model on the peripheral subchannel flow in the roughened region of the fuel element; the effect is substantial. Although neither equivalent friction factor model is empirically verified at this time, the parallel resistance model, see Table 3.2, is believed to be the more accurate model.

Figure 3.6 gives typical flows for peripheral and interior subchannels in laminar flow. The rod-to-wall gap sizes (0.100 - 0.140 in.) were selected to be in the range of the optimum gap; the power/flow is the same as in Figure 3.4. It will be noted that there are no effects of surface roughening in laminar flow, cf., any Moody friction factor chart for commercial pipe.

Figure 3.7 shows the influence of flow regime (an operating condition) on the ratio of peripheral-to-interior subchannel flow rates. The transition of flow from turbulent to laminar strongly influences the division of flow between subchannel types, i.e., the fuel element flow split, due to (A) the change in the Reynolds number exponent in the friction factor correlation and (B) the absence of the effects of surface roughening.

The dependence of the ratio of peripheral-to-interior subchannel flows on the rod-to-wall gap is shown

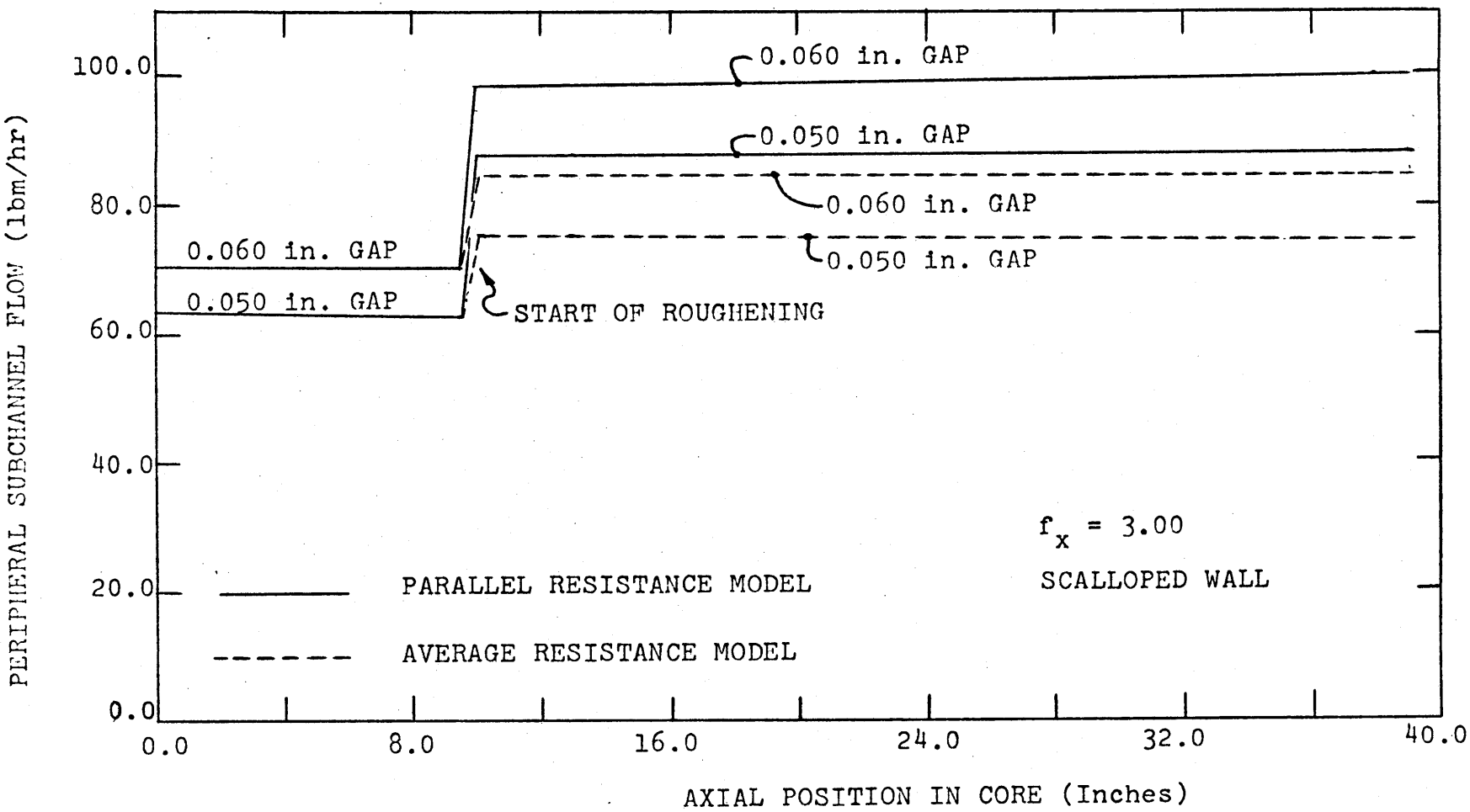

FIGURE 3.5 - THE EFFECT OF EQUIVALENT FRICTION FACTOR MODEL ON PERIPHERAL SUBCHANNEL FLOW, TURBULENT FLOW

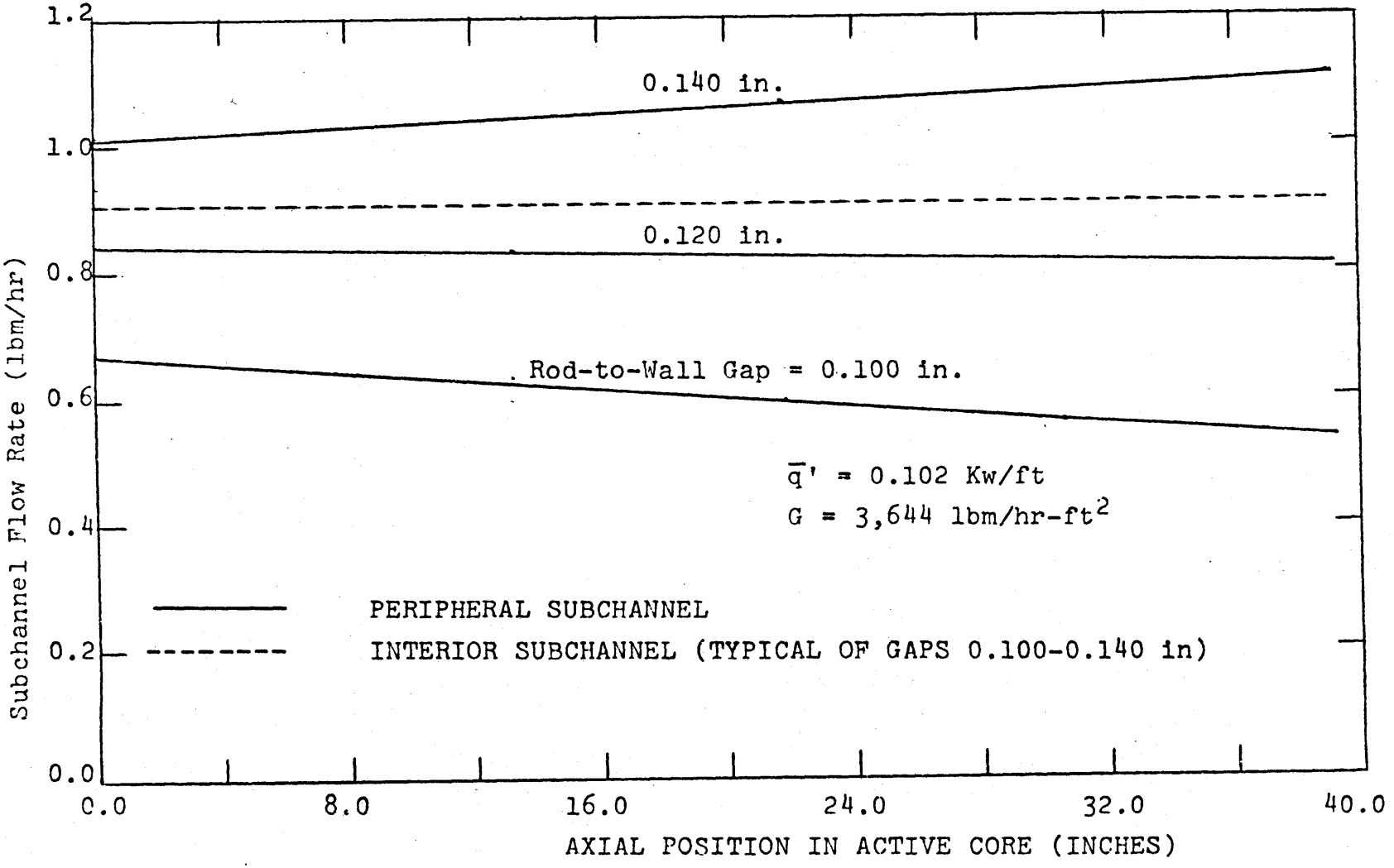

FIGURE 3.6 - TYPICAL SUBCHANNEL FLOW RATES IN LAMINAR FLOW

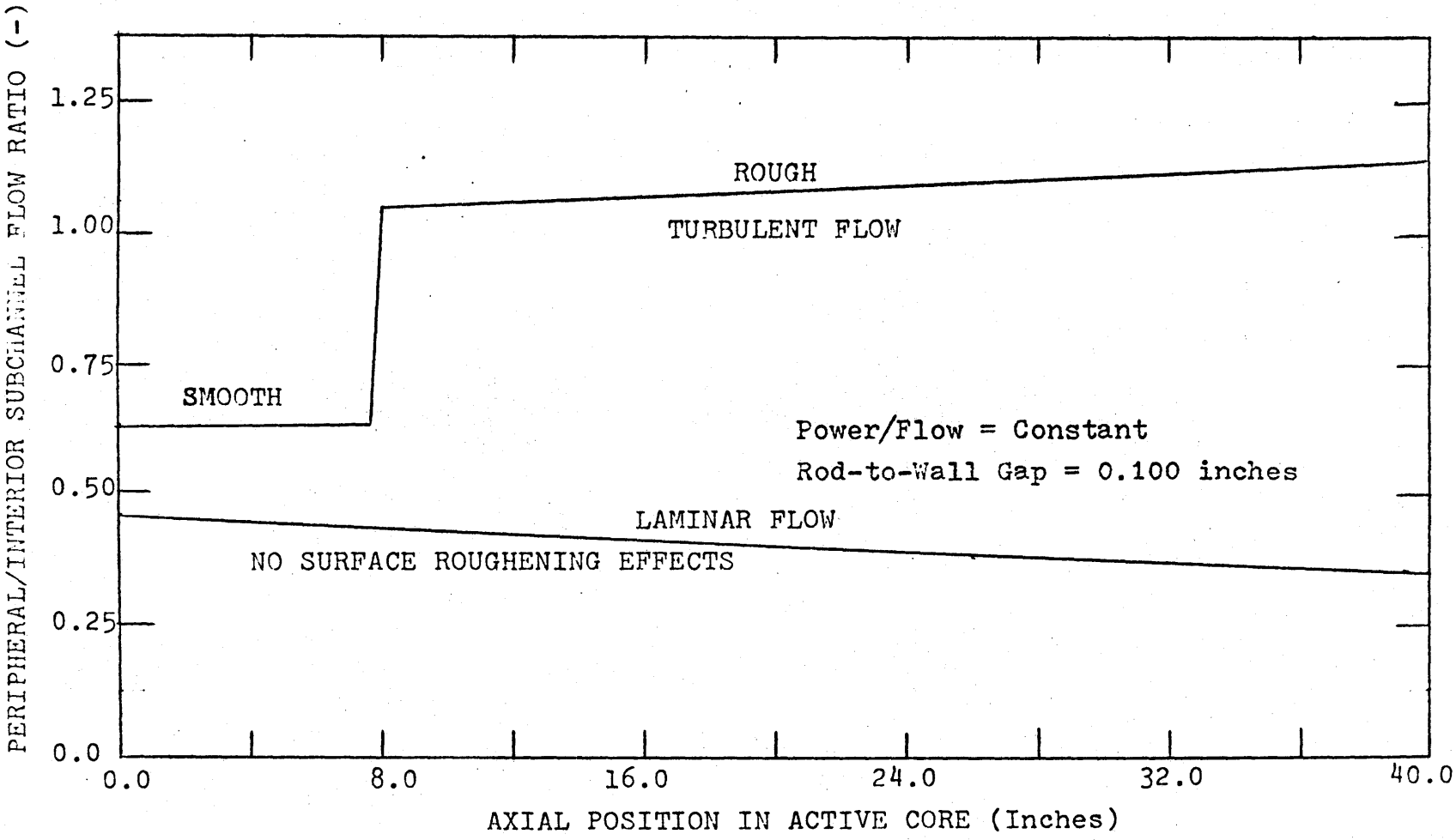

FIGURE 3.7_ TYPICAL RATIOS OF PERIPHERAL-TO-INTERIOR SUBCHANNEL FLOWS VERSUS CORE POSITION AS INFLUENCED BY FLOW REGIME

in Figure 3.8 for the case of turbulent flow. The line of the approximate optimum of this ratio, i.e., the ratio of flows which equals the ratio of heated perimeteres, has been shown. The effect of wall design is shown in the figure, and the effect is pronounced. From the figure the optimum rod-to-wall gap is predicted to be (in the roughened region) -

0.030 in (0.762 mm): Flat Wall, Parallel Resistance Model for Equivalent Friction Factor,

0.048 in (1.22 mm): Scalloped Wall, Parallel Model

0.062 in (1.57 mm): Scalloped Wall, Average Model,

and (in the smooth region) -

0.050 in. (1.27 mm): Flat Wall,

0.083 in. (2.11 mm): Scalloped Wall.

Figure 3.9 gives the ratio of peripheral-to-interior subchannel flows in laminar flow. The optimum flow ratios occur at a rod-to-wall gap of 0.127 in. (3.23 mm) for the scalloped wall and 0.071 in. (1.80 mm) for the flat wall design. The optimum design of the peripheral subchannel depends on flow regime; design for optimum rod-to-wall gap at full power operation will result in under-cooling of the peripheral subchannels in low flow situations (laminar flow).

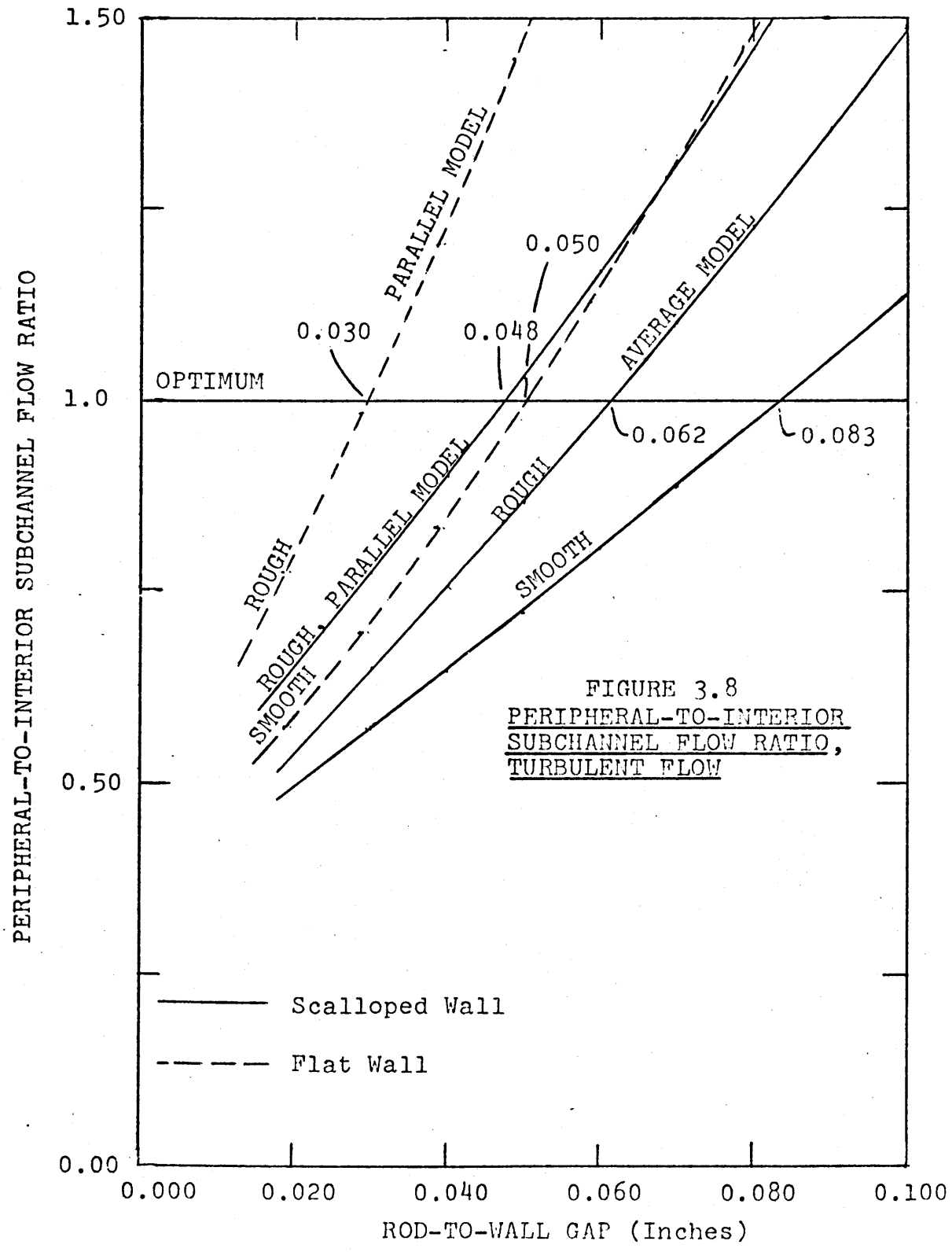

FIGURE 3.8
PERIPHERAL-TO-INTERIOR SUBCHANNEL FLOW RATIO, TURBULENT FLOW

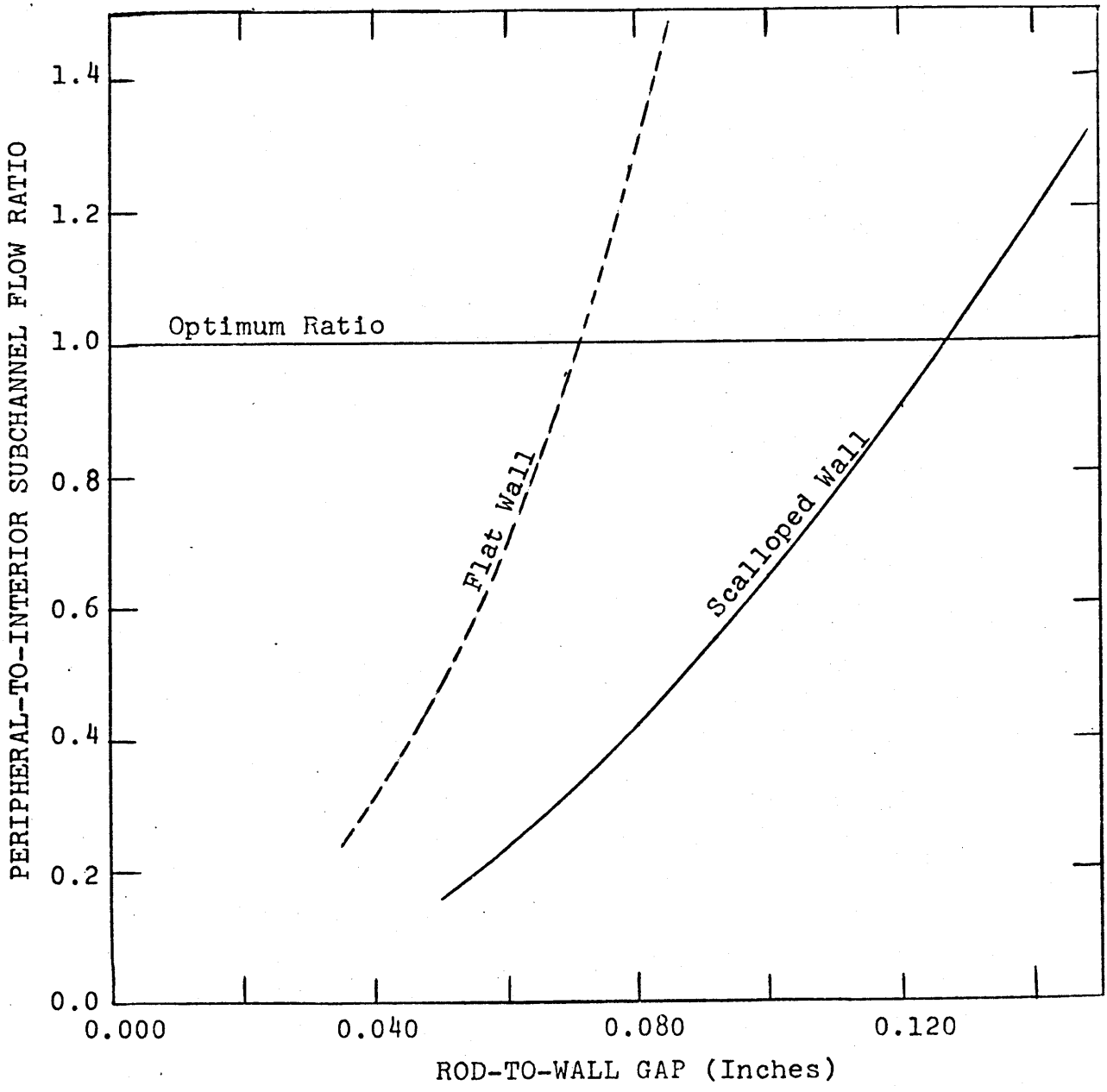

FIGURE 3.9 - RATIO OF PERIPHERAL-TO-INTERIOR SUBCHANNEL FLOWS VERSUS ROD-TO-WALL GAP, LAMINAR FLOW

The optimum rod-to-wall gap can also be determined using Equation 3.15. In using this equation, an optimum gap must be guessed; if the guess is too low, the calculated optimum gap will be higher than guessed. If the guess is too high, the calculated will be lower. Regardless, the technique will converge to exactly the same values of optimum rod-to-wall gaps reported above.

3.6.2 Sensitivity of Peripheral (or Corner) Subchannel Flow to Gap Variations

The change of flow in a peripheral subchannel with respect to a change in the rod-to-wall gap g may be seen to be directly influenced by the following variables, cf. Eq. 3.12 with i=2 for a peripheral subchannel (or i=3 for a corner subchannel): A. the flow area of the peripheral subchannel A_2 (the interior subchannel flow area A_1 is assumed constant), B. the viscosity in both peripheral and interior subchannels, C. the density in both peripheral and interior subchannels, D. the flow regime, E. the flow in the interior subchannel, W_1, and F. the equivalent friction factor multiplier in the peripheral subchannel, f_{x2},

The results of finite difference calculations gave the following results for the behavior of the peripheral subchannel flow as influenced by changes in

the rod-to-wall gap:

A. The sensitivity of peripheral subchannel flow decreases with increases in rod-to-wall gap,

B. $\Delta W_p/\Delta g$ depends significantly on the shape of the unheated wall, i.e., whether scalloped or flat,

C. $\Delta W_p/\Delta g$ is lower for the scalloped wall design,

D. the sensitivity of W_p is lower in turbulent flow than laminar flow,

E. the sensitivity of W_p is less in the smooth region than in the roughened region for turbulent flow,

F. the sensitivity of W_p in the roughened region (turbulent flow) is slightly dependent on the equivalent friction factor model,

E. the sharp cornered, corner subchannel design is less sensitive to changes in the rod-to-wall gap than is the rounded corner design,*

F. the corner subchannel is the most sensitive to changes in rod-to-wall gap.*

Computational results of the finite difference method for determining the sensitivity of peripheral

* See Reference [E1]

subchannel flow to changes in the rod-to-wall gap are given in Figures 3.10 and 3.11. Figure 3.10 shows the influence of flow regime, surface roughness (turbulent regime only), and equivalent friction factor on the peripheral flow sensitivity versus rod-to-wall gap curves. Figure 3.11 is a more detailed plot of the turbulent regime; it shows the effect of wall shape, i.e., either scalloped or flat, on the peripheral flow sensitivity. The scalloped wall design has a lower sensitivity of flow to changes in rod-to-wall gap. Furthermore, the sensitivity of all subchannels to changes in rod-to-wall gap is considerable higher in laminar flow than in turbulent flow..

3.7 Detailed Thermal-Hydraulic Analysis of Roughened, Gas-Cooled Nuclear Fuel Elements

As was noted earlier, several simplifying assumptions were required in order to arrive at a convenient expression for the subchannel flows used in the RUFHYD code (cf. Table 3.1). Although the results of the RUFHYD code provide a valuable illumination of the thermal-hydraulic behavior of roughened, gas-cooled nuclear fuel elements a detailed thermal-hydraulic analysis will be required in order to optimize the rod array geometry and to specify the thermal-hydraulic operating limits for a given reactor design.

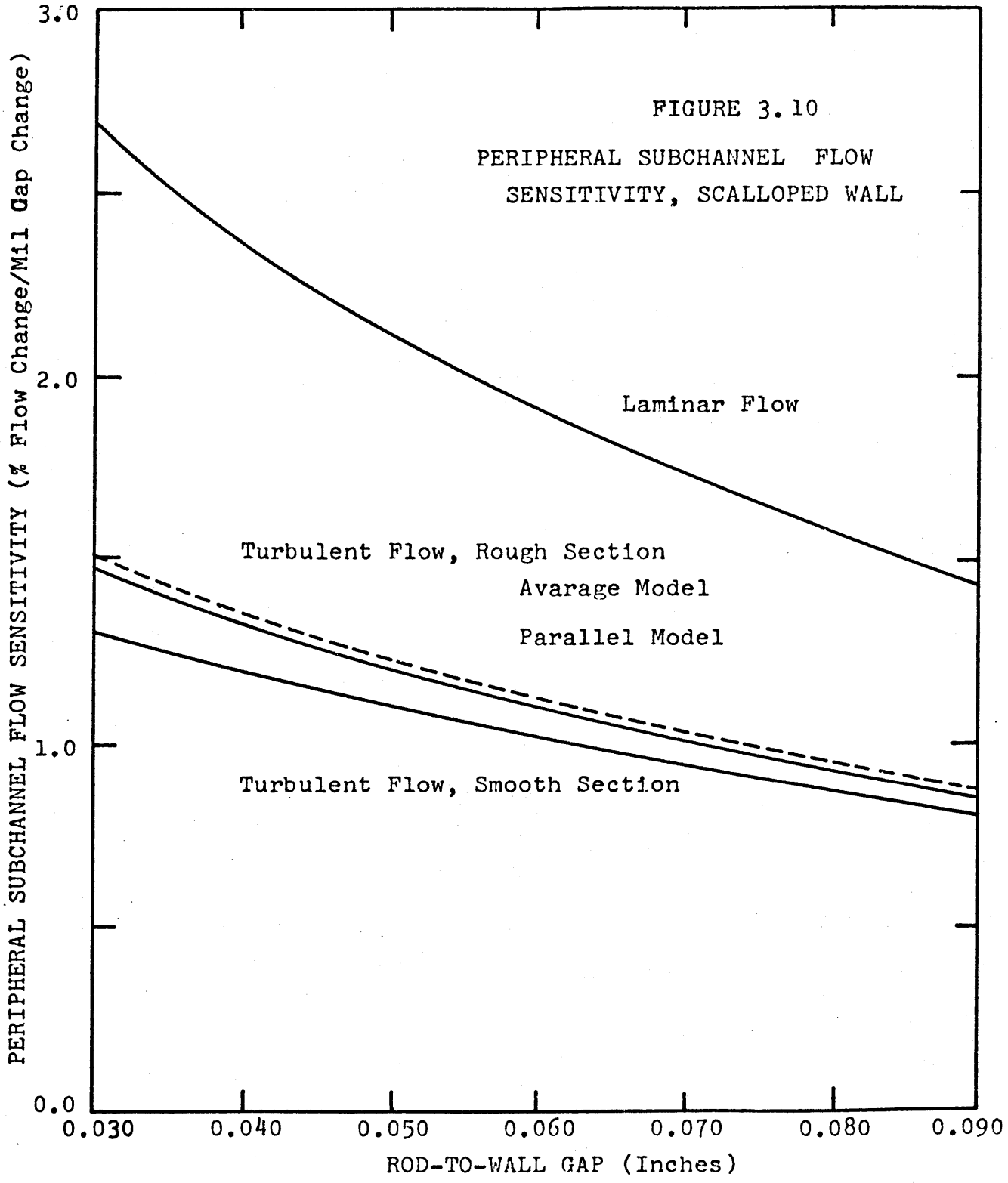
FIGURE 3.10
PERIPHERAL SUBCHANNEL FLOW
SENSITIVITY, SCALLOPED WALL
Laminar Flow
Turbulent Flow, Rough Section
Avarage Model
Parallel Model
Turbulent Flow, Smooth Section
PERIPHERAL SUBCHANNEL FLOW SENSITIVITY (% Flow Change/Mil Gap Change)
3.0
2.0
1.0
0.0
0.030
0.040
0.050
0.060
0.070
0.080
0.090
ROD-TO-WALL GAP (Inches)

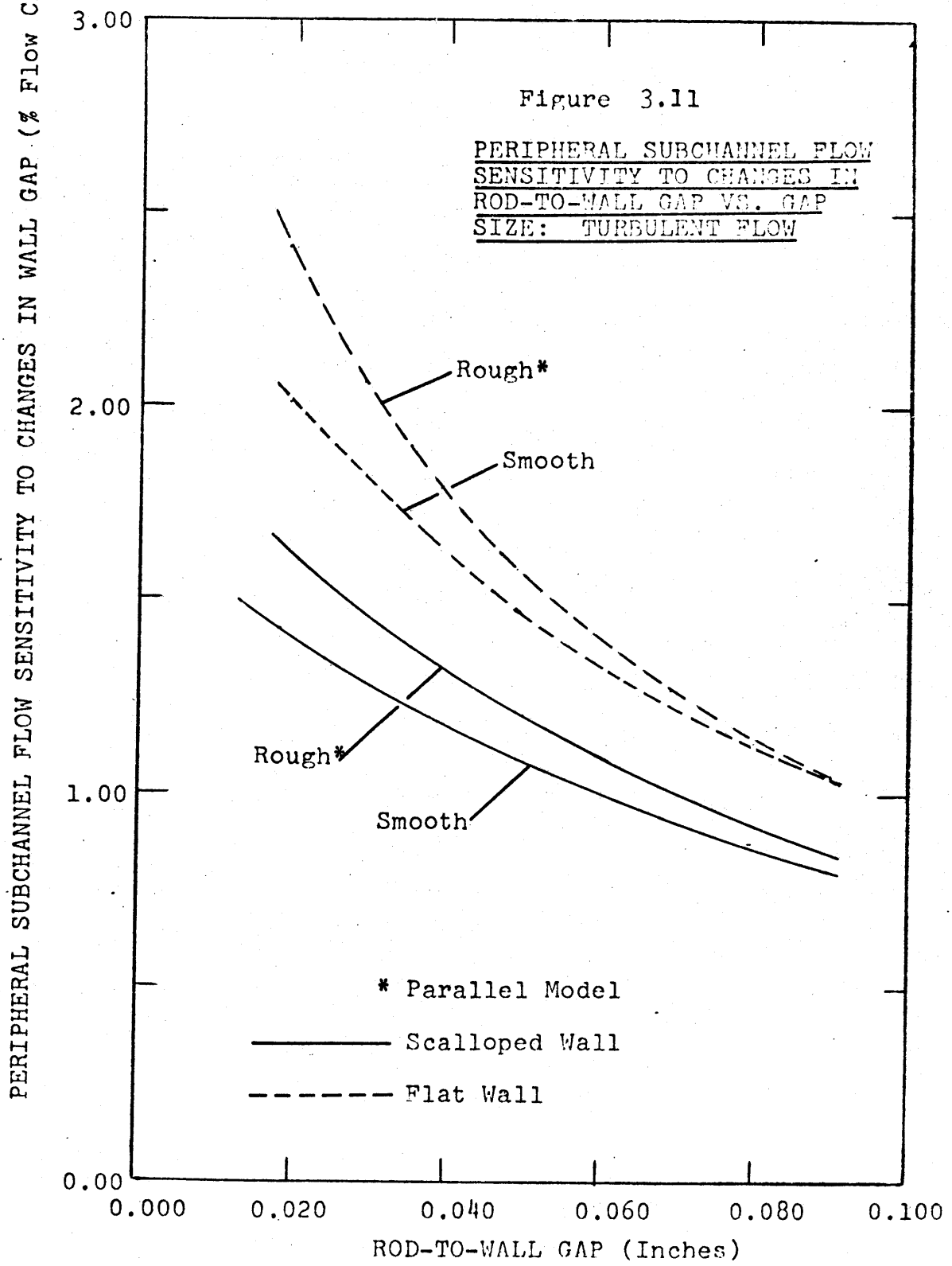

Figure 3.11

PERIPHERAL SUBCHANNEL FLOW SENSITIVITY TO CHANGES IN ROD-TO-WALL GAP VS. GAP SIZE: TURBULENT FLOW

Of particular importance in a detailed thermal-hydraulic analysis would be the inclusion of the effects of interchannel coolant mixing, radial pressure gradients (flow development) and radial power gradients. Consideration of these effects requires that the flow and temperature of each subchannel be uniquely determined at each axial location considered throughout the fuel element.

Computer codes which perform detailed thermal-hydraulic analyses of rod array type nuclear fuel elements are readily available; however, these codes (to date) have not dealt with roughened rod arrays using single-phase gaseous coolants. One of the more common series of codes for performing detailed rod arrays thermal-hydraulic analyses, the COBRA codes, is limited by the restrictions noted.

The COBRA codes [R2, R3, R4, R5, W5] can deal with rapid axial changes in density such as those occurring in a boiling water reactor BWR. Therefore, the COBRA codes can be expected to deal effectively with the density changes typical of a GCFR, i.e., an inlet density of 0.43 lbm/ft^3 and outlet density of 0.29 lbm/ft^3. Very importantly, however, the COBRA codes with their tabular look-up of two-phase coolant properties cannot deal with the pressure and temperature dependence of helium

thermodynamic and transport properties. Although the COBRA codes can be run with liquid coolants, e.g., subcooled water or liquid metals, without modification; this is not possible with a gaseous coolant.

The modifications to the COBRA-3C code required to permit its use with roughened, gas-cooled, rod array-type nuclear fuel elements have been completed as part of this project. Limitations in time and money have prevented verification of the modified version of the code which is called COBRA-3H.

Included in the modifications was the deletion of the following capabilities from the code: (A) two-phaseflow, (B) fluid property tables, (C) wire-wrap spacers, and (D) plate type fuel elements; the following subroutines were removed from the COBRA-3C code: VOID, BVOID, HCOOL, CHF, CHF1, CHF2, SCQUAL, ELAP, TOD, and DOY; the following subroutines (as well as the main program) were modified significantly: TEMP, PROP, and FORCE. The following subroutines were added to the code: TPPROP (HELIUM) and TFIND. For future development work, it might be desirable to add two addition subroutines: ROUGH and GEOMET. The modified code COBRA-3H has approximately 1000 cards less than the original COBRA-3C

(approximately 3300 cards).

Subroutine TPPROP (HELIUM) was added during the modification in order to calculate the properties of helium. Knowing the temperature TT and absolute pressure PP, TPPROP calculates thermodynamic properties using an equation of state and transport properties using correlations. The following quantities are calculated: specific heat at constant pressure, density, enthalpy, dynamic viscosity, thermal conductivity, and Prandtl number. Subroutine TFIND was added to determine the coolant temperature when only pressure PFIND and enthalpy HFIND are known.

For future work it might be convenient to add a subroutine GEOMET to calculate geometrical information for the various subchannel types. The addition of a subroutine ROUGH to determine the roughened surface performance within the nuclear fuel element might also be desirable.

The COBRA-3H code (unverified) has not been listed here in order to conserve space (40 pages). Listings of the code and additional details may be obtained from the author.

CHAPTER IV

THE EXPERIMENTAL PROGRAM

This work included a substantial experimental effort using a 37-rod hexagonal rod array. The experimental determination of pressure losses, velocity profiles, and coolant mixing is a mandatory requirement for the verification of analytical methods and for the determination of empirical coefficients for computer codes.

4.1 The Experimental Objectives

4.1.1 The Data Desired

The objectives of the experimental program were to determine (a) rod array friction factors and spacer grid loss coefficients using an axially moving static pressure tap, (B) outlet velocity profiles using a pitot tube, and (c) interchannel cooling mixing using salt solution tracer tehcniques.

4.1.2 The Parameters Varied

All experimental data was taken using both smooth and rough for arrays; in this manner the effects of surface roughening on rod array hydraulics were determined. The effect of flow regime, i.e., laminar or turbulent, was determined in both cases. It was also of interest to determine the effect of Reynolds number on the hydraulic behavior of the rod arrays in turbulent flow. The effect

of injection subchannel type, i.e., whether an interior or peripheral subchannel, was determined for each case considered.

The experimental data collected and the parameters varied have been summarized in Table 4.1. The balance of this Chapter discusses the experimental facility and the instrumentation method used for the experiments. The experimental results are given in Chapter 5.

4.2 Experiment Design and Construction

Briefly, the experimental facility was a 37-rod, hexagonal bundle similar to the AGATHE bundle at E.I.R.: the rod diameter was 0.331 inches (0.841 mm) with a lattice pitch-to-diameter ratio of 1.30. Water was used for the flow media. The hydraulic facilities were capable of operating the experimental rod bundle at Reynolds numbers as high as 50,000.

Overall pressure losses of the experimental rod bundle were measured using Bourdon tube gages. Rod bundle friction factors and spacer grid losses were determined using an axially traversing static pressure tap. Exit velocity profiles were measured using a pietotube. Interchannel coolant mixing experiments were performed using an axially traversing salt tracer injection technique developed by Eaton and Todreas [E2].

TABLE 4.1

THE EXPERIMENTAL PROGRAM

I. Rod Array Pressure Losses:
Friction Factors and Grid Loss Coefficients
- Roughened Surface Effects
  - Smooth Rod Array
  - Rough Rod Array
- Flow Rate Effects
  - Turbulent Flow Regime
- Subchannel Effects
  - Interior Subchannel
  - Peripheral Subchannel

II. Rod Array Outlet Velocity Profiles
- Roughened Surface Effects
  - Smooth Rod Array
  - Rough Rod Array
- Flow Rate Effects
  - Turbulent Flow Regime
- Subchannel Type Effects
  - Interior Subchannels
  - Peripheral Subchannels
  - Corner Subchannels

III. Interchannel Coolant Mixing Data
- Roughened Surface Effects
  - Smooth Rod Array
  - Rough Rod Array
- Flow Rate Effects
  - Laminar Flow Regime
  - Turbulent Flow Regime
- Injection Subchannel Type Effects
  - Interior Subchannel Injection
  - Peripheral Subchannel Injection

4.2.1 The Experimental Rod Array

In order to perform the hydraulic experiments, a 37-rod test section was constructed. The rod array had a hexagonal overall shape and was 60 inches (1520 cm) in length. The rod diameter used was 0.331 inches (8.41 mm) and the rod-to-rod pitch was 0.430 inches (10.9 mm); the pitch-to-diameter ratio was 1.30.

The design of the experimental rod array was governed by the decision to use AGATHE grid spacers which were supplied to this project by the General Atomic Company [The AGATHE tests are a series of heated rod array experiments (which use gaseous cooling) that are being performed at E.I.R. in Switzerland]. The "egg crate" rod spacer assembly was about 3/4 inches thick and was welded to the base of a 7-3/4 inch long flow shroud. The test section contained eight grid assemblies positioned end-to-end so that the top of the grid assemblies was flush with the flow outlet of the test section. The test section was assembled with the rod spacer grid located on the downstream end of the spacer assemblies. Complete details regarding the AGATHE grid spacer geometry are given in reference [Z1]. The grid spacer is illustrated in Figure 4.1.

Details of the MIT hydraulic experiment test section

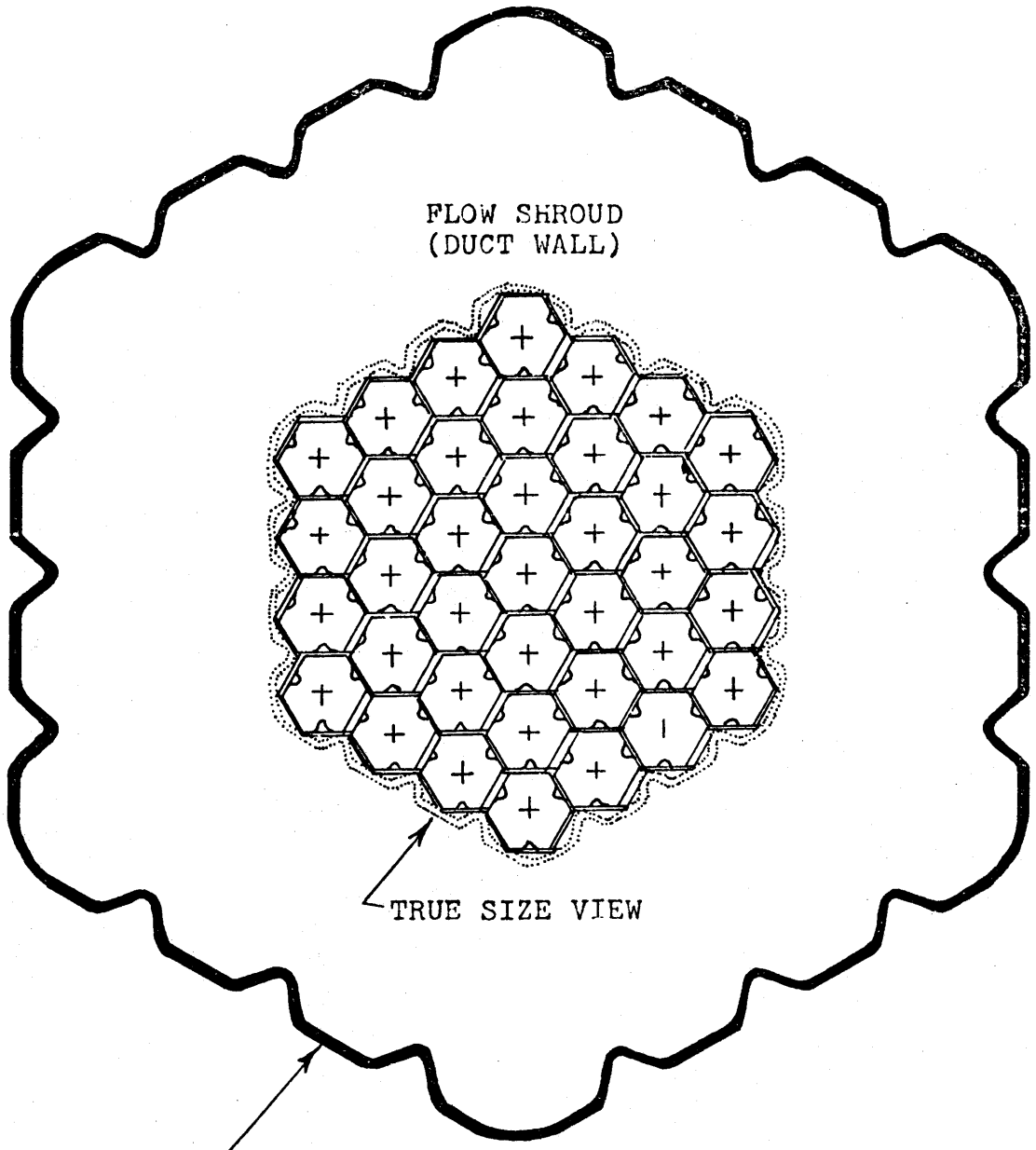

FIGURE 4.1

THE AGATHE 37-ROD, HEXAGONAL SPACER GRID ASSEMBLY

are given in Table 4.2 along with the respective values for a typical GCFR fuel element, see also Table 4.3.

A cross section of the test section is shown in Figure 4.2; the flow duct is made of two "Vee-Channels" and two end plates (a brass end plate and lucite end plate). Bolts passing through the end plates and the Vee-Channel every two inches held the assembly together. It is important to note that the fluted shroud on the rod array spacer assembly formed the flow boundary, and the flow duct acted only as a pressure boundary, see Figure 4.1.

Two sets of rods were manufactured for use with the rod array: a smooth set and a rough set. The rods were turned down to 0.331 in. O.D. from an original O.D. of 0.375 in. using a lathe. Cutting tool marks were removed from the rods by progressive sanding with 120 and 240 emery paper. The roughened rods were roughened over the downstream half of the rod length (30 in.). In the GCFR, the smooth rod length in the axial blanket on the upstream end is 17.7 inches and the smooth rod length in the active core region is 9.8 inches so that experimental rods with a 30 inch roughened length and a 30 inch smooth length were similar to the GCFR fuel element, i.e., 27.5 inches smooth and 29.4 inches rough. Hydraulic

TABLE 4.2

EXPERIMENTAL ROD ARRAY AND
GCFR FUEL ELEMENT PARAMETERS*

	EXPERIMENT	GCFR
Rod Diameter - Outside Diameter (Smooth), Over Ribs (Rough)	0.331 (8.41)	0.285 (7.24)
Rod Root Diameter - Roughened Region	0.319 (8.10)	0.273 (6.93)
Rod-to-Rod Pitch -	0.430 (10.9)	0.389 (9.88)
Rod Pitch-to-Diameter Ratio -	1.30	1.36
Rod-to-Wall Gap -	0.065 (1.65), Nominal	0.048 (1.22), Nominal
Number of Rods -	37	271
Rod Array Shape - (Overall)	Hexagonal	Hexagonal
Rod Array Lattice	Triangular (Equilateral)	Triangular (Equilateral)
Rod Length	60.0 (1525)	39.2 (996), Active Core

TABLE 4.2 (continued)

Roughened Length -	30.0 (762), Downstream End	29.4 (747)[a] Downstream End
Roughened Surface Rib Height, e -	0.006 (0.152)	0.006 (0.152)
Roughened Surface Rib Pitch, p -	0.072 (1.83) p/e = 12	0.072 (1.83) p/e = 12
Roughened Surface Rib Helix Angle -	12.7° Single Start Helical Rib	0.0° Transverse Rib
Roughened Surface Rib Width, w -	0.018 (0.457) w/e = 3	0.018 (0.457) w/e = 3
Roughened Surface Rib Geometry -	Trapezoidal[b]	Trapezoidal[b]
Relative Surface Roughness, e/d_e -	0.025	0.021
Equivalent Hydraulic Diameter (Bundle Average) -	0.238 (6.05)	0.284 (7.21)

TABLE 4.2 (concluded)

Flow Duct Width (Across Flats)	2.70 (68.6)	6.44 (164.)
Spacer Type -	AGATHE Grid (Similar to GCFR)	Grid
Spacer Grid Axial Separation -	7-3/4 (197) Nominal	10. (254) Nominal

* Dimensions given are in inches (millimeters)

a 3/4 of active core length on the downstream end.

b See Figure 4. 3, same as General Atomic Co. Drwg. No. 5001-15, 30 April 1973.

TABLE 4.3

EXPERIMENTAL ROD BUNDLE PARAMETERS*

Rod Diameter = 0.331 (8.41), Smooth and Over Ribs
Rod Root Diameter - 0.319 (8.10), Rough
Rod-to-Rod Pitch = 0.430 (10.9)
Pitch-to-Diameter Ratio = 1.30
Rod-to-Wall Gap = 0.065 (1.65)[1] (nominal)
Number of Rods = 37
Rod Bundle Shape (Overall) = HEXAGONAL
Rod Bundle Lattice - Equilateral Triangular
Rod Leng = 60.0 (1525)
Roughened Length = 30 (762) on Downstream End
Roughened Surface Rib Height = 0.006 (0.152), e
Relative Roughness = 0.018, e/D
Roughened Surface Rib Pitch = 0.072 (1.83), p/e = 12
Roughened Surface Rib Width = 0.018 (0.457), w/e = 3
Roughened Surface Rib Helix Angle = 12.7°, Single Start
Roughened Surface Rib Geometry = Trapezoidal[2]
Rod Material = Phosphor Bronze, Free Machining
AGATHE Grid Spacer Material = 304 SS
AGATHE Grid Spacer Across Flats Dimension = 2.80 (71.1), nominal

EXPERIMENTAL TEST SECTION DETAILS*

Across Flats, Hexagonal Duct Inside Dimension = 2.800 (71.1)
Vee Channel Wall Material = Brass, Free Machining
Flat Channel Wall Materials = One (1), 1/4" Brass, Free Machining
= (1), 1" Lucite
Channel Length = 60 (1525)
Plenum Material = 8" steel pipe (Sch 40)
Test Section Connecting Piping = 3" Steel Pipe (Sch 40)
Test Section Drain Piping = 4" Plastic Pipe (Sch 40)
Main Flow Meter = Oriface By-Pass Rotameter (370 GPM Max.)
Pressure Gage = High Accuracy Bourdon Tube Gage
(± 1/4% accuracy, 150 psig max.)
Assembly Bolt Size = 1/4
Assembly Bolt Material = Brass
O-Ring Seal Material = Neoprene, 0.125 in D
Channel Overall Outside Dimensions = 4-5/8 × 4-1/8
Channel Overall Outside Geometry = Rectangular
Assembly Bolt Spacing = 2
Assembly Bolts Required = 60
Weight ≈ 220 pounds (100 kg)

Notes: * All dimensions in inches (millimeters)
1 - Dimension given for AGATHE grid spacer
2 - Refer to General Atomic Co. Drawing 5001-15, dated 30 April 1973.

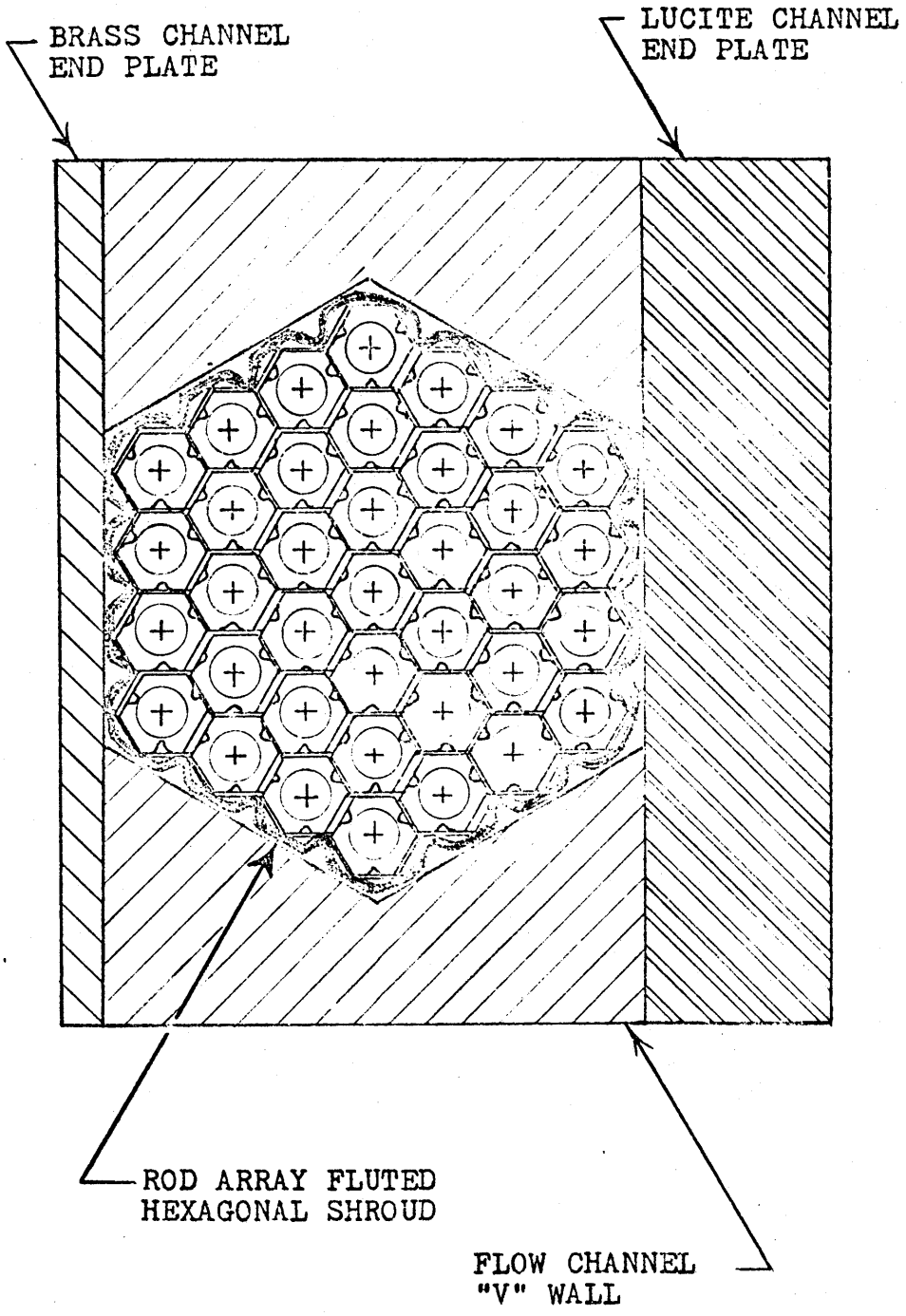

FIGURE 4.2 - CROSS SECTION OF THE TEST SECTION BUILT FOR THE HYDRAULIC EXPERIMENTS (MIT)

conditions at the test section outlet were expected to be similar to those at the GCFR fuel element outlet in that the upstream geometries were similar.

The roughened surface design used for the test section rod array was similar to that used in the GCFR. However, the relative roughness was slightly different for the test section and the GCFR (0.021 vs. 0.020, respectively) due to differences in rod array geometry. The roughened surface geometry is illustrated in Figure 4.3. Based on the author's review of the literature, the design of the roughened surface appears to be near optimum.

4.2.2. The Tracer Injection System

The salt solution tracer used in the interchannel coolant mixing experiments was uniformly mixed with a known salt concentration and poured into a 30 gallon injection tank. The tank was pressurized with laboratory compressed air to cause the tracer solution to flow into the experimental rod array. During the experiment, the injection flow was held constant and was carefully metered. The injection flow rate was determined from the "equal velocity criterion" which is discussed later in Article 4.3.4.

The primary hardware item in the injection system was the axially traversing tracer injection device

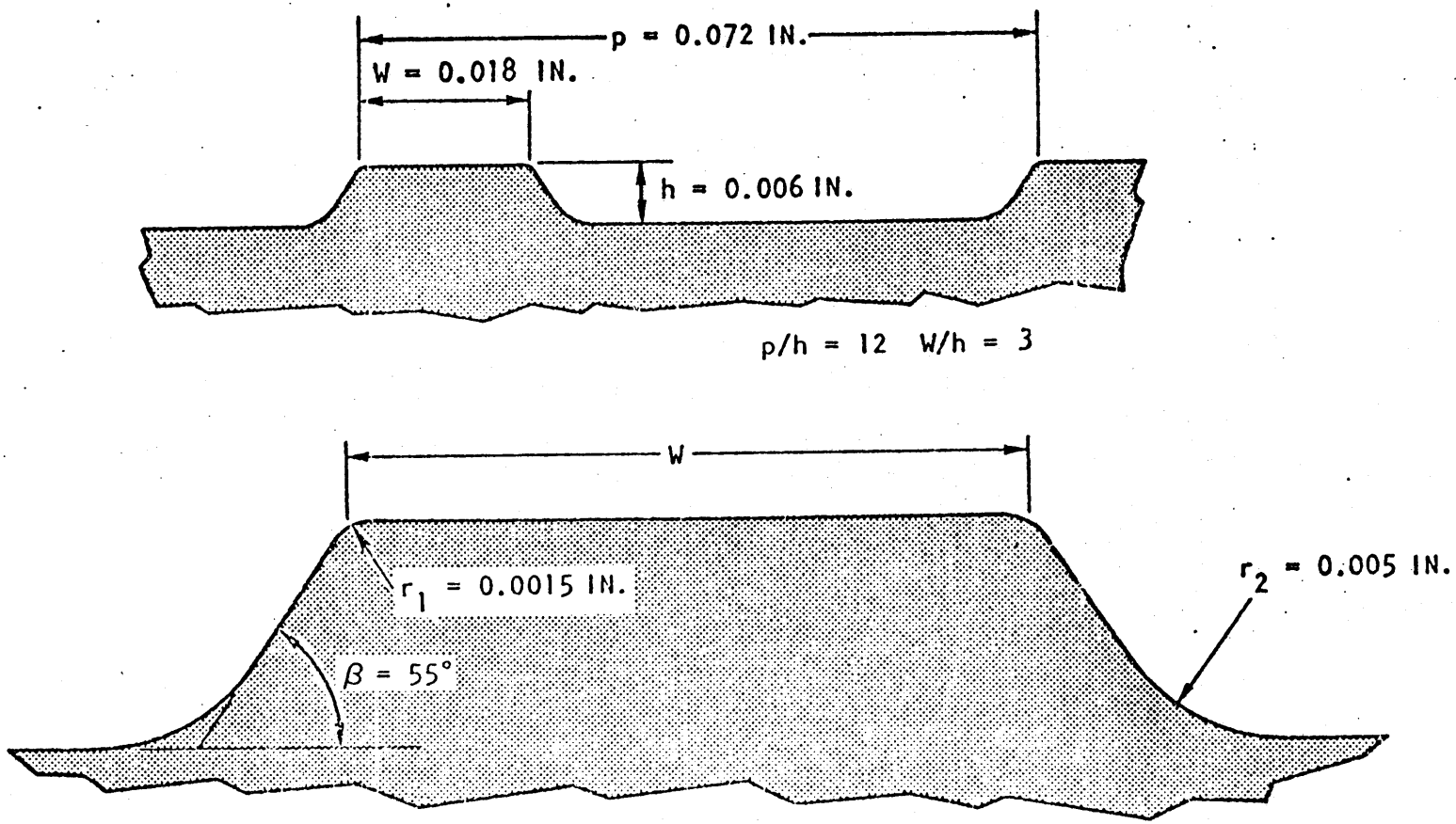

FIGURE 4.3

DETAILS OF THE SURFACE ROUGHENING OF THE ROD ARRAY

conceived by T.E. Eaton in Summer, 1971, with subsequent development reported in USAEC Report COO-2245-9 TR [E2]. The injection device was basically two concentric tubes of which the inner tube was free to move axially. The outer tube had a narrow slot machined along the upper half of its length, see Figure 4.4. The outer tube was oriented such that the slot was positioned toward the centroid of the injection subchannel. The moving inner tube had a 0.033 in. I.D. (0.84 mm) stainless steel hypodermic tube mounted so that it extended through the tube wall at an axial position near the tube midpoint. This hypodermic tube was mounted with its centerline passing through the centerline of the moving tube at the smallest angle practical (typically 20°-25°), see Figure 4.5. This mounting technique resulted in the minimum-practical disturbance of the main flow due to the injector design [E2]. The inner tube was positioned radially so that the tracer stream flowing through the hypodermic tube passed through the slot in the outer tube and into the injection subchannel.

From the early coolant mixing experiments done for this project, it was observed that the tracer stream was remaining inside the slot (0.040 inches wide × 0.07 inches deep) in the wall of the outer concentric tube of the injection rod assembly. To alleviate this problem, a

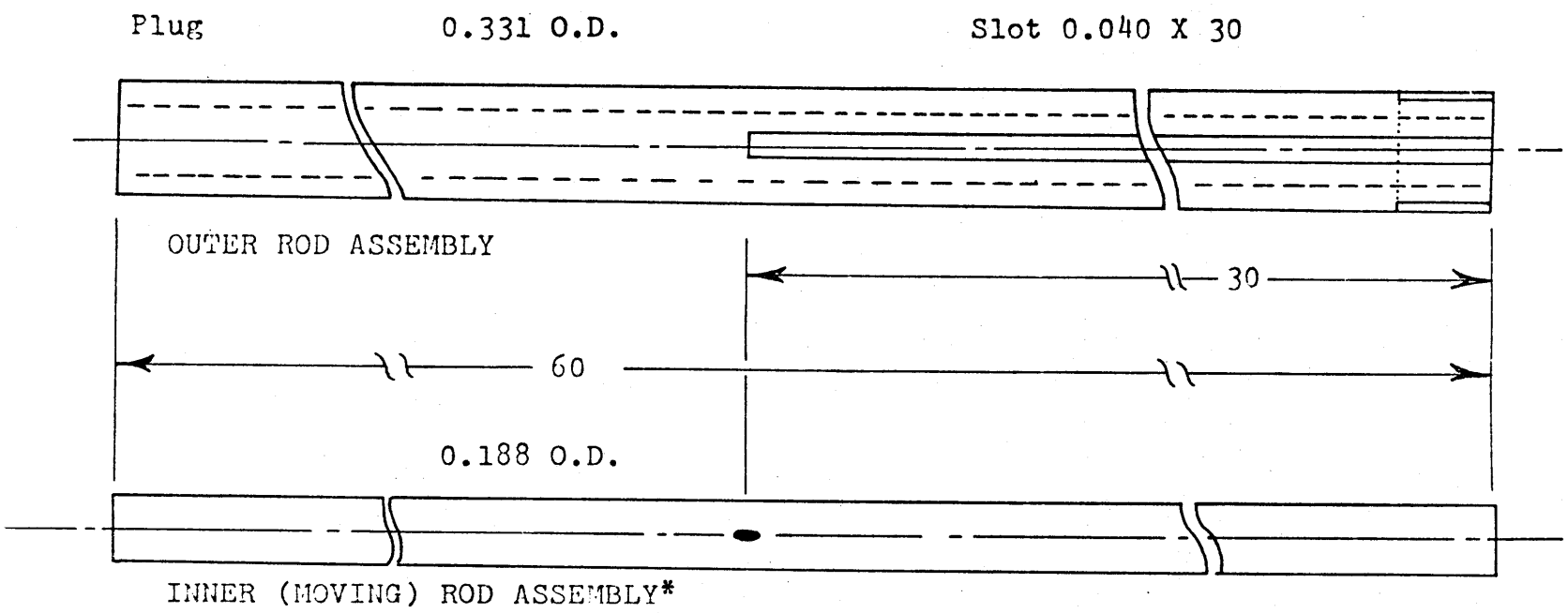

* Inner rod must move freely inside outer rod after assembly

Note: Dimensions in Inches
Scale 2 X True Size
Material - 304 SS

FIGURE 4.4

INJECTION ROD ASSEMBLY DETAILS

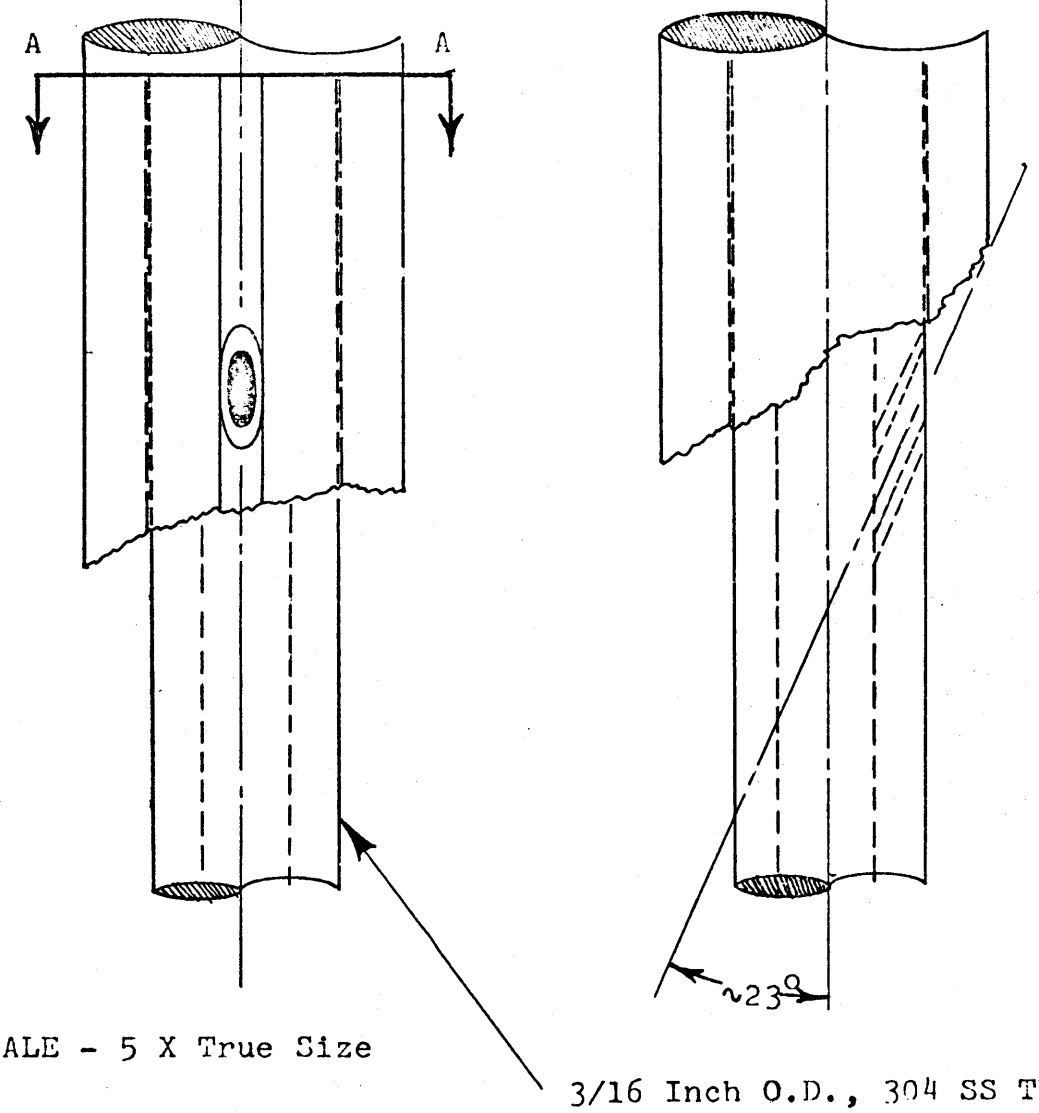

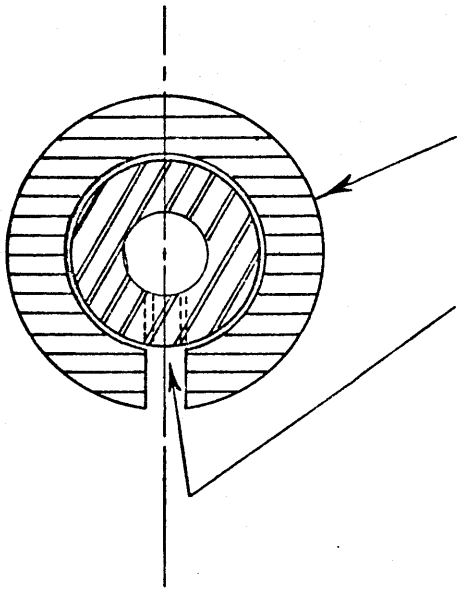

FIGURE 4.5

INJECTOR DETAILS

"follower" device was attached to the inside tube of the injection rod assembly so as to force the flow contained within the slot out into the injection subchannel. This follower device was located about one inch downstream from the injector needle and filled the slot for a distance of about two inches.

4.2.3 The Main Flow System

The main flow system provided the flow through the experimental, rod array test section. The flow media used for the experiments was water that was drawn from a large (∿ 50,000 gallons) subfloor canal near the experimental facility. The water was pumped by two centrifugal pumps arranged so that they could be operated either in series (for high outlet pressure) or in parallel (for high operating flows). The pump facility served either of two experiments and was provided with flow regulating valves, see Figure 4.6.

The main flow discharged from the pumps was metered before entering the high pressure plenum of the experimental facility. Either of two parallel main flow paths could be used to measure the main flow: the high flow loop and the intermediate flow loop. The high flow meter was a by-pass oriface plate meter which measured flows between 50 to 370 GPM ± 15 GPM. The intermediate flow loop

measured main flows from 5 to 50 GPM (± 1 GPM) using two large rotameters connected so as to be used either independently or in parallel.

The main flow entered the high pressure (lower) plenum horizontally and was turned upward. It then passed through a flow straightening device and entered the test section. The test section was 60 inches long (1.5 meters) and contained eight grid spacers. The main flow discharged into an open outlet plenum and then to the subfloor canal via a PVC drain line. The main flow returned to the canal about 35 feet from the pump intake. Because the canal is continuously purged and because the salt solution tracer flow was small, changes in the background (main flow) conductivity were small.

Although the GCFR uses a compressed gas (helium) as a coolant, the experiment used water, an incompressible fluid, to model the flow media of the GCFR. During normal operation, the coolant flow velocity in the GCFR is of the order of 300 ft/sec; the sonic velocity of the coolant rages from 5000 to 6000 ft/sec. Because the ratio of coolant flow velocity to sonic velocity, i.e., the Mach number, is less than 0.3, the flow of the GCFR fuel element may be considered as incompressible. A Mach number of 0.06 is well within the range of incompressible

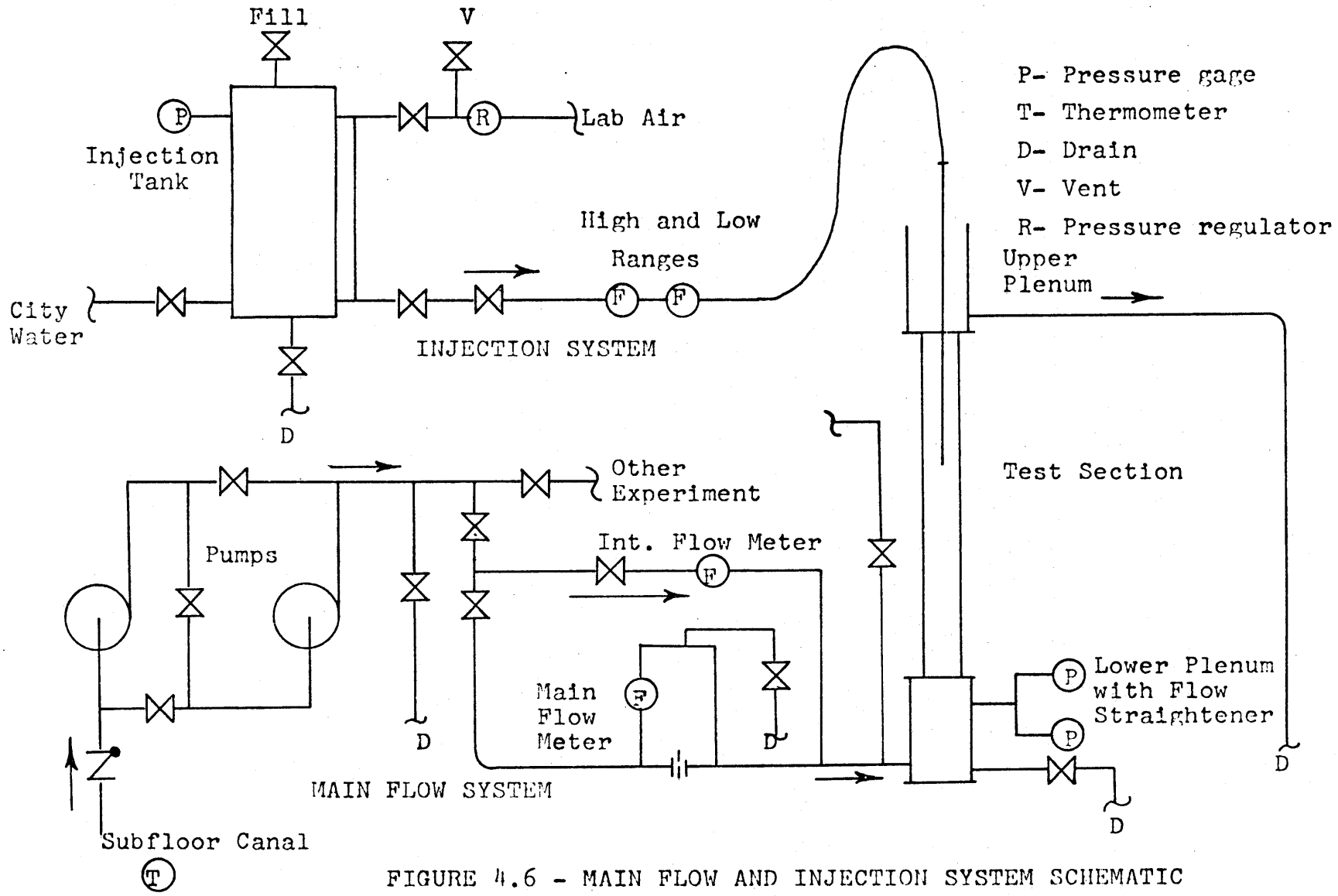

FIGURE 4.6 - MAIN FLOW AND INJECTION SYSTEM SCHEMATIC

flow, generally considered to range from Mach numbers of 0.0 to 0.3 or 0.5. Because the helium flow in the GCFR is incompressible, water could be used to model the helium flow.

4.2.4 Subchannel Conductivity Probe Design and Operation

The subchannel salt solution concentration in the coolant mixing experiments was measured using a custom-designed conductivity probe, i.e., an electrolytic conductivity cell, which was initially developed by Eaton and Todreas [E2].

The conductivity probe is illustrated in Figure 4.7; the two platinum wires extending from the end of the probe constituted the heart of the conductivity cell. Once these platinum wires had been properly platinized and the cell calibrated, the probe could be used to determine the solute concentration of an electrolytic solution in which it was submerged.

Complete details on the use of conductivity probes for interchannel coolant mixing experiment may be found in Eaton and Todreas (E2); the report discusses the electrical behavior of electrolytic solutions and conductivity cells, as well as conductance measurement techniques.

4.3 The Instrumentation and Measurement Techniques

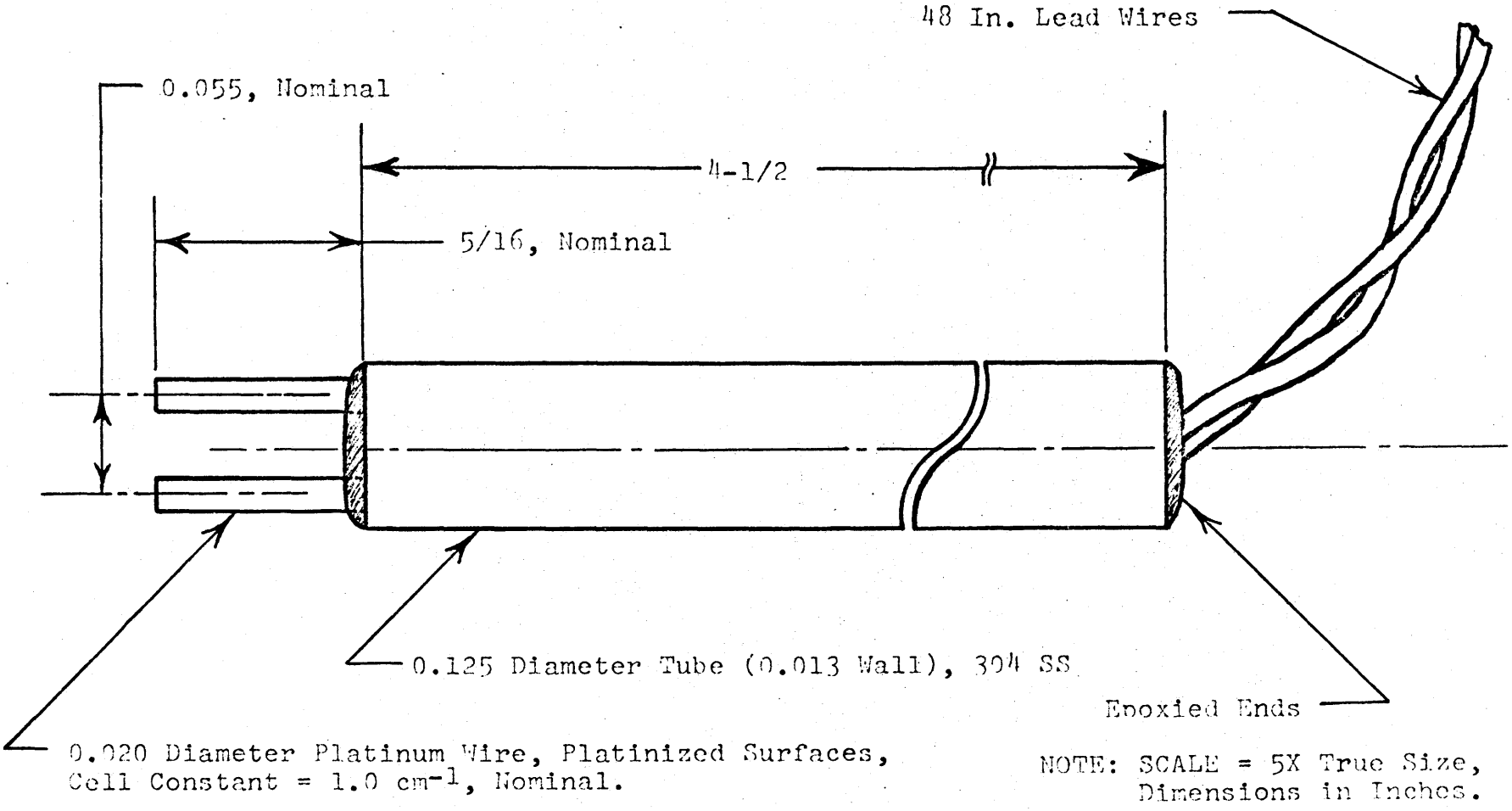

FIGURE 4.7

CONDUCTIVITY CELL INSTRUMENTATION (DETECTION) PROBE

4.3.1 Pressure Loss and Flow Velocity Measurements

Axial profiles of the local static pressure in an interior and a peripheral subchannel of the rod array were measured using an axially traversing pressure tap. The injection device used to insert the salt solution tracer into the main flow during the coolant mixing experiments was used for the mobile pressure tap, cf. section 4.2.2. (This experimental technique was conceived by the author during this project in December 1974.) The static pressure inside the rod array was measured using a bellows-type differential pressure gage with the high pressure side connected to the static tap and the low pressure side connected to the flow outlet plenum (bundle exit pressure). From the plotted results of pressure versus axial position, it was possible to determine the friction factors and the spacer grid pressure loss coefficients for the experimental flow conditions (see Chapter 5 for details of the experimental results).

Total test section pressure losses were measured using high accuracy bourdon tube gages connected to the inlet and outlet plenums. The static pressure difference between the lower and upper plenums was taken as the total

test section pressure loss.

The flow velocity in various subchannels of the rod array was measured at the test section exit using a commercial pitot-static probe which measured both total and static pressure. The total and static pressure taps were connected to the high and low pressure side, respectively, of a bellows-type differential pressure gauge. With this arrangement, the dynamic pressure P_d (in Inches of Water) was measured directly and was related to flow velocity V (ft/sec) by

$$V = 2.32 \sqrt{P_d} \ . \qquad \text{(Eq. 4.1)}$$

The pitot-static probe used had a total pressure sensing diameter of 0.020 inches (0.51 mm). The static pressure was measured with several static taps located 0.25 inches (6.4 mm) above the total pressure tap. Further details on the velocity probe are given in reference [U1] while all equipment used for the experiments has been listed in Appendix 4.

4.3.2 Interchannel Coolant Mixing Experiments Using Salt Solution Tracers

In order to assess the interchannel coolant mixing in the experimental rod array, a salt solution tracer was injected into the main flow of an interior

and a peripheral subchannel of the test section. The injected tracer then traveled with the main flow and was dispersed transversely by the various fluid mixing mechanisms discussed in Appendix 3.

The injection device, discussed earlier in Section 4.2.2, was used to inject tracer over the upper 28 inches (110 cm) of the rod array while conductivity probes (see section 4.2.4) monitored the transverse tracer dispersion at the rod array outlet.

In the data gathering process, the injector-detector (probe) separation distance was held constant as the probe electrical signals were recorded in each subchannel of interest at the rod array outlet. The injector-detector separation was then changed and the subchannel data again recorded; this process continued, using whatever axial injector travel increments the experimenter selected until all the data for a given experiment had been taken. This axially detailed coolant mixing data provided a lucid view of the mixing phenomenon; this experimental technique was developed under the sponsorship of the USAEC Coolant Mixing Project at MIT, see Reference [E2] for complete details.

The processing of salt solution tracer data from coolant mixing experiments performed at MIT using smooth

and rough rod arrays was done using a computer code anmed MITMIX-R (modified from Eaton [E2]). Further details regarding the MITMIX-R code are given in Appendix 5.

4.3.4 Operating Procedures for the Coolant Mixing Experiments

The data for the coolant mixing experiments was taken using an automated data acquisition system constructed by A.S. Hanson (MIT: USAEC Coolant Mixing Project). This system, illustrated schematically in Figure 4.8, used a parallel resistor, current-dividing technique to determine a resistance characteristic of a specific subchannel solution; further details regarding this system are available in references [H1, H2].

Each of the subchannel probes (approximately 50 are required) was connected to an automatic switching device, a multiplexer, which individually connected each of the probes to the resistance measurement circuit. The probe signal was processed and then digitized by a digital voltmeter. The digitized signal was then recorded on a teletype machine which produced a paper tape record of the data. Under the control of the serial transmitter, the system sequentially recorded the signal in each subchannel and stopped. Under the control of the operator,

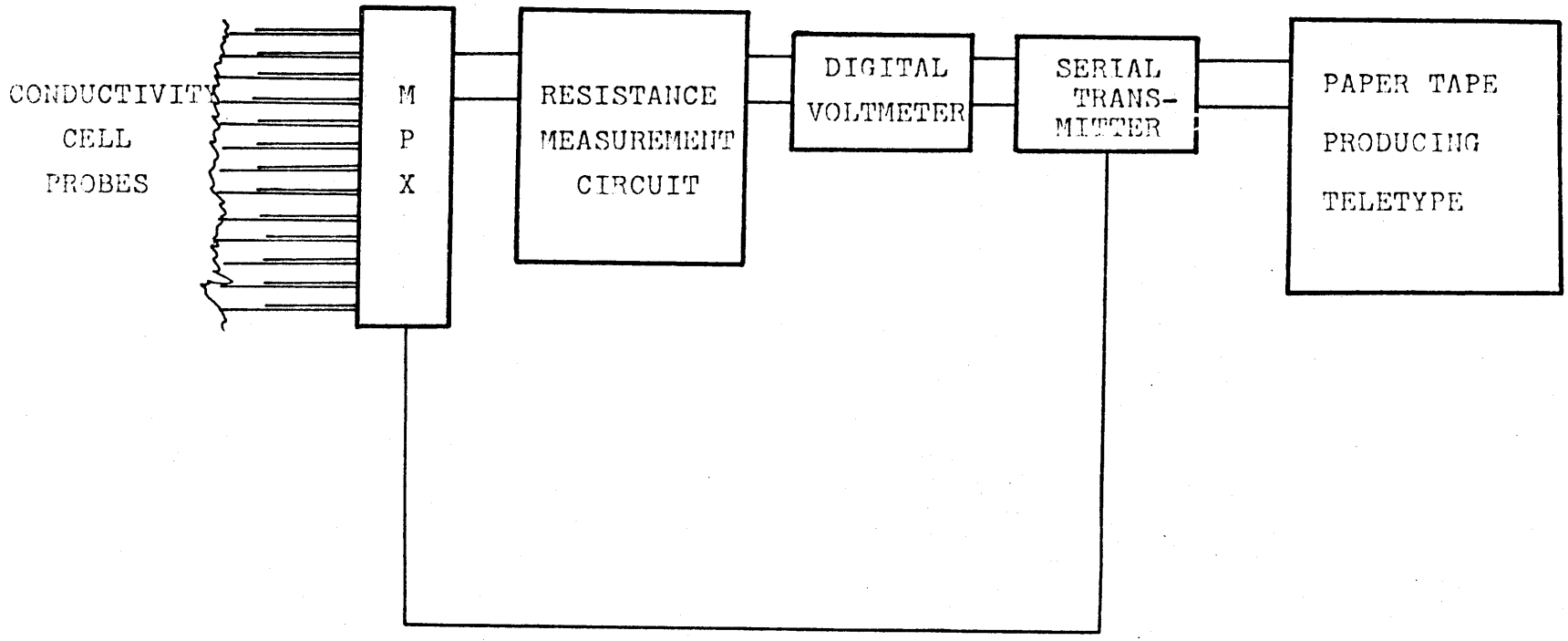

FIGURE 4.8 - SCHEMATIC OF THE INTERCHANNEL COOLANT MIXING DATA ACQUISITION SYSTEM

the injector-detector (probe) separation distance was changed, and the recording cycle initiated. In this manner, an axially -detailed set of coolant mixing data was obtained.

An important operating criterion for the coolant mixing experiments was the ratio of injection flow to injection subchannel flow. In prior development work [E2], it was shown that the minimum main flow perturbation due to tracer injection occurs when the average axial injection velocity was approximately equal to the average axial velocity of the injection subchannel. Main flow perturbations were found to increase with increasing injection velocity, and the best experimental results were obtained using the "equal average axial velocity criterion."

Using the equal velocity criterion, the injection flow rate W_{inj} was given by

$$W_{inj} = \frac{W_i A_{inj}}{\cos(\alpha)\ A_i} = \frac{X_{ib} W_b A_{inj}}{\cos(\alpha)\ A_i} \qquad \text{(Eq. 4.2)}$$

where α was the angle the injector hypodermic tube made with the vertical, W_i was the flow rate in the injection subchannel, and A_i and A_{inj} were the respective flow areas of the injection subchannel and the injection tube. W_{inj} was related to the total test section flow

rate W_b using the injection subchannel flow split factor X_{ib}. Flow split factors could be determined experimentally or analytically and were influenced by the flow regime, surface roughening and subchannel geometry. Typical errors in determining the parameters in Eq. 4.2 do not cause errors in the injection flow rate which are large enough to significantly influence the coolant mixing results, cf. reference [E2].

Before the experiment, a calibration curve was generated for each conductivity probe with the probe in position for the experiment. The calibration procedure involved mixing several solutions of known concentration and using them to fill the test section. When the test section had been filled with a calibration solution, the electrical signal of each subchannel probe was recorded using the data acquisition system. The solution was then drained, and the test section filled with another calibration solution. Finally, a calibration curve of probe signal versus concentration was obtained via a curve-fit of the calibration data.

The probe calibration curve was used to translate the probe signal obtained during the coolant mixing experiments into salt solution (tracer) concentrations. The primary distinction between the mixing experiment

measurement conditions and the calibration conditions was that in the case of the calibration, the solution was uniformly mixed.

However, in the case of the experiments, the solution was flowing and may or may not have been uniformly mixed. Within the experimental rod array the tracer was dispersed almost entirely by coolant mixing mechanisms. This non-uniform concentration consideration was important because conductivity probes function properly only when submerged in solutions of uniform concentration. Because of the nature of the tracer mixing, non-uniform tracer concentrations were expected to be a problem primarily when the injector-detector separation was small, say less than about 6 inches.

4.3.5 The Tracer Mass Balance

As a check of the accuracy of the results of a coolant mixing experiment (using a salt solution tracer), the mass of salt detected was compared to that known to be injected, i.e., the tracer"mass balance". The tracer mass injection rate M_i was determined from the metered injection flow rate W_i (constant) and the given tracer injection concetnration C_i (constant) so that:

$$M_i = W_i C_i \quad \text{(grams/min)}.$$

The tracer mass detection rate $M_d(z)$ was determined from the measured subchannel salt concentration $C_{dj}(z)$ and the subchannel flow rate W_j (constant) with the total detection rate being the sum of the rates in each of the n subchannels, i.e.,

$$M_d(z) = \sum_{j=1}^{n} W_j C_{dj}(z) \quad \text{(grams/min)}.$$

The mass balance criterion was simply

$$M_i = M_d(z) \qquad \text{(grams/min)}.$$

Note that the subchannel salt concentrations and thus the tracer detection rate were functions of the separation distance z between the movable injector and the stationary detectors.

The axial dependence of the subchannel salt concentrations resulted from the flow field within the rod array. The subchannel flows were also an important part of the tracer mass balance calculations; from this it was apparent that the main flow or total bundle mass flow W_b (determined from the main flow meter, W_m, in the bundle inlet piping) be equal to the sum of the subchannel flows W_j, i.e.,

$$W_b = \sum_{j} W_j = W_m + W_i \quad \text{(lbm/min)}.$$

W_j was determined either

(1) from analytical flow split calculations or

(2) from experimental velocity measurements.

CHAPTER V

EXPERIMENTAL RESULTS

The results of the rod array experiments regarding outlet velocity profiles, axial pressure profiles and coolant mixing behavior are summarized in Table 5.1.

The subchannel and rod identfiication numbers used for the experimental rod array are shown in Figure 5.1. The salt solution tracer injectors and the static pressure taps were contained within rods 1 and 25 and were oriented toward subchannels 1 (interior) and 48 (peripheral), respectively.

In all pressure profile and coolant mixing experimental result plots, the flow direction is from left-to-right.

5.1 Rod Array Outlet Velocity Profiles

One-dimensional velocity profiles were taken at the rod array outlet using a pitot tube. Four different traverses were used: (A) Central, (B) Offset Central, (C) Corner, and (D) Offset Corner. Prior to the velocity measurement experiments, the pitot tube was visually aligned with the top of the rod array so that the probe traverse corresponded to the velocity traverse indicated in Figure 5.1. The alignment was rechecked at the end of each experiment.

Table 5.1

A Summary of the Experiments

I. Outlet Velocity Profiles

Smooth Rod Array

100 GPM:	Central Profile[2]
	Offset Central Profile
	Corner Profile
200 GPM:	Offset Central Profile
	Corner Profile
250 GPM:	Central Profile
	Offset Central Profile

Rough Rod Array

100 GPM:	Central Profile
	Central Offset Profile
	Corner Profile
	Offset Corner Profile
200 GPM:	Central Profile
	Offset Corner Profile
	Corner Profile
	Offset Corner Profile
250 GPM:	Offset Central Profile

II Axial Pressure Profile Experiments

Smooth Rod Array

50 GPM:	Interior,	Peripheral[1]
100 GPM:	"	"
150 GPM:	"	"
200 GPM:	"	"
250 GPM:	"	"

Rough Rod Array

50 GPM:	Interior,	Peripheral
100 GPM:	"	"
150 GPM:	"	"
200 GPM:	"	"
250 GPM:	"	"

(Table 5.1 continued)

(Table 5.1 concluded)

Spacer Pressure Profiles

Smooth Rod Array, Spacers 6, 7, 8:
200 GPM: Interior, Peripheral

Rough Rod Array, Spacers 6, 7, 8:
200 GPM: Interior, Peripheral
100 GPM: Interior, Peripheral

III. Interchannel Coolant Mixing Experiments

Smooth Rod Bundle

4.8 GPM: Interior, Peripheral[3]
49. GPM: " "
100 GPM: " "
150 GPM " "
200 GPM " "

Spacer Details, Spacers 6, 7, 8:
150 GPM: Interior, Peripheral

Rough Rod Bundle

4.8 GPM: Interior, Peripheral
49 GPM: " "
100 GPM: " "
150 GPM: " "
200 GPM: " "
250 GPM: " "

Spacer Details, Spacers 6, 7, 8:
100 GPM: Interior, Peripheral
200 GPM: " "

IV. Miscellaneous Experiments

Total Test Section Pressure Losses
Rod - Spacer Interaction Forces
Rod Array Exit Presure Profiles

1. Refers to an axially traversing, static pressure probe in either an interior or peripheral subchannel.

2. See Figure 5.1for an illustration of the various velocity profile traverses.

3. Refer to salt solution tracer injection into either an interior or peripheral subchannel.

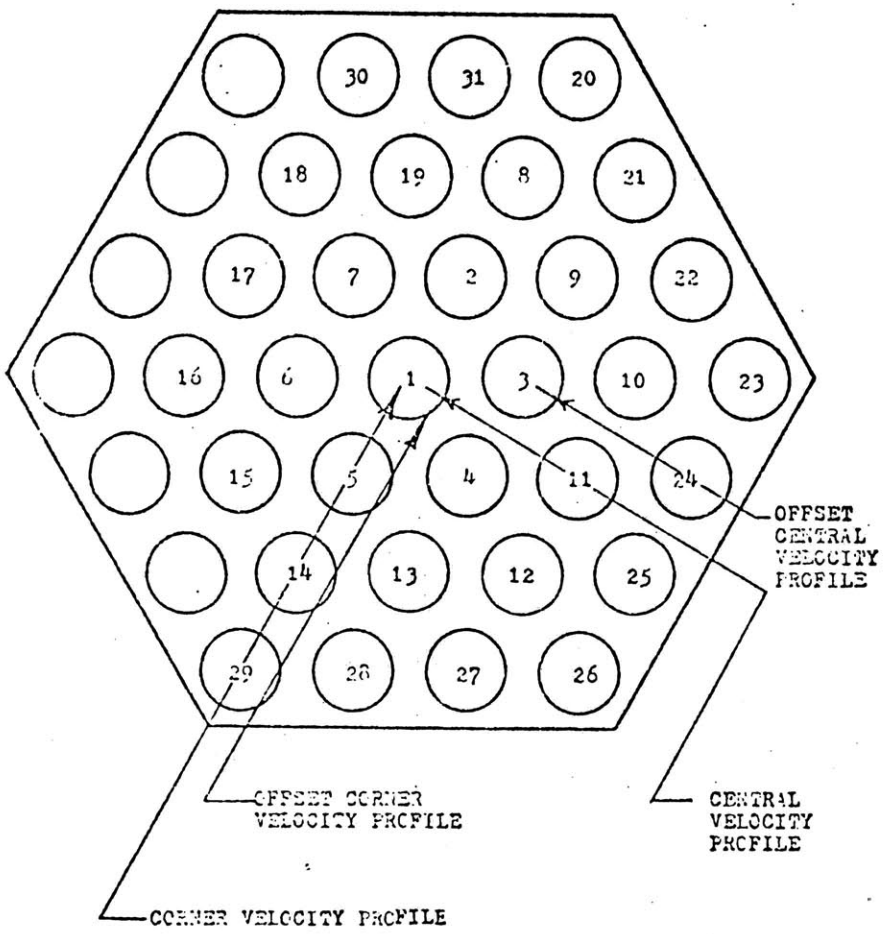

ROD IDENTIFICATION NUMBERS AND VELOCITY PROFILE LOCATIONS

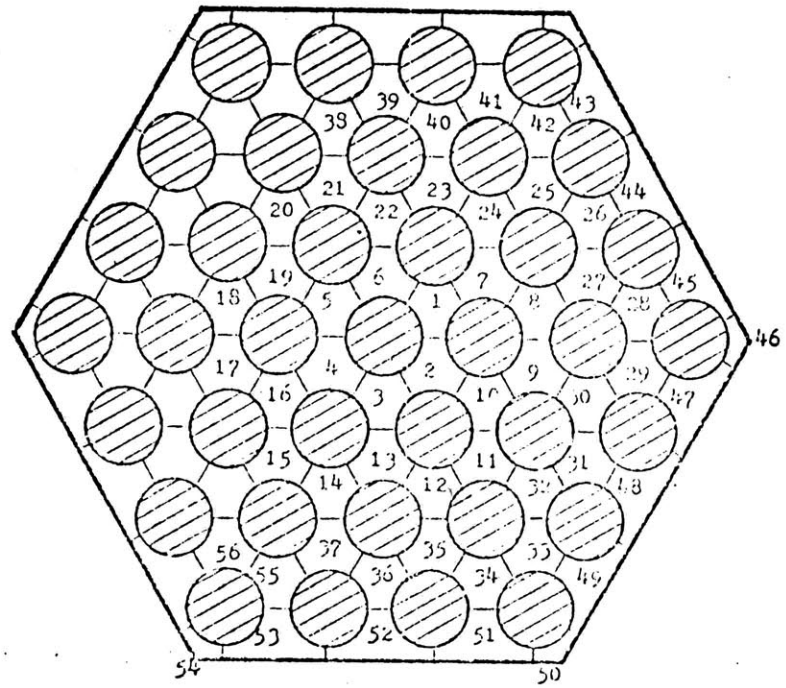

SUBCHANNEL IDENTIFICATION NUMBERS

FIGURE 5.1

SUBCHANNEL AND ROD IDENTIFICATION NUMBERS, VELOCITY PROFILE LOCATIONS

5.1.1 Velocity Profile Results

The velocity profile data has been presented in Figures 5.2 through 5.9. The offset central velocity profiles are shown in Figures 5.2 (100, 200, and 250 GPM) and 5.3 (100, 200, and 250 GPM) for the smooth and rough rod arrays, respectively.

From the offset central velocity profiles, the following observations were noted: (A) the velocity gradients near the roughened walls of the rough rod array were not as steep as was the case for the same walls in the smooth rod array; (B) the velocity in the rod-to-wall gap was higher in the roughened case than the smooth case, and the differences between results for rough and smooth cases increased with Reynolds number; (C) the velocity in the rod-to-rod gap was lower in the roughened case and the differences increased with Reynolds number; (D) the peak-to-average velocity ratio was higher in the roughened rod array, and this ratio increased with Reynolds number in both the smooth and the rough rod arrays (see also section 5.1.4).

The above observations are explained by the increase in flow resistance characteristic of roughened surfaces. Recall that the flow resistance on roughened surfaces when compared to smooth surfaces increases with Reynolds number. Because the flow resistance was higher near the rod surfaces in the rough array than in the smooth array, the flow

FIGURE 5.2

OFFSET CENTRAL VELOCITY PROFILE, SMOOTH ROD ARRAY

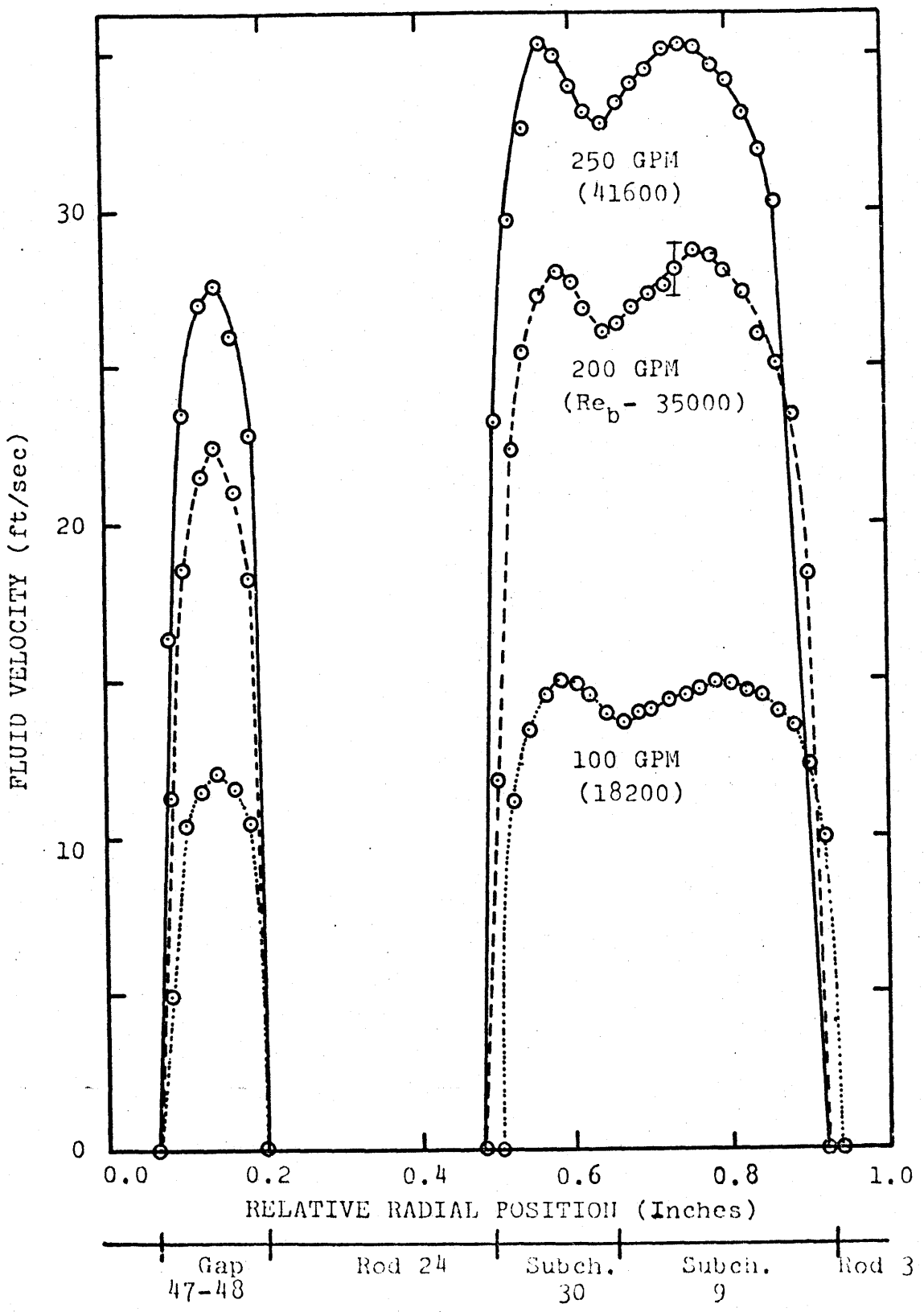

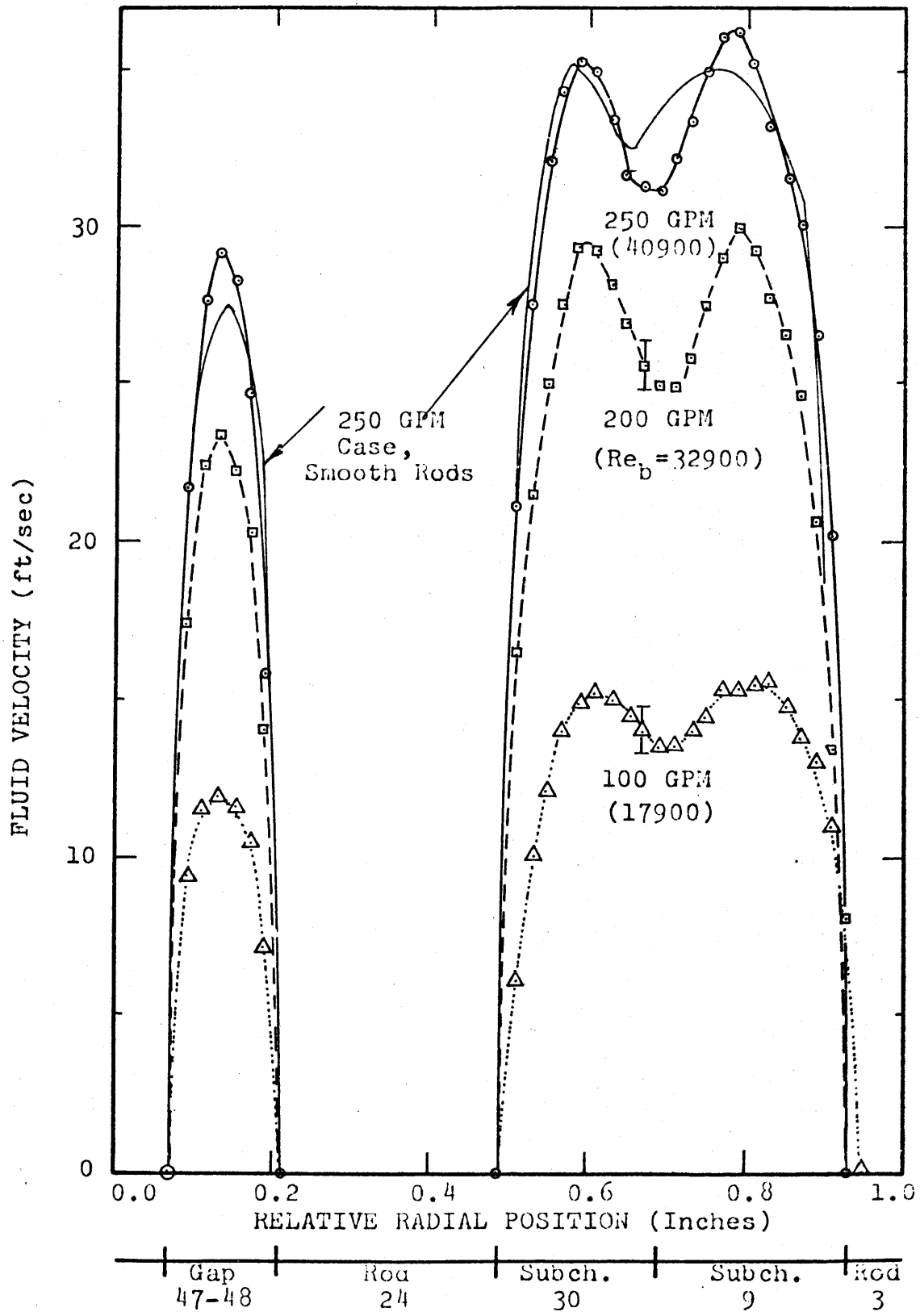

FIGURE 5.3

OFFSET CENTRAL VELOCITY PROFILE, ROUGH ROD ARRAY

velocities in the subchannel centriod region were expected to be higher than in the smooth array. This also explained why the peak-to-average velocity ratio was higher in the rough rod array, why the velocity in the rough rod-to-smooth wall gap was higher, and why the velocity in the rough rod-to-rod gap was lower.

From geometrical considerations, the flow in subchannel numbers 9 and 30, cf., Figure 5.2, was expected to be symmetric about the rod-to-rod gap. The location of the rod-to-rod gap between subchannels 9 and 30 was clearly displaced in the direction of subchannel 30. The gap location was determined by the low velocity point between the subchannels. The nonsymmetric location of the gap can only be explained by a distorted rod array geometry at the velocity measuring plane (outlet), see section 5.1.2.

The central velocity traverses for the smooth and rough rod arrays are shown in Figures 5.4 (100 and 250 GPM) and 5.5 (100 and 200 GPM), respectively.

From comparisons of the figures, the following observations were noted: (A) the velocity in the peripheral subchannel number 48 was considerably higher in the rough rod array than in the smooth rod array, (B) the velocity gradient along the smooth duct wall of the roughened rod array was higher than in the smooth rod array, (C) the peak-to-average subchannel velocities were higher in the rough rod array than the smooth array (especially in subchannels near

FIGURE 5.4

CENTRAL VELOCITY PROFILE, SMOOTH ROD ARRAY

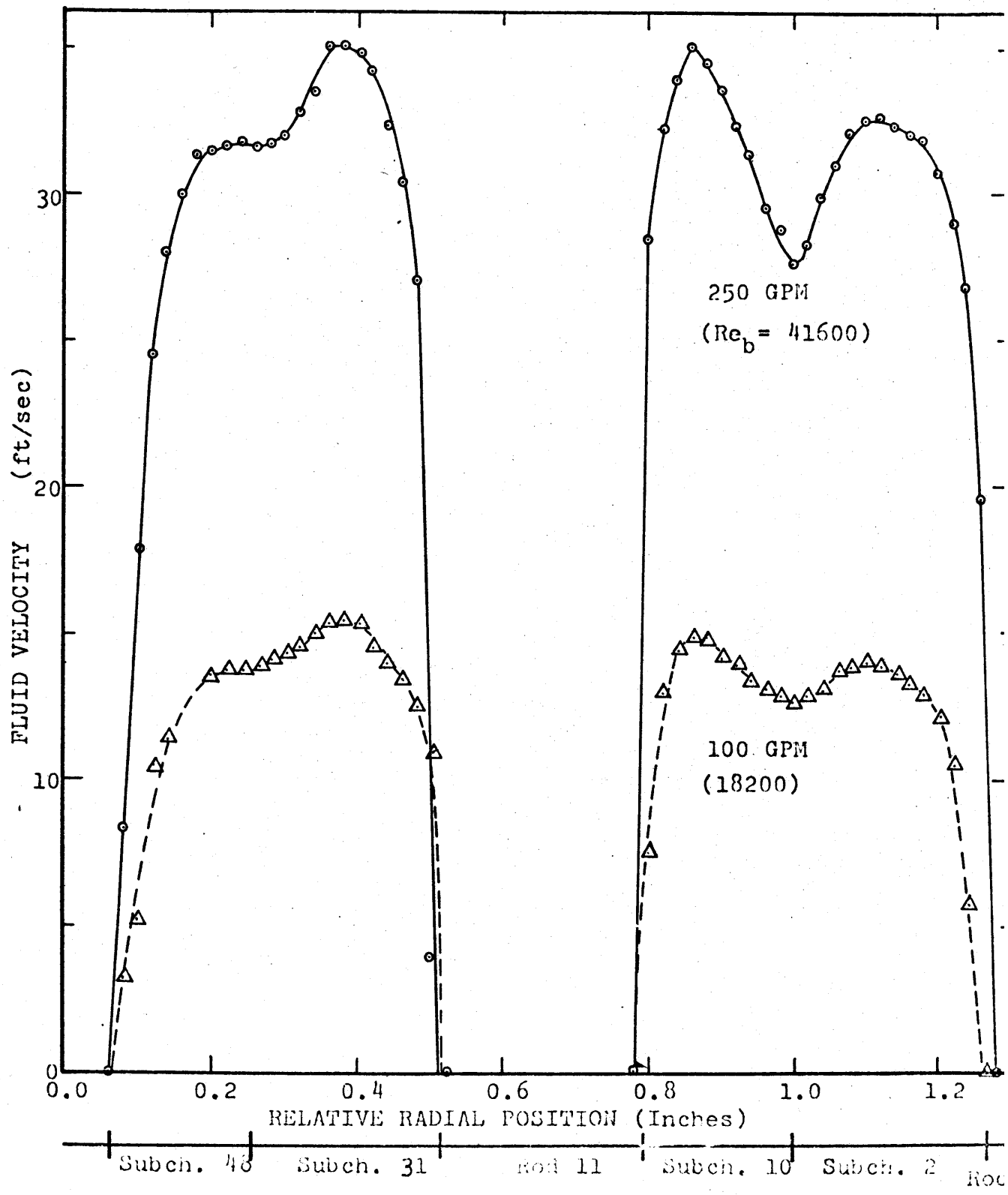

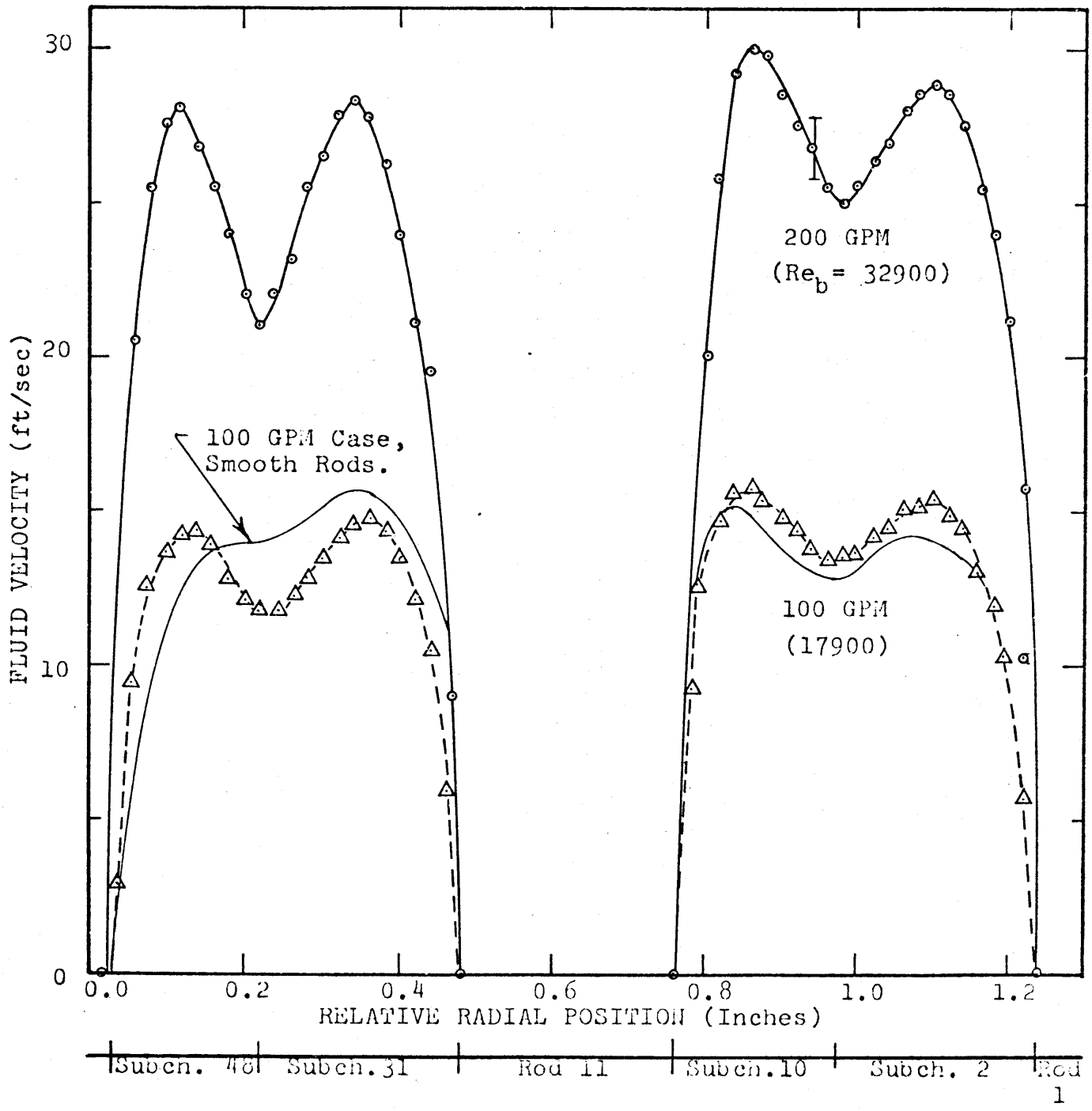

FIGURE 5.5

CENTRAL VELOCITY PROFILE, ROUGH ROD ARRAY

the smooth wall of the rough array), and the ratios increased with Reynolds number, (D) the velocities in the subchannel centroid region were higher in the rough array and (E) the velocities in the rod-to-rod gap region were lower in the rough array.

As was discussed earlier, the above observations are explained by the roughened surface behavior. The increase in peripheral subchannel velocity, i.e., by-pass flow, in the roughened array was of particular interest because of the partially roughened nature of the subchannels. That is, because the relative change in the friction factor in a partially roughened subchannel was less than in a fully roughened subchannel, e.g., 1.5 versus 3.0, the flow ratio between a partially roughened peripheral and a fully roughened interior subchannel will be higher than would be the case if all surfaces were smooth.

The corner velocity profiles (100 and 200 GPM) are shown in Figures 5.6 and 5.7 for the smooth and rough rod arrays, respectively. The following observations were noted from comparison of the figures: (A) the velocity in the corner subchannel increases faster than that expected based on flow rate considerations alone, (B) the velocity gradients are steeper near the smooth rods than the rough rods, (C) the peak gap velocities increased as the smooth rod array center was approached and decreased as the rough rod array center was approached.

FIGURE 5.6

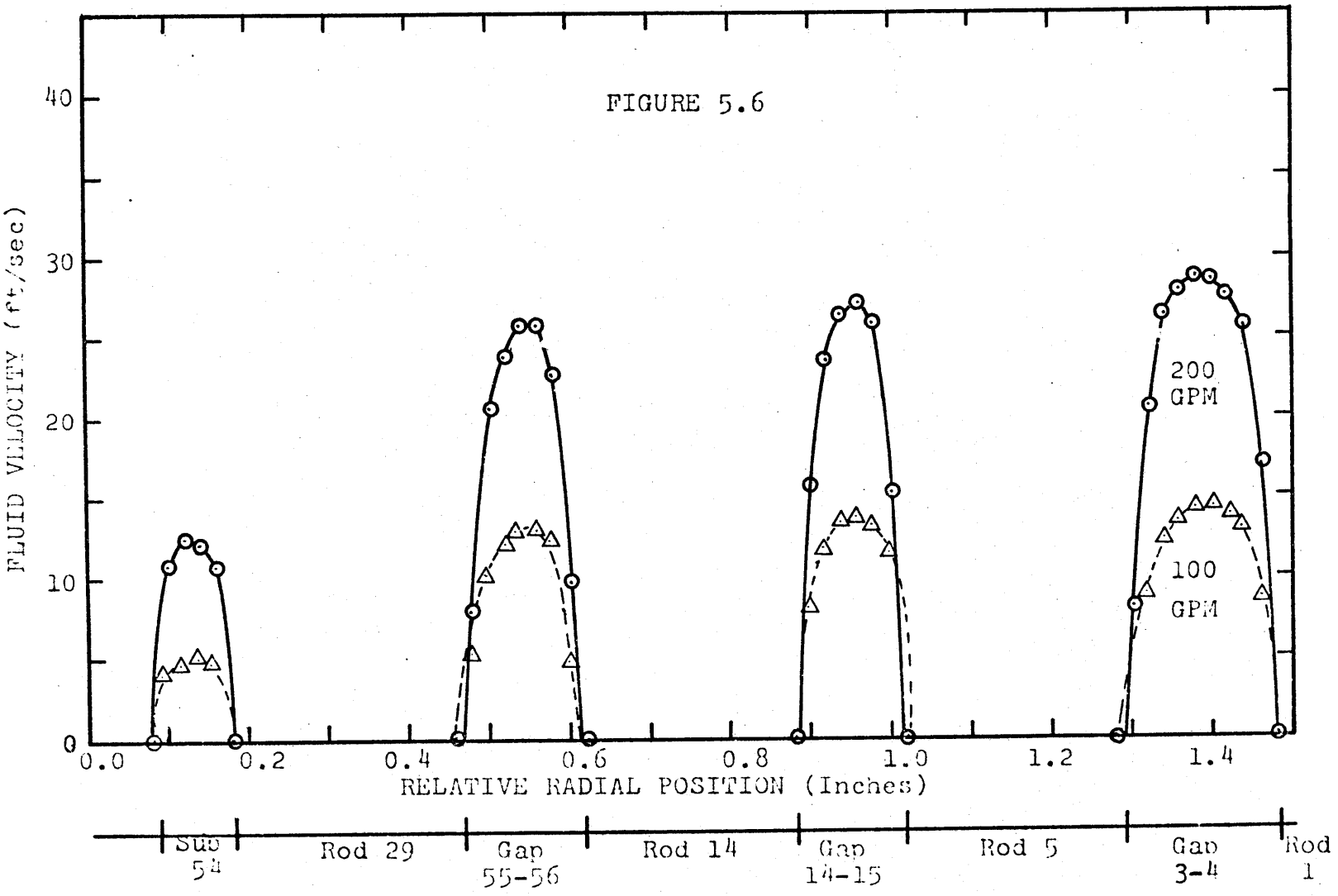

CORNER VELOCITY PROFILE, SMOOTH ROD ARRAY

FIGURE 5.7

CORNER VELOCITY PROFILE, ROUGH ROD ARRAY

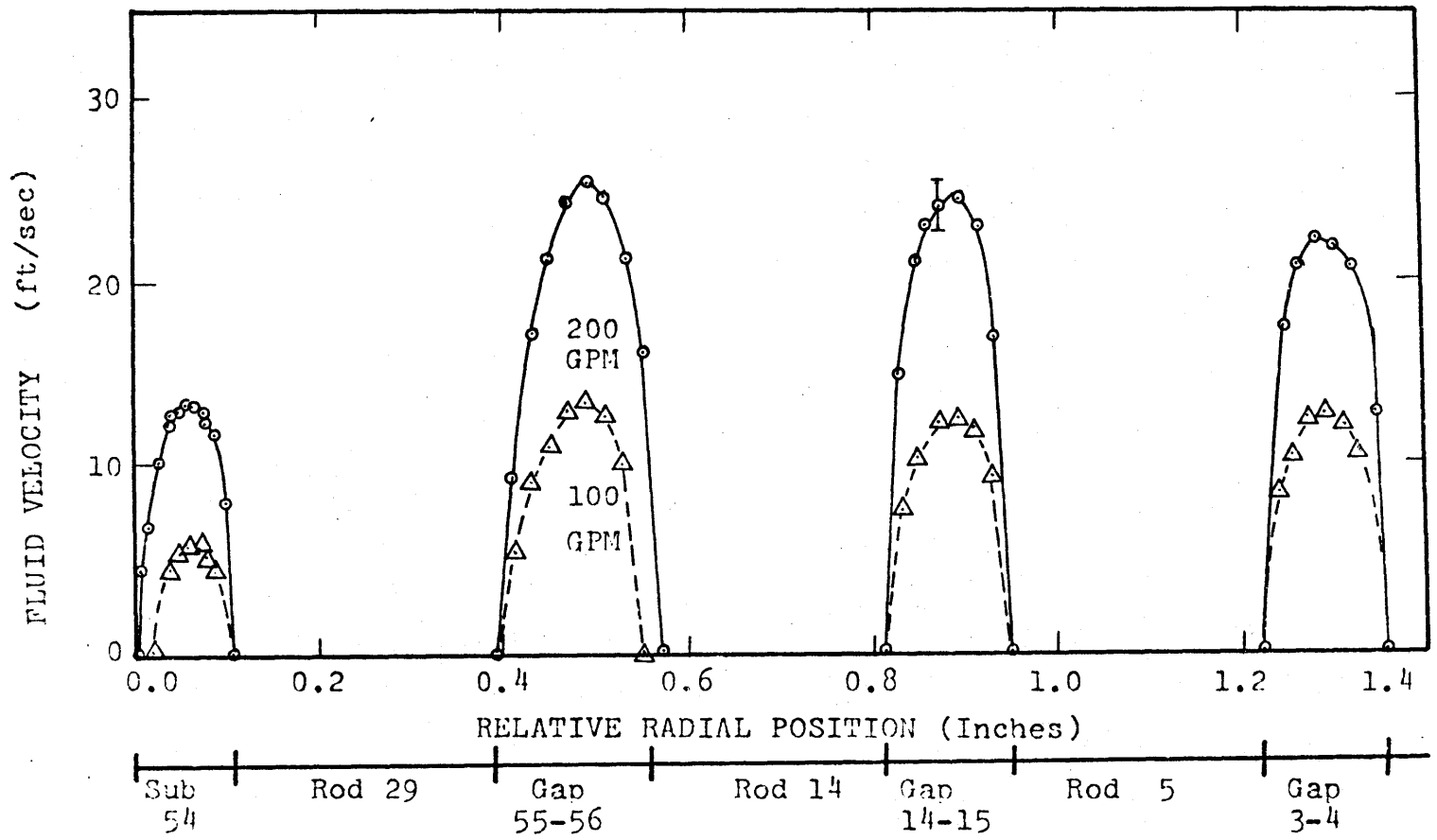

Upon reviewing the main flow split equation, Eq. 3.12, the corner subchannel velocity behavior in the smooth rod array could not be explained from the simplified hydraulic analysis. This was because the geometry and coolant properties were constant, and there were no roughening effects. In both the smooth and the rough rod arrays, the increase in corner subchannel velocity at a rate faster than the total bundle flow rate can be explained by transverse momentum exchange. Interaction of peripheral subchannel flow with the slower flowing corner subchannel fluid will cause the corner subchannel velocity to increase. In the roughened rod array, the corner velocity increased faster with flow than in the smooth array; this was because the interaction between subchannels in the roughened bundle was higher, see section 5.4.

The variation of maximum gap velocity with radial position may have been caused by (A) errors in probe positioning, (B) by interaction of the interior rod array flow with the flow at the rod array perimeter or (C) by distortions in the rod array inlet velocity profile. Whatever the cause, the data for all corner and offset corner velocity profiles (presented later) showed the same trend for the respective rod surface conditions. In the central and offset central velocity profiles, the flow maldistributions were attributed to rod array geometry distortions because of the nature of the velocity data. With the corner and offset corner

profiles, it was not possible to determine if flow maldistributions were due to probe positioning errors or rod array geometrical distortions because of the reorientation of the probe traverse with respect ot the rod array geometry.

Regarding bundle entrance flow maldistributions, the experiments were plagued by failures in the lower plenum - rod bundle seal (located at the bundle entrance). Although every effort was made to keep this seal in good condition, bundle inlet seal failures may have caused flow maldistributions at the bundle entrance, i.e., limited flow blockage. However, even if entrance blockages were occurring, it was very doubtful they would have influenced the outlet velocity profiles because the bundle entrance and outlet were separated by eight spacer grids and over 250 hydraulic diameters of flow passage ($L/d_e = 252$).

If one neglects the mechanical problems, the variation in peak velocity with radial position might have been explained by coolant mixing, i.e., transverse momentum transfer. (Recall, the simplified hydraulic analysis, cf., Chapter 3, predicts the same flow in all subchannels of the same type.) In the smooth rod array, the flow region between the outer rod row and the hexagonal duct offers more resistance to flow than the rod array interior. Interchannel coolant mixing in the smooth array would cause interior subchannel flows to decrease as the outer rod row was approached. In

the rough array, the roughened rod surfaces cause the rod array interior to offer a higher risistance to flow than the rod array perimeter. (Recall, the hexagonal duct was not roughened.) In the rough array, coolant mixing would cause the velocity in interior subchannels to decrease in the direction away from the rod array perimeter.

The offset corner velocity profiles are shown in Figures 5.8 (200 GPM) and 5.9 (100 and 200 GPM) for the smooth and rough rod arrays, respectfully. From comparison of the Figures, the following observations are noted: (A) the velocities between the rod surfaces and the subchannel centriod region were less in the rough array than in the smooth array, (B) the velocity adjacent to the corner subchannel was higher in the rough bundle (200 GPM) than in the smooth bundle, (C) the peak subchannel velocities increased as the smooth rod array center was approached and decreased as the rough rod array center was approached.

From the velocity profiles, rod number 5 appeared to be out of position in the direction of subchannel number 16. The observations regarding the offset corner profiles were discussed earlier after the corner profile observations.

5.1.2 Rod Array Geometry Distortions at the Exit Plane

The results of the velocity measurements were plagued by a poor rod array geometry at the rod array flow exit plane. Several of the rods in the array were found to

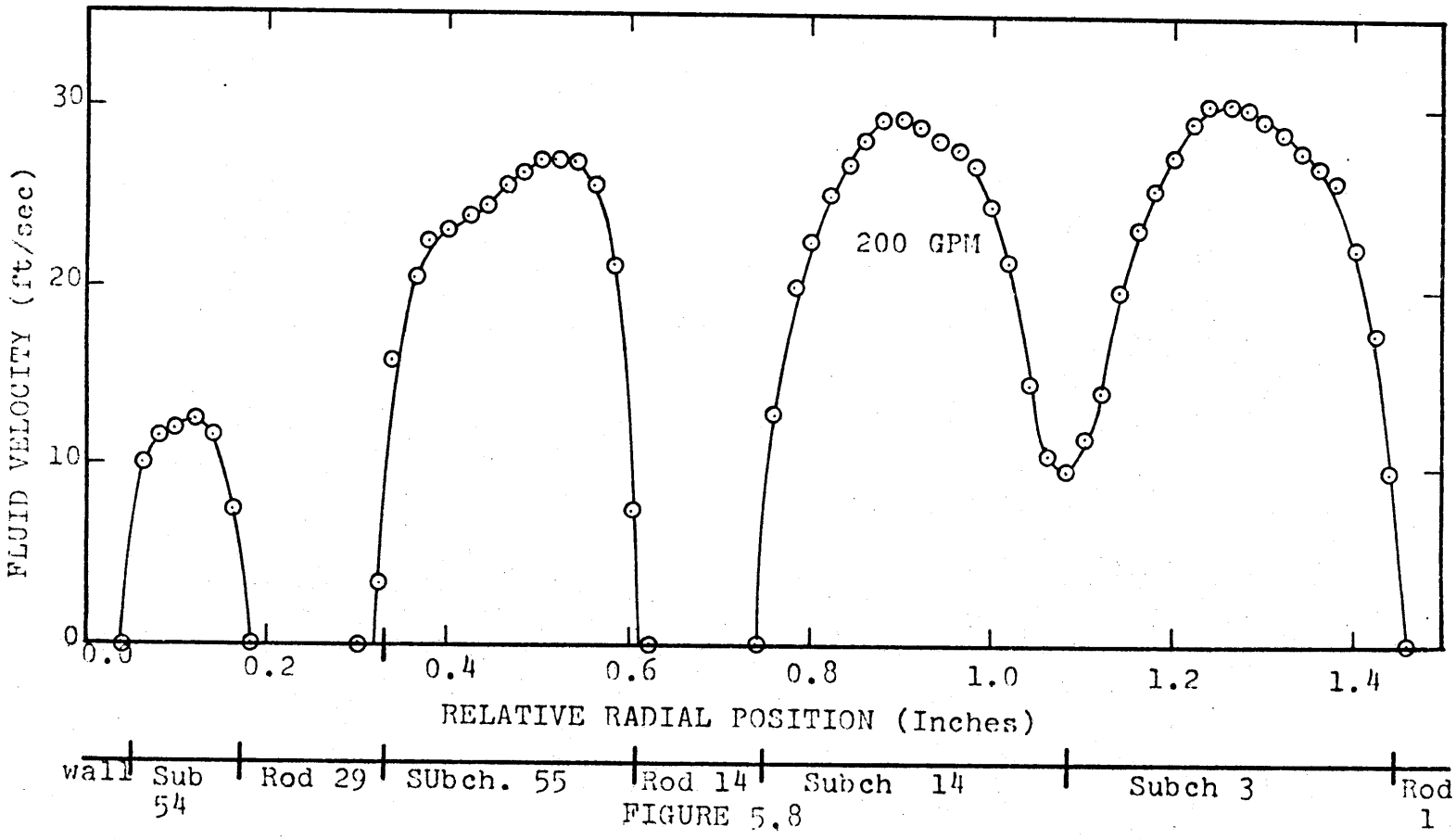

FIGURE 5.8

OFFSET CORNER VELOCITY PROFILE, SMOOTH ROD ARRAY

FIGURE 5.9

OFFSET CORNER VELOCITY PROFILE, ROUGH ROD ARRAY

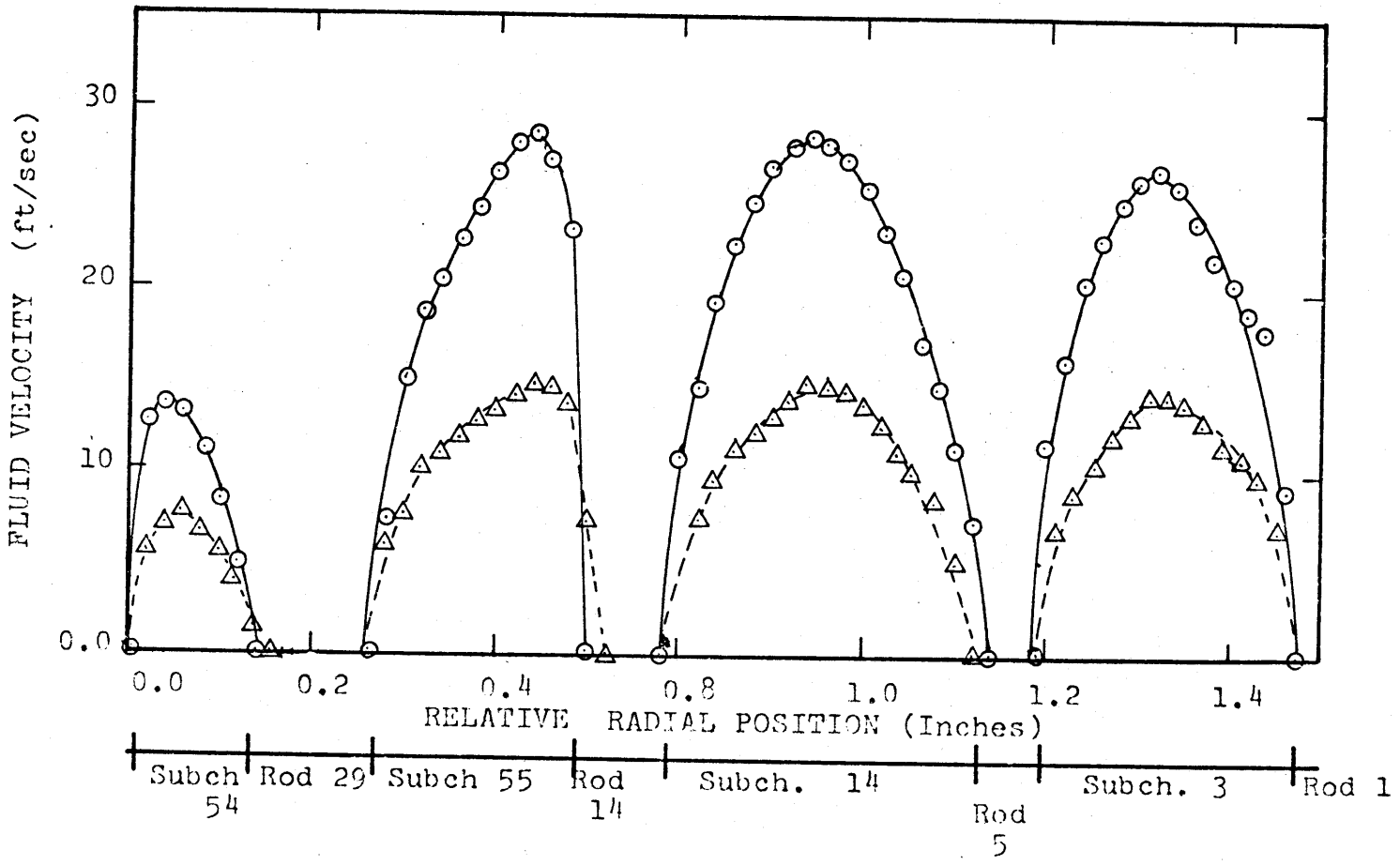

be notably out of true position by observing the outlet velocity profiles. The rods were not noted as being out of position during visual examination under no flow conditions.

The distortions in the rod array outlet geometry were not due to bent rods. Visual examination of the rods before, during, and after the experiments showed the rods to be straight. That the distorted outlet geometry was not due to bent rods was further verified by the fact that the distortions indicated by the velocity profiles were similar for two different sets of rods, i.e., the smooth and rough rod arrays.

The reasons believed to be responsible for the distorted rod array geometry are given below.

(A) In order to allow the pitot tube to pass over the tops of the rods, the rod array was unsupported at the rod array outlet. The rods were thus cantiliver supported from the top spacer grid (grid no. 8) over a length of 7-1/2 inches (19 cm). In all other axial regions, the rods were supported every 7-3/4 inches. Because of the difference in the nature of the rod support between the rod array outlet and the rod array interior, the outlet rod array geometry could have been expected to be notably distorted.

(B) Another possible cause of the distorted outlet rod array geometry was the spacer grids supplied for use with the test section. The spacer grid assemblies (as fabricated)

did not allow free axial motion of the outer row of rods during test section assembly, see Appendix 6. The corner rods were particularly difficult to slide. These fabrication problems apparently resulted from welding the "egg-crate" grid assembly to the spacer hanger (flow shroud or duct).

One reference was noted with similar flow maldistributions in a grid spaced rod array which had a square rod lattice.

> ". . . . velocity distribution tests performed at APDA (Atomic Power Development Associates) on certain types of subassembly prototypes furnished by the fuel manufacturers; Velocity traverses measured with pitot tubes indicate flow maldistributions (± 30%) which varies, furthermore, according to the longitudinal position of the probe in the bundle. No explanation has been found for these velocity distribution results, ..." [S2]

The rod array outlet geometry influenced the velocity experiment data primarily because the velocities were measured at the rod array outlet. The static pressure data was taken over an axial length of 27 inches and was influenced by outlet geometry only over a short axial length. Further, axial pressure profiles near the rod array exit did not influence the determination of either friction factor or grid loss coefficient data.

The salt tracer concentrations, discussed later in section 5.3, were measured at the rod array outlet but were the consequence of coolant mixing over the entire injector-detector separation distance. The actual tracer

concentration measurements were essentially independent of velocity. The influence of rod array geometry distortions on mixing experiment results was only apparent in the subchannel flows used in the mass balance calculations.

5.1.3 Determination of the Average Subchannel Velocity

From the measured velocity profiles, the average velocity of interior, peripheral and corner subchannels was determined using an area weighted averaging technique. The accuracy of the results was severely limited by the nature of the velocity measurement instrumentation. Accurate average subchannel velocities can by determined experimentally only from two-dimensional velocity profile data, i.e., from velocity data taken over the entire flow area of interest.

The average value of interior subchannel velocity data was determined by using the concentric ring, area weighting factors illustrated in Figure 5.10. The average value of the two data points appearing at locations symmetric to the central (largest velocity) position were weighted by the area of the rings in which they were located. As the data points became farther and farther away from the central point, the weighting area was reduced accordingly. Also, when the rings intersected a flow boundary, only one data point was available for use in the average velocity equation. The average subchannel velocity was determined by

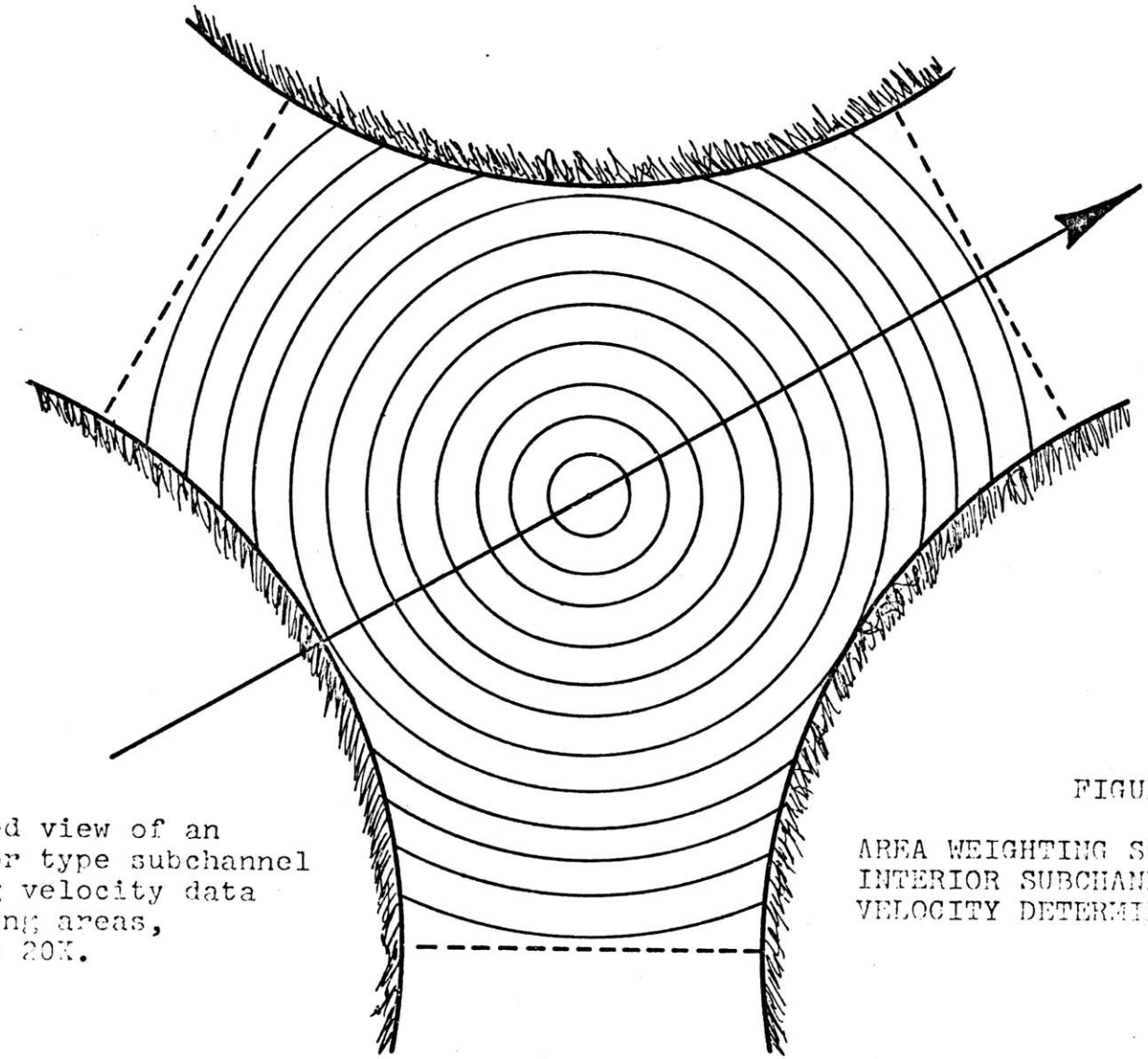

Enlarged view of an interior type subchannel showing velocity data weighting areas, scale - 20X.

FIGURE 5.10

AREA WEIGHTING SCHEME USED FOR INTERIOR SUBCHANNEL AVERAGE VELOCITY DETERMINATION

$$\bar{V}_i = \frac{\sum_{j=1}^{n} A_j V_j}{\sum_{j=1}^{n} A_j} = \sum_{j=1}^{n} V_j \frac{A_j}{A_i} \qquad \text{(Eq. 5.1)}$$

where A_j/A_i is the area weighting factor applying to velocity data point V_j.

In peripheral subchannels, two velocity data sets were available for obtaining the average velocity. One set was obtained from a "central velocity profile" traverse; the other from a "offset central velocity profile" traverse. In order to obtain the average peripheral subchannel velocity, the numerical average of the central traverse (passing through the rod-to-rod gap) was weighted by the six-sided area A_6 shown in Figure 5.11. The average numerical value of the offset central velocity traverse (passing through the rod-to-wall gap) was multiplied by the area of both rod-to-wall gap regions A_g. Because the rod-to-wall separation was nearly constant in the side areas, the offset velocity profile data was considered typical of the entire region. The average peripheral subchannel velocity was determined by

$$\bar{V}_p = \frac{\bar{V}_6 A_6 + \bar{V}_g (2 A_g)}{A_6 + 2 A_g} \qquad \text{(Eq. 5.2)}$$

The average velocity of the corner subchannel, see Figure 3.1, was determined by taking the numerical average

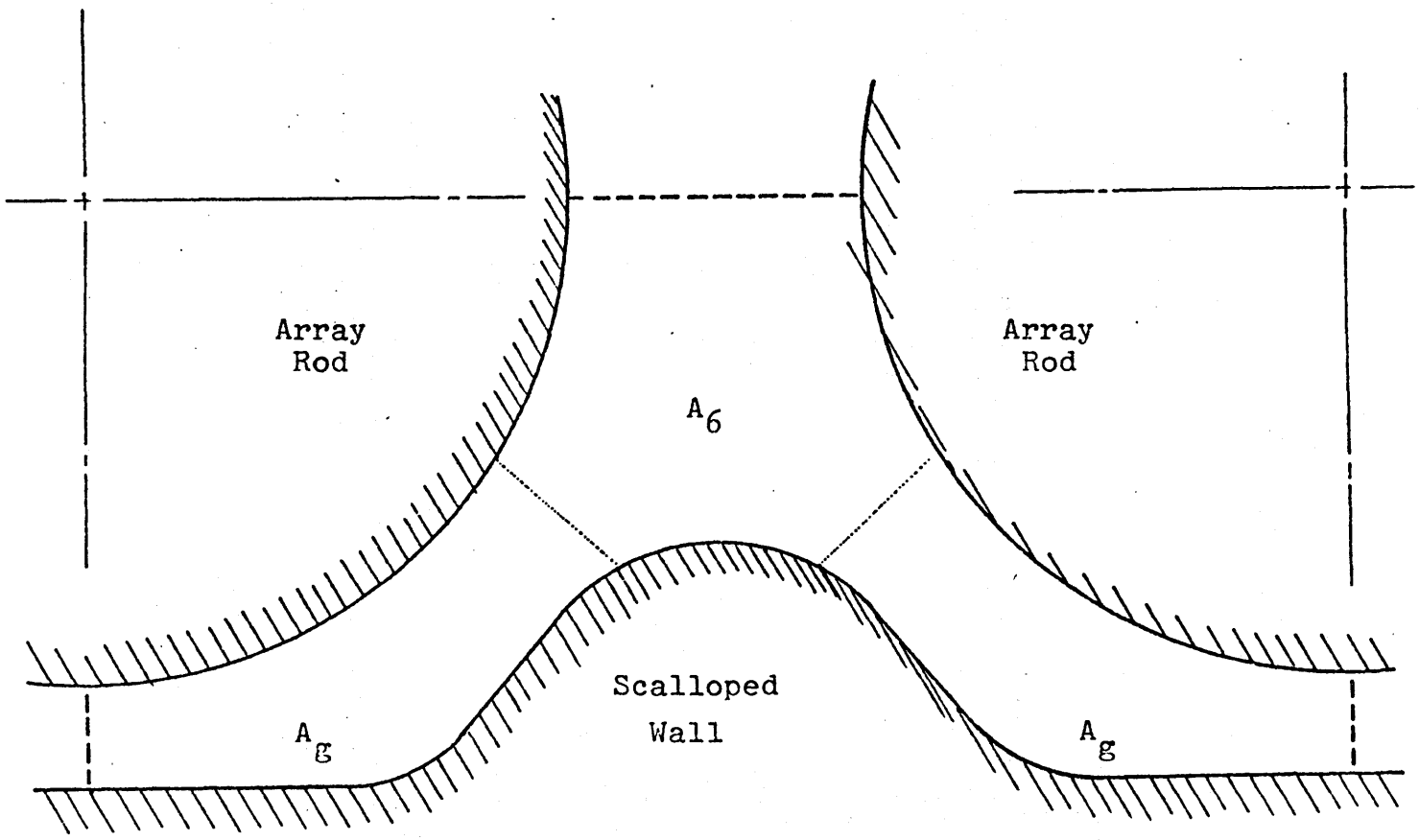

Scale: 16 Times True Size
Details from EIR TM-IN-545 [Z1]

FIGURE 5.11

ENLARGED VIEW OF A PERIPHERAL SUBCHANNEL

of the corner subchannel velocity data taken in a "corner velocity profile" traverse. Because the subchannel was an annulus shape, the area weighting factors were approximately the same for all data points. The average corner velocity was simply

$$\bar{V}_c = \sum_{j=1}^{n} V_j/n \quad . \qquad \text{(Eq. 5.3)}$$

It is important to note, that the discussion has delt only with perfect rod array geometries. In the actual determination of interior subchannel average velocities, some accommodation of rod array distortions was attempted. No such accommodations were made for peripheral and corner subchannels. However, with the velocity data available, further sophistication in determining the average velocity was not justifiable. The experimentally determined average subchannel velocities presented herein can only be considered as estimates of the actual values because of limitations in the velocity measuring instrumentation and because of distortions in the rod array outlet geometry.

5.1.4 Average Subchannel Velocity Results

The average subchannel velocities for the various experiments are listed in Table 5.2. The average velocities are given for each subchannel or gap where the velocity profile was determined for a specified traverse and main flow. Average velocities from the offset corner velocity

Table 5.2

Specific Subchannel Average and Maximum Velocities

Main Flow	Subchannel (Gap) No., Type	Average Velocity (ft/sec)		Peak Velocity (ft/sec)		Peak/Average	
		Smooth Rods	Rough Rods	Smooth Rods	Rough Rods	Smooth Rods	Rough Rods
100	2-I	13.1	13.4	14.0	15.3	1.07	1.1
	10-I	13.3	13.3	14.9	15.7	1.12	1.1
	31-I	13.9	12.6	15.5	14.7	1.12	1.1
	48-P	12.8	12.8	14.0	14.3	1.09	1.1
200	2-I	-	25,0	-	28.7	-	1.1
	10-I	-	23.9	-	30.1	-	1.2
	31-I	-	22.5	-	28.2	--	1.2
	48-P	-	22.1	-	28.1	-	1.2
250	2-I	30.2	-	32.5	-.	1.08	-
	10-I	30.3	-	35.1	-	1.16	-
	31-I	31.9	-	35.0	-	1.1	-
	48-P	26.6	-	31.8	-	1.20	-
100	9-I	14.0	13.7	14.8	15.6	1.06	1.1
	30-I	13.5	12.4	15.0	15.1	1.11	1.2
	47,48-P,P*	10.1	10.9	12.1	11.8	1.20	1.0
200	9-I	26.0	25.5	28.2	29.9	1.08	1.1
	30-I	26.4	24.3	28.3	29.4	1.07	1.2
	47,48-P,P	19.0	21.0	22.0	23.3	1.16	1.1
250	9-I	33.3	30.2	35.2	36.2	1.06	1.2
	30-I	31.3	29.6	34.8	35.3	1.11	1.1
	47,48-P,P	23.9	24.6	28.4	29.1	1.19	1.1
100	3,4-I,I	12.5	10.3	14.3	11.7	1.14	1.1
	14,15-I,I	12.1	10.8	13.7	12.7	1.13	1.1
	55,56-I,I	10.2	10.8	13.1	13.4	1.28	1.2
	54-C	4.8	4.7	5.2	5.4	1.11	1.1
200	3,4-I,I	23.4	19.7	28.7	22.5	1.23	1.1
	14,15-I,I	22.3	21.0	27.1	24.9	1.22	1.1
	55,56-I,I	19.5	20.2	25.8	25.9	1.32	1.2
	54-C	11.5	10.9	12.5	13.7	1.09	1.2

tion indicates either a rod-to-rod or rod-to-wall gap.

profiles were not determined; the offset corner traverses were oriented to the subchannel geometries such that average velocities could not be determined from the data.

The average subchannel and gap velocity data was used to determine the average flow velocities in specific subchannel types for the various flow conditions. In the case of the interior subchannels, it was possible to numerically average the average subchannel velocities of several subchannels in determining the average subchannel velocity reported in Table 5.3; for peripheral and corner subchannels only one average subchannel velocity was available. The average velocities for the various subchannel types are given in Table 5.3 along with the analytically predicted average subchannel velocities for the same flow conditions. For all analytical data, the nominal main flow indicated by the main flow meter was used, i.e., 100, 200 or 250 GPM.

The analytical data listed in Table 5.3 was calculated using the RUFHYD code. These calculations assumed ideal rod array geometry and neglected interchannel coolant mixing. For the RUFHYD results (and MITMIX-R) reported in Chapter 5, the dependence of the roughened surface friction factor multiplier on Reynolds number was calculated using Eq. A1.9:

$$f_x = 0.24\ Re_1^{0.21} \qquad \text{(Eq. A1.9)}$$

where $7{,}000 < Re < 70{,}000$. An iterative process was required

DISCLAIMER

Page has been ommitted due to a pagination error by the author.

211

TABLE 5.3

AVERAGE VELOCITY IN THE VARIOUS SUBCHANNEL TYPES

Rod Surface	Smooth				Rough			
Source	Experimental (51°F)		Analytical		Experimental (47°F)		Analytical[$]	
Bundle Flow: Subchannel Type	Velocity* (ft/sec)	Flow Split Factor (X_{ib})	Velocity (ft/sec)	Flow Split Factor (X_{ib})	Velocity (ft/sec)	Flow Split Factor (X_{ib})	Velocity (ft/sec)	Flow Split Factor (X_{ib})
Bundle Flow (GPM)	115		100		113		100	
Interior - 1	13.6	0.0138	12.2	0.0141	13.1	0.0136	11.6	0.0133
Peripheral - 2	11.3	0.0139	8.7	0.0123	11.7	0.0148	10.2	0.0143
Corner - 3	4.8	0.0018	7.4	0.0031	4.7	0.0018	8.8	0.0037
Bundle Flow (GPM)	221		200		208		200	
Interior - 1	26.2	0.0140	24.4	0.0141	24.2	0.0135	22.8	0.0131
Peripheral - 2	(21.3)	(0.0138)	17.5	0.0123	21.5	0.0146	21.1	0.0149
Corner - 3	11.5	0.0022	14.8	0.0031	10.9	0.0022	18.3	0.0039
Bundle Flow	263		250		258		250	
Interior - 1	31.4	0.0138	30.5	0.0141	29.9	0.0134	28.3	0.0131
Peripheral - 2	25.1	0.0135	21.8	0.0123	26.7	0.0146	26.7	0.0151
Corner - 3	(14.4)	0.0023	18.5	0.0031	13.7	0.0022	23.2	0.0039

$ Rough Bundle analysis was done using $f_x = 0.24\ Re_1^{0.21}$ with the perimeter-weighted, parallel resistance model for the equivalent friction factor.

*Numbers in parenthesis indicate non-experimental values obtained by extrapolation or interpolation of available experimental data.

to determine the flow and friction factor of the roughened interior subchannels. In the code results reported, the interior subchannel flow and friction factor were converged. The friction factor multiplier of the interior subchannel was used in conjunction with the perimeter-weighted, parallel resistance, equivalent friction factor model to calculate the friction factor of the partially roughened peripheral and corner subchannels. Uncertainties in the analytical models for calculating the friction factors in the peripheral and corner subchannels precluded any improvement in the flow calculations by converging the flow and friction factors in the peripheral and corner subchannels.

The main flow rate was estimated from experimental data using the average subchannel velocity data in Table 5.3. The experimental total flows were generally 5 - 10% higher than those indicated by the main flow meter. Only one experimental total flow was outside the flow meter manufacturer's accuracy range ($\pm$ 15 GPM), cf., Table 5.3, 200 GPM, Smooth; it was determined using only two subchannel average velocities.

The average subchannel velocities determined using experimental data were approximately 10% too high because the pitot tube was unable to reliably measure velocity data within 0.020 inches of a flow boundary. Thus, low velocity data could not be included in the averages; further details

regarding experimental uncertainties are given in section 5.5.

The subchannel flow split factors, i.e., the ratio of the average flow rate in a subchannel of a given type i to that in the total bundle ($X_{ib} = W_i/W_b$), have also been given in Table 5.3.

The consideration of experimental uncertainty in the average velocity data restricts the conclusions which can be drawn from the data. From consideration of the flow split factors, the ratios of subchannel flow to bundle flow, the following observations maybe noted. (A) The flow area of the corner subchannel was reduced by rod array distortions. In all cases, the corner subchannel flow fraction was less than that analytically predicted; (B) The peripheral subchannels had higher flow fractions in the rough bundle than in the smooth bundle; this behavior was expected because of the partially roughened perimeter. (C) Analytical methods predict an interior-to-peripheral subchannel flow ratio which was higher in the smooth rod bundle and lower in the rough rod array than was experimentally observed. This may be explained by the neglect of interchannel coolant mixing in the analytical model.

The experimentally determined hydraulic data for the various subchannel types and the rod bundle have been given in Table 5.4.

TABLE 5.4

Experimentally Determined Subchannel Hydraulic Data

	Interior Subchannel	Peripheral Subchannel	Corner Subchannel	Bundle Average
d_e(in)	0.285	0.179	0.142	0.238
A(in^2)	0.0370	0.0452	0.0135	2.894
		Smooth Rod Array		
100 GPM (115)				
V (ft/sec)	13.6	11.3	4.8	12.7
Re -	23300	12100	4100	18200
P_D (in H_2O)	34.4	23.8	4.3	30.0
200 GPM (221)				
V	26.2	(21.3)	11.5	24.4
Re	44900	22900	9810	35000
P_D	128.	84.3	24.6	111
250 GPM (263)				
V	31.4	25.1	(14.1)	29.1
Re	53800	27000	12000	41600
P_D	183	117.	36.9	157

Table 5.4 continued

Rough Rod Array

100 GPM (113)				
V	13.1	11.7	4.7	12.5
Re	22400	12600	4010	17900
P_D	31.9	25.5	4.10	29.0
200 GPM (208)				
V	24.2	21.5	10.9	23.0
Re	41400	23100	9300	32900
P_D	109.	85.9	22.1	98.3
250 GPM (258)				
V	29.9	26.7	13.7	38.6
Re	51200	28700	11700.	40900.
P_D	166	132	34.9	152.

$Re_i = 6008\ Vd_e$; $P_{di} = 0.186\ V^2$; $V_{10} = 0.111\ Q$

(Table 5.4 concluded)

5.2 Rod Array Axial Pressure Profiles

Axial profiles of the static pressure within interior subchannel no. 1 and peripheral subchannel 48 were taken over the upper 28 inches (nominal) of the rod array, i.e., from the approximate rod array mid-point to the exit. Typical results of this procedure are shown in Figure 5.12 for the case of interior subchannel no. 1 in the roughened rod array with a total flow rate of 200 GPM.

The static pressure profile in Figure 5.12 shows the effects of friction pressure losses, grid spacer pressure losses and rod array outlet flow expansion. The parallel straight lines decreasing from left-to-right are the friction pressure losses. Recall, the firction pressure loss equation predicts a linear change in pressure with distance;

$$\frac{\Delta P_f}{L} = \frac{f}{d_e} \frac{\rho V^2}{2 g_c} = \frac{f}{d_e} P_d \qquad \text{(Eq. 5.4)}$$

where all of the variables (see the nomenclature listing) are characteristic of the flow area to which the static pressure corresponds.

The three sharp decreases in pressure were due to the grid spacer losses at grids no. 6, 7, and 8. Detailed axial, static pressure profiles were taken in the vicinity of the grid spacers; Figure 5.13 shows typical results of static pressure profiles taken in the region of grid no. 8 for the smooth rod array at 200 GPM.

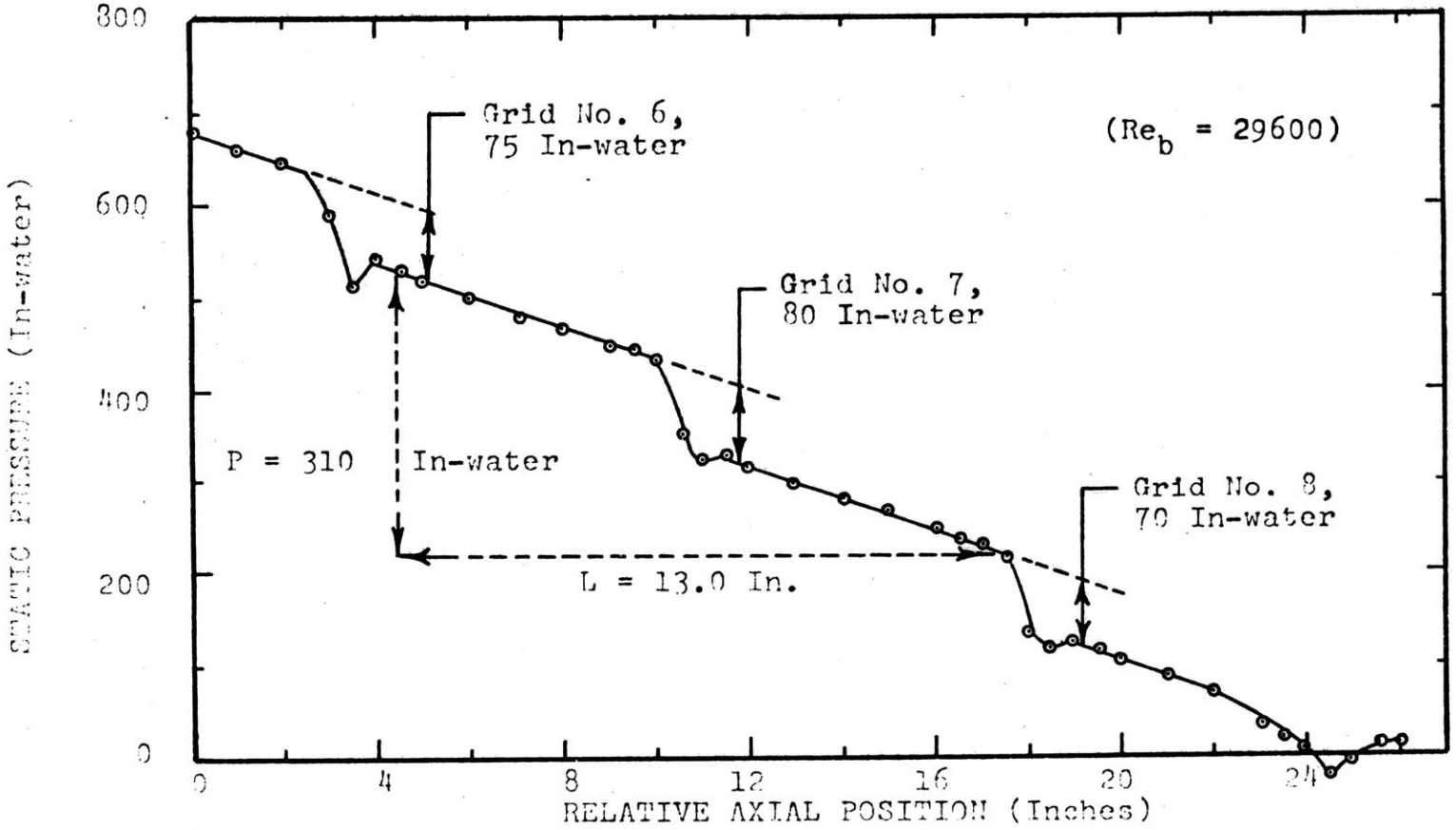

FIGURE 5.12

ROUGH ROD ARRAY, AXIAL PRESSURE PROFILE: INTERIOR SUBCHANNEL, 200 GPM

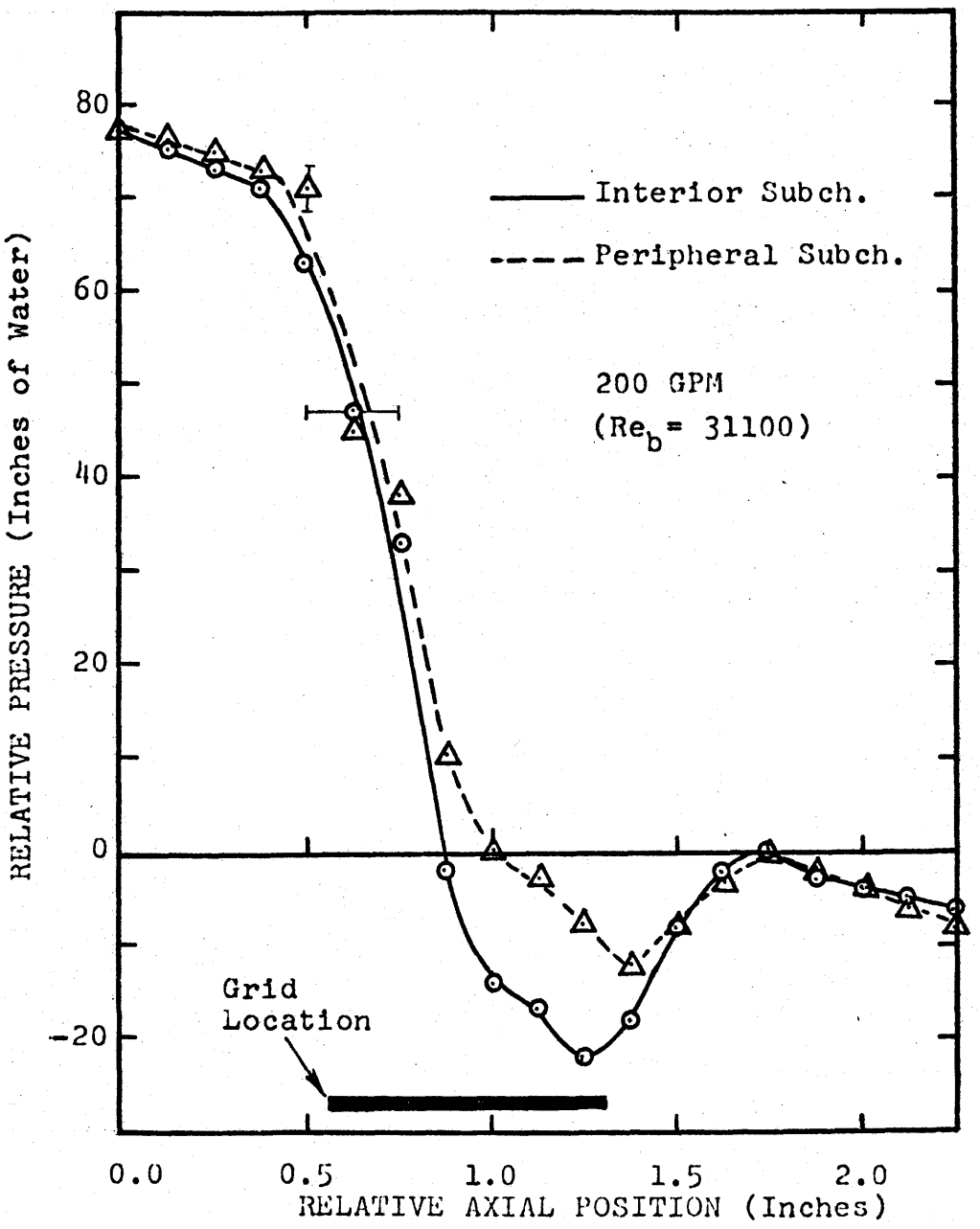

FIGURE 5.13

AXIAL PRESSURE PROFILE, SPACER NO. 8,
SMOOTH ROD ARRAY

The static pressure decreased very rapidly as the flow entered the spacer region because of flow acceleration (the spacer blocks 24% of the flow area) and increased friction losses. Upon leaving the grid, the flow decelerated and some static head was recovered.

The pressure losses assigned to the spacer grid was the difference in pressure between the parallel friction loss lines on either side of the grid spacer. This technique was chosen to separately account for the change of pressure drop in the axial region near the grid due to the presence of the grid. The friction losses in the grid region which would occur in the rod array with the grids removed were not charged to the spacer grid. When using the grid loss coefficients reported herein, the friction losses of the rod array should be calculated using an axial length which includes the axial region enclosed by the spacer grid.

A representative frictional pressure loss ΔP_f over an axial distance L was obtained from the plotted results. This procedure was illustrated in Figure 5.12; a total pressure loss of 310 inches of water was observed over an axial distance of 13.0 inches. The frictional pressure along the distance L was the total pressure loss less the pressure loss due to grid no. 7 (ΔP_7), i.e., 310 in. - 80 in. = 230 inches of water.

5.2.1 Axial Pressure Profile Data Reduction

Axial pressure profiles for the smooth and the rough rod arrays (for both interior and peripheral subchannel static pressure traverses) have been given in Appendix 7. In each of the four cases, axial pressure profiles were taken for total bundle flows of 50, 100, 150, 200, and 250 GPM.

The data for determining the rod array friction factors and spacer grid loss coefficients was summarized in Table 5.5. In determining the friction factors and grid loss coefficients from the data in Table 5.5, it was necessary to specify the average dynamic pressure P_d ($= \rho V^{-2} / 2\, g_c$) and the equivalent hydraulic diameter d_e of the flow geometry of interest for the flow conditions of the experiment. For this work the data was reduced by using both analytically calculated and experimentally measured values of the average velocity (dynamic pressure). Further, the flow geometry of both the measurement subchannel and the overall rod bundle was used. The various data reduction procedures are summarized below.

DATA REDUCTION PROCEDURES

Flow Geometry	Measurement Subchannel	Overall Rod Array
Source of Flow Information for the Data Reduction	Experimental Measurement	Experimental Measurement
	Analytical Calculation	Analytical Calculation

Table 5.5

Rod Array Pressure Loss Data Summary

Smooth Rod Array

Main Flow (GPM)	Probe Subchannel	ΔP_f (in. of Water)	L (in.)	ΔP_6 (in. of Water)	ΔP_7 (in. of Water	ΔP_8 (in. of Water	Water Temp. (°F)	$\overline{\Delta P}_g$	Figure No.
50	I*	15.6	16.0	8.0	5.8	8.0	49	7.3	A7.1
100	I	55	19.0	21	20	21	49	20.7	A7.2
150	I	118	19.0	40	38	40	49	39.3	A7.3
200	I	160	17.0	70	58	62	50	63.3	A7.4
250	I	214	16.0	92	96	90	50	92.7	A7.5
50	P	14.5	16.0	6.5	6.5	6.0	48	6.3	A7.6
100	P	50	17.0	22	20	21	49	21.0	A7.7
150	P	103	16.0	42	37	38	48	39.0	A7.8
200	P	200	18.4	50	55	55	49	53.3	A7.9
250	P	204	15.0	86	90	92	48	89.3	A7.10

(Table 5.5 continued)

Rough Rod Array

50	I	11.5	12.0	5.8	5.0	5.0	46	5.3	A7.11
100	I	58	13.0	22	22	22	46	22.0	A7.12
150	I	161	16.0	46	46	45	46	45.7	A7.13
200	I	230	13.0	75	80	70	46	75.0	5.13
250	I	370	14.4	100	100	102	46	101	A7.14
50	P	14.0	12.6	5.4	5.8	5.6	46	5.6	A7.15
100	P	54	12.6	23	24	22	46	23.0	A7.16
150	P	130	13.0	45	47	42	46	44.7	A7.17
200	P	231	13.2	76	73	69	46	72.3	A7.18
250	P	398	15.9	117	110	100	46	109	A7.19

(Table 5.5 concluded)

By rearranging Eq. 5.4, an expression for determining the friction factor of the rod bundle (or measurment subchannel) may be obtained;

$$f = \frac{\Delta P_f}{L} \frac{d_e}{\left(\frac{\rho}{2} \frac{\bar{V}^2}{g_c}\right)} = \frac{\Delta P_f}{L} \frac{d_e}{P_d} \qquad \text{(Eq. 5.5)}$$

where $\Delta P_f/L$ is the slope of the friction pressure loss line.

The grid loss coefficient was determined from the experimentally measured grid pressure loss ΔP_g and the dynamic pressure P_d corresponding to the flow area of interest;

$$K_g = \Delta P_g / P_d \, . \qquad \text{(Eq. 5.6)}$$

The friction factors and grid loss coefficients obtained from pressure profile data transformation using analytically determined average velocities and Reynolds numbers are given in Table 5.6. The same results obtained from data transformation using experimentally determined average velocities and Reynolds numbers are given in Table 5.7.

Typical uncertainties have been illustrated along with the various plots of the results. Experimental uncertainty estimates are discussed in detail in section 5.5.

Table 5.6

Analytical Pressure Profile Data Transformation

Main Flow (GPM)	Water Temp (°F)	P_{d-b} (in-H_2O)	P_{d-i} (in-H_2O)	Re_b -	Re_i -	f_b -	f_i -	K_{6-b} -	K_{6-i} -	K_{7-b} -	K_{7-i} -	K_{8-b} -	K_{8-i} -
---------- Smooth Rod Array, Interior Subchannel Data, i=1 ----------													
50	49	5.74	6.94	7770	10200	0.040	0.040	1.39	1.15	1.01	0.84	1.39	1.15
100	49	22.9	27.7	15500	20400	0.030	0.030	0.92	0.76	0.87	0.72	0.92	0.76
150	50	51.6	62.4	23300	30600	0.029	0.028	0.78	0.64	0.74	0.61	0.78	0.64
200	50	91.8	111.	31100	40800	0.024	0.024	0.76	0.63	0.63	0.52	0.68	0.56
250	50	143.	173.	38800	51000	0.022	0.022	0.64	0.53	0.67	0.55	0.63	0.52
---------- Smooth Rod Array, Peripheral Subchannel Data ----------													
50	48	5.74	3.56	7610	4490	0.038	0.046	1.13	1.83	1.13	1.83	1.05	1.68
100	49	22.9	14.2	15500	9200	0.031	0.037	0.96	1.55	0.87	1.41	0.92	1.48
150	48	51.6	32.1	22800	13500	0.030	0.036	0.81	1.31	0.72	1.15	0.74	1.18
200	49	91.8	57.0	31100	18300	0.028	0.034	0.55	0.88	0.60	0.96	0.60	0.96
250	48	143.	89.0	38000	22500	0.023	0.028	0.60	0.97	0.63	1.01	0.64	1.03
---------- Rough Rod Array, Interior Subchannel Data ----------													
50	46	5.74	6.41	7410	9360	0.040	0.043	1.01	0.90	0.87	0.78	0.87	0.78
100	46	22.9	24.9	14800	18500	0.046	0.051	0.96	0.88	0.96	0.88	0.96	0.88
150	46	51.6	55.1	22200	27400	0.046	0.052	0.89	0.83	0.89	0.83	0.87	0.82
200	46	91.8	96.7	29600	36300	0.046	0.052	0.82	0.78	0.87	0.83	0.76	0.72
250	46	143.	150.	37000	45200	0.043	0.049	0.70	0.67	0.70	0.67	0.71	0.68
---------- Rough Rod Array, Peripheral Subchannel Data ----------													
50	46	5.74	4.47	7410	4900	0.046	0.044	0.94	1.21	1.01	1.30	0.98	1.25
100	46	22.9	19.3	14800	10200	0.045	0.040	1.00	1.19	1.05	1.24	1.96	1.14
150	46	51.6	45.3	22200	15700	0.046	0.040	0.87	0.99	0.91	1.04	0.81	0.93
200	46	91.8	83.2	29600	21100	0.045	0.038	0.83	0.91	0.80	0.88	0.75	0.83
250	46	143.	133.	37000	26800	0.042	0.034	0.82	0.88	0.77	0.91	0.70	0.75

Table 5.7

Experimental Pressure Loss Data Transformation

Main Flow (GPM)	Water Temp (°F)	P_{d-b} (in-H_2O)	P_{d-i} (in-H_2O)	Re_b	Re_i	f_b	f_i	K_{6-b}	K_{6-i}	K_{7-b}	K_{7-i}	K_{8-b}	K_{8-i}
Smooth Rod Array, Interior Subchannel Data, i=1													
100	51	29.5	34.4	18100	23300	0.023	0.024	0.71	0.61	0.68	0.58	0.71	0.61
200	51	107.	128.	34400	44900	0.021	0.021	0.65	0.55	0.54	0.45	0.58	0.48
250	51	157.	183.	41600	53800	0.020	0.021	0.59	0.50	0.61	0.53	0.57	0.49
Smooth Rod Array, Peripheral Subchannel Data, i=2													
100	51	30.0	23.8	18200	12100	0.023	0.022	0.73	0.92	0.67	0.84	0.70	0.88
200	51	111.	84.3	35000	22900	0.023	0.023	0.45	0.59	0.50	0.65	0.50	0.65
250	51	157.	117.	41600	27000	0.021	0.021	0.55	0.74	0.57	0.77	0.59	0.79
Rough Rod Array, Interior Subchannel Data, i=1													
100	47	28.1	31.9	17600	22400	0.038	0.040	0.78	0.69	0.78	0.69	0.78	0.69
200	47	98.3	109.	32900	41400	0.043	0.046	0.76	0.69	0.81	0.73	0.71	0.64
250	47	152.	166.	40900	51200	0.040	0.044	0.66	0.60	0.66	0.60	0.67	0.67
Rough Rod Array, Peripheral Subchannel Data, i=2													
100	47	29.1	25.5	17900	12600	0.035	0.030	0.79	0.90	0.82	0.94	0.76	0.86
200	47	98.3	85.9	32900	23100	0.042	0.036	0.77	0.88	0.74	0.85	0.70	0.80
250	47	152.	132.	40900	28700	0.039	0.034	0.77	0.88	0.72	0.83	0.66	0.76

5.2.2 Friction Factor Results

The plots of subchannel friction factors for the smooth and rough rod arrays (interior and peripheral subchannel data) are given in Figure 5.14. For comparison, the various analytical correlations for the subchannel friction factors have been shown.

The smooth surface friction factor f_s was evaluated using Eq. A1.5, the Blasius equation:

$$f_s = 0.316\ Re^{-0.25} \qquad \text{(Eq. A1.5)}$$

Although this expression was not recommended at Reynolds numbers greater than 30,000, the Blasius equation was found to be within $\pm$ 4% of values from the recommended equation for Reynolds numbers up to 100,000. The roughened surface friction factor of the interior subchannel was estimated using Eq. A1.9 developed in Appendix 1:

$$f_{r1} = 0.076\ Re^{-0.04} \qquad \text{(Eq. A1.9)}$$

The equivalent friction factor of the partially roughened peripheral subchannel was estimated using Eq. A1.9 in conjunction with the perimeter-weighted average and perimeter-weighted parallel models, i.e., $\bar{f}_{r2}$ and $\bar{\bar{f}}_{r2}$, respectively (see section 3.1.1). Typical numerical values of the aforementioned procedures are given in Table 5.8.

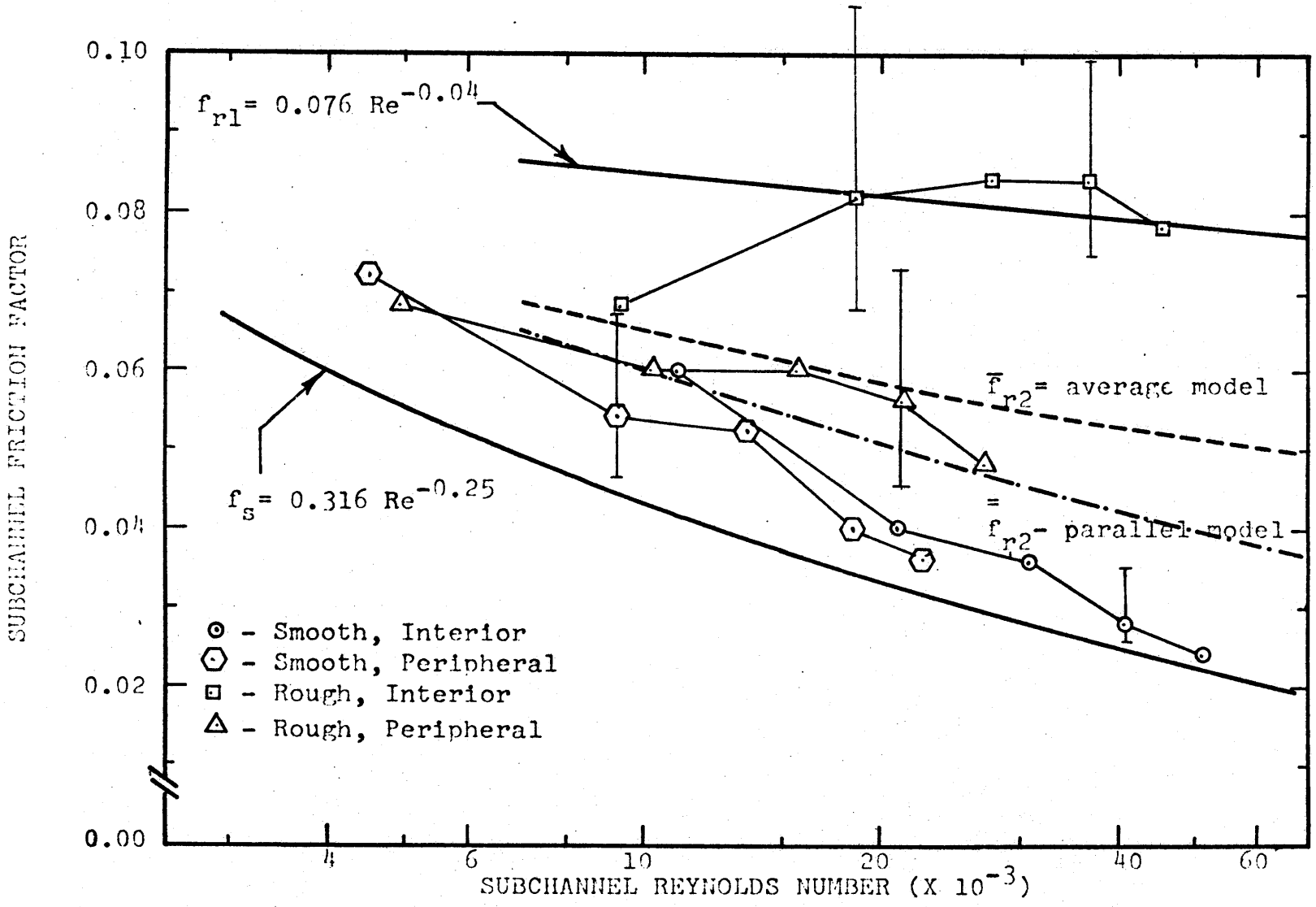

FIGURE 5.14

ANALYTICALLY DETERMINED SUBCHANNEL FRICTION FACTORS

Table 5.8

Theoretical Prediction of Subchannel Friction Factors and Friction Factor Multipliers in the Experimental Rod Array

Re_i	f_x	$\bar{f}_{x2}$	$\bar{\bar{f}}_{x2}$	f_s	f_{r1}	$\bar{f}_{r2}$	$\bar{\bar{f}}_{r2}$	$\bar{f}_{xb}$	$\bar{\bar{f}}_{xb}$	$\bar{f}_{rb}$	$\bar{\bar{f}}_{rb}$
4000	-	-	-	0.0397	-	-	-				
6000	-	-	-	0.0359	-	-	-				
7000	1.54	1.28	1.22	0.0345	0.0531	0.0442	0.0421	1.43	1.38	0.0493	0.0476
10000	1.66	1.34	1.26	0.0316	0.0525	0.0423	0.0398	1.52	1.46	0.0480	0.0461
15000	1.81	1.42	1.30	0.0286	0.0517	0.0406	0.0372	1.64	1.55	0.0469	0.0443
20000	1.92	1.47	1.33	0.0266	0.0511	0.0391	0.0354	1.73	1.61	0.0460	0.0428
30000	2.09	1.56	1.37	0.0240	0.0502	0.0374	0.0329	1.86	1.70	0.0446	0.0408
40000	2.22	1.63	1.39	0.0223	0.0495	0.0363	0.0310	1.97	1.77	0.0439	0.0395
50000	2.33	1.68	1.42	0.0211	0.0491	0.0354	0.0300	2.05	1.83	0.0433	0.0386
60000	2.42	1.73	1.43	0.0202	0.0489	0.0349	0.0289	2.12	1.87	0.0428	0.0378
70000	2.50	1.77	1.45	0.0194	0.0485	0.0343	0.0281	2.19	1.91	0.0425	0.0371
80000	-	-	-	0.0188	-	-	-	-	-		

$f_s = 0.316\ Re^{-0.25}$ (Eq. A1.5) $\bar{f}_{x2} = 1 + H_2(f_x - 1)$ Eq.3.13) $H_b = 38.5/48.6 - 0.792$

$f_{ri} = 0.076\ Re^{-0.04}$ (Eq. A1.9) $\bar{\bar{f}}_{x2} = f_x/[(1 - H_2)\ f_x + H_2]$ (Eq.3.14)

$f_{r2} = f_{ri} \times f_x$ $H_2 = P_{H2}/P_{w2} = 0.520/1.011 = 0.514$

$f_{x1} = 0.24\ Re^{0.21}$ (Eq. A1.9)

From the plotted results in Figure 5.14, the subchannel friction factors are found to be in agreement with the analytically predicted friction factors at Reynolds numbers greater than 20,000. Experimental uncertainties were larger than the calculated difference between equivalent friction factor models. The behavior of the data below Reynolds numbers of 15,000 does not follow the analytical predictions. Further, this was a region where flow transition effects were strongest.

The bundle or rod array average friction factors (based on rod bundle average hydraulic diameter and dynamic pressure) are plotted versus Reynolds number in Figure 5.15. By using analytically determined flow information for the data reduction, the smooth rod bundle average friction factors are seen to be in good agreement with analytical predictions at Reynolds numbers greater than 10,000. At Reynolds numbers above 15,000, in the rough rod array, the friction factors are in agreement with those predicted using Eq. A1.9 along with the equivalent friction factor models. Experimental uncertainties again were larger than the calculated differences between the two equivalent friction factor models.

The bundle average friction factors are seen to be nearly equal for the interior and peripheral subchannel data for both smooth and rough rod bundles; this indicates that radial pressure gradients are either small or negligible over

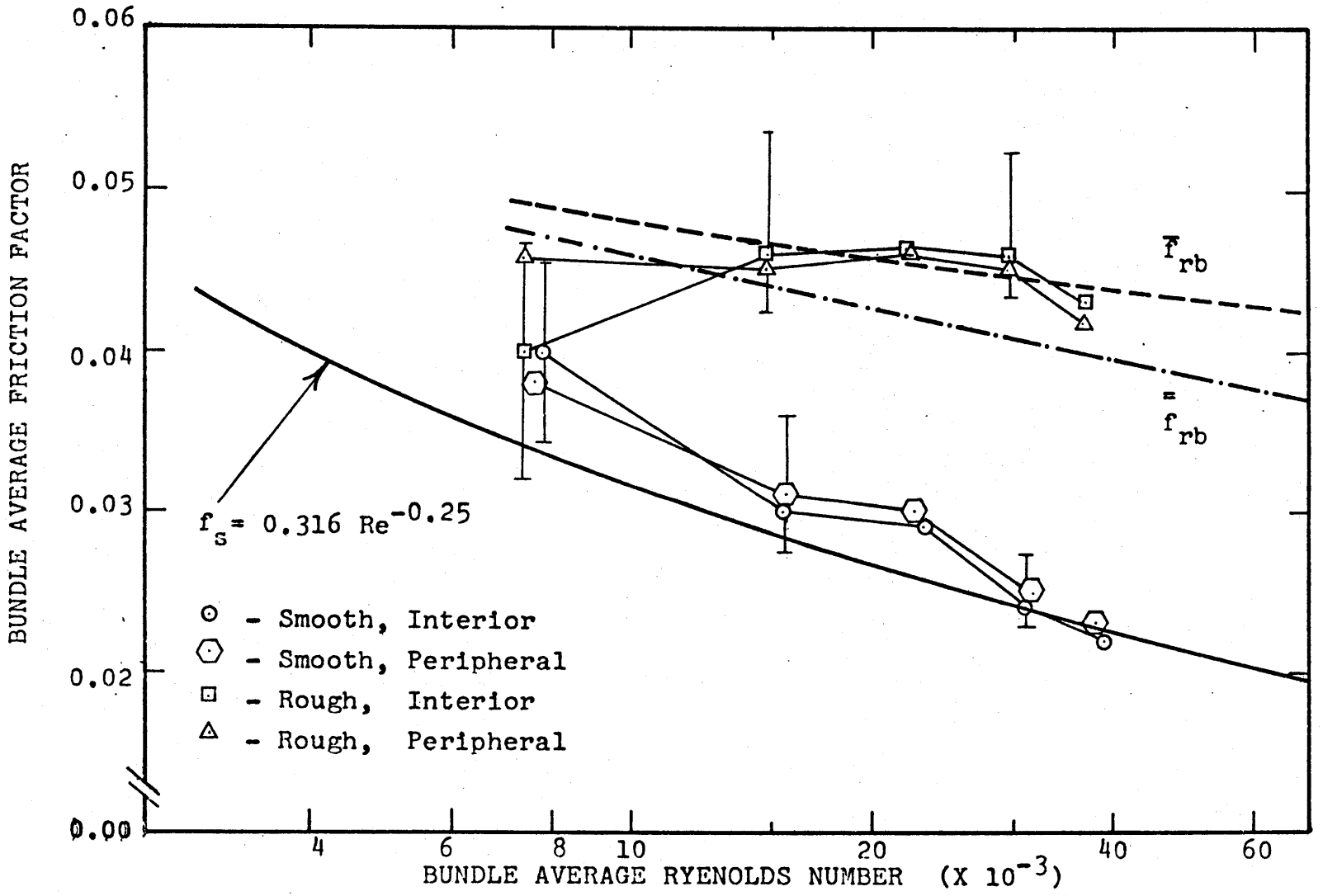

FIGURE 5.15

ANALYTICALLY DETERMINED ROD ARRAY FRICTION FACTORS

the axial region of interest. Experimental uncertainty prohibited the determination of the value of the magnitude (if any) of radial pressure gradients in the rod bundle.

The following notes are made regarding the calculation of the smooth rod bundle friction factors. Rogers and Tahir [R6] have suggested that the rod bundle average friction factor f_b should be calculated according to

$$f_b = 0.179\ Re_b^{-0.194} \qquad \text{(Eq. 5.6)}$$

However, no Reynolds number range was specified. This correlation was stated to be in "excellent agreement" with a survey of rod bundle friction factor data (smooth) by Rehme [R7].

Eq. 5.6 was found to be almost identical to the smooth tube firction factor correlation (Eq. A1.4) for the Reynolds number range 30,000 - 1,000,000. For this work the smooth tube friction factor correlation (the Blasius equation) for the Reynolds number range 5,000 - 30,000 was used throughout for the calculation of smooth rod bundle friction factors because (A) it was in good agreement with Eqs. 5.6 and A1.4 at Reynolds numbers greater than 25,000 and (B) Eq. Eq. A1.4 did not apply at Reynolds numbers below 30,000.

The results of the experimentally determined subchannel friction factors are plotted versus Reynolds number in Figure 5.16 and are shown along with the analytical predictions of

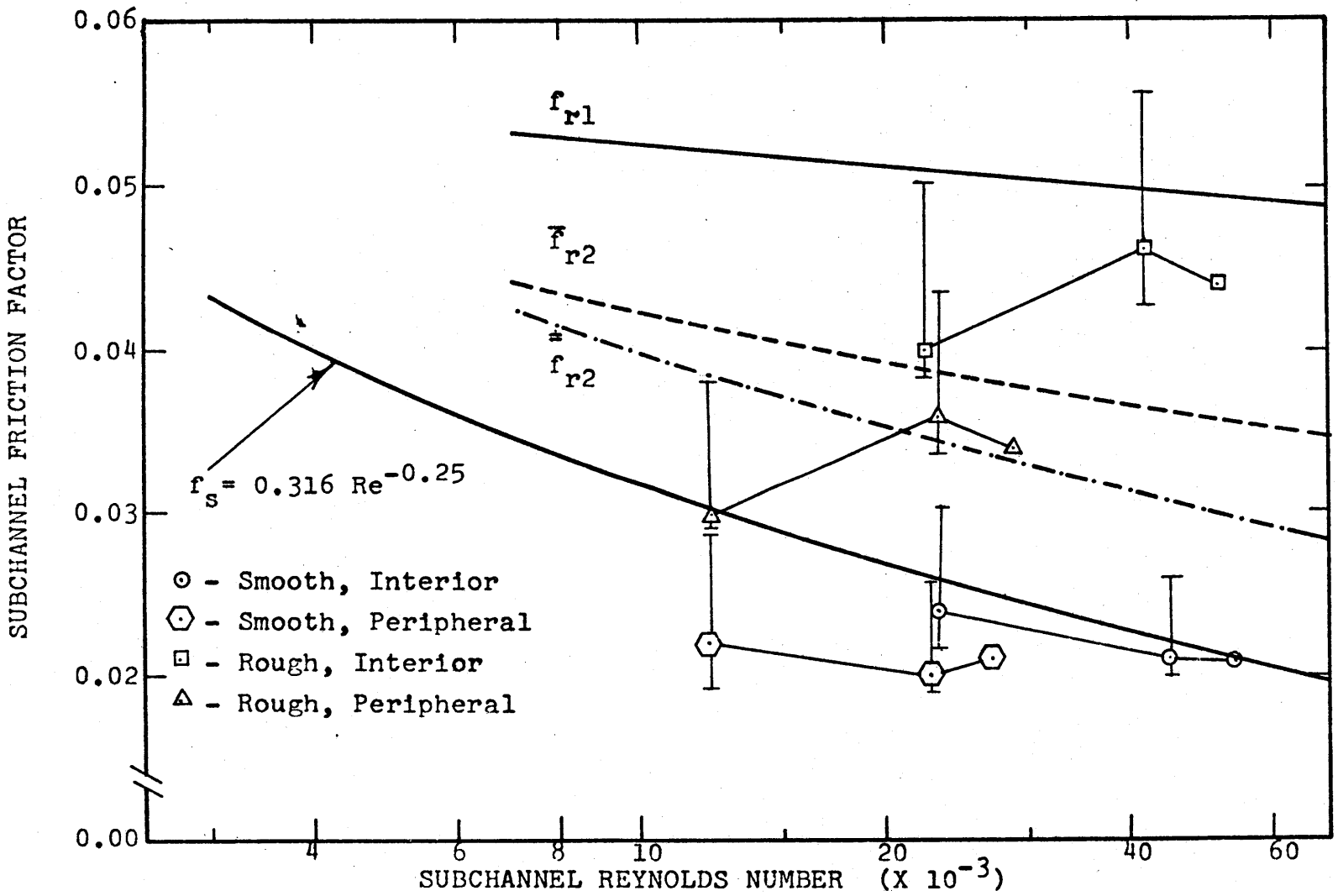

FIGURE 5.16

EXPERIMENTALLY DETERMINED SUBCHANNEL FRICTION FACTORS

the various subchannel friction factors. The interior subchannel friction factors for the smooth rod bundle agreed with the predictions using the Blasius equation. The rough bundle, interior subchannel firction factors were somewhat lower than those predicted using Eq. A1.9. The smooth and rough bundle friction factors for the peripheral subchannel were lower than those analytically predicted. While the axial pressure drop in the peripheral subchannel was about the same as in the interior subchannel, the experimentally measured average velocity in the peripheral subchannel was higher than that calculated due to coolant mixing effects and instrumentation limitations. With this, the dynamic pressure in the peripheral subchannel was higher than that calculated, and the experimentally determined friction factor was lower than expected.

The experimentally determined friction factors for the overall rod array are shown in Figure 5.17. The smooth bundle friction factors were slightly below analytical predictions while those for the rough rod bundle were in agreement with bundle average friction factors predicted using the weighted perimeter models for the equivalent friction factor of the overall rod bundle, see Table 5.8.

5.2.3 Friction Factor Multiplier Results

The friction factor multipliers for the rough rod array were determined by dividing the friction factor

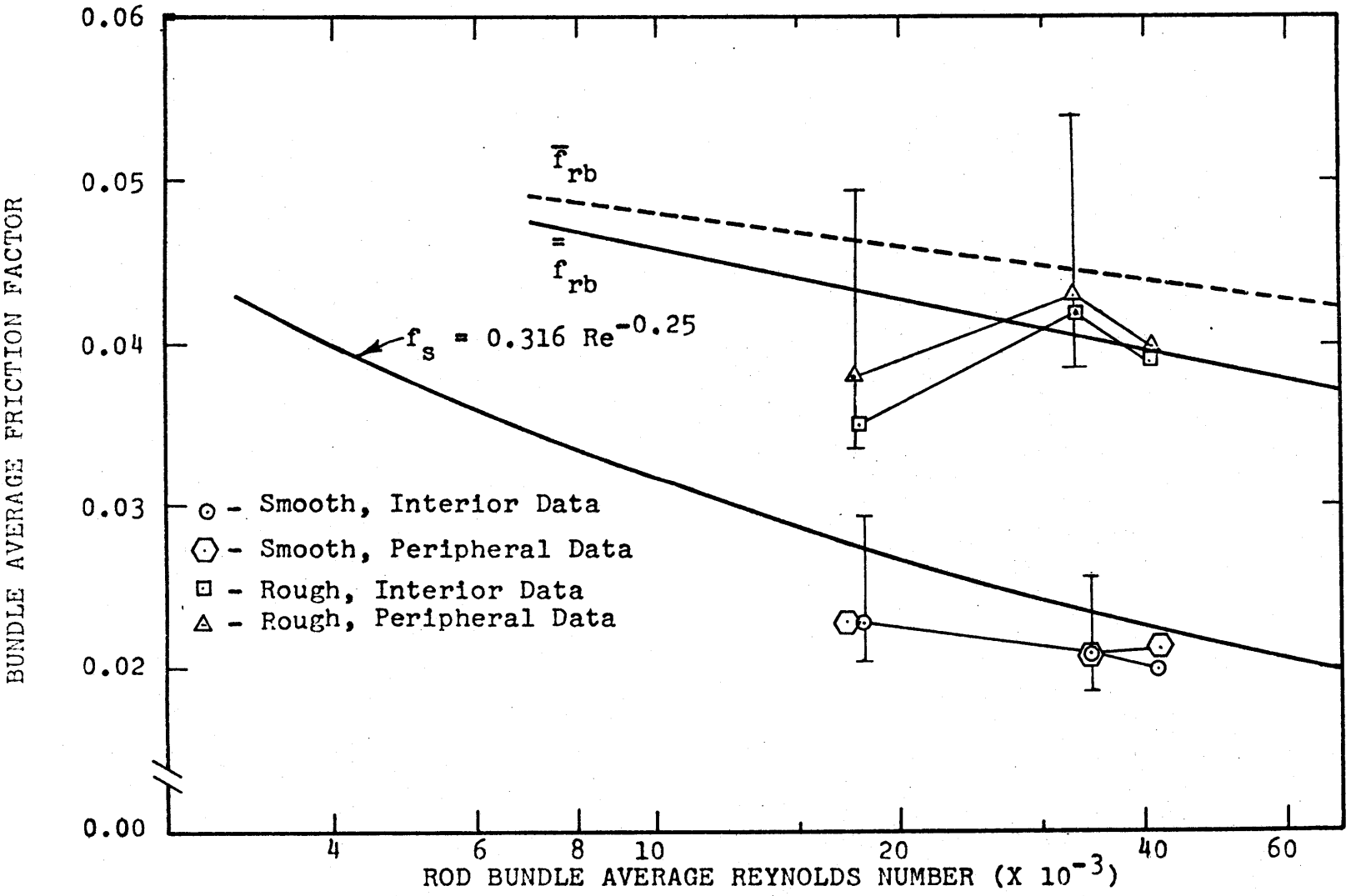

FIGURE 5.17

EXPERIMENTALLY DETERMINED ROD BUNDLE AVERAGE FRICTION FACTORS

of the rough bundle by those of the smooth bundle for the same flow conditions and geometry. The friction factor multiplier results were obtained using the friction factor data in Tables 5.6 and 5.7 and are tabulated in Table 5.9.

The friction factor multipliers determined by using analytically predicted flow information in the data reduction are shown in Figure 5.18. All of the data tended to support the observation that the roughened surface flow was undergoing a transition at Reynolds numbers below 15,000. This was because all of the friction factor multiplier dat was below that analytically predicted. At Reynolds numbers higher than 15,000, the friction factor multipliers tended to agree with the analytically predicted values. The peripheral subchannel friction factor multipliers were slightly lower than those predicted. The rod bundle friction factor multipliers were within the range of values predicted using the perimeter-weighted, equivalent friction factor models (see Table 5.8).

The friction factor multipliers determined using the experimentally measured flow information are shown in Figure 5.19 along with the analytically predicted friction factor multipliers for the interior and peripheral subchannels, as well as, the overall rod array. The data does agree somewhat with the predictions.

Table 5.9

Experimental Friction Factor Multipliers

Main Flow (GPM)	$\overline{Re}_1$	f_{x1}	$\overline{Re}_2$	f_{x2}	$\overline{Re}_b$	f_{xb} (Inter. Data)	f_{xb} (Periph. Data)
			Analytical Data Reduction				
50	9980	1.08	4700	0.96	7590	1.00	1.21
100	19599	1.70	9700	1.08	15200	1.53	1.45
150	29000	1.86	14600	1.11	22800	1.59	1.53
200	38600	2.17	19700	1.12	30400	1.92	1.61
250	48100	2.23	24700	1.21	37900	1.95	1.83
			Experimental Data Reduction				
100	22850	1.67	18050	1.36	17850	1.65	1.52
200	43150	2.19	33950	1.53	33650	2.05	1.83
250	52500	2.10	41250	1.62	41250	2.00	1.86

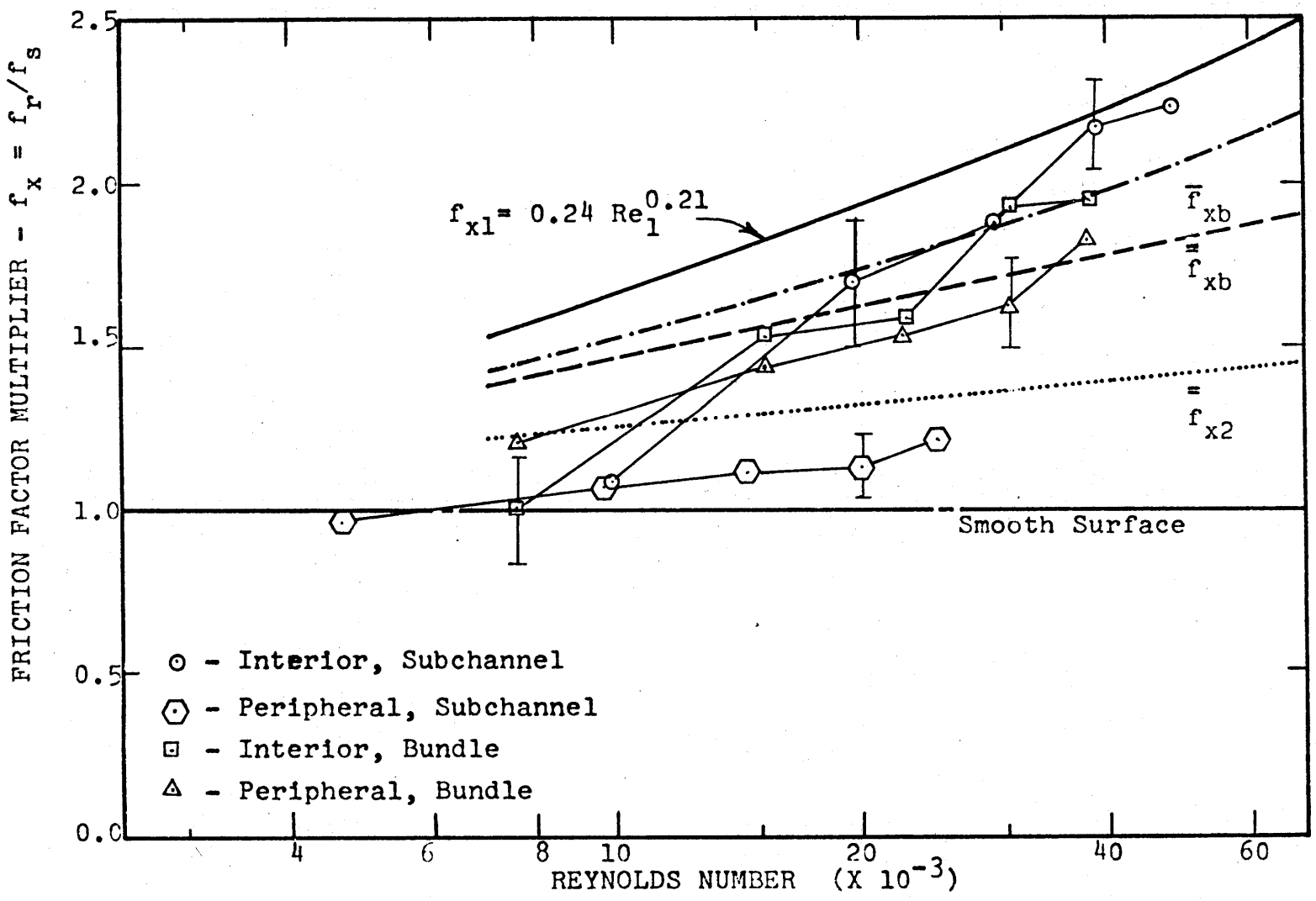

FIGURE 5.18

ANALYTICALLY DETERMINED SUBCHANNEL AND ROD BUNDLE FRICTION FACTOR MULTIPLIERS

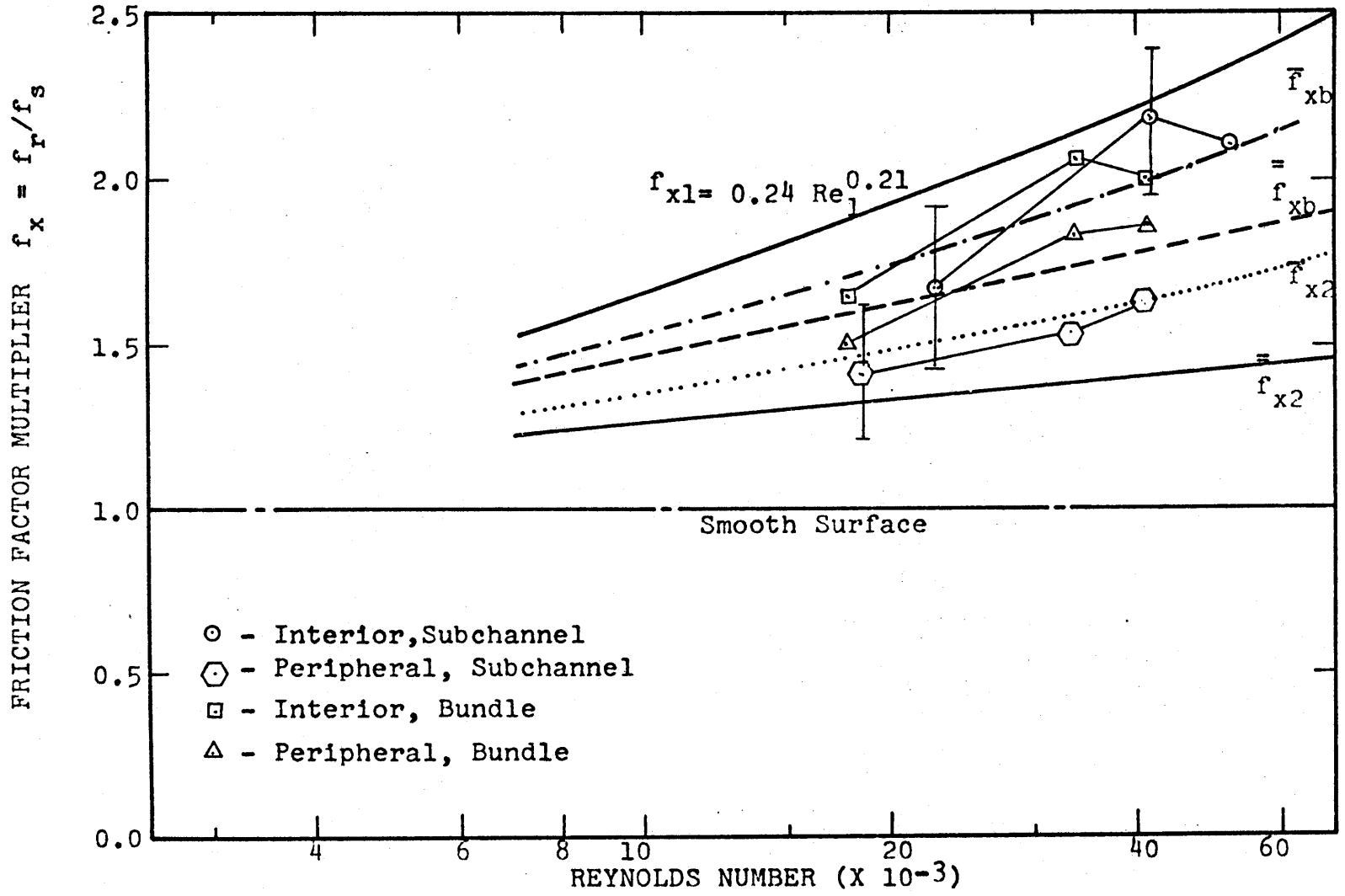

FIGURE 5.19 - EXPERIMENTALLY DETERMINED SUBCHANNEL AND ROD BUNDLE FRICTION FACTOR MULTIPLIERS

5.2.4 Spacer Grid Loss Coefficient Results

The grid spacer pressure losses measured in the various axial pressure profile experiments were tabulated in Table 5.5 and discussed in more detail in section 5.2.1. The analytically and experimentally determined dynamic pressures used to obtain the loss coefficients were listed in Tables 5.6 and 5.7, respectively. The spacer grid loss coefficients were determined for the specific subchannel in which the data was collected and for the rod bundle average.

The average value of the pressure losses measured for the three grids $\overline{\Delta P}_g$ was used to establish the average grid loss coefficient for the measurement subchannel $\bar{K}_{gi}$ and the overall rod array $\bar{K}_{gb}$. The average spacer grid loss coefficients in smooth and rough rod arrays calculated from interior and peripheral subchannel data are listed in Table 5.10; loss coefficients determined using experimental flow information have been given in parenthesis in Table 5.10. The average loss coefficients determined using analytical flow information are given in Figure 5.20; the same data for the specific grids is plotted in Figure 5.21. The loss coefficients have been shown along with those predicted using the correlation of Buettiker developed at E.I.R. for "clean" AGATHE spacers [B1] :

$$\bar{K}_{gb} = 20.73 \ Re_b^{-0.5} + 0.452 \quad . \qquad \text{(Eq. 5.7)}$$

Table 5.10

Average Spacer Grid Loss Coefficients*

Main Flow (GPM)	Smooth Rod Array $\overline{\Delta P_g}$ (in-H_2O)	Smooth Rod Array $\overline{K_i}$	Smooth Rod Array $\overline{K_g}$	Rough Rod Array $\overline{\Delta P_g}$ (in-H_2O)	Rough Rod Array $\overline{K_i}$	Rough Rod Array $\overline{K_g}$
Interior Subchannel Data						
50	7.3	1.05	1.27	5.3	0.83	0.92
100	20.7	0.75 (0.60)+	0.90 (0.69)	22.0	0.88 (0.69)	0.96 (0.76)
150	39.3	0.63	0.76	45.7	0.83	0.89
200	63.3	0.57 (0.49)	0.70 (0.57)	75.0	0.78 (0.69)	0.82 (0.76)
250	92.7	0.54 (0.51)	0.65 (0.59)	101.	0.67 (0.61)	0.71 (0.66)
Peripheral Subchannel Data						
50	6.3	1.77	1.10	5.6	1.25	0.98
100	21.0	1.48 (0.88)	0.92 (0.70)	23.0	1.19 (0.90)	1.00 (0.79)
150	39.0	1.21	0.76	44.7	0.99	0.87
200	53.3	0.94 (0.63)	0.58 (0.48)	72.3	0.87 (0.84)	0.79 (0.74)
250	89.3	1.00 (0.76)	0.62 (0.57)	109.	0.82 (0.83)	0.76 (0.72)

*The Reynolds numbers and dynamic pressures corresponding to the data points are given in Tables 5.6 and 5.7 .

+Values in parenthesis were determined using experimental flow data, all other values were determined using analytical flow data.

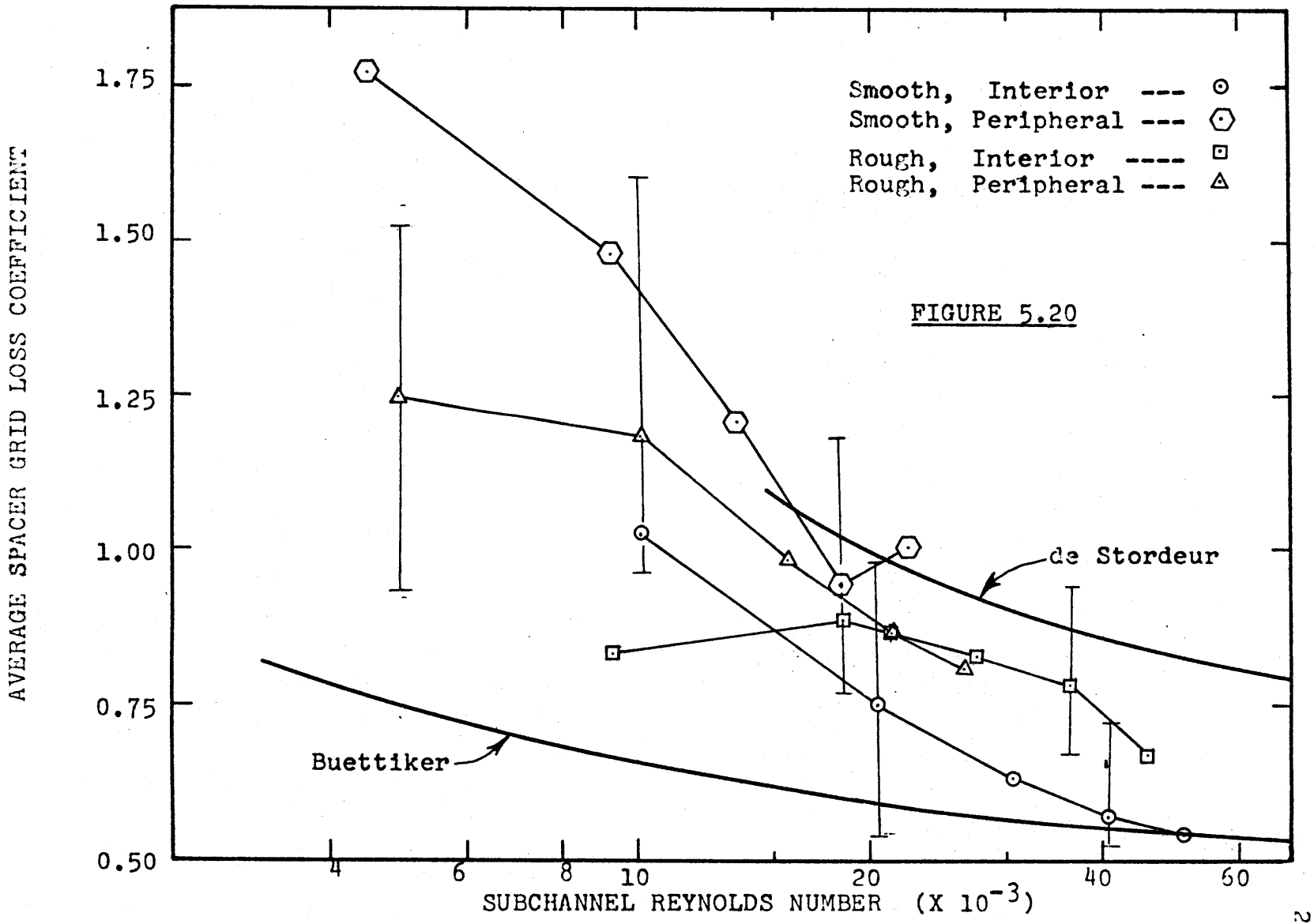

FIGURE 5.20

ANALYTICALLY DETERMINED SUBCHANNEL AVERAGE, SPACER GRID LOSS COEFFICIENTS

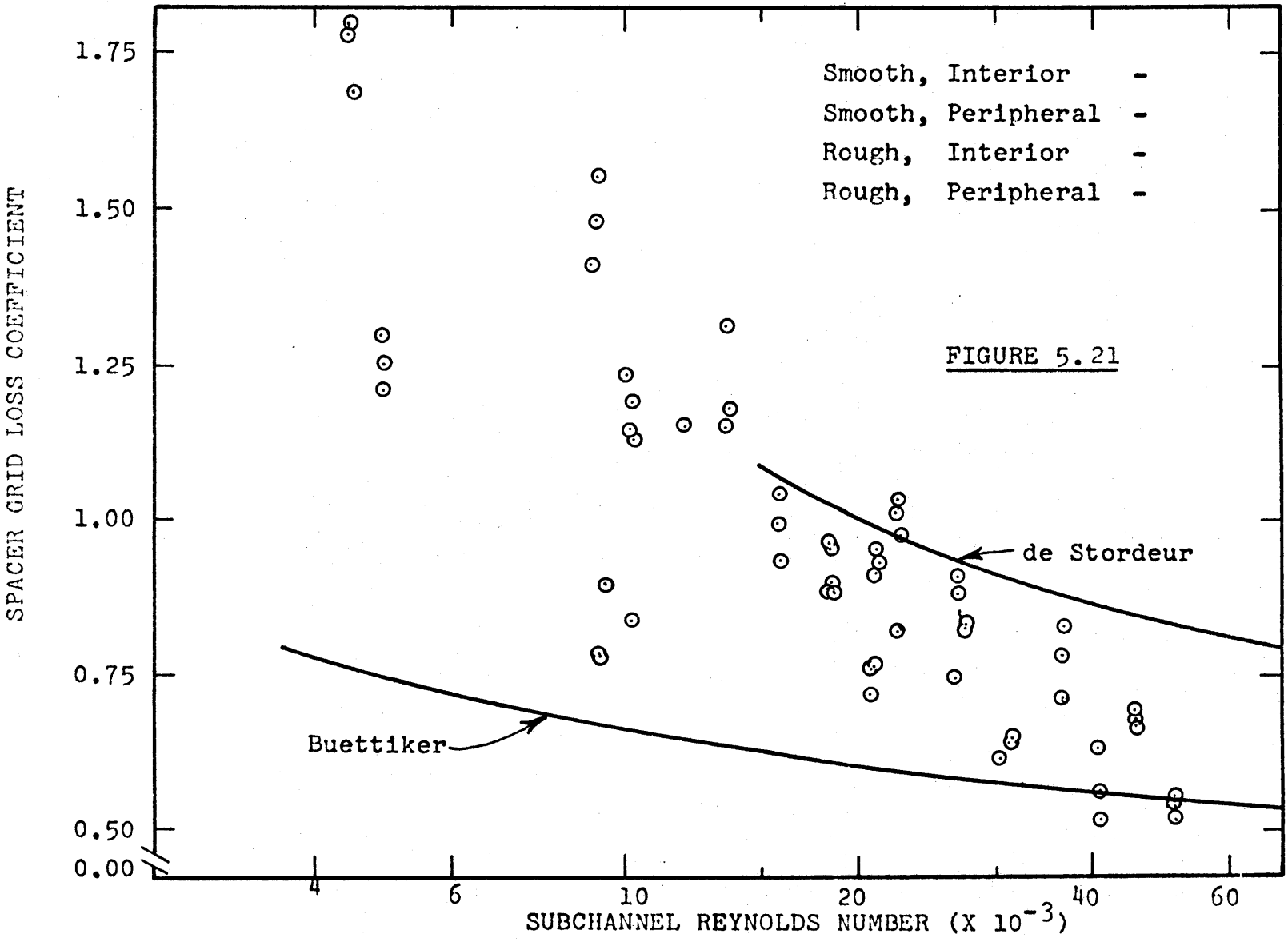

FIGURE 5.21

ANALYTICALLY DETERMINED SPACER GRID LOSS COEFFICIENTS

The grid loss predicted using the method of de Stordeur, see references [S2, L3] for calculational details, was developed from data applying to honeycomb grids for square lattice rod arrays typical of the Fermi liquid-metal cooled, fast breeder reactor. The data is seen to fall between the values predicted by the two correlations.

The rod bundle average, grid loss coefficients determined using analytical flow information are plotted in Figure 5.22. The average grid loss coefficients based on measurement subchannel data which was experimentally determined is shown in Figure 5.23. The average grid loss coefficients based on rod bundle data which was experimentally determined is shown in Figure 5.24. In general, the loss coefficients for the the spacer grids tested were higher than the values predicted by the Buettiker correlation - particularly at Reynolds numbers below 20,000. Although experimental uncertainty prevents any definite conclusions, it was observed that the grid loss coefficients in the rough bundle were typically 10% higher than those of the smooth bundle. Further experimental study will be required to determine if the grid loss coefficient varies with surface roughness. Nevertheless, the grid losses in a roughened surface region might be expected to be larger than in a smooth region because, in the rough array, the velocity gradients on the smooth grid surfaces are higher and because the peak-to-

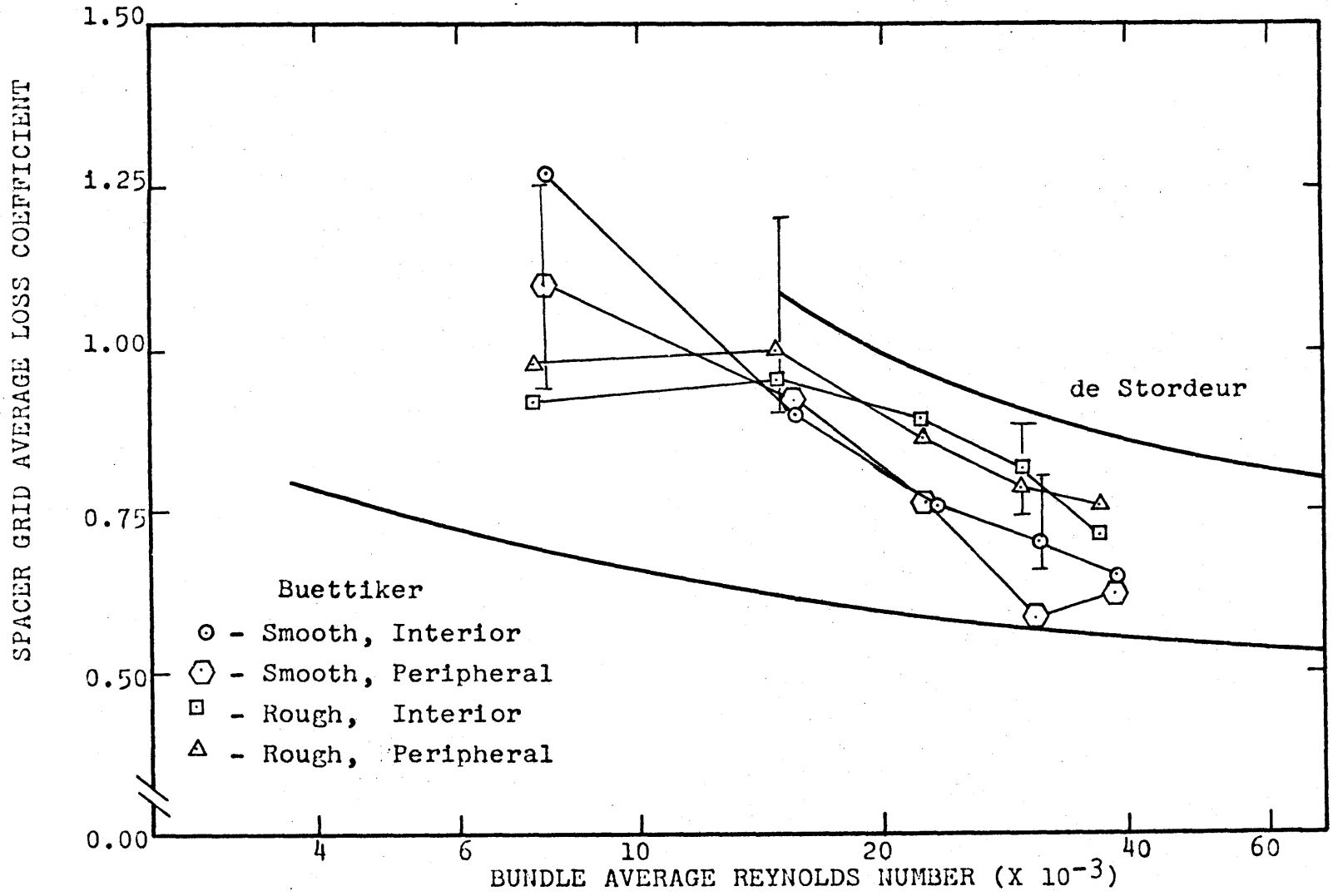

FIGURE 5.22

ANALYTICALLY DETERMINED ROD BUNDLE AVERAGE, SPACER GRID LOSS COEFFICIENTS

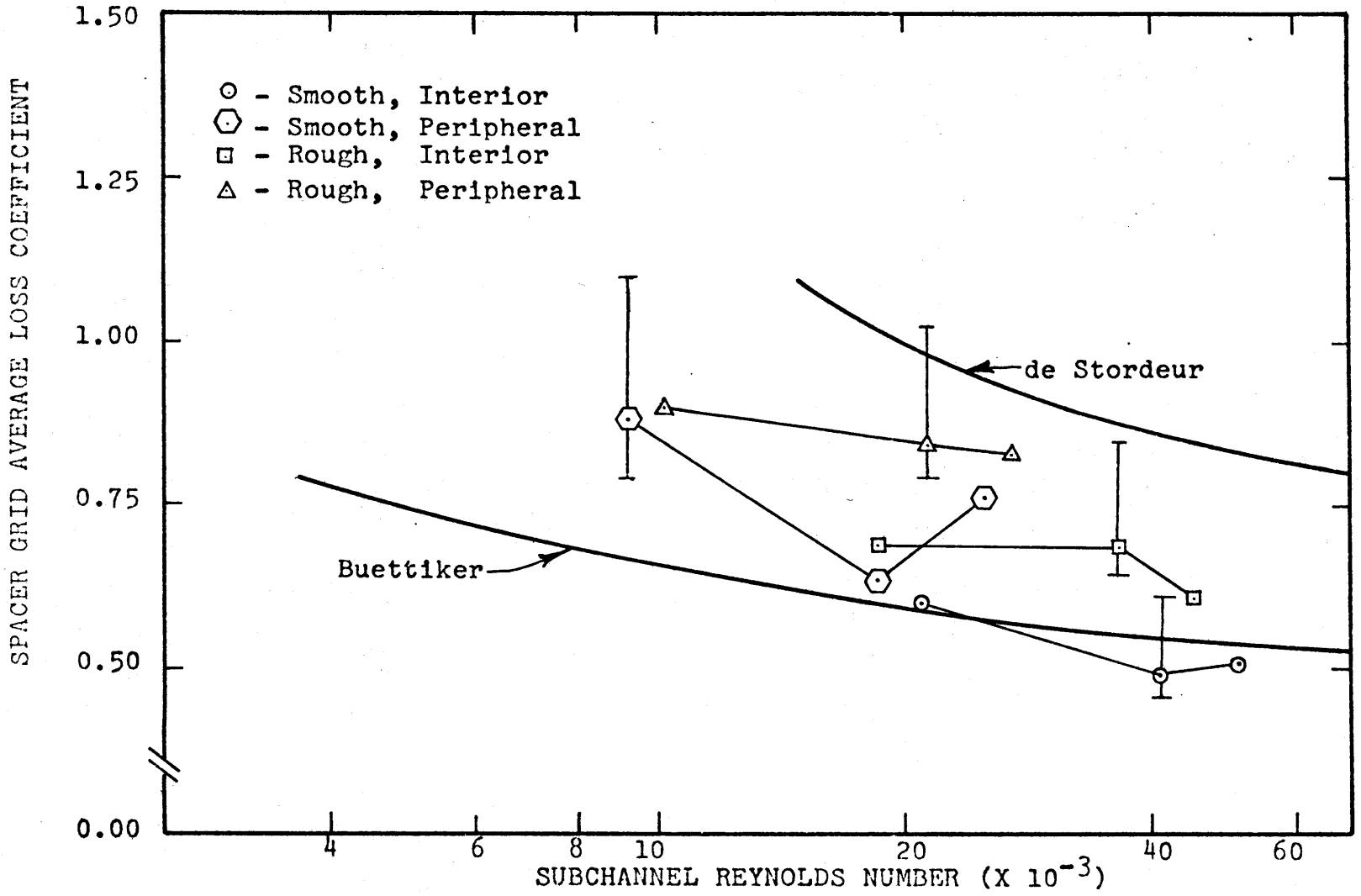

FIGURE 5.23

EXPERIMENTALLY DETERMINED AVERAGE, SUBCHANNEL SPACER GRID LOSS COEFFICIENTS

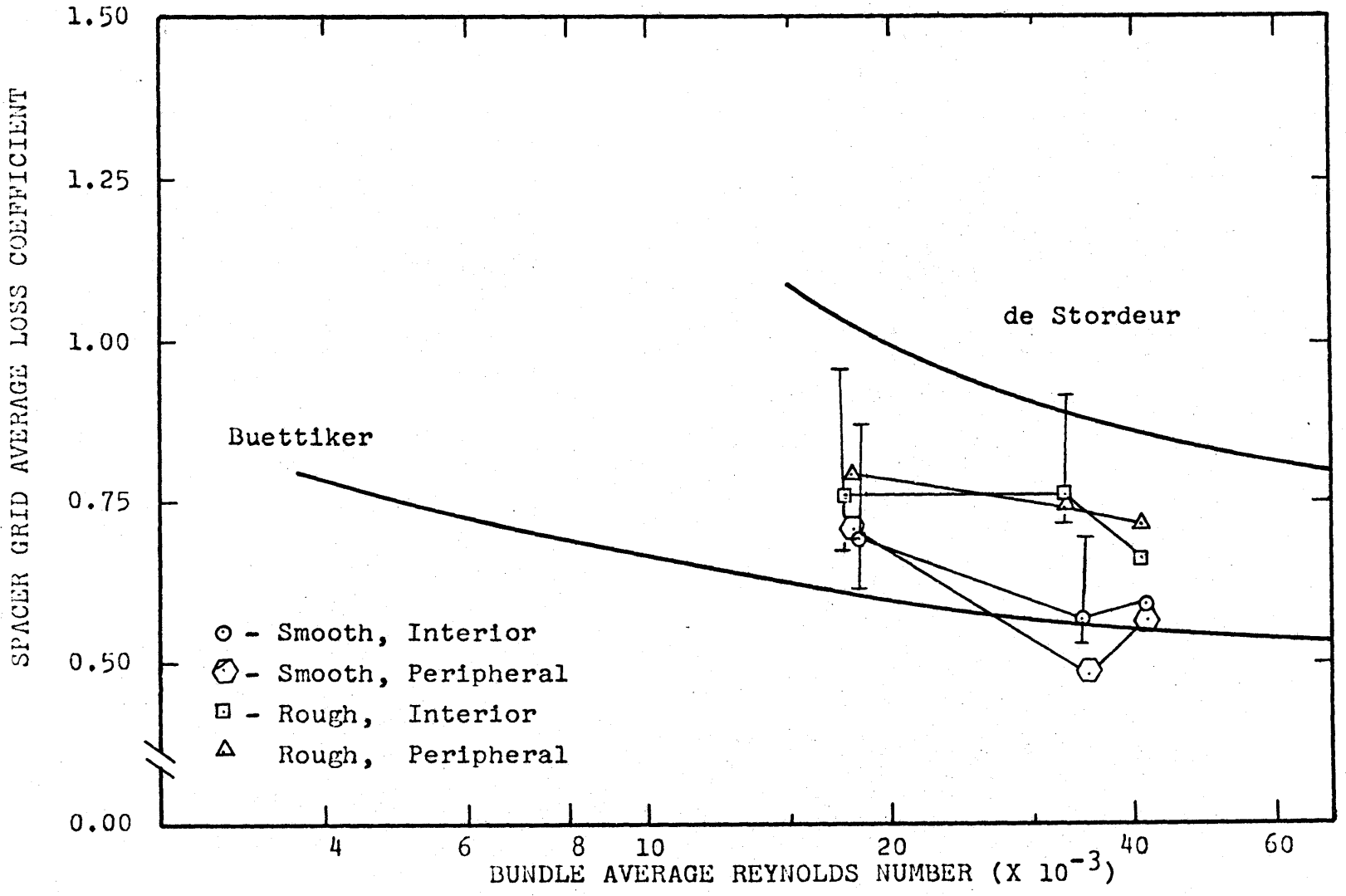

FIGURE 5.24

EXPERIMENTALLY DETERMINED ROD BUNDLE AVERAGE, SPACER GRID LOSS COEFFICIENT

average velocity in the subchannels are higher than in the smooth array.

5.3 Interchannel Coolant Mixing Experiments

Experiments were performed with salt solution tracer injection into interior subchannel no. 1 and peripheral subchannel no. 48 of the experimental rod array in order to determine interchannel coolant mixing behavior in both smooth and rough rod arrays. Further discussion of coolant mixing is given in Appendix 3. Details of the experiment design and procedures are given in Chapter 4. The experimental mixing data was processed by a computer code called MITMIX-R which is discussed in Appendix 5.

Recall that the tracer solution was injected over a variable axial position into the downstream 27 inches of the the rod array. Salt solution conductance probes were located within the last 1/4 inch of the rod array next to the exit plane. The coolant mixing experiments were performed with five to six different Reynolds numbers (main flows); each experiment included 12 to 50 different axial separation distances between the tracer injection device and the detector probes. In addition to the experiments noted, more axially detailed data was taken in the vicinity of the grid spacers. The coolant mixing experiments performed during this work are listed in Table 5.11 along with various details regarding the experiments. Hydraulic data for the

Table 5.11

A Summary of the Interchannel Coolant Mixing Experiments

Exp. No.*	Date	Main Flow (GPM)	Inj. Flow (gr/min)	No. Axial Loc.	No. Subch. Monit.	Water Temp. (°F)	Note
---------- Smooth Rod Array, Interior Subchannel Injection ----------							
SI-1	17 Mar	4.8	25.	34	32	45	Laminar Flow
SI-2	17 Mar	49.	72.	24	52	44	Turbulent Flow
SI-3	17 Mar	100.	140.	25	52	44	"
SI-4	17 Mar	150.	200.	34	52	44	"
SI-5	24 Mar	200.	260.	25	32	46	"
SI-6	21 Mar	49.	75.	12	32	45	Spacer No. 6
SI-7	21 Mar	49.	75.	10	32	45	Spacer No. 7
SI-8	21 Mar	150.	203.	12	32	45	Spacer No. 6
SI-9	21 Mar	150.	203.	11	32	45	Spacer No. 7
---------- Smooth Rod Array, Peripheral Subchannel Injection ----------							
SP-1	21 Mar	4.8	25.	25	52	45	Laminar Flow
SP-2	21 Mar	49.	55.	25	52	45	Turbulent Flow
SP-3	18 Mar	100.	100.	25	52	45	"
SP-4	18 Mar	150.	100.	34	52	45	"
SP-5	24 Mar	200.	205.	26	52	46	"
SP-6	21 Mar	150.	150.	11	52	45	Spacer No. 6
SP-7	21 Mar	150.	150.	11	52	45	Spacer No. 7
---------- Rough Rod Array, Interior Subchannel Injection ----------							
RI-1	6 May	4.8	17	12	24	54	Laminar Flow
RI-2	6 May	49.	76	25	32	54	Turbulent Flow
RI-3	6 May	100.	126	26	32	54	"
RI-4	6 May	150.	177	25	32	54	"
RI-5	7 May	200.	255	27	32	54	"
RI-6	7 May	250.	280	26	32	54	"
RI-7	7 May	100.	127	16	32	54	Spacer No. 6
RI-8	7 May	100.	127	15	32	54	Spacer No. 7
RI-9	7 May	100.	127	15	32	54	Spacer No. 8
RI-10	7 May	200.	255	16	32	54	Spacer No. 6
RI-11	7 May	200.	255	16	32	54	Spacer No. 7
RI-12	7 May	200.	255	15	32	54	Spacer No. 8
---------- Rough Rod Array, Peripheral Subchannel Injection ----------							
RP-1	9 May	4.8	17.	14	36	54	Laminar Flow
RP-2	9 May	49.	65.	15	36	54	Turbulent Flow
RP-3		100.	126.	54	52	58	"
RP-4	9 May	150.	180.	26	36	54	"
RP-5	20 May	200.	240.	49	52	58	"
RP-6	9 May	250.	290.	15	36	54	"
RP-7	20 May	100.	126.	15	52	58	Spacer No. 6
RP-8	20 May	100.	126.	15	52	58	Spacer No. 7
RP-9	20 May	100.	126.	15	52	58	Spacer No. 8
RP-10	20 May	200.	240.	15	52	58	Spacer No. 6
RP-11	20 May	200.	240.	15	52	58	Spacer No. 7
RP-12	20 May	200.	240.	10	52	58	Spacer No. 8

coolant mixing experiments are given in Table 5.12.

In each experiment, the injection flow rate was approximately equal to the value calculated by using the equal axial velocity criterion. The average subchannel velocities used to determine the injection flows were calculated by using the RUFHYD code.

5.3.1 Coolant Mixing Experiment Results, Smooth Rod Array, Interior Subchannel Injection

Coolant mixing experiments with tracer injection into interior subchannel no. 1 of the smooth rod array were done for main flows from 4.8 to 200 GPM. The experimental results of subchannel salt solution concentration versus injector-detector separation (axial position) are given in Appendix 8; the results for the 200 GPM case (Experiment no. SI-5, Table 5.11) are given in Figures 5.25 through 5.27. Recall that the various subchannel identification numbers were illustrated in Figure 5.1.

For each experiment the total rate of tracer detection at each axial measurement plane was compared to that injected. This "mass balance" procedure is duscussed in detail in section 4.3.5 and is illustrated in Figure 5.25. For the smooth rod experiments, the detected tracer rate was about two-thirds of the injected for injector positions below about 16 inches (upstream of grid no. 8). In the rough rod experiments, the mass balance results were much better, see sections 5.3.3 and 5.3.4. Downstream of

TABLE 5.12

HYDRAULIC DATA FOR THE COOLANT MIXING EXPERIMENTS

EXP. NO.	MAIN FLOW (GPM)	$\bar{V}_1$ (ft/sec)	$\bar{V}_2$ (ft/sec)	f_{x1}	Re_1	Re_2	Re_b
-----	Smooth Rod Array, Interior Subchannel Injection ------						
SI-1	4.8	0.66	0.26	1.00	1022	250	830
SI-2	49.	6.09	4.36	1.00	9320	4190	8040
SI-3	100.	13.6	10.9	*	20760	10490	18200
SI-4	150.	18.3	13.1	1.00	28000	12600	24200
SI-5	200.	26.2	20.0	*	41500	19900	36100
SI-6	49.	6.09	4.36	1.00	9320	4190	8040
SI-7	49.	6.09	4.36	1.00	9320	4190	8040
SI-8	150.	18.3	13.1	1.00	28400	12800	24500
SI-9	150.	18.3	13.1	1.00	28400	12800	24500
-----	Smooth Rod Array, Peripheral Subchannel Injection ----						
SP-1	4.8	0.66	0.26	1.00	1020	250	830
SP-2	49.	5.97	4.27	1.00	9300	4170	8020
SP-3	100.	13.6	10.9	*	21100	10700	18500
SP-4	150.	18.3	13.1	1.00	28400	12800	24500
SP-5	200.	26.2	20.0	*	41500	19900	36100
SP-6	150.	18.3	13.1	1.00	28400	12800	24500
SP-7	150.	18.3	13.1	1.00	28400	12800	24500
-----	Rough Rod Array, Interior Subchannel Injection ------						
RI-1	4.8	0.66	0.26	1.00	1170	290	950
RI-2	49.	5.73	4.82	1.67	10200	5400	9000
RI-3	100.	13.1	10.9	*	23300	12200	20500
RI-4	150.	17.1	15.7	2.10	30500	17500	27300
RI-5	200.	24.2	21.5	*	43200	24040	38400
RI-6	250.	29.9	26.7	*	53300	29900	47500
RI-7	100.	13.1	10.9	*	23300	12200	20500
RI-8	100.	13.1	10.9	*	23300	12200	20500
RI-9	100.	13.1	10.9	*	23300	12200	20500
RI-10	200.	24.2	21.5	*	43200	24040	38400
RI-11	200.	24.2	21.5	*	43200	24040	38400
RI-12	200.	24.2	21.5	*	43200	24040	38400
-----	Rough Rod Array, Peripheral Subchannel Injection -----						
RP-1	4.8	0.66	0.26	1.00	1170	290	950
RP-2	49.	5.75	4.77	1.61	10200	5340	9000
RP-3	100.	13.1	10.9	*	25100	13200	22100
RP-4	150.	17.1	15.6	2.10	30600	17500	27300
RP-5	200.	24.2	21.5	*	46600	25900	41400
RP-6	250.	29.9	26.7	*	53300	29900	47500
RP-7	100.	13.1	10.9	*	25100	13200	22100
RP-8	100.	13.1	10.9	*	25100	13200	22100
RP-9	100.	13.1	10.9	*	25100	13200	22100
RP-10	200.	24.2	21.5	*	46600	25900	41400
RP-11	200.	24.2	21.5	*	46600	25900	41400
RP-11	200.	24.2	21.5	*	46600	25900	41400

* Not applicable, Experimental velocity data was used.

FIGURE 5.25

CASE SI-5: MASS BALANCE VERSUS INJECTOR TRAVEL

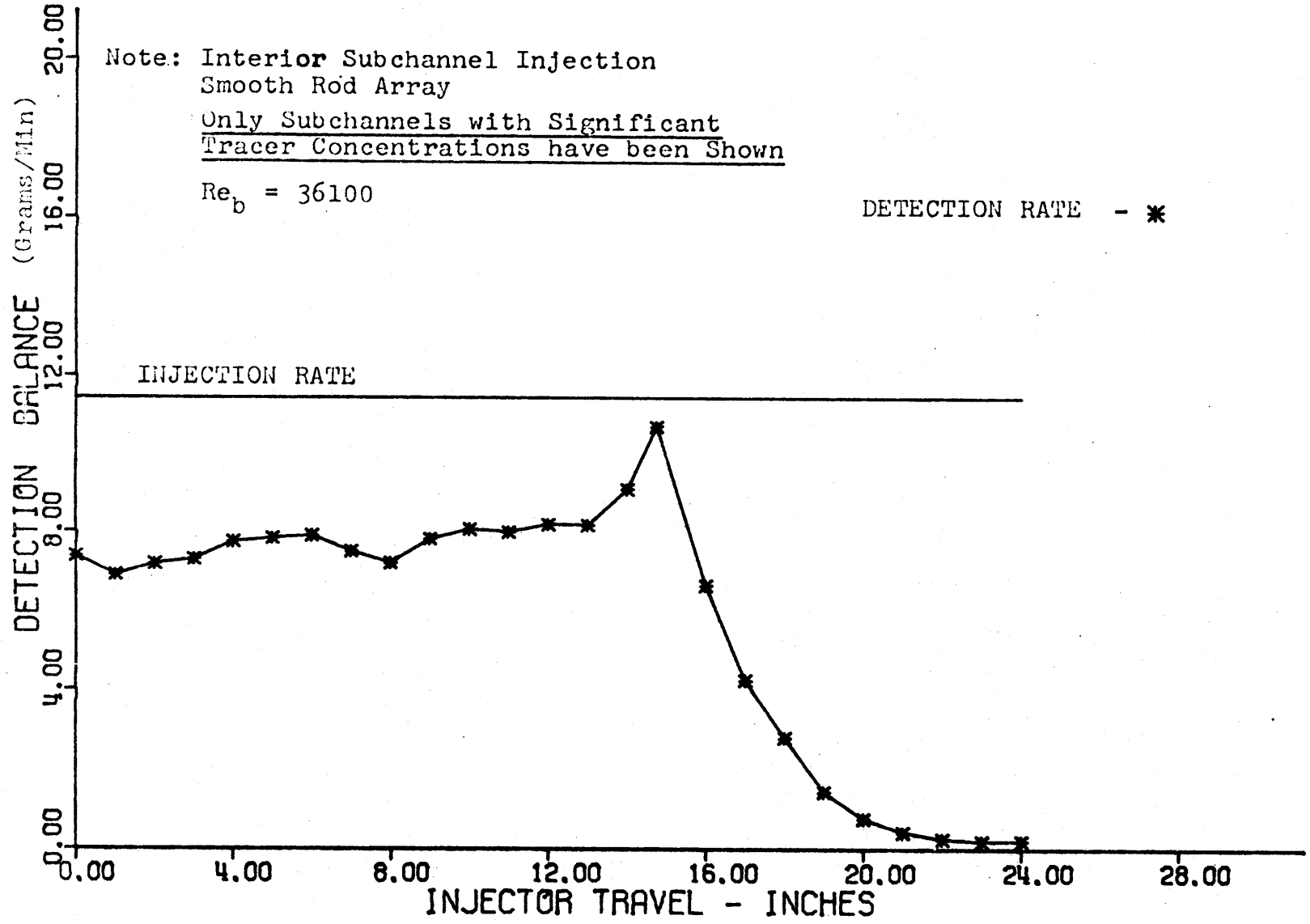

FIGURE 5.26

CASE SI-5; AXIAL TRACER CONCENTRATRATION, SUBCHANNELS 2, 1, 3, 4

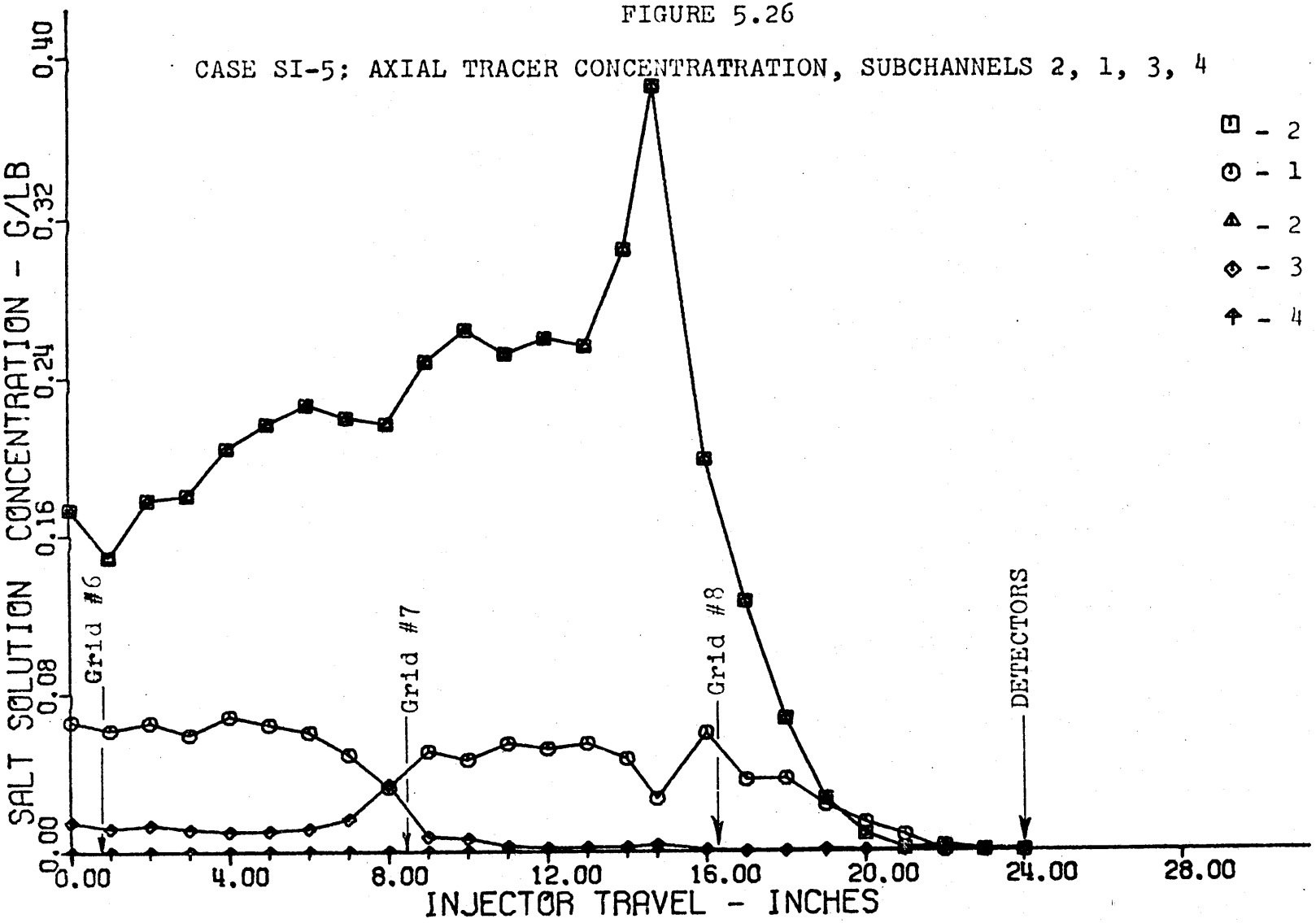

FIGURE 5.27

CASE SI-5: AXIAL TRACER CONCENTRATIONS, SUBCHANNELS 2, 5, 6, 7, 8

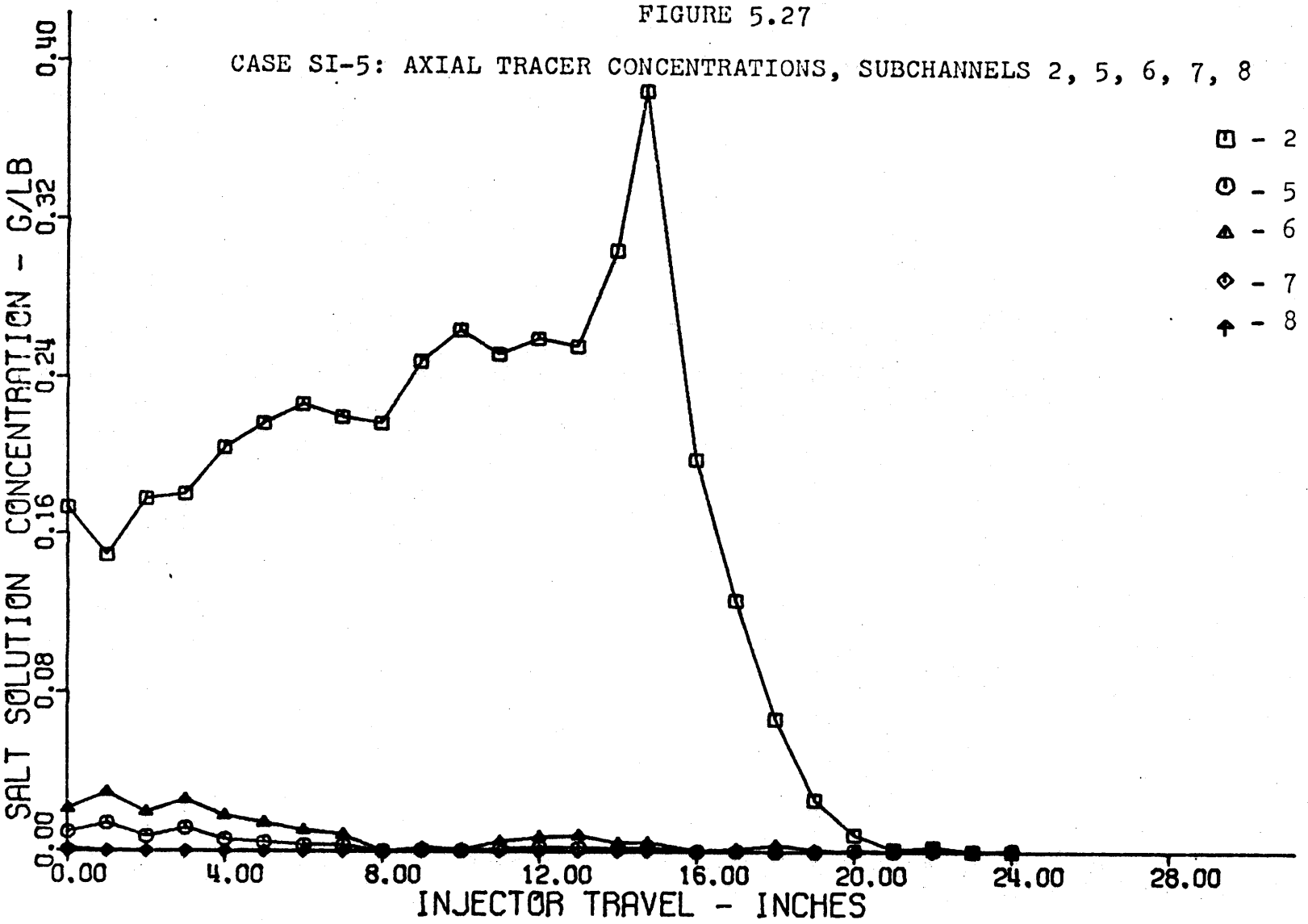

grid no. 8, the tracer detection rate diminished rapidly due to inherent instrumentation design limitations.

Proper operation of the solution conductance measurement instrumentation requires a uniform salt solution concentration. In order to detect all of the tracer injected, the tracer must be nearly uniformly mixed in all subchannels where tracer occurs. If during the mixing process large gradients of tracer concentration occur in some of the subchannels or similarly if the tracer solution has not mixed uniformly within the injection subchannel, then the detection probes cannot accurately measure the tracer concentration.

In the smooth rod array, the mass balance behavior was similar to that of Figure 5.25 in all turbulent flow cases. Upstream of grid no. 8 (16 3/4 inches), the tracer had not mixed uniformly in the injection subchannel; downstream of grid no. 8, the loss of tracer was due to tracer gradients in the subchannels contiguous to the injection subchannel, as well as, within the injection subchannel.

Concerning tracer gradients in the injection subchannel, it was possible that a tracer flow was passing through the detection plane by remaining inside the slot in the injection rod. Although the flow inside the slot was forced to mix with the injection subchannel flow over a 2 inch length by a flow tripping device, the slot flow was unpreturbed (except by spacers) after reestablishing downstream of the

flow tripper. The possibility that the slot contained a significant tracer flow was reinforced by the observation that the mass balance results were considerably lower (in the smooth bundle) before the slot flow tripping device was added.

Salt solution concentrations of subchannel nos. 1, 2, 3, and 4 are shown versus axial position (injector traver) in Figure 5.26. In all of the smooth rod array results, the spacer grid nos. 6, 7, and 8 are located at 3/4 in., 8-1/2 in., and 16-1/4 in., respectively. (The grid assemblies were 3/4 in. wide axially beginning at the location noted.)

The highest salt solution concentration at all axial positions was expected to be that of the injection subchannel, i.e., subchannel no. 1. In all experiments with interior subchannel injection, however, the salt concentration was observed to be highest in subchannel no. 2 when the injector was upstream of grid number 8, i.e., less than 16-1/4 inches. Careful inspection of the injection rod and the probe wire connections showed no errors during assembly. Further, inspection of the experimental results indicated that salt solution tracer dispersion in the smooth rod array, coolant mixing experiments was dominated by flow diversions occurring at the spacer grid assemblies. It was not possible to determine whether the tracer diversion was caused by interference of the grids with the unmixed tracer stream or by a large scale diversion of flow from one subchannel to

another.

Tracer mixing into subchannel 3 from subchannel 2 may also be seen in Figure 5.26. Figure 5.27 shows some tracer mixing into subchannel 6 from 1 and then from subchannel 6 to 5. For the case presented, there was little or no mixing from subchannel 1 to 7 or from subchannel 2 to 10.

In each plot of the subchannel tracer concentration versus injector travel (axial position), the data for the subchannel with the highest tracer concentration has been included so as to maintain a perspective of the amount of salt transferred. Because the injection rate was constant in all experiments, the tracer flow rate in all of the subchannels was constant. Thus, when the tracer concentration in one subchannel changed, the changes in tracer concentration in contiguous subchannels should have been equal and opposite.

From the laminar flow results (Figs. A8.1-A8.3) of subchannel tracer concentration versus injector travel, the tracer mixing was observed to be negligible. There was some flow scattering in the vicinity of the grids, but little of the tracer injected was detected.

The axial plots of subchannel tracer concentrations (Figs. A8.4 - A8.17 and 5.25 -5.27) revealed that the principal influence of Reynolds number on tracer dispersion

was that the relative amount of tracer flow diverted from subchannel 1 to 2 decreased with decreases in Reynolds number. As the flow decreased the fraction of observed tracer in subchannels contiguous to the subchannel with the largest salt concentration, i.e., nos. 1, 6, and 7, increased. The tracer data in subchannels 3 and 5 indicates turbulent interchange mixing from subchannel 2 to 3 and from subchannel 6 to 5, respectively. The tracer behavior typical of turbulent interchange mixing appears when the difference in tracer concentration between two contiguous subchannels decreases as injector-detector separation increases (injector travel decreases). Quantitative estimates of turbulent interchange are discussed in section 5.3.5.

Details of the axial behavior of the tracer dispersion were obtained in the vicinity of grid spacers no. 6 and 7 for interior subchannel injection and main flows of 50 and 150 GPM. The plotted results are given in Figures A8.18 - A8.31. Although the spacer grids significantly perturbed the tracer dispersion in the vicinity of the grids, the disturbances were settled within 3 to 4 inches of the grids.

5.3.2 Coolant Mixing Experiment Results, Smooth Rod Array, Peripheral Subchannel Injection

Using the smooth rod array, the experiments discussed in section 5.3.1 were repeated with the injection

subchannel changed to peripheral subchannel no. 48.

The laminar flow tracer dispersion experiment gave nearly the same results with peripheral subchannel injection as was observed with interior injection. Only a small amount of the tracer injected was detected. The tracer was chiefly observed only in the injection subchannel and in the one contiguous interior subchannel (no. 31). The axial tracer concentration plots (Figs. A8.33 and A8.34) indicated tracer dispersion was due solely to tracer scattering at the spacer grids.

As with interior subchannel injection, the mass balances with peripheral subchannel injection showed the detection rate was about two-thirds of the injection rate downstream of grid no. 8. Rough rod array experiments with peripheral subchannel injection had better mass balance results.

In the turbulent flow, peripheral injection mixing experiments (smooth rods), Figures A8.35 - A8.54, the tracer remained primarily within injection subchannel no. 48. Nearly all of the tracer transferred out of the injection subchannel went into subchannel 31. The axial behavior of the tracer concentrations in subchannels 48 and 31 indicated that the tracer transfer was due to both flow scattering at the grids and turbulent interchange. Some tracer appeared in subchannel 49 when the injector-detector was nearly maximum. Turbulent interchange mixing was recognized between subchannels 49 and 50, subchannels 31 and 30, as

well as between subchannels 31 and 32. The experimental mixing results for the 200 GPM case differed somewhat from the other cases without explanation.

Typical results of a peripheral subchannel injection, smooth rod array mixing experiment are given in Figures 5.28 through 5.30 (Case SP-3, 100 GPM)

Details of the tracer dispersion in the axial region of spacer numbers 6 and 7 were obtained for the case of 150 GPM main flow (Figs. A8.46 - A8.51).

5.3.3 Coolant Mixing Experiment Results, Rough Rod Array, Interior Subchannel Injection

Interchannel coolant mixing experiments were done in a rod array with roughened surfaces over the flow range from 4.8 to 250 GPM. Mass balance and subchannel tracer concentration results (interior subchannel injection) have been given in Appendix 8, Figures A8.52 - A8.98, with the exception of the 200 GPM flow results (Case RI-4) which are Presented in Figures 5.31 - 5.36. In the roughened rod array, the axial reference location (injector travel = 0.00) was changed so that the spacer grid numbers 6, 7, and 8 occurred at injector travels of 4, 11-3/4, and 19-1/2 inches, respectively.

The turbulent flow, rough rod array, interior subchannel injection, tracer mixing experiment results are given in

FIGURE 5.28

CASE SP-3: MASS BALANCE VERSUS INJECTOR TRAVEL

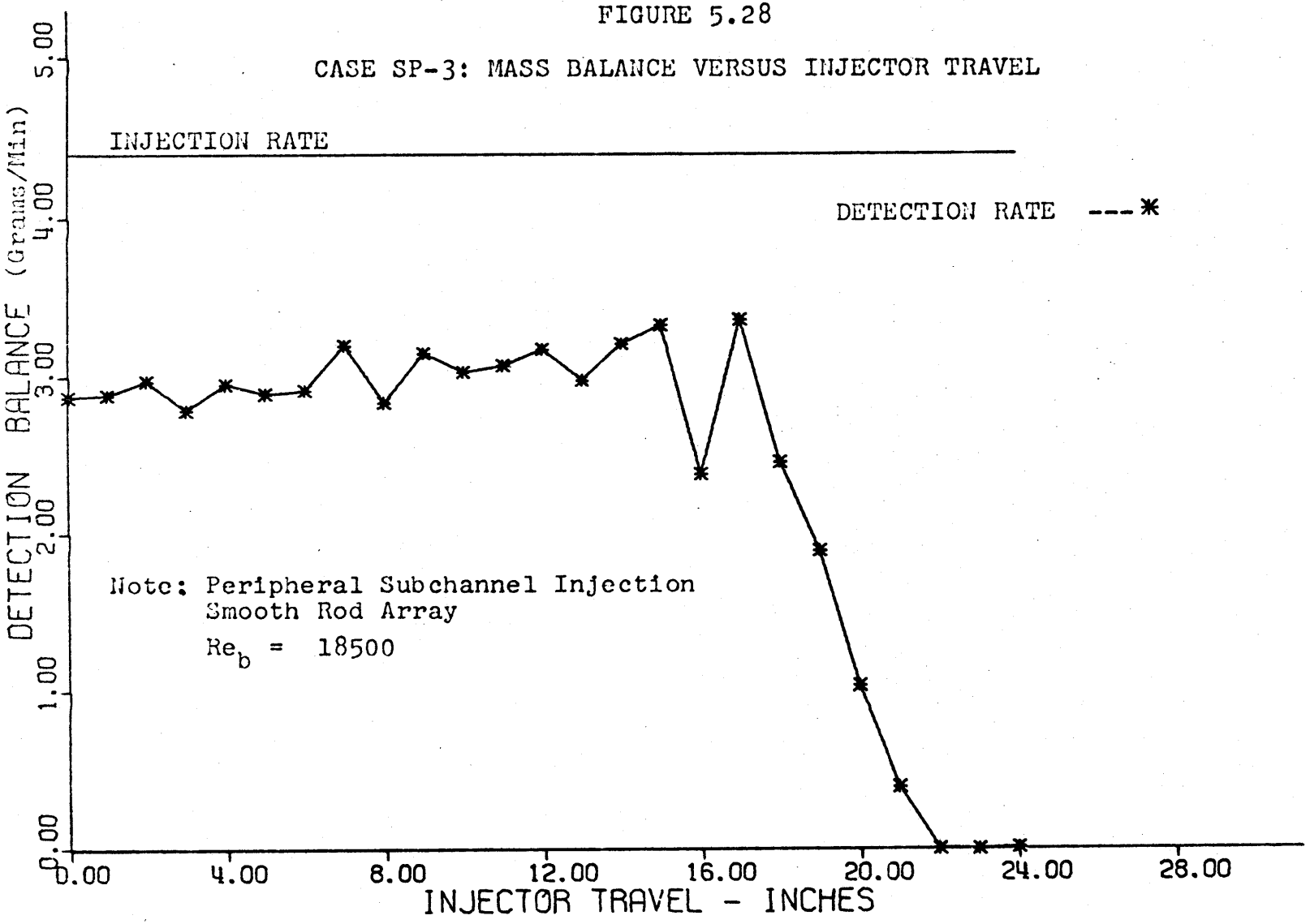

FIGURE 5.29

CASE SP-3: AXIAL TRACER CONCENTRATION, SUBCHANNELS 48, 29, 30, 31, 32.

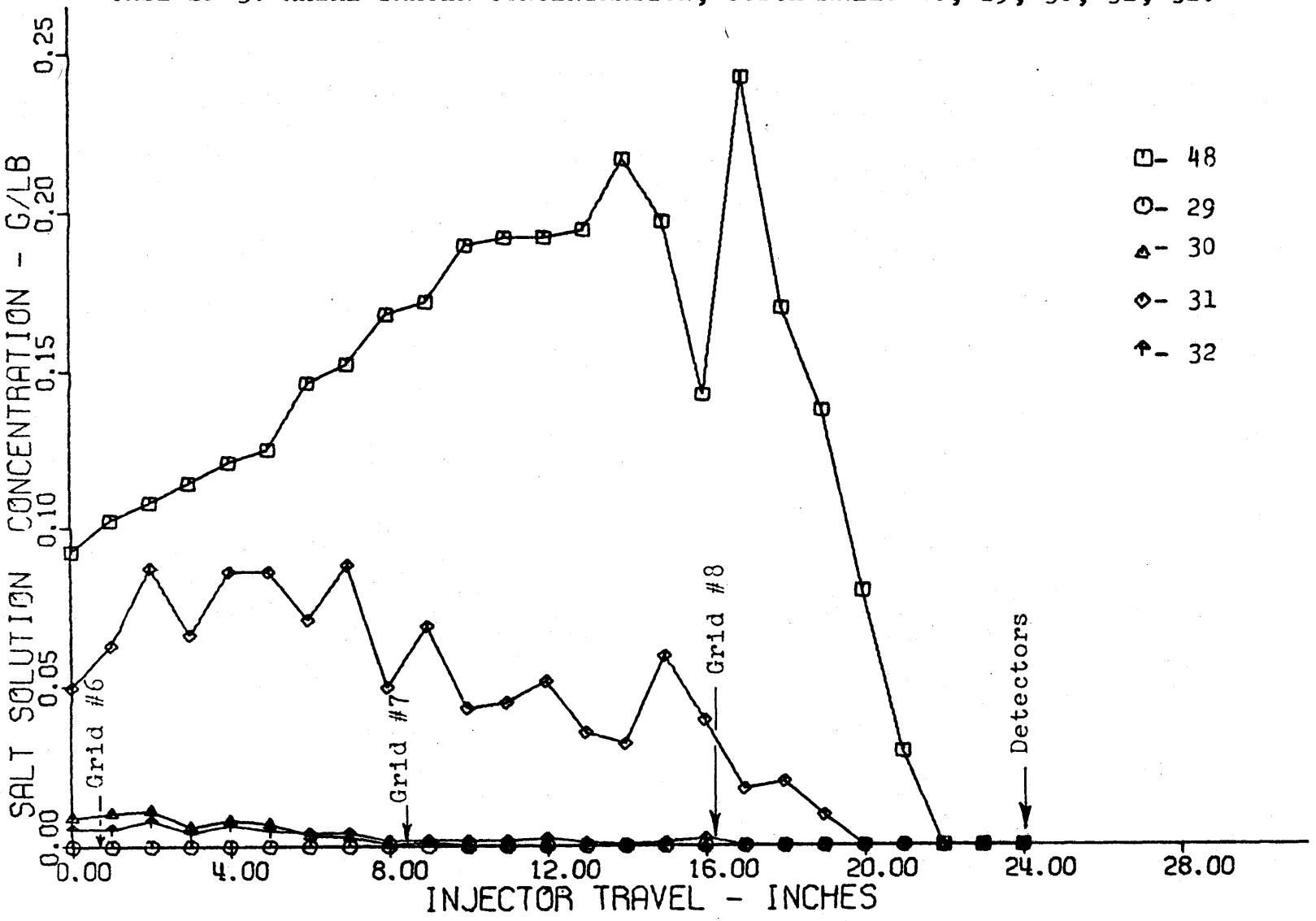

FIGURE 5.30

CASE SP-3: AXIAL TRACER CONCENTRATION, SUBCHANNELS 48, 49, 50, 51, 52

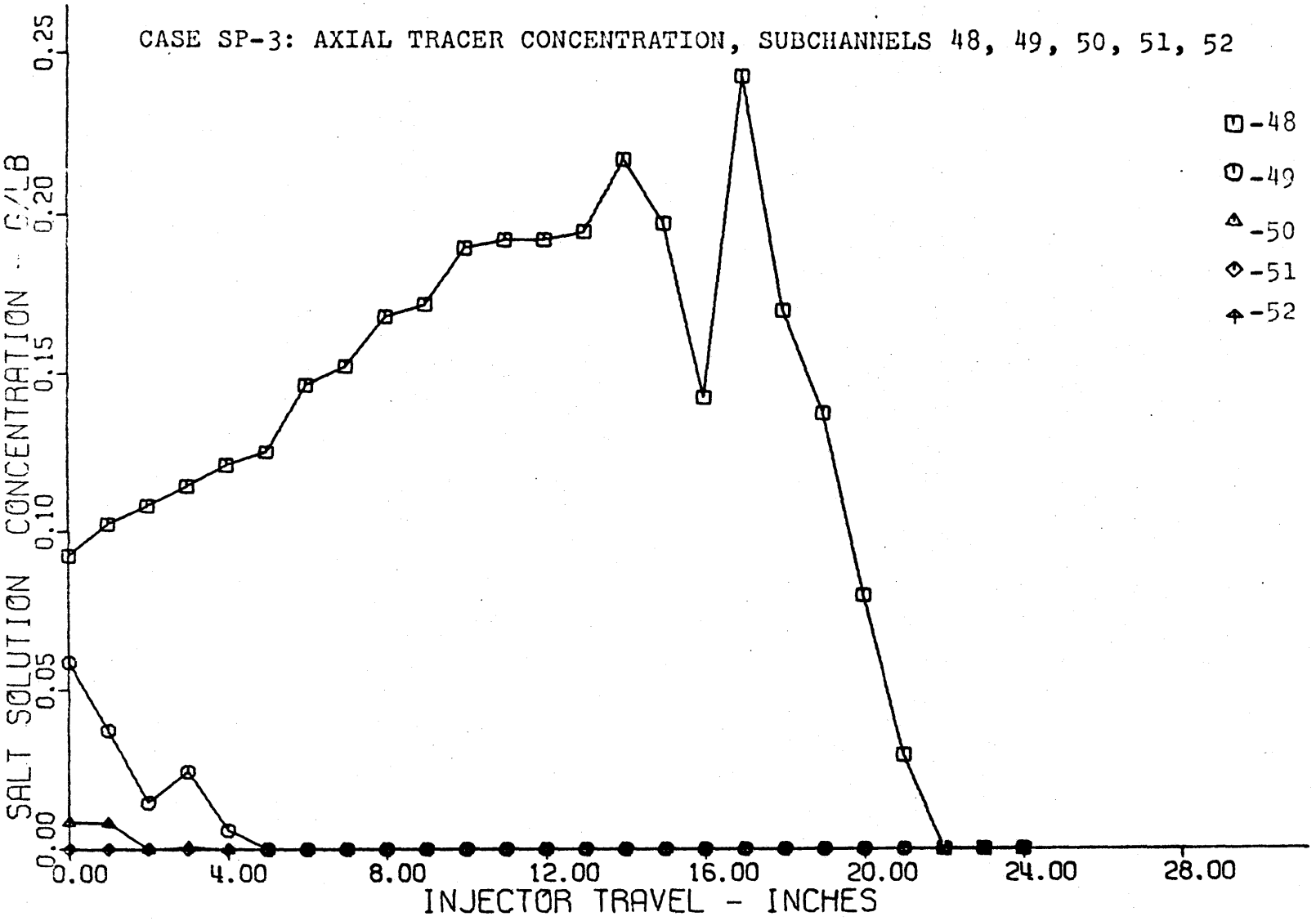

FIGURE 5.31

CASE RI-5: MASS BALANCE VERSUS INJECTOR TRAVEL

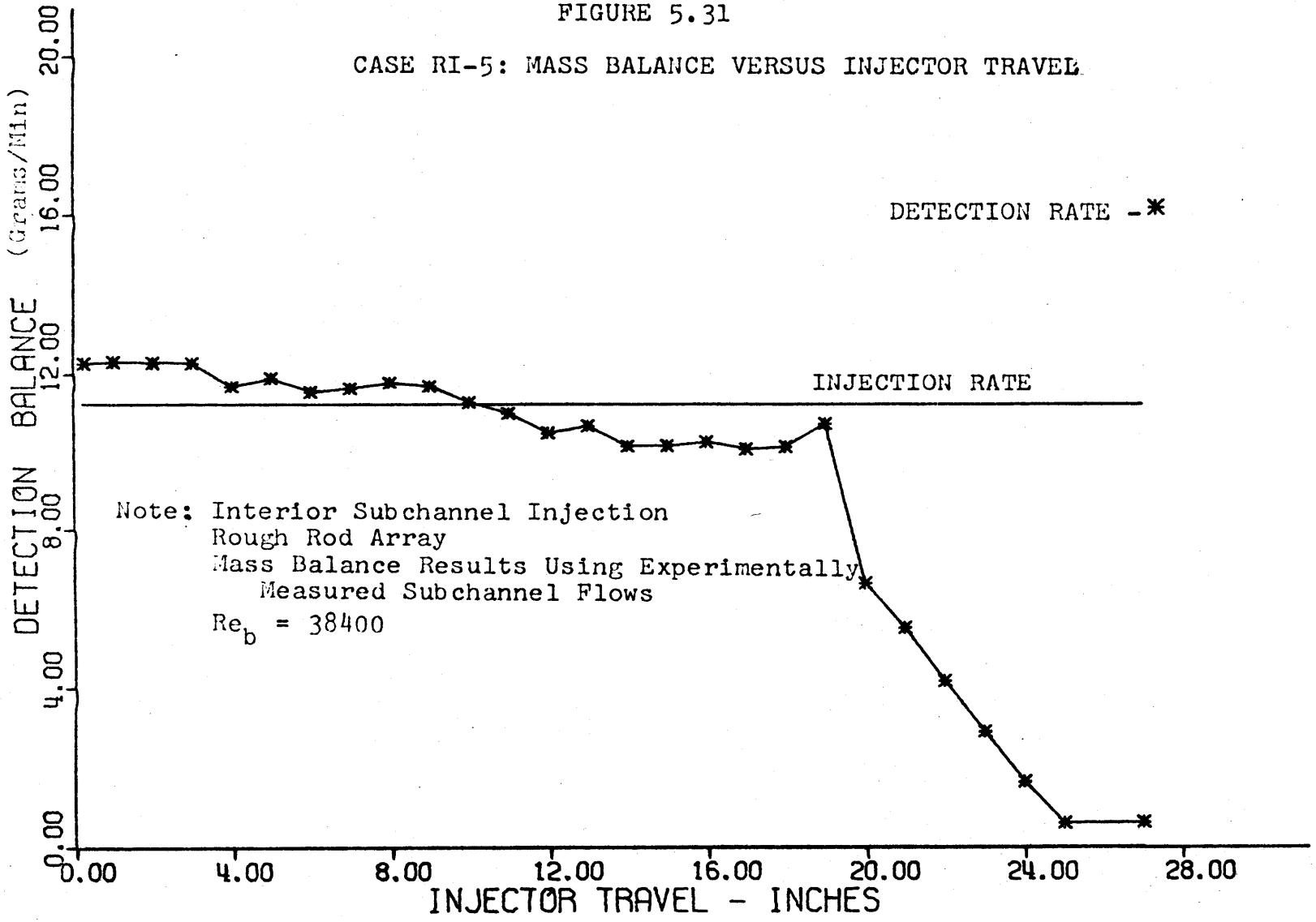

FIGURE 5.32

CASE RI-5: MASS BALANCE VERSUS INJECTOR TRAVEL

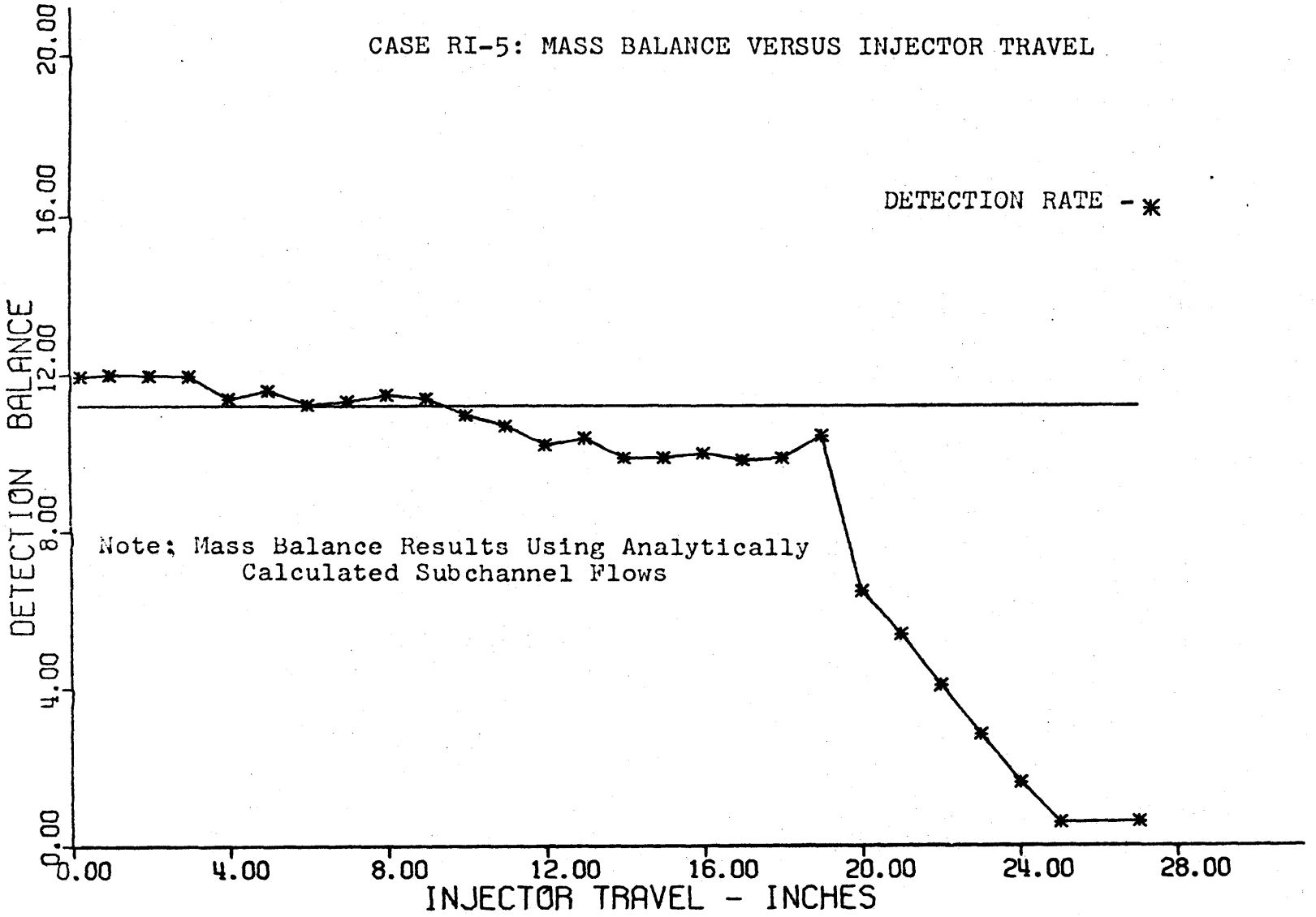

FIGURE 5.33

CASE RI-5: AXIAL TRACER CONCENTRATION, SUBCHANNELS 2, 1, 3, 4

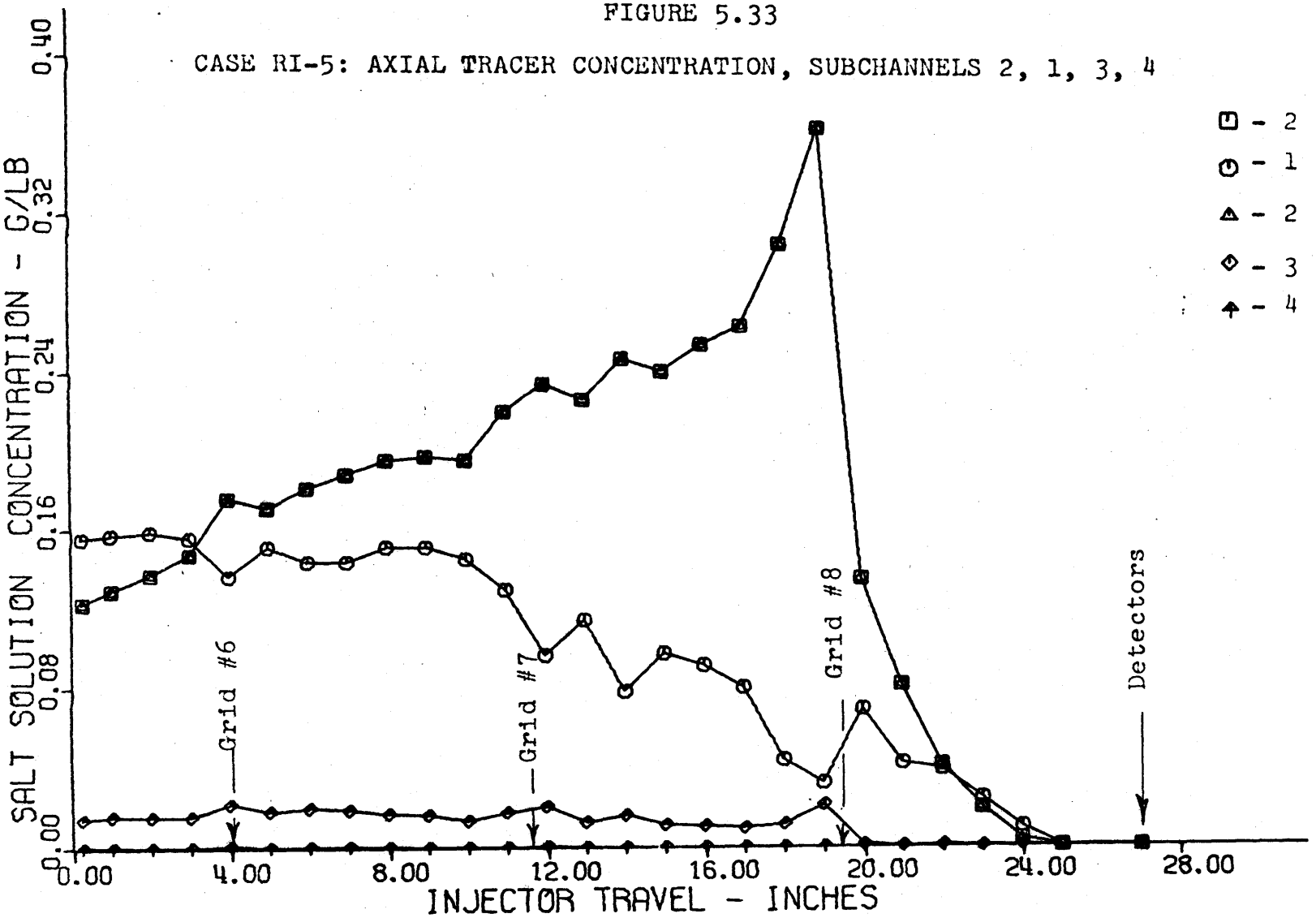

FIGURE 5.34

CASE RI-5: AXIAL TRACER CONCENTRATIONS, SUBCHANNELS 2, 5, 6, 7, 8

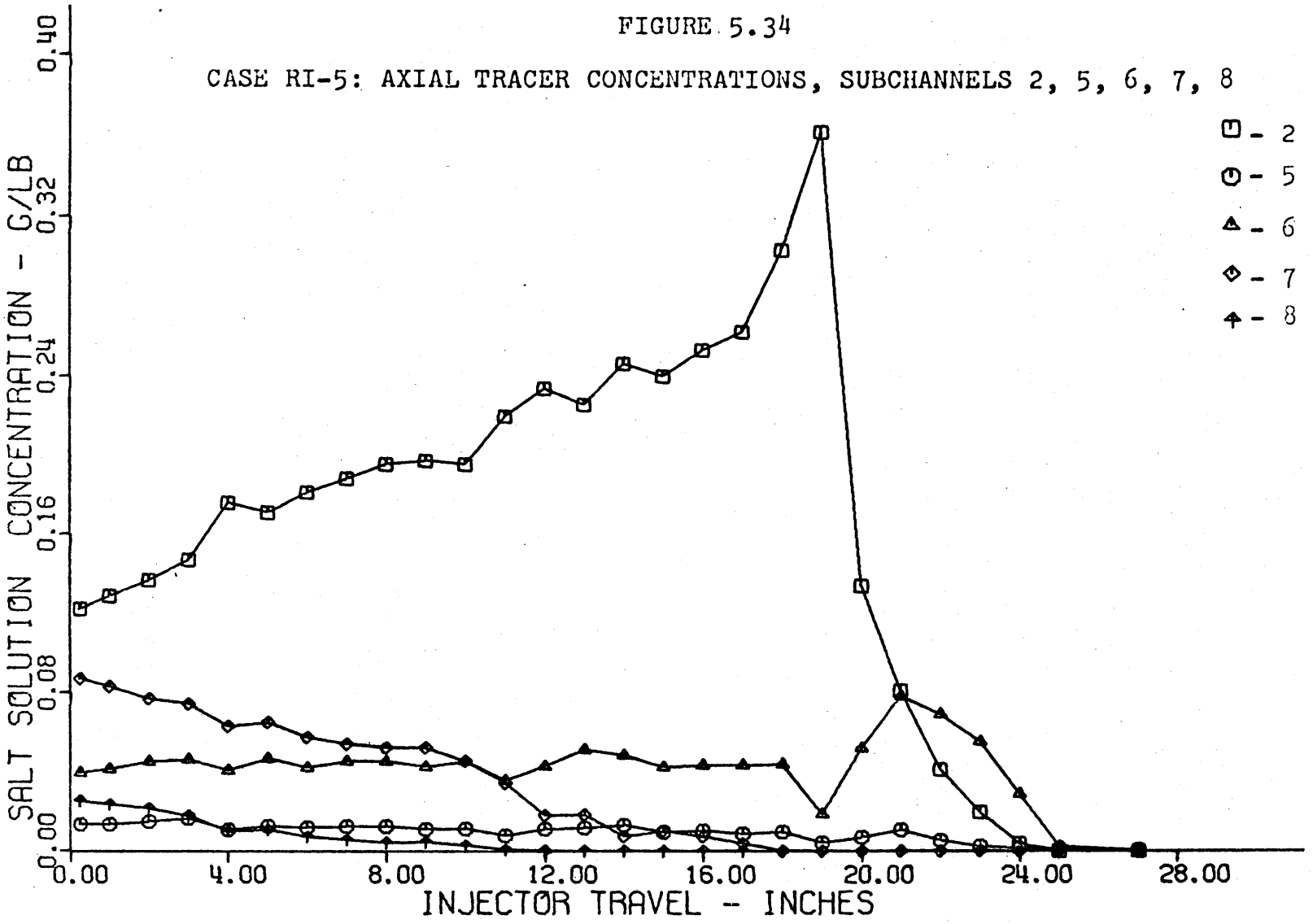

FIGURE 5.35

CASE RI-5: AXIAL TRACER CONCENTRATION, SUBCHANNELS 2, 9, 10, 11, 12

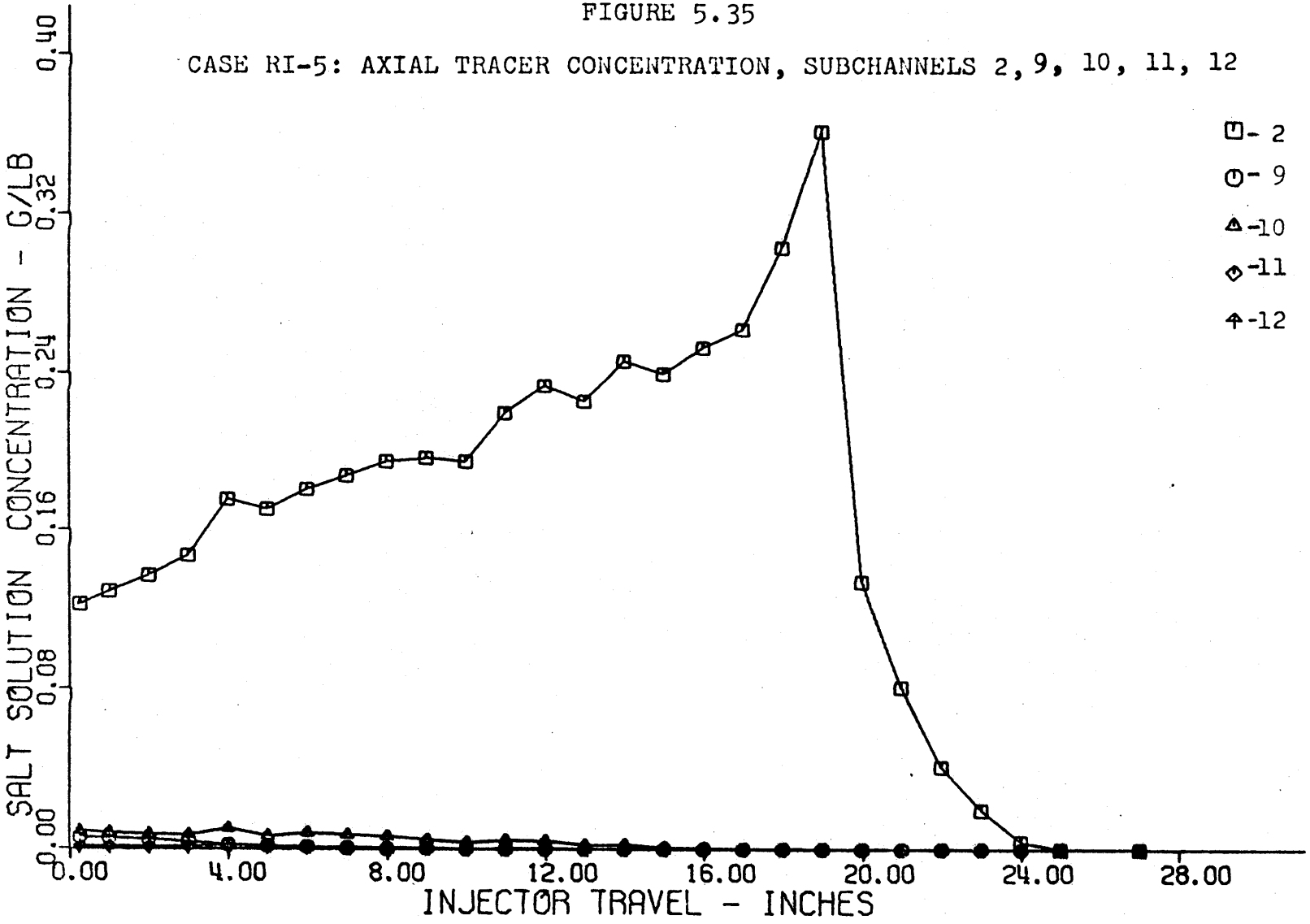

FIGURE 5.36

CASE RI-5: AXIAL TRACER CONCENTRATIONS, SUBCHANNELS 2, 21, 22, 23, 24

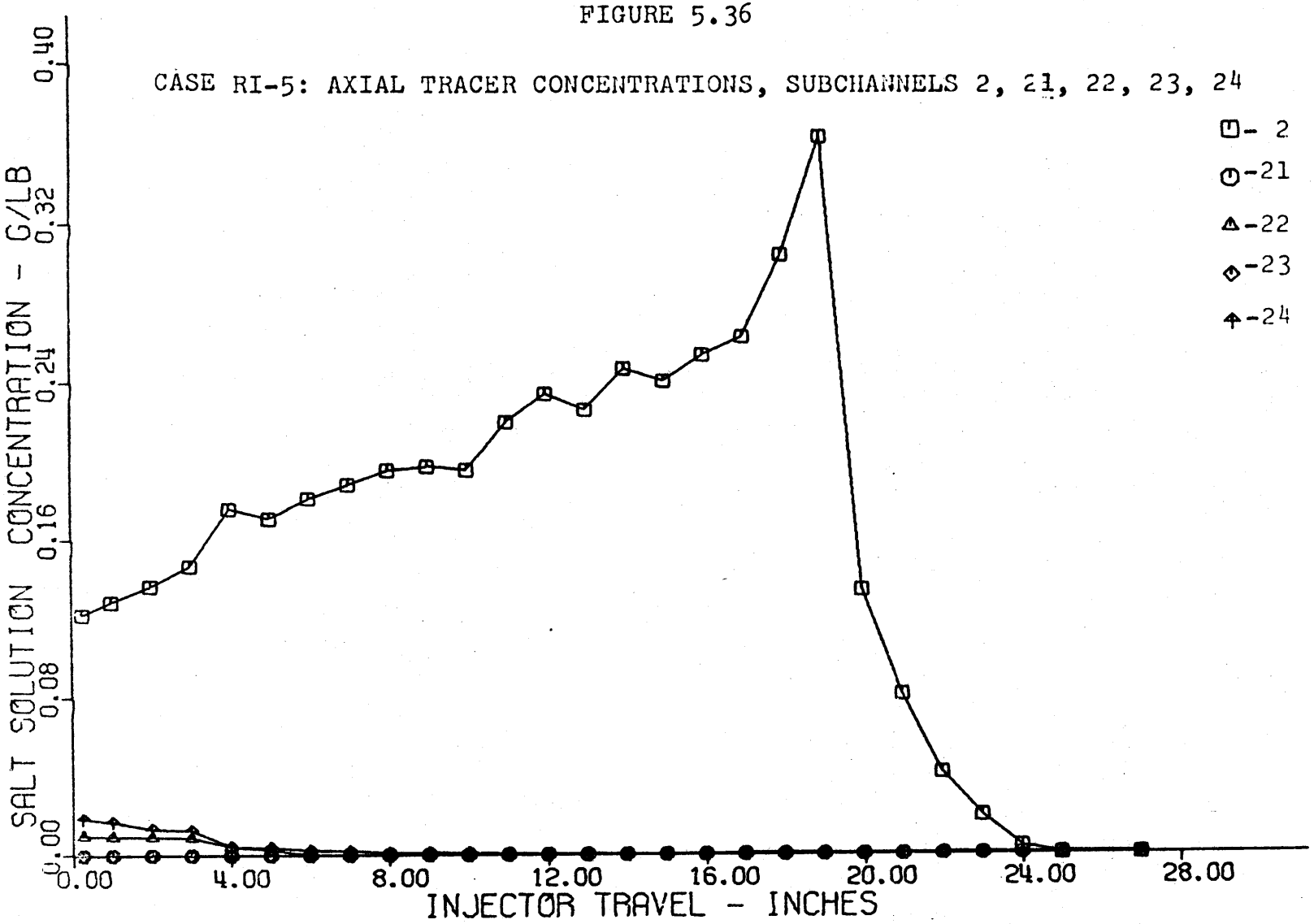

Figures A8.55 - A8.98 and 5.31 - 5.36. All data indicates that the turbulent interchange in the rough rod array was considerably higher than in the smooth array. The detected mass balance results were within +10% to -15% of the injected tracer rates in most cases. Significant tracer scattering occurred in the vicinity of the spacer grids. The magnitude of the grid disturbances reduced with increases in Reynolds number.

As was the case in the smooth array, the highest concentration of tracer occurred in subchannel no. 2 other than in the injection subchannel (no. 1). This was again explained by tracer diversion at grid no. 8.

The relative amount of tracer in subchannels 1 and 6 with respect to subchannel no. 2 decreased significantly with increases in Reynolds number. This may be explained by the higher turbulent interchange mixing in the rough array which would cause the tracer to be more uniformly mixed within a given subchannel. Thus flow scattering would have less of an influence on the scattering of the tracer from certain regions with a subchannel.

Turbulent interchange also affected the tracer dispersion patterns in the axial regions between the spacers. More tracer was observed two subchannels away from the injection subchannel than was the case in the smooth bundle. and was indicative of the wider transverse tracer dispersion in the rough bundle compared to the smooth bundle. For

example, the relative amount of tracer in subchannel 7 compared to subchannel 1 and subchannel 8 compared to 7 was higher in the rough array than the smooth. Discussion of the quantitative differences between turbulent interchange in the rough and smooth rod arrays is given in section 5.3.5.

Axial details of the transverse dispersion of the tracer in the region of the grids were taken for grids no. 6, 7, and 8 for main flows of 100 and 200 GPM; the results of these experiments are given in Figures A8.75 -A8.98. The flow scattering by the grids is most severe in the vicinity of the grid and appear to be damped out of the flow within four inches downstream of the grids.

The strong diversion of the tracer into subchannel 2 by grid no. 8 may be observed in Figures A8.85, 86, 97 and 98. Unfortunately, just after the injector passed through the spacer, the mass balance revealed that most of the tracer was not being detected.

The tracer detection rates for the spacer region mixing experiments were in good agreement with the tracer injection rate for spacers 6 and 7. At spacer 8, the tracer detection deteriorated rapidly as the detectors were approached.

Figures 5.31 and 5.32 show the mass balance results for

the 200 GPM, interior injection case using experimentally and analytically determined subchannel flows, respectively. In all cases where experimental and analytical subchannel flow rates were used in comparative mass balance calculations, the detection rates were in good agreement.

The laminar flow results, Figures A8.52 - A8.54, indicated that the laminar flow tracer dispersion in the rough rod array was due to flow scattering at the spacer grids. A larger fraction of the tracer injected was detected but turbulent interchange mixing was absent.

5.3.4 Interchannel Coolant Mixing Experiment Results, Rough Rod Array, Peripheral Subchannel Injection

Rough rod array mixing experiments were done for main flows varing from 4.8 to 250 GPM with tracer injection into peripheral subchannel no. 48. The laminar flow case (4.8 GPM) gave results similar to all others, i.e., most of the tracer was undetected because of a lack of turbulent interchange. Some tracer dispersion was observed due to flow scattering by the spacer grids.

The turbulent flow cases with peripheral subchannel injection showed a higher level of turbulent interchange in the rough array than in the smooth array. This was particularly evidenced by the axial behavior of the tracer dispersion in subchannels 30, 31, 32 and 49. Flow scattering

FIGURE 5.37

CASE RP-4: MASS BALANCE VERSUS INJECTOR TRAVEL

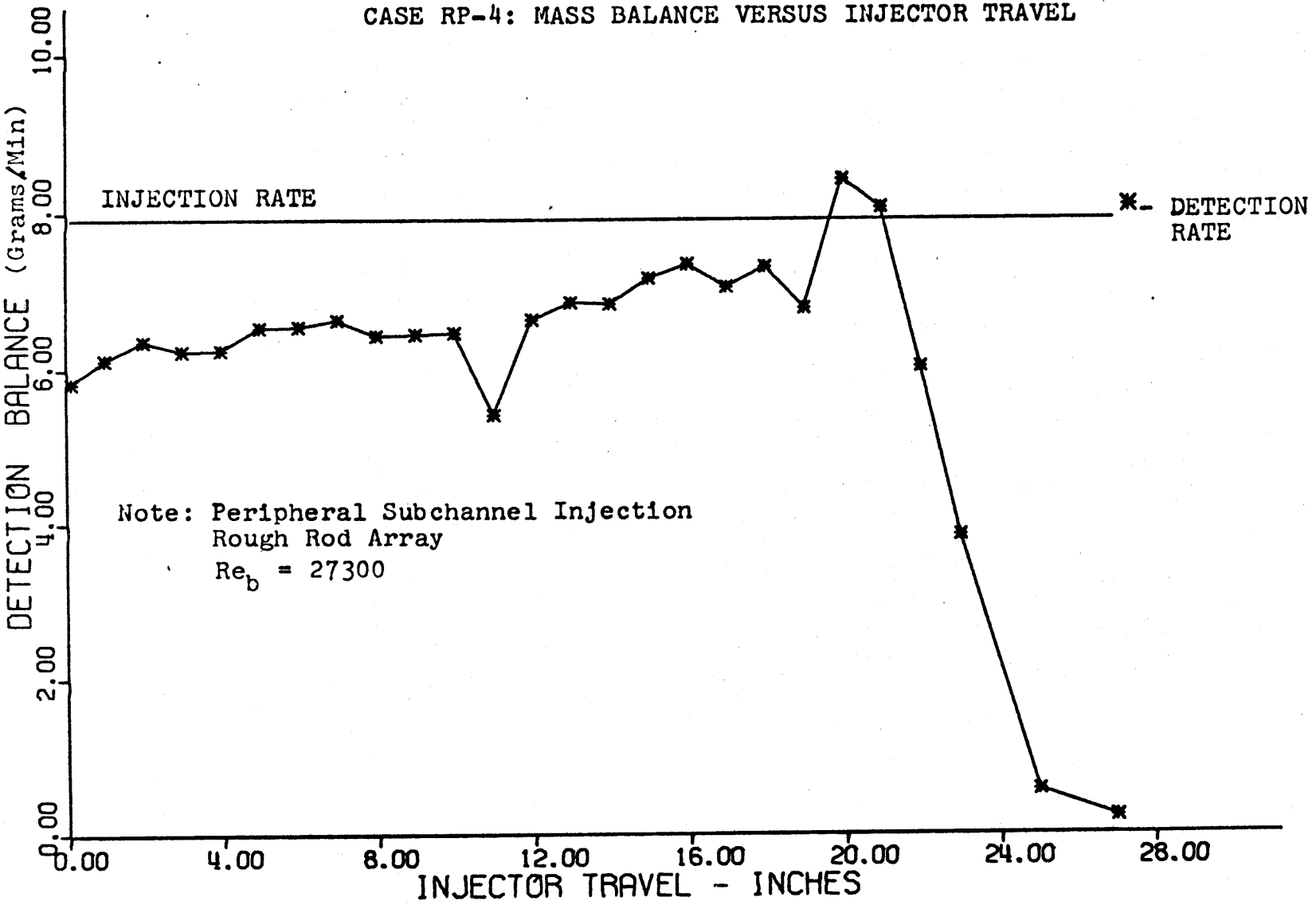

FIGURE 5.38

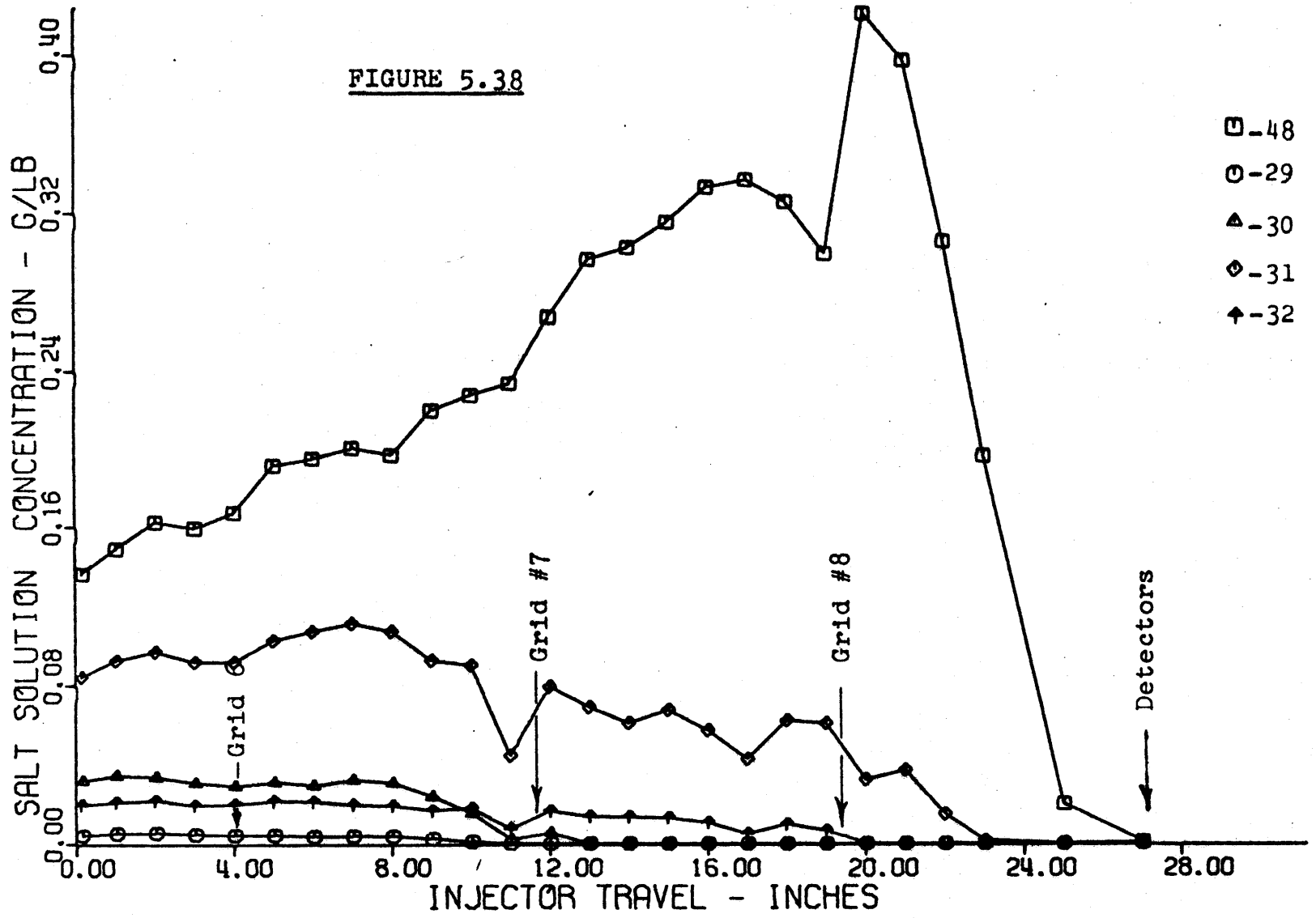

CASE RP-4: AXIAL TRACER CONCENTRATION, SUBCHANNELS 48, 29, 30, 31, 32.

FIGURE 5.39

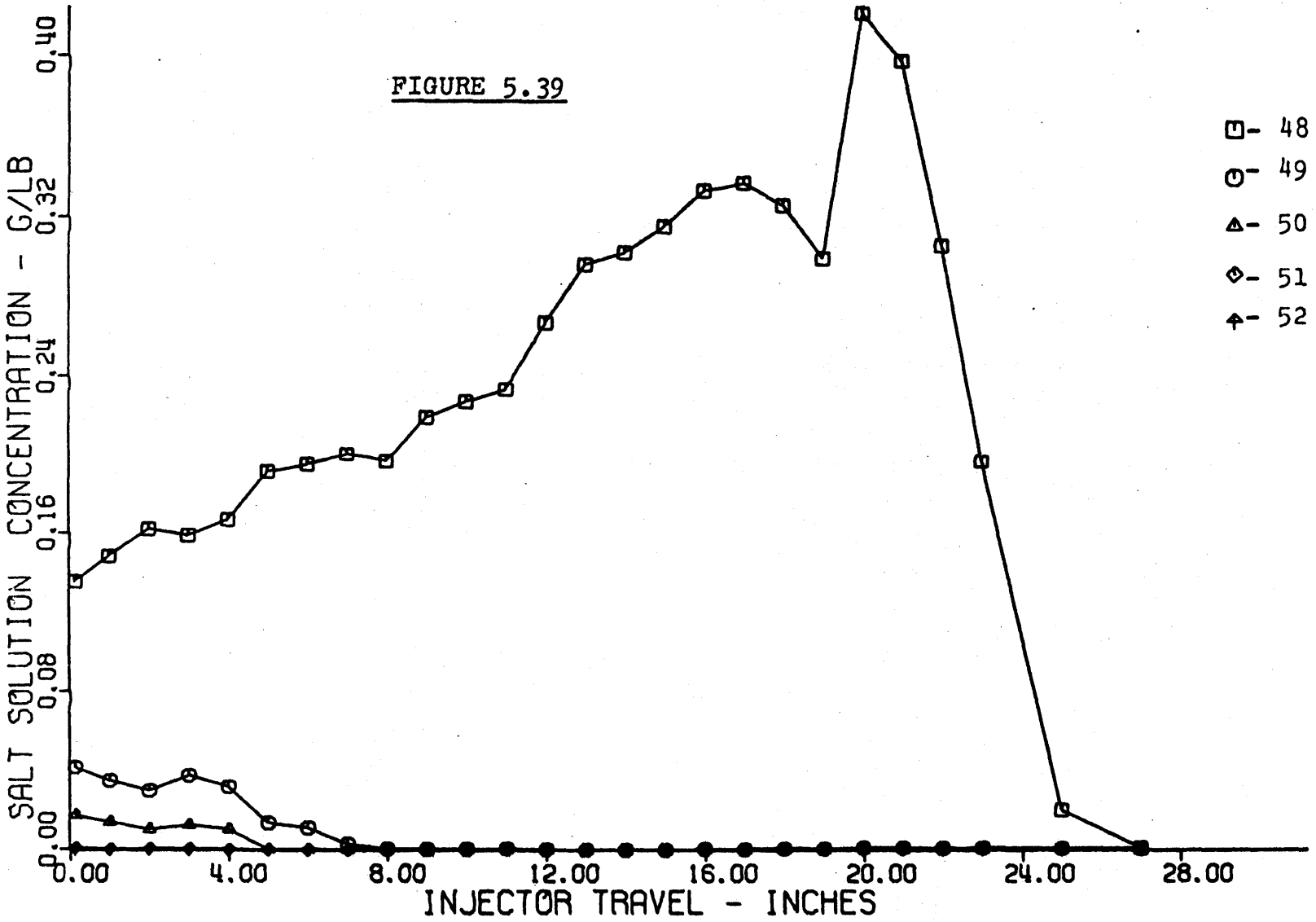

CASE RP-4: AXIAL TRACER CONCENTRATION, SUBCHANNELS 48, 49, 50, 51, 52.

near the spacers continued to play a significant role in the tracer dispersion, see Figures 5.37 - 5.39.

The tracer detection rates were in closer agreement to the injected rates in the rough bundle for flow cases 50, 150 and 250 GPM than in the smooth array; this to indicated a higher level of turbulent interchange mixing. For the 100 and 200 GPM main flow cases (including the spacer axial resolution experiments), the calibration curve for the injection subchannel (no. 48) was in error at salt concentrations greater than about 0.30 grams/lbm due to a failure in the calibration curve fit at higher concentrations. This calibration curve error resulted in the over-estimation of the tracer concentraiton in subchannel 48 when the concentration was over 0.30 grams/lbm. This was why the tracer detection rate was too high in the axial region between grid 7 and grid 8 in the 100 and 200 GPM cases.

The tracer mixing data in the regions of the spacer grids was taken with small axial increments in experiments RP-3 and RP-5. This data for spacers 6, 7, and 8 at flows of 100 and 200 GPM has been plotted to show the tracer dispersion detail near the grids in Figures A8.116 - A8.136. These figures reinforce the earlier observations regarding the higher tracer dispersion due to increased turbulent interchange in the rough bundle compared to the smooth. Also, the flow scattering by the grids was most noticable in

the vicinity of the grids and had damped-out within four inches downstream of grids 6 and 7.

5.3.5 Quantitative Evaluation of the Dimensionless Coolant Mixing Coefficient

Using the technique discussed in section A3.3, attempts were made to determine the dimensionless mixing coefficient β_{ij} between subchannels i and j. From the data available, it was difficult to quantitatively evaluate the mixing coefficient because the tracer was not always uniformly mixed within the subchannels. It was found that the accurate determination of the dimensionless mixing coefficient required a long unperturbed length in which turbulent interchange was the only operative coolant mixing mechanism; this was especially true when the coolant mixing coefficient was low in value.

Coolant mixing in the rough rod array was definitely higher than in the smooth array; this permitted an estimation of the mixing coefficient because the unpreturbed axial distance required for the extimate was shorter and because the tracer perturbations caused by the grids were less severe. From the tracer dispersion data in the rough rod array with spacer grids, the dimensionless mixing coefficient was estimated to be 0.020 ± 0.005 in the turbulent flow regime, cf. section A3.3. The nature of the experimental data prevented the determination of the effect

of Reynolds number or gap type on the mixing coefficient. In both smooth and rough rod arrays, the recommended laminar flow mixing coefficient is effectively zero - a conclusion reflecting the inablilty in this experiment to detect any mixing.

Determination of the dimensionless mixing coefficient in the smooth rod array will require salt tracer experiments with injector - detector separation distance of the range 60 to 20 inches, and preferably, Reynolds numbers above 40,000. Reduction of the error in the rough rod array mixing coefficient ,as well as, the determination of the gap type and Reynolds number effects on the mixing coefficient will require salt tracer mixing experiments with injector - detector separation distances of the range 50 to 10 inches. In future experiments, it is recommended that the tracer mixing expeirments be performed with both bare and grid spaced rod arrays. This will allow the determination of the effect of the spacer grids on the coolant mixing coefficient.

Although the smooth rod array mixing coefficient could not be evaluated from the tracer dispersion data, an estimate was obtained as discussed below.

Recently Rogers and Tahir [R6] have suggested that the dimensionless mixing coefficient β_{ij} could be calculated via the following correlations;

for interior-to-interior subchannels,

$$\beta_{ij} = 0.0018 \left(\frac{g}{d_r}\right)^{-1.40} , \qquad \text{(Eq. 5.8)}$$

for interior-to-peripheral or peripheral-to-peripheral subchannels,

$$\beta_{ij} = 0.0054 \left(\frac{g}{d_r}\right)^{-0.95} . \qquad \text{(Eq. 5.9)}$$

The calculated mixing coefficients using the respective equations for the smooth experimental array are 0.010 and 0.019. It should be noted however, that the reference does not contain information regarding tracer mass balances or rod spacer devices.

5.4 Miscellaneous Experimental Results

5.4.1 Overall Rod Array Pressure Losses

The overall pressure loss across the smooth and the rough rod arrays have been shown in Figure 5. . The inlet plenum-to-outlet plenum pressure drop was seen to be approximately 30% higher in the rough bundle than the smooth even though the friction factor multiplier in the rough bundle was of the range 1.5 to 2.1. The total pressure losses did not increase proportionately to the friction factor because friction losses are only partially responsible for the total pressure losses, cf., entrance and exit losses, spacer losses, and smooth section losses (only half of the rod length was roughened).

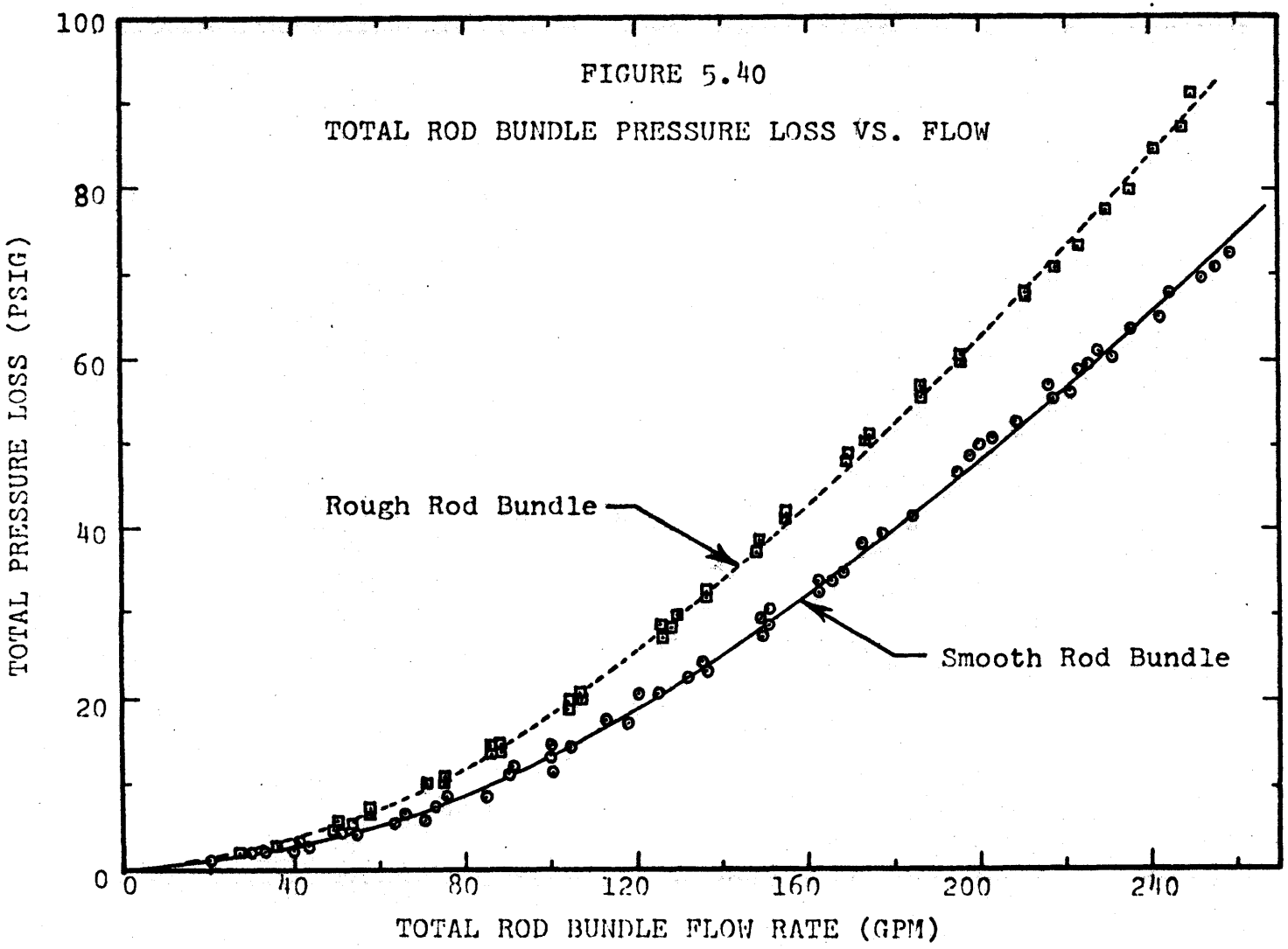
FIGURE 5.40
TOTAL ROD BUNDLE PRESSURE LOSS VS. FLOW
TOTAL PRESSURE LOSS (PSIG)
100
80
60
40
20
0
0
40
80
120
160
200
240
TOTAL ROD BUNDLE FLOW RATE (GPM)
Rough Rod Bundle
Smooth Rod Bundle

5.4.2 Static Pressure Profiles at the Rod Array Outlet

At the rod array outlet plane there was a sudden increase in the flow area of the test section. Static pressure profiles were taken with axial detail at the outlet plane. A typical plot of these results is given in Figure 5.41. Recall that the nature of the rod array outlet static pressure has been introduced in Figure 5.13 where the static pressure profile of the entire upper half of the rod array was illustrated.

The static pressure , as the rod array outlet was approached from the bundle interior, was observed to deviate from the straight-line behavior characteristic of friction pressure losses about four inches (15 hydraulic diameters) upstream of the exit plane. From Figure 5.41, the deviation of the static pressure from that of the pure friction case increases as the exit is approached; at the exit plane, a substantial negative gage pressure occurred. Further downstream, the static head rapidly recovered due to deceleration of the flow. The exit region behavior described above was strongly flow, i.e., velocity, dependent.

5.5 A Discussion of Experimental Uncertainty

The uncertainty in the experimental results was due to the accummulation of various uncertainties in the measurements and in the data used for the data reduction. The

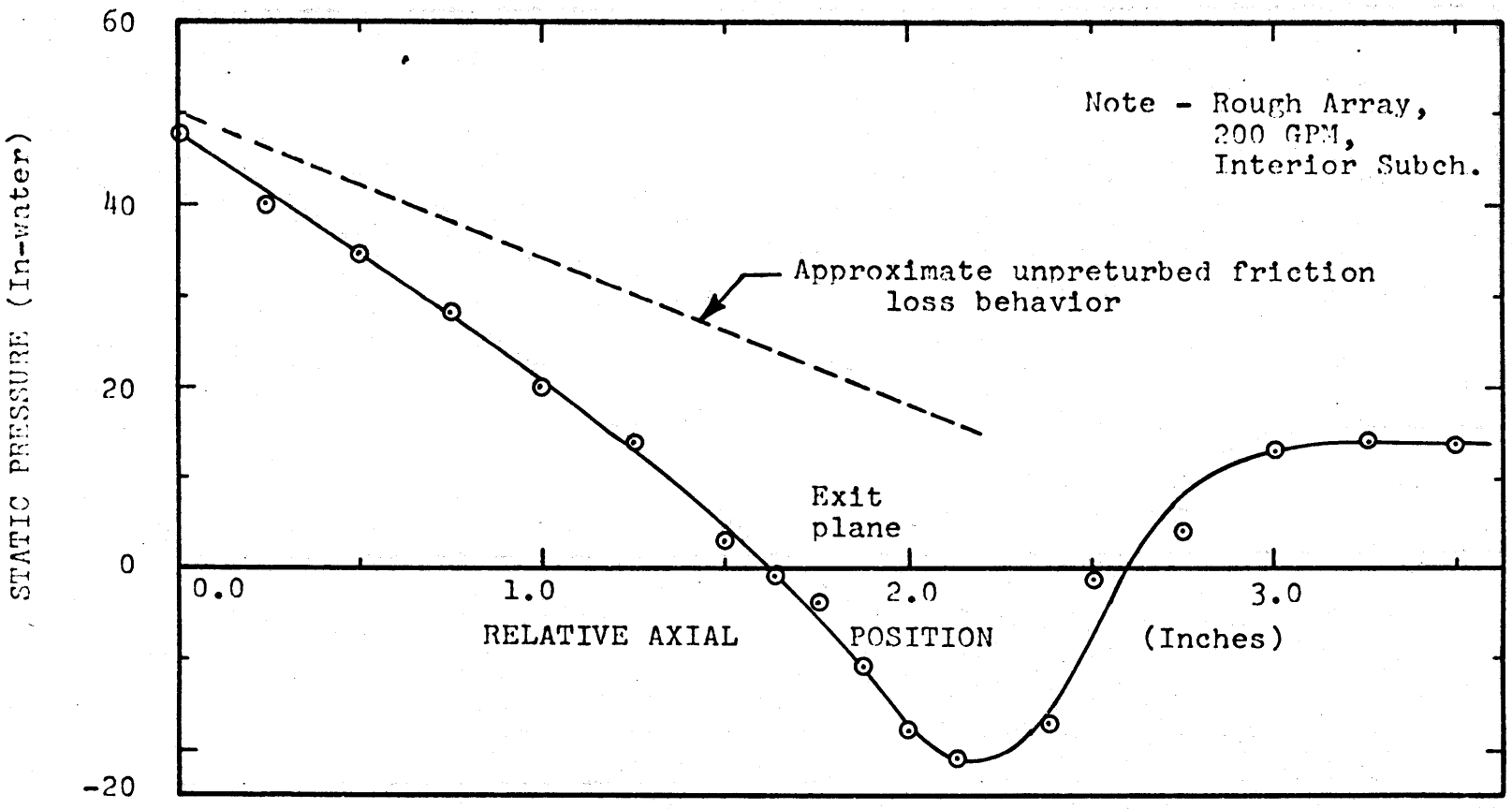

FIGURE 5.41

TYPICAL STATIC PRESSURE PROFILE IN THE VICINITY OF THE ROD ARRAY EXIT PLANE

determination of the average subchannel velocities for the data reduction caused the greatest uncertainty in the results of friction factor and grid loss coefficient.

The uncertainties which occurred during this work were both systematic and random in nature. In the estimates of the experimental uncertainties given in Table 5.12, every effort has been made to accurately estimate the effects of systematic errors (where known) and random errors. Further, the estimated uncertainties were selected to be conservative. The uncertainty values selected were based on both manufacturer's specifications of instrument accuracy (where available) and the author's experiences during experimental operations and data analysis. Other than give an exhausting discussion of the numerious experimental uncertainties, the principal considerations are discussed below.

For this work, the uncertainties were stated according to the "usual understanding" given in Baumeister [B7], i.e., the true value (of the variable), as far as can be determined, "is just as likely to lie inside as outside the interval." The true value than lies within the stated range of uncertainty with a confidence of 50% - at least.

The local fluid velocity was measurable only when the pressure sensing portion of the pitot tube was not over a flow boundary. Thus, velocities measured within 0.020 inches

TABLE 5.13

A SUMMARY OF ESTIMATED EXPERIMENTAL UNCERTAINTIES

Variable	Estimated Error (%)	@ 50 GPM (%)	@ 100 GPM (%)	@ 200 GPM (%)
T	$\pm$ 1°F	-	-	-
Q	+0/Q -10/Q	$\pm 4^{+}$	+0 -10	+0 -5
P_s	$\pm$3/Q	$\pm$6	$\pm$3	$\pm$2
V	+2/Q+0.02 -2/Q-0.02	$\pm$6	$\pm$4	$\pm$3
$\bar{V}$	-4+2/Q -8-2/Q	+0 -12	-2 -10	-3 -9
$\bar{V}_{al\text{-}smooth}$	+0*Q+e_Q -2*Q-e_Q	+4 -5	+0 -12	+0 -9
$\bar{V}_{a2\text{-}smooth}$	+5*Q+e_Q -0*Q-e_Q	+7 -4	+5 -10	+10 -5
$\bar{V}_{al\text{-}rough}$	+2*Q+e_Q -2*Q-e_Q	$\pm$6	+2 -12	+4 -9
$\bar{V}_{a2\text{-}rough}$	+5*Q+e_Q -5*Q-e_Q	$\pm$9	+5 -15	+10 -15
$\bar{V}_{be}$	-5+2/Q -10-2/Q	-1 -14	-3 -12	-4 -11
$\bar{V}_{ba}$	+0 -10/Q	$\pm 4^{+}$	+0 -10	+0 -5
$\Delta P_f/L$	*	$\pm$8	$\pm$6	$\pm$4
$\overline{\Delta P_g}$	*	$\pm$8	$\pm$6	$\pm$4
P_{d1}	$\sim 2e_{\bar{V}_1}$	Included below		
Re_{1e}, Re_{be}	2+$e_{\bar{V}_e}$ 2-$e_{\bar{V}_e}$	+2 -14	+0 -12	-1 -11

Variable	Estimated Error (%)	@ 50 GPM (%)	@ 100 GPM (%)	@ 200 GPM (%)
Re_{1a}	+2+$e_{\bar{V}_{al}}$ -2-$e_{\bar{V}_{al}}$	+6 -7	+2 -14	+2 -11
Re_{ba}	+2+$e_{\bar{V}_{ba}}$ -2-$e_{\bar{V}_{ba}}$	$\pm$6	+2 -12	+2 -7
f, $\bar{K}_g$	$\sim e_{\Delta P_g/2e_{\bar{V}_i}}$,	$\sim e_{K_g/2e_{\bar{V}_i}}$		
", $"_e$	","	+30 -8	+26 -10	+22 -7
"," al-smooth	","	+18 -16	+30 -6	+22 -4
"," a2-smooth	","	+16 -20	+26 -16	+14 -24
"," al-rough	","	$\pm$22	+30 -10	+22 -12
"," a2-rough	","	$\pm$24	+36 -16	+34 -24
"," be	","	+36 -10	+30 -12	+26 -12
"," ba	","	$\pm$16	+26 -6	+14 -4
f_{x_e}	+8+4/Q -8-4/Q	$\pm$14	$\pm$13	$\pm$12
$f_{x_{al}}$	+8+2(e_{V_s}+e_{V_r}) -8-2(e_{V_s}+e_{V_r})	+28 -30	+32 -36	+26 -32
$f_{x_{al}}$	*	+40 -34	+48 -38	+58 -38
$f_{x_{be}}$	*	$\pm$16	$\pm$12	$\pm$8
$f_{x_{ba}}$	*	$\pm$16	$\pm$12	$\pm$8

+ Rotameters were used for this flow measurement rather than the main flow meter

* Best Estimate

of a rod or wall were not reliable. This was a significant error in the average velocity data because the low velocity fluid in the vicinity of the flow boundaries could not be included in the velocity averaging procedure. The average subchannel velocities were estimated to be 4 to 8% higher than the actual due to this limitation and due to rod array distortions at the outlet. This systematic error was based on the fraction of the flow area which was not included in the average velocity calculation.

Uncertainties in determining the analytical average subchannel velocity were due chiefly to the neglection of coolant mixing in the calculational model. Because of the nature of the influence of mixing on average peripheral subchannel velocities observed in the experiments, the estimated uncertainty in the analytical velocities was increases with main flow rate. Because the peripheral and interior subchannel velocities were more nearly equal in the rough bundle, the mixing error was estimated to be less in that case.

Much of the error in the experimental measurements was dependent on flow because instrument manufacturers specify accuracy as a percentage of the full scale instrument reading. This type of uncertainty occurred in the measurement of flow and pressure.

Estimates of the various errors in the measurements and the reduced data have been shown in Table 5.12. The error in the experimentally determined flow data decreased with flow rate because of the increased accuracy of the instruments.

The results of the data recuction based on the bundle average flow data were more accurate than those based on the subchannel flow results because the problem of determining the flow split between subchannel types did not arise.

Because of the comparative nature of the friciton factor multiplier data, i.e., smooth rod array results versus rough array results, the uncertainties were less than in the absolute measurements because part of the experimental uncertainty was consistent between smooth and rough experiments.

Regarding the coolant mixing experiments, the instrumentation could measure the salt solution concentration in a subchannel with an estimated accuracy of $\pm 3\%$ in the no flow case. In the flowing case, the instrument uncertainties were monitored through mass balances, i.e., comparing the tracer injection rate with the detection rate. The main uncertainties in calculating the detection rate were due to uncertainties in determining subchannel flows and due to nonuniform tracer concentrations. The mass balance results have been discussed earlier in section 5.3.

To summarize, the experimental results determined using rod array average flow data were the more accurate results reported.

5.5.1 The Effect of Temperature Variations on the Experimental Results

The various experiments were performed with main flow temperatures which varied between 44°F and 59°F. The variation of Reynolds number with turbulent flow temperature was the principal effect of concern and was caused by the strong dependence of dynamic viscosity on temperature.

Because the flow density was nearly constant with temperature, the dynamic pressure varied only with velocity. In the smooth rod array, the flow velocity of the subchannels was independent of temperature. In both smooth and rough rod arrays, the average velocity was independent of temperature. However, in the rough array the subchannel velocities were influenced by Reynolds number through the roughened surface effect. Estimates using Eq. 3.12 and A1.9 revealed that the worst observed extremes in temperature caused the peripheral-to-interior subchannel velocity ratio to change less than 3%.

The axial pressure profile experiments were mainly incluenced by flow temperature through the variation of

friction factor with Reynolds number. The friction factor changed less than 6% due to temperature variations.

Temperature variations of the flow influenced the coolant mixing experiments chiefly through the variation of Reynolds number.

In all cases, the changes in temperature of the flow media were significant only because of resulting changes in Reynolds number. Secondary temperature effects, such as variations in flow split factors X_{ij} or friction factors were less than 6% for the extremes of temperature variation observed. In most cases, the effect of temperature changes was less than that of the extreme.

The Reynolds number did vary by as much as 25% due to the change of dynamic viscosity with temperature. Since the effect of flow on the experimental results was usually evaluated by variations of Reynolds number, the primary effect of flow temperature variations was inherently included in the data reduction. The secondary effects of temperature variations were not considered in the data reduction.

CHAPTER 6

RECOMMENDATIONS FOR FUTURE WORK

During the course of this investigation, it has been shown that the use of a gaseous coolant with surface roughening in a rod array - type nuclear fuel element leads to a thermal-hydraulic behavior which is considerably more complicated than that which occurs in the case of a liquid-cooled fuel element.

This chapter briefly discusses recommendations for future work regarding the thermal-hydraulic analysis and experimental testing of gas-cooled, surface roughened nuclear fuel elements.

6.1 The Influence of Coolant Property Variations on Fuel Element Thermal-Hydraulics

Because of the temperature and pressure dependence of coolant density and dynamic viscosity, radial power gradients can distort coolant flow distributions through a property variation feedback effect. Coolant property variations are also of concern because of temperature variations within the subchannels adjacent to heated walls, i.e., the convection film property variations. The influence of film property variations on the determination

of the friction factor and the convection coefficient should be investigated with attention given to the effects of Reynolds number and surface roughening.

Of particular interest in investigating the coolant property feedback effect are the following concerns: non-optimum subchannel geometry, radial power gradients (including fuel element rotation effects), power-to-flow ratio variations, flow regime, and roughened surface performance.

In order to investigate coolant property variation effects, it will be necessary to perform heated rod array experiments using a gaseous coolant. The coolant property variation feedback effect could be observed by making velocity profile measurements across the rod bundle operating with various radial power gradients. The significance of property variations through the convection film could be determined by measuring local fluid bulk temperatures and rod wall temperatures during heated rod experiments.

6.2 The Influence of Surface Roughening Behavior on Fuel Element Thermal-Hydraulics

The changes in Stanton number and friction factor characteristic of roughened surfaces compared to smooth surfaces are a major complicating factor in the thermal-hydraulic analysis of rod array type nuclear fuel elements. The effects of Reynolds number and relative roughness in

both fully roughened and partially roughened subchannels must be understood before a complete thermal-hydraulic analysis can be performed.

The influence of surface roughening on spacer grid loss coefficients and fuel rod vibrations is also of interest.

Because the unheated duct wall is not roughened in the GCFR fuel element, the problem of determining the effect of partial wetted perimeter roughening on performance of the roughened surface in peripheral and corner subchannel geometries must be considered. This problem arises because the relative change in the subchannel friction factor is higher in the fully roughened interior subchannels than in the partially roughened peripheral subchannels, e.g., 3.0 versus 1.5, respectively. It is interesting to note that much of the research activity in roughened surface experiments has delt with the problem of isolating the roughened rod surface behavior from that of a partially roughened annular flow channel. In roughened nuclear fuel elements, a related but inverted problem of determining roughened surface behavior in partially roughened subchannel geometries is also a major concern.

Because of the increased resistance to flow near a roughened surface, the peak-to-average subchannel flow velocities are higher in a rough rod array than in a smooth

array. The effect of circumferential variations of the forced convection heat transfer coefficient on the rod surfaces should be considered in the fuel element hot-spot analysis.

The investigation of surface roughening behavior should be done in heated rod array experiments. Roughened surface performance can be determined from measurements of local static pressure, fuel rod surface temperatures, and bulk fluid temperatures. Flow distributions should be measured using two-dimensional velocity profiles. Circumferential variations in heat transfer coefficient may be determined from measurements of radial temperature distributions on specific rod surfaces.

6.3 Interchannel Coolant Mixing Behavior

The coolant mixing level in roughened rod arrays was found to be significantly larger than in smooth rod arrays. However, tracer scattering by the spacer grids prevented the determination of the mixing coefficient in the smooth rod array as well as the influence of Reynolds number and subchannel geometry on the mixing coefficient.

In future rod bundle experiments, it is recommended that the effects of Reynolds number and subchannel geometry be investigated in both smooth and rough rod arrays

with grid spacers typical of the fuel element design. Using heated rod experiments and monitoring temperature distributions within the rod array, it should be possible to determine the dimensionless coolant mixing coefficients. If additional experimentation is done using salt solution tracer techniques, tracer insertion at injector-detector separations of typically 60 - 10 inches is recommended.

Further assessment of the coolant mixing coefficient is also significant in the investigation of flow distributions between the various subchannel types, of the sensitivity of subchannel flows to distortions in the ideal rod array geometry, and of the flow behavior in non-optimum subchannel geometry conditions.

6.4 GCFR Fuel Element Design Recommendations

Concerning the design of the GCFR fuel element, the following design recommendations are presented: (A) grid spacers instead of the alternative twisted-tape designs, (B) a sharp cornered versus rounded corner subchannel design, (C) a scalloped flow boundary at the rod array perimeter, and (D) the possible use of full length roughening. The various advantages and disadvantages of the alternative spacer designs have been discussed in section 2.3.4. Discussion of the other alternative design recommendations may be found in Chapter 4 of reference [E1].

Because of the effects of coolant property variations with temperature and surface roughening with flow variations, it is important that these phenomenon be considered during the specification of operating criteria for power and flow in the GCFR fuel elements.

Consideration should be given to hot-spot factors, coolant mixing, flow rate, surface roughening, and coolant property variations in the design of peripheral and corner subchannels, as well as, in the assessment of fuel element geometry distortions.

6.5 GCFR Fuel Element Thermal-Hydraulic Analysis

The RUFHYD code, discussed in Chapter 3, does provide an illumination of the thermal-hydraulc behavior of gas-cooled, roughened, fast breeder reactor fuel elements; however, the RUFHYD calculational model was restricted by the neglect of coolant mixing and flow development (or redistribution). For future work, a more sophisticated thermal-hydraulic analysis code is recommended. Details for modifying the COBRA-3C code to work with a gaseous coolant and roughened surfaces were given in section 3.7.

Regardless of the specific computer code used, it will be necessary to supply such a code with empirically determined coolant mixing ocefficients and roughened surface performance predictions.

REFERENCES

[B1] Buettiker, P. "Pressure Loss of AGATHE HEX Spacer," Spacer," Swiss Federal Institute for Reactor Research Report E.I.R. TM-IN-482, 19 October 1973.

[B2] Bergles, A.E., "Survey and Evaluation of Techniques to Augment Convective Heat and Mass Transfer," Progress in Heat and Mass Transfer, V1 (Oxford, Pergamon Press, 1969), pp. 331-424.

[B3] Bernath, L., "Alternate GCFR Fuel Element Spacer - The Twisted Tape," GGA Internal Correspondence 730619-01, to J.B. Dee, dated 19 June 1973.

[B4] Bergles, A.E. and R.L. Webb, editors, Augmentation of Convective Heat and Mass Transfer (NY, ASME, 1970).

[B5] Barnett, P.G., "The Influence of Wall Thickness, Thermal Conductivity and Method of Heat Input on the Heat Transfer Performance of Some Ribbed Surfaces," Intl. Journal of Heat and Mass Transfer, V15, 1972, pp. 1159-1169.

[B6] Bergles, A.E., "Techniques to Augment Heat Transfer," Section 10, Handbook of Heat Transfer, ed. by W.M. Rohsenow and J.P. Hartnet (New York, McGraw-Hill, 1973).

[B7] Baumeister, T. and L.S. Marks, eds., Standard Handbook for Mechanical Engineers (New York, McGraw-Hill, 1967), p. 2-33.

[D1] Dee, J.B., P. Fortesque and J.A. Larrimore, "Gas-Cooled Fast Breeder Reactor Studies," Gulf General Atomic Co. Report GA-10678, June 1971.

[E1] Eaton, T.E., "Hydraulic Analysis of Nuclear Fuel Elements Using Roughened Surfaces and Gaseous Coolants," MIT General Atomic Company Project Report, August 1975.

[E2] Eaton, T.E. and N.E. Todreas, "Instrumentation Methods for Interchannel Coolant Mixing Studies in Wire-Wrap Spaced Nuclear Fuel Assemblies," USAEC Report COO-2245-9 TR, Massachusetts Institute of Technology, June 1974.

[E3] Eckert, E.R.G., "Radiation, Part A, Relations and Properties," Section 15, Handbook of Heat Transfer, ed. by W.M. Rohsenow and J.P. Hartnett (New York, McGraw-Hill, 1973), p. 15-21.

[E4] Eaton, T.E., Letters and Comments, Mechanical Engineering V95, N7, July 1973, p. 62.

[E5] Eaton, T.E., "Comments on the Calculation of Thermodynamic and Transport Properties of Helium," Massachusetts Institute of Technology, Department of Nuclear Engineering Report MITNE-166, November 1974.

[E6] Eaton, T.E., "A List of References Relating to the Use of Roughening Surfaces for the Augmentation of Forced Convection Heat Transfer," General Atomic Company Project, Nuclear Engineering Dept., Massachusetts Institue of Technology, 1975.

[E7] Eaton, T.E., D.D. Lanning and N.E. Todreas, "Gas-Cooled Fast Breeder Reactor Fuel Element Thermal-Hydraulic Investigations, Semiannual Progress Report for the Period 1 October 1973 through 31 March 1974," Nuclear Engineering Dept., Massachusetts Institute of Technology, June 1974.

[G1] Goodman, J., V. Jovanovic, J.T. Ganley, R.E. Covert, "The Thermodynamic and Transport Properties of Helium," General Atomic Company Report, March 1975 (DRAFT).

[G2] Gambill, W.R. and R.D. Bundy, "An Evaluation of the Present Status of Swirl Flow Heat Transfer," USAEC Report 61-4-61, 1961; also ASME Paper 61-HT-42, 1962.

[G3] GCFR Project Staff, "Gas-Cooled Fast Breeder Reactor Preliminary Safety Information Document," General Atomic Company Report GA-10298, February 1971, and revisons.

[G4] Gatehouse, M.H.T., A.G. Hutton, M.H. Lee and G.H. Lyall, "HELICAL-3: A program for Calculation of Detailed Can and Coolant Temperature Distributions in AGR Clusters," CEGB Report RD/B/N2437, Berkeley, October, 1972.

[H1] Hanson, A.S. and N.E. Todreas, "Coolant Mixing in Rod Bundles, Report for the Period June 1, 1974 - August 31, 1974," USAEC Report COO-2245-13.

[H2] Hanson, A.S., "FLuid Mixing Studies in an Hexagonal 61-Pin, Wire-Wrapped Rod Bundle," Doctor of Science Thesis, Department of Nuclear Engineering, Massachusetts, Institute of Technology, Cambridge, Mass. 1975.

[H3] Hudina, M. "Experimental Investigation of the Thermo-hydraulic Characteristics of Some Rough Surfaces at Low Reynolds Number," EIR Report SL-R/10, May 1973.

[H4] High Pressure Gas as a Heat Transport Medium, Institution of Mechanical Engineers Proceedings 1966-67, V181, Part 3I (London, IME, 1967).

[H5] Hudina, M. ,"Heat Transfer and Pressure Drop Measurements with Surfaces Roughened by Photo-Etching," Paper 12, Report SL-R/3, Specialists Meeting on Thermal Hydraulics, Windscale, May 1972.

[H6] Hall, W.B., "Heat Transfer in Channels Having Rough and Smooth Surfaces," Journal of Mechanical Engineering Science, V4, N3, 1962, pp. 287-291 (Also, "Heat Transfer in Channels Composed of Rough and Smooth Surfaces," Report IGN-TN/W.832).

[K1] Kattchee, N. and W.V. Mackewicz, "Heat Transfer and Fluid Friction Characteristics of Tube Clusters with Boundary-Layer Turbulence Promoters," ASME Paper 63-HT-1, 1963.

[K2] Kattchee, N. and W.V. Mackewicz, "Effects of Boundary Layer Turbulence Promoters on the Local Film Coefficients of ML-1 Fuel Elements," Nuclear Science and Engineering, V16, 1963, pp. 31-38.

[K3] Kjellstrom, B. and S. Hedberg, "On Shear Stress Distribution for Flow in Smooth or Partially Rough Annuli," AE-243, 1966, AE-RTL-796, 1965 (Also: Paper at EAES Heat Transfer Symposium, Bern, 1966).

[K4] Klein, D.E. and K.O. Lund, "Evaluation of Transformation Methods for Rough Rods Tested in an Annulus," General Atomic Company Internal Correspondence 741113226-GCFR, 13 November 1974, not published.

[K5] Knudsen, J.G. and D.L. Katz, Fluid Dynamics and Heat Transfer (New York, McGraw-Hill, 1958).

[K6] Kays, W.M. and H.C. Perkins, "Forced Convection, Internal Flow in Ducts," Section 7, Handbook of Heat Transfer, ed. by W.M. Rohsenow and J.P. Hartnett (New York, McGraw-Hill, 1973)

[L1] Lewis, M.J., "Errors that Arise when Estimating the Heat-Transfer Characteristics of Rough Surfaces from 'Bulk' Measurements in Annular Channels," Swiss Federal Institute for Reactor Research - EIR Report TM-In-535, Wurenlungen, Switzerland, May 1973.

[L2] Lewis, M.J., "A New Method for Analysing the Subsonic Flow Over Any Rough Surface at All Reynolds Numbers," Swiss Federal Institute for Reactor Research - EIR Report TM-IN-535, May 1973.

[L3] Levy, S. "Fluid Flow," Chapter 15, The Technology of Nuclear Reactor Safety, V2, Reactor Materials and Engineering, ed. by T.J. Thompson and J.G. Beckerley (Cambridge, MIT Press, 1973), pp. 298 - 301.

[M1] Moody, L.F., "Friction Factors in Pipe Flow," Trans. of the ASME, V66, November 1944, p. 671.

[M2] Markoczy, G. "Core Heat Transfer and Fluid Flow in the GCFR," Transactions of the ANS, V14, N1, pp. 275-276.

[M3] Markoczy, G., Letter to L. Bernath (Gulf General Atomic Company) from EIR, Switzerland, date 1 Oct. 1973.

[M4] Melese-d'Hospital, G. "Performance of GCFR's with Artificially Roughened Fuel Elements," Nuclear Science and Engineering, V33, 1968, pp. 271 - 283.

[M5] Maubach, K. and K. Rehme, "Pressure Drop for Parallel Flow Through a Roughened Rod Cluster," Nuclear Eng. and Design, V25, 1973, pp. 369 - 378.

[M6] Mantle, P.L., A.R. Freeman and J. Watts, "Conductivity Effects on Ribbed Surface Heat Transfer," International Journal of Heat and Mass Transfer, V14, 1971, pp. 1825 - 1834.

[M7] Mantle. P.L., "Improvements in or Relating to Fuel Element Assemblies for Nuclear Reactors," Patent Specification #1224465, British Patent Office, 17 May 1967.

[M8] Mantle, P.L., "A Programme of Work to Develop a Modified Type of AGR Fuel Cluster Offering a Large Improvement in Heat Transfer Performance," CEGB Report RD/B/N.833, 1967.

[M9] Mantle, P.L. and A.G. Morss, "Measuring the Heat Transfer Performance of Nuclear Reactor Fuel Element Clusters using the Technique of Superposition of Temperature Distributions," Heat Transfer 1970, Vol. VII (Amsterdam, Elsevier), Paper MT 2.6.

[M10] Mantle, P.L., "Secondary Gas Flows Produced by Multi-Start Helically Ribbed Rods," C.E.G.B., Unpublished Work.

[N1] Norris, R.H., "Some Simple Approximate Heat Transfer Correlations for Turbulent Flow in Ducts with Rough Surfaces," Augmentation of Convective Heat and Mass Transfer (NY, ASME, 1970), pp. 16-26.

[P1] Poppendick, H.F. and W.R. Gambill, "Helical, Forced-Flow, Heat Transfer and Fluid Dynamics in Single and Two-Phase Systems," Proc. Third Intl. Conference on Peaceful Uses of Atomic Energy, V8 (New York, UN, 1965), pp. 274 - 282.

[R1] Rapier, A.C. "Forced Convection Heat Transfer in Passages with Varying Roughness and Heat Flux Around the Perimeter," UKAEA Report TRG 519(W), 1963.

[R2] Rowe, D.S. and C.W. Angle, "Crossflow Mixing Between Parallel Flow Channels During Boiling, USAEC Report BNWL-371, "Part I: COBRA Computer Program for Coolant Boiling in Rod Arrays," March 1967, "Part II: Measurements of Flow and Enthalpy in Two Parallel Channels," December 1967, "Part III: Effect of Spacers on Mixing Between Two Channels," January 1969.

[R3] Rowe, D.S., "COBRA-II: A Digital Computer Program for Thermal Hydraulic Sub-Channel Analysis of Rod Bundle Nuclear Fuel Elements," USAEC Report BNWL-1229, August 1970.

[R4] Rowe, D.S., "COBRA-III: A Digital Computer Program for Steady State and Transient Thermal-Hydraulic Analysis of Rod Bundle Nuclear Fuel Elements, USAEC Report, BNWL-B-82.

[R5] Rowe, D.S., COBRA-III C: A Digital Computer Program for Steady State and Transient Thermal-Hydraulic Analysis of Rod Bundle Nuclear Fuel Elements," USAEC Report BNWL-1695, March 1973.

[R6] Rogers, J.T. and M.E.E. Tahir, "Turbulent Interchange Mixing in Rod Bundles and the Role of Secondary Flows," ASME Paper 75-HT-31, 1975.

[R7] Rehme, K. "Pressure Drop Performance of Rod Bundles in Hexagonal Arrangements," International Journal of Heat and Mass Transfer, V15, 1972, pp. 2499-2517.

[R8] Rogers, J.T. and N.E. Todreas, "Coolant Interchannel Mixing in Reactor Fuel Rod Bundles: Single-Phase Coolants," Heat Transfer in Rod Bundles (NY, ASME, 1968), pp. 1 - 56.

[S1] Sangster, W.A., "Calculation of Rod Bundle Pressure Loss," ASME Paper 68-WA/HT-35, 1968.

[S2] de Stordeur, A.N., "Drag Coefficients for Fuel-Spacers," Nucleonics, V19, No. 6, June 1961, pp. 74 -80.

[S3] Sheriff, N. and P. Gumley, "Heat Transfer and Friction Properties of Surfaces with Discrete Roughness," International Journal of Heat and Mass Transfer, V9, 1966, pp. 1297 - 1320.

[T1] Tang, I.M. and R.A. Fazzolare, "Heat Transfer from the Roughened Surface of a GCFR Fuel Rod," Transactions of the ANS, V19, October 1974, pp. 320 - 321.

[U1] United Sensor and Control Corp., "Probes for Measuring Temperature, Total and Static Pressure, Velocity and Flow Direction of Fluids, Gases and Liquids," Catalog S-7, Revision - A, USCC, 85 School St., Watertown, Mass. 02172.

[V1] Varadi, G., "Thermodynamische Stoffwerte von Helium," Swiss Federal Institute for Reactor Research - EIR Report TM-IN-410, Wurenlingen, March 1969 (In German) (English Translation - G. Varadi, "Thermodynamic Properties of Helium," EIR Report TM-IN-410, translated by T.E. Eaton and P.B. Bon-MIT).

[W1] Wilkie, D. "Forced Convection Heat Transfer from Surfaces Roughened by Transverse Ribs," Third International Heat Transfer Conference, Vol. 1 (AIChE, 1966), pp. 1-19.

[W2] Williams, F. and J. Watts, "The Development of Rough Surfaces with Improved Heat Transfer Performance and a Study of Mechanisms Involved," Paper FC 5.5, Heat Transfer 1970 (Amsterdam, Elsevier, 1970).

[W3] White, L. and D. Wilkie, "The Heat Transfer and Pressure Loss Characteristics of Some Multi-Start Ribbed Surfaces," Augmentation of Convective Heat and Mass Transfer, Ed. by A.E. Bergles and R.L. Webb (NY, ASME, 1970), pp. 55-62.

[W4] Wilkie, D., "Calculation of Heat Transfer and Flow Resistance of Rough and Smooth Surfaces Contained in a Single Passage," Proceedings of the Institution of Mechanical Engineers, 1964, pp. 20 - 31 (Also: Proceedings of the Third Intl. Heat Transfer Conference, Chicago 1966, Paper no. 2).

[W5] Wheeler, C.L., G.C. Main and D.C. Kolesan, "COBRA II-A: A Program for Thermal Hydraulic Analysis of Very Large Bundles of Fuel Pins," USAEC Report, BNWL-1422, August 1970.

[Z1] Zimmermann, M.W., "Geometrical Data of the AGATHE - Hex Spacer," Swiss Federal Institute of Reactor Research Report EIR TM-IN-545, September 1973.

NOMENCLATURE*

A - Flow Area

A_g - Gap region weighting area in peripheral subchannel, average velocity determination, section 5.1.3

A_{inj} - Injection tube flow area

A_j - Data weighting area in interior subchannel, average velocity determination, section 5.1.3

A_6 - Six-sided weighting area in peripheral subchannel, average velocity determination, section 5.1.3

C - Salt solution tracer concentration

C_i - Injection tracer, solution concentration, Chap. 4, Friction factor correlation constant, Chap. 3

C_p - Specific heat at constant pressure

d_e - Equivalent hydraulic diameter

d_r - Rod diameter

e - Roughened surface rib height

e/d_e - Relative roughness (also d_e/e)

e - Estimated experimental uncertainty, Table 5.13

f - Friction factor

F - Force, Appendix 6

f_x - Ratio of rough surface to smooth surface friction factors, $f_x = f_r/f_s$

$\bar{f}_x$ - Friction factor multiplier determined using the perimeter-weighted, average equivalent friction factor multiplier model, see section 3.2

$\tilde{f}_x$ - Friction factor multiplier determined using the perimeter-weighted, parallel equivalent friction factor multiplier model, see section 3.2

G - Mass velocity

NOMENCLATURE (Continued)

$\overline{G_{ij}}$ - Average mass velocity in subchannels i and j

g - Rod-to-rod gap, Chapter 5; Rod-to-wall gap Chapter 3

g_c - Gravitational constant

h - Forced convection coefficient

H - Ratio of heated-to-wetted perimeter - P_h/P_w

K - Spacer grid loss coefficient

$\overline{K}$ - Average spacer grid loss coefficient for grids 6, 7, and 8.

L - Length

l - Roughened surface helical rib lead length

L_r - Roughened length (rod length, Appendix 6, only)

m - Friction factor correlation, Reynolds number exponent, i.e., $f = C/Re^m$

$M_d(z)$ - Tracer mass detection rate as a function of axial position

M_i - Tracer mass injection rate

M_{ij} - Mixing Stanton number

n - Number of velocity data points used in an average velocity determination

N_j - Number of subchannels of type j

N_s - Number of helical rib starts

ns - Number of specific flow boundaries making-up the wetted perimeter of a flow area

Nu - Nusselt number

P - Pressure

p - Roughened surface rib-to-rib pitch

NOMENCLATURE (Continued)

P_d - Dynamic pressure

P_j - Perimeter of a specific subchannel flow boundary

P_h - Heated perimeter

P_r - Prandtl number

P_w - Wetted perimeter

Q - Main flow rate ($= W_b$)

$\bar{q}'$ - Average fuel rod linear power

q'' - Fuel rod surface heat flux

Re - Reynolds number

St - Stanton number

St_x - Ratio of rough-to-smooth surface Stanton numbers

T - Temperature

V - Fluid velocity

$\bar{V}_i$ - Average fluid velocity for area i

$\overline{V_c}$ - Average corner subchannel velocity

$\overline{V_g}$ - Average velocity in rod-to-wall gap

$\overline{V_6}$ - Average peripheral subchannel velocity, central velocity profile

W - Flow rate

w - Roughened surface rib width

W_b - Bundle or main (total) flow rate ($=W_m$)

w_{ij} - Transverse flow per unit length

W_i - Flow rate in subchannel type i

W_{inj} - Injection flow rate

NOMENCLATURE (Continued)

W_p - Peripheral subchannel flow rate

W_t - Total bundle flow rate

X_{hc} - Ratio of hot-to-cold side subchannel flow rates

X_{ij} - Ratio of flow in area i -to- flow in area j

Z - Axial position

----- Greek Letters -----

α - Roughened surface rib helix angle, Chapter 2; Injection stream angle to axial flow, Chapter 4

β_{ij} - Dimensionless mixing coefficient between subchannels i and j, see section A3.3

ΔP_f - Pressure difference due to friction

ΔP_g - Pressure difference due to spacer grid

$\Delta W_p/\Delta g$ - Change in peripheral subchannel flow rate per change in rod-to-wall gap

ϵ - Emissivity

ρ - Fluid density

ρ_r - Rod density, Appendix 6

σ - Radiative transfer (Stefan-Boltzman) constant

μ - Fluid dynamic viscosity

----- Subscripts (Not noted above) -----

a - analytical

b - Bundle or rod array overall

e - Experimental

i - Subchannel type i

NOMENCLATURE (Concluded)

g - Grid spacer

r - Rough rod surface

s - Smooth rod surface

---

* Note - A line over the variable indicates the average value.

See Table A2.1 for helium property correlation nomenclature.

APPENDIX 1

ROUGHENED SURFACE PERFORMANCE OBSERVATIONS TAKEN FROM THE FRICTION FACTOR DIAGRAM

Some insight into the behavior of nuclear fuel elements which use roughened surfaces is readily available from observations of the common Moody friction factor chart [M1], see Figure A1.1. It is useful to recall that the GCFR Demonstration Plant fuel element uses a roughness height e of 0.006 in. (0.152 mm); the relative roughness e/d_e is 0.020 in interior subchannels, 0.29 in peripheral subchannels, 0.053 in corner subchannels, and 0.021 averaged over the fuel element. [Rod-to-wall gap = 0.048 in (1.22 mm), typical]. The Reynolds number range of interest varies from 0.0 to 120,000.

From the Moody chart, it is found that

A. the surface roughness effect is negligible in laminar flow,

B. the Reynolds number dependence of the friction factor decreases with increases in relative roughness from an exponent of 0.20 (nominal) for $e/d_e = 0.0000$ to approximately 0.00 for $e/d_e = 0.05$, (in laminar flow the Reynolds number dependence is -1.00, and it is independent of relative roughness),

C. the friction factor multiplier decreases with

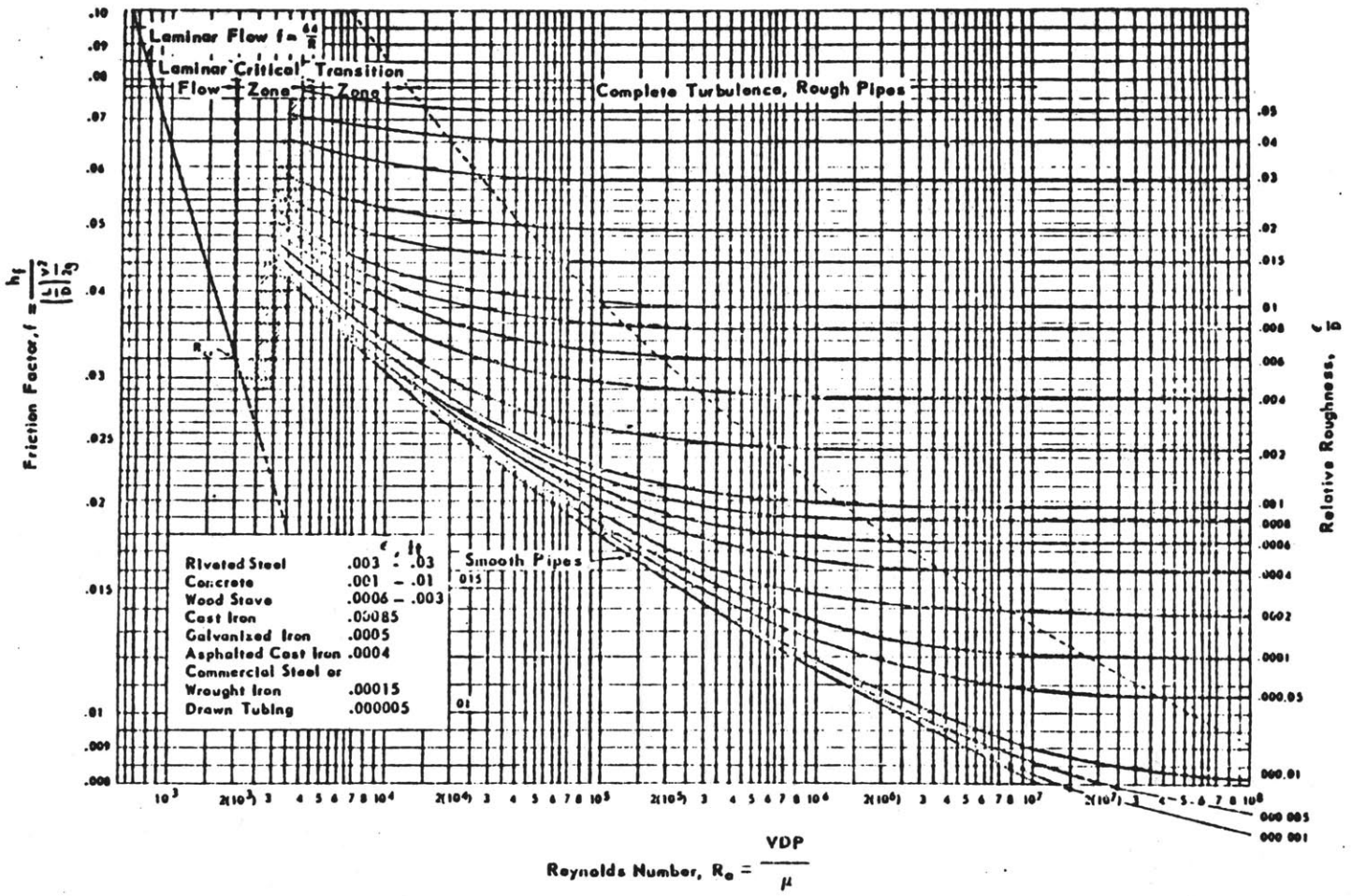

FIGURE A1.1 - THE FRICTION FACTOR CHART FROM MOODY [M1]

decreases in Reynolds number (e.g., for $e/d_e = 0.02$, typically from about 3.0 at Re = 100,000 to 2.0 at Re = 10,000 to 1.0 at Re < 2000), see Figure A1.2 D. the friction factor multiplier (and its variation with Reynolds number) varies with subchannel type due to the differences of relative roughness e/d_e and to differences in the Reynolds number, see Figure A1.2. (This will result in changes in the subchannel flow split factors with changes in total fuel element flow).

It should be noted that the friction factor chart was produced from circular tube geometry data. Further, the influence of partially roughened wetted perimeters on roughened surface behavior is not well understood. The effects of relative roughness and Reynolds number on roughened surface performance in partially roughened flow geometries complicate the problem.

A1.1 The Influence of Reynolds Number on the Friction Factor Multiplier

From the Moody chart, Figure A1.1, the friction factor for rough tubes may be seen to become constant as the Reynolds number increases. Further, the larger the relative roughness e/d_e, the higher the fully developed friction factor, and the sooner the friction factor becomes constant. Knudsen and Katz [K5] have

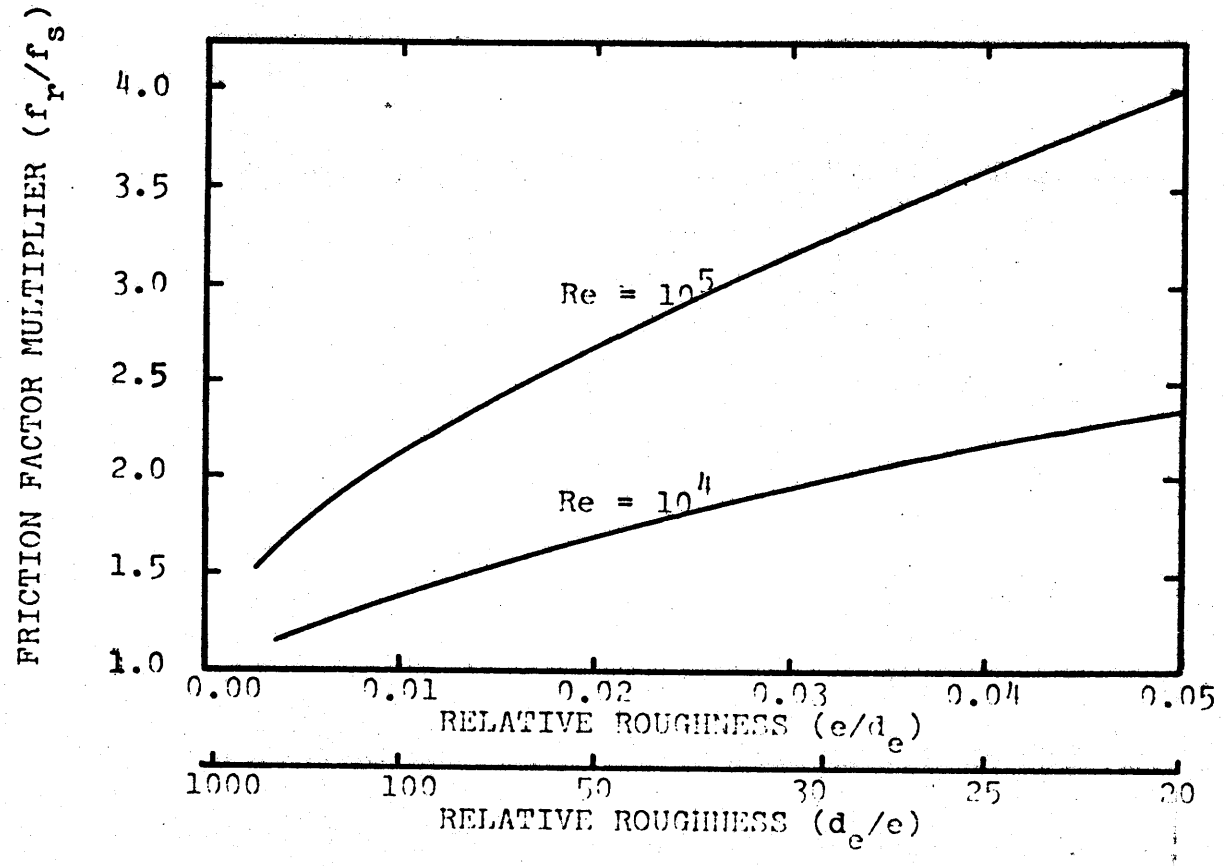

FIGURE A1.2

FRICTION FACTOR MULTIPLIER VS. RELATIVE ROUGHNESS DERIVED FROM THE MOODY FRICTION FACTOR DIAGRAM [M1]

recommended that the friction factor for fully developed, turbulent flow in a rough tube is given by [K6]

$$\frac{1}{\sqrt{f_r}} = 0.87 \ln(d_e/e) + 1.14 \qquad \text{(Eq. A1.1)}$$

for the Reynolds number range given by

$$Re > \frac{(d_e/e)}{0.005\sqrt{f_r}} \qquad \text{(Eq. A1.1a)}$$

where f_r is the Darcy friction factor and d_e/e is the relative roughness. Using Eq. A1.1, Eq. A1.1a may be expressed as a function of relative roughness only:

$$Re > (d_e/e)[174(\ln(d_e/e)) + 228.] \qquad \text{(Eq. A1.1b)}$$

It is important to note that the fully developed rough tube friction factor depends only on the relative roughness. In the flow development region, the rough tube friction factor depends on both Reynolds number and relative roughness. The transition of flow from laminar (no relative roughness effect) to fully turbulent (no Reynolds number effect) occurs in the Reynolds number range:

$$2{,}000 \lesssim Re < \frac{(d_e/e)}{0.005\sqrt{f_r}} \qquad \text{(Eq. A1.2)}$$

the friction factor of a smooth tube f_s in fully developed turbulent flow is given by the Karman-Nikuradse relation:

$$\frac{1}{\sqrt{f_s}} = -0.8 + 0.87 \ln\left(Re \sqrt{f_s}\right) \qquad \text{(Eq. A1.3)}$$

This expression is closely approximated by

$$f_s = 0.184 \, Re^{-0.20} \qquad \text{(Eq. A1.4)}$$

for $30{,}000 < Re < 1{,}000{,}000$.

For the Reynolds number range $5{,}000 < Re < 30{,}000$ the Blasius equation may be used as a good approximation:

$$f_s = 0.316 \, Re^{-0.25} \qquad \text{(Eq. A1.5)}$$

With the above, the friction factor multiplier, i.e., the ratio of the roughed surface friction factor to the smooth surface friction factor f_r/f_s, may be found to be

$$f_x = \frac{f_r}{f_s} = \frac{7.18 \, Re^{0.20}}{[\ln(d_e/e) + 1.31]^2} \quad ; \qquad \text{(Eq. A1.6)}$$

Equation A1.6 is limited by the range $30{,}000 < Re < 1{,}000{,}000$ and by the condition of equation A1.1b. A similar equation may be obtained using the Blasius equation (Eq. A1.5):

$$f_x = \frac{4.18 \, Re^{0.25}}{[\ln(d_e/e) + 1.14]^2} \quad ; \qquad \text{(Eq. A1.7)}$$

Equation A1.7 is limited by the range 5,000 < Re < 30,000 and by the condition of equation A1.1b. For the case of the GCFR fuel element with normal flow conditions and a relative roughness of 50. (0.3005 in./0.006 in.) Eq. A1.6 applies:

$$f_x = 0.26\ Re^{0.20} \quad (\text{i.e., } f_r = 0.048) \qquad \text{(Eq. A1.8)}$$

for 46,000 < Re < 1,000,000

In the case of the experiments, limitations in the flow facilities restricted much of the experimental results to the range of transition flow, i.e., for the experimental case 2,000 $\lesssim$ Re < 52,000. Because equation A1.6 did not apply in the transition flow region, a semilog plot of friction factor multiplier versus Reynolds number was produced taking smooth and rough tube friction factors directly from the Moody chart (Figure A1.1). The plot was prepared for a relative roughness e/d_e of 0.02 ($d_e/e = 50$) and is given in Figure A1.3. Using this figure, the following correlations for the transition flow, rough tube, friction factor multipler were obtained for a relative roughness $e/d_e = 0.02$:

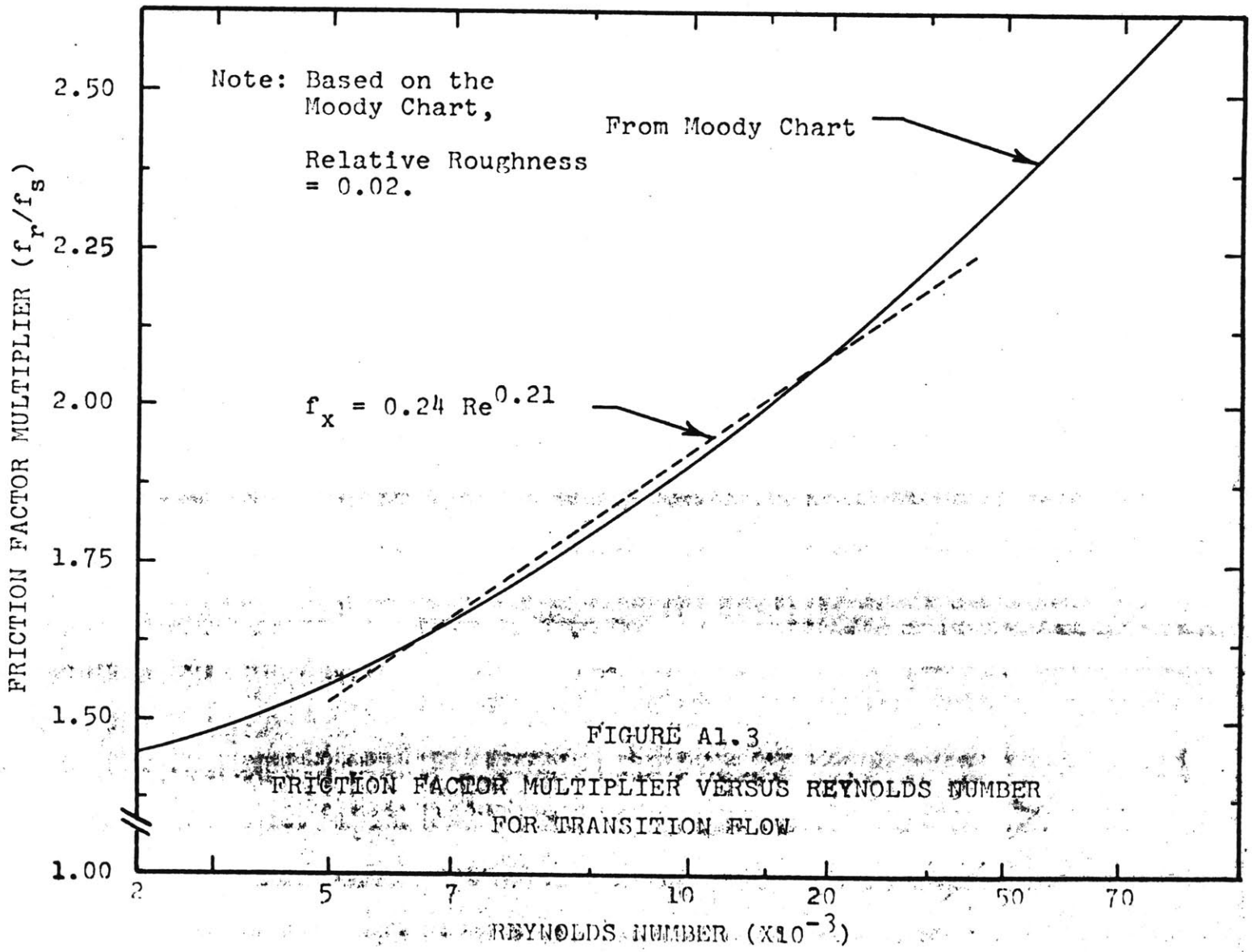

FIGURE A1.3
FRICTION FACTOR MULTIPLIER VERSUS REYNOLDS NUMBER FOR TRANSITION FLOW

A. $f_x = 0.24\ Re^{0.21}$ ($f_r = 0.076\ Re^{-0.04}$)

$7{,}000 < Re < 70{,}000$ (Eq. A1.9)

B. $f_x = 0.22\ Re^{0.22}$

$20{,}000 < Re < 100{,}000$ (Eq. A1.10)

The above correlations predict the friction factor multiplier with an accuracy of ±5% in the Reynolds number range specified. Recall that the theoretical expression for f_x in the Reynolds number range $46{,}000 < Re < 1{,}000{,}000$ was given as Eq. A1.8 for the same relative roughness.

A1.2 The Influence of Reynolds Number on the Stanton Number Multiplier

Norris has shown that the Stanton number multiplier St_x may be related to the friction factor multiplier by the following approximation [N1]:

$$St_x = f_x^{0.6} \qquad \text{(Eq. A1.11)}$$

From this and Eq. A1.6, the approximate dependence of Stanton number multiplier on Reynolds number may be determined:

$$St_x = \frac{3.27\ Re^{0.12}}{[\ln(d_e/e) + 1.31]^{1.2}} \qquad \text{(Eq. A1.12)}$$

For the case of a GCFR interior subchannel, d_e = 0.3005 in, e = 0.006 in, equation A1.12 becomes

$$St_x = 0.45\ Re^{0.12} \qquad \text{(Eq. A1.13)}$$

The above equations for St_x are limited to the range 46,000 < Re < 1,000,000 and by the condition of equation A1.1b. At Re = 100,000 equation A1.13 predicts St_x = 1.79. Using equation A1.9, St_x may be estimated in the transition flow region to be

$$St_x = 0.42\ Re^{0.13} \qquad \text{(Eq. A1.14)}$$

$$7{,}000 < Re < 70{,}000$$

The theoretically predicted, friction factor and Stanton number multiplers for fully developed turbulent flow (defined by equation A1.1b) have been plotted in Figure A1.4. The equations used were those established for the GCFR fuel element, i.e., equation A1.8 for the friction factor multiplier and equation A1.13 for the Stanton number multiplier.

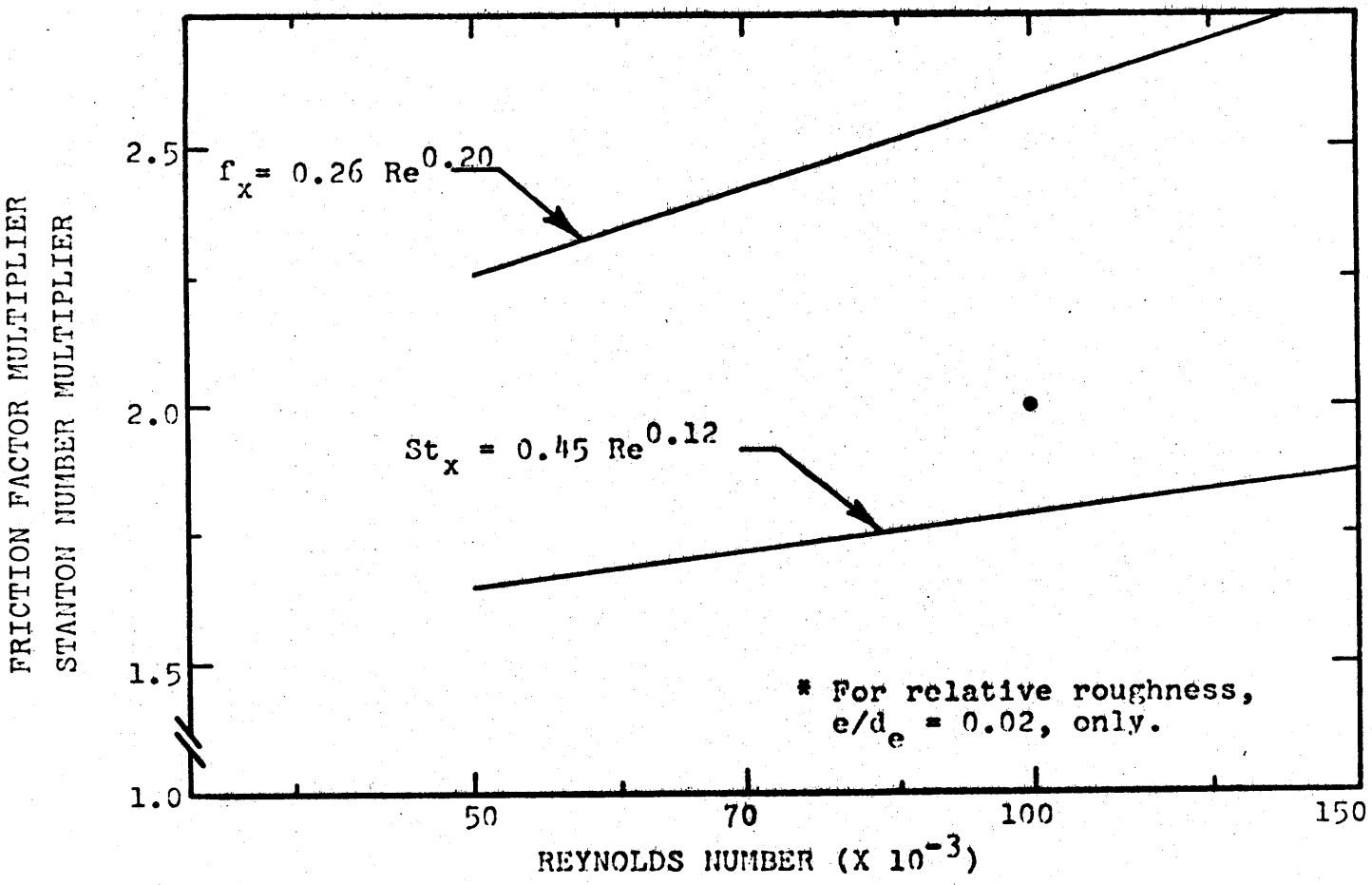

FIGURE A1.4 - THEORETICAL PREDICTION OF THE REYNOLDS NUMBER DEPENDENCE OF ROUGHENED SURFACE PERFORMANCE

APPENDIX 2

CALCULATION OF HELIUM THERMODYNAMIC AND TRANSPORT PROPERTIES

Performing the thermal-hydraulic analysis of a GCFR fuel element requires the calculation of the thermodynamic and transport properties of helium gas. The reader is referred to two reports: Goodman (G5) and Eaton (E5). It is important to note that helium, with its low atomic weight, closely approximates ideal gas behavior. Currently available analytical methods may be used to calculate thermodynamic properties with good accuracy; however, the transport property correlations, particularly the correlations for thermal conductivity, do not give as accurate results. This problem is due primarily to difficulties with experimental measurements. Further consideration of the calculation of helium thermal conductivity is recommended for future work.

Table A2.1 gives a summary of equations for calculating helium properties as reported by Varadi (V1). The Varadi equations are sufficient for engineering calculations; however, the reader is cautioned to selected helium property correlations cautiously if extensive utilization is required.

TABLE A2.1

A SUMMARY OF EQUATIONS SUGGESTED FOR CALCULATING HELIUM THERMAL-PHYSICAL PROPERTIES BY VARADI (EIR TM-IN-410) [V1]

---------- ENGLISH UNITS $ ----------

$T = {}^{o}R$ $P = psia$ $T_o = 491.67\ {}^{o}R$ $P_o = 14.504\ psia$

$R = 0.4965\ BTU/lbm\text{-}{}^{o}R$

$$Z = 1.0 + (0.1850)\frac{BP}{RT}$$

$$B = B(T) = C_1 + \frac{C_2}{1-C_3T} + \frac{C_4}{1+C_5T} \qquad (ft^3/lbm)$$

$C_1 = 1.520017 \times 10^{-2}\ ft^3/lbm$ $C_2 = 1.526208 \times 10^{-2}\ ft^3/lbm$

$C_3 = 1.900378 \times 10^{-2}\ {}^{o}R^{-1}$ $C_4 = 4.388083 \times 10^{-2}\ ft^3/lbm$

$C_5 = 5.227289 \times 10^{-4}\ {}^{o}R^{-1}$

$$B' = \frac{\partial B(T)}{\partial T} = \frac{C_2C_3}{(1-C_3T)^2} - \frac{C_4C_5}{(1+C_5T)^2} \qquad (ft^3/lbm\,{}^{o}R)$$

$$B'' = \frac{\partial^2 B(T)}{\partial T^2} = \frac{2C_2C_3^2}{(1-C_3T)^3} + \frac{2C_4C_5^2}{(1+C_5T)^3} \qquad (ft^3/lbm\text{-}{}^{o}R^2)$$

$$\rho = \frac{P}{(5.4054)RT + BP} \qquad (lbm/ft^3)$$

$C_{po} = 1.242\ BTU/lbm\text{-}{}^{o}F$ $C_{vo} = 0.7456\ BTU/lbm\text{-}{}^{o}F$

$C_p = C_{po} - 0.1850)\ TB''P \quad (BTU/lbm\text{-}{}^{o}F)$

$C_v = C_{vo} - (0.1850)P[TB'' + B'(2.0+(0.1850)B'P/R)] \quad (BTU/lbm\,{}^{o}F)$

$H_o = 2.390\ BTU/lbm$ $S_o = 6.6930\ BTU/lbm\text{-}{}^{o}F$

$S = S_o + C_{po}\ln(T/T_o) - R(\ln(P/P_o)) - 0.1850\ B'P \quad (BTU/lbm\text{-}{}^{o}F)$

$H = H_o + C_{po}T + (0.1850)\ P(B - B'T) \qquad (BTU/lbm)$

$$V_s = (158.29)\, Z \sqrt{RT\, C_p/C_v} \qquad \text{(ft/sec)}$$

$$\mu = 0.04488\, (T/T_o)^{0.68} \qquad \text{(lbm/hr-ft)}$$

$$K(P,T) = 0.08368(T/T_o)^{0.68}[1.0+(1.665\times10^{-4})(P/P_o)^{1.17}/(T/T_o)^{1.85}] \qquad \text{(BTU/hr-ft-}^{o}\text{F)}$$

$$Pr = 0.666[1.0+(1.665\times10^{-4})(P/P_o)^{1.17}/(T/T_o)^{1.85}]^{-1}$$

---------- METRIC UNITS $ ----------

$T = {}^{o}K \quad P = N/m^2 \quad T_o = 273.15\ {}^{o}K \quad P_o = 10^5\ N/m^2$

$R = 2077.1\ J/kg^{o}K$

$$Z = 1.0 + \frac{BP}{RT}$$

$$B = B(T) = C_1 + \frac{C_2}{1-C_3T} + \frac{C_4}{1+C_5T} \qquad (m^3/kg)$$

$C_1 = 9.489433 \times 10^{-4}\ m^3/kg \quad C_2 = 9.528079 \times 10^{-4}\ m^3/kg$

$C_3 = 3.420680 \times 10^{-2}\ {}^{o}K^{-1} \quad C_4 = 2.739470 \times 10^{-3}\ m^3/kg$

$C_5 = 9.409120 \times 10^{-4}\ {}^{o}K^{-1}$

$$B' = \frac{\partial B(T)}{\partial T} = \frac{+C_2C_3}{(1-C_3T)^2} - \frac{C_4C_5}{(1+C_5T)^2} \qquad (m^3/kg\text{-}{}^{o}K^2)$$

$$B'' = \frac{\partial B(T)}{\partial T^2} = \frac{+C_2C_3^2}{(1-C_3T)^3} + \frac{2C_4C_5^2}{(1+C_5T)^3} \qquad (m^3/kg\text{-}{}^{o}K^2)$$

$$\rho = \frac{P}{RT + BP} \qquad (kg/m^3)$$

$C_{po} = 5198$ J/kg-^oK $\qquad C_{vo} = 3121$ J/kg-^oK

$$C_p = C_{po} - TB"P \qquad (J/kg-^oK)$$

$$C_v = C_{vo} - P[TB" + B'(2.0 + \frac{B'P}{R})] \qquad (J/kg-^oK)$$

$H_o = 5557$ J/kg $\qquad S_o = 28016$ J/kg

$$S = S_o + C_{po}(\ln(T/T_o)) - R(\ln(P/P_o)) - B'P \qquad (J/kg-^oK)$$

$$H = H_o + C_{po}T + P(B - B'T) \qquad (J/kg)$$

$$V_s = Z\sqrt{RT(C_p/C_v)} \qquad (m/sec)$$

$$\mu = 1.855 \times 10^{-5} (T/T_o)^{0.68} \qquad (kg/m-sec)$$

$$K(P,T) = 0.1448(T/T_o)^{0.68}[1.0 + 1.665 \times 10^{-4}(P/P_o)^{1.17}/(T/T_o)^{1.85}] \qquad (W/m-^oC)$$

$$Pr = 0.666\,[1.0 + 1.665 \times 10^{-4}(P/P_o)^{1.17}/(T/T_o)^{1.85}]^{-1}$$

$ NOMENCLATURE

B = Second Viral Coefficient - ft^3/lbm (m^3/kg)*

B' = $\partial B/\partial T$ - ft^3/lbm-^oF (m^3/kg-^oK)

B" = $\partial^2 B/\partial T^2$ - ft^3/lbm-^of (m^3/kg-$^oK^2$)

C_p = Specific Heat at Constant Pressure - BTU/lbm-^oF (J/kg-^oK)

C_v = Specific Heat at Constant Volume - BTU/lbm-^oF (J/kg-^oK)

H = Enthalpy - BTU/lbm (J/kg)

K = Thermal Conductivity - BTU/hr-ft-^{o}F (J/hr-m-^{o}K)

P = Pressure - psia (N/m^2)

P_o = 14.504 psia = 10^5 N/m^2

R = Gas Constant for Helium BTU/lbm-^{o}R (J/kg-^{o}K)

S = Entropy - BTU/lbm-^{o}F (J/kg-^{o}K)

T = Absolute Temperature - ^{o}R (^{o}K)

T_o = 491.67^{o}R = 273.15^{o}K

V_s = Sonic Velocity - ft/sec 9m/sec)

Z = Compressibility Factor

ρ = Fluid Density - lbm/ft^3 (kg/m^3)

μ = Dynamic Viscosity - lbm/hr-ft (kg/sec-m)

---

* (metric equation units)

APPENDIX 3

A DISCUSSION OF INTERCHANNEL COOLANT MIXING

A3.1 Mixing in Nuclear Fuel Assemblies

Many nuclear power reactor cores are made up of fuel assemblies composed of an array of fuel bearing tubes called fuel rods. The fuel rods are arranged into an array and are held in the lattice arrangement by a spacer device, e.g., spacer grids or wire-wraps. The spacer devices serve primarily to maintain the coolant flow passages and to prevent fuel rod vibrations. The fuel rod array may be contained within a box structure to provide support for the rods and to contain the coolant within the array. The rod array is constructed so as to provide for transverse communication of the coolant as it passes axially through the fuel assembly. The transverse exchange or transfer of coolant and energy within the fuel assembly is the subject of interchannel coolant and energy mixing. The word interchannel is introduced in rod array or rod bundle thermal-hydraulic analysis where the coolant flow passages are divided into unit flow areas called subchannels.

Transverse coolant and energy transfer or mixing occurs via natural or inherent mechanisms and by forced or mechanical (design) mechanisms. Fluid transfer or coolant mixing inherently gives rise to energy mixing as well; however, thermal conduction within fuel assembly materials and radiation (possible with gaseous coolants) transfers energy without coolant transfer. The design option of using extended surfaces (fins) to promote energy transfer can be considered a mechanical mechanism to promote energy mixing. The natural coolant and energy mixing effects are turbulent interchange and diversion cross flow while the forced or mechanical coolant (and energy) mixing mechanisms are turbulence promotion (flow scattering) and flow sweeping. These mechanisms of coolant and energy mixing are summarized in Table A3.1 Additional discussion of mixing effects may be found in Rogers and Todreas [R8].

Natural Mixing Effects

The primary natural mixing effect is turbulent interchange (resulting from transverse eddy transport) of coolant and energy within the gaps between fuel rods where the fluid flowing axially in the rod array communicates transversely (across the artificial subchannel boundaries); turbulent interchange does not involve a

Table A3.1

A Summary of Mechanisms for Interchannel Coolant and Energy Mixing Effects Within Nuclear Fuel Assemblies[†]

	NATURAL	FORCED or MECHANICAL
FLUID AND ENERGY MIXING EFFECTS	TURBULENT INTERCHANGE DIVERSION CROSS FLOW[*]	TURBULENCE PROMOTION (Flow Scattering) FLOW SWEEPING[*]
ENERGY MIXING EFFECTS ONLY	THERMAL CONDUCTION RADIATIVE TRANSFER	THERMAL CONDUCTION IN EXTENDED SURFACES (FINS)

[†]Adapted from Rogers and Todreas [R8]

[*]Directional Coolant Mixing Effects

net fluid transfer but can result in net energy transfer from one flow region to another. Diversion cross flow is a directional inherent mixing mechanism which results from changes in the differences of hydraulic resistance between flow subchannels. An excellent example of diversion cross flow is the flow development in rod arrays enclosed within a fuel assembly box or can. The flow normally enters the rod array from a plenum with a uniform velocity and is redistributed as hydraulic flow development occurs due to differences in the hydraulic resistance of the various subchannels. An example of diversion cross flow arises when a gaseous coolant is used in a fuel assembly subjected to radial power gradients; density decreases in higher powered regions result in a transverse or diversion cross flow to the cooler side of the fuel assembly.

Secondary flow occurs naturally whenever the wetted perimeter (hydraulic resistance) is not distributed uniformly around the flow area. These non-circular flow geometries give rise to transverse pressure gradients which generate secondary flows (superimposed on the main axial flow). Although secondary flows are not

responsible for the transfer of coolant from one subchannel to another, such internal subchannel flows can be expected to have a influence on the transfer of coolant and energy in the vicinity of the subchannel gaps.

Forced Mixing Effects

Forced mixing results from coolant flow interaction with mechanical components within the assembly . Several types of forced mixing effects are possible, e.g., turbulence promotion, which inlcudes flow scattering, and flow sweeping. Turbulence promotion is a non-directional mechanical method of increasing the level of background or natural turbulence; this forced mixing effect is introduced into the fuel assembly by using roughened surfaces of various types. Turbulence promotion (which is used to improve the convective heat transfer coefficient is usually desirable only in the active fuel region of the assembly and thus gives rise to diversion cross flow at the start (and termination) of roughening.. This is because only the heated surfaces are roughened, and the increase in hydraulic resistance is greater within the rod array than along the smooth periphery of the fuel element. Flow scattering is a non-directional type of turbulence promotion which results from mechanical protuberances in the flow field, e.g., spacer

grids.

Flow sweeping is a directional forced mixing effect which is caused by such mechanical devices as wire-wrap spacers or grid spacer turning vanes that are oriented with an angle to the axially flowing coolant.

The Significance of Mixing

Interchannel coolant and energy mixing are important in the thermal-hydraulic and thermal-mechanical design of nuclear fuel assemblies because its mechanisms influence the coolant temperature profile and reduce hot spot temperatures. These considerations of thermal-hydraulic analysis are particularly important in fast breeder reactors where both coolant and structural temperatures are high and where structural materials undergo volumetric swelling in a strongly temperature dependent manner.

It is important to note that no interchannel coolant mixing effect has the capability to transfer coolant over length scales larger than those typical of the fuel rod pitch. The length scale typical of mixing mechanisms limits the ability of mixing to reduce temperature gradients over lengths greater than a few rod pitches, e.g., the radial assembly temperature tilt occurring in fuel assemblies subjected to steep radial power gradients.

Mixing effects can be very effective in reducing local temperature differences in fuel assemblies but cannot be effective in reducing temperature differences across the entire assembly. Figure A3.1 shows typical results of increasing mixing levels on the temperature tilt across a fast breeder reactor fuel assembly. The steep temperature gradients near the array sides in Figure A3.1 are due to a by-pass flow that over-cools the near-wall region; this by-pass flow results from the mechanical design of the fuel element which, for the case illustrated, has a lower flow resis tance at the array edge than in the array interior.

A3.2 Definition of the Mixing Coefficient

The dimensionlass mixing coefficient, commonly referred to as "beta", is defined as

$$\beta_{ij} = \frac{w_{ij}}{\bar{G}_{ij} g_{ij}} \qquad \text{(Eq.A3.1)}$$

where β_{ij} is the dimensionless mixing coefficient between subchannel i and subchannel j, w_{ij} is the transverse flow per unit length between subchannels i and j, g_{ij} is the gap width of the common boundary between subchannels i and j, and $\bar{G}_{ij}$ is the average axial mass velocity in subchannels i and j, i.e.,

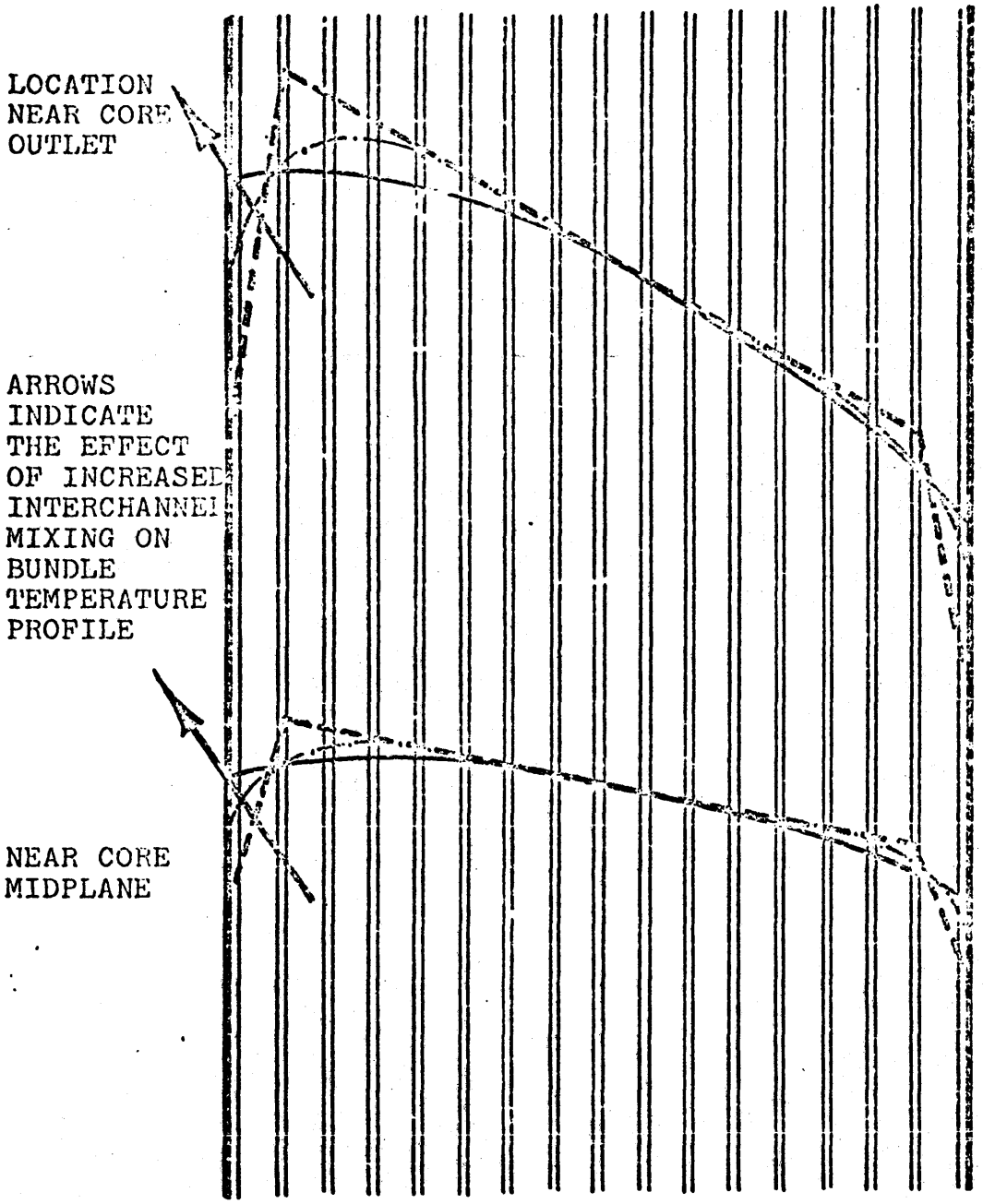

FIGURE A3.1- INFLUENCE OF INTERCHANNEL COOLANT AND ENERGY MIXING ON THE TRANSVERSE BUNDLE TEMPERATURE PROFILE ARISING FROM RADIAL POWER GRADIENTS*

* Adopted from Markóczy [M2]

$$\overline{G}_{ij} = \frac{G_i + G_j}{2} \quad . \qquad \text{(Eq. A3.2)}$$

β_{ij} is related to the Mixing Stanton Number M_{ij} by

$$M_{ij} = \frac{\beta_{ij}\overline{G}}{G_i} = \frac{w_{ij}}{G_i g_{ij}} \qquad \text{(Eq. A3.3)}$$

It is also convenient to note that the fraction of flow exchanged between subchannels i and j per unit length is given by w_{ij}/W_i where W_i is the mass flow rate in subchannel i.

A3.3 Evaluation of the Dimensionless Mixing Coefficient From Salt Solution Tracer Experiment Data

The salt solution tracer used in the coolant mixing experiments discussed in Chapters 4 and 5 was injected into one subchannel and was transversely dispersed by coolant mixing mechanisms. Typical injection subchannels have been labelled i in Figure A3.2. The tracer injected into the flow in subchannel i communicates with the flow in subchannel j across the common artificial boundary at the gap between the fuel rods, g_{ij}. Because the transverse transfer of salt tracer is caused only by coolant mixing (for all practical purposes), the coolant mixing coefficient in dimensionless form may be evaluated using data from a mixing experiment which provides subchannel

FIGURE A3.2

ILLUSTRATION OF THE VARIOUS DIMENSIONLESS MIXING COEFFICIENTS DETERMINED FROM THE SALT TRACER EXPERIMENT DATA

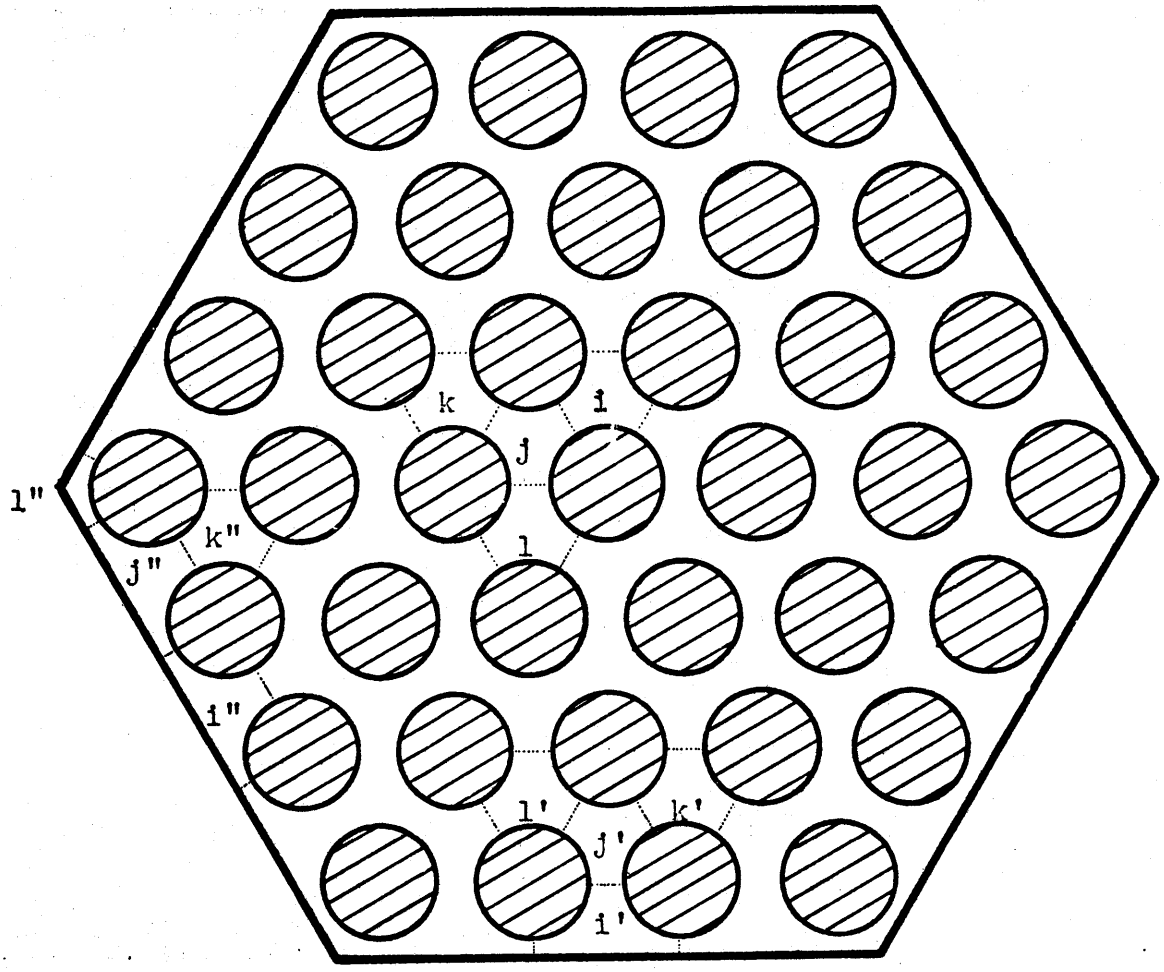

The three geometrically distinct interchannel mixing coefficients illustrated above are

A. Interior-to-Interior Subchannels: $\beta_{11} = \beta_{ij}$

B. Peripheral-to-Interior Subchannels: $\beta_{21} = \beta_{i'j'}$

C. Peripheral-to-Peripheral Subchannels: $\beta_{22} = \beta_{i"j"}$

tracer concentrations as a function of axial position.

In any rod array, coolant mixing occurs across all of the rod gaps simultaneously so that the general problem of determining the mixing rate between two subchannels, subchannels i and j, is complicated in nature and requires the solution of a large set of simultaneous equations. Because of the nature of the rod array experiments presented herein, it was possible to develop a simplified evaluation of the mixing coefficient as discussed below.

The amount of tracer flowing within a given subchannel is the product of the concentration of the tracer dissolved within the subchannel C_j and the flow rate of the subchannel W_j. If one considers the change in tracer flow rate over a given axial distance (assume the subchannel flow W_j to be constant), cf. Figure A3.2, it may be seen to be due to the transfer of salt into subchannel j by coolant mixing with a contiguous subchannel (s), say i, with a higher salt concentration. A change in the tracer flow rate in subchannel j may also be caused by the transfer of tracer out of subchannel j by coolant mixing with contiguous subchannels, say k and l, which have lower tracer concentrations than subchannel j. Regarding the experimental data, where i is the injection subchannel,

the primary tracer transfer is from subchannel i to j. Because the change of tracer flow rate in subchannel j is influenced by coolant mixing between subchannels j and k, as well as, subchannels j and l; this tracer transfer is a second order effect. The tracer concentration in subchannels k and l influences the tracer transfer from subchannels k to j and from l to j, respectively. Thus, the tracer transfer to subchannels k and l to contiguous subchannels (other than j) also influences the transfer from j to k and j to l, respectively. Tracer transfer out of subchannels k and l is a third order effect and may be neglected in the case at hand.

For the purposes of determining the mixing coefficient in the salt solution tracer experiments discussed in Chapters 4 and 5, it is important to note that the tracer moves transversely from regions of high concentration to regions (subchannels) of lower concentration via coolant mixing. Because the tracer was not observed to be widely dispersed transversely within the rod array, it is possible to obtain an accurate estimate of the mixing coefficient of a subchannel by considering only the tracer concentrations in contiguous subchannels. Referring to Figure A3.2, if i is the injection subchannel, then the crossflow in gap g_{ij} may be determined by considering axial changes in the tracer flow rates in

subchannels i, j, k and l. The change in tracer flow in subchannel j per change in axial position $\Delta(C_jW_j)/\Delta Z$ is the crossflow rate in gap g_{ij} times the average difference in concentration between i and j over the distance ΔZ, less the amount of tracer transferred to subchannels k and l from j over the distance ΔZ. As was noted earlier, changes in the tracer flow rate of subchannels contiguous to k and l (other than j) are third order effects and may be neglected. That is, assuming fully developed flow,

$$\frac{\Delta C_jW_j}{\Delta Z} = w_{ij}(\overline{C}_i - \overline{C}_j) - \Delta C_kW_k - \Delta C_lW_l \ . \qquad \text{(Eq. A3.4)}$$

This equation may be rewritten in finite difference form as:

$$w_{ij} \cong \frac{2\sum_{m=j}^{l} W_m(C_{m,Z'} - C_{m,Z})}{(Z' - Z)\left[(C_{i,Z'} + C_{i,Z}) - (C_{j,Z'} + C_{j,Z})\right]} \qquad \text{(Eq. A3.5)}$$

In the experimental rod array with tracer injection into only one subchannel, the mixing process transfers fluid with high concentration levels from the injection subchannel to the contiguous receiving subchannel. In turn, the injection subchannel concentration is reduced because fluid leaving the injection subchannel is replaced with fluid from an adjacent subchannel with a lower salt

concentration. Therefore, the net transfer of tracer is determined by the difference in salt concentrations between the subchannels of interest at the axial position of interest. For the purposes of this treatment, the average tracer concentration between the axial data points taken was used to evaluate the mixing coefficient.

With the above and the assumption that the tracer is uniformly distributed with the subchannel of interest, the transverse flow per unit length between subchannels i and j - W_{ij} - across the gap g_{ij} may be determined by

$$w_{ij} \cong \frac{2 \sum_{m=j}^{l} W_m (C_{m,z'} - C_{m,z})}{\Delta Z \left[(C_{i,z'} + C_{i,z}) - (C_{j,z'} + C_{j,z}) \right]} \quad \text{(Eq.A3.6)},$$

where m=j accounts the change in the tracer concentration in subchannel j and m=1 and m=k account for tracer removal from subchannel j. The combined effects of the change and removal of tracer from subchannel j is approximately equal to the tracer transferred from subchannel i to j between axial positions Z and Z', (ΔZ). Recalling the definition of the dimensionless mixing coefficient beta:

$$\beta_{ij} = \frac{w_{ij}}{\bar{G}_{ij} g_{ij}} \quad \text{(Eq. A3.2)}$$

where $$\overline{G}_{ij} = \frac{G_i + G_j}{2} \qquad \text{(Eq. A3.2)}$$

Substituting Eq. A3.1 into Eq. A3.6, one obtains an estimate of beta using the salt tracer experiment data:

$$\beta_{ij} \simeq \frac{4 \sum_{m+j}^{1} W_m(C_{m,\,z'} - C_{m,z})}{(G_i + G_j)g_{ij}\Delta Z\left[(C_{i,z'} + C_{i,z}) - (C_{j,z'} + C_{j,z})\right]} \cdot$$

(Eq. A3.7)

Using the equation developed for the dimensionless mixing coefficient β_{ij} (Eq. A3.7), an expression for the mixing Stanton number M_{ij} may be easily obtained recalling the relationship between M_{ij} and β_{ij}:

$$M_{ij} = \frac{\beta_{ij}\overline{G}}{G_i} = \frac{ij}{G_i g_{ij}} \qquad \text{(Eq. A3.3)}$$

thus,

$$M_{ij} = \frac{2 \sum_{m=j}^{1} W_m(C_{m,z'} - C_{m,z})}{(Z' - Z)G_i g_{ij}\left[(C_{i,z'} + C_{i,z}) - (C_{j,z'} + C_{j,z})\right]}$$

(Eq. A3.8)

From Figure A3.2, it may be seen that three distinct gap types were involved in coolant mixing in the interior and peripheral subchannel injection experiments discussed in Chapter 5, i.e., (A) interior-to-interior subchannel mixing, β_{11}, (B) peripheral-to-interior subchannel mixing, β_{21}, and (C) perpheral-to-peripheral subchannel mixing. The specific subchannels used to determine the various mixing coefficients listed above (β_{ij}) have been summarized in Table A3.2.

Table A3.2

SUBCHANNEL DATA USED TO DETERMINE THE MIXING COEFFICIENT USING EQ. A3.7

Gap Type	β_{ij}	i	j	k	l	Gap (in.)
INTERIOR INJECTION						
1,1	1,2	1	2	3	10	0.100
1,1	1,6	1	6	5	22	0.100
1,1	1,7	1	7	8	24	0.100
1,1	2,3	2	3	4	13	0.100
1,1	2,10	2	10	9	11	0.100
1,1	6,5	6	5	4	19	0.100
1,1	6,22	6	22	21	23	0.100
1,1	7,8	7	8	9	27	0.100
1,1	7,24	7	24	23	25	0.100
PERIPHERAL INJECTION						
2,1	48,31	48	31	30	32	0.100
2,2	48,47	48	47	29	46	0.065
2,2	48,49	48	49	33	50	0.065
1,1	31,30	31	30	9	29	0.100
1,1	31,32	31	32	11	33	0.100
2,1	47,29	47	29	28	30	0.100
2,3	47,46	47	46	45	--	0.065
2,1	49,33	49	33	32	34	0.100
2,3	49,50	49	50	51	--	0.065

APPENDIX 4

EQUIPMENT LIST

Hydraulic Equipment:

Main Flow Meter: Fischer Porter Co., Precision Bore Flowrator, Model 10A3567A, SN 6610A4743B1, Tube No. FP-2-27-6-10/83, Float T602GNSWGT-98, 0-37 GPM Water.

Main Flow Meter: Fischer Porter Co., Precision Bore Flowrator, Model 10A3563A, SN 6612A408681, Tube No. FP 1-1/2-27-G-10/83, Float No. T6-1-1/2-GNSWG 9-86, 0-20 GPM Water.

Main Flow Meter: Fischer Porter Co., By-Pass Oriflowrator, Model No. B3565-7-3-G-D-BSY, SN 7404A0514A2, Oriface Plate No. 625A016U06, 0-370 GPM Water.

Injection Flow Meter: Fischer Porter Co., Precision Bore Flowrator, Tube No. 2-F-1/4-20-5/70, 0.0-0.5 lbm/min Water, Glass Float.

Injection Flow Meter: Emil Greiner Co., Catalog No. G-9148, 3/8 in. Rotameter, Glass Float, Manufactured by the Fischer Porter Co.

Motor-Pump Sets: Bell and Gossett Co., Hydro-Flow Centrifugal Pumps, Factory Numbers 436983 11W and 436984 11W, Catalog No. 2-1/2A 7AB, 1510 Type B, 20 HP @ 3450 RPM, 300 GPM @ 180 Ft. (78 PSIG) Water.

Reliance Electrical and Engineering Co., Precision Built Electric Motor, Frame 284U, From P/BP, 3 Phase, Continuous Duty, SN N611379A3 and N611379A4, 20 HP @ 3520 RPM, 208/220/440V AC, 54.8/52/26 Amps., 60Hz., Code F, 40°C Rise, Design B.

Coupler, Pump PW1Z-429 Motor PWZ-529, Disc PW-5415.

Bourdon Tube Pressure Gages: Helicoid Gage Co., Test Gage 0-60 psig; Test Gage 0-150 psig; Test Gage 30 Inches of Mercury Vacuum - 15 psig; Test Gage Accurace = ± 1/4 of 1% Full Scale Reading.

Bellows-Type Differential Pressure Gages: ITT Barton, 0-50 Inches of Water, SN 227-57463; 0-400 Inches of Water, SN 227-57467.

ELECTRICAL EQUIPMENT:

Sweep Generators (Oscillator): Wavetek, Model 134, SN 011552.

Digital Voltmeter: Keithley Instruments, Model 160, SN 28265.

Teletype: Teletype Corp., Model 33TC.

Platinizing Kit: Yellow Springs Instrument Co., Model YSI 3139.

Transformer: Triad Division of Litton Industries, TY - 38X Interstage Transformer, 3 kiloohms, CT. 4 ma to 1K. ohm CT. 200 MW.; TY - 36X Transistor Interstage Transformer, 2K, ohm 2 ma to 1500 ohms CT. 200 MW.

CHEMICALS AND SOLUTIONS:

Salt Tracer, Sodium Chloride, Mallinckrodt Chemical Work, No. 7581, A.C.S. Purity

Platinizing Solution, Yellow Springs Instrument Co., YSI 3140, Description - Platinum Chloride 3% dissolved in 0.025% Lead Acetate solution.

Cell Cleaner, 100 millliliters Isopropyl Alcohol, 100 millliliters Ethyl Ether, 50 millliliters concentrated Hydrochloric Acid, and 50 millliliters distilled Water.

Large Balance Scale: Ohaus Scale Co., Model 1119, Capacity 20 Kg.

Small Balance Scale: Central Scientific Co., EPL No. 86A, Capacity 1.11 Kg.

TABLE A4.1

NOMINAL OPERATING RANGE OF THE EXPERIMENTAL EQUIPMENT

Inlet Plenum Pressure	0-90 psig
Channel Water Temperature	45-60°F
Oscillator Frequency (Nominal)	1000 Hertz
Oscillator Voltage	0.10 VAC-RMS
Injection Tank Pressure	10-100 psig
Main Flow: Laminar	40 lbm/min
Turbulent	50-250 GPM
Injection Flow:	15-300 grams/min

APPENDIX 5

PROCESSING OF THE COOLANT MIXING EXPERIMENT DATA

Once the experimental coolant mixing data had been recorded on a punched paper-tape by the automatic data collection system, it was then converted from paper-tape to punched computer cards. The mixing data card decks were verified by comparing a card listing with the original data listing typed by the teletype machine during the experiment. The edited data was then processed by the MITMIX-R code.

The MITMIX - R computer code performed the following functions:

A. generating an analytical curve fit of the conductance cell probe calibration data,

B. plotting the calibration data and the cell calibration curves,

C. converting the electric signal value to a salt solution concentration via the calibration curves,

D. performing the tracer mass balance calculations to verify correct operation of the experiment,

E. plotting the experimental results in terms of subchannel salt concentrations versus axial position,

F. calculating the dimensionless mixing coefficient

from the experimental data (see Appendix 3), and

G. calculating, if necessary, an analytical flow split for the rod bundle using the RUFHYD model discussed in Chapter 3.

The MITMIX-R code recorded instructions for producing the various computer generated plots onto a magnetic tape; the magnetic tape was then transferred to a Calcomp plotting device to physically generate the plots.

Additional details regarding the functions of the MITMIX-R code may be obtained from a listing available from the author. Details regarding the RUFHYD analytical method for calculating the analytical flow split are given in section 3.2; details regarding the calculation of the salt tracer mass balance for the coolant mixing experiments may be found in section 4.3.5.

Using a static calibration procedure, the salt solution concentration in the subchannels during the mixing experiments could be related to a probe electrical signal recorded by the data collection instrumentation. An analytical curve fit of the calibration data provided a calibration curve for use in translating the recorded experimental data into subchannel salt concentrations. A typical plot of calibration data is shown in Figure A5.1; the line through the data points in this figure was drawn using the analytical curve fit.

FIGURE A5.1

TYPICAL CALIBRATION DATA AND CURVE FIT

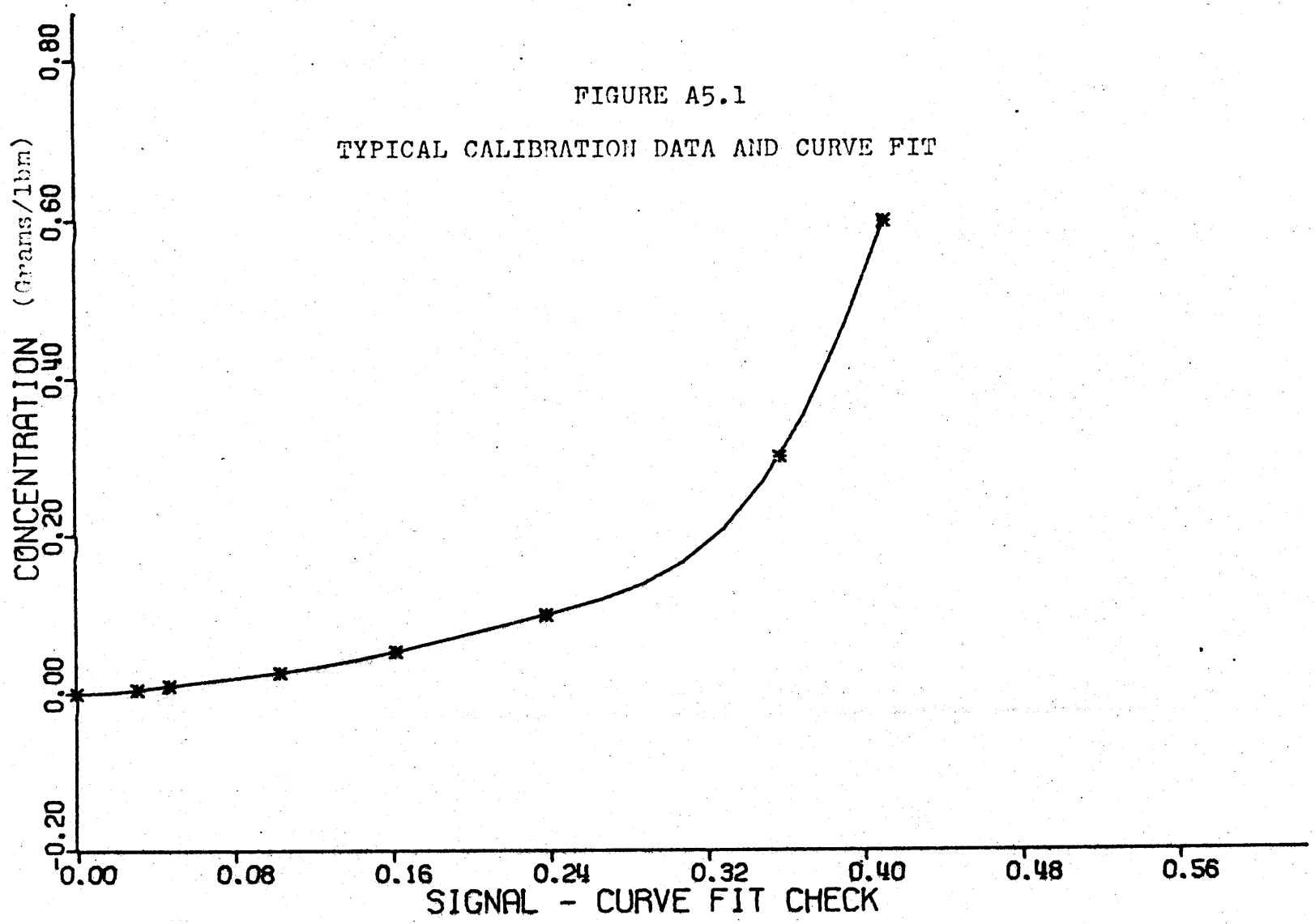

APPENDIX 6

OBSERVATIONS OF ROD BUNDLE - SPACER INTERACTION FORCES

The design of the rod bundle test section has been discussed earlier in Chapter IV; recall that the final assembly of the rod array was accomplished by sliding the rods into the assembled flow channel which contained the eight spacer grid assemblies. During the process of changing from the smooth rod array to the partially roughened rod array, the forces required to slide the rods in the assembled test section were monitored.

In general, it was found that the rod would move freely with the test section in the horizontal position with axial forces in the range of 5 - 12 pounds. In the vertical position, it was found that rods would rise at bundle flow rates between 200 and 250 GPM. If one uses the total bundle pressure drop ΔP_b (see Figure 5.40) and accounts for gravity and bouyancy effects, the lifting force on the rods may be shown to be

$$F = \Delta P_b A_r - (\rho_b - \rho_w) A_r L_r \quad . \qquad \text{(Eq. A6.1)}$$

With Eq. A6.1, the rod lifting force is found to be in the range of 3 - 4 pounds with the bundle vertical and subjected to a water flow. The higher rod sliding forces observed with the rod bundle in the horizontal position are believed to be due to the weight of the rods, about 1.5 pounds,

bearing on the grid spacers and due to the absence of flow induced rod vibrations. The rod sliding forces were approximately independent of both wetness and rod surface roughening. The above rod sliding forces are believed to be typical of a well fabricated grid spacer assembly mounted in a well fabricated hexagonal fuel element duct.

However, it is important to note that a few of the rods in the experimental test section required considerably more than 20 pounds force in order to achieve axial motion. Several rods required forces in the range 12 - 20 pounds to achieve axial motion. Most of the rods requiring forces greater than 12 pounds to move were located in the outer row; further, the rods requiring abnormally high forces were the corner rods. Because the rods in the outer rod row were the hardest to move, it was felt that the abnormally high forces required for axial rod motion were caused primarily by the fabrication of the grid spacer. The grid spacer, hexagonal cells for the outer row of rods were apparently distorted when the grid spacer was welded to the hexagonal, flutted shroud.

Another complication of the fabrication of the grid spacer assemblies was that the eight grids received on 6 March 1974 (the grid assemblies were fabricated by the

General Atomic Company) had outside flat-to-flat distances which varied between 2.78 and 2.84 inches. The hexagonal flow channel was designed to be 2.80 inches; thus, when the test section was assembled, some grid flat-to-flat distances were forced to conform to a 2.80 inch flat-to-flat distance.

Some of the rods were noticed as being scratched by the spacer grids during assembly of the rod bundle. The severity of scratching varied with the force required to move the rods. The scratches were estimated to be mainly of the order of a few ten-thousandths (2/10,000 - 5/10,000) of an inch deep and were never more than 0.001 inches deep. The roughened section of the partially roughened rods was visually determined to be insignificantly effected by scratches.

Appendix 7

AXIAL PROFILES OF ROD ARRAY STATIC PRESSURE

TABLE A7.1

A LIST OF ROD ARRAY AXIAL PRESSURE PROFILES

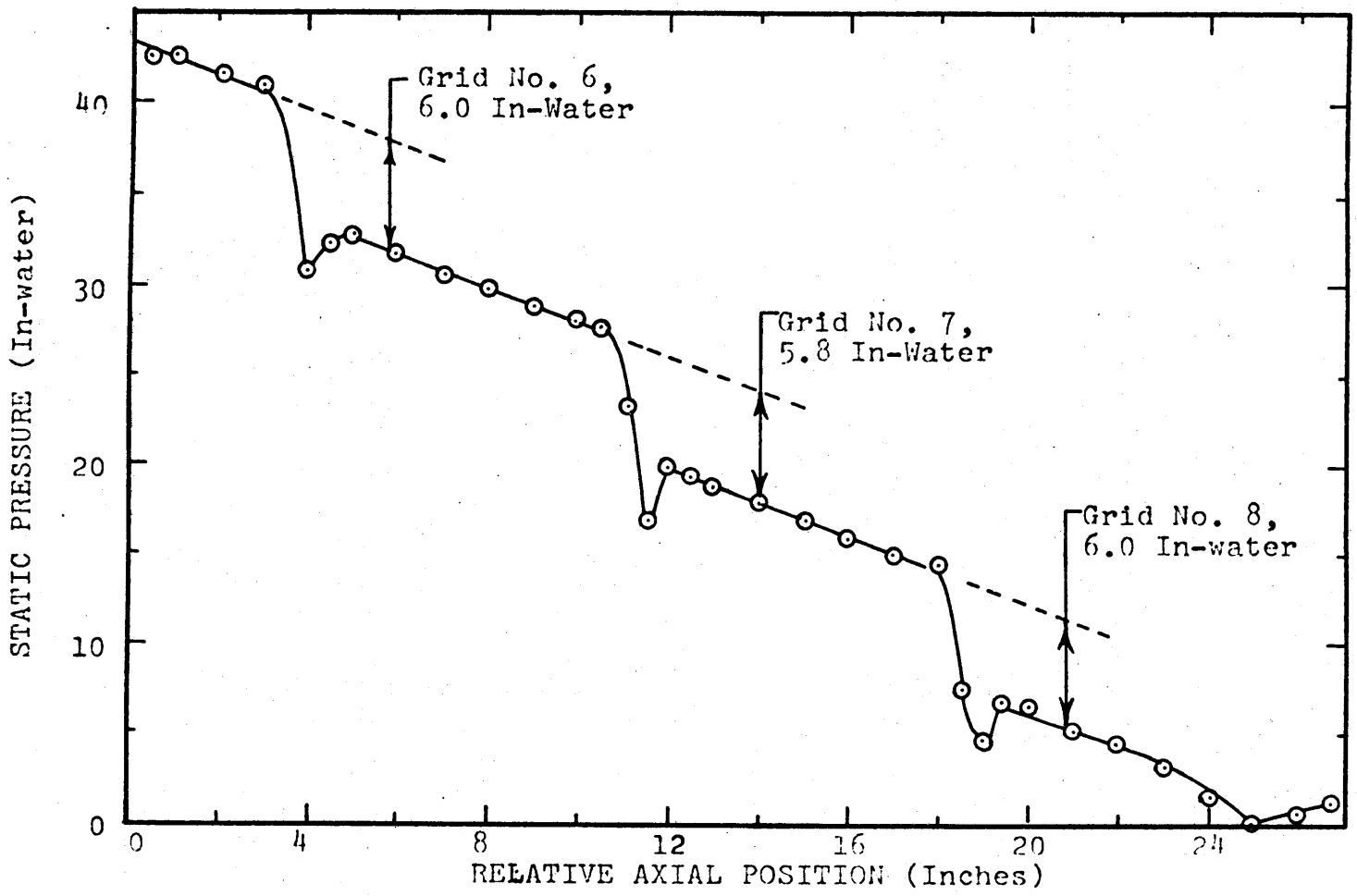

FIGURE A7.1

SMOOTH ROD ARRAY, AXIAL PRESSURE PROFILE: INTERIOR SUBCHANNEL, 50 GPM

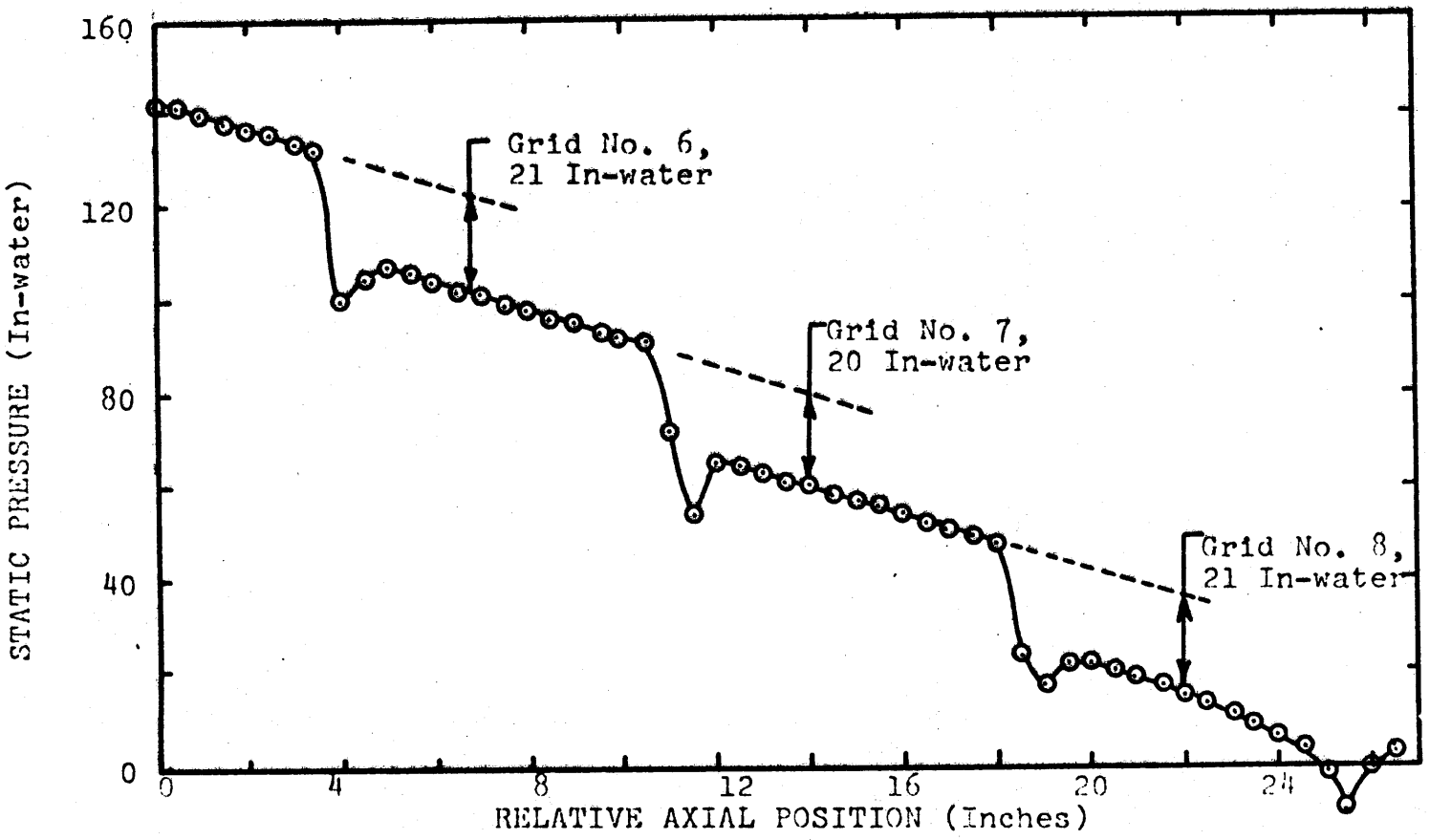

FIGURE A7.2

SMOOTH ROD ARRAY, AXIAL PRESSURE PROFILE: INTERIOR SUBCHANNEL, 100 GPM

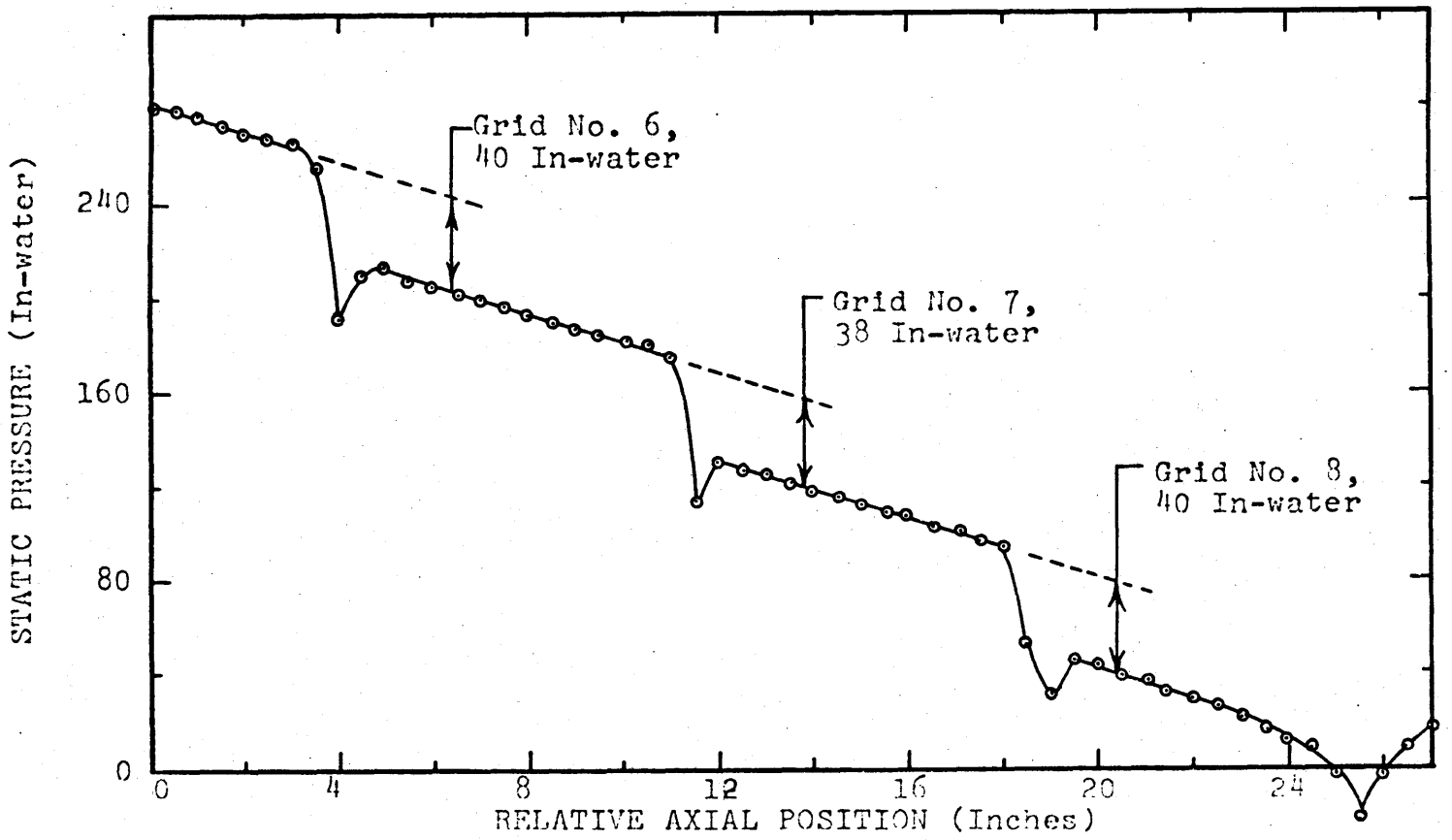

FIGURE A7.3

SMOOTH ROD ARRAY, AXIAL PRESSURE PROFILE: INTERIOR SUBCHANNEL, 150 GPM

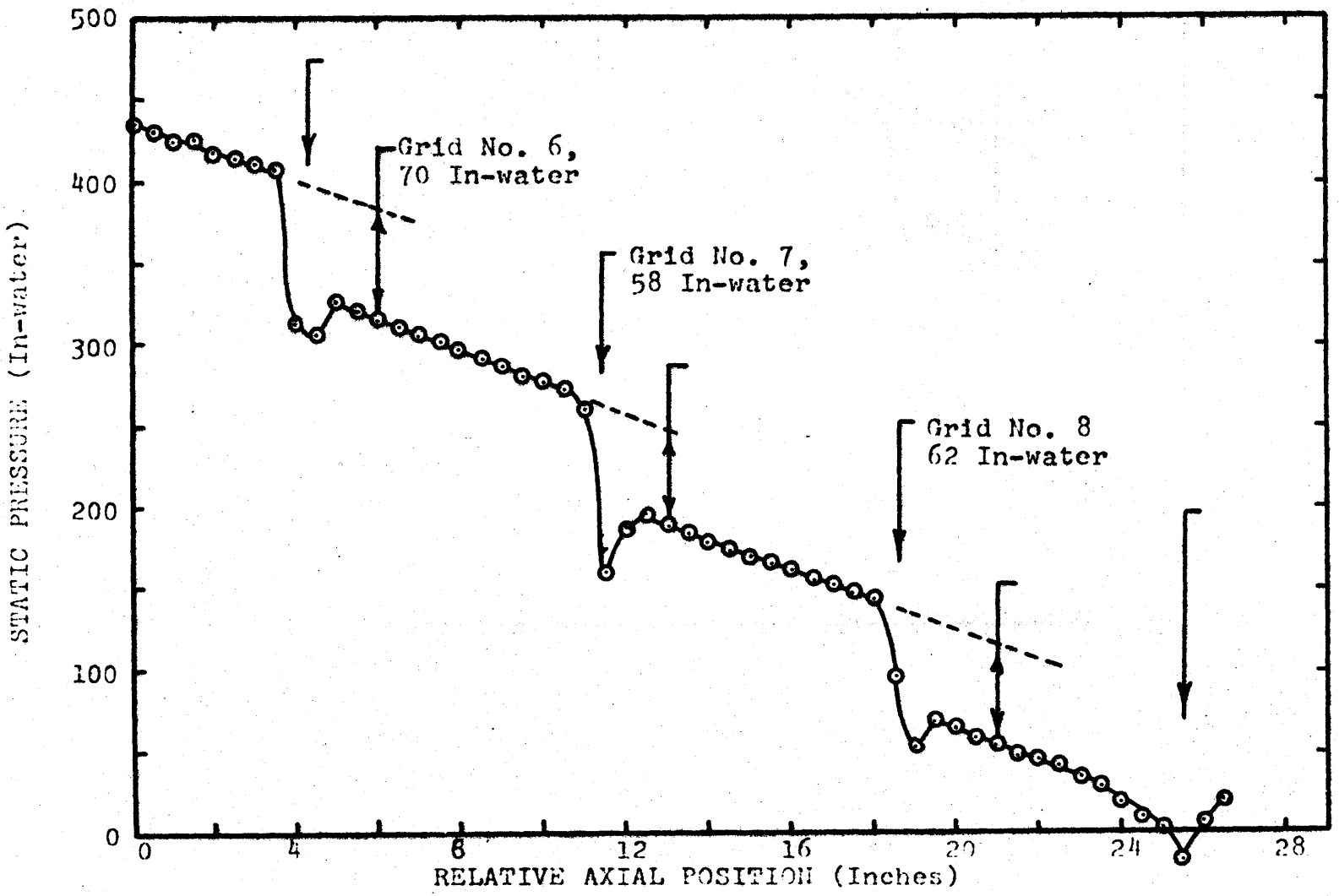
Grid No. 6,
70 In-water
Grid No. 7,
58 In-water
Grid No. 8
62 In-water
STATIC PRESSURE (In-water)
500
400
300
200
100
0
0
4
8
12
16
20
24
28
RELATIVE AXIAL POSITION (Inches)

FIGURE A7.4

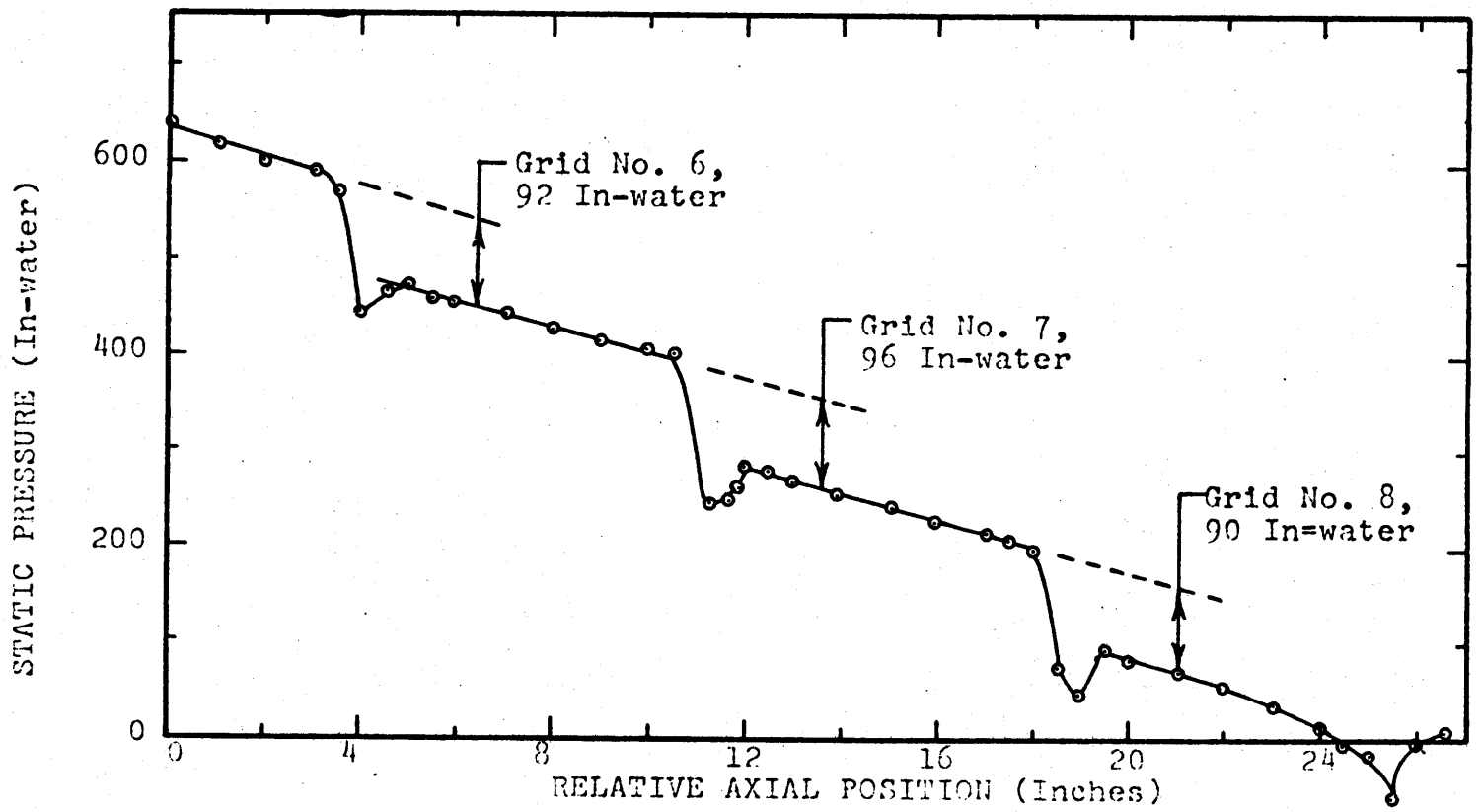

FIGURE A7.5

SMOOTH ROD ARRAY, AXIAL PRESSURE PROFILE: INTERIOR SUBCHANNEL, 250 GPM

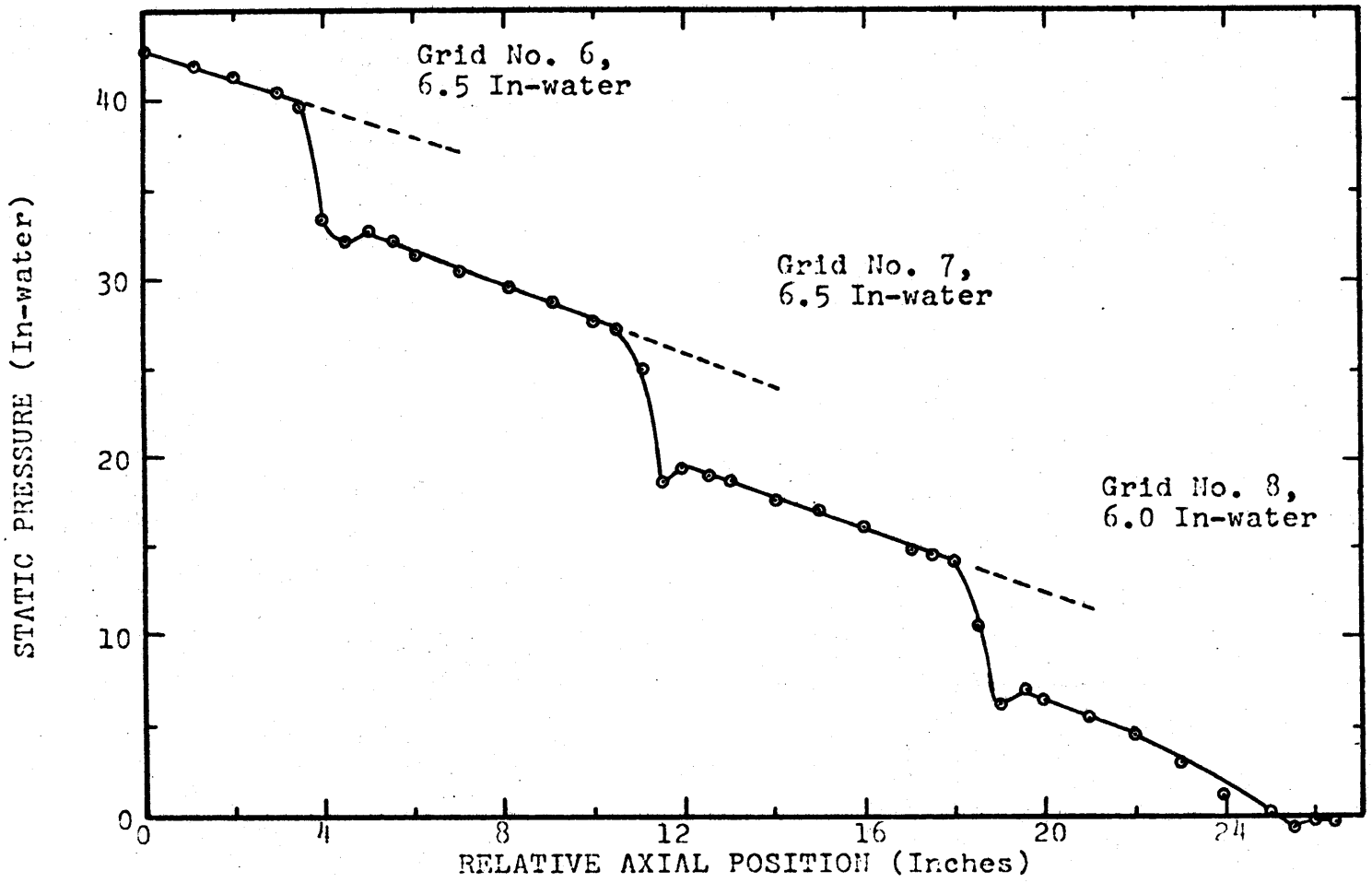

FIGURE A7.6

SMOOTH ROD ARRAY, AXIAL PRESSURE PROFILE: PERIPHERAL SUBCHANNEL, 50 GPM

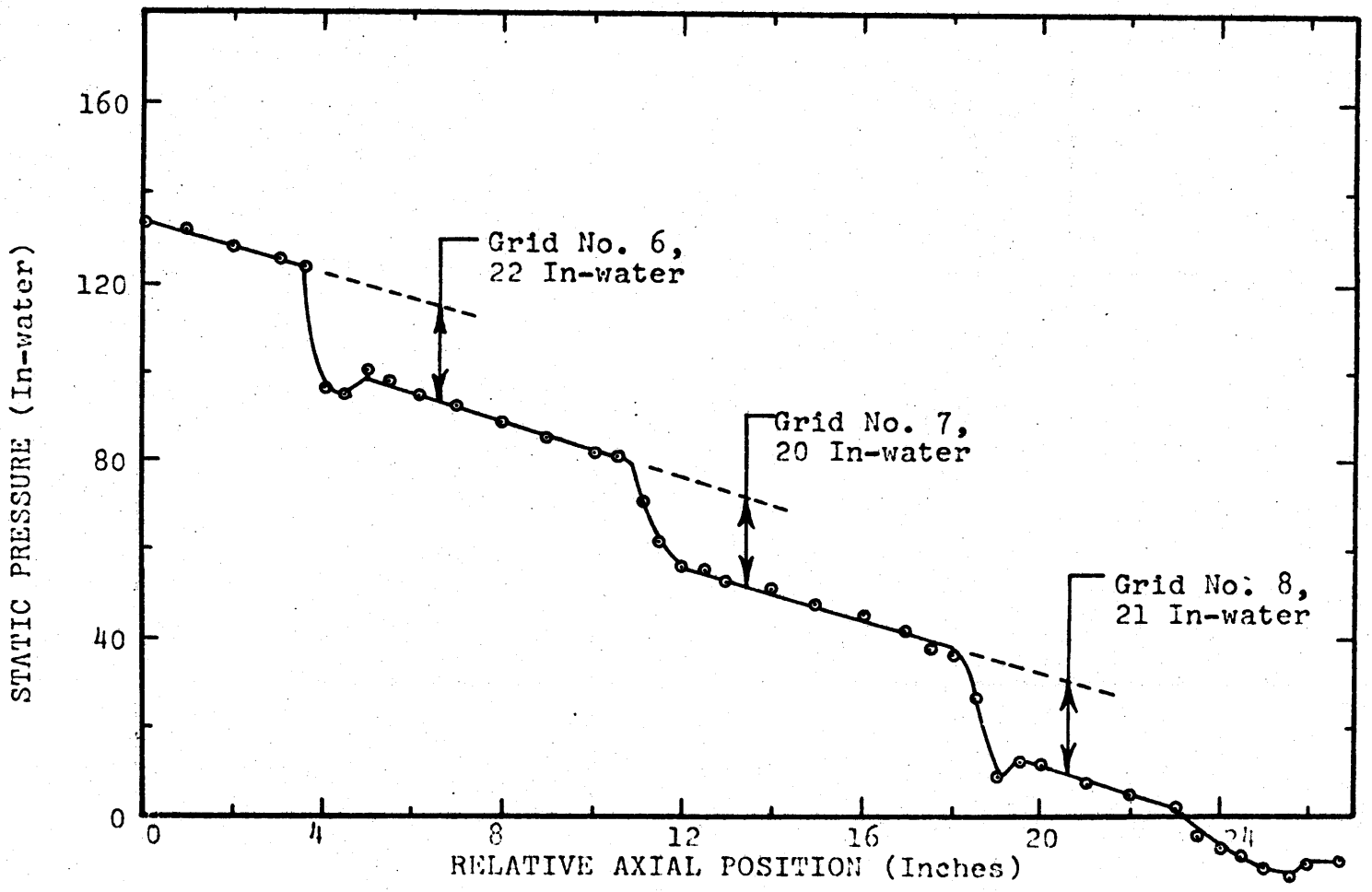

FIGURE A7.7

SMOOTH ROD ARRAY, AXIAL PRESSURE PROFILE: PERIPHERAL SUBCHANNEL, 100 GPM

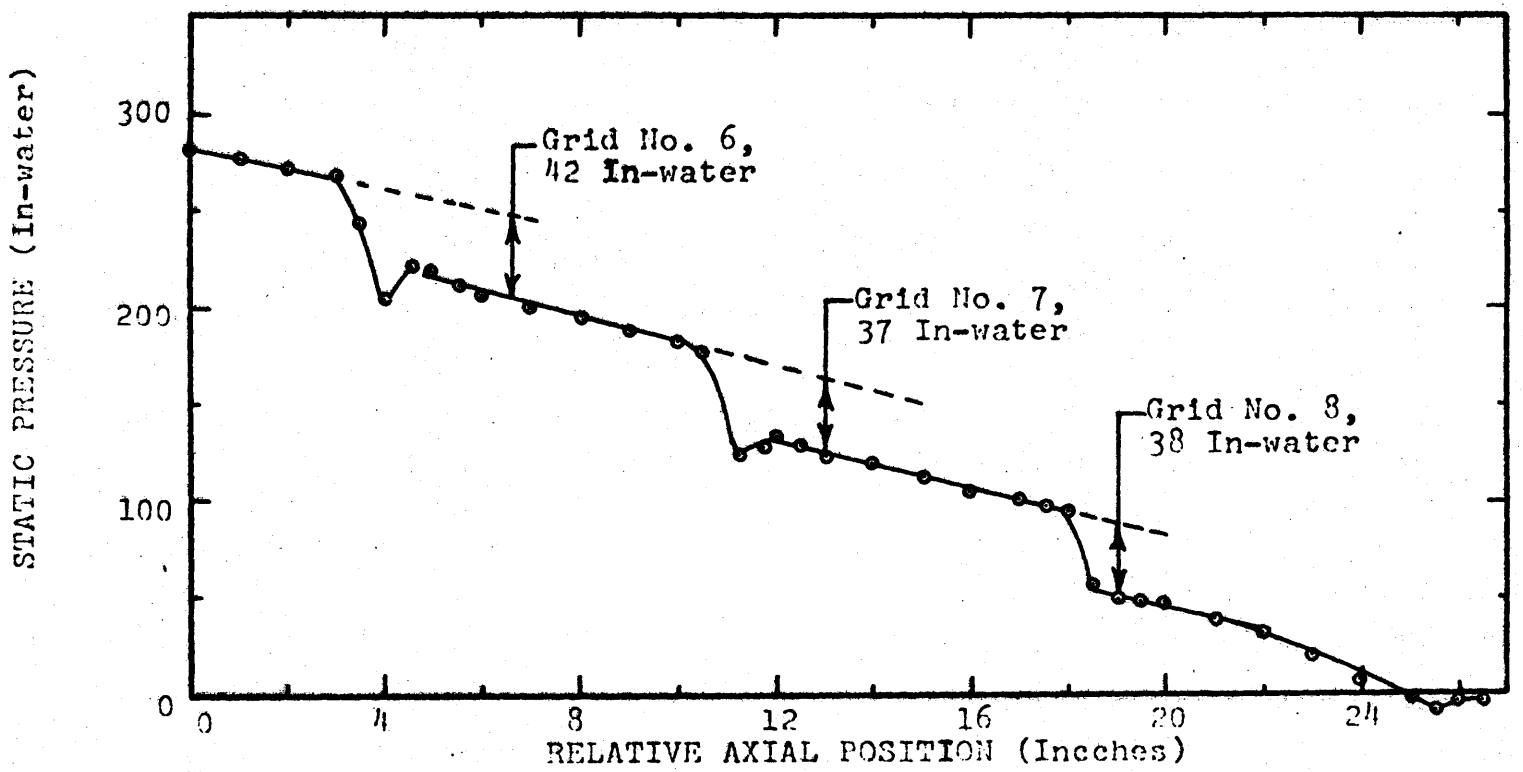

FIGURE A7.8

SMOOTH ROD ARRAY, AXIAL PRESSURE PROFILE: PERIPHERAL SUBCHANNEL, 150 GPM

FIGURE A7.9

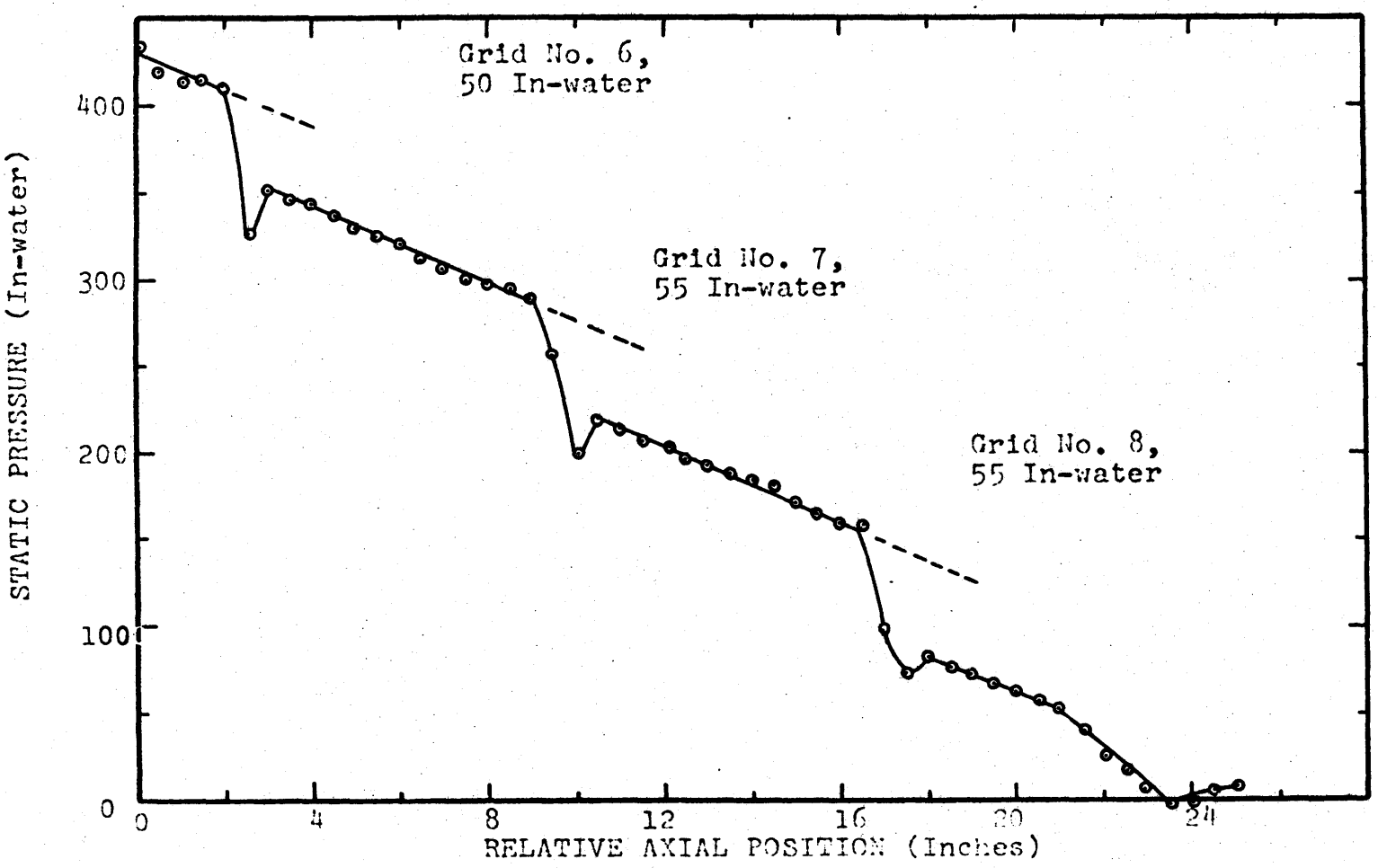

SMOOTH ROD ARRAY, AXIAL PRESSURE PROFILE; PERIPHERAL SUBCHANNEL, 200 GPM

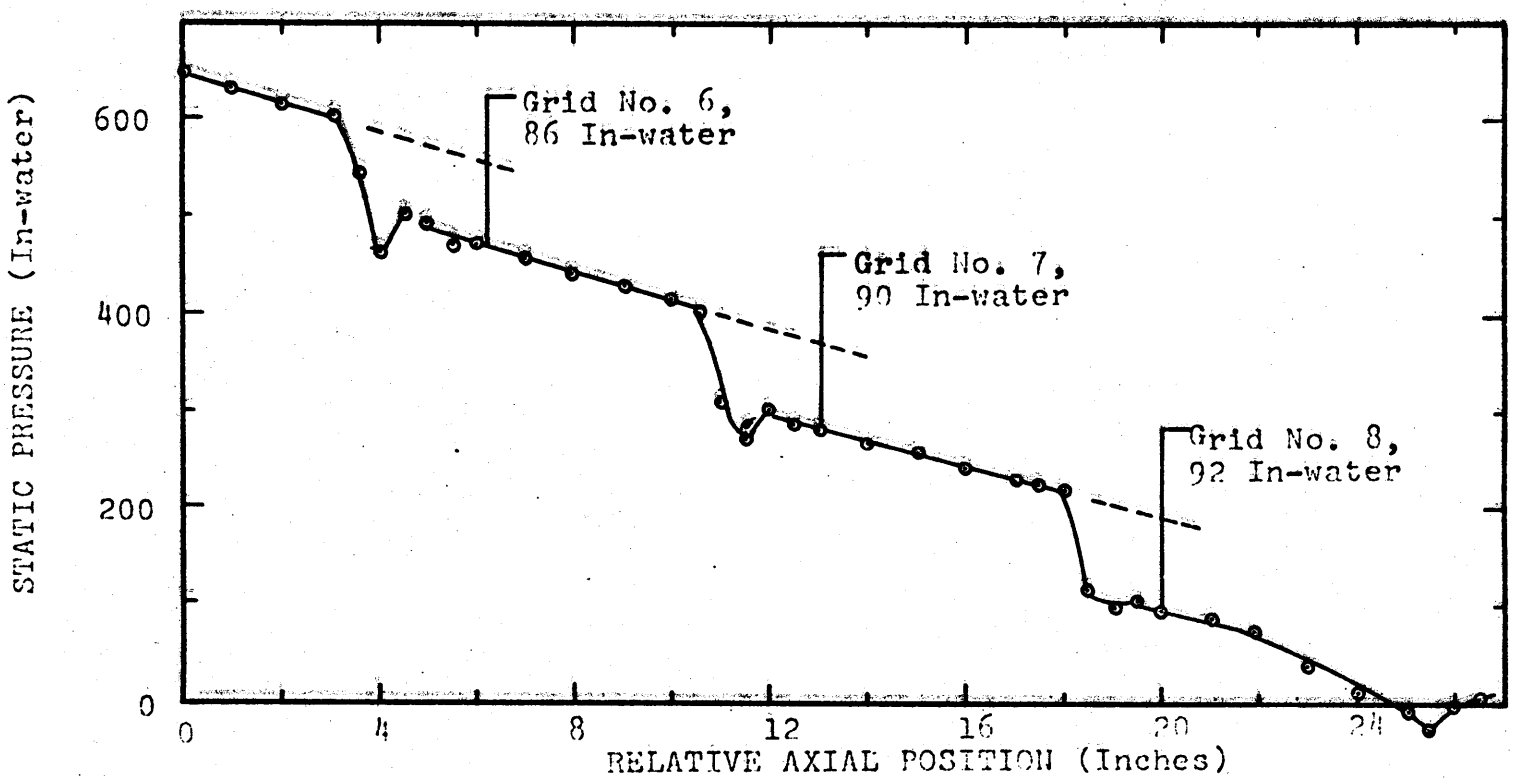

FIGURE A7.10

SMOOTH ROD ARRAY, AXIAL PRESSURE PROFILE: PERIPHERAL SUBCHANNEL, 250 GPM

FIGURE A7.11

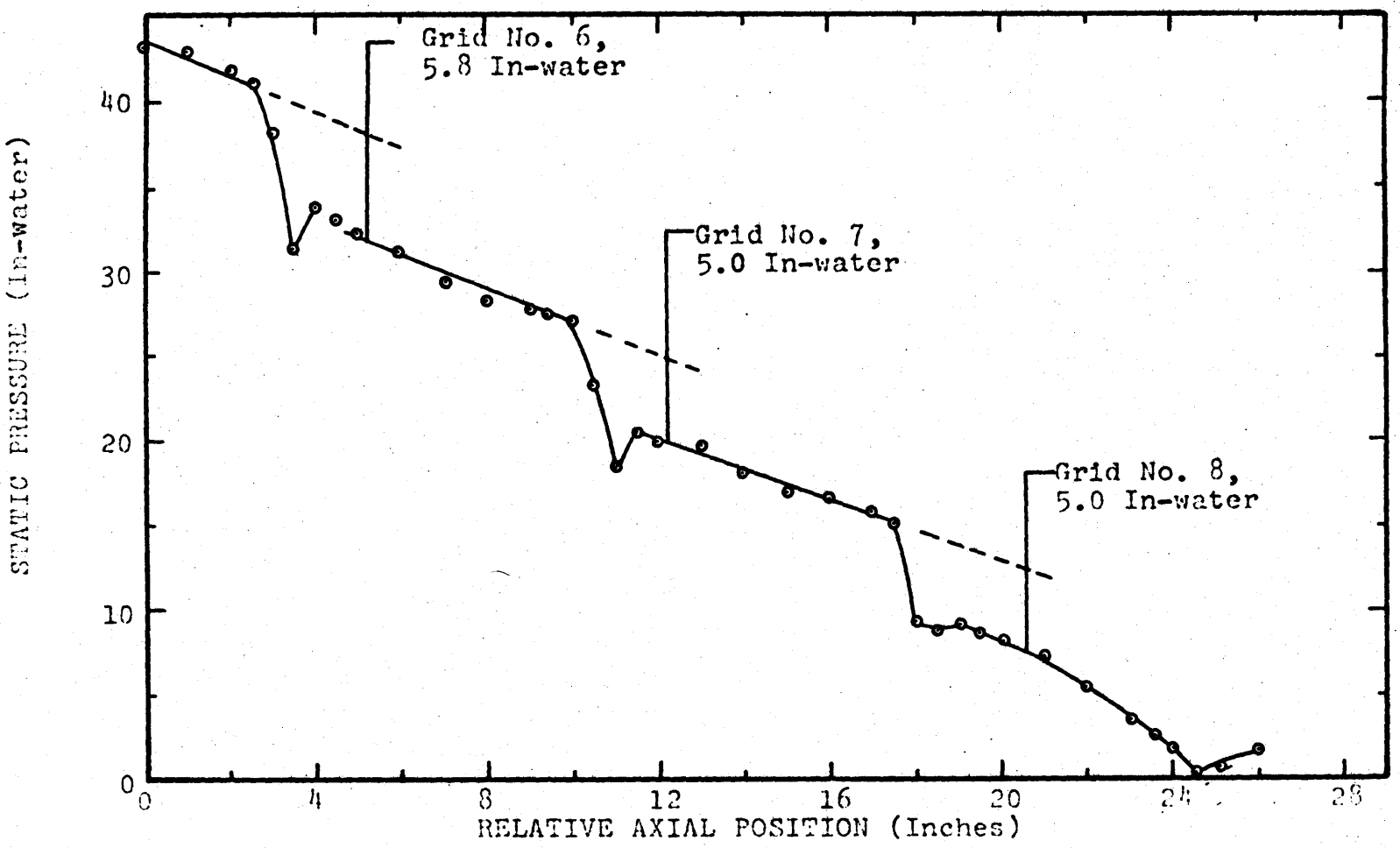

ROUGH ROD ARRAY, AXIAL PRESSURE PROFILE; INTERIOR SUBCHANNEL, 50 GPM

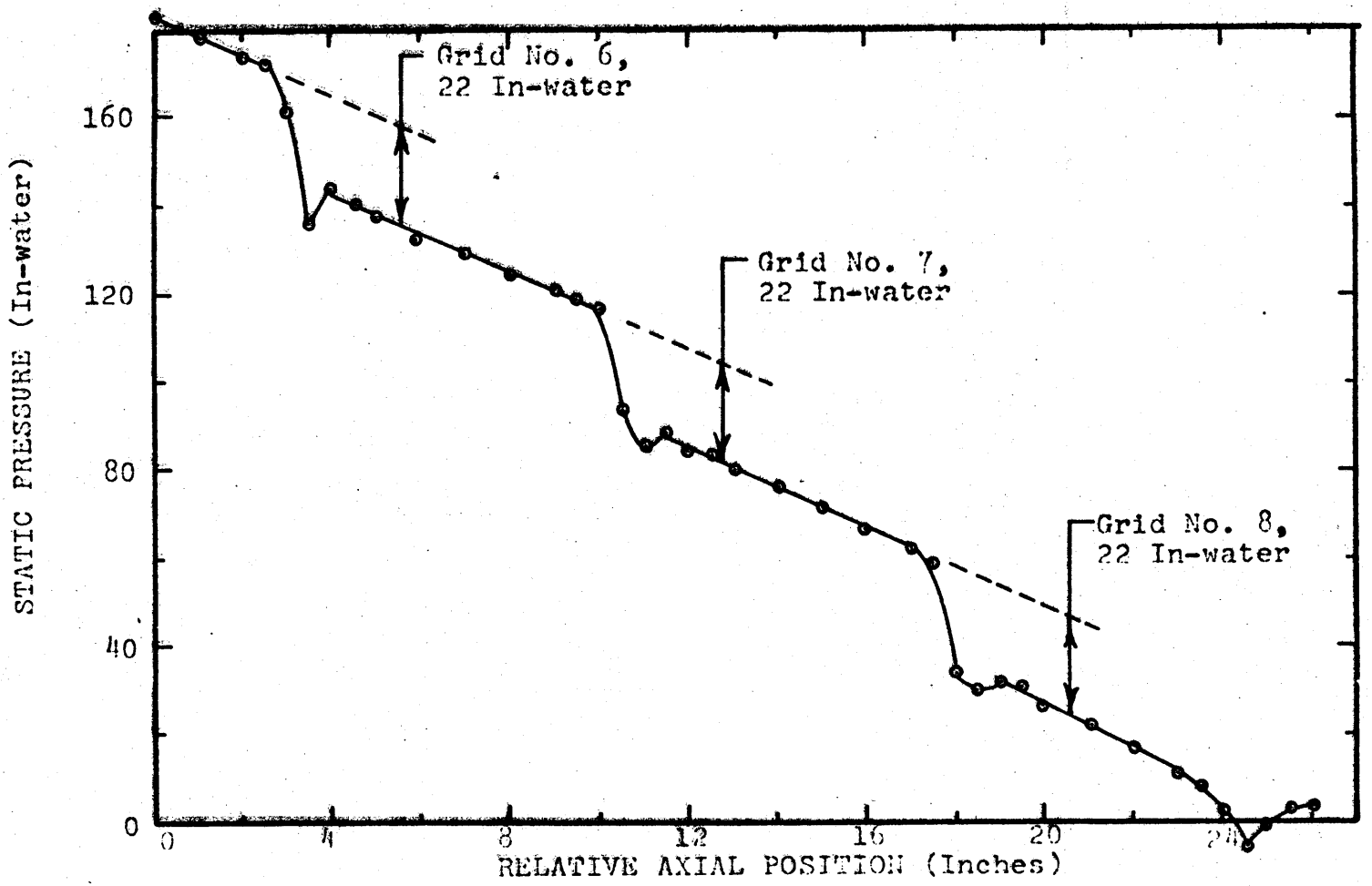

FIGURE A7.12

ROUGH ROD ARRAY, AXIAL PRESSURE PROFILE: INTERIOR SUBCHANNEL, 100 GPM

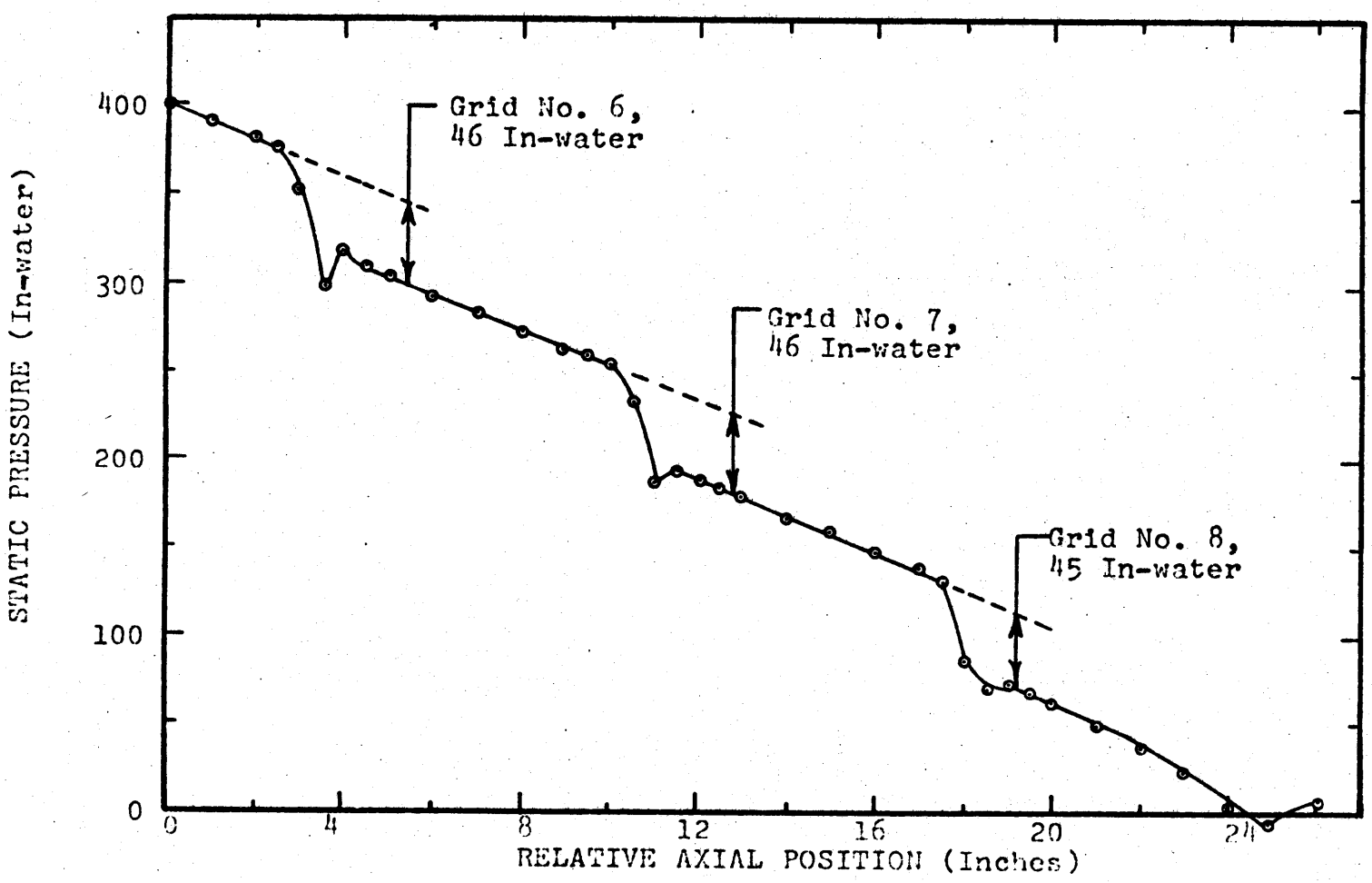

FIGURE A7.13

ROUGH ROD ARRAY, AXIAL PRESSURE PROFILE: INTERIOR SUBCHANNEL, 150 GPM

FIGURE A7.14

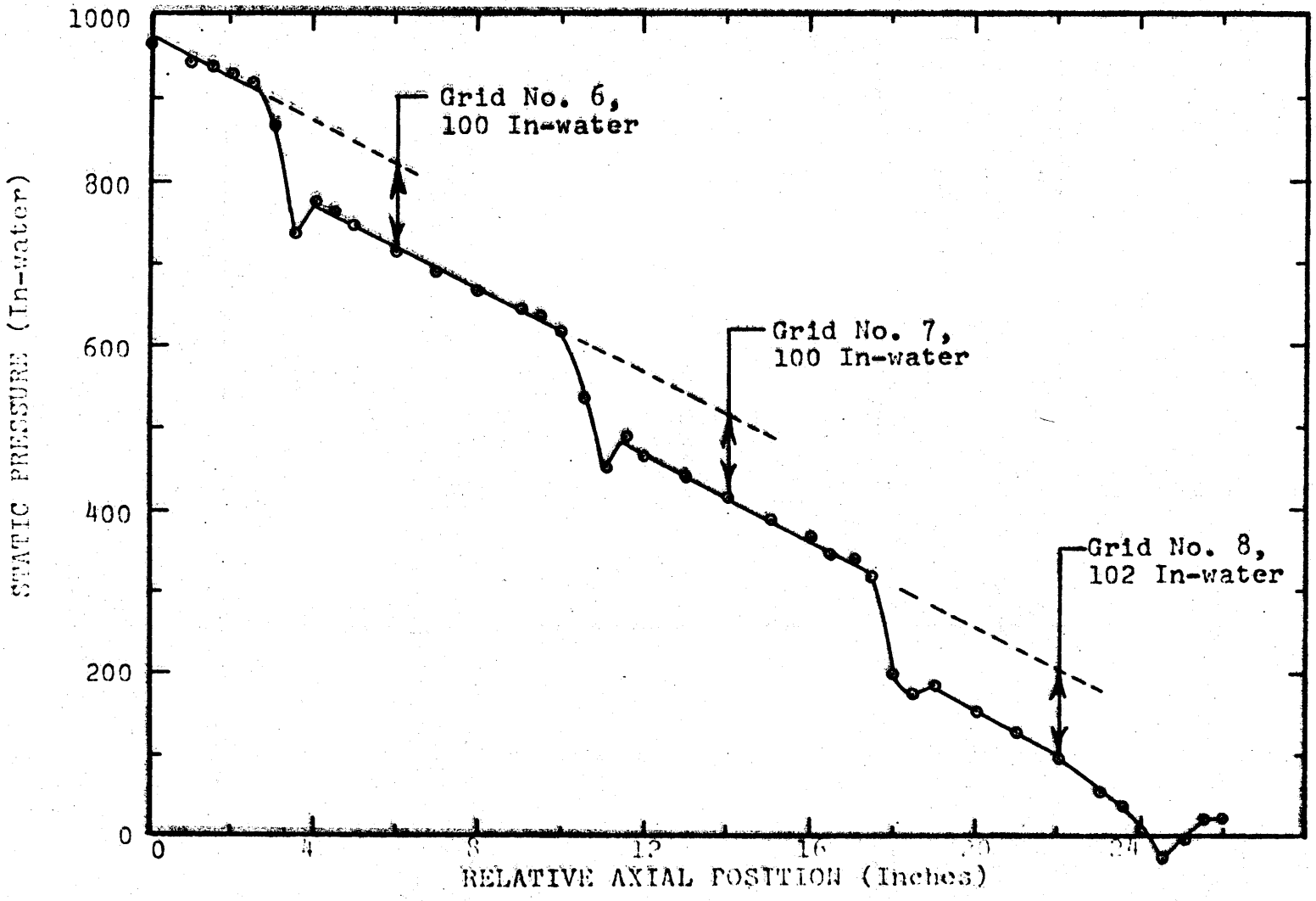

ROUGH ROD ARRAY, AXIAL PRESSURE PROFILE: INTERIOR SUBCHANNEL, 250 GPM

FIGURE A7.15

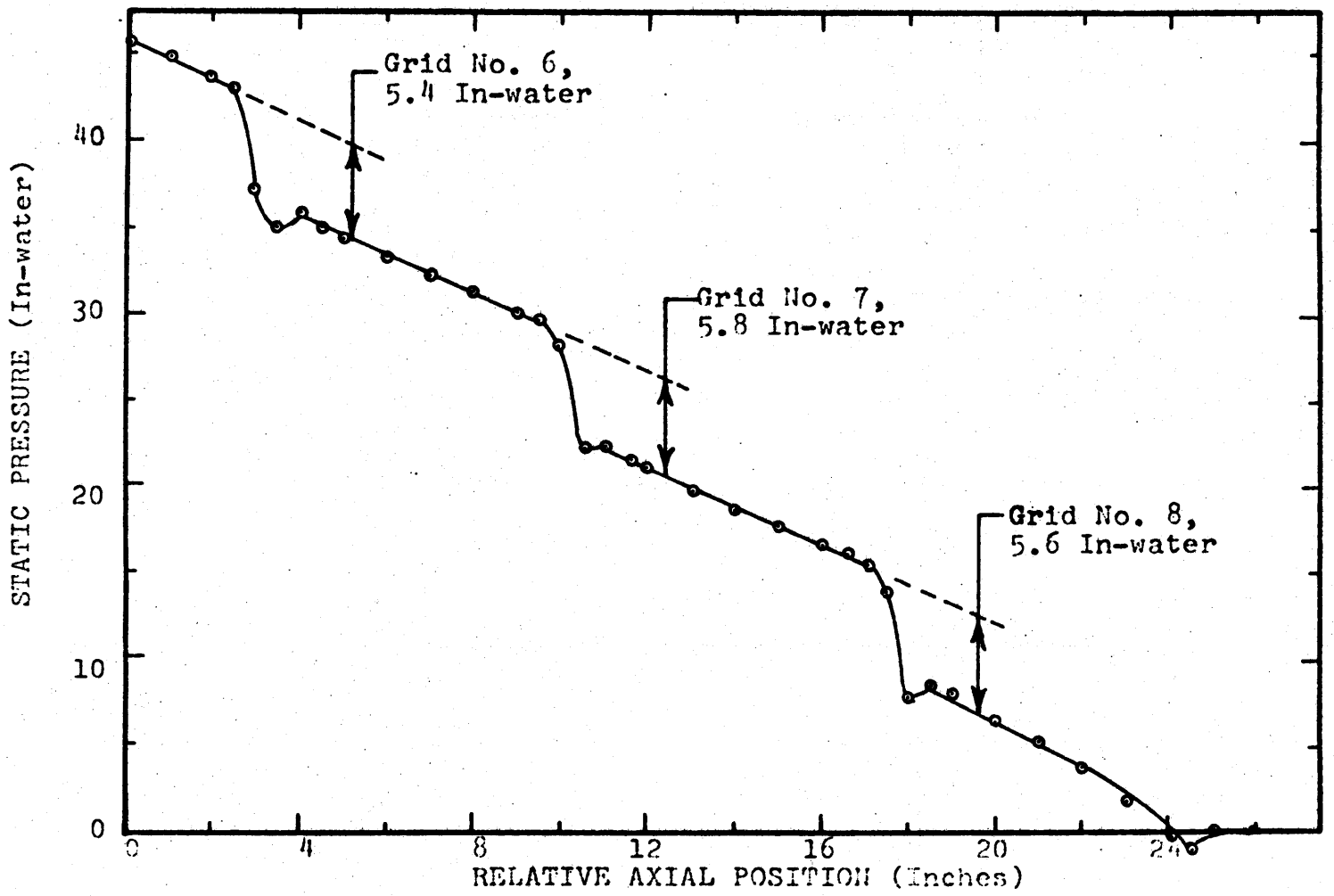

ROUGH ROD ARRAY, AXIAL PRESSURE PROFILE; PERIPHERAL SUBCHANNEL, 50 GPM

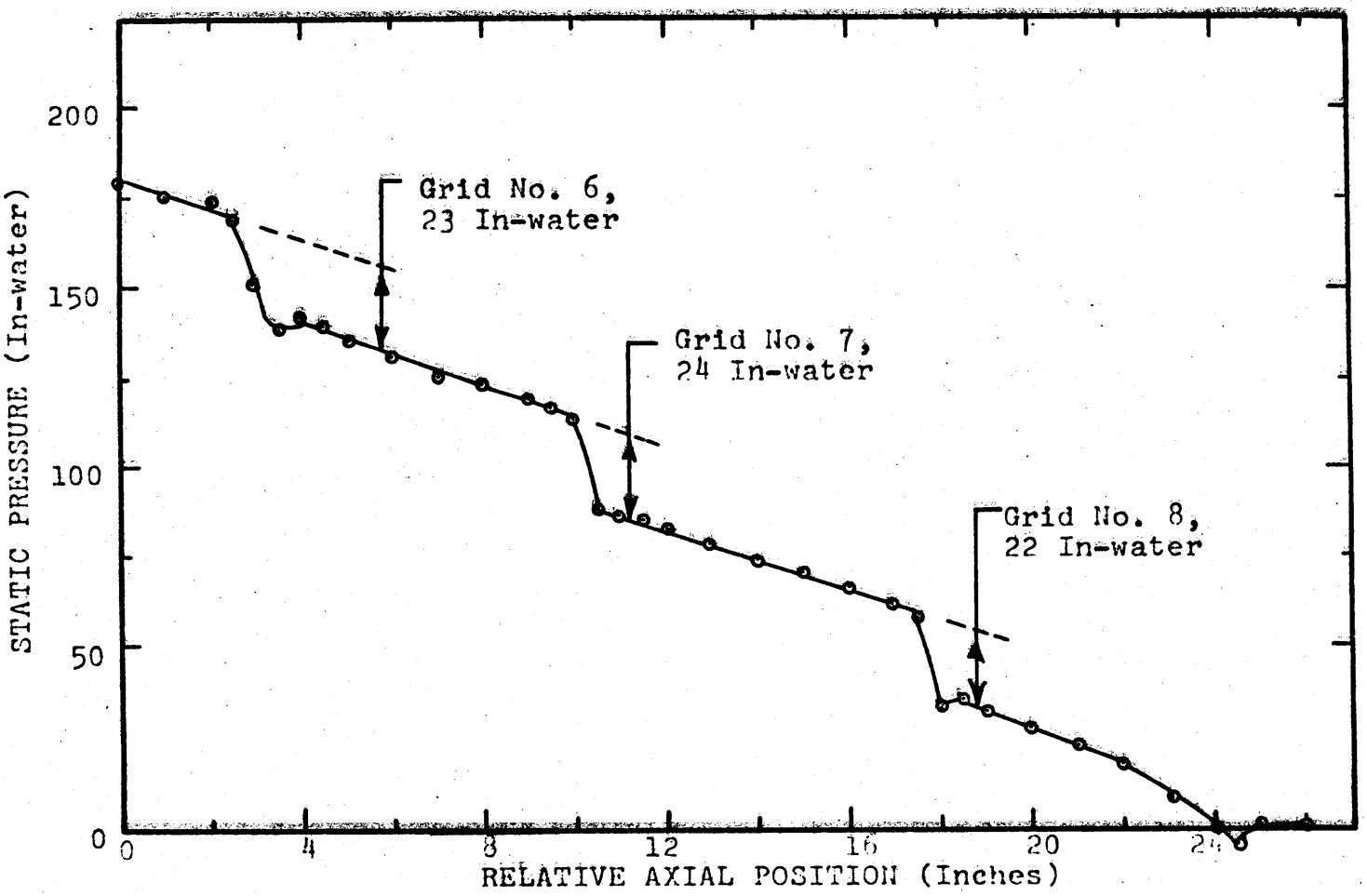

FIGURE A7.16

ROUGH ROD ARRAY, AXIAL PRESSURE PROFILE: PERIPHERAL SUBCHANNEL, 100 GPM

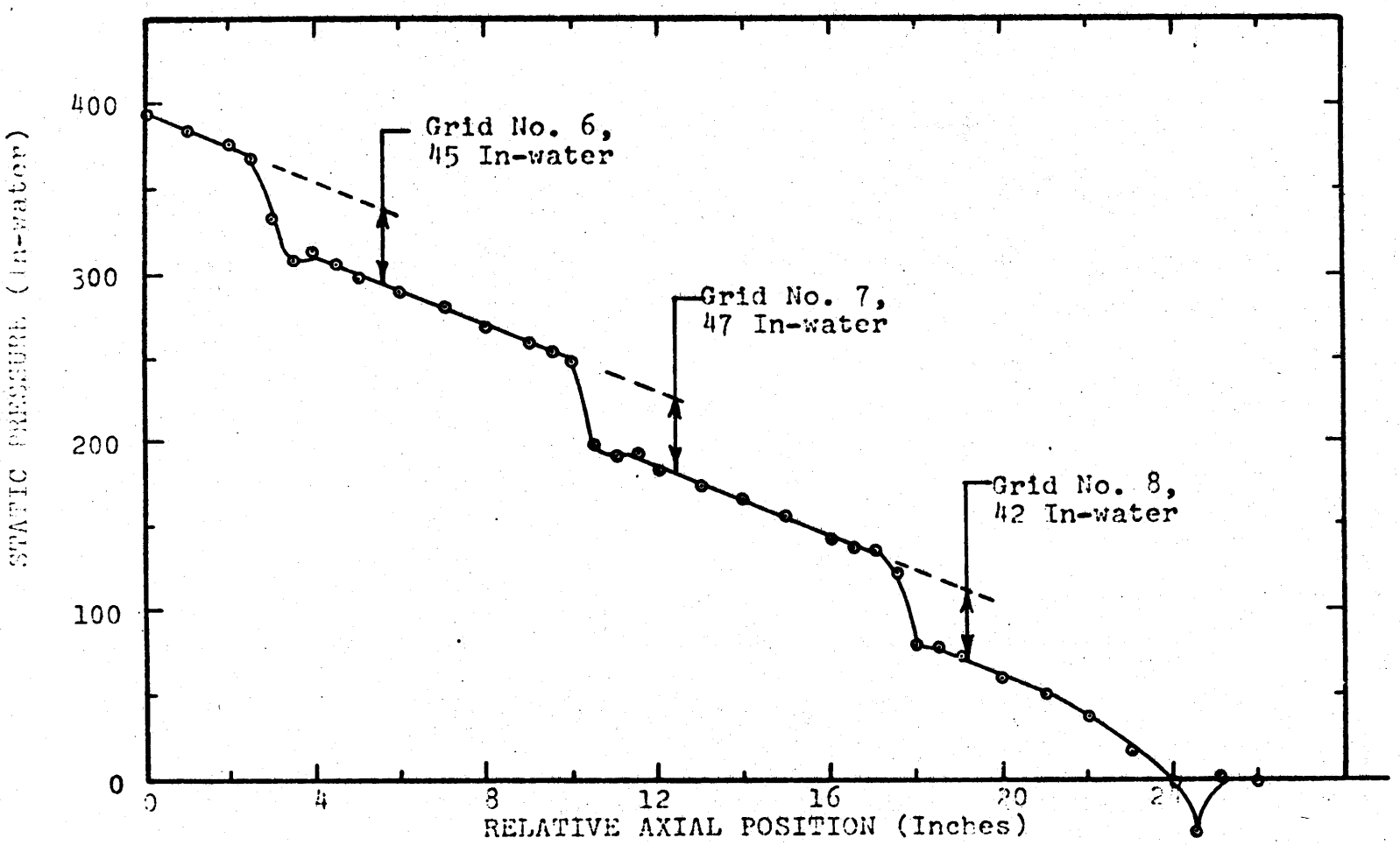

FIGURE A7.17

ROUGH ROD ARRAY, AXIAL PRESSURE PROFILE: PERIPHERAL SUBCHANNEL, 150 GPM

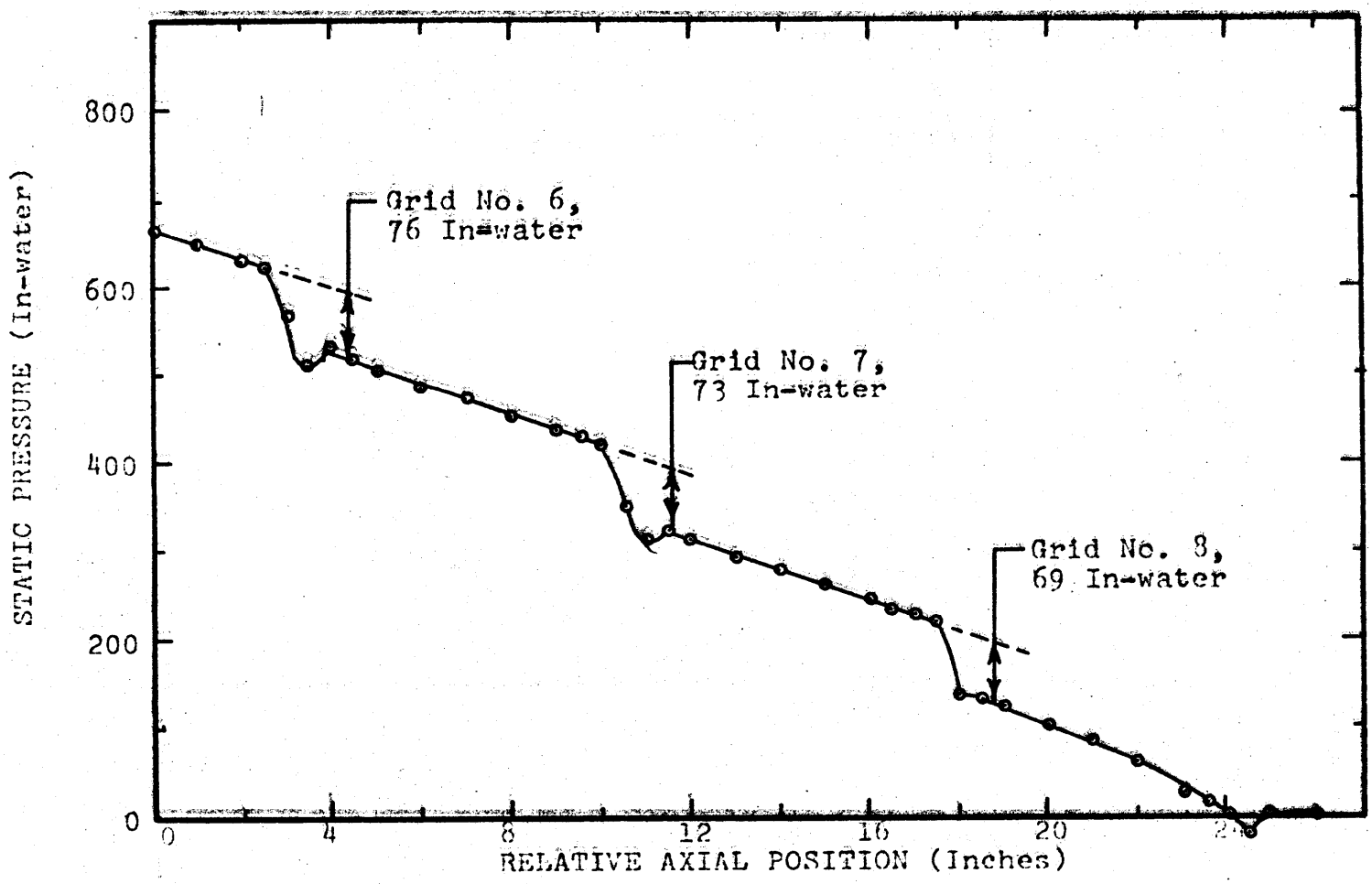

FIGURE A7.18

ROUGH ROD ARRAY, AXIAL PRESSURE PROFILE; PERIPHERAL SUBCHANNEL, 200 GPM

FIGURE A7.19

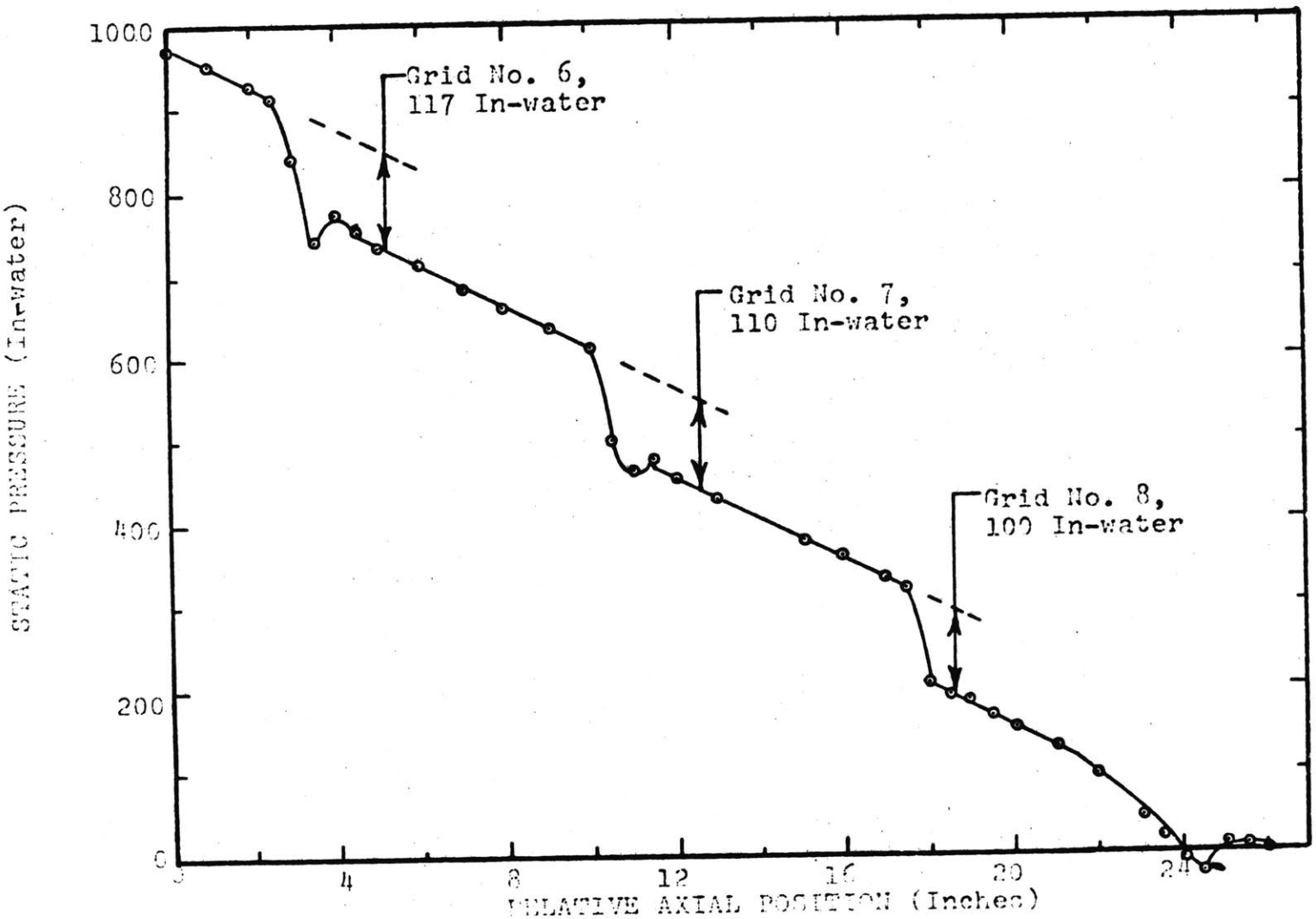

ROUGH ROD ARRAY, AXIAL PRESSURE PROFILE: PERIPHERIAL SUBCHANNEL, [illegible] GPM

APPENDIX 8

INTERCHANNEL COOLANT MIXING EXPERIMENT RESULTS

See Tables 5.11 and 5.12 for additional details regarding the coolant mixing experiments

TABLE A8.1

A LIST OF FIGURES OF INTERCHANNEL COOLANT MIXING RESULTS

----- SMOOTH ROD ARRAY, INTERIOR SUBCHANNEL INJECTION ----

TABLE A8.1 (Continued)

FIGURE A8.1

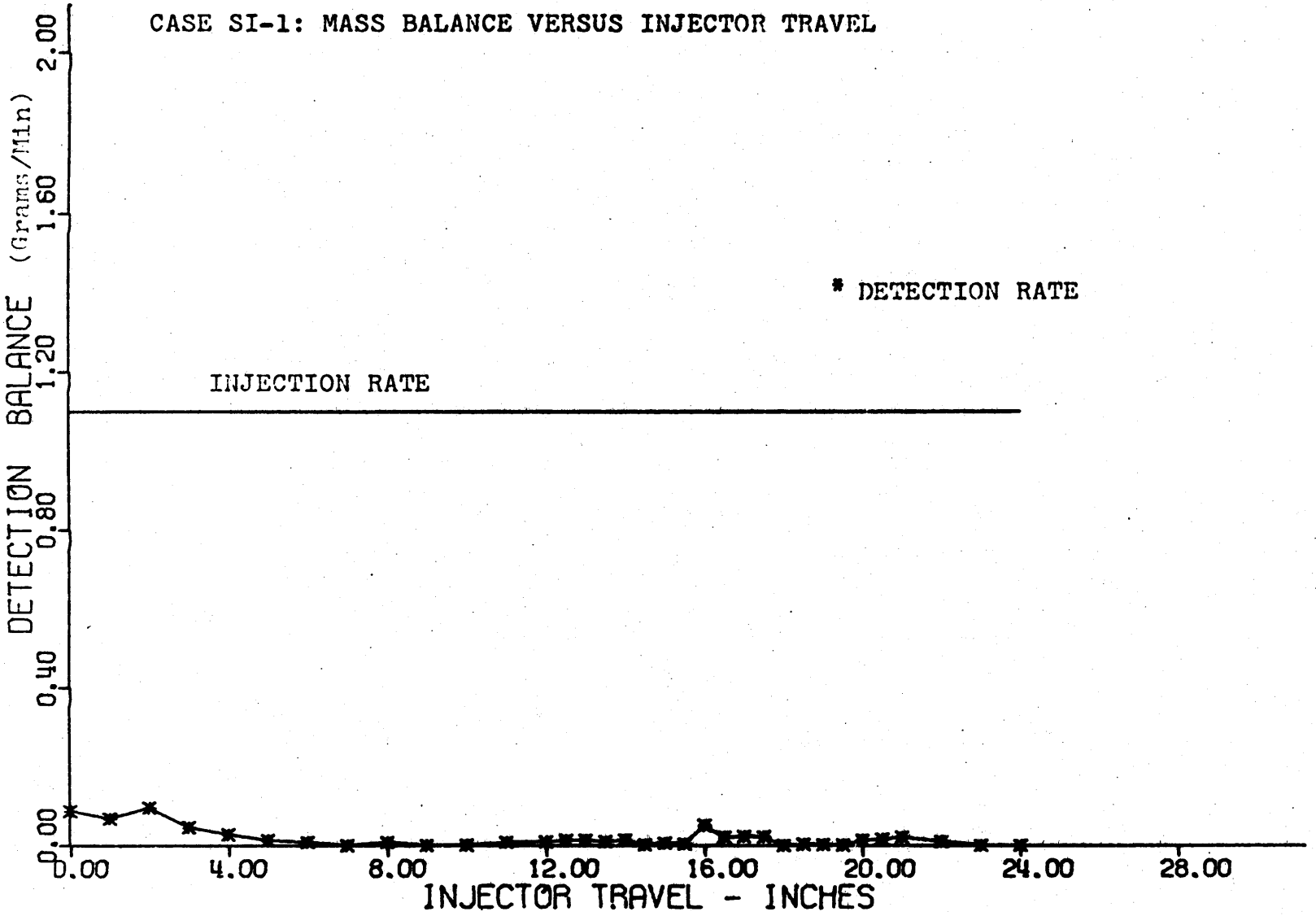
CASE SI-1: MASS BALANCE VERSUS INJECTOR TRAVEL
DETECTION BALANCE (Grams/Min)
2.00
1.60
1.20
0.80
0.40
0.00
* DETECTION RATE
INJECTION RATE
0.00
4.00
8.00
12.00
16.00
20.00
24.00
28.00
INJECTOR TRAVEL - INCHES

FIGURE A8.2

CASE SI-1: AXIAL TRACER CONCENTRATIONS, SUBCHANNELS 2, 1, 3, 4.

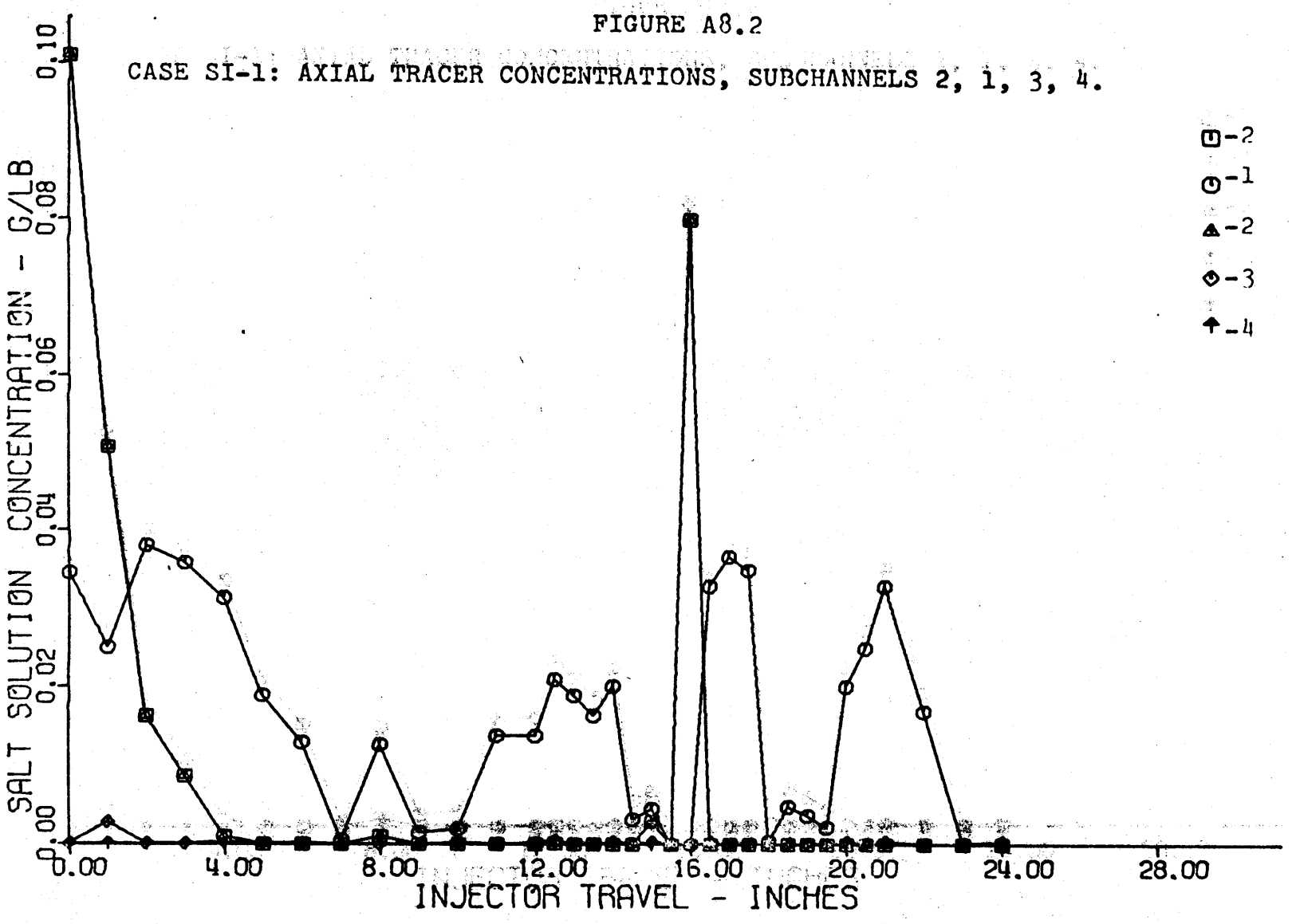

FIGURE A8.3

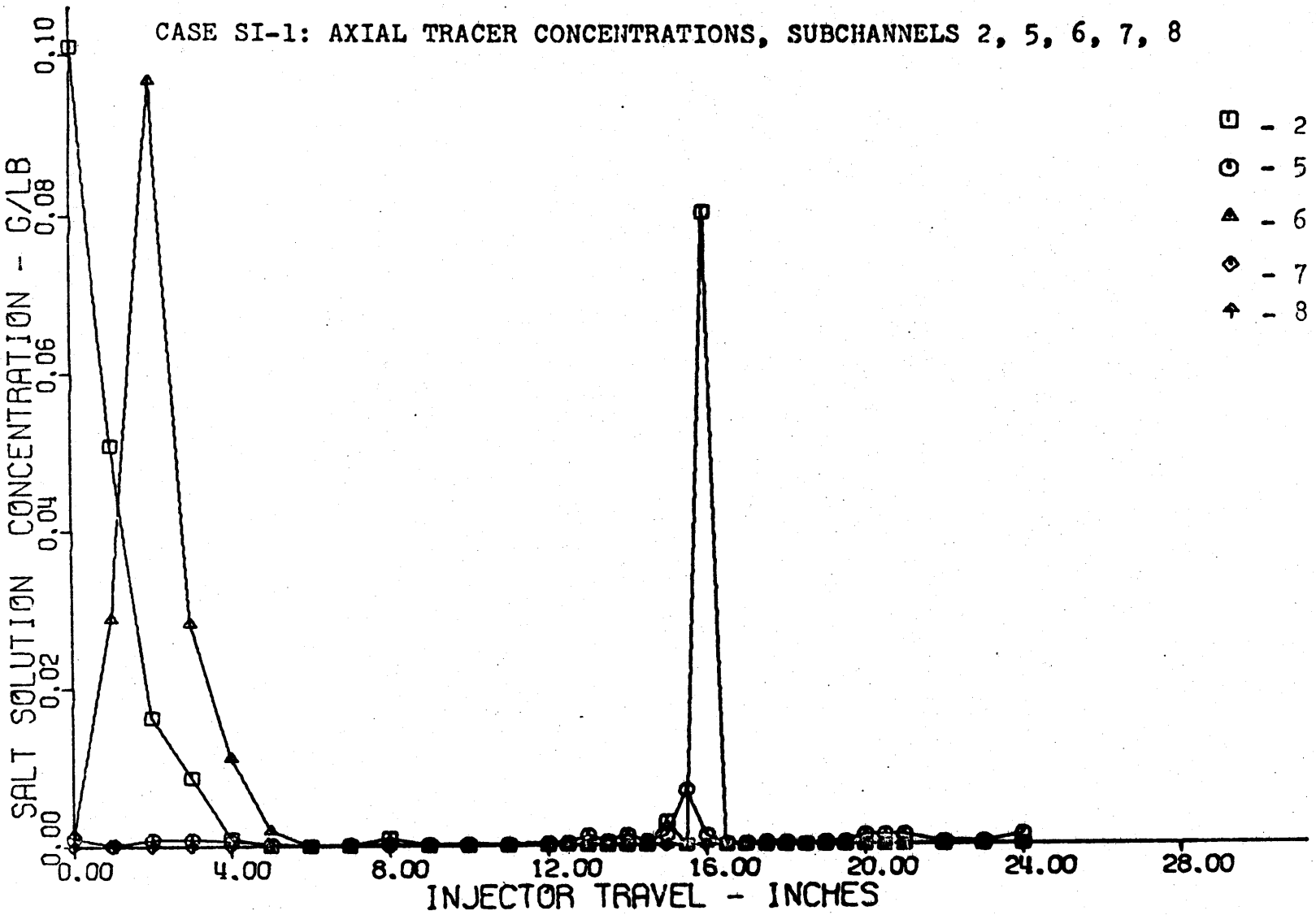
CASE SI-1: AXIAL TRACER CONCENTRATIONS, SUBCHANNELS 2, 5, 6, 7, 8
SALT SOLUTION CONCENTRATION - G/LB
0.00
0.02
0.04
0.06
0.08
0.10
0.00
4.00
8.00
12.00
16.00
20.00
24.00
28.00
INJECTOR TRAVEL - INCHES
- 2
- 5
- 6
- 7
- 8

FIGURE A8.4

CASE SI-2: MASS BALANCE VS. INJECTOR TRAVEL

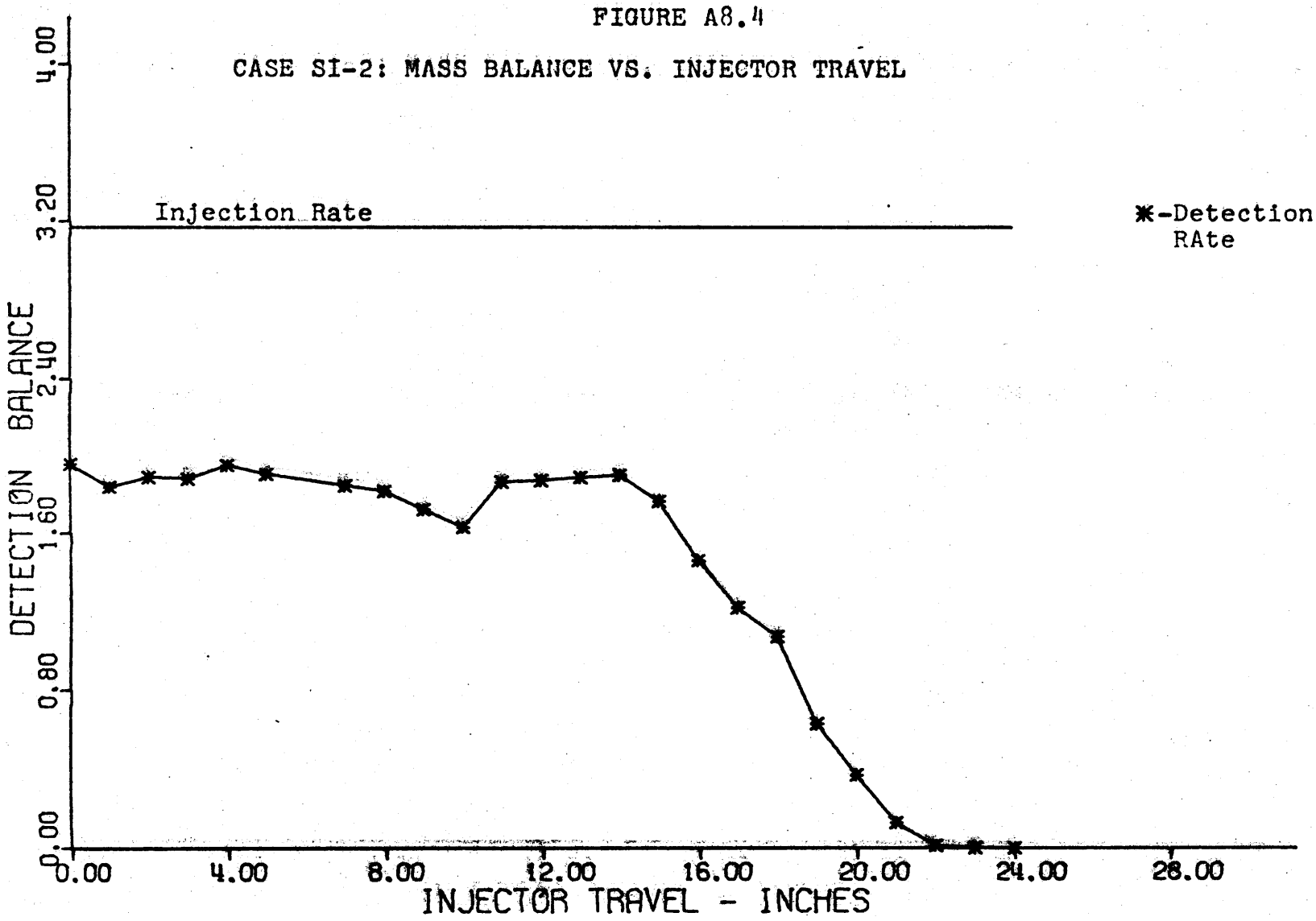

FIGURE A8.5

CASE SI-2: AXIAL TRACER CONCENTATION, SUBCHANNELS 2, 1, 3, 4

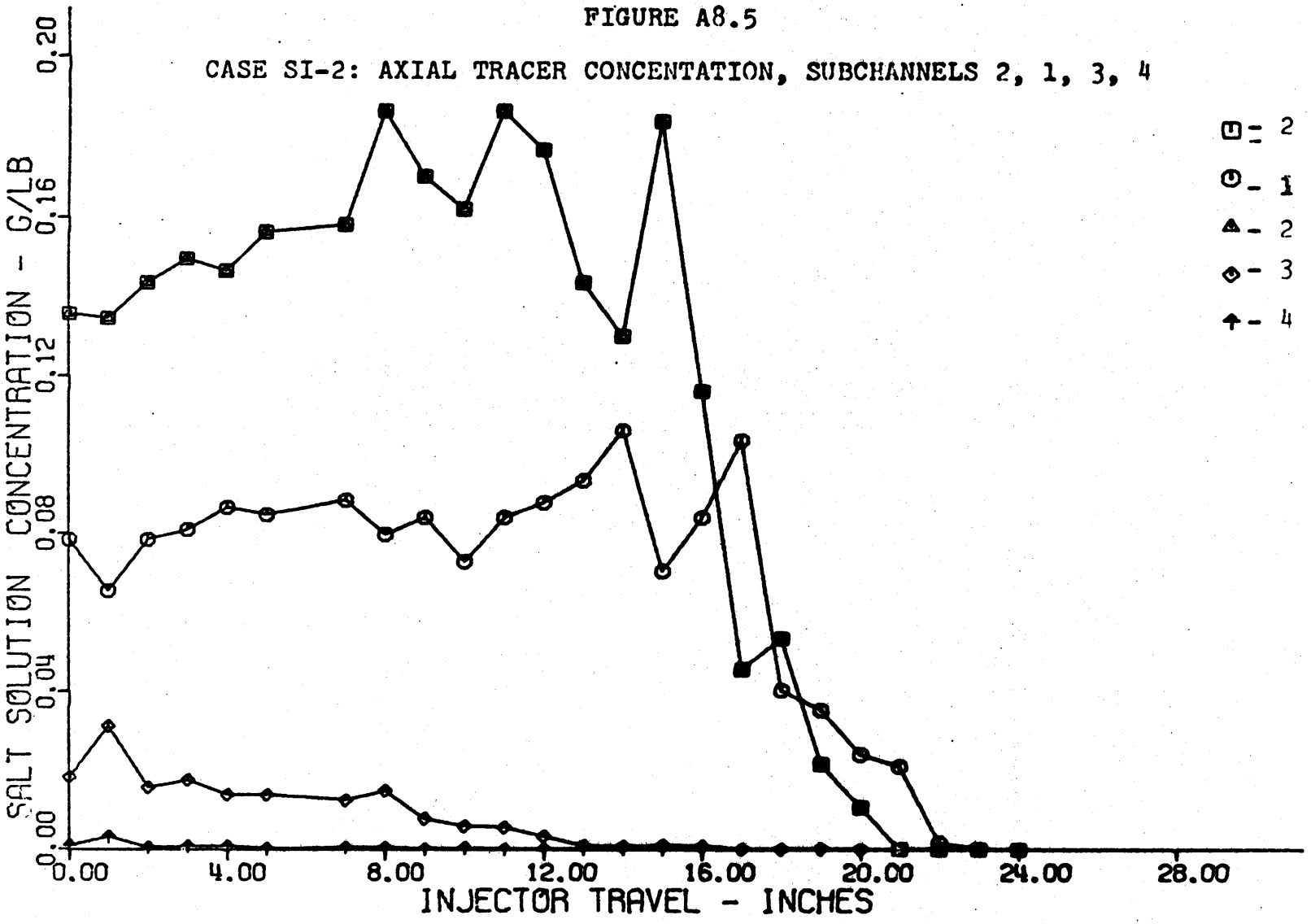

FIGURE A8.6

CASE SI-2: AXIAL TRACER CONCENTRATIONS, SUBCHANNELS 2, 5, 6, 7, 8

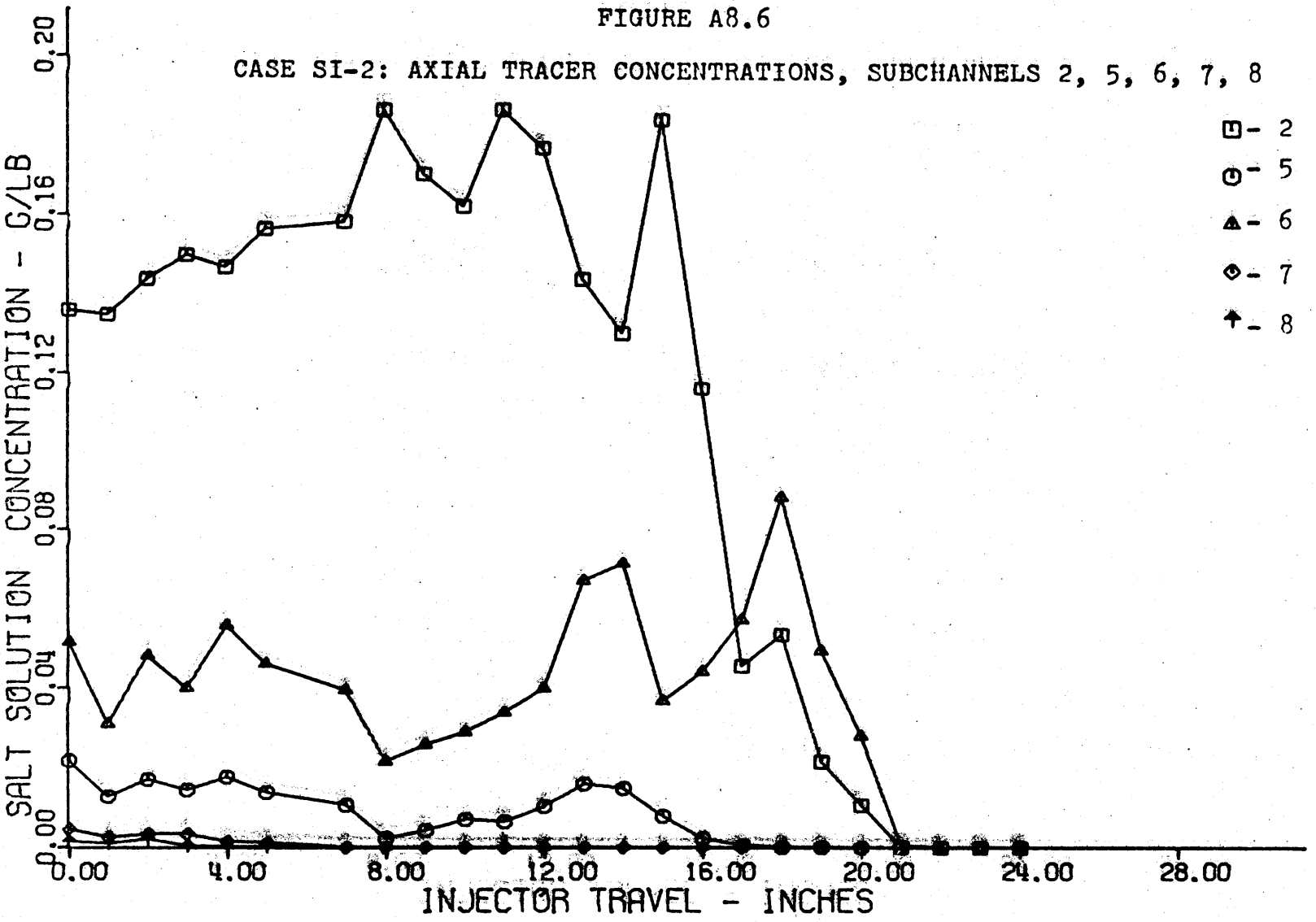

FIGURE A8.7

CASE SI-2: AXIAL TRACER CONCENTRATION, SUBCHANNELS 2, 9, 10, 11, 12.

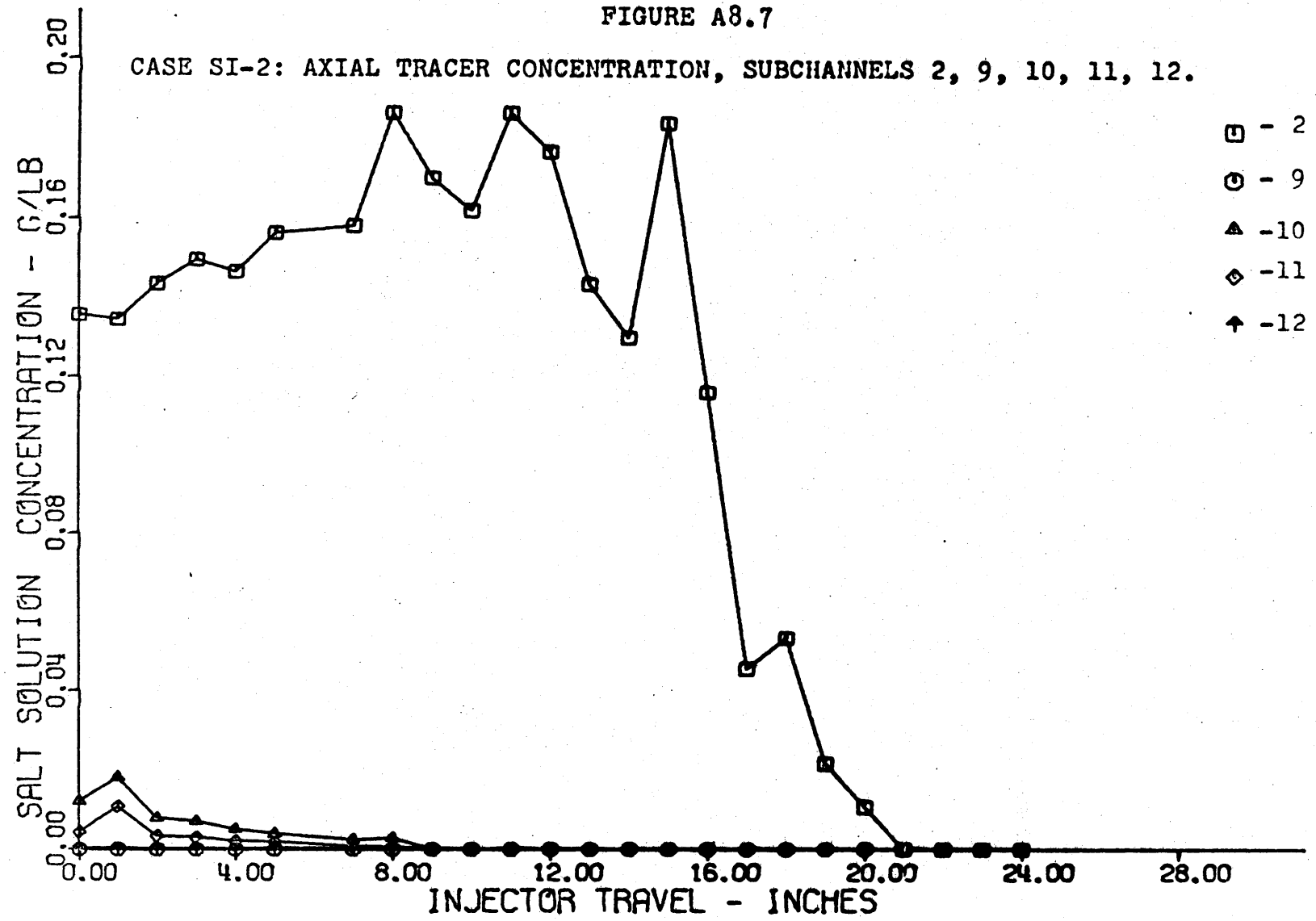

FIGURE A8.8

CASE SI-2: AXIAL TRACER CONCENTRATIONS, SUBCHANNELS 2, 17, 18, 19, 20.

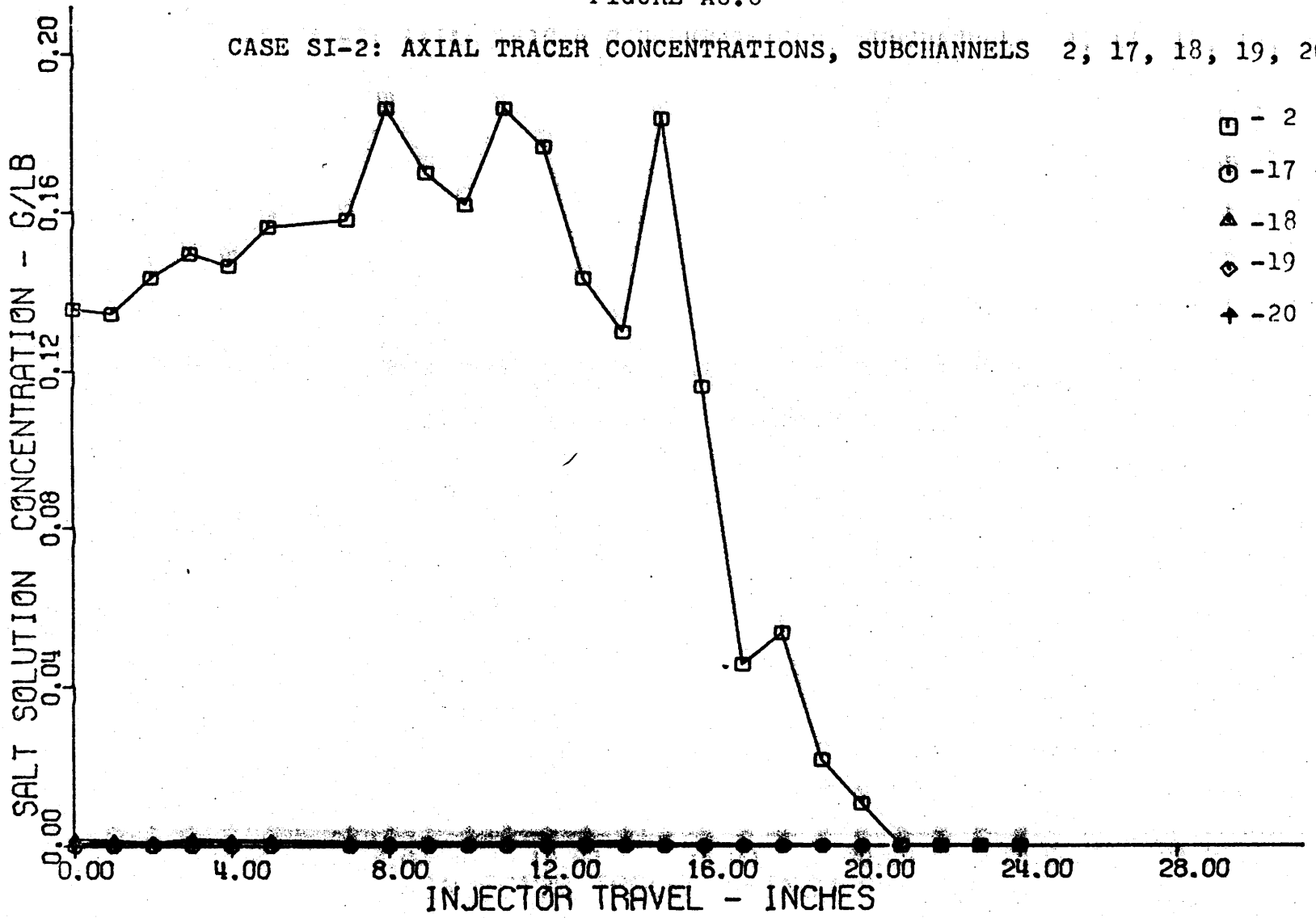

FIGURE A8.9

CASE SI-3: MASS BALANCE VS. INJECTOR TRAVEL

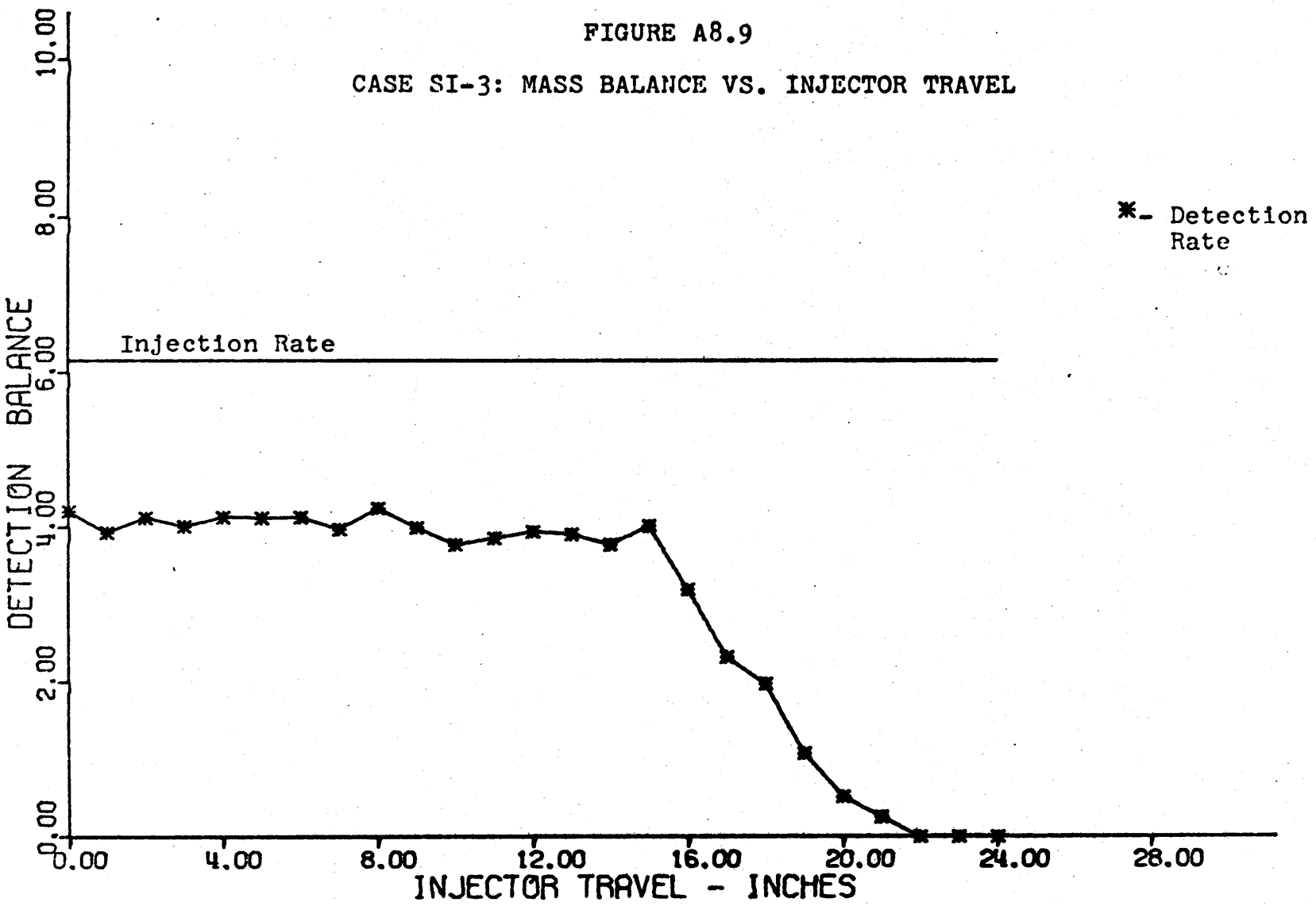

FIGURE A8.10

CASE SI-3: AXIAL TRACER CONCENTRATION, SUBCHANNELS 2, 1, 3, 4

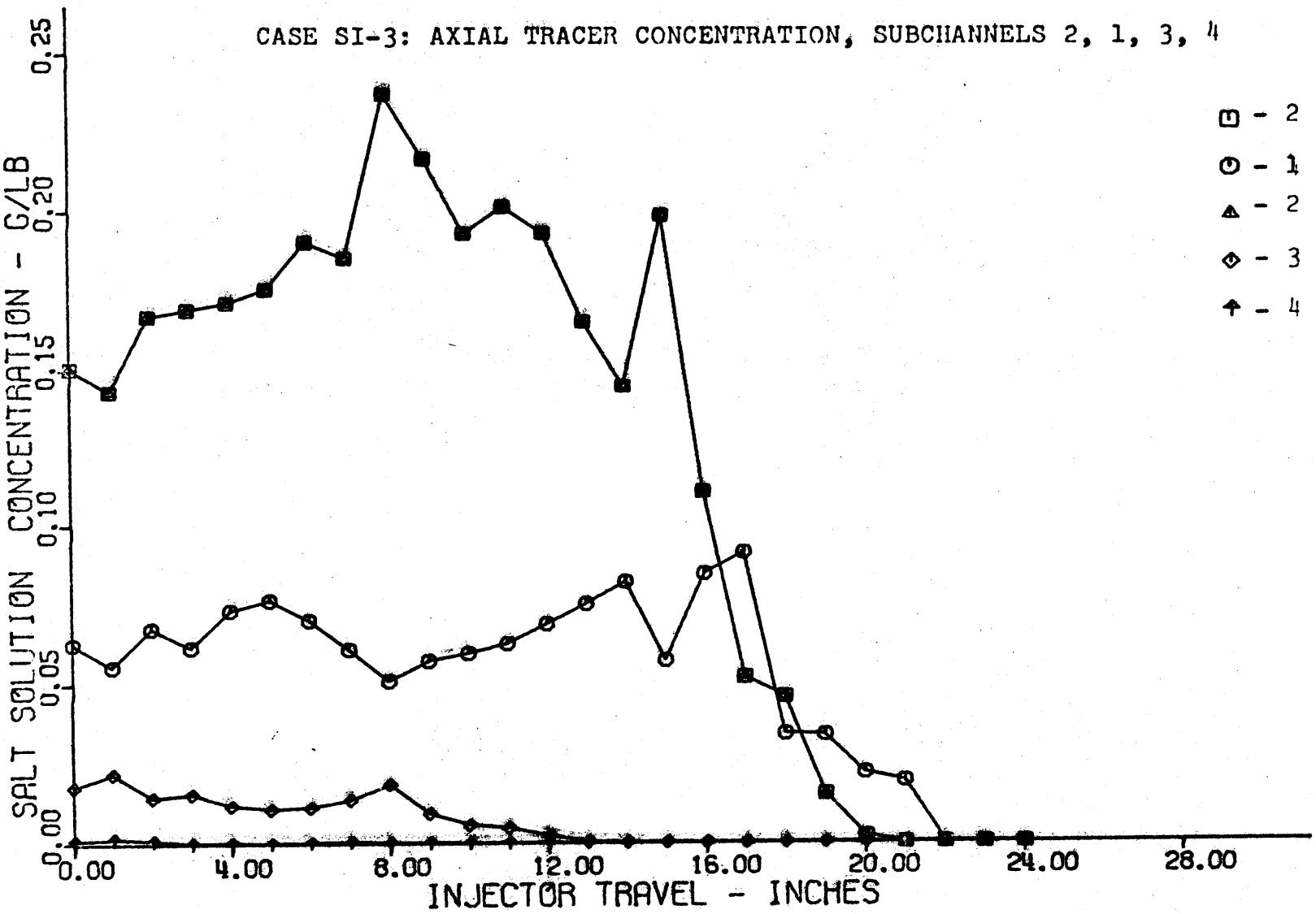

FIGURE A8.11

CASE SI-3: AXIAL TRACER CONCENTRATION, SUBCHANNELS 2, 5, 6, 7, 8

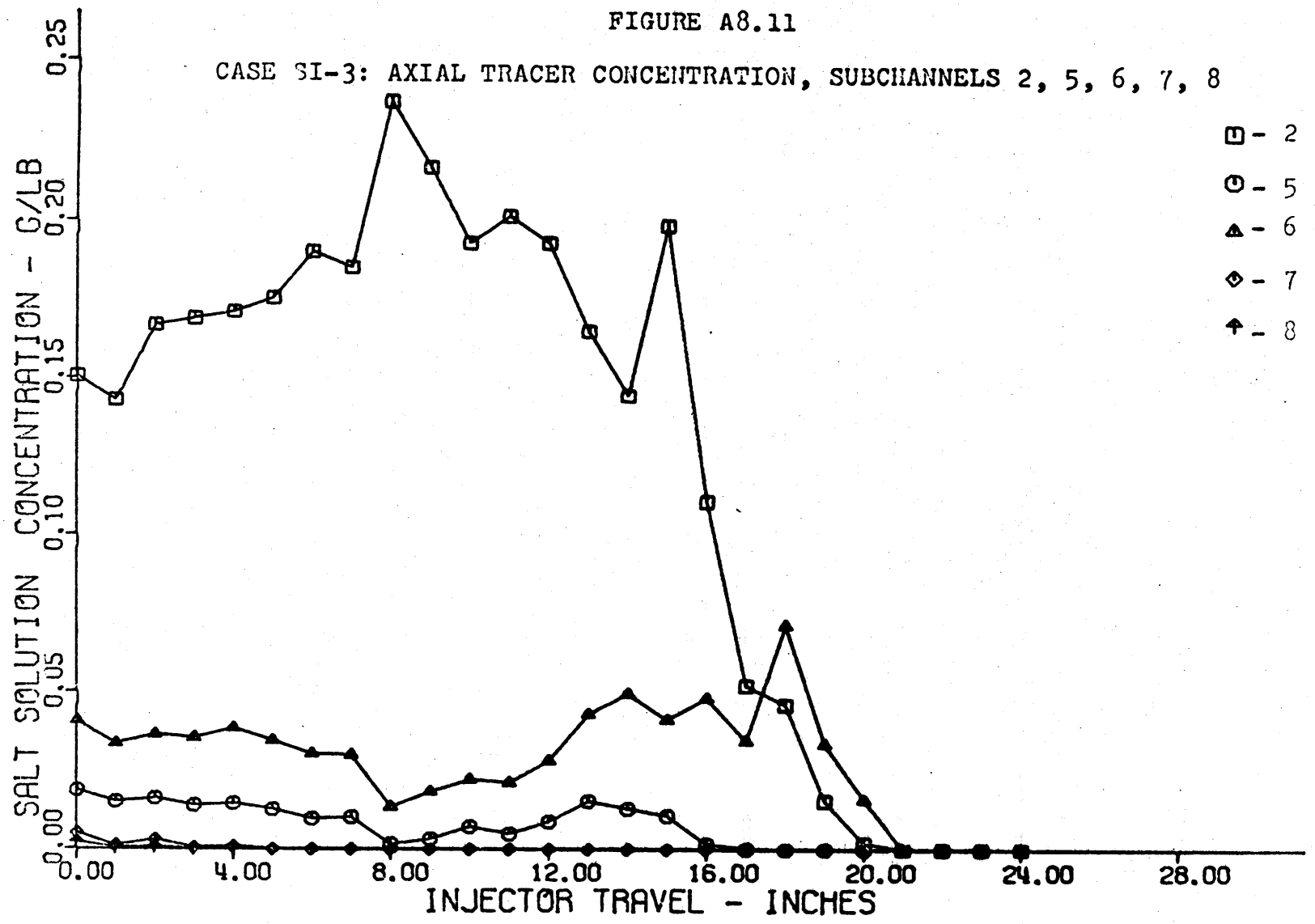

FIGURE A8.12

CASE SI-3: AXIAL TRACER CONCENTRATION, SUBCHANNELS 2, 9,10,11,12

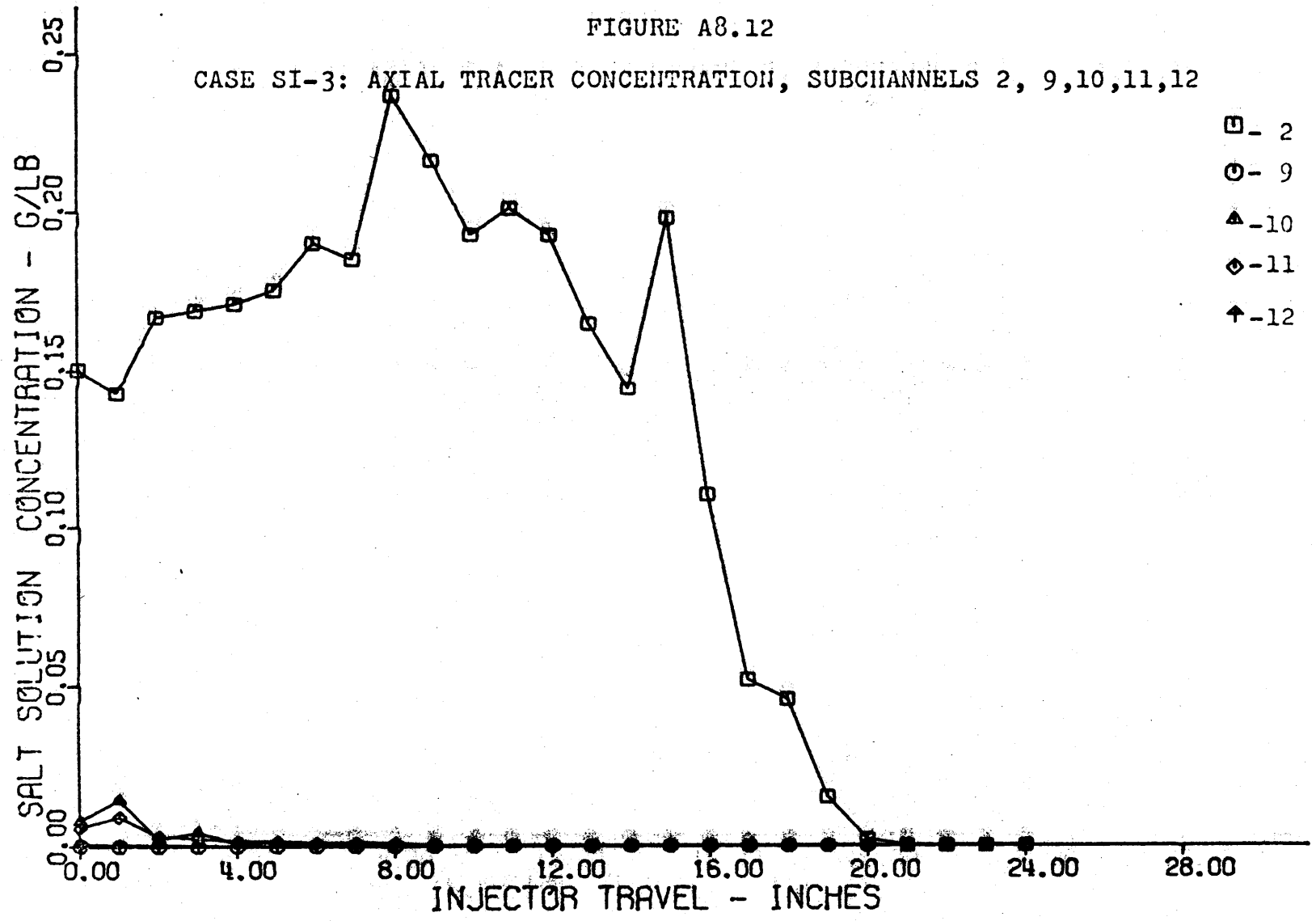

FIGURE A8.13

CASE SI-3: AXIAL TRACER CONCENTRATION, SUBCHANNELS 2,17,18,19,20

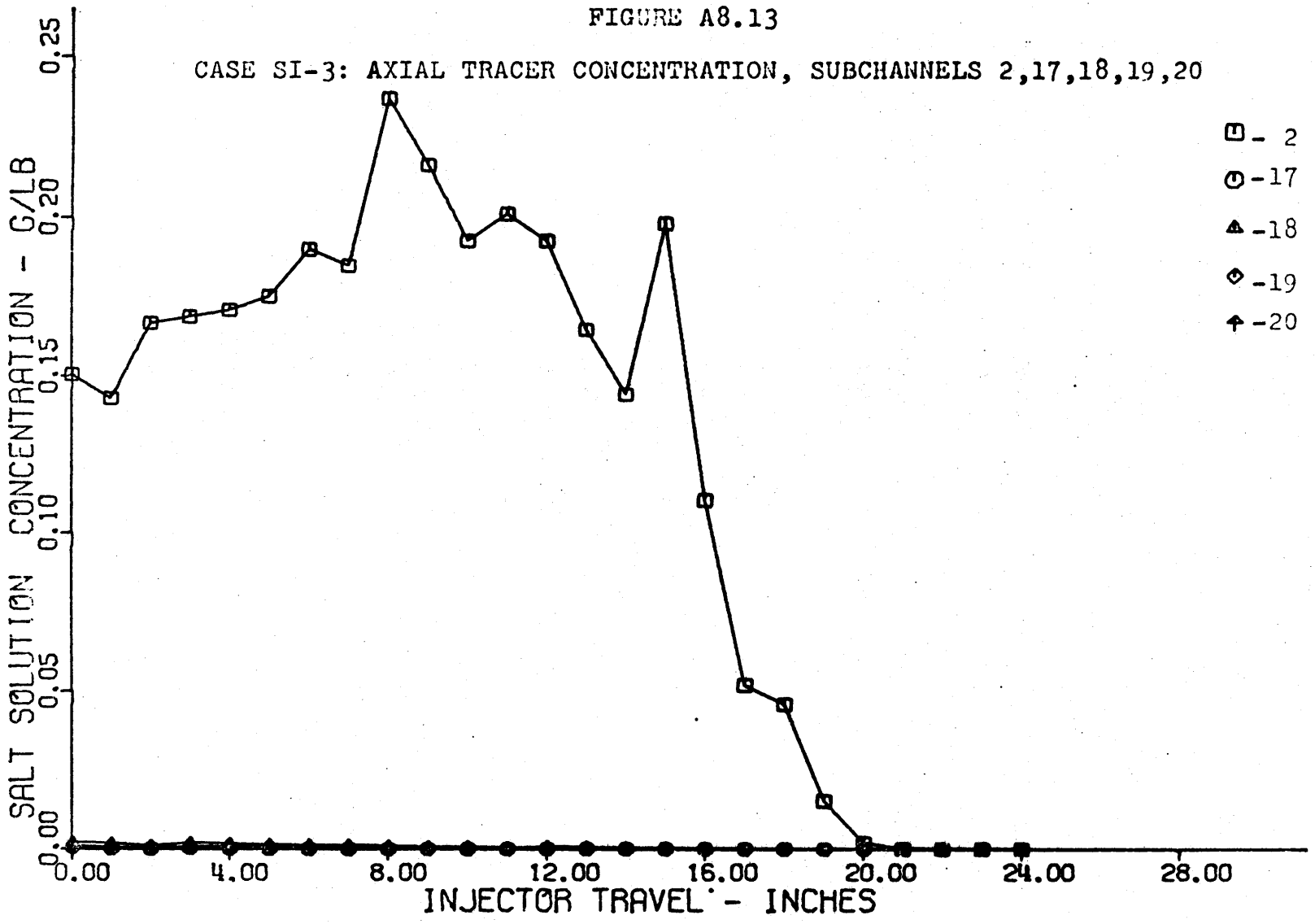

FIGURE A8.14

CASE SI-4: MASS BALANCE VERSUS INJECTOR TRAVEL

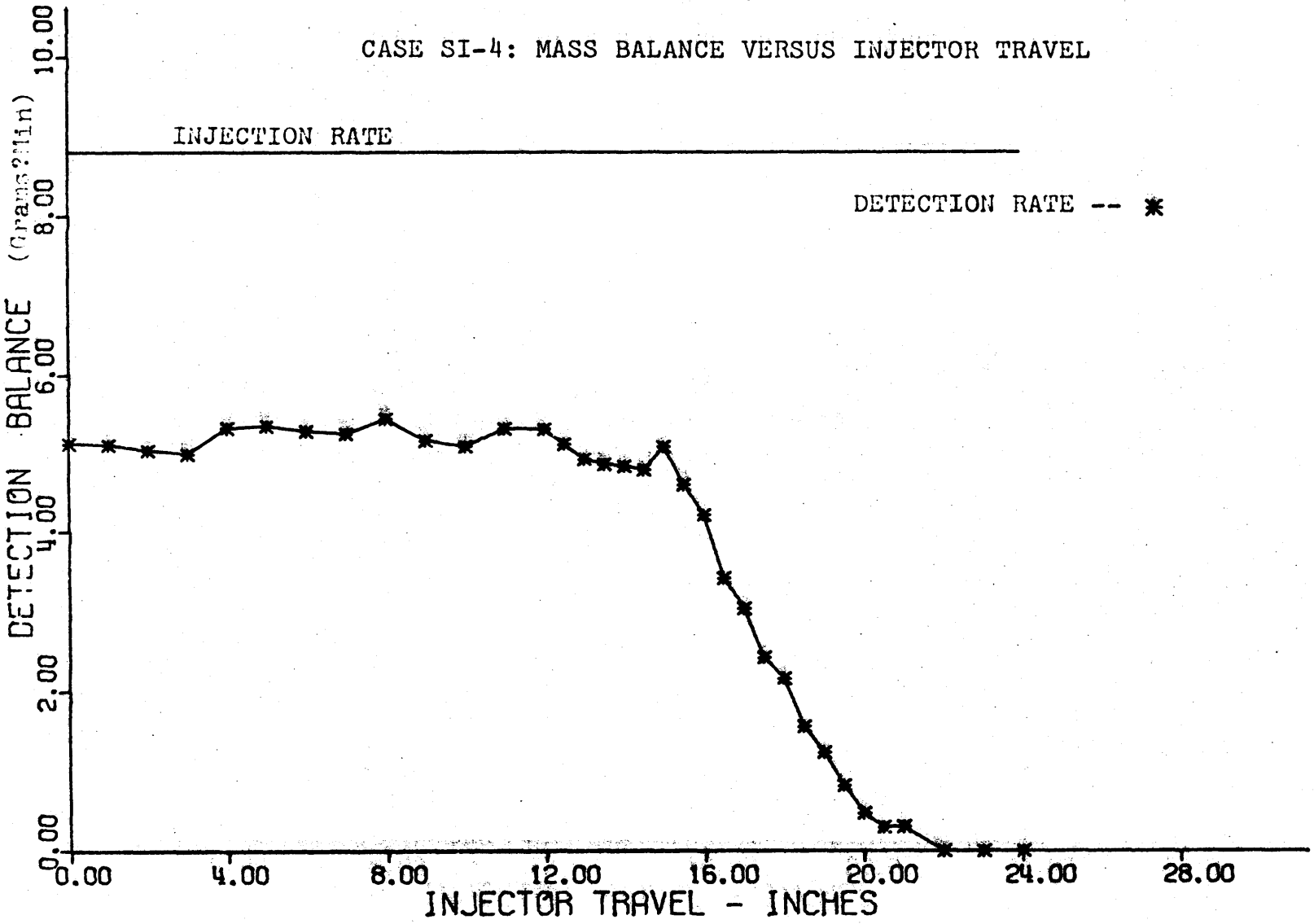

FIGURE A8.15

CASE SI-4: AXIAL TRACER CONCENTRATION, SUBCHANNELS 2, 1, 3, 4

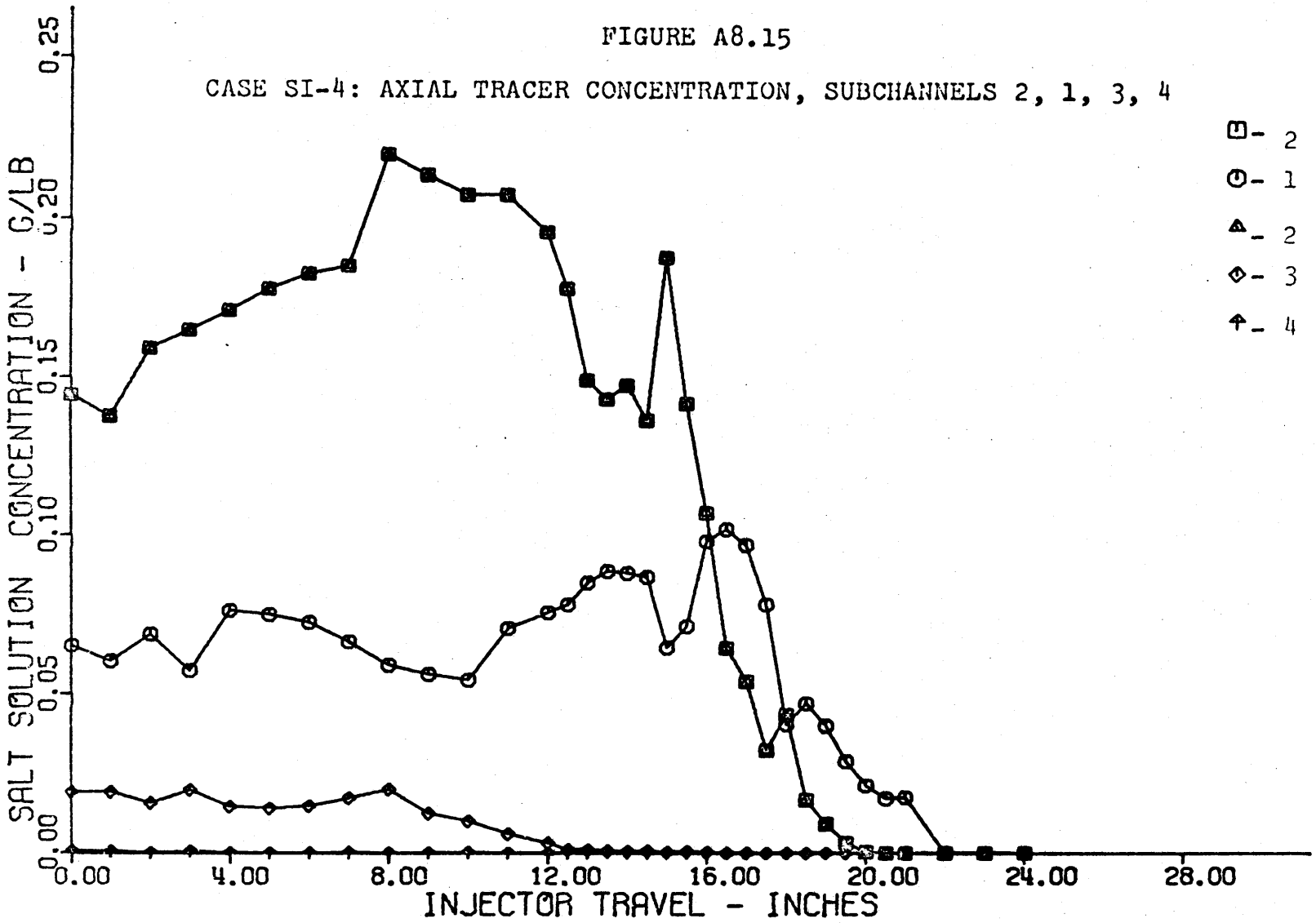

FIGURE A8.16

CASE SI-4: AXIAL TRACER CONCNETRATION, SUBCHANNELS 2, 5, 6, 7, 8

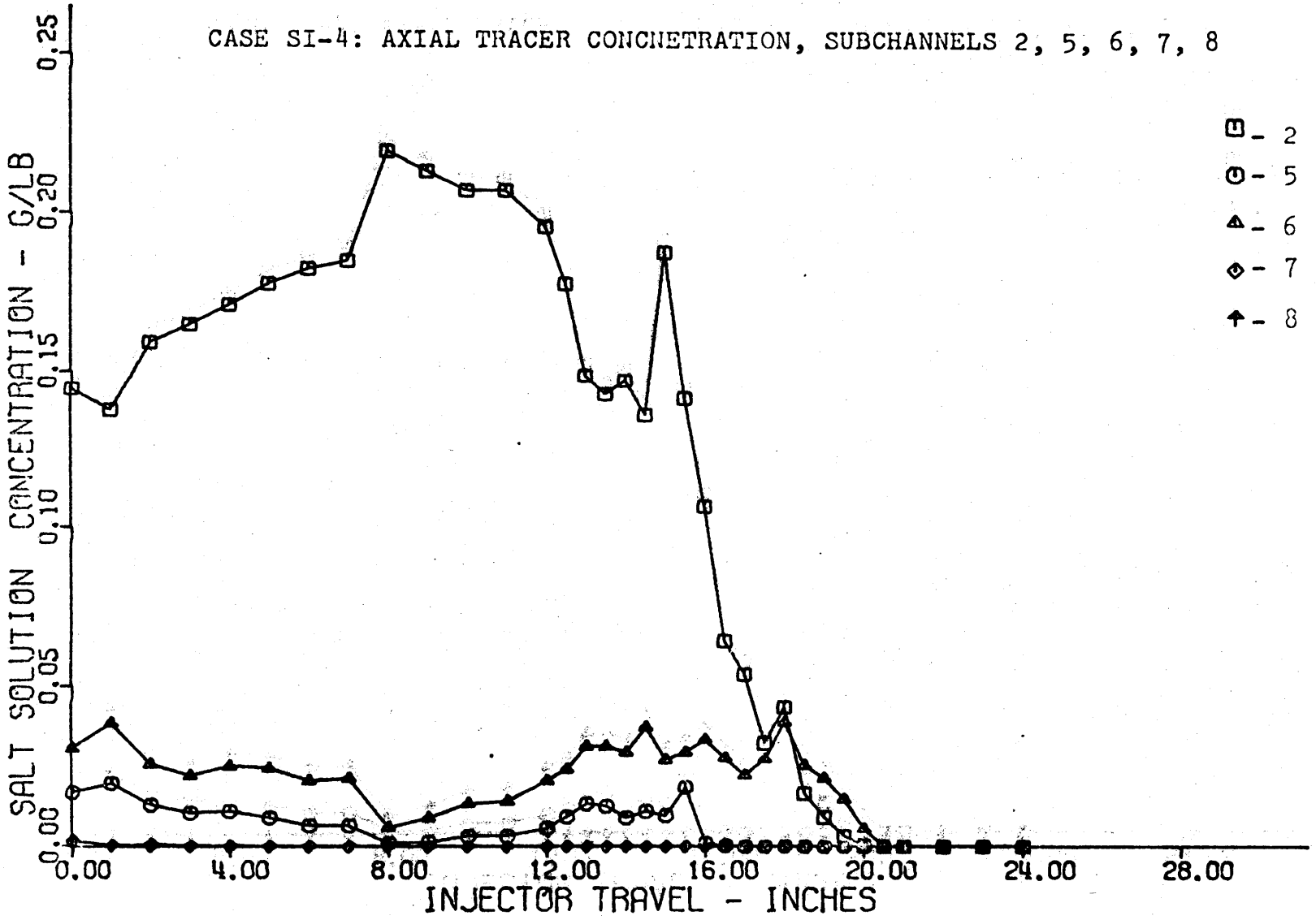

FIGURE A8.17

CASE SI-4: AXIAL TRACER CONCENTRATION, SUBCHANNELS 2, 9,10,11,12

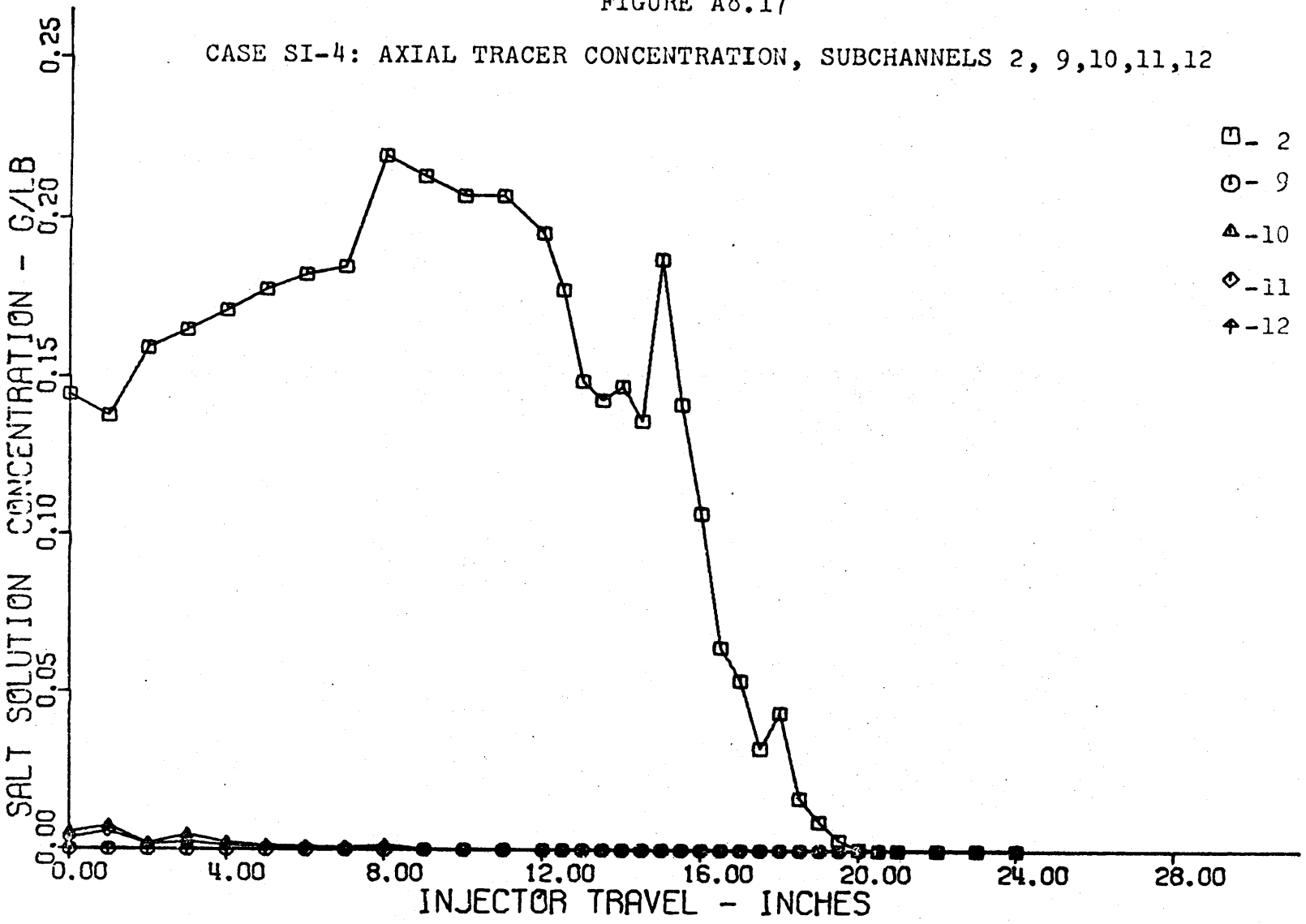

FIGURE A8.18

CASE SI-6: MASS BALANCE VERSUS INJECTOR TRAVEL

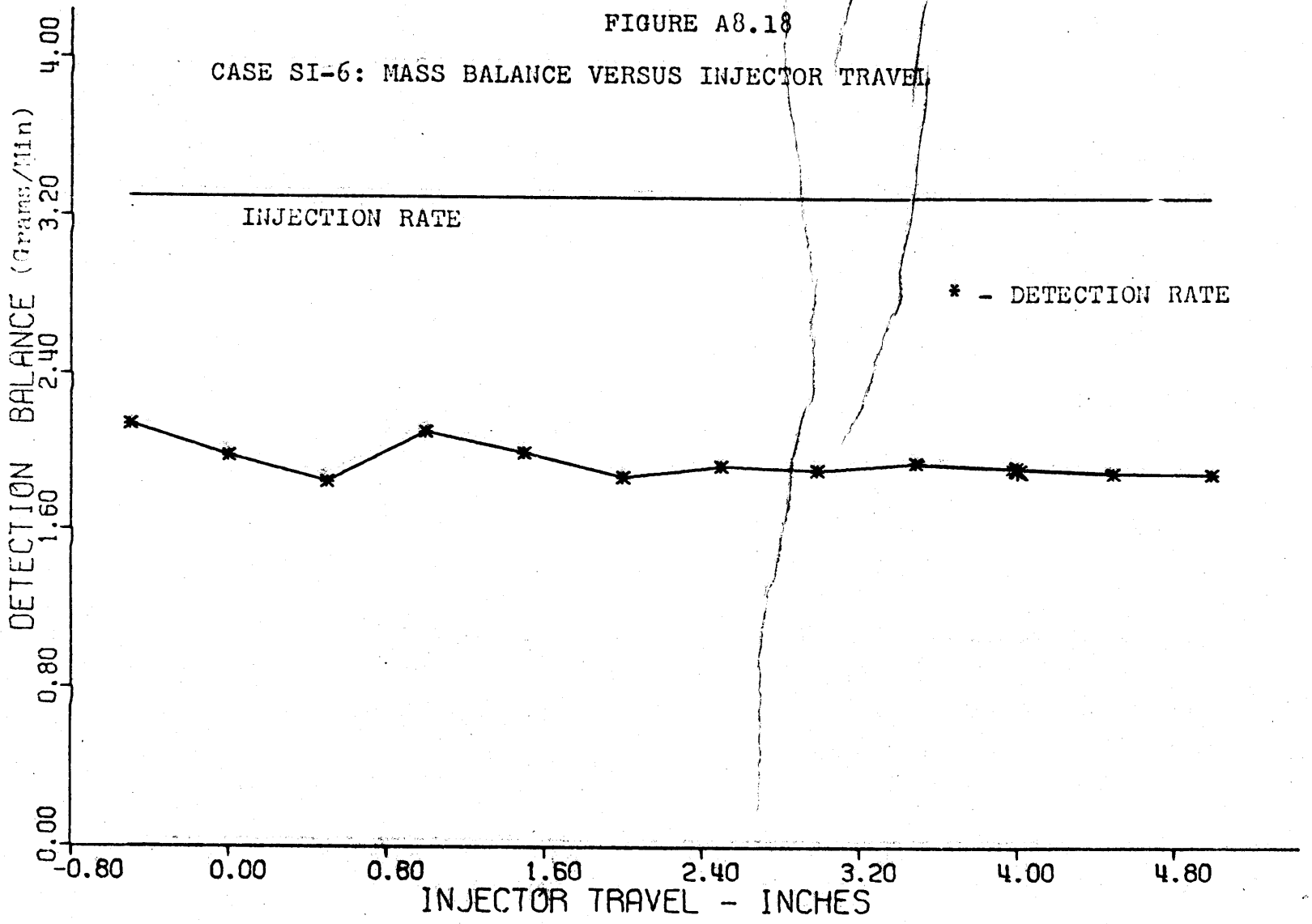

FIGURE A8.19

CASE SI-6: AXIAL TRACER CONCNETRATION, SUBCHANNELS 2, 1, 3, 4

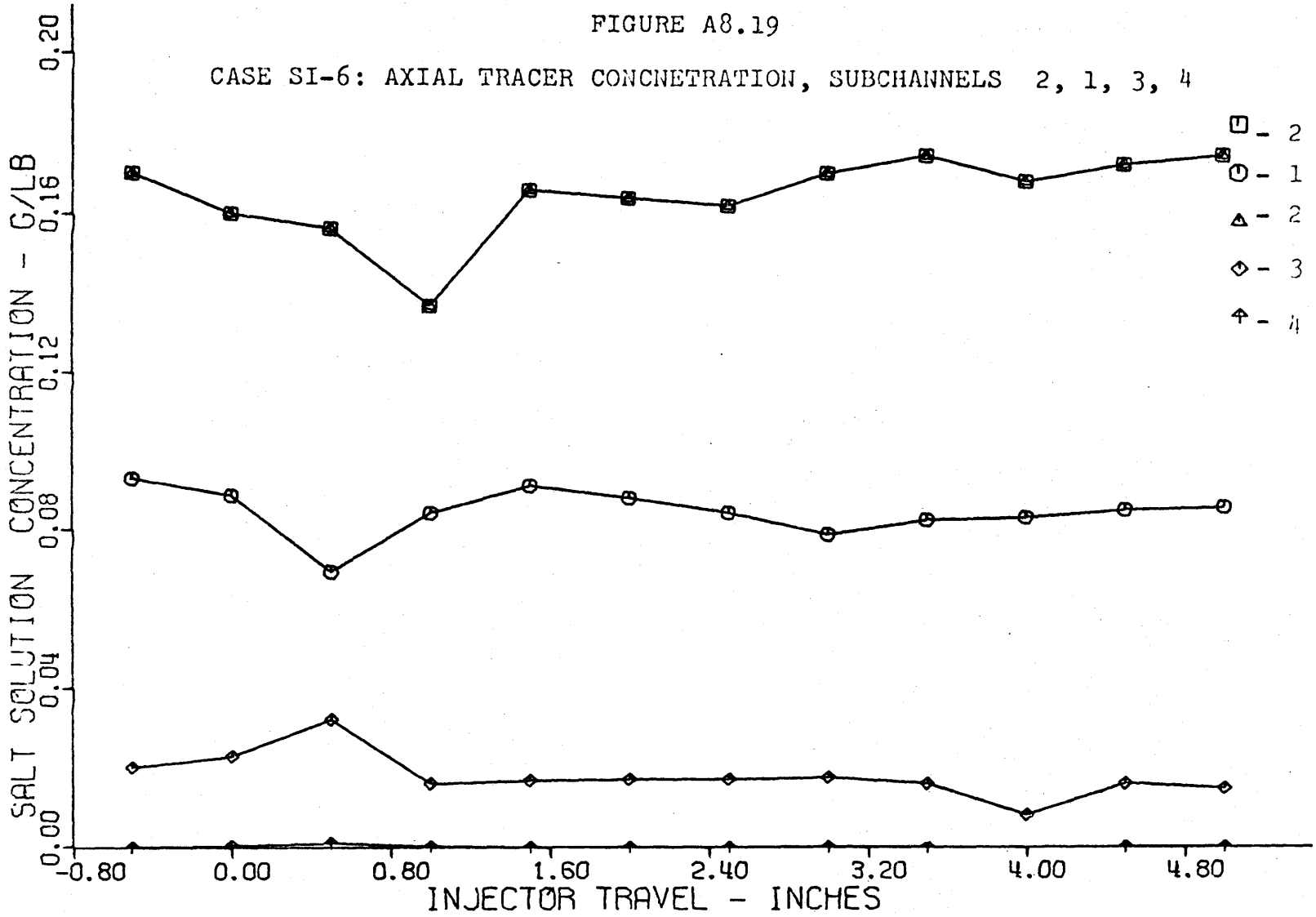

FIGURE A8.20

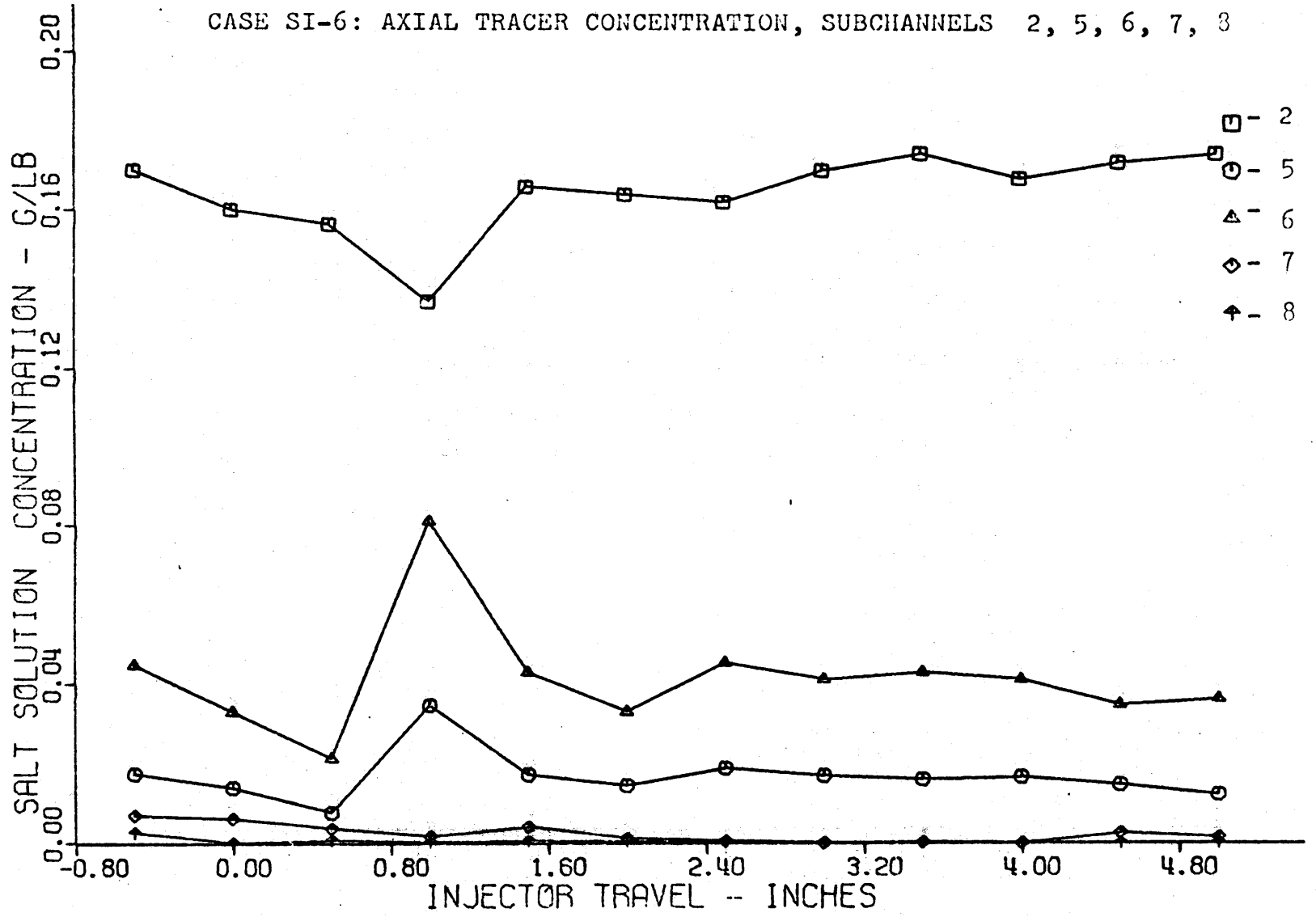
CASE SI-6: AXIAL TRACER CONCENTRATION, SUBCHANNELS 2, 5, 6, 7, 8
SALT SOLUTION CONCENTRATION - G/LB
0.00
0.04
0.08
0.12
0.16
0.20
-0.80
0.00
0.80
1.60
2.40
3.20
4.00
4.80
INJECTOR TRAVEL -- INCHES
2
5
6
7
8

FIGURE A8.21

CASE SI-6: AXIAL TRACER CONCENTRATION, SUBCHANNELS 2, 9,10,11,12

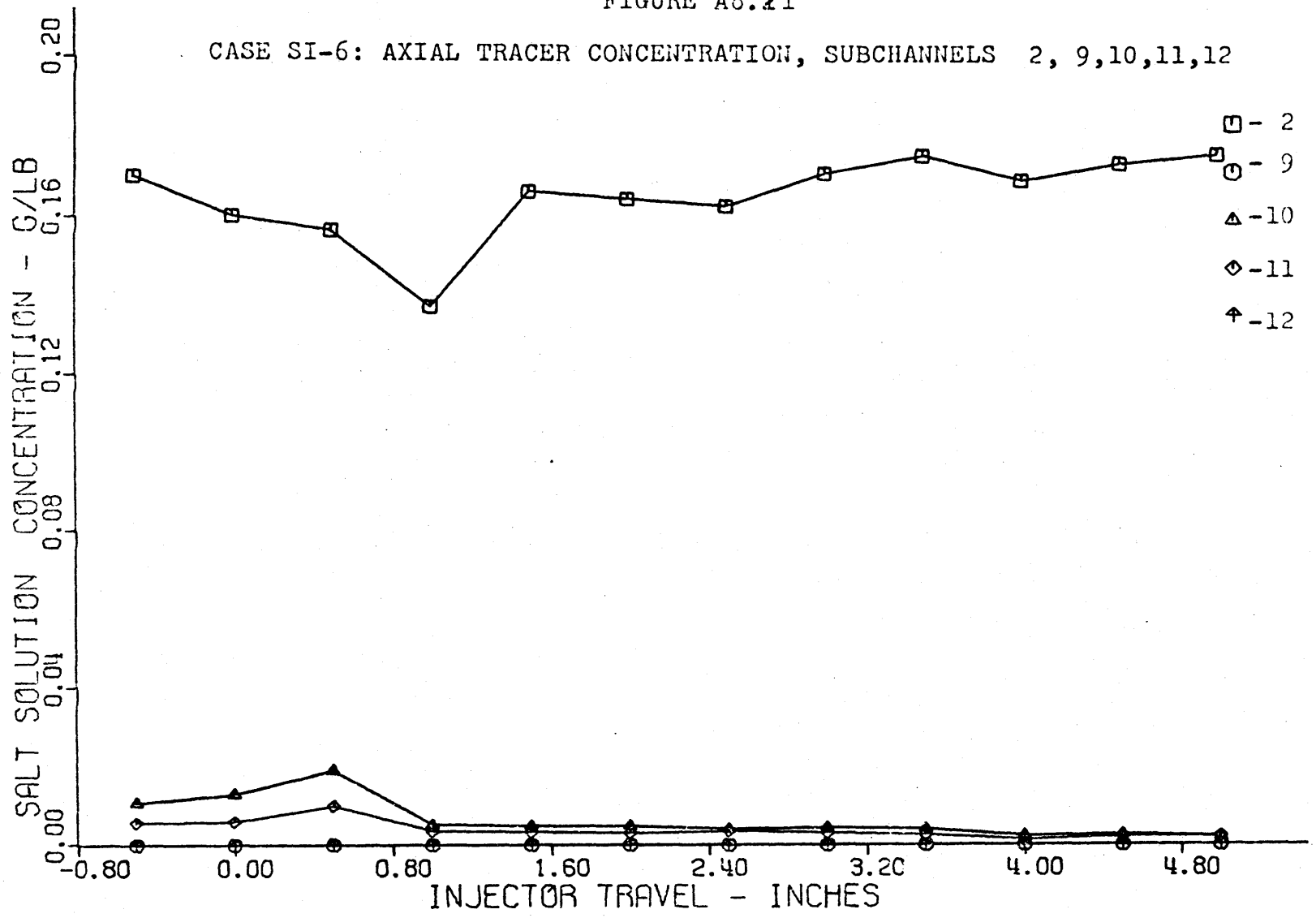

FIGURE A8.22

CASE SI-7: MASS BALANCE VERSUS INJECTOR TRAVEL

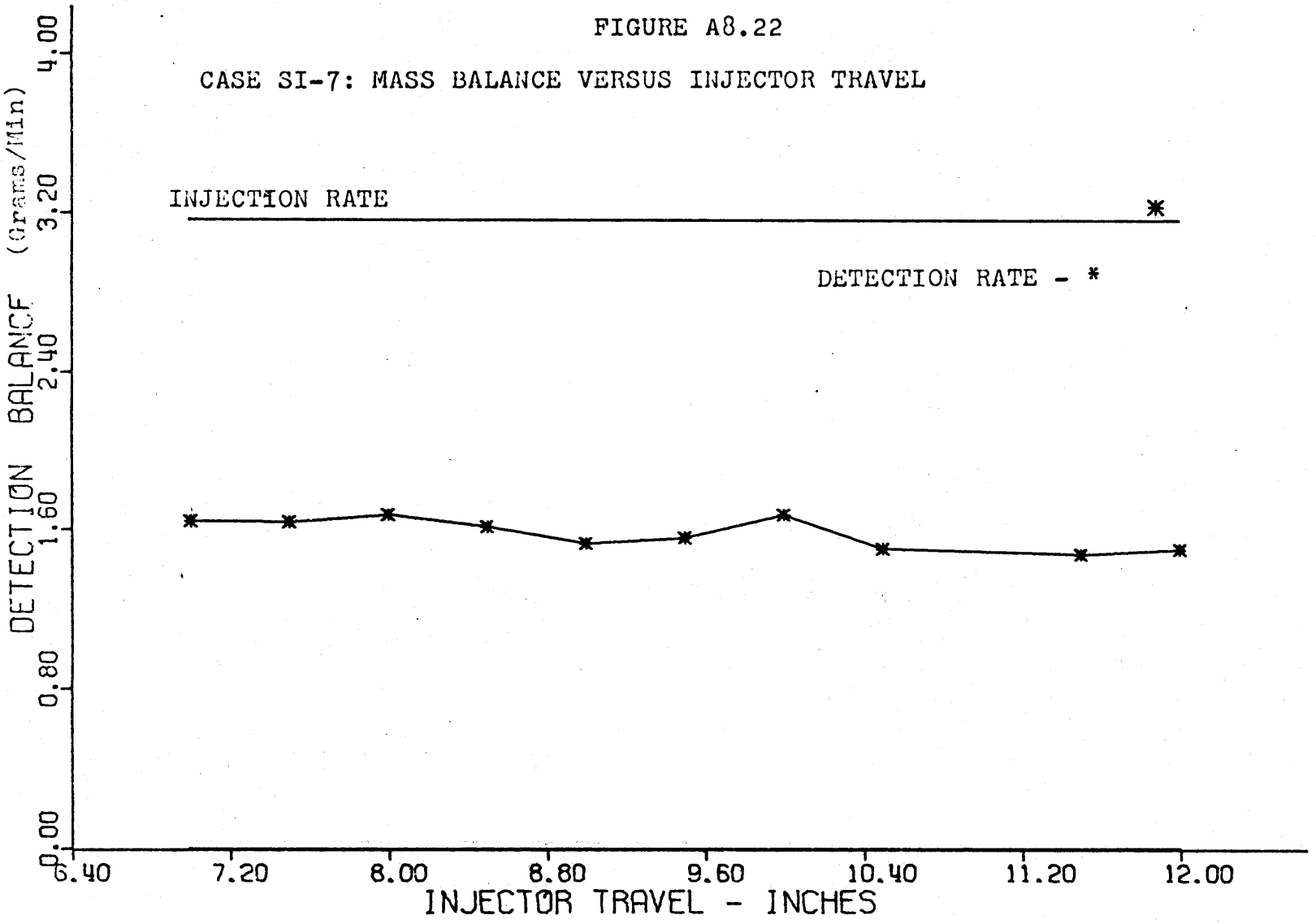

FIGURE A8.23

CASE SI-7: AXIAL TRACER CONCENTRATION, SUBCHANNELS 2, 1, 3, 4

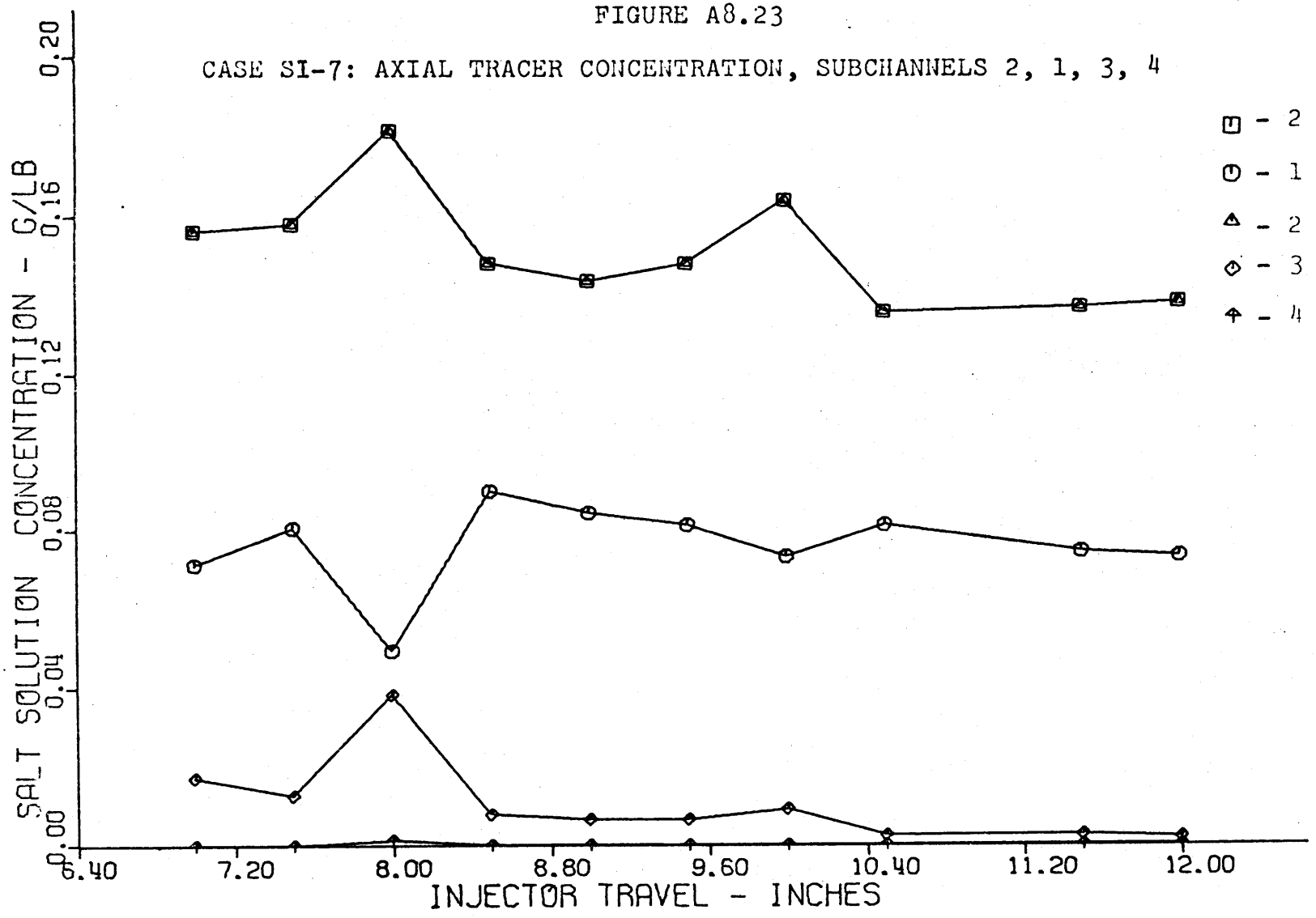

FIGURE A8.24

CASE SI-7: AXIAL TRACER CONCENTRATION, SUBCHANNELS 2, 5, 6, 7, 8

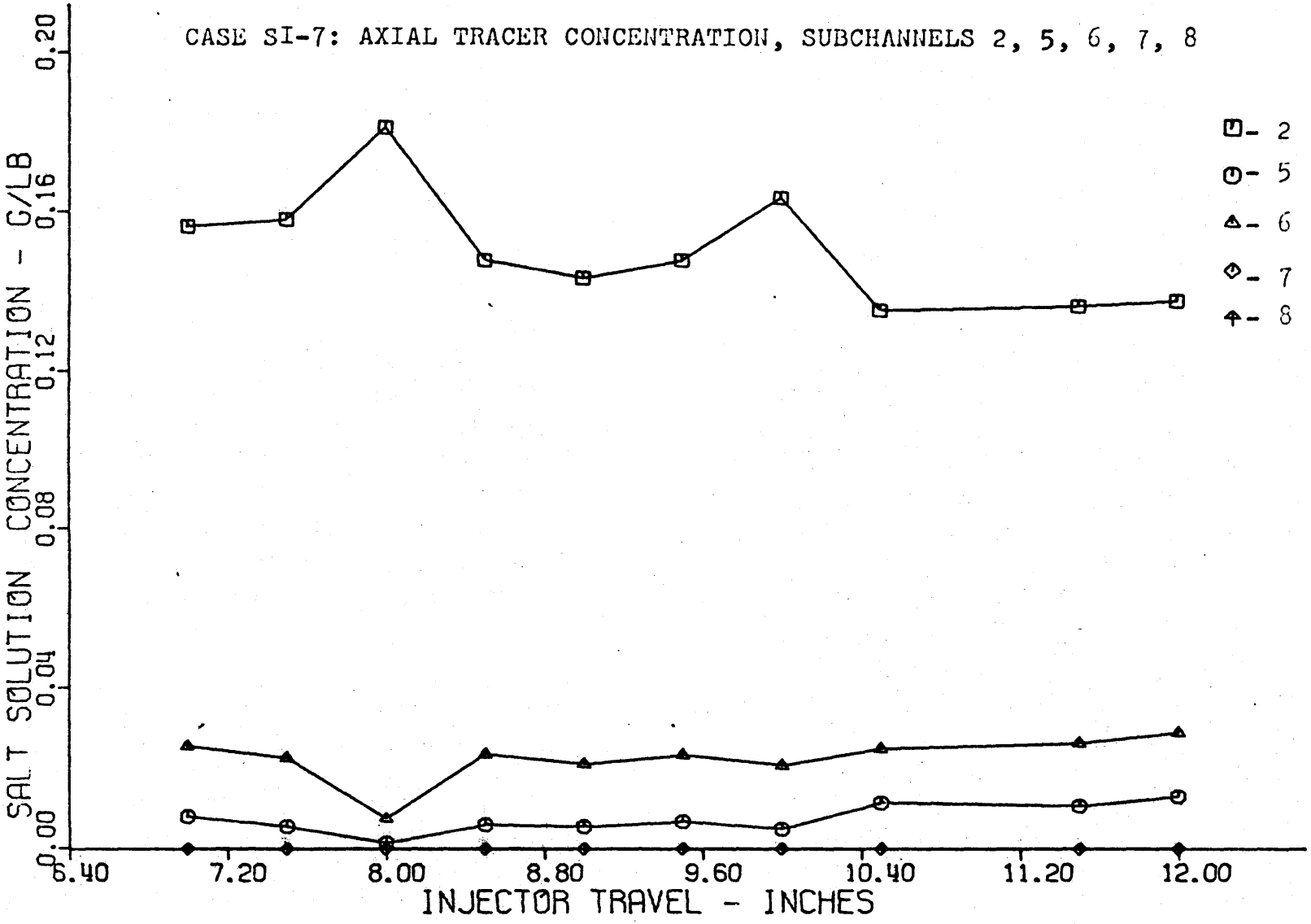

FIGURE A8.25

CASE SI-8: MASS BALANCE VERSUS INJECTOR TRAVEL

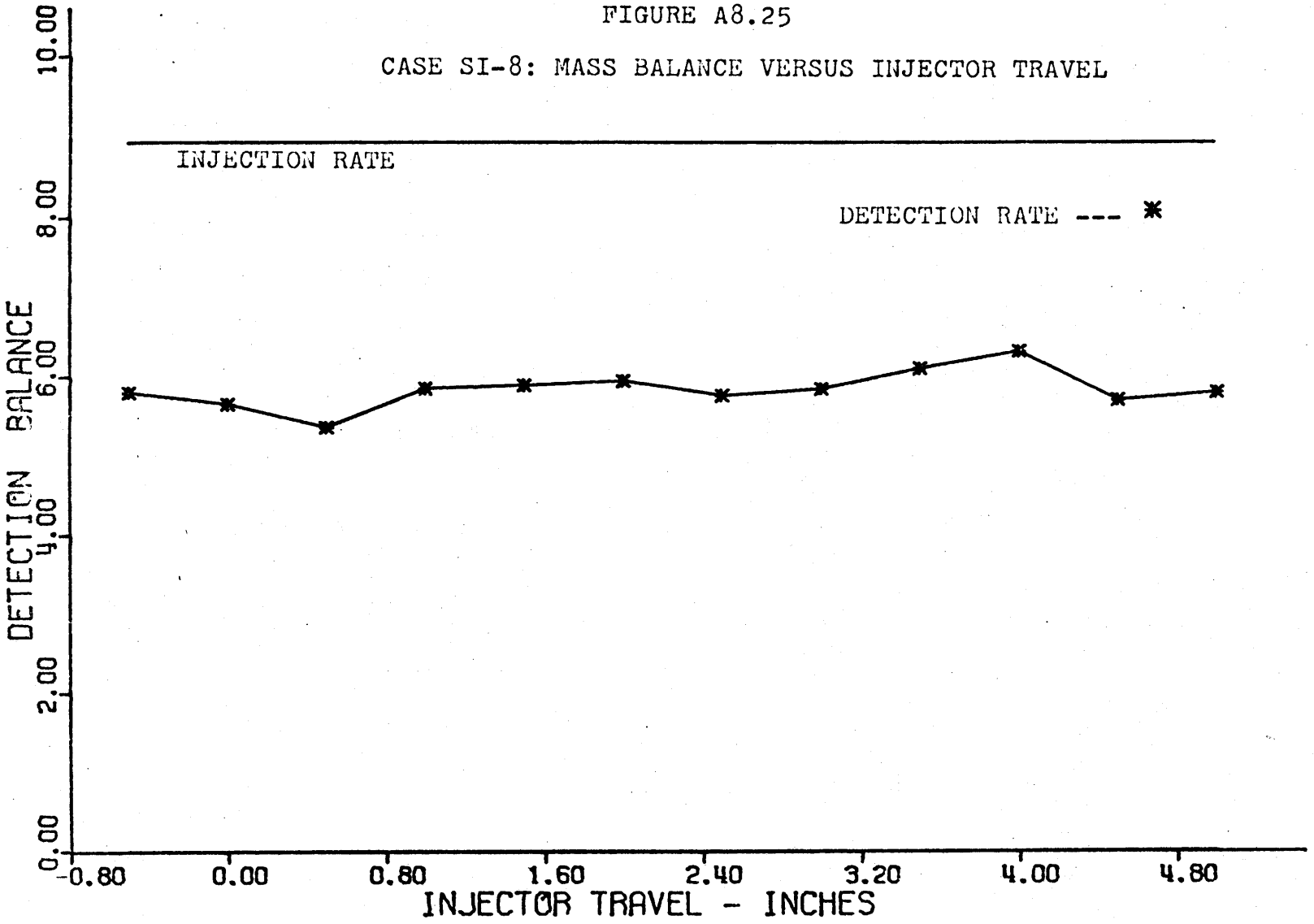

FIGURE A8.26

CASE SI-8: AXIAL TRACER CONCENTRATION, SUBCHANNELS 2, 1, 3, 4

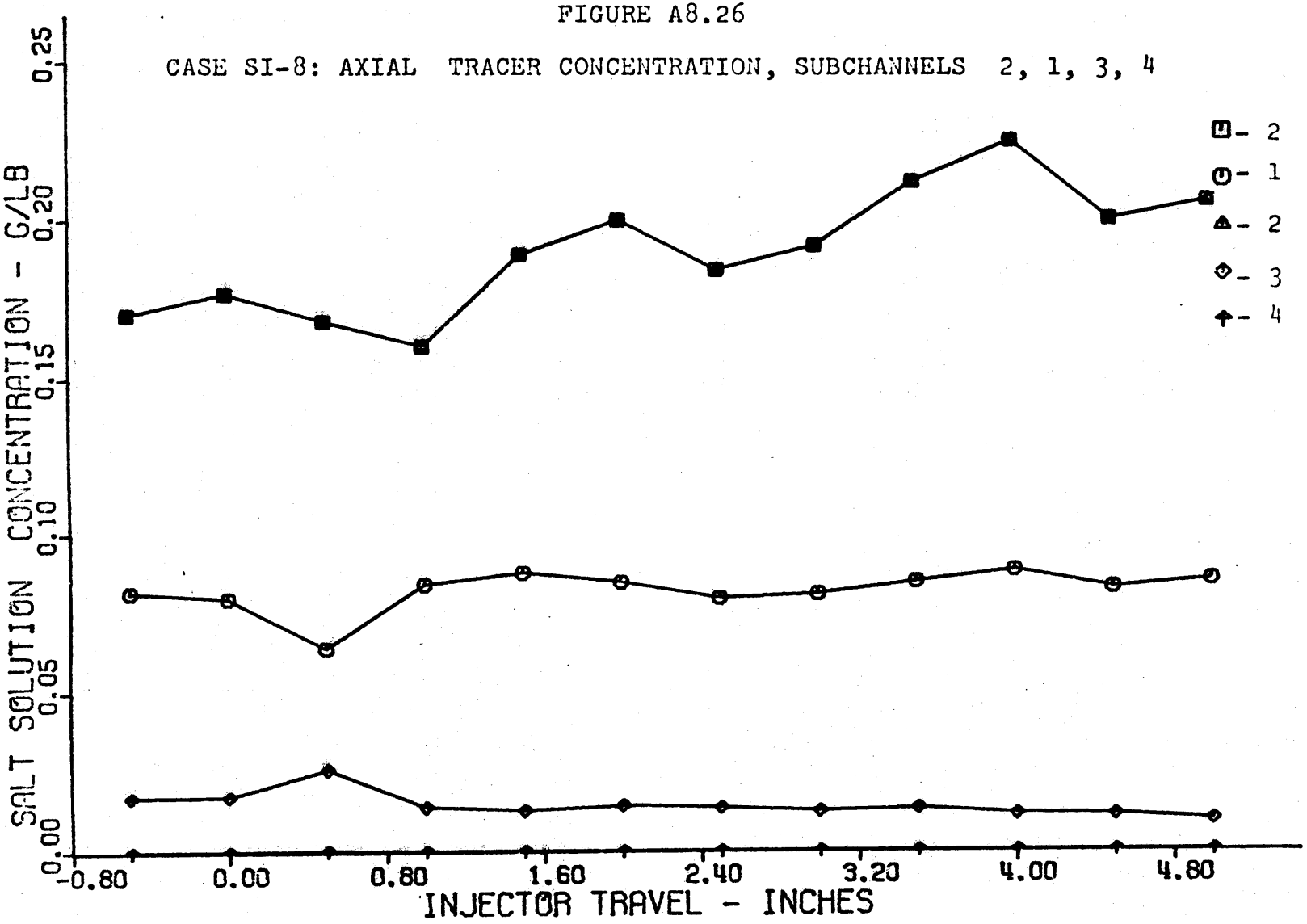

FIGURE A8.27

CASE SI-8: AXIAL TRACER CONCENTRATION, SUBCHANNELS 2, 5, 6, 7, 8

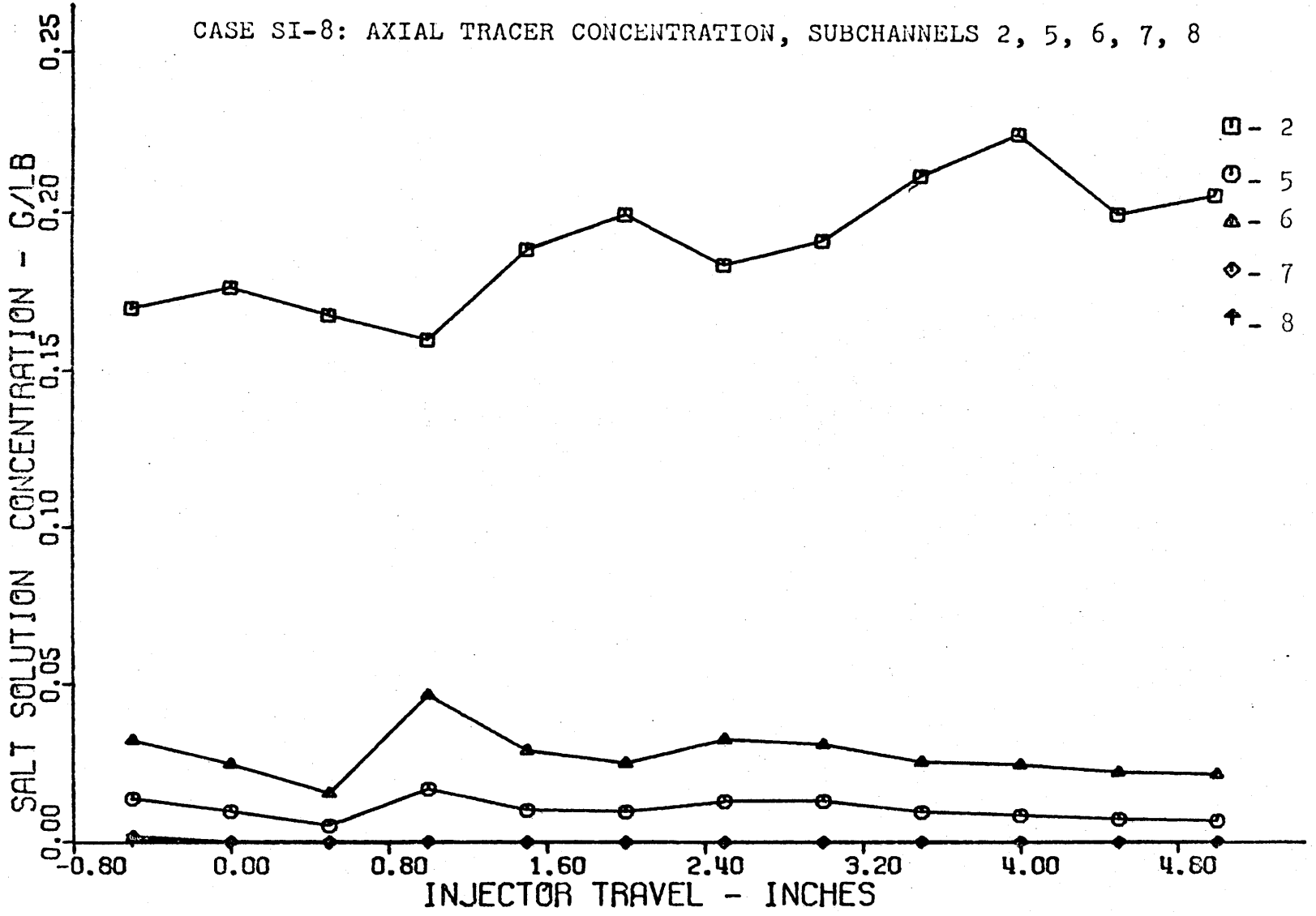

FIGURE A8.28

CASE SI-8: AXIAL TRACER CONCENTRATION, SUBCHANNELS 2, 9,10,11,12

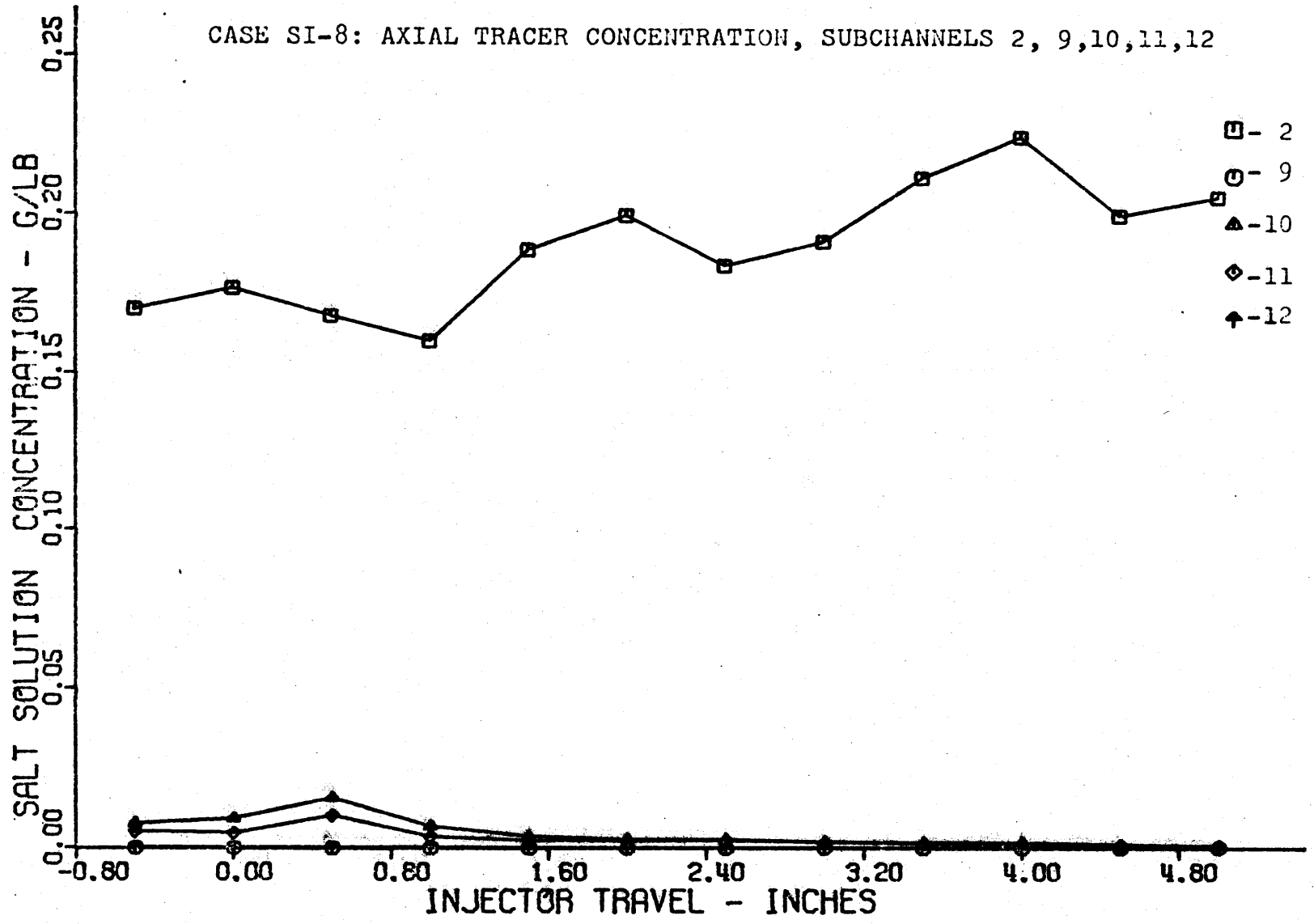

FIGURE A8.29

CASE SI-9: MASS BALANCE VERSUS INJECTOR TRAVEL

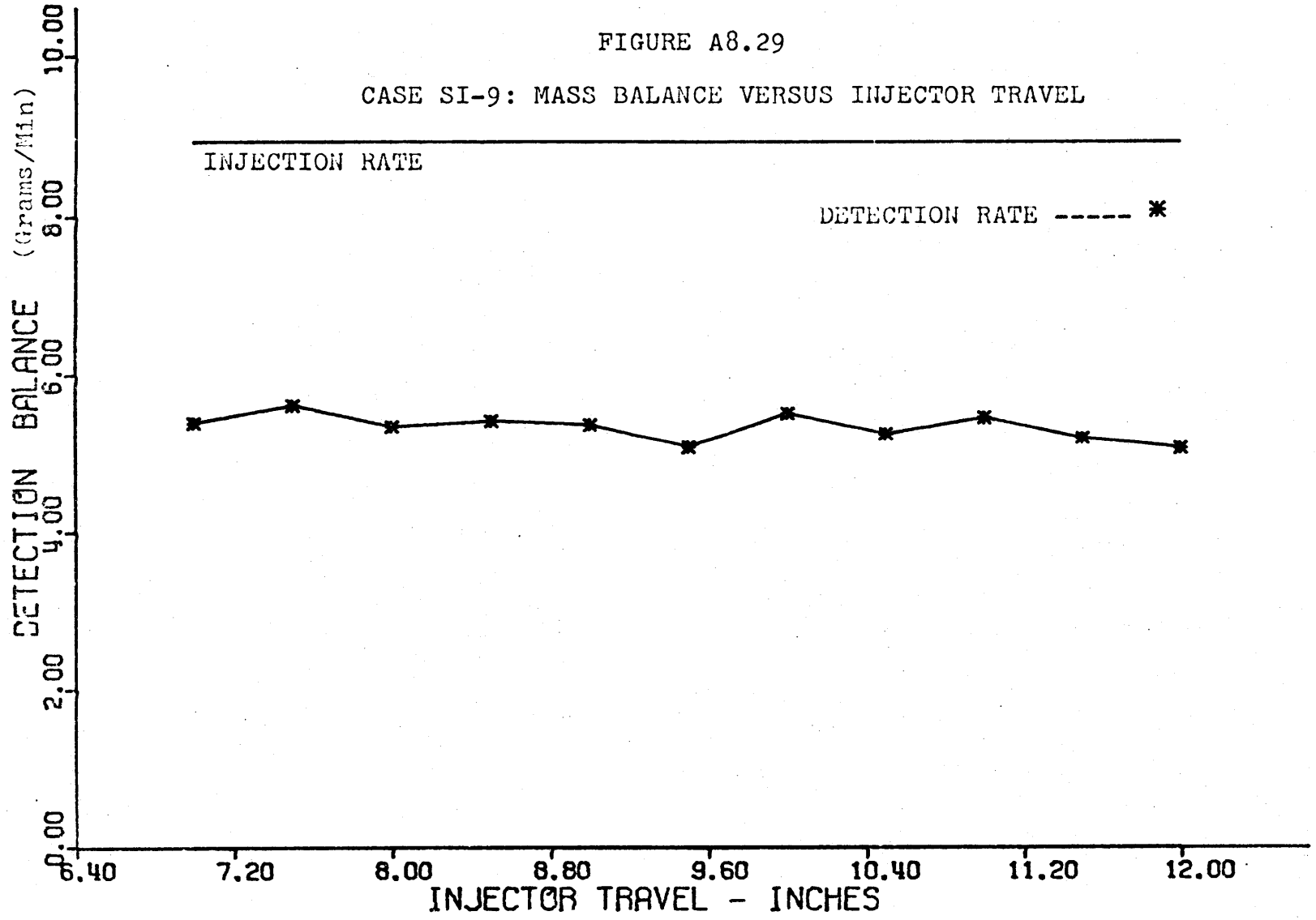

FIGURE A8.30

CASE SI-9: AXIAL TRACER CONCENTRATION, SUBCHANNELS 2, 1, 3, 4

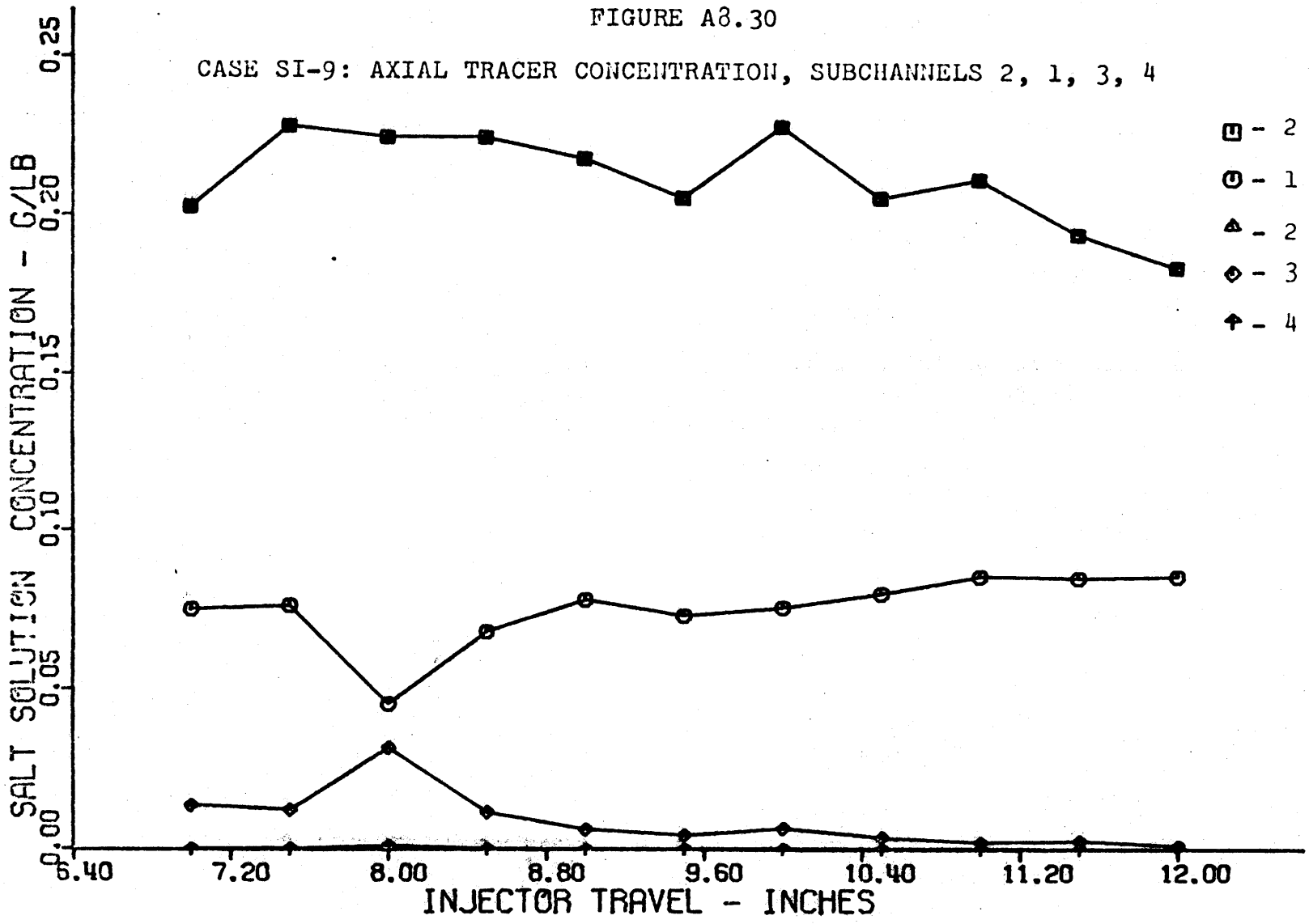

FIGURE A8.31

CASE SI-9: AXIAL TRACER CONCENTRATIONS, SUBCHANNELS 2, 5, 6, 7, 8

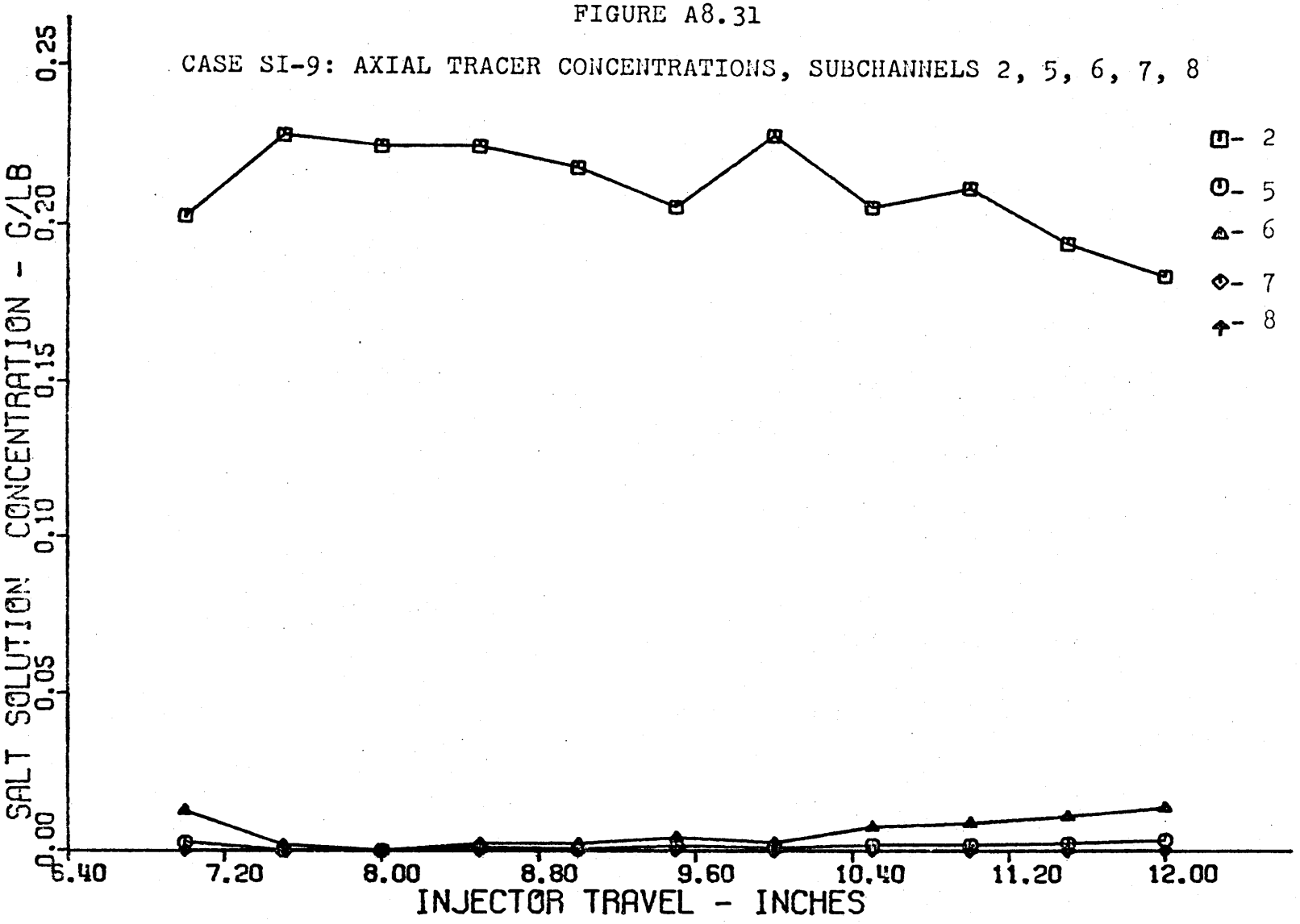

FIGURE A8.32

CASE S CASE SP-1: MASS BALANCE VERSUS INJECTOR TRAVEL

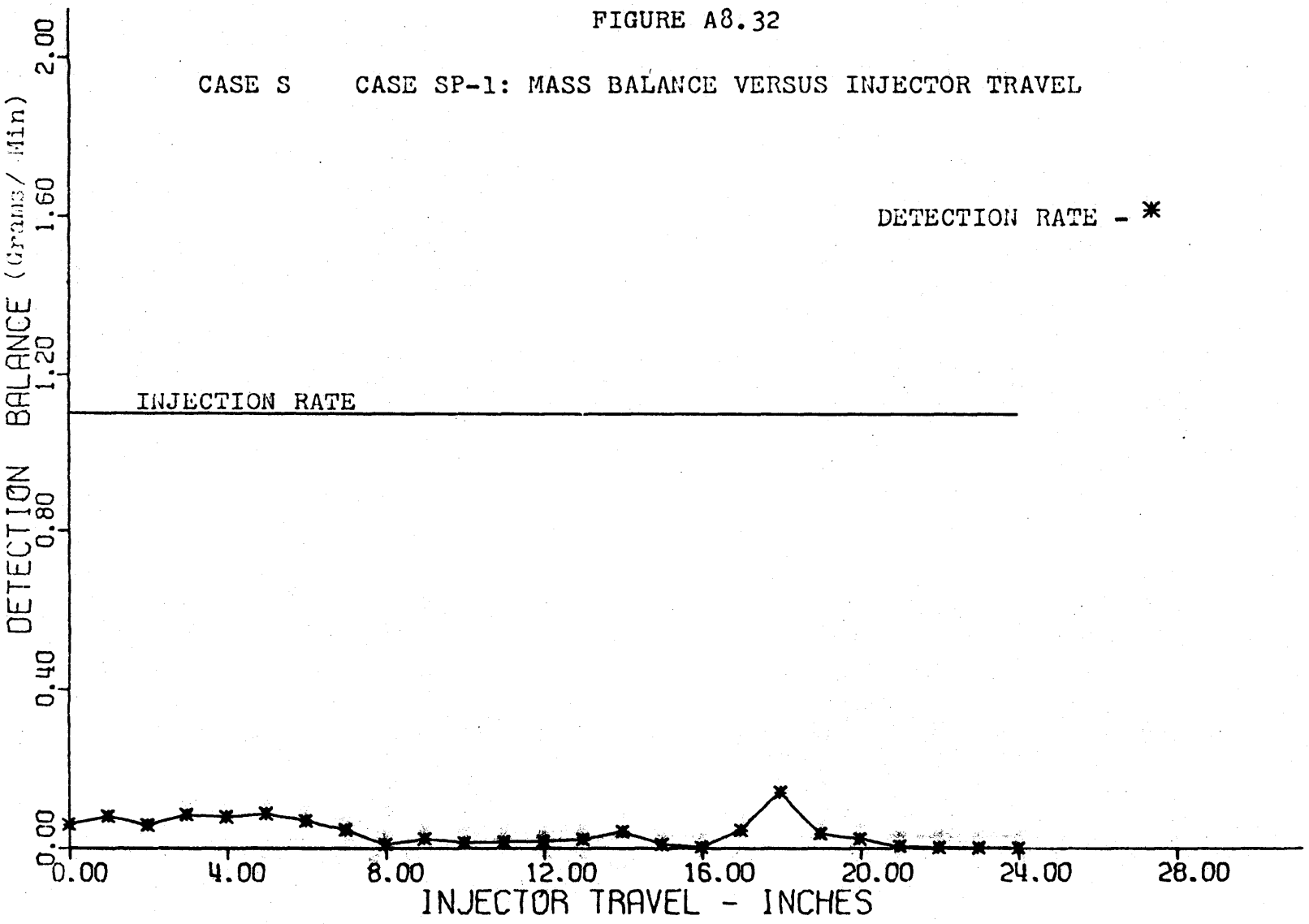

FIGURE A8.33

CASE SP-1: AXIAL TRACER CONCENTRATION, SUBCHANNELS 29,30,31,32

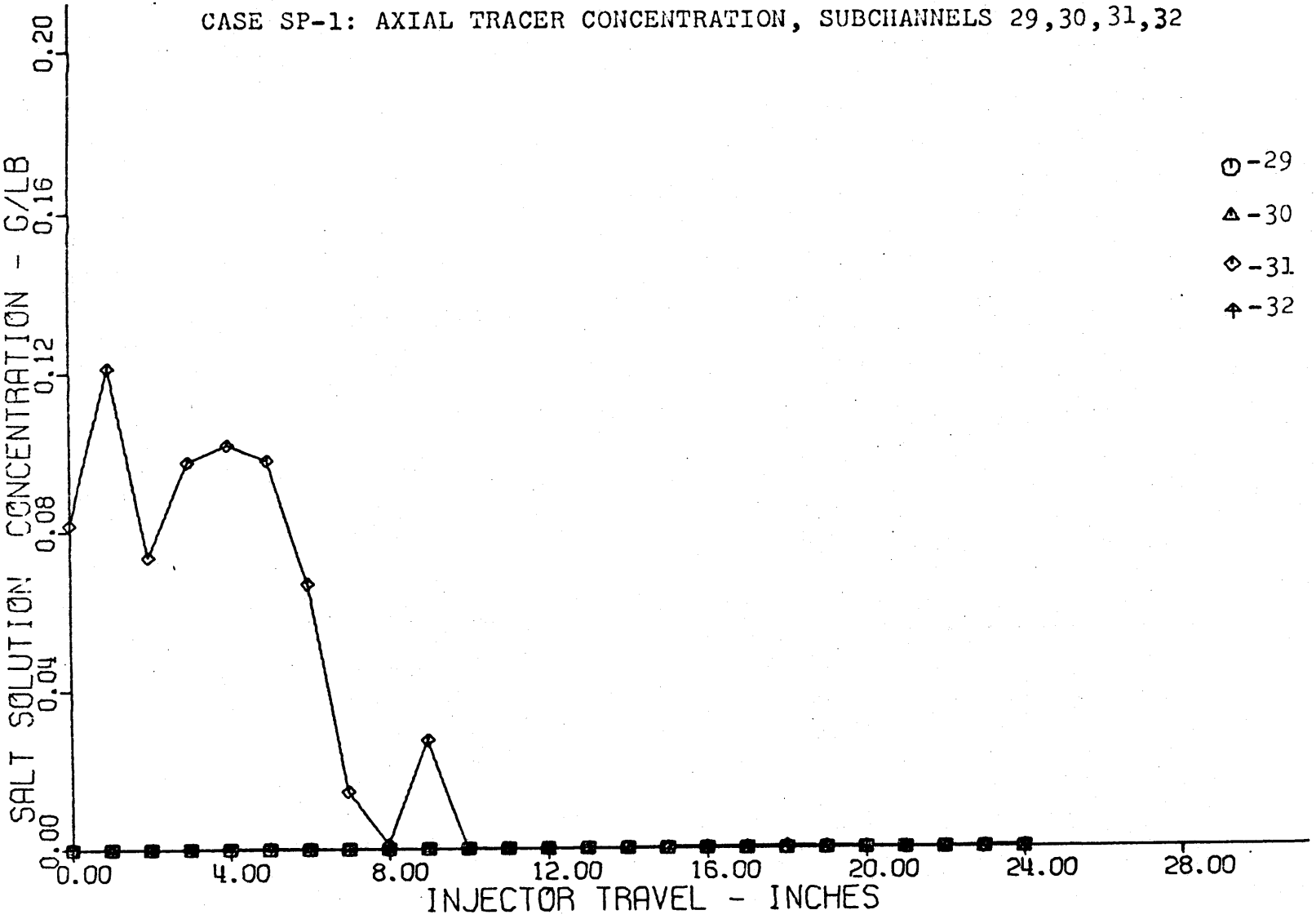

FIGURE A8.34

CASE SP-1: AXIAL TRACER CONCENTRATION, SUBCHANNELS 48,45,46,47

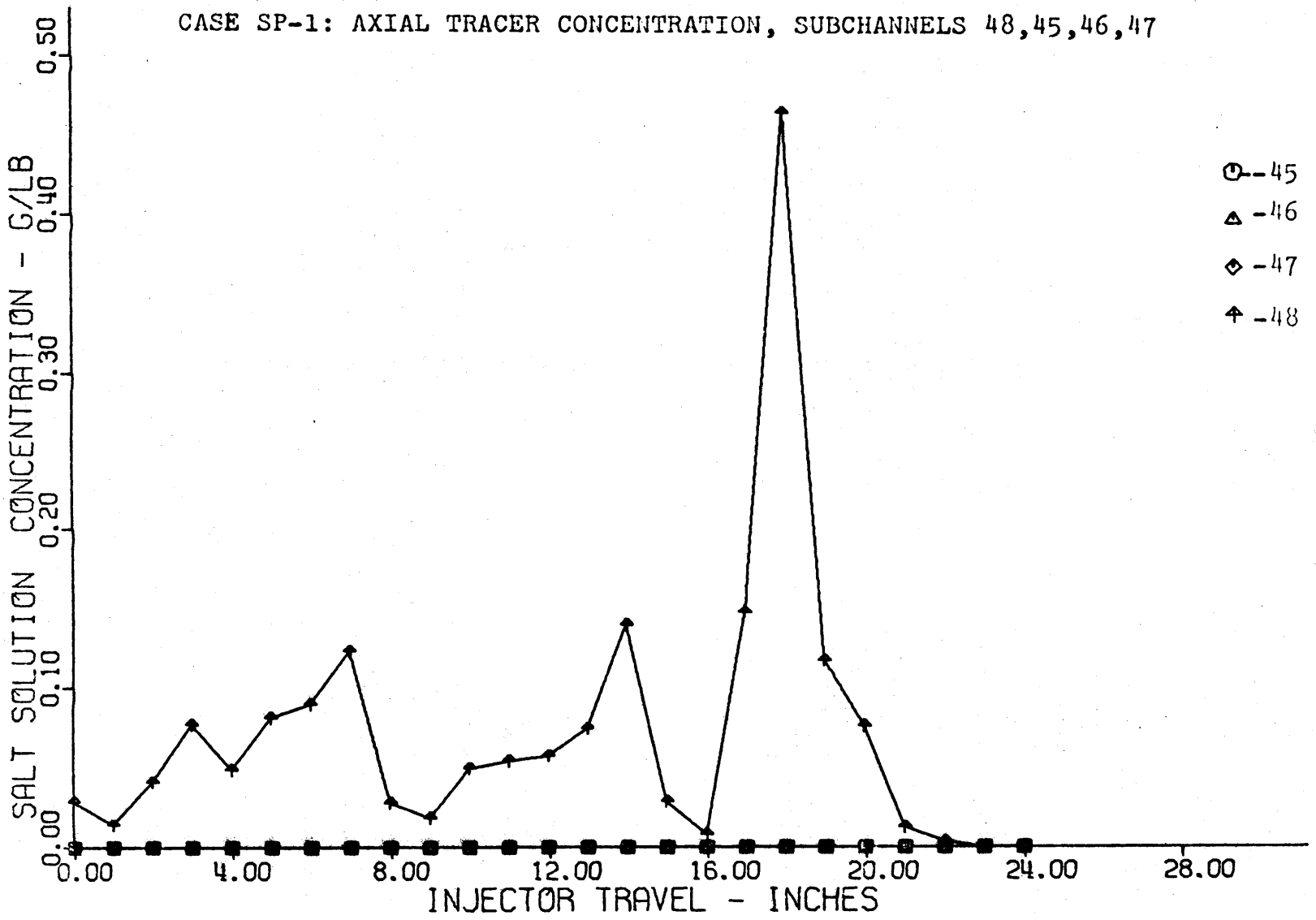

FIGURE A8.35

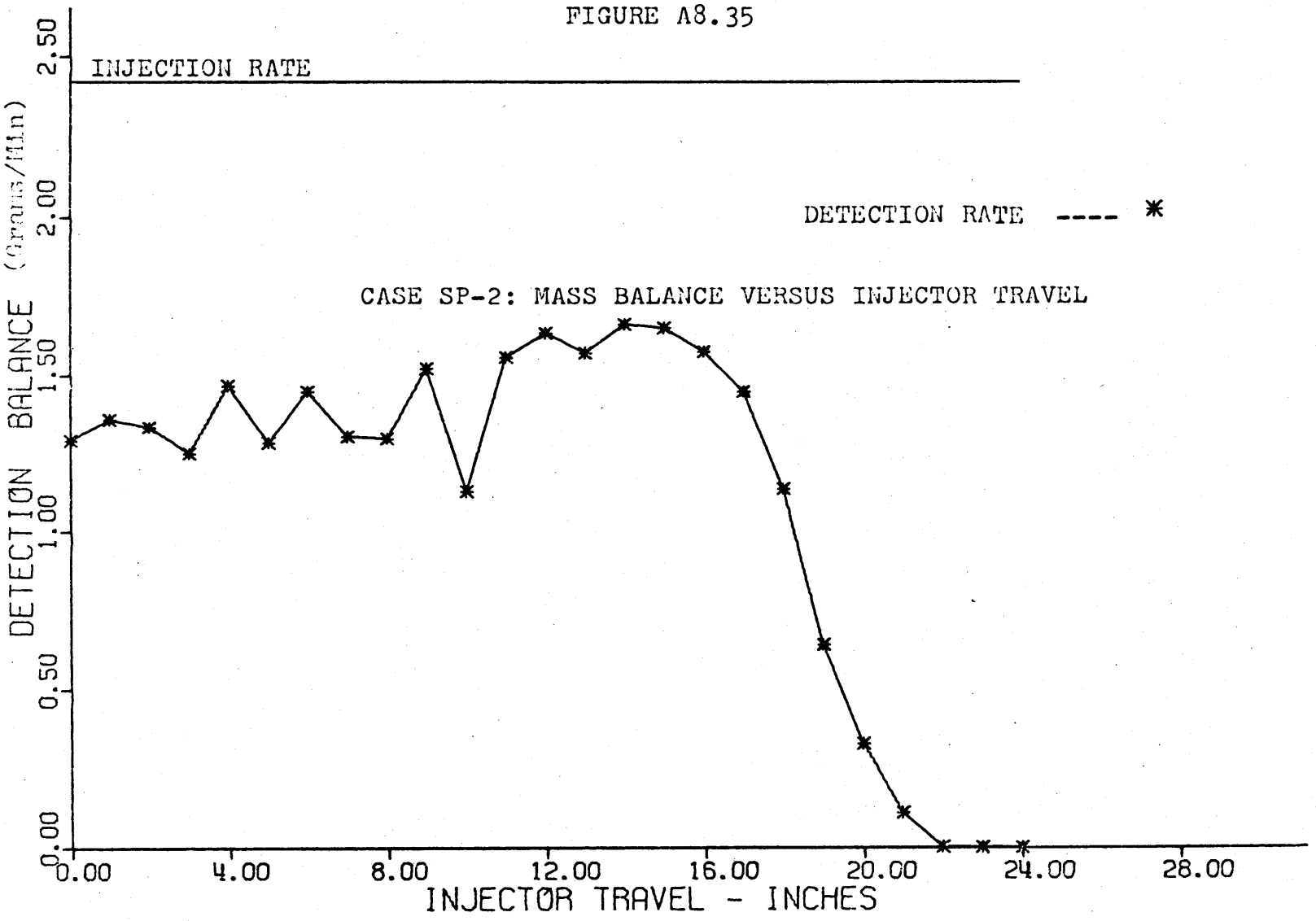
INJECTION RATE
DETECTION RATE ---- *
CASE SP-2: MASS BALANCE VERSUS INJECTOR TRAVEL
DETECTION BALANCE (Grams/Min)
2.50
2.00
1.50
1.00
0.50
0.00
0.00
4.00
8.00
12.00
16.00
20.00
24.00
28.00
INJECTOR TRAVEL - INCHES

FIGURE A8.36

CASE SP-2: AXIAL TRACER CONCENTRATION, SUBCHANNELS 48,29,30,31,32

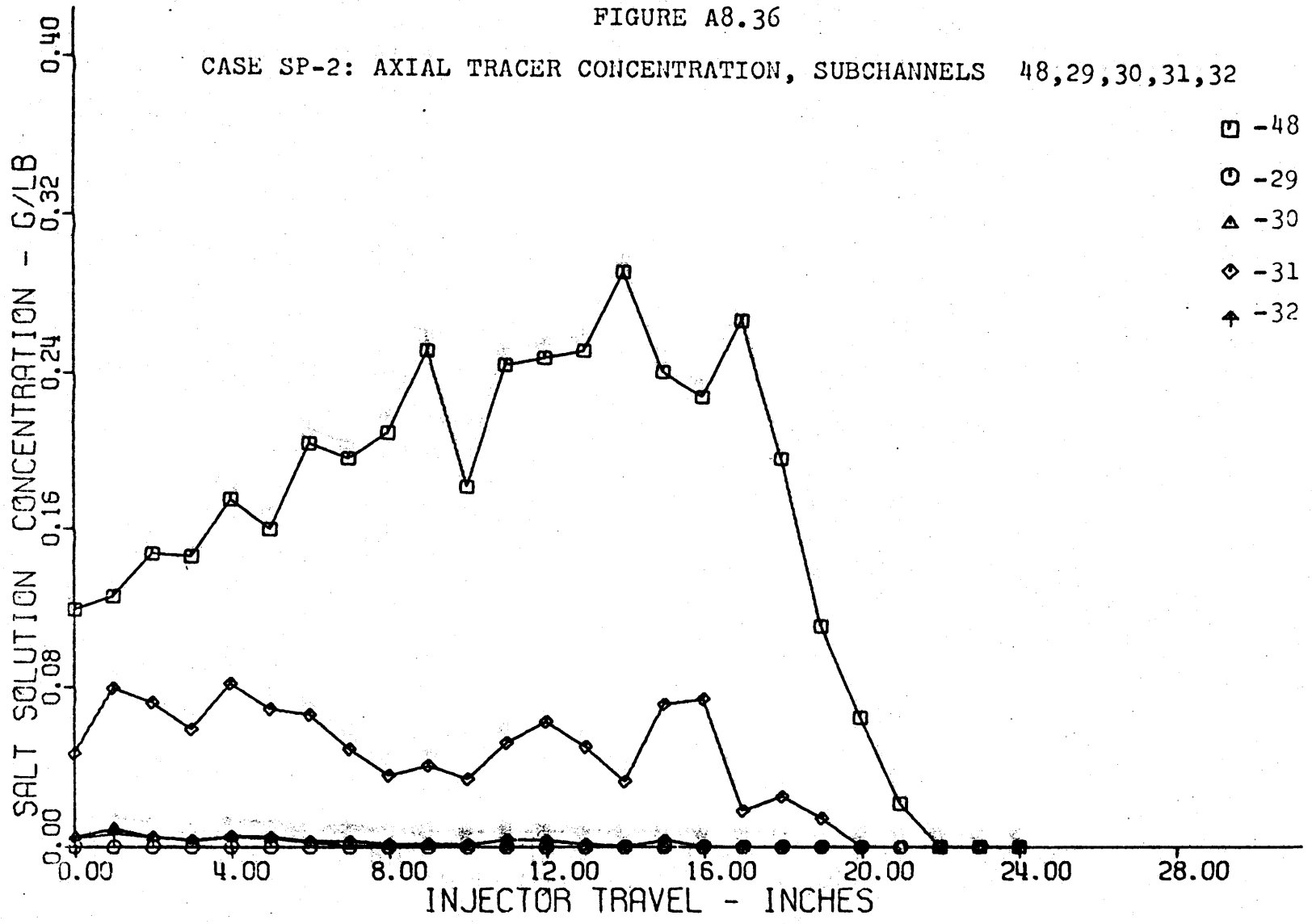

FIGURE A8.37

CASE SP-2: AXIAL TRACER CONCENTRATION, SUBCHANNELS 48,45,46,47

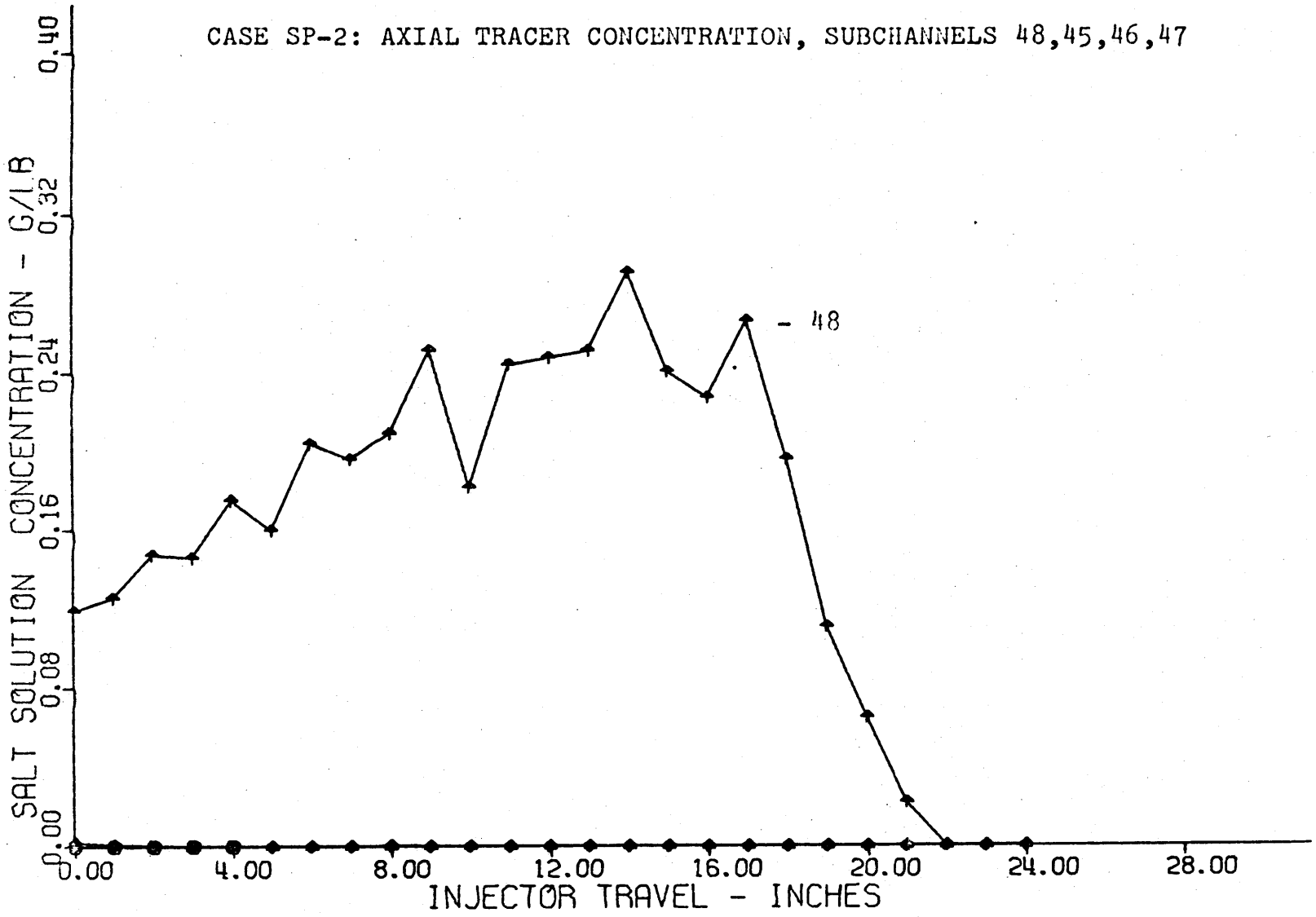

FIGURE A8.38

CASE SP-2: AXIAL TRACER CONCENTRATION, SUBCHANNELS 48,49,50,51,52

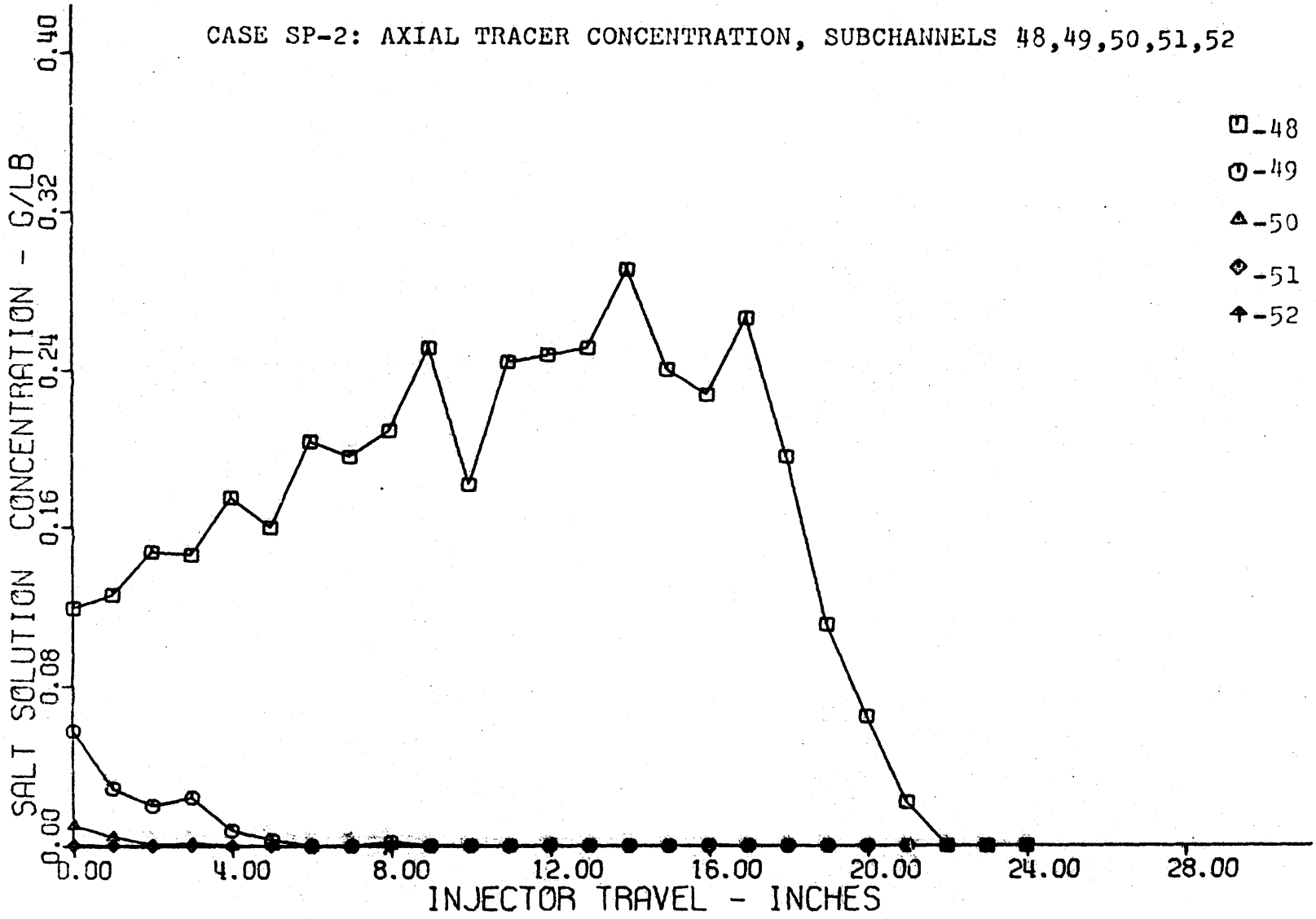

FIGURE A8.39

CASE SP-4: MASS BALANCE VERSUS INJECTOR TRAVEL

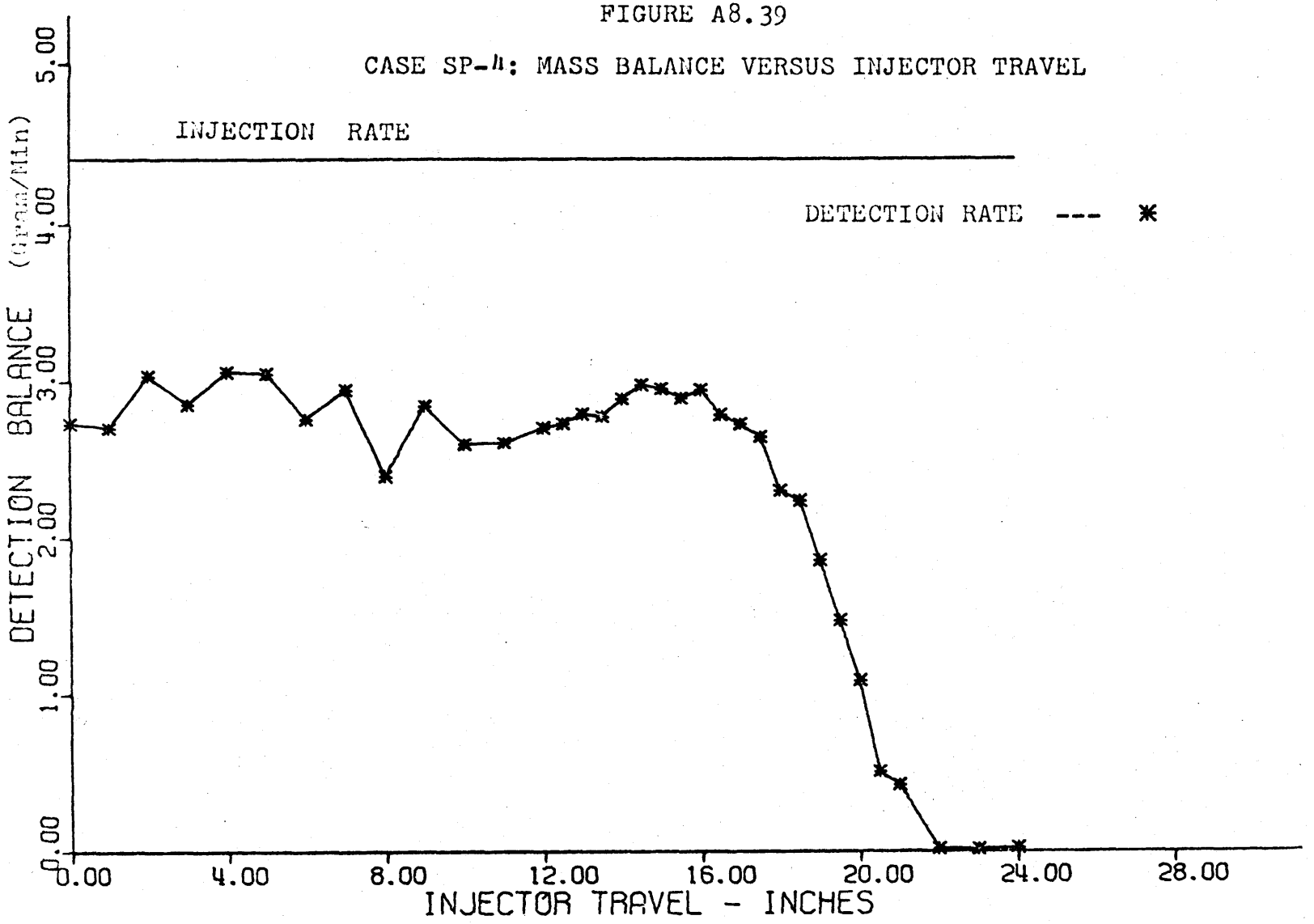

FIGURE A8.40

CASE SP-4: AXIAL TRACER CONCENTRATION, SUBCHANNELS 48,29,30,31,32

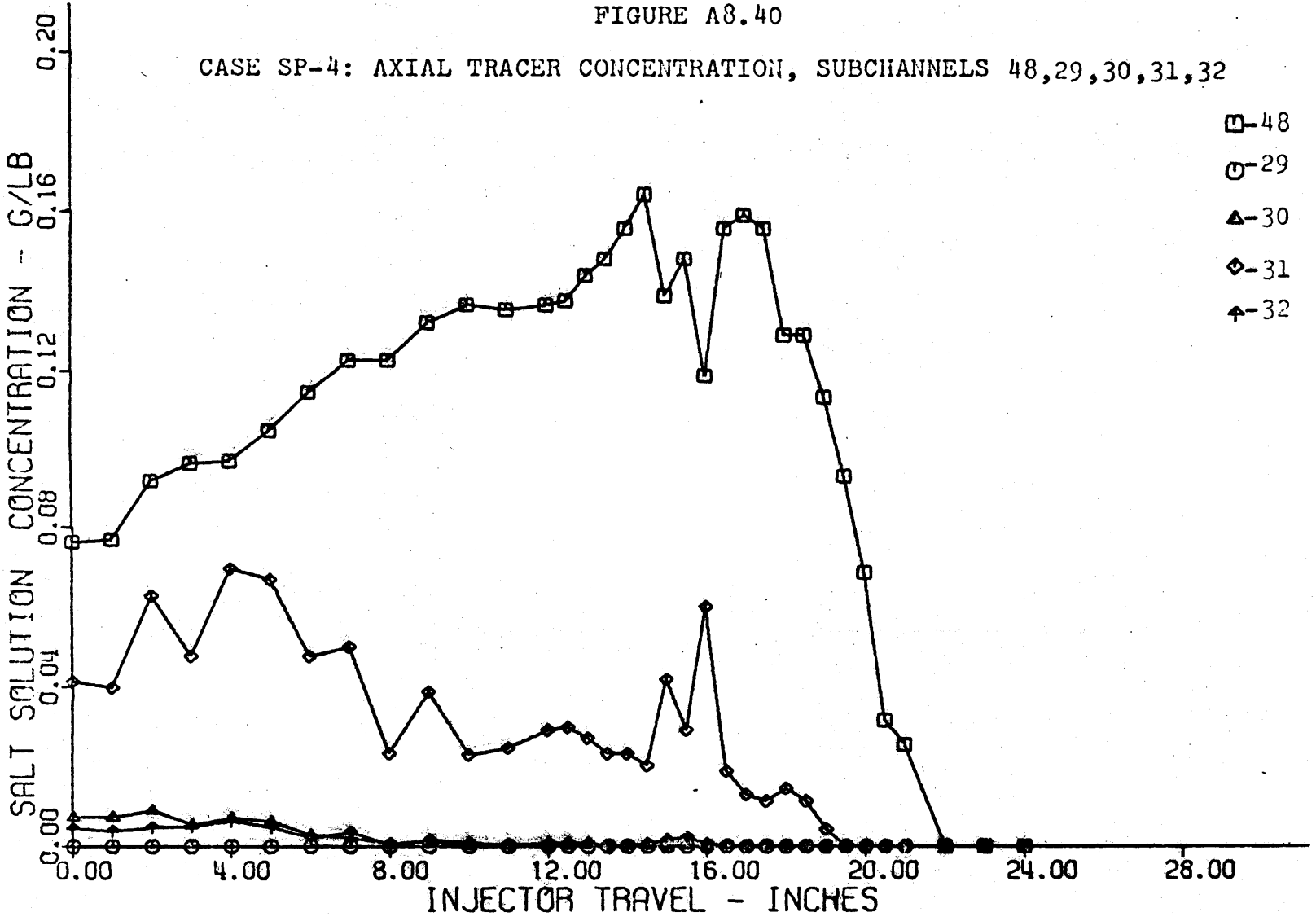

FIGURE A8.41

CASE SP-4: AXIAL TRACER CONCENTRATION, SUBCHANNELS 48,49,50,51,52

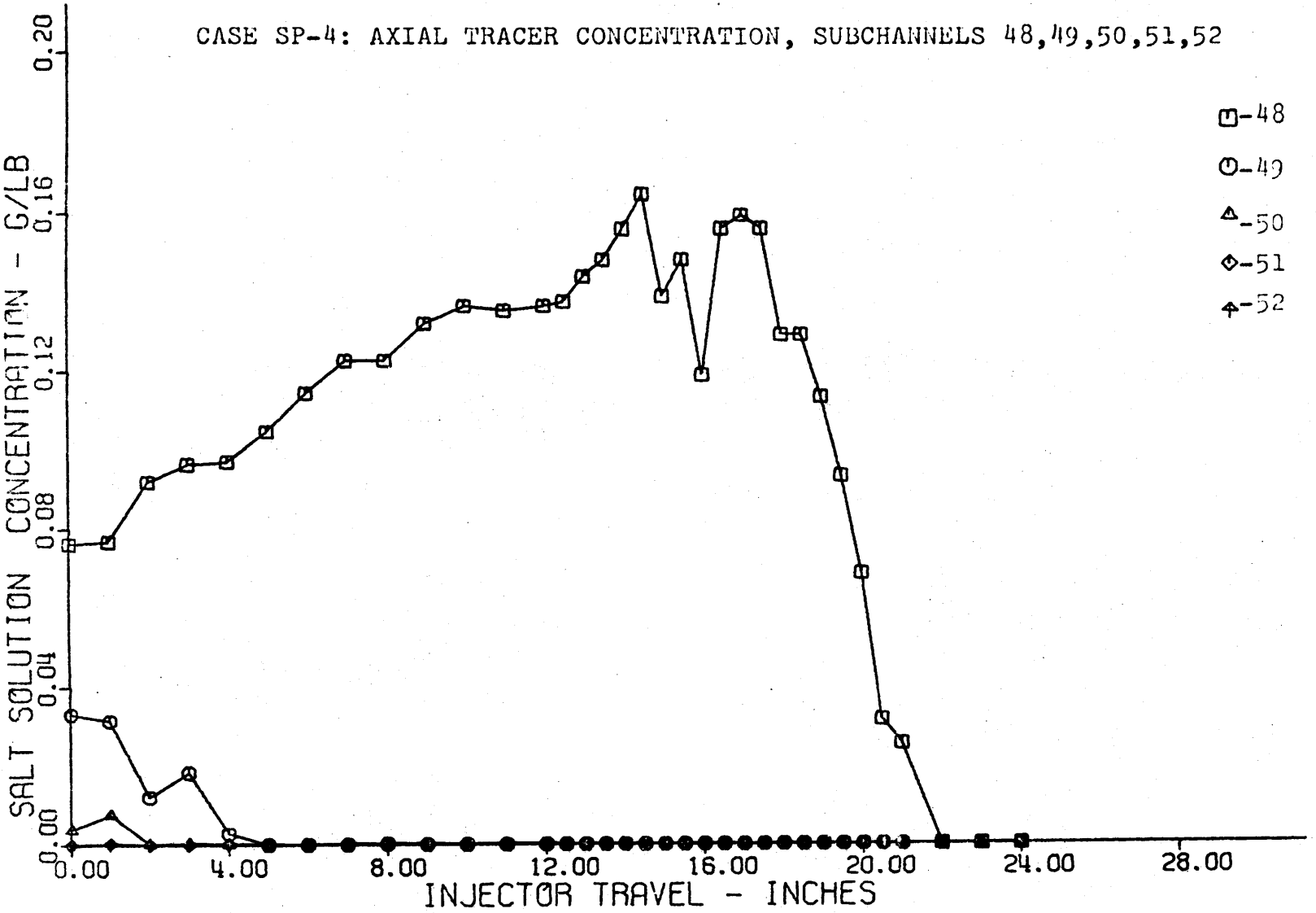

FIGURE A8.42

CASE SP-5: MASS BALANCE VERSUS INJECTOR TRAVEL (Experimental)

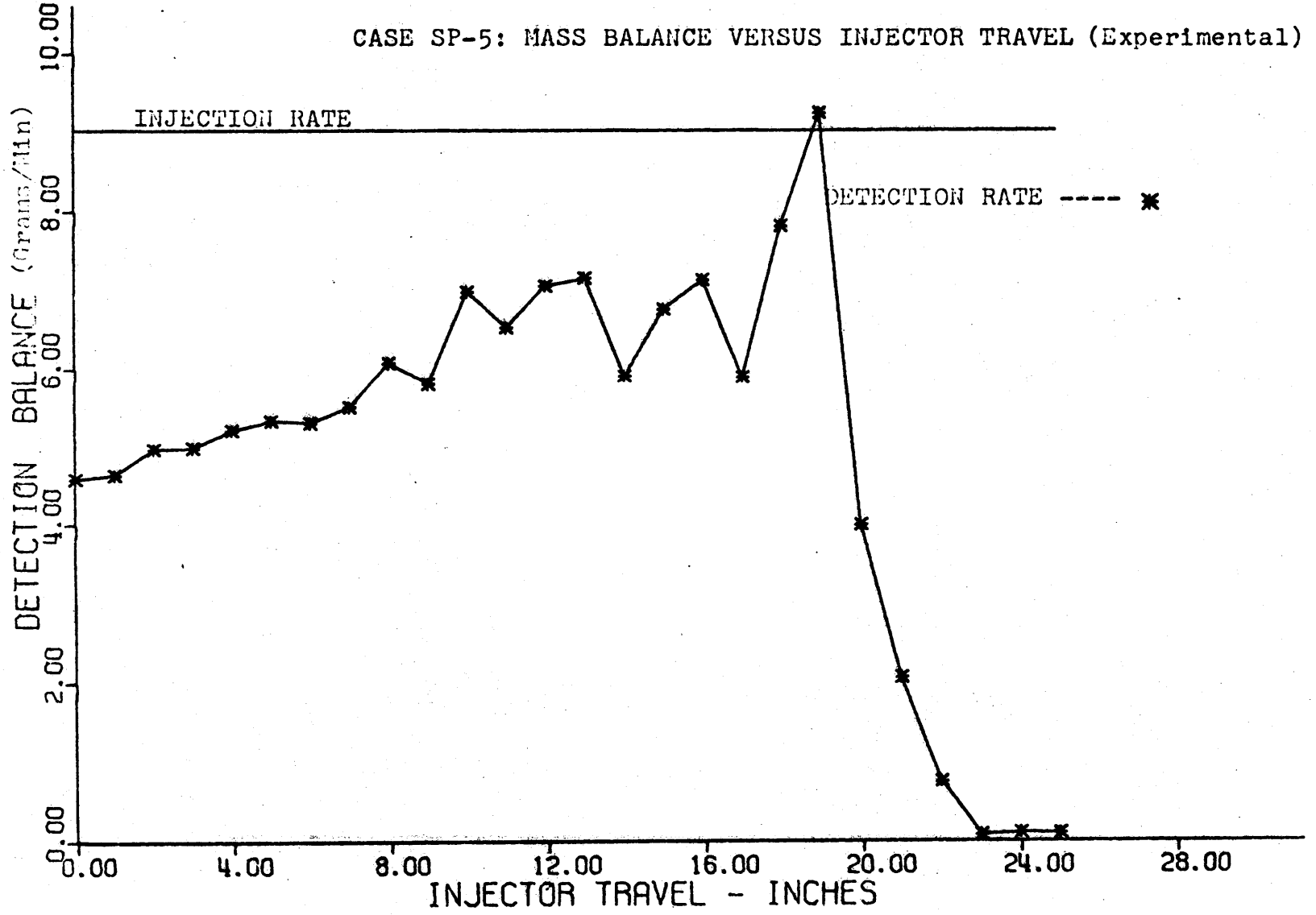

FIGURE A8.43

CASE SP-5: MASS BALANCE VERSUS INJECTOR TRAVEL (Analytical)

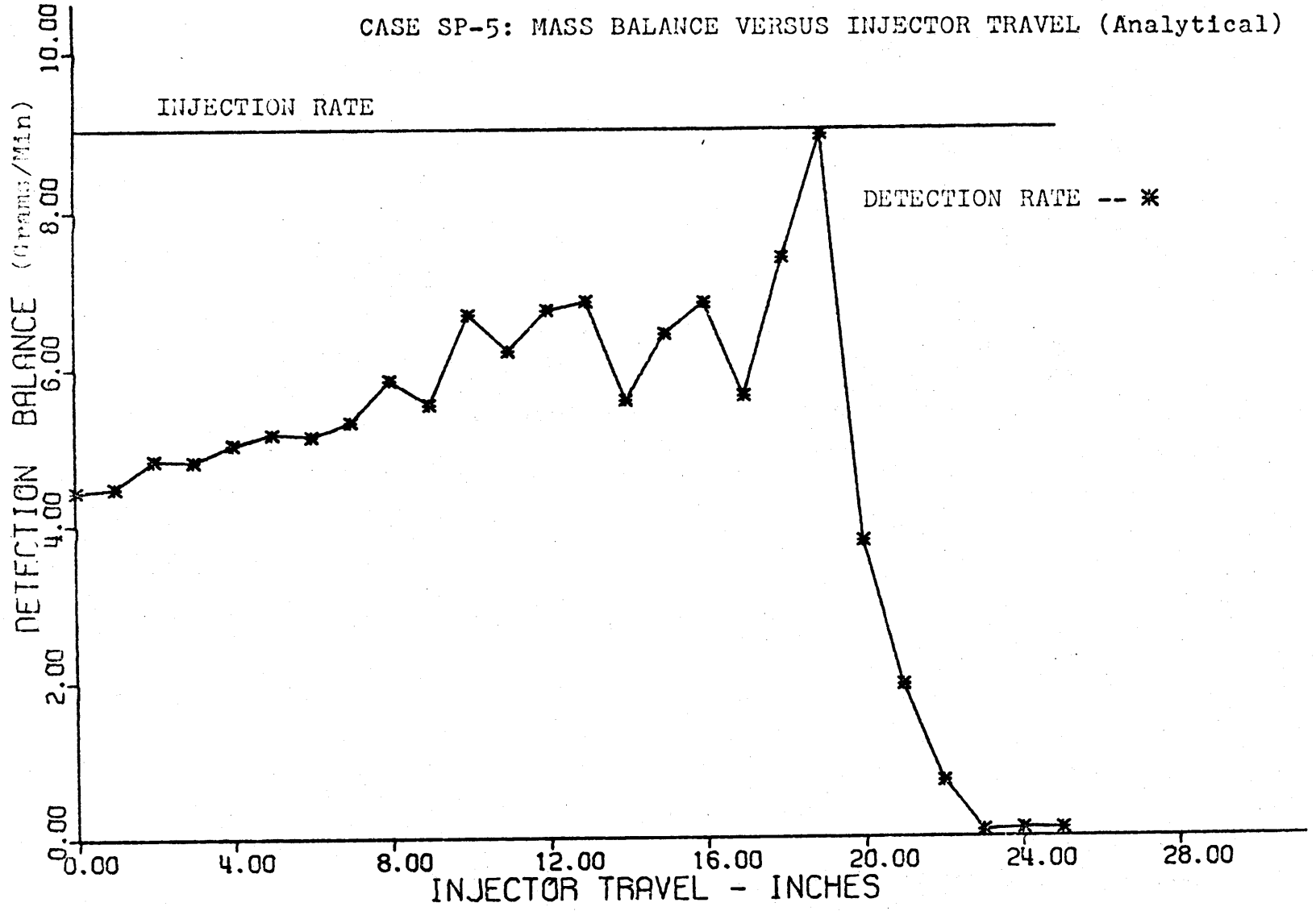

FIGURE A8.44

CASE SP-5: AXIAL TRACER CONCENTRATION, SUBCHANNELS 48,29,30,31,32

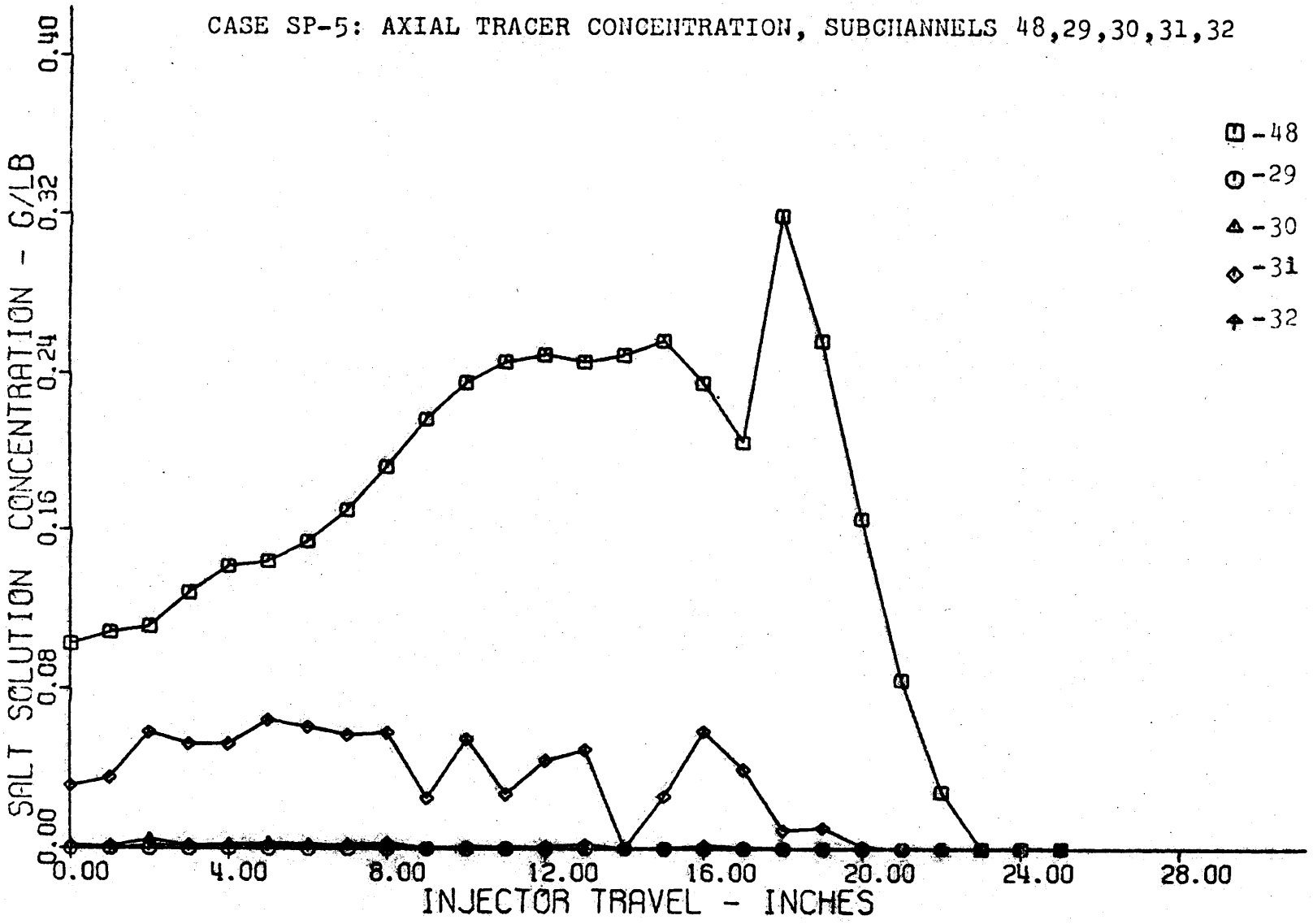

FIGURE A8.45

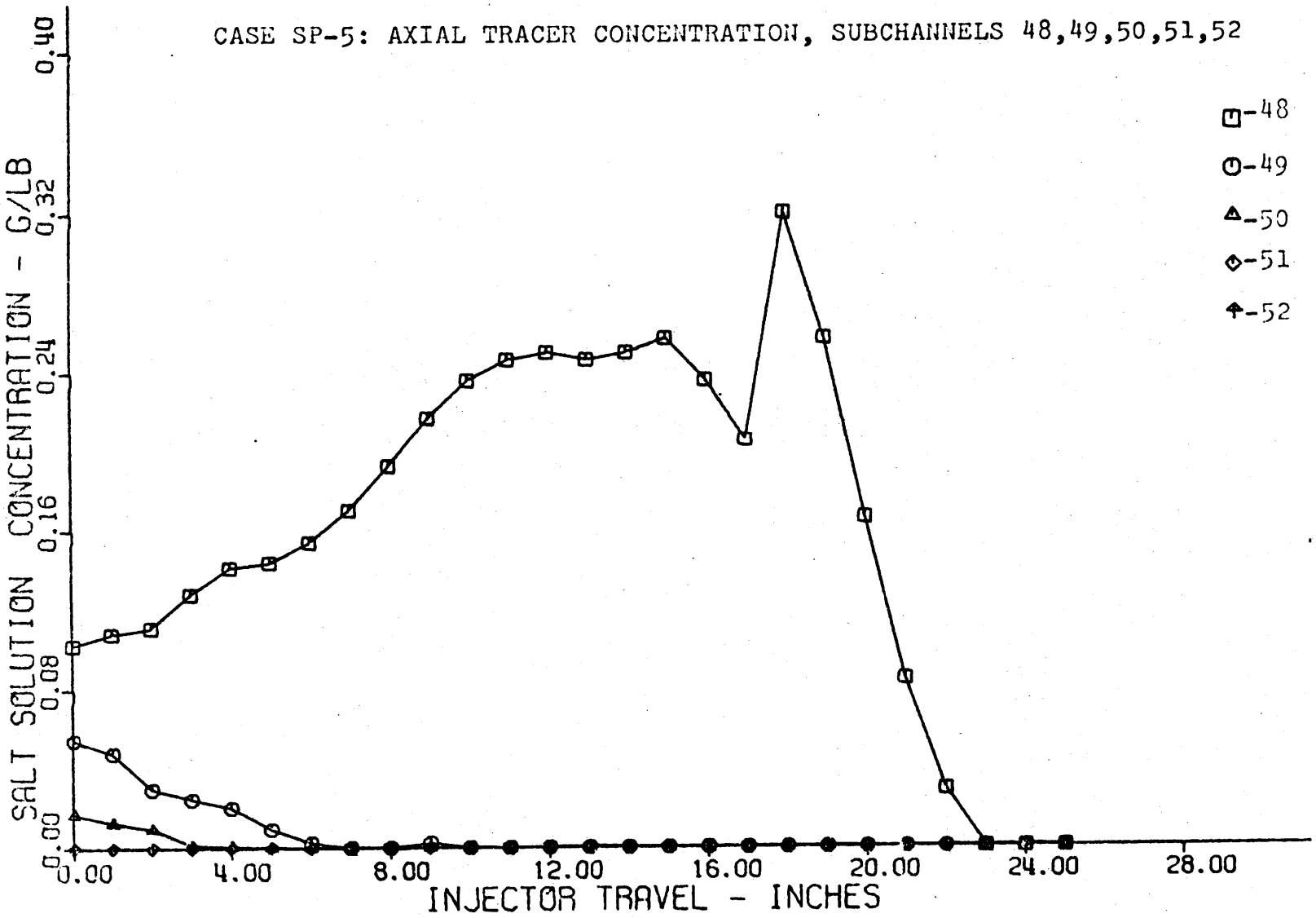
CASE SP-5: AXIAL TRACER CONCENTRATION, SUBCHANNELS 48,49,50,51,52
SALT SOLUTION CONCENTRATION - G/LB
0.00
0.08
0.16
0.24
0.32
0.40
0.00
4.00
8.00
12.00
16.00
20.00
24.00
28.00
INJECTOR TRAVEL - INCHES
-48
-49
-50
-51
-52

FIGURE A8.46

CASE SP-6: MASS BALANCE VERSUS INJECTOR TRAVEL

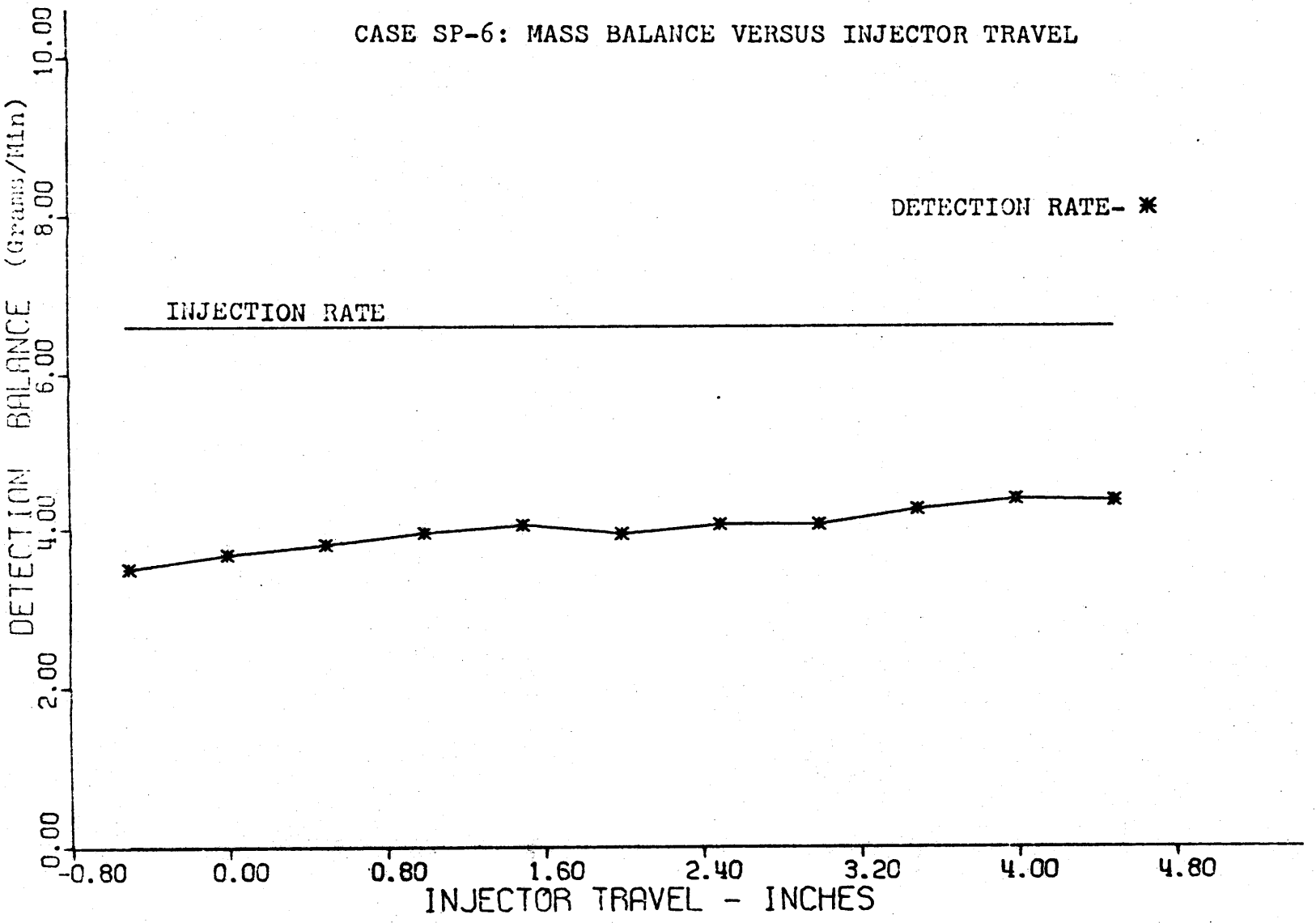

FIGURE A8.47

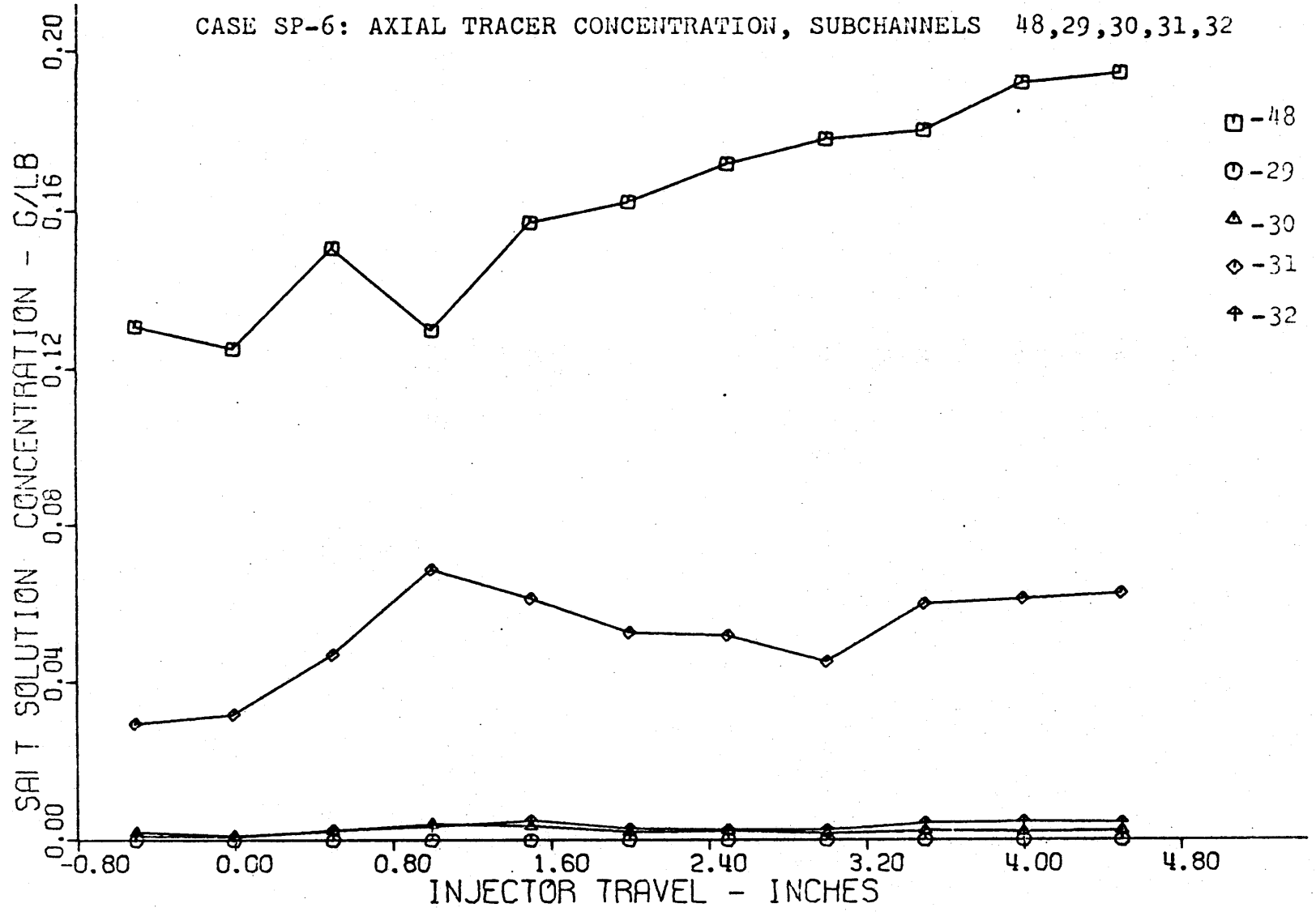
CASE SP-6: AXIAL TRACER CONCENTRATION, SUBCHANNELS 48,29,30,31,32
SALT SOLUTION CONCENTRATION - G/LB
0.00
0.04
0.08
0.12
0.16
0.20
-0.80
0.00
0.80
1.60
2.40
3.20
4.00
4.80
INJECTOR TRAVEL - INCHES
-48
-29
-30
-31
-32

FIGURE A8.48

CASE SP-6: AXIAL TRACER CONCENTRATION, SUBCHANNELS 48,45,46,47

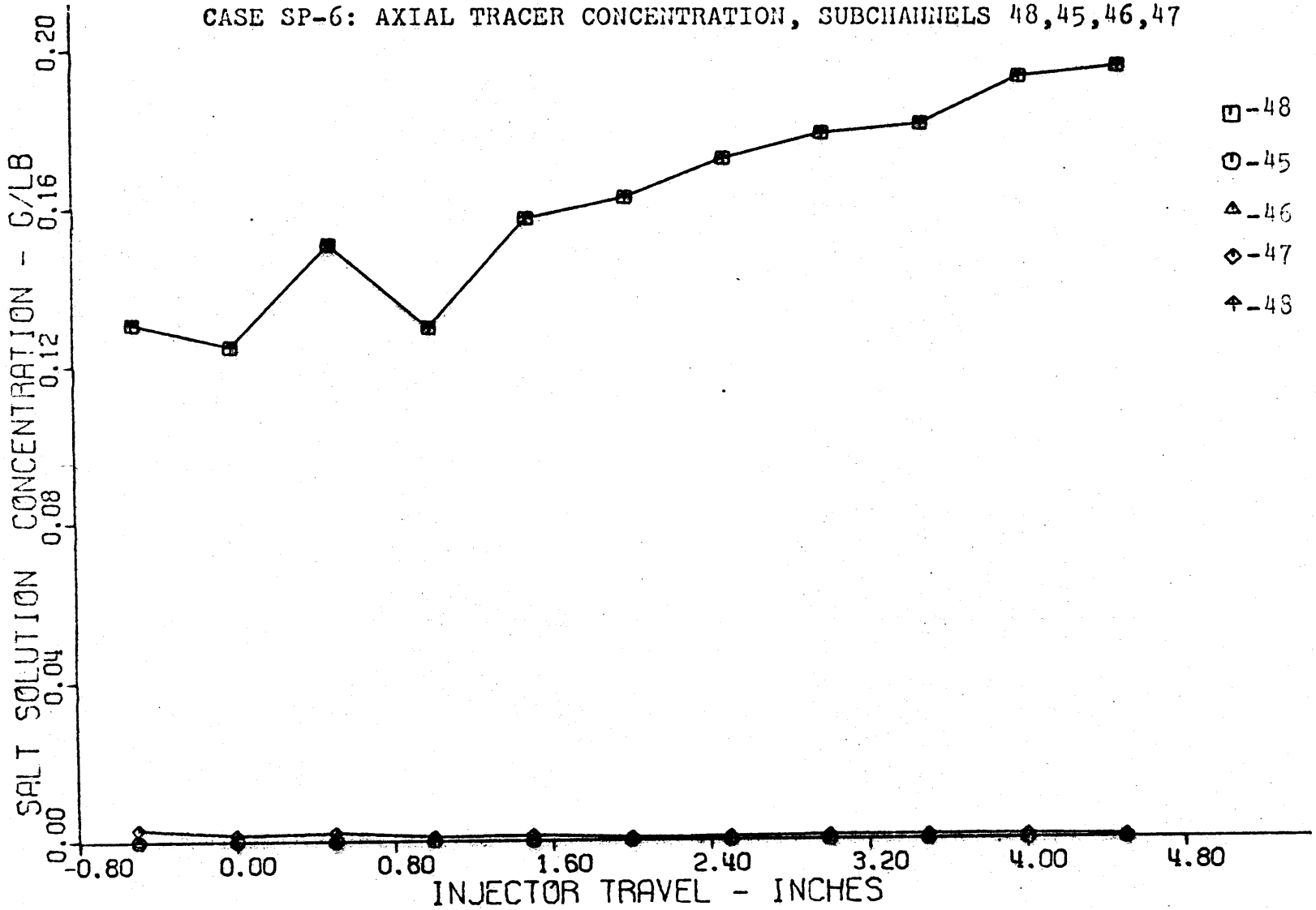

FIGURE A8.49

CASE SP-6: AXIAL TRACER CONCENTRATION, SUBCHANNELS 48,49,50,51,52

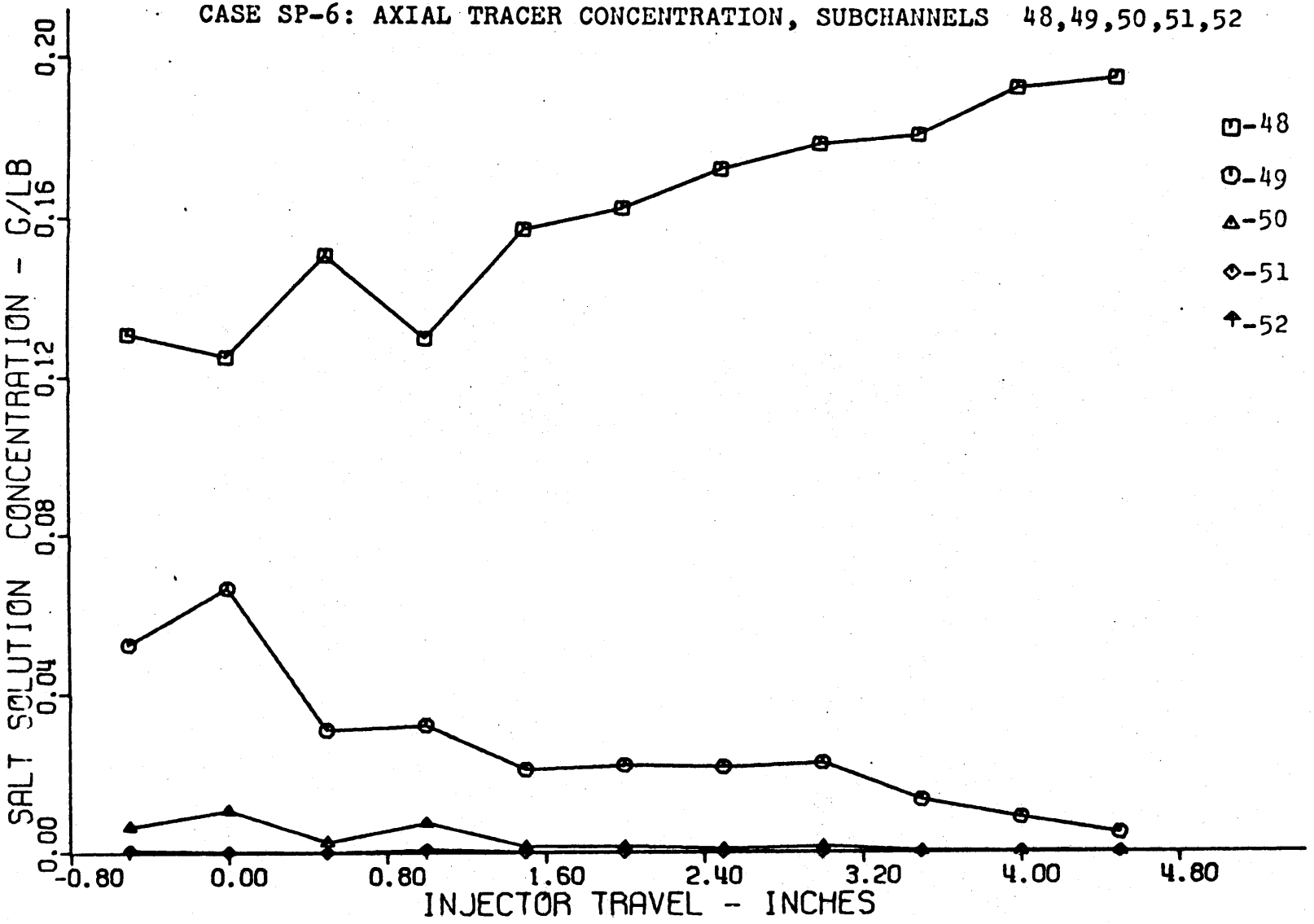

FIGURE A8.50

CASE SP-7: MASS BALANCE VERSUS INJECTOR TRAVEL

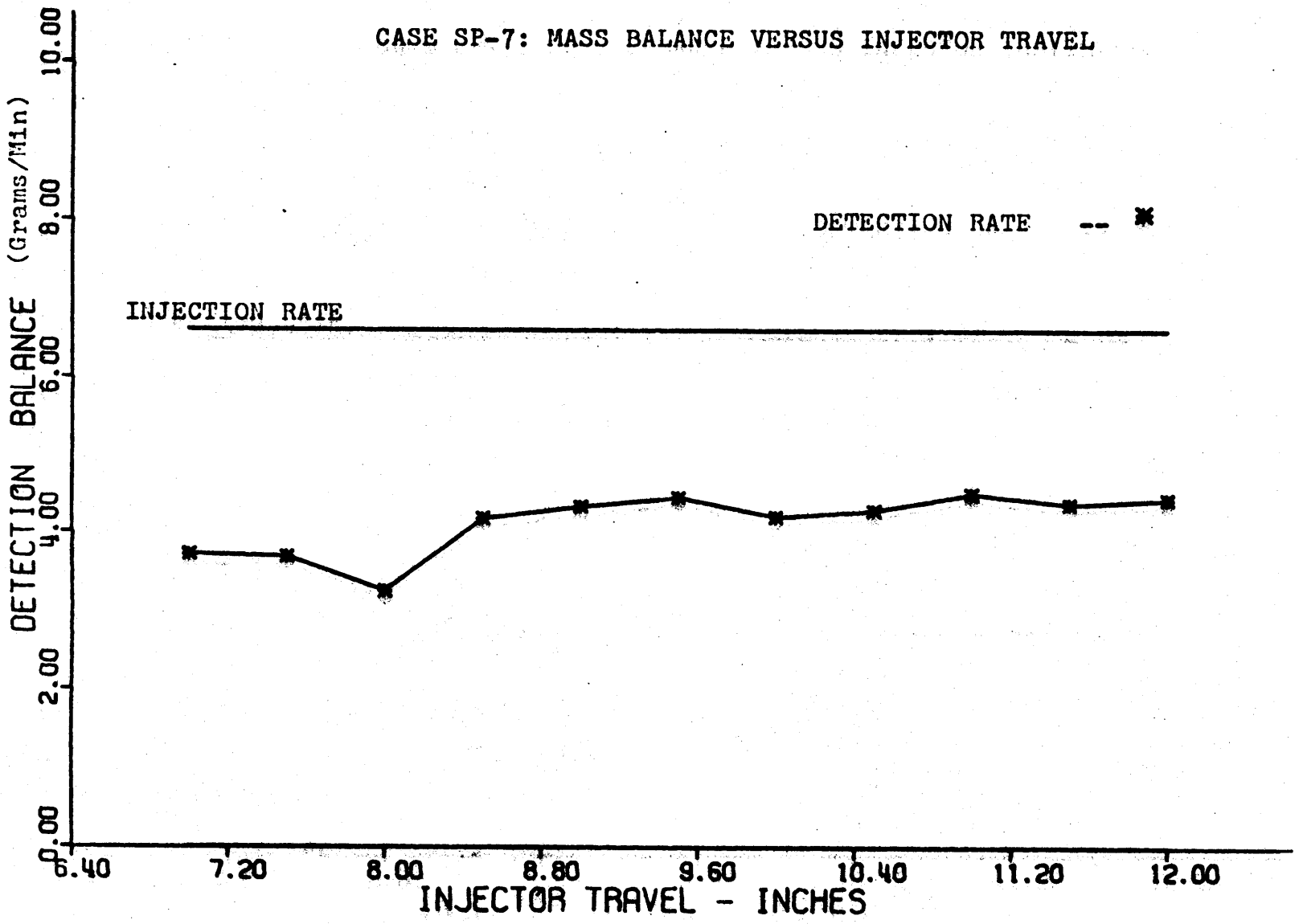

FIGURE A8.51

CASE SP-7: AXIAL TRACER CONCENTRATION, SUBCHANNELS 48,29,30,31,32

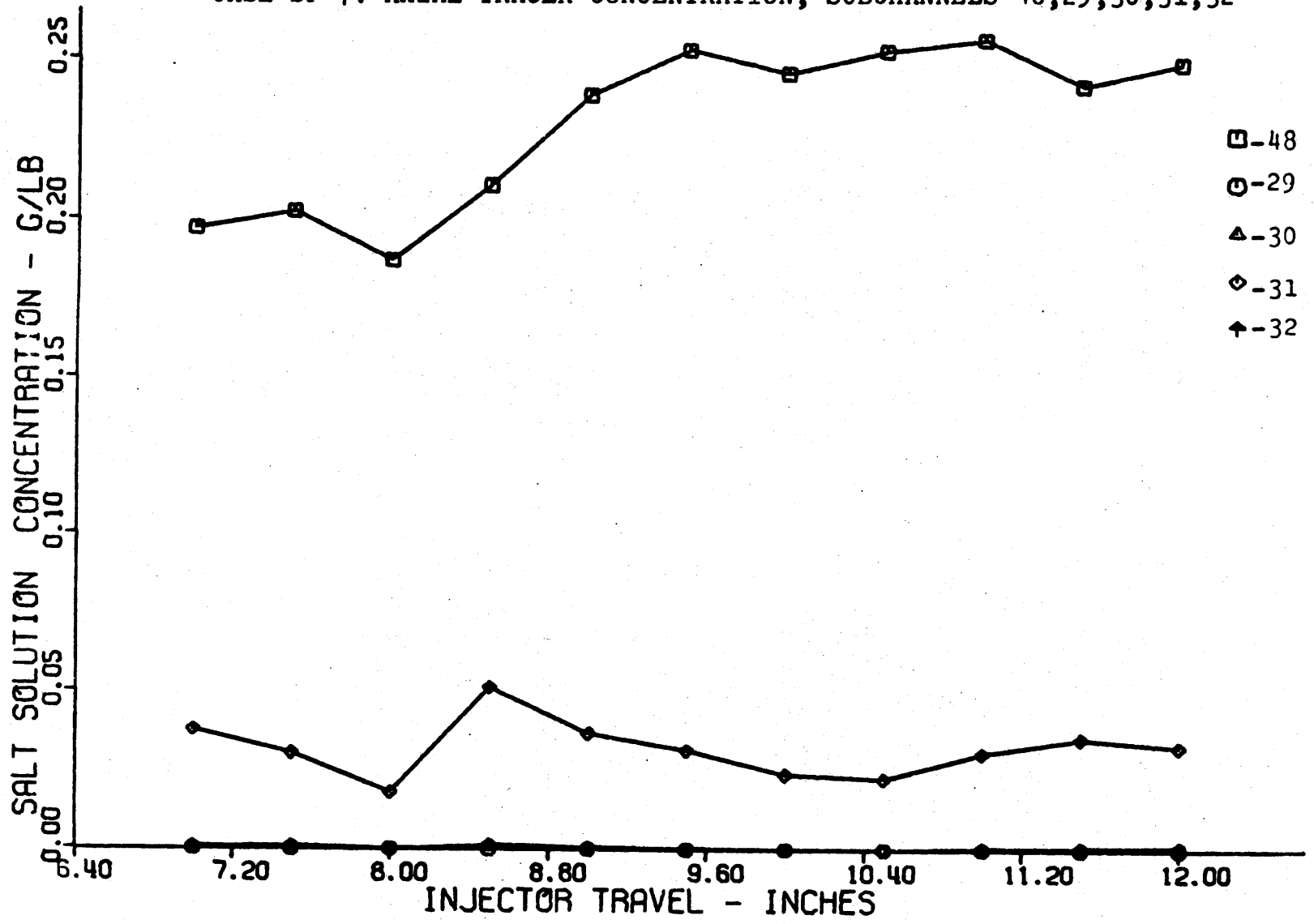

TABLE A8.2

A LIST OF FIGURES OF INTERCHANNEL COOLANT MIXING EXPERIMENT RESULTS

----- ROUGH ROD ARRAY, INTERIOR SUBCHANNEL INJECTION -----

TABLE A8.2 (Continued)

TABLE A8.2 (Continued)

TABLE A8.2 (Concluded)

FIGURE A8.52

CASE RI-1: MASS BALANCE VERSUS INJECTOR TRAVEL

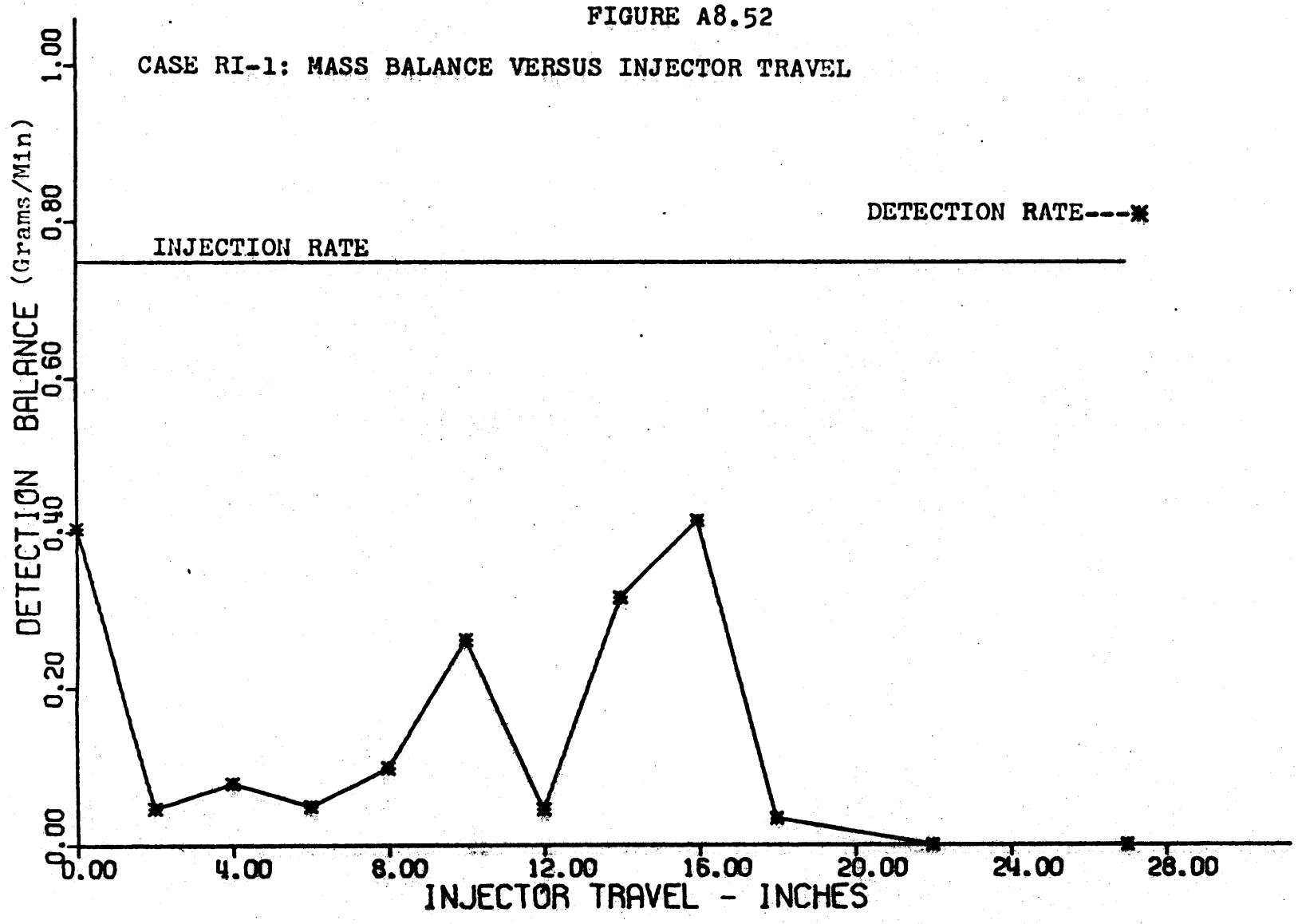

FIGURE A8.53

CASE RI-1: AXIAL TRACER CONCENTRATION, SUBCHANNELS 2, 1, 3, 4

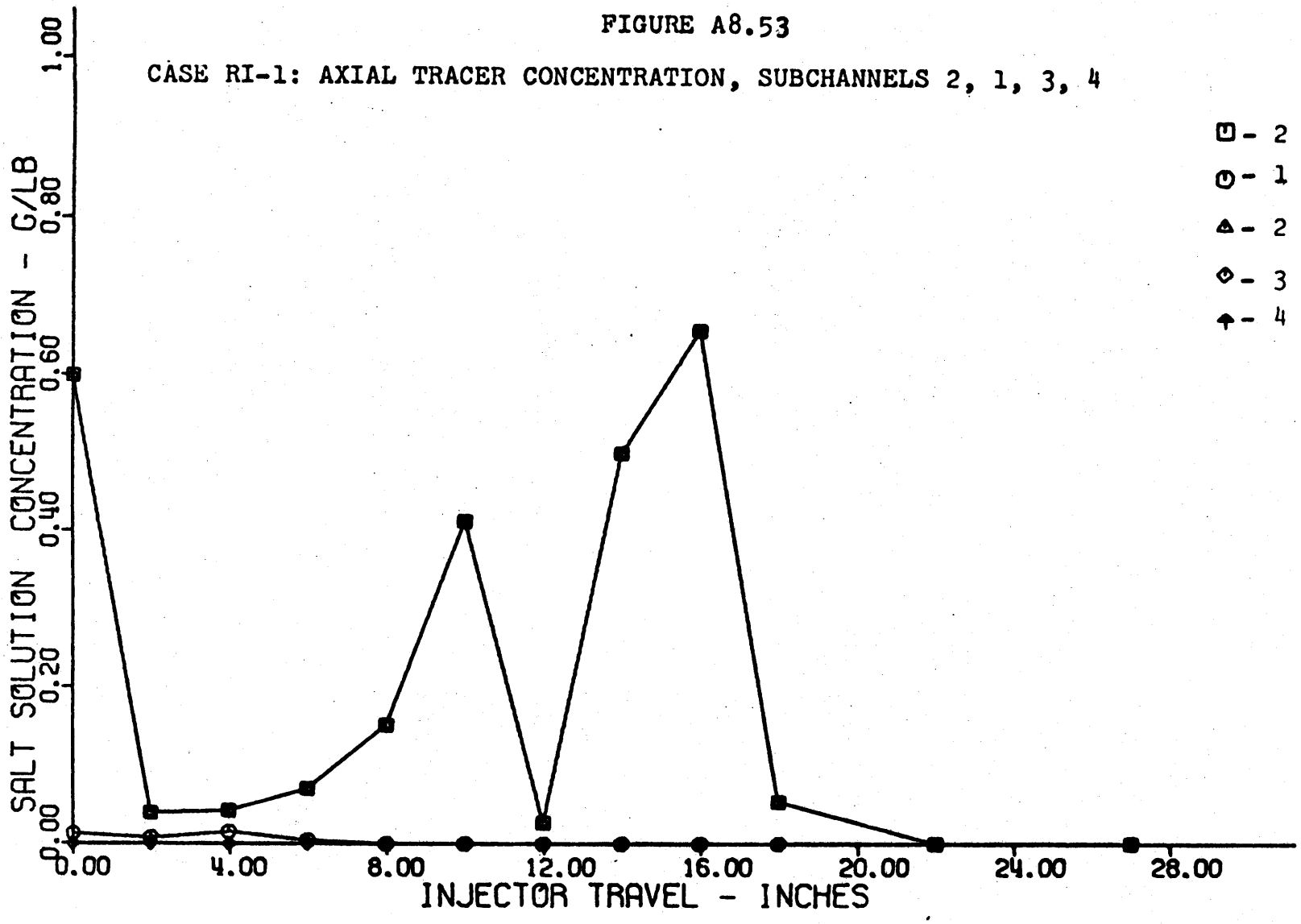

FIGURE A8.5

CASE RI-1: AXIAL TRACER CONCENTRATION, SUBCHANNELS 2, 5, 6, 7, 8

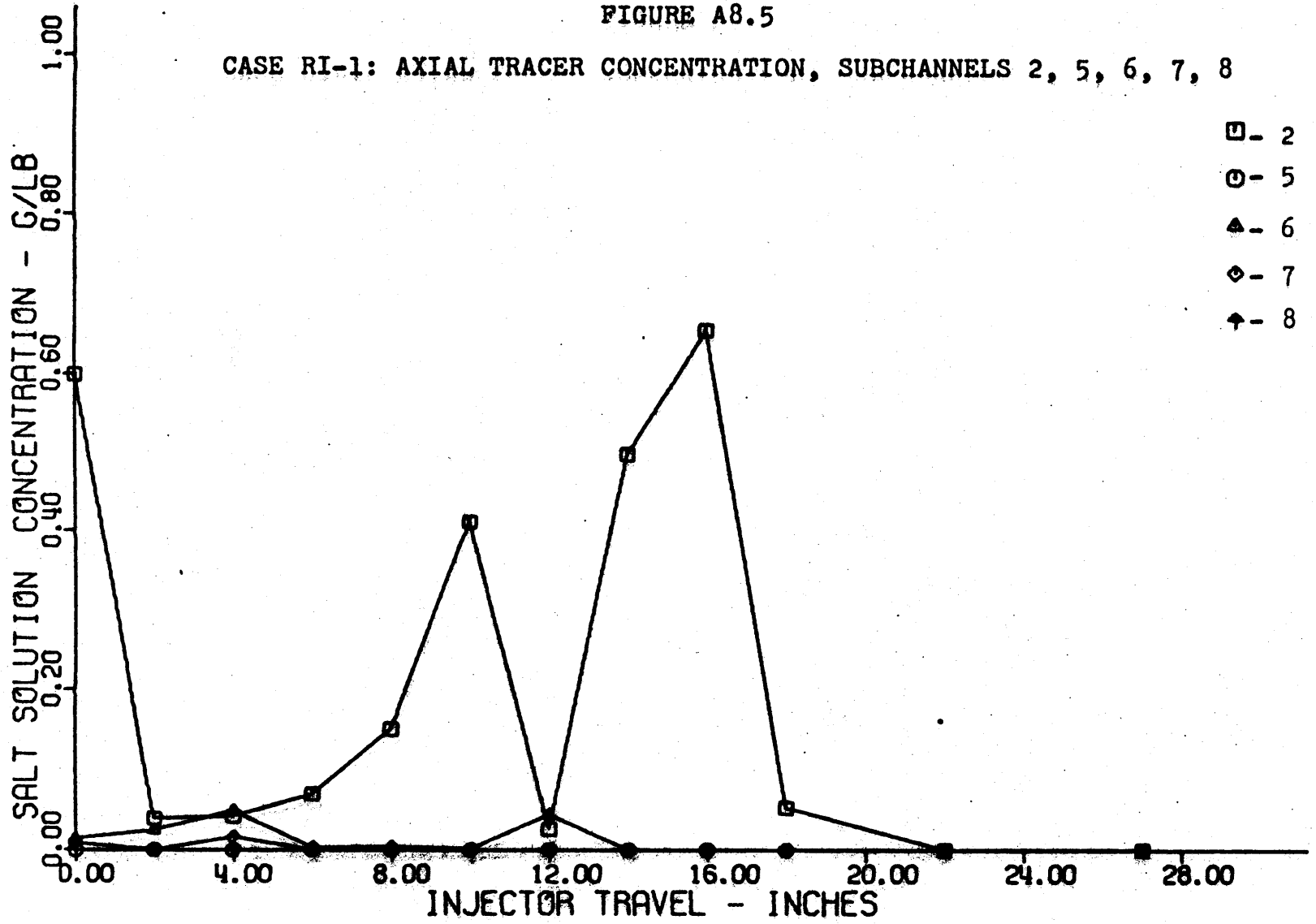

FIGURE A8.55

CASE RI-2: MASS BALANCE VERSUS INJECTOR TRAVEL

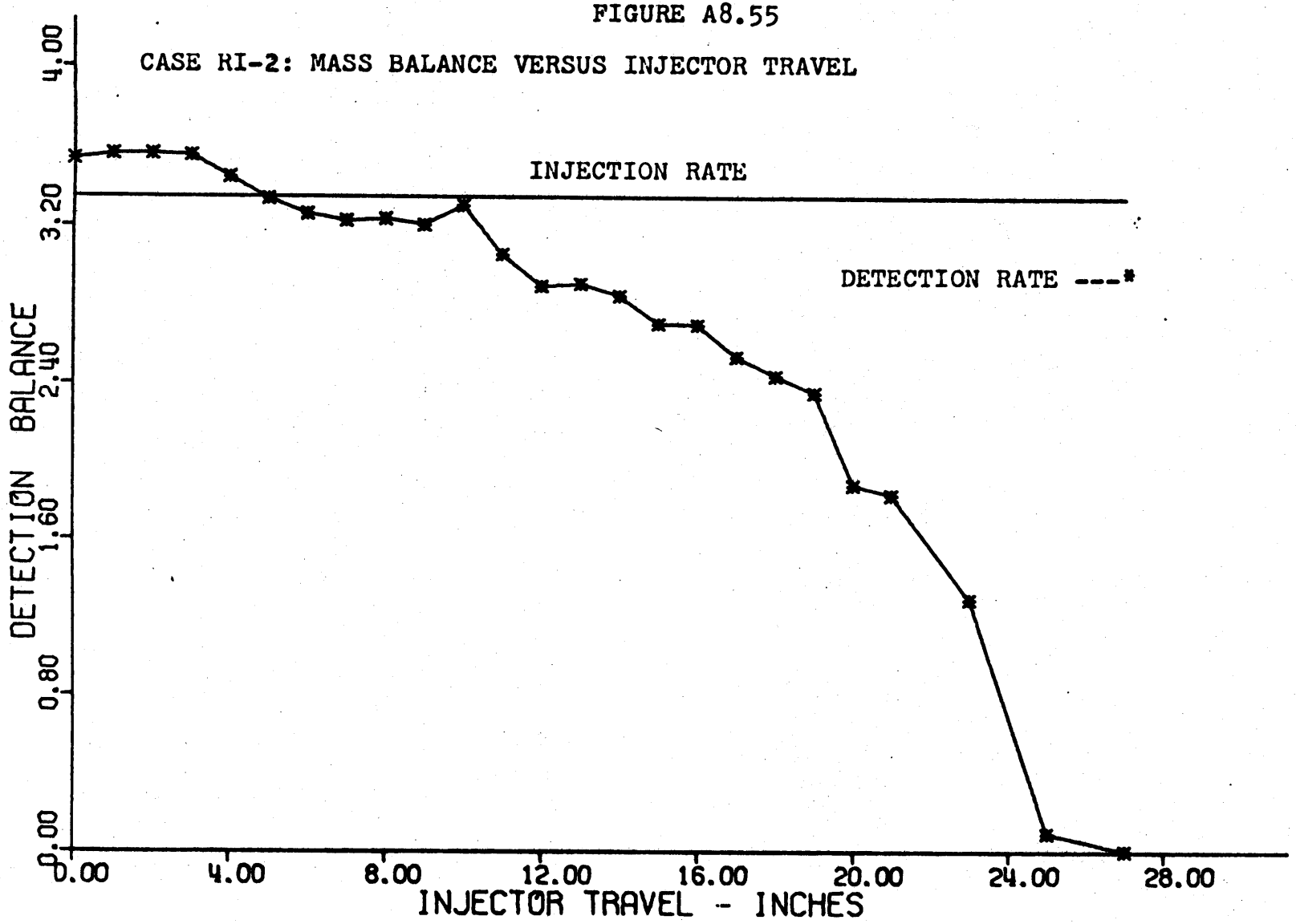

FIGURE A8.56

CASE RI-2: AXIAL TRACER CONCENTRATIONS, SUBCHANNELS 2, 1, 3, 4

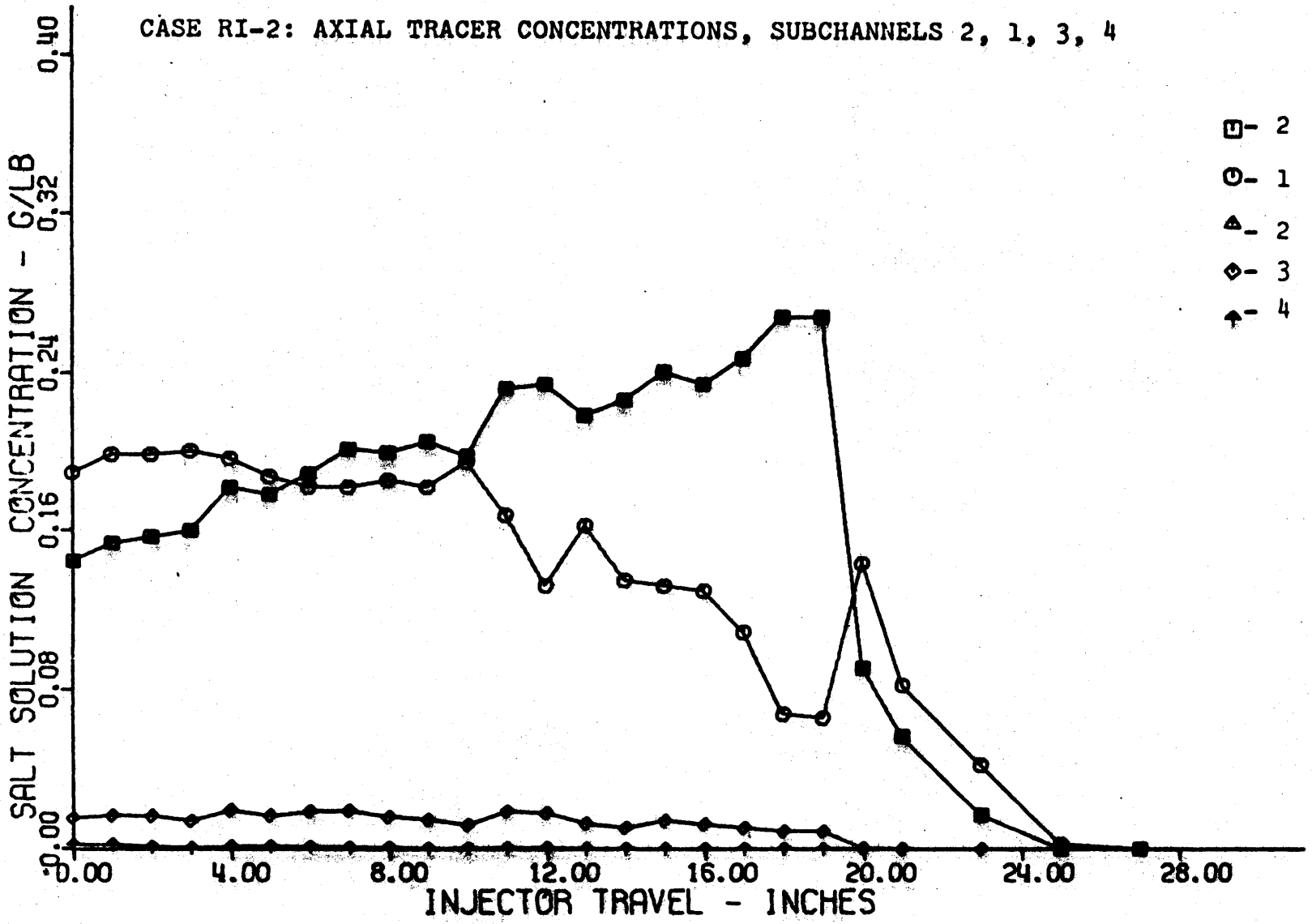

FIGURE A8.57

CASE RI-2: AXIAL TRACER CONCENTRATION, SUBCHANNELS 2, 5, 6, 7, 8

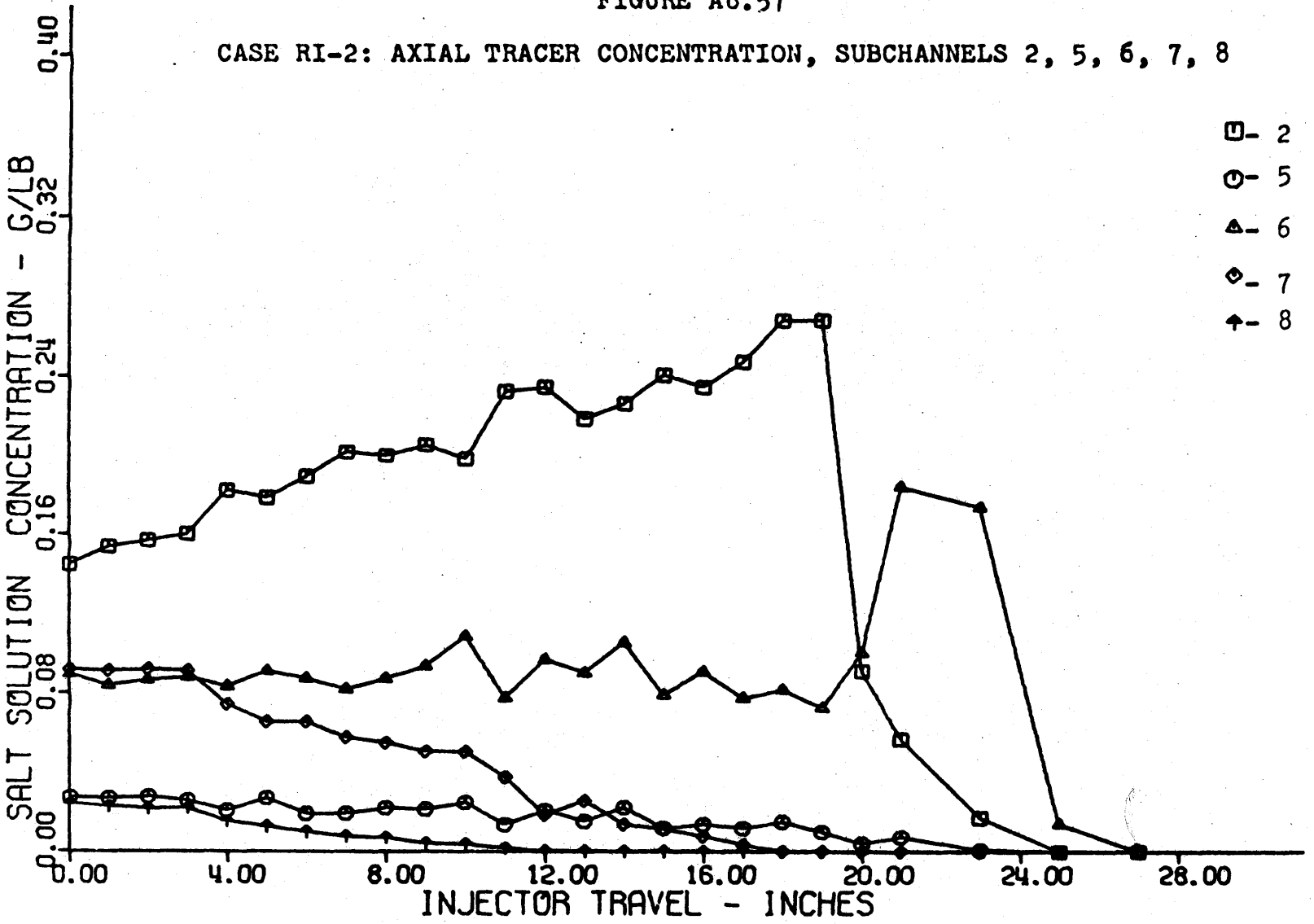

FIGURE A8.58

CASE RI-2: AXIAL TRACER CONCENTRATION, SUBCHANNELS 2, 9,10,11,12

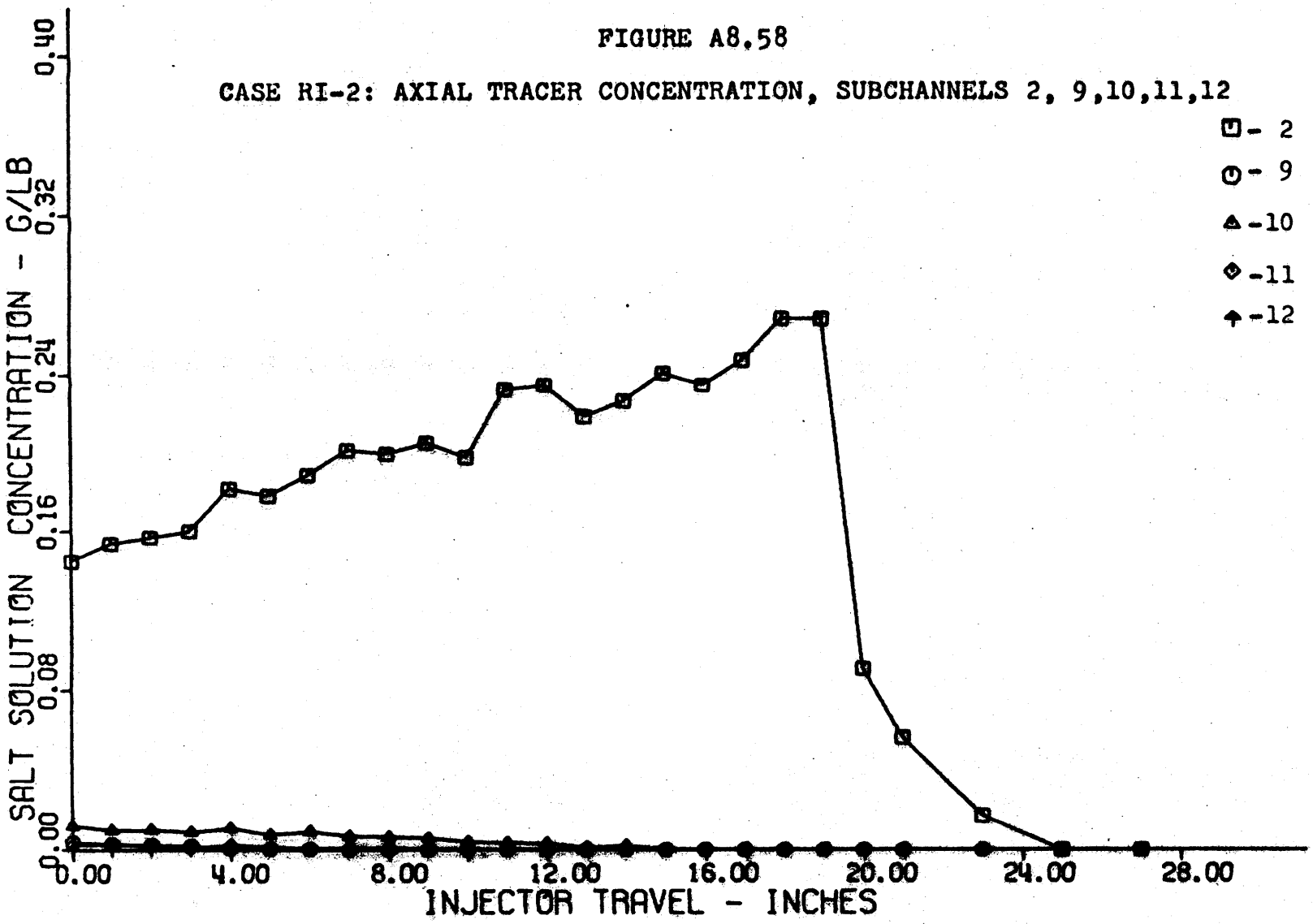

FIGURE A8.59

CASE RI-2: AXIAL TRACER CONCENTRATION, SUBCHANNELS 2,21,22,23,24

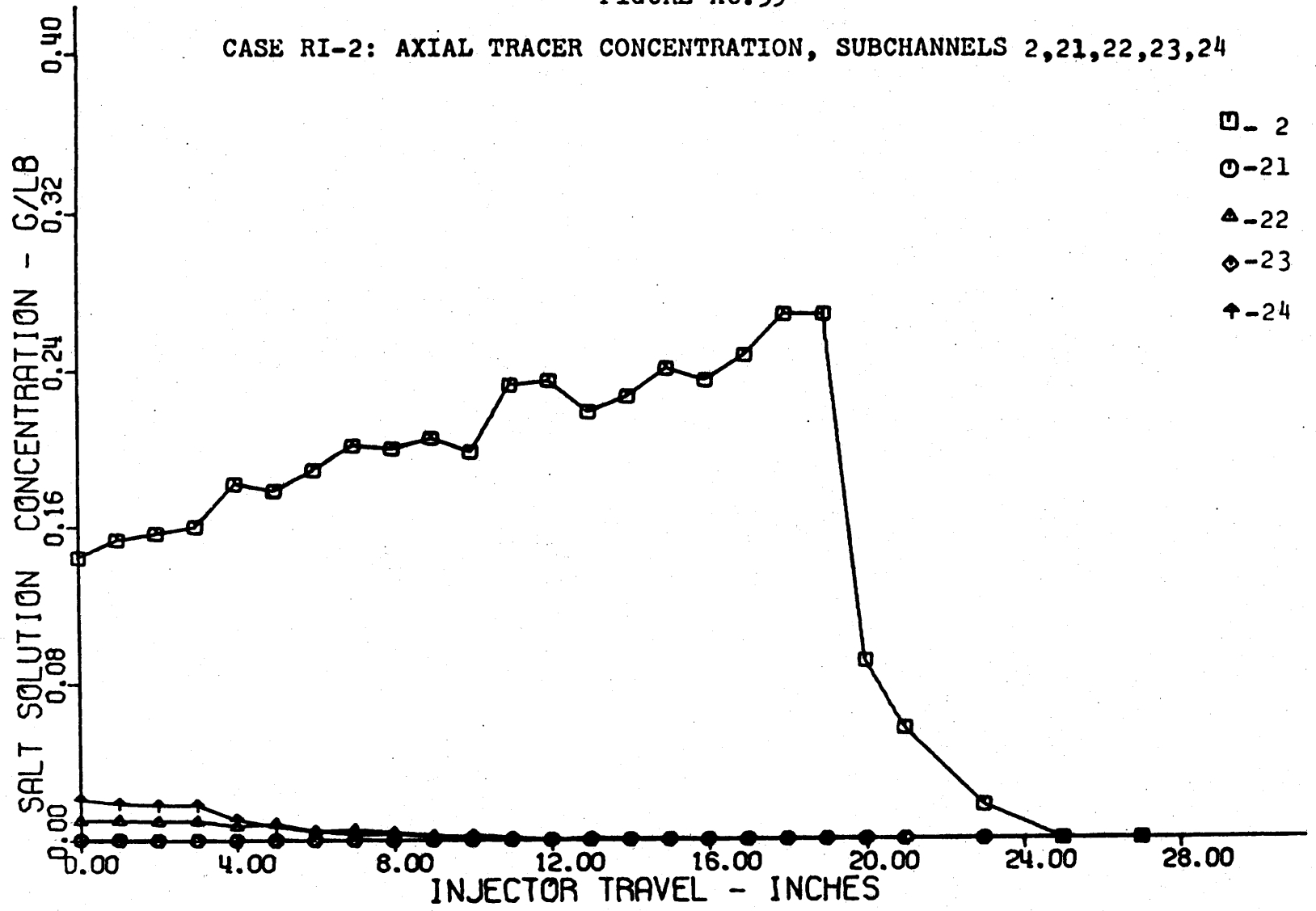

FIGURE A8.60

CASE RI-3: MASS BALANCE VERSUS INJECTOR TRAVEL

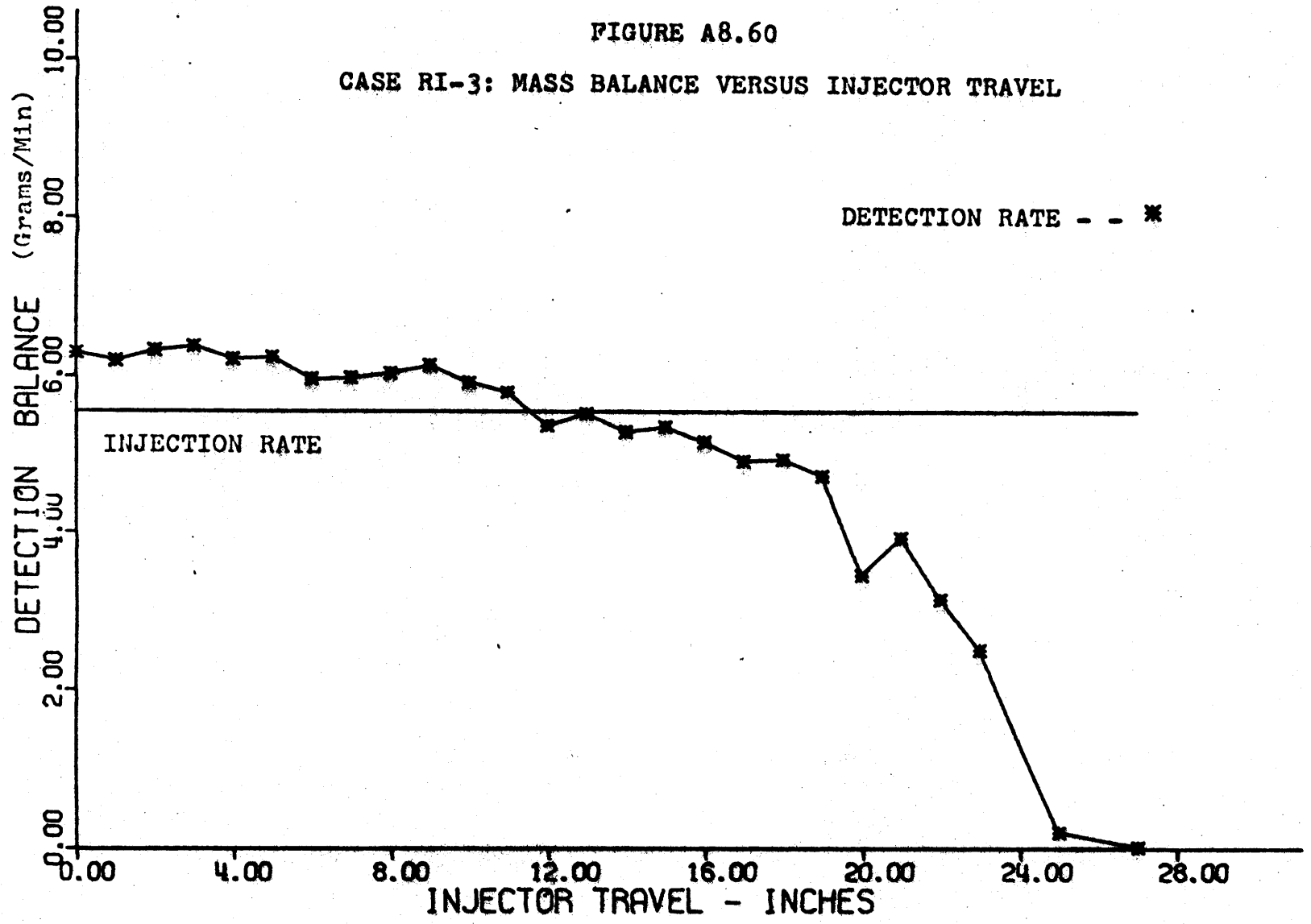

FIGURE A8.61

CASE RI-3: AXIAL TRACER CONCENTRAITON, SUBCHANNELS 2, 1, 3, 4

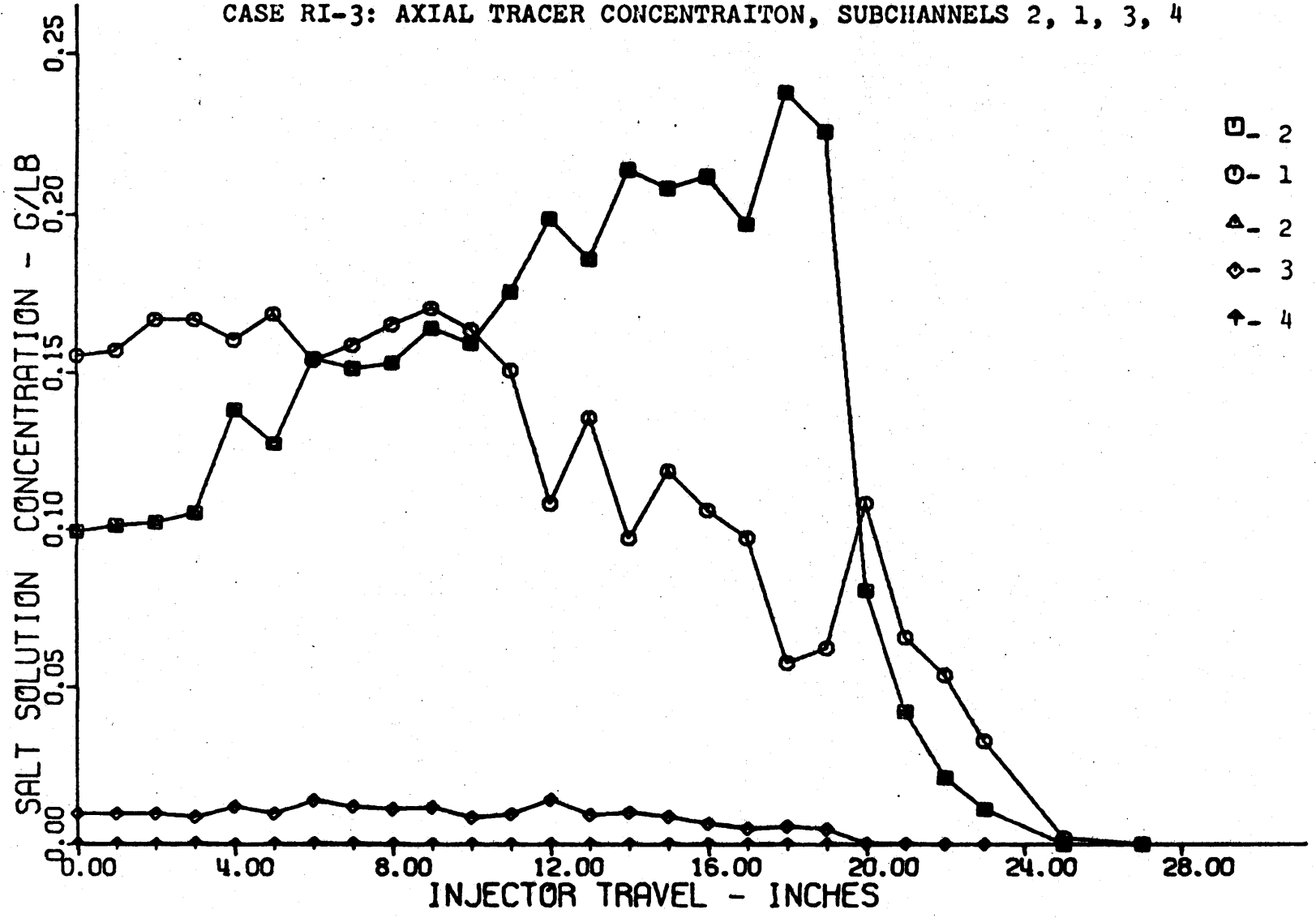

FIGURE A8.62

CASE RI-3: AXIAL TRACER CONCENTRATION SUBCHANNELS 2, 5, 6, 7, 8

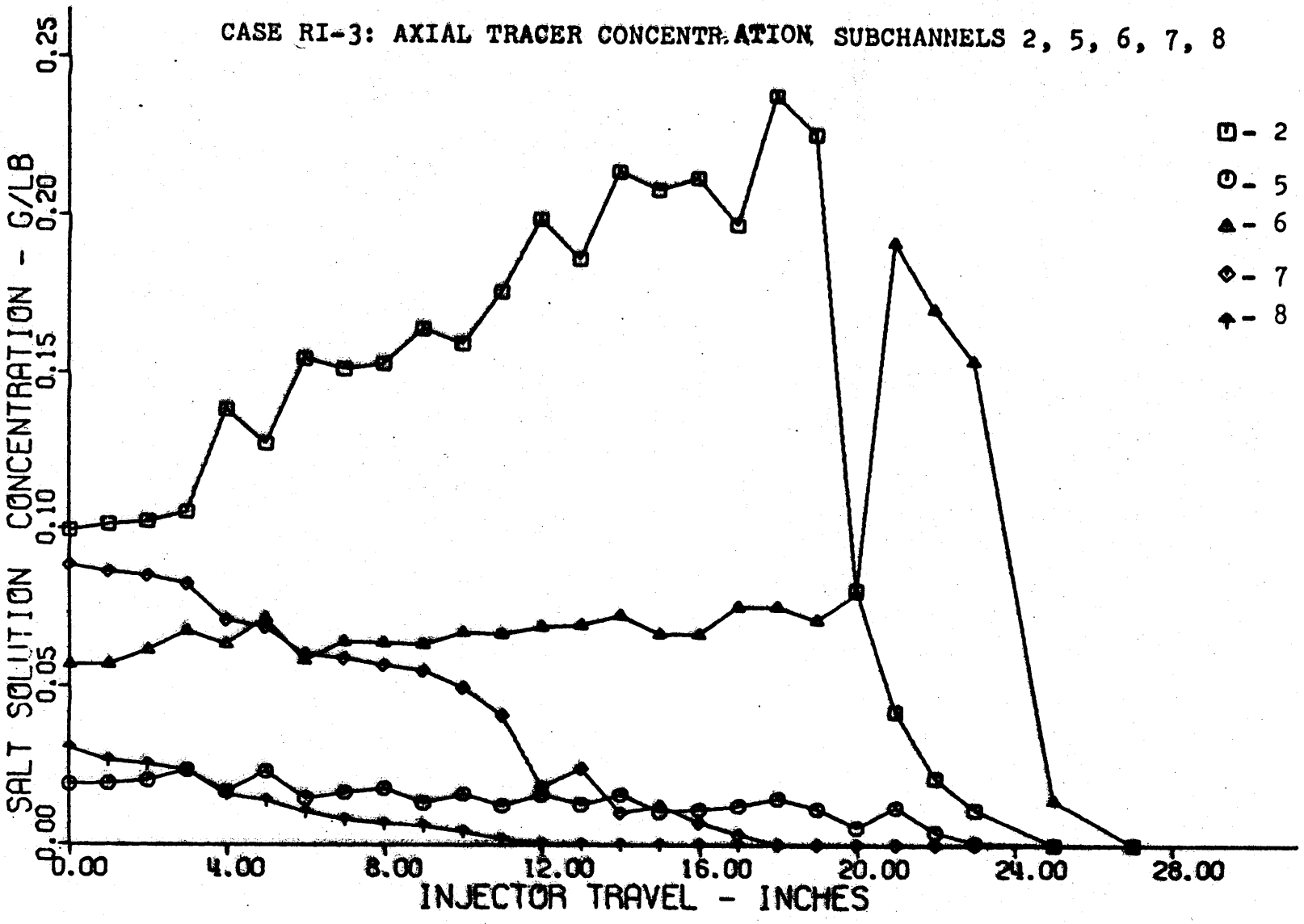

FIGURE A8.63

CASE RI-3: AXIAL TRACER CONCENTRATION, SUBCHANNELS 2, 9,10,11,12

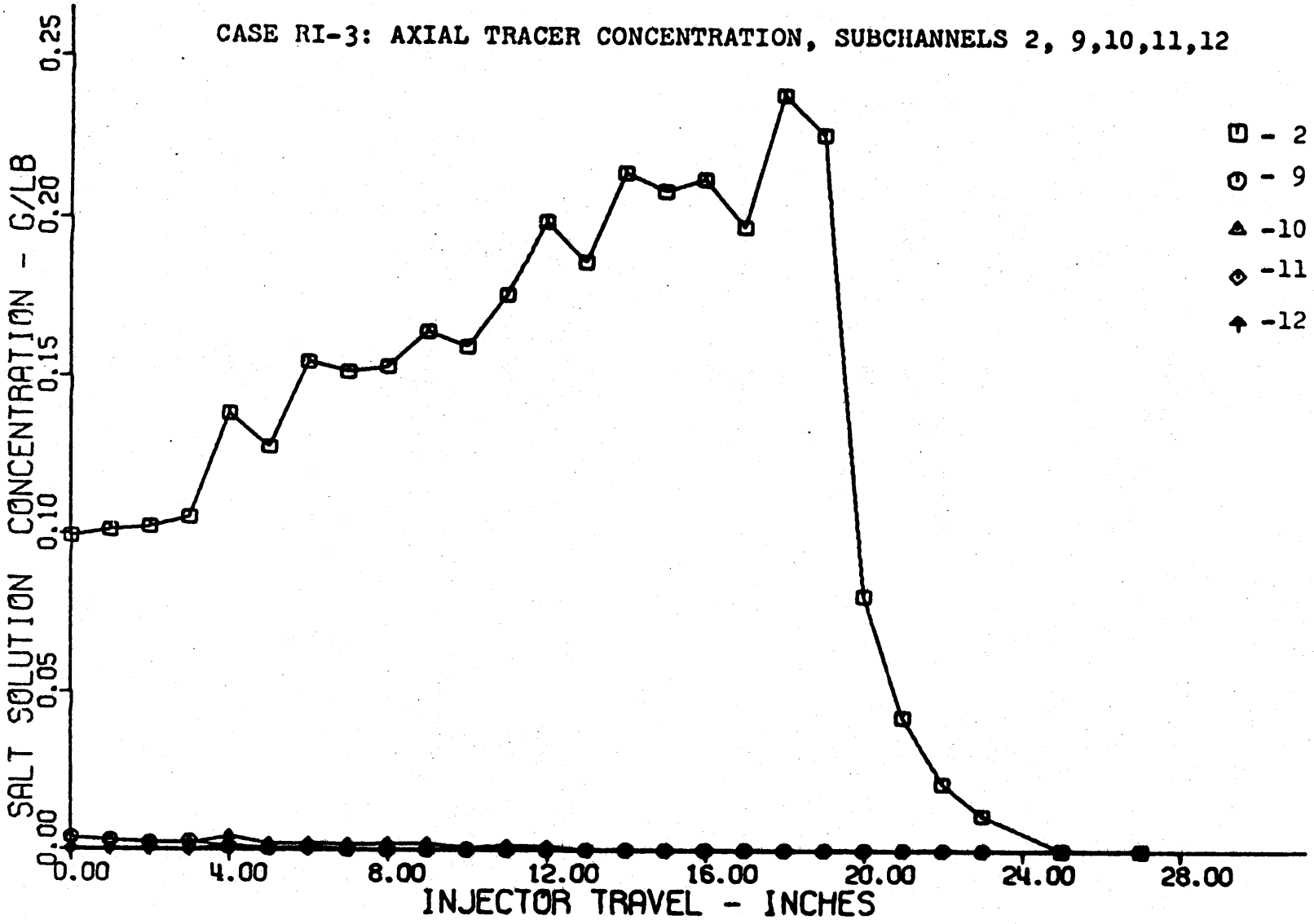

FIGURE A8.64

CASE RI-3: AXIAL TRACER CONCENTRATION, SUBCHANNELS 2,21,22,23,24

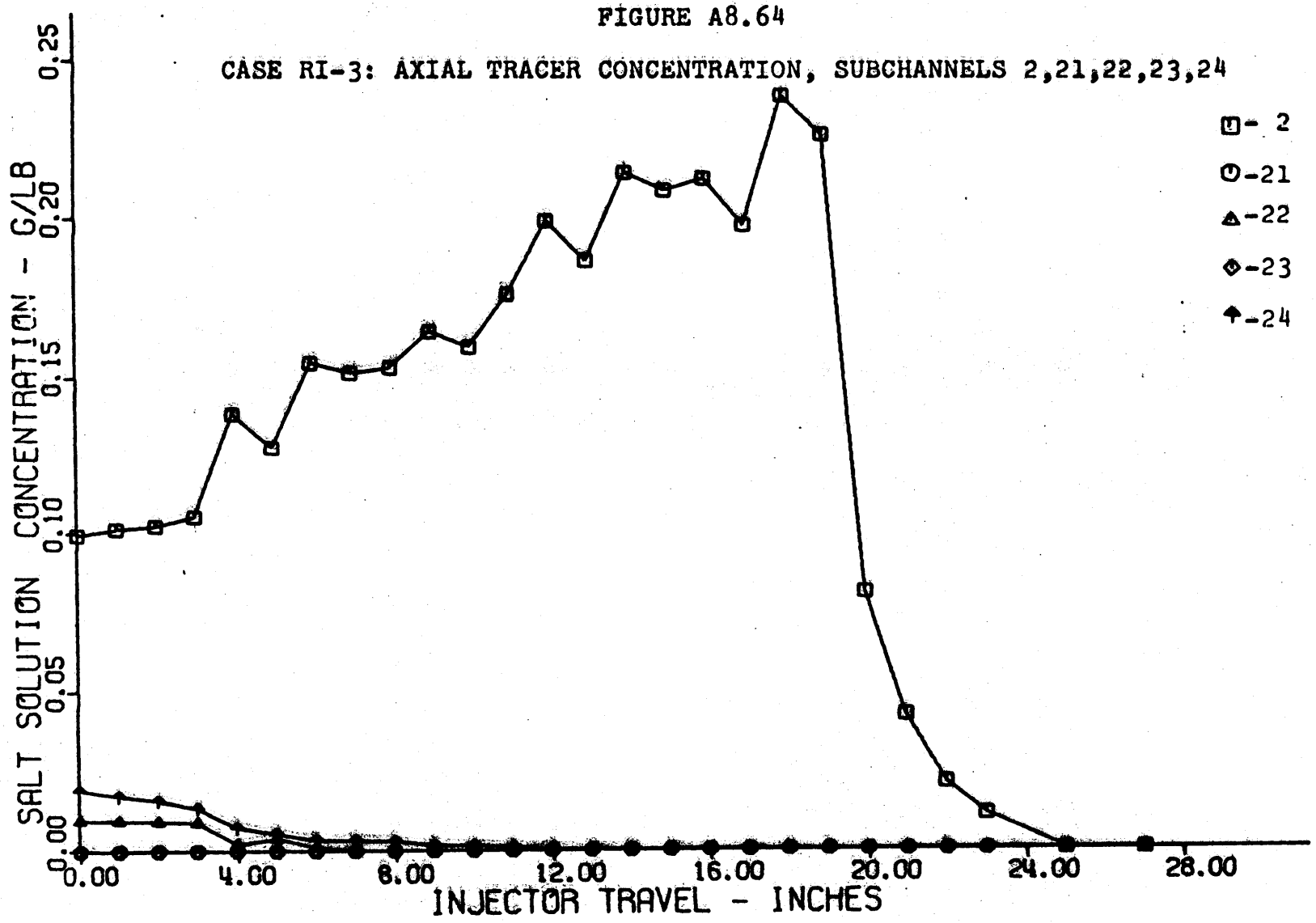

FIGURE A8.65

CASE RI-4: MASS BALANCE VERSUS INJECTOR TRAVEL

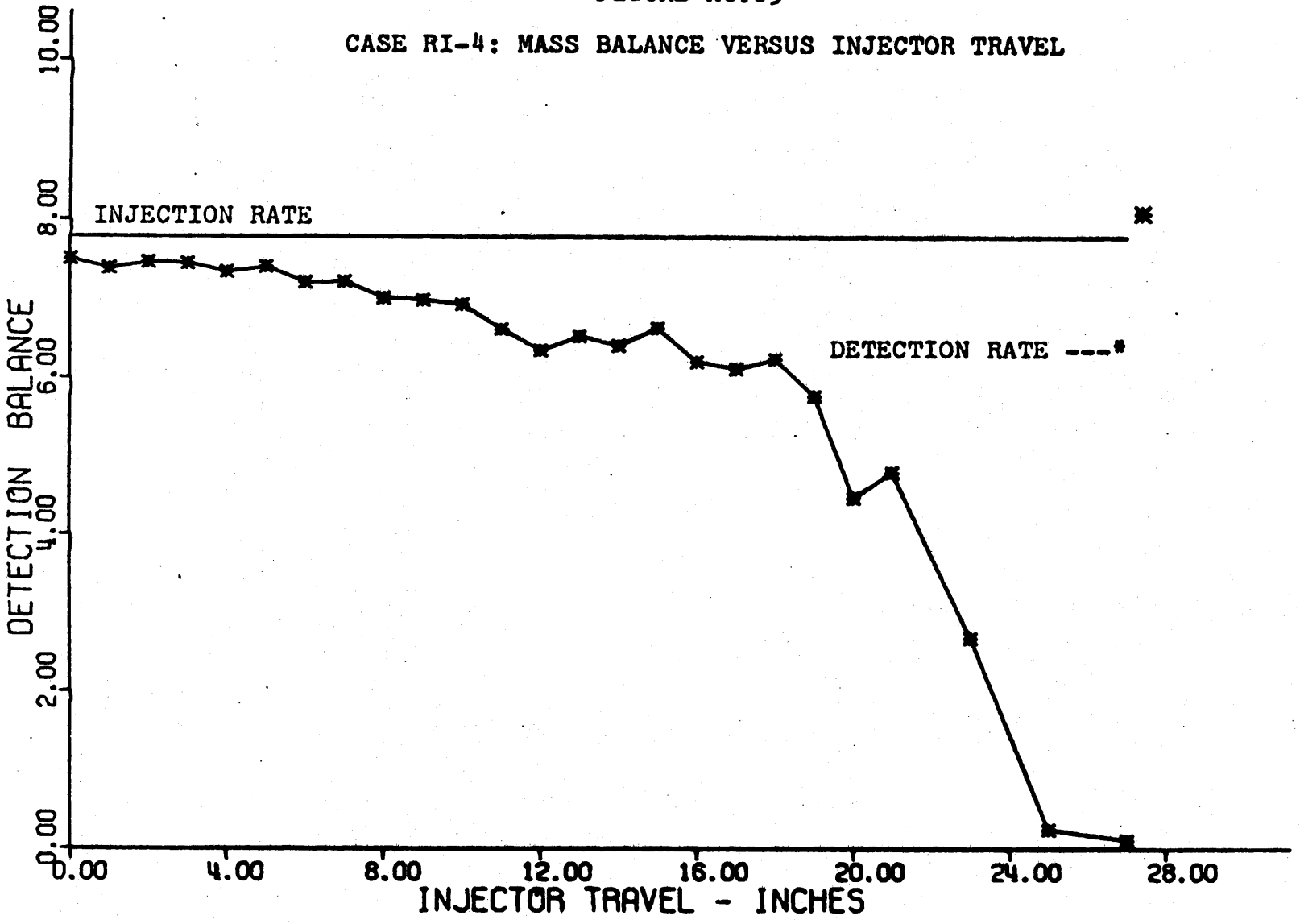

FIGURE A8.66

CASE RI-4: AXIAL TRACER CONCENTRATION, SUBCHANNELS 2, 1, 3, 4

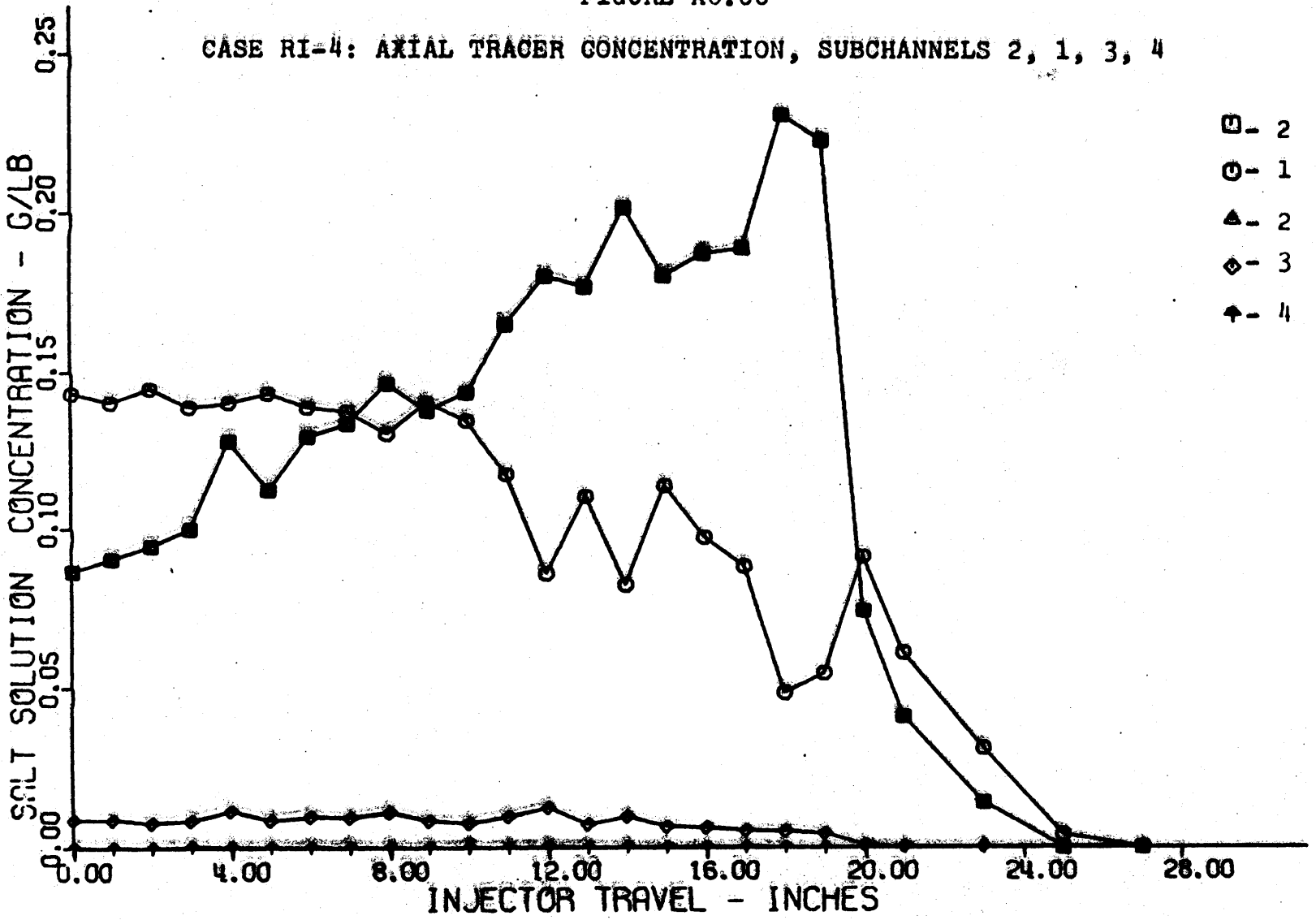

FIGURE A8.67

CASE RI-4: AXIAL TRACER CONCENTRATION, SUBCHANNELS 2, 5, 6, 7, 8

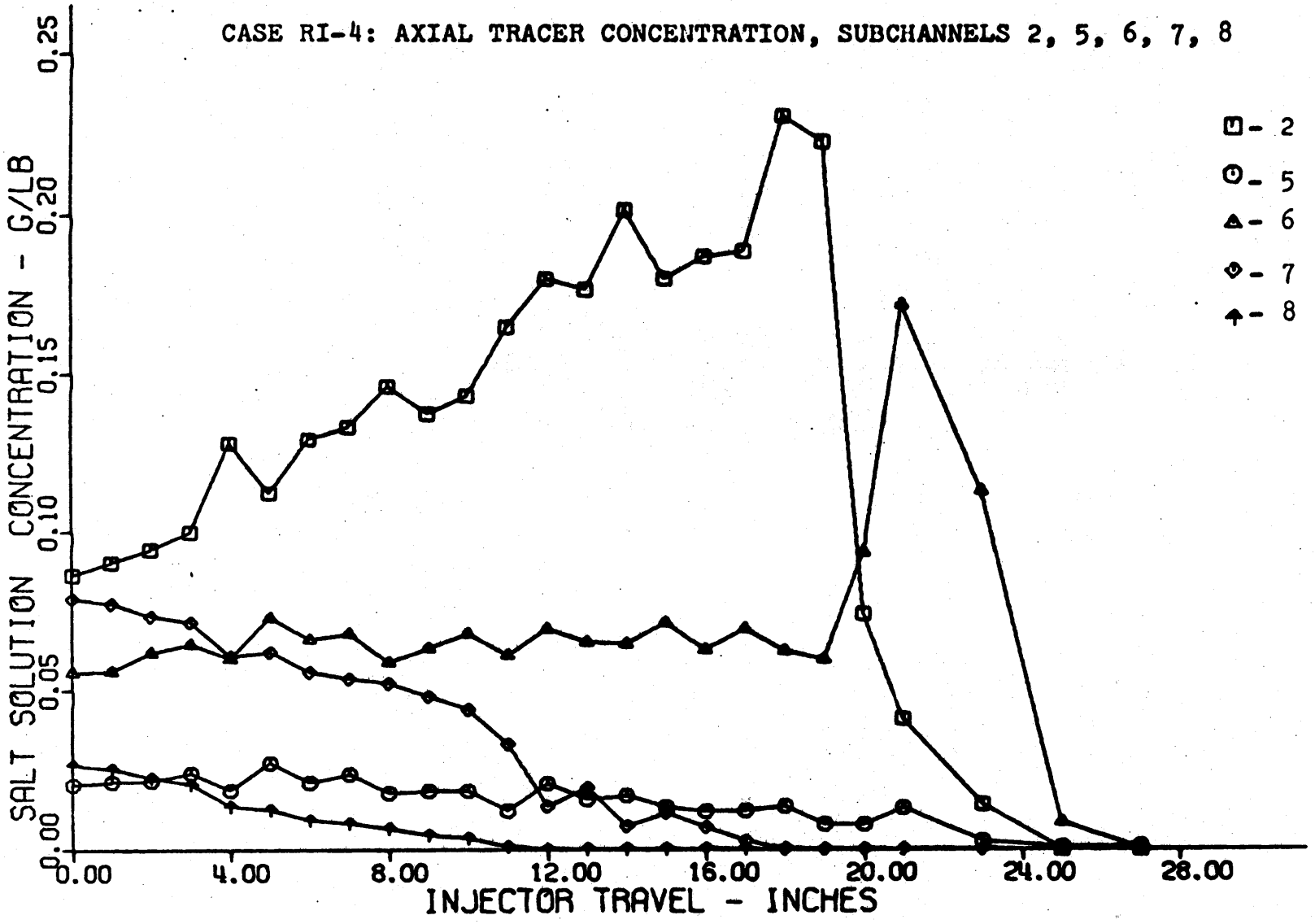

FIGURE A8.68

CASE RI-4: AXIAL TRACER CONCENTRAITON, SUBCHANNELS 2, 9,10,11,12

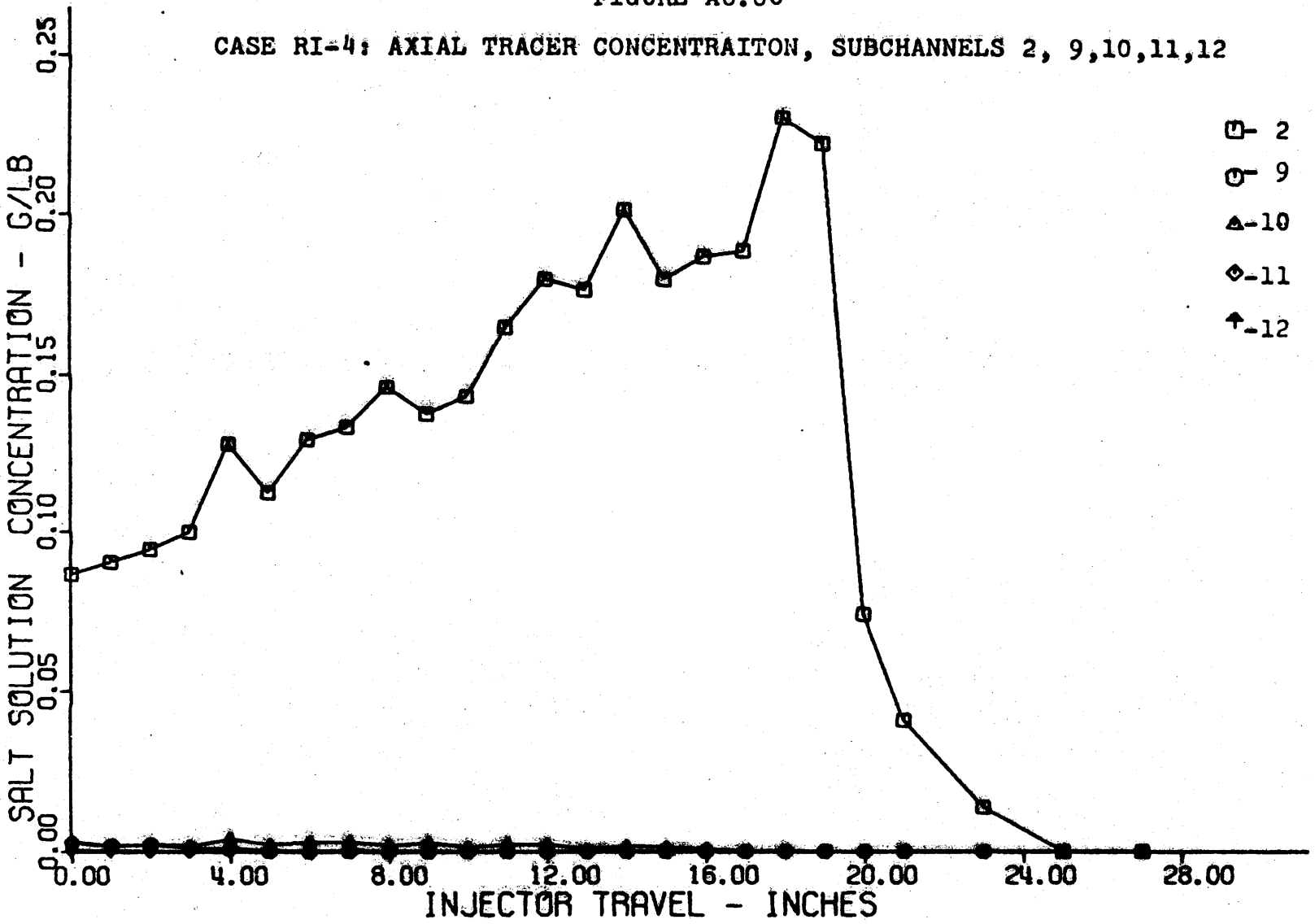

FIGURE A8.69

CASE RI-4: AXIAL TRACER CONCENTRATION, SUBCHANNELS 2,21,22,23,24

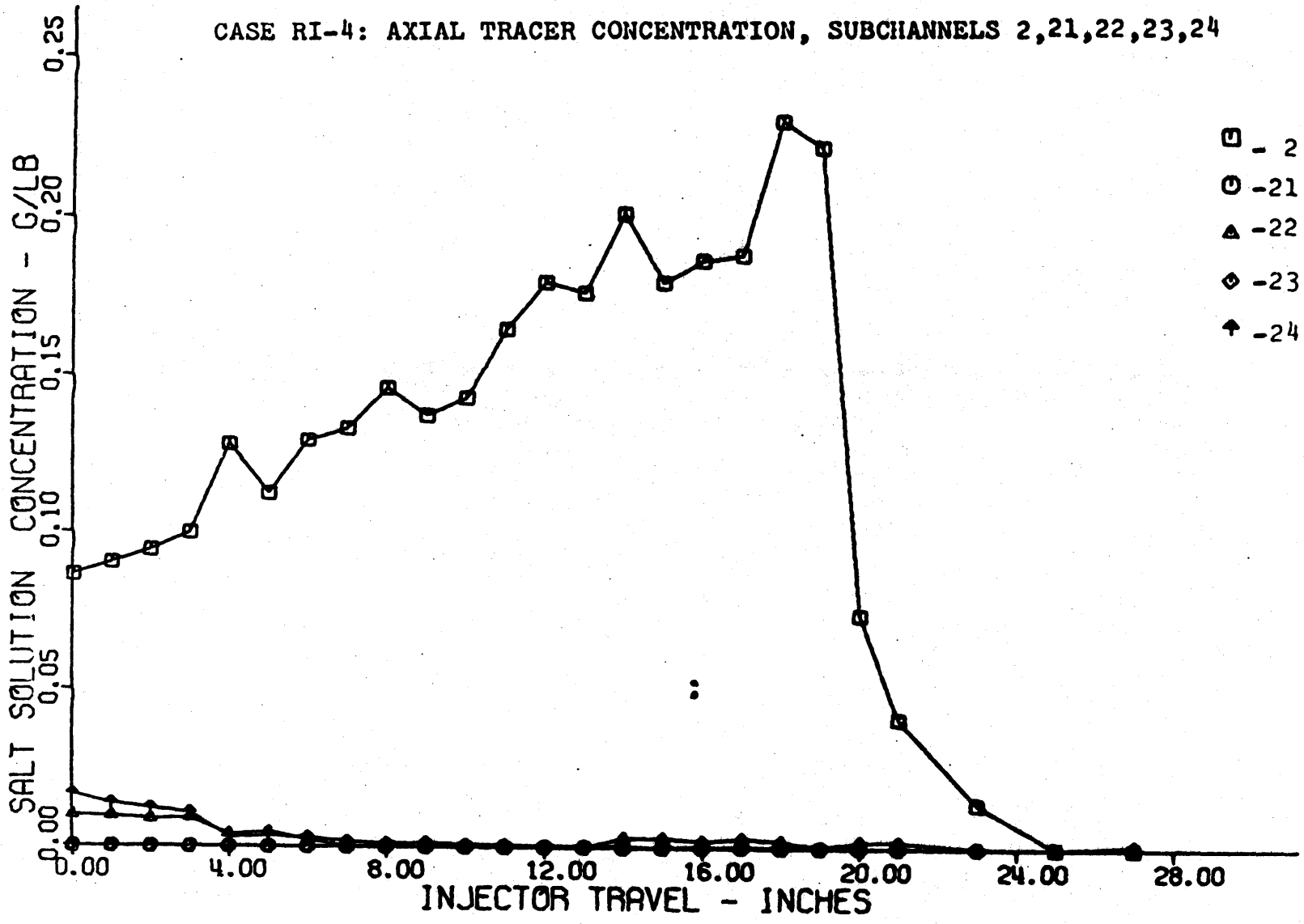

FIGURE A8.70

CASE RI-6: MASS BALANCE VERSUS INJECTOR TRAVEL

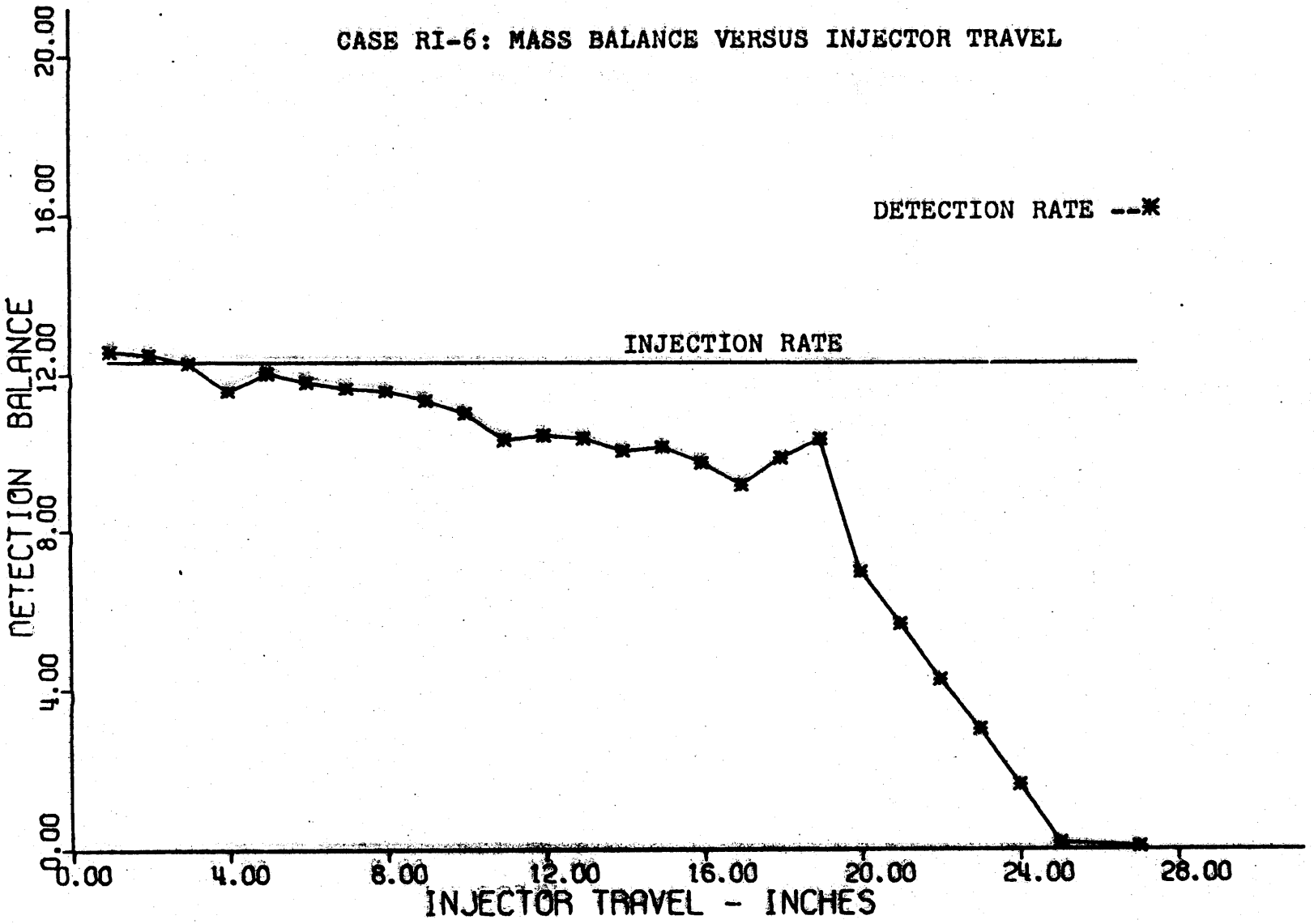

FIGURE A8.71

CASE RI-6: AXIAL TRACER CONCENTRATION, SUBCHANNELS 2, 1, 3, 4

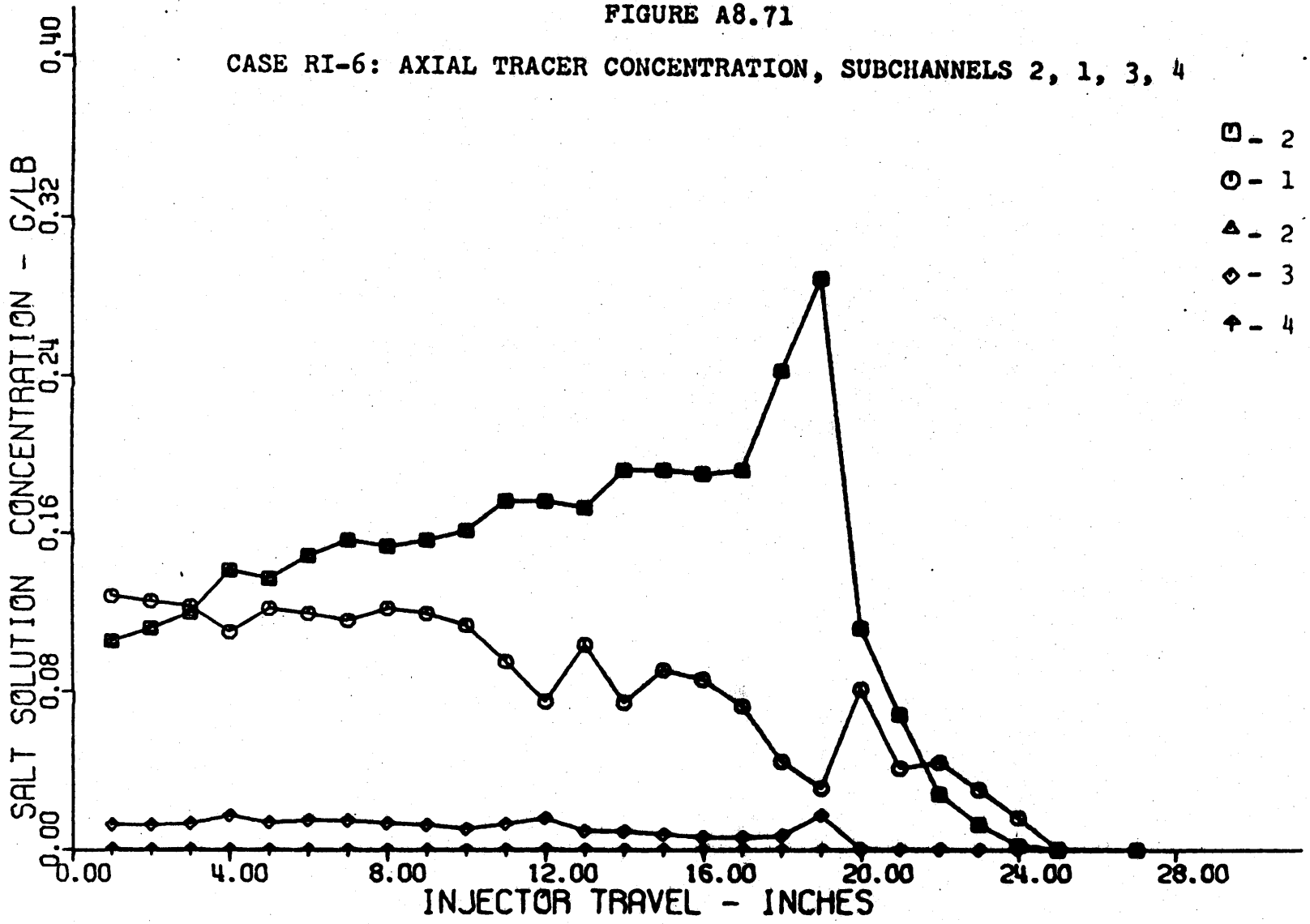

FIGURE A8.72

CASE RI-6: AXIAL TRACER CONCENTRATION, SUBCHANNELS 2, 5, 6, 7, 8

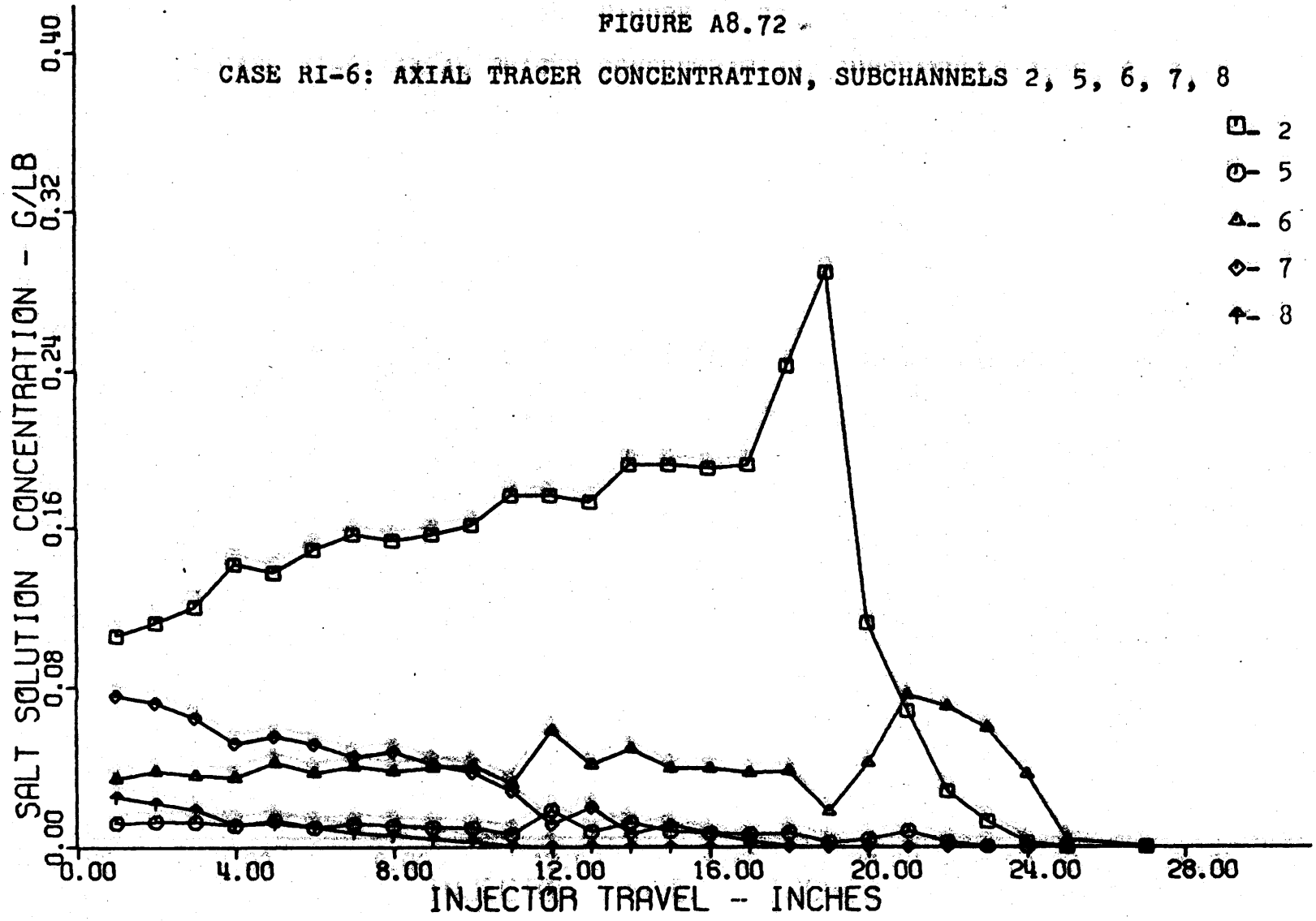

FIGURE A8.73

CASE RI-6: AXIAL TRACER CONCENTRATION, SUBCHANNELS 2, 9,10,11,12

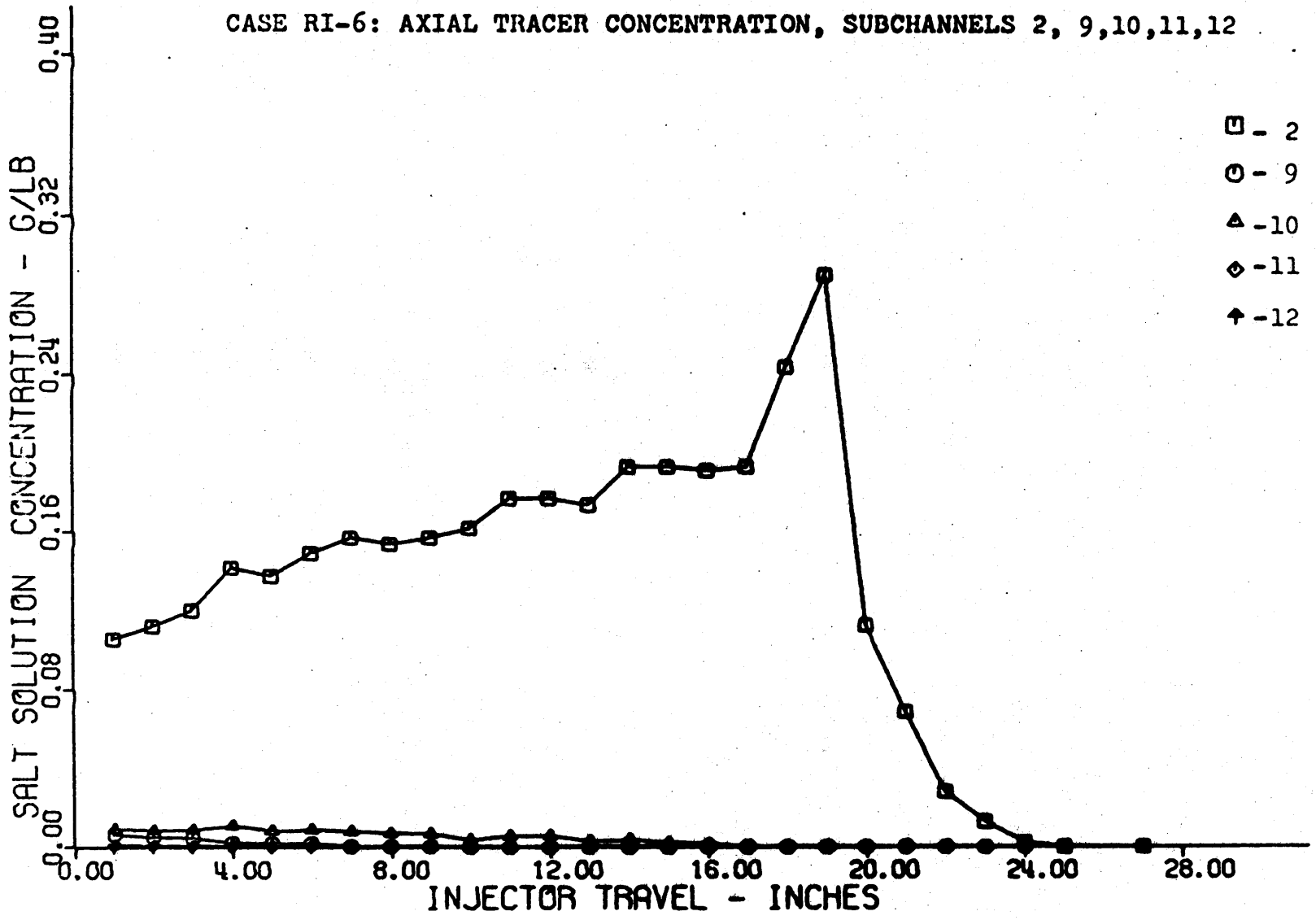

FIGURE A8.74

CASE RI-6: AXIAL TRACER CONCENTRATION, SUBCHANNELS 2,21,22,23,24

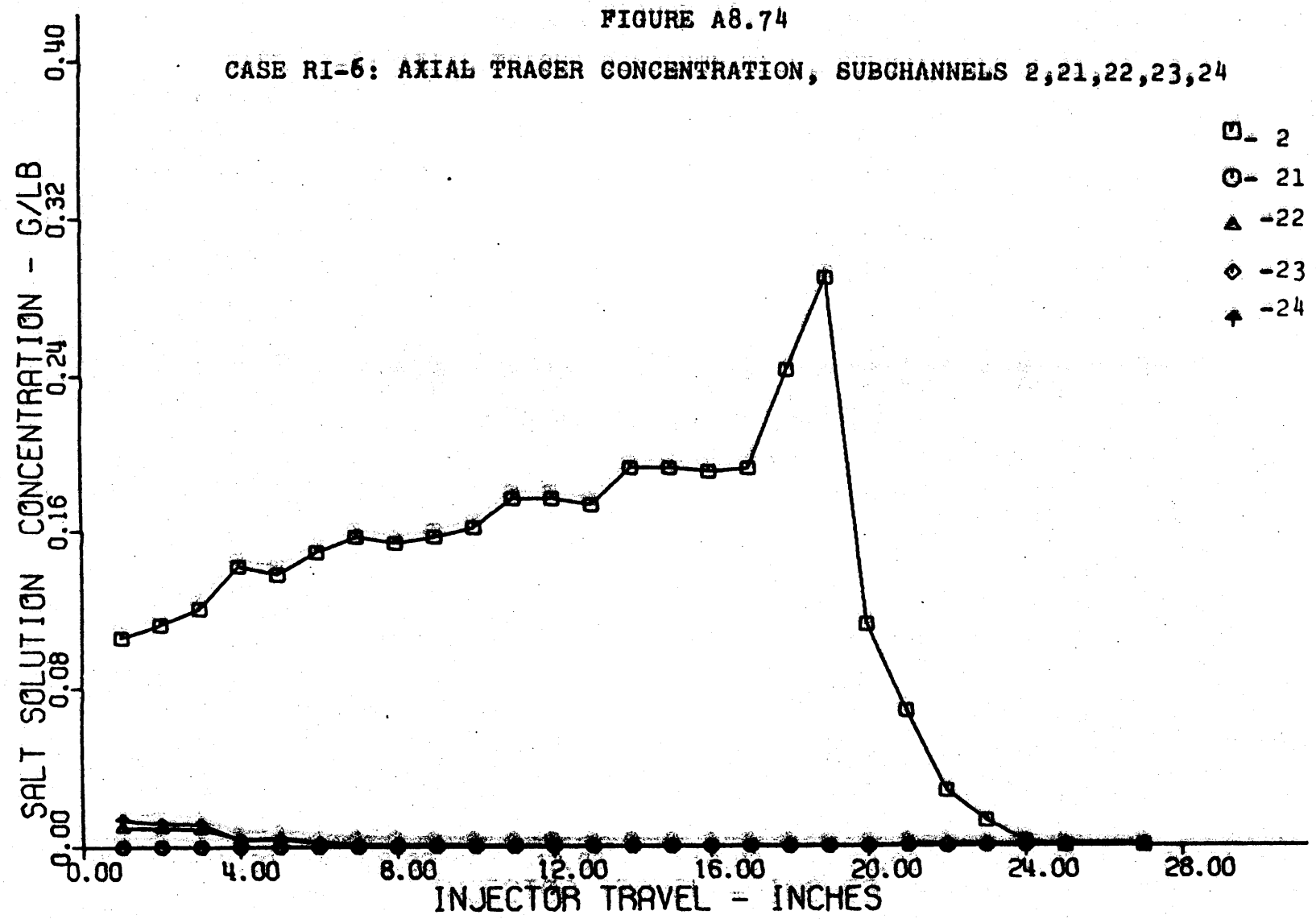

FIGURE A8.75

CASE RI-7: MASS BALANCE VERSUS INJECTOR TRAVEL

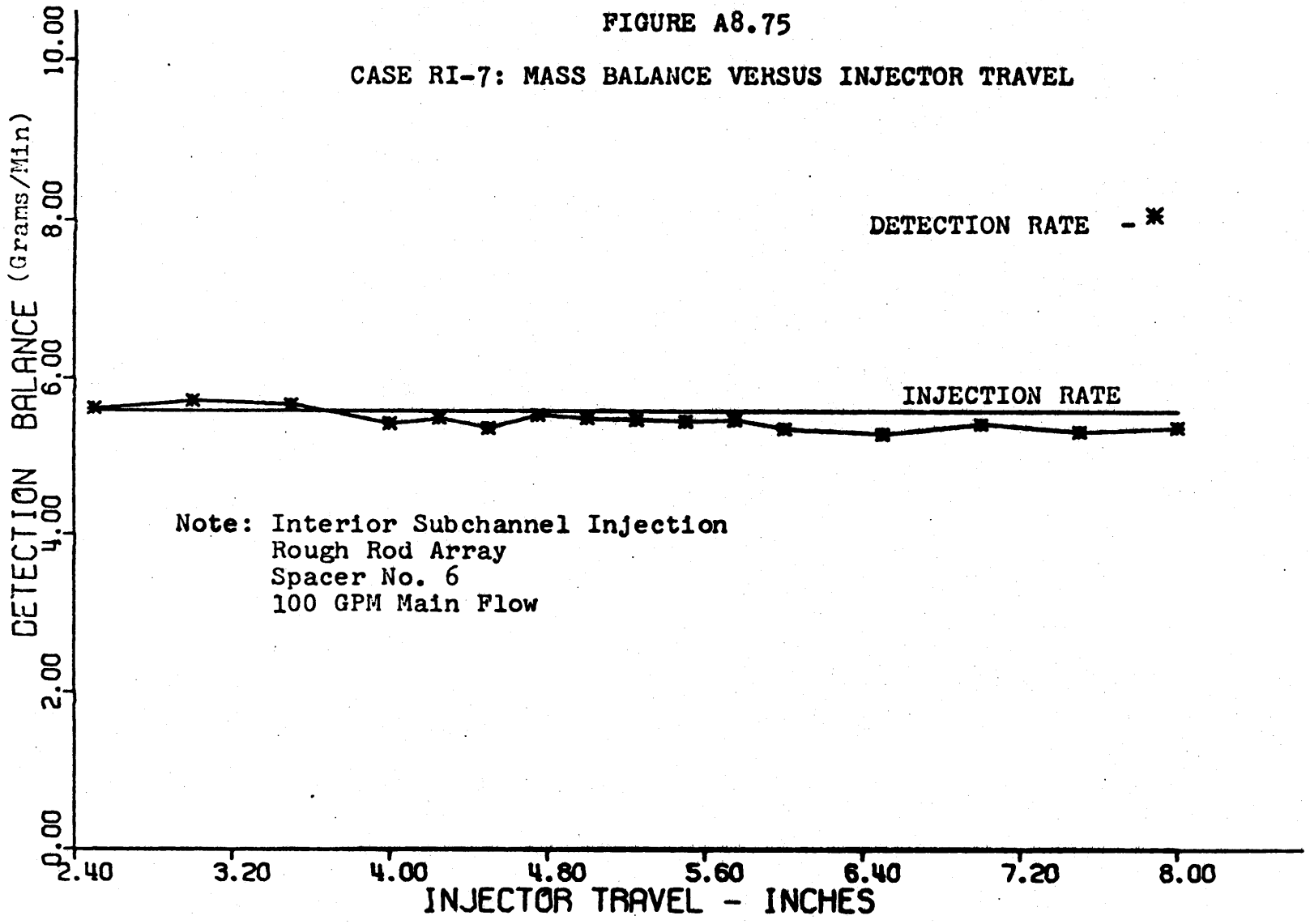

FIGURE A8.76

CASE RI-7: AXIAL TRACER CONCENTRATION; SUBCHANNELS 2, 1, 3, 4

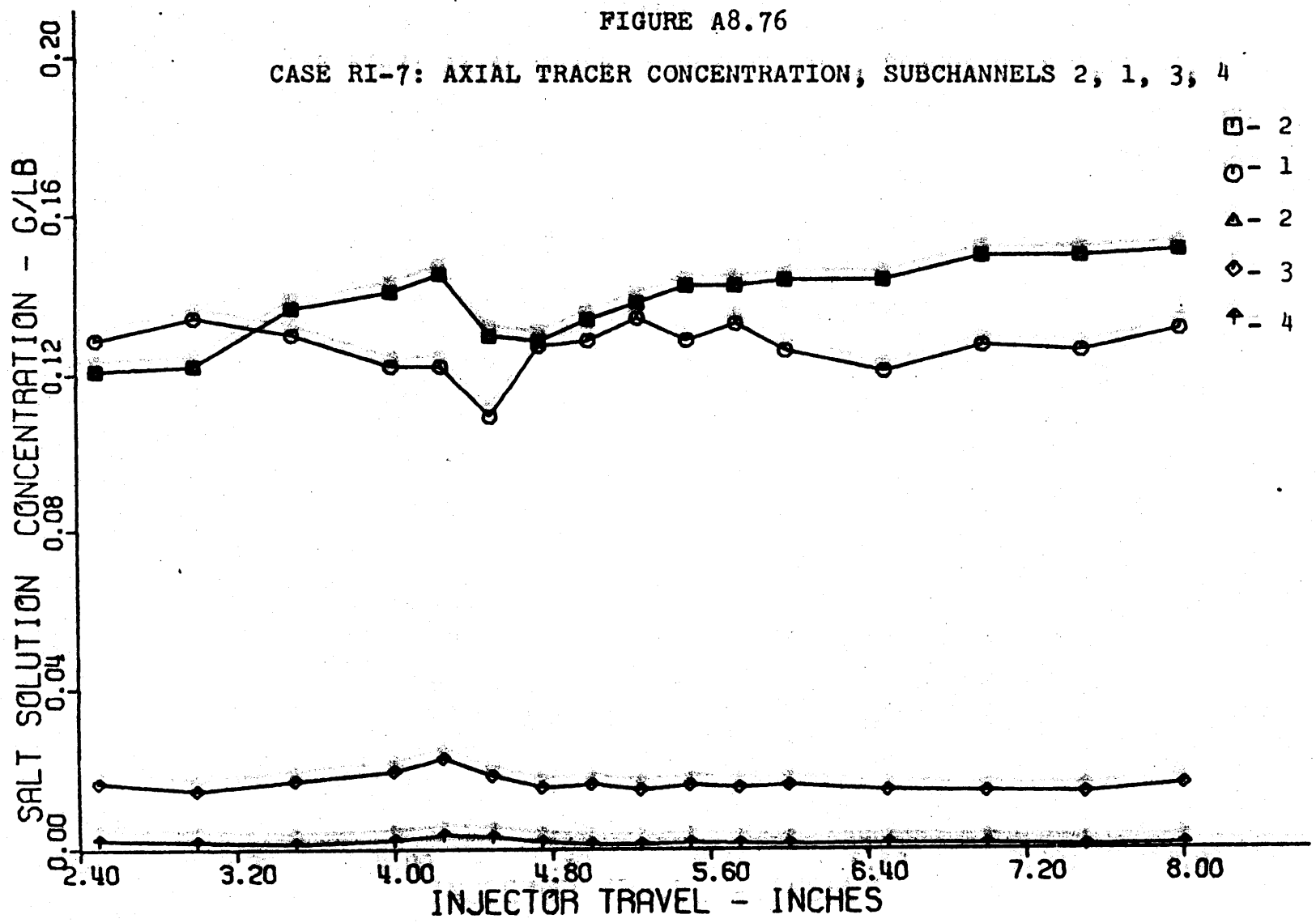

FIGURE A8.77

CASE RI-7: AXIAL TRACER CONCENTRATIONS: SUBCHANNELS 2, 5, 6, 7, 8

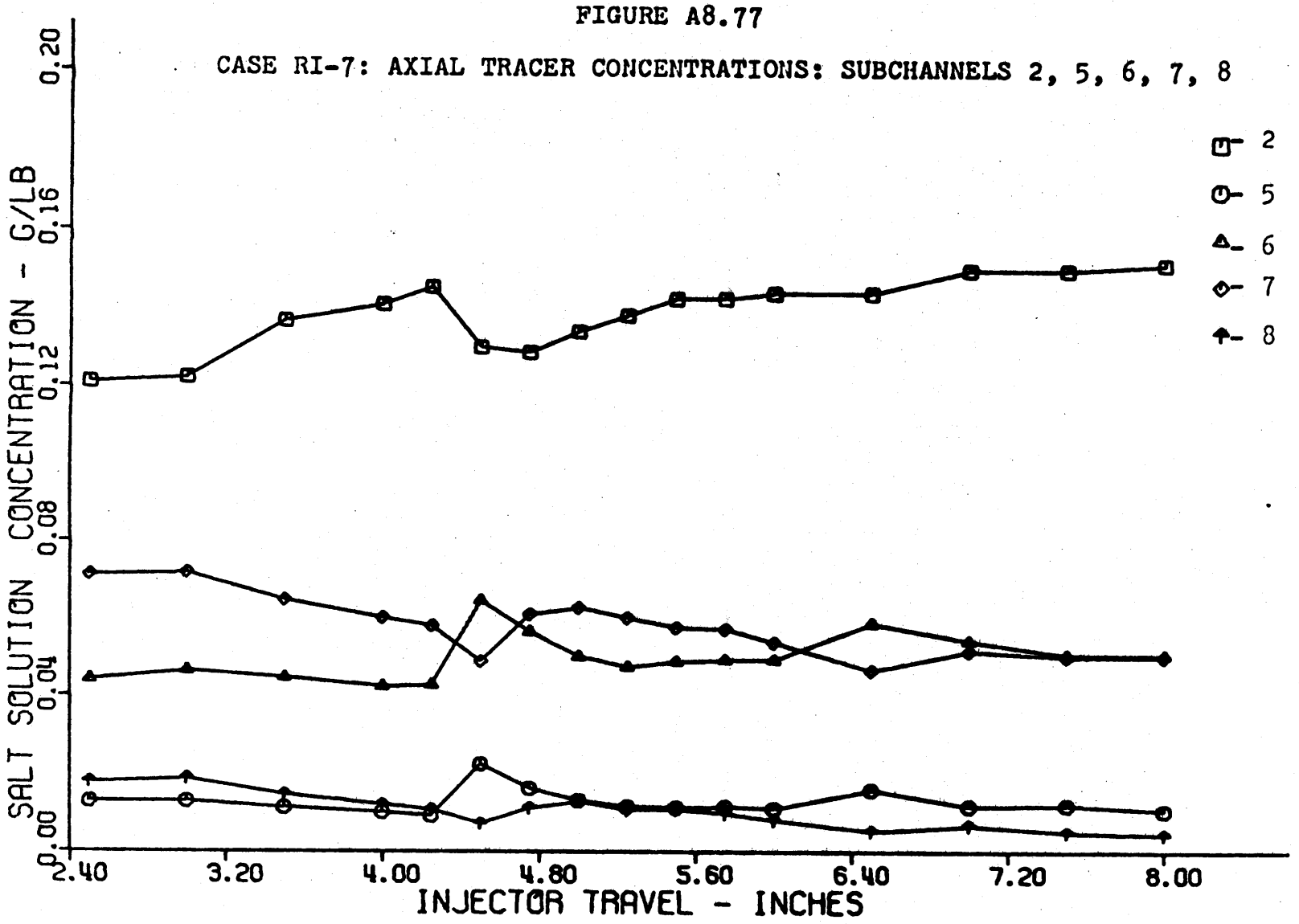

FIGURE A8.78

CASE RI-7: AXIAL TRACER CONCENTRATION, SUBCHANNELS 2, 9, 10, 11, 12

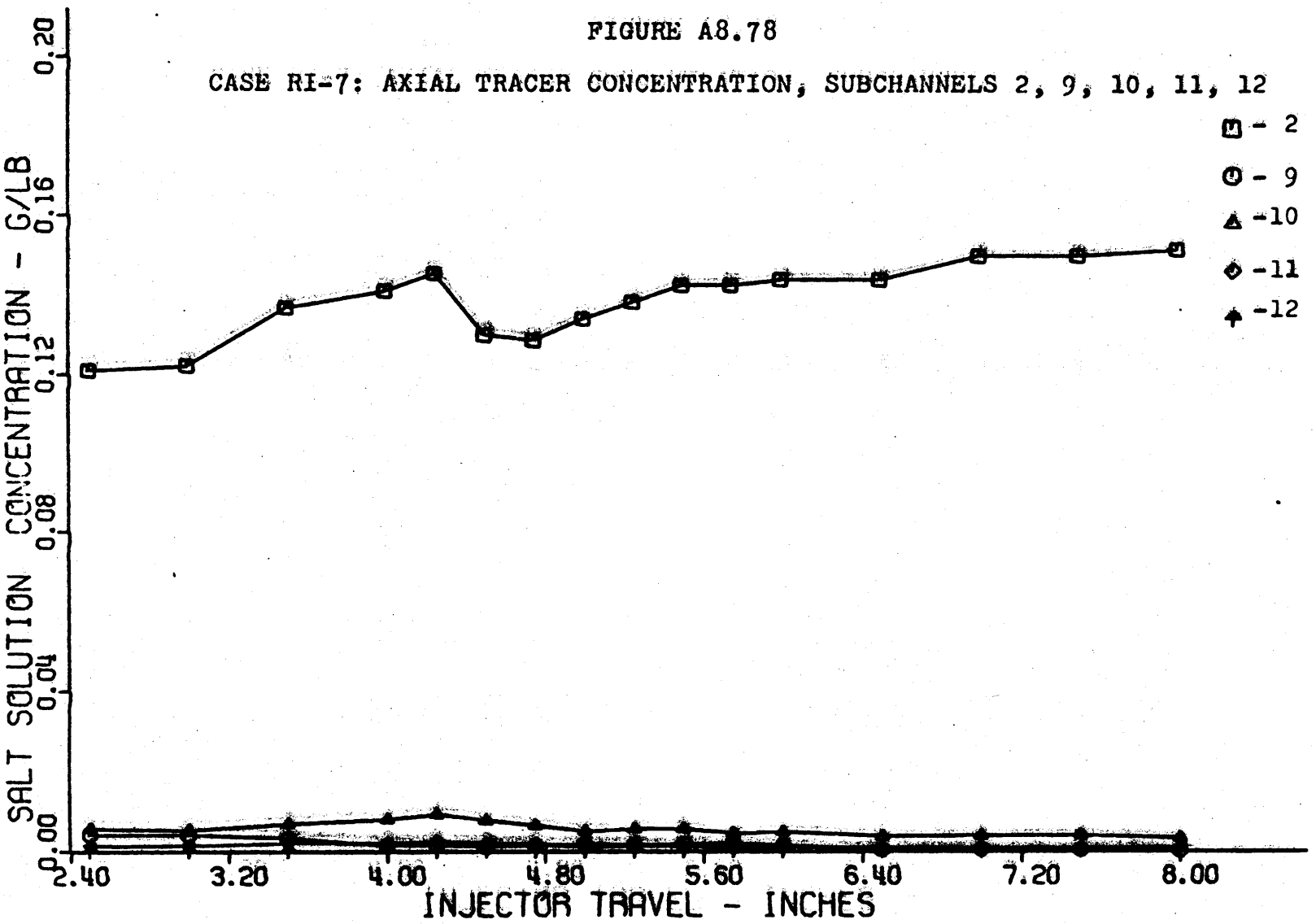

FIGURE A8.79

CASE RI-7: AXIAL TRACER CONCENTRATIONS; SUBCHANNELS 2, 21, 22, 23, 24.

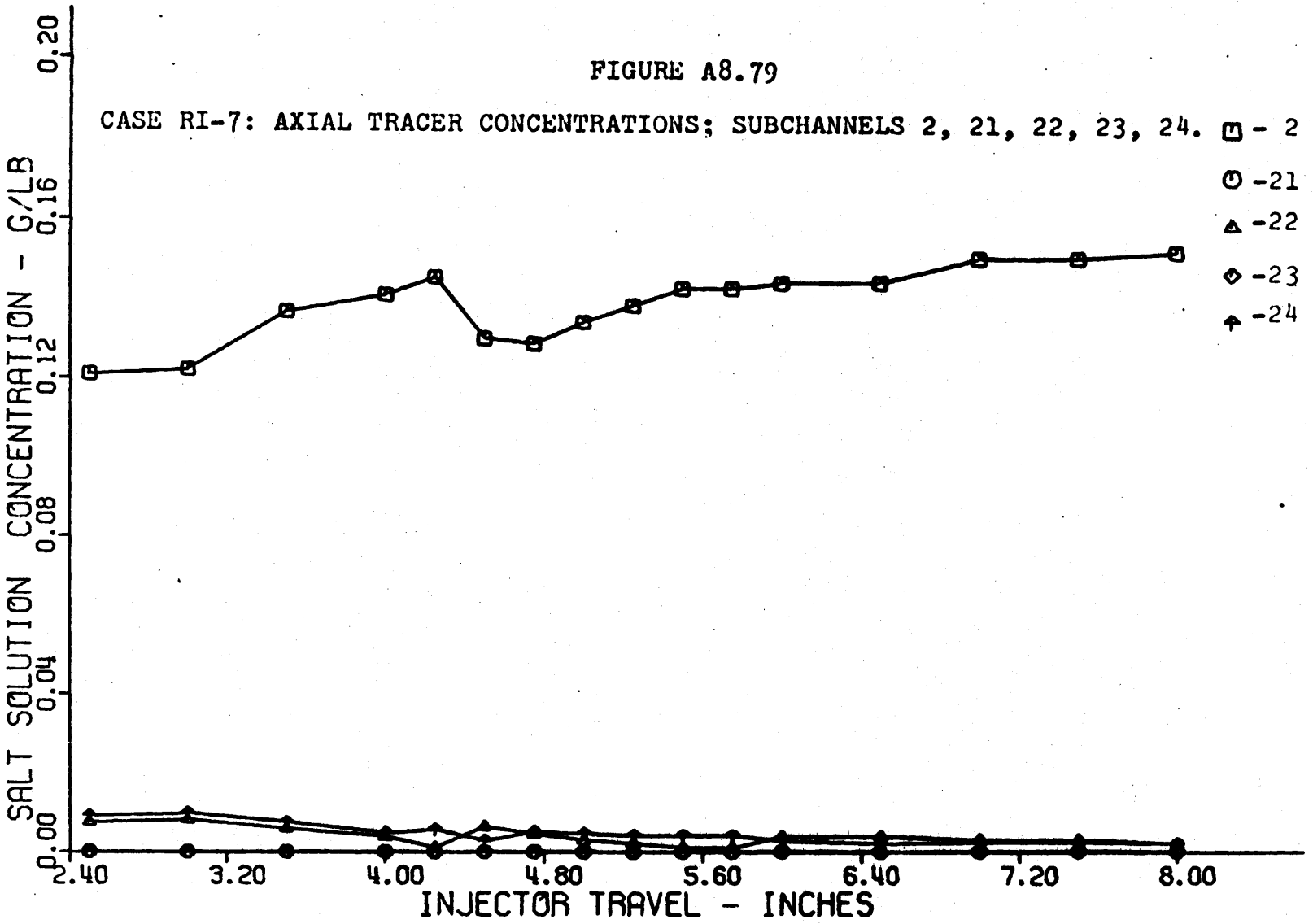

FIGURE A8.80

CASE RI-8: MASS BALANCE VERSUS INJECTOR TRAVEL

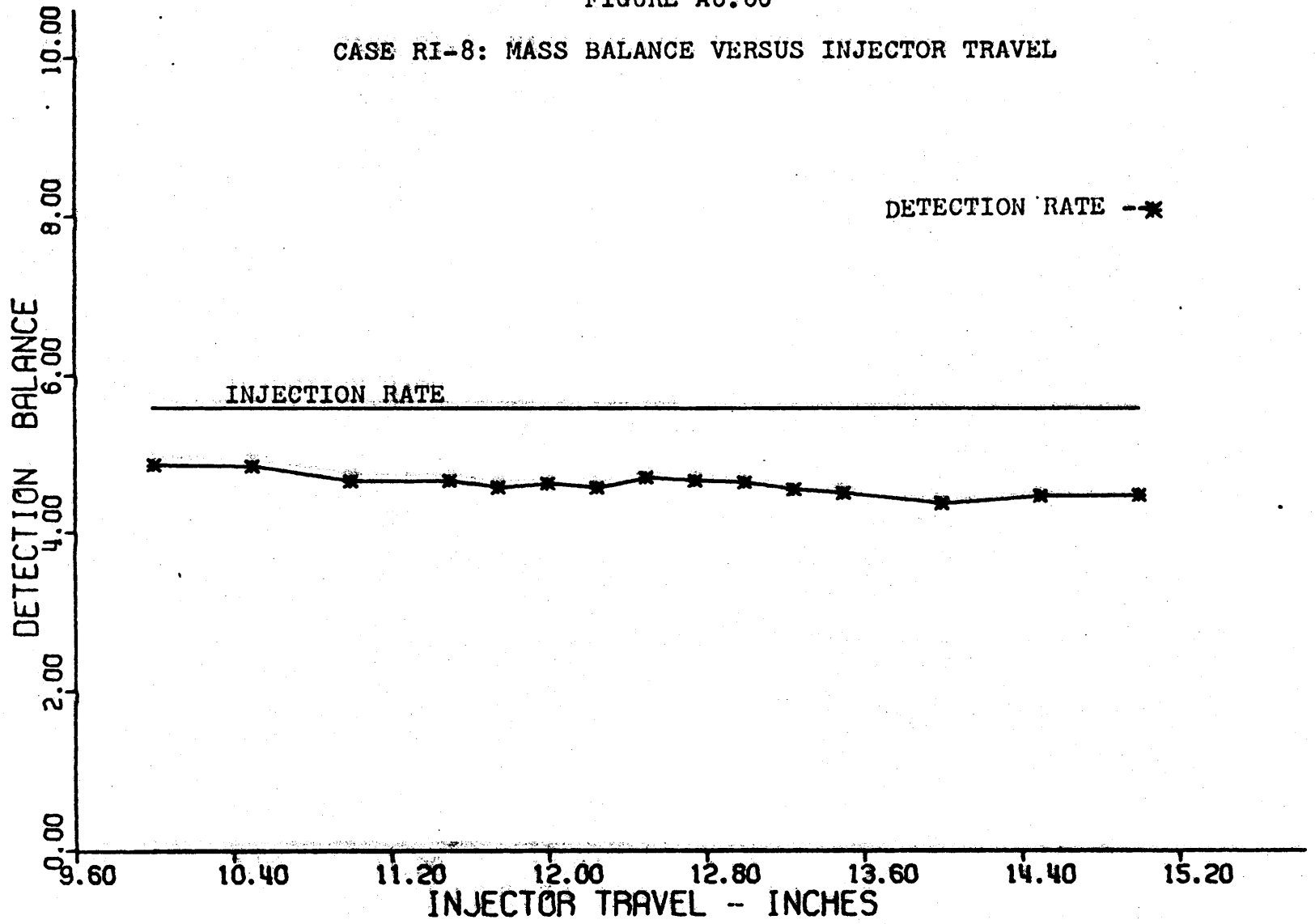

FIGURE A8.81

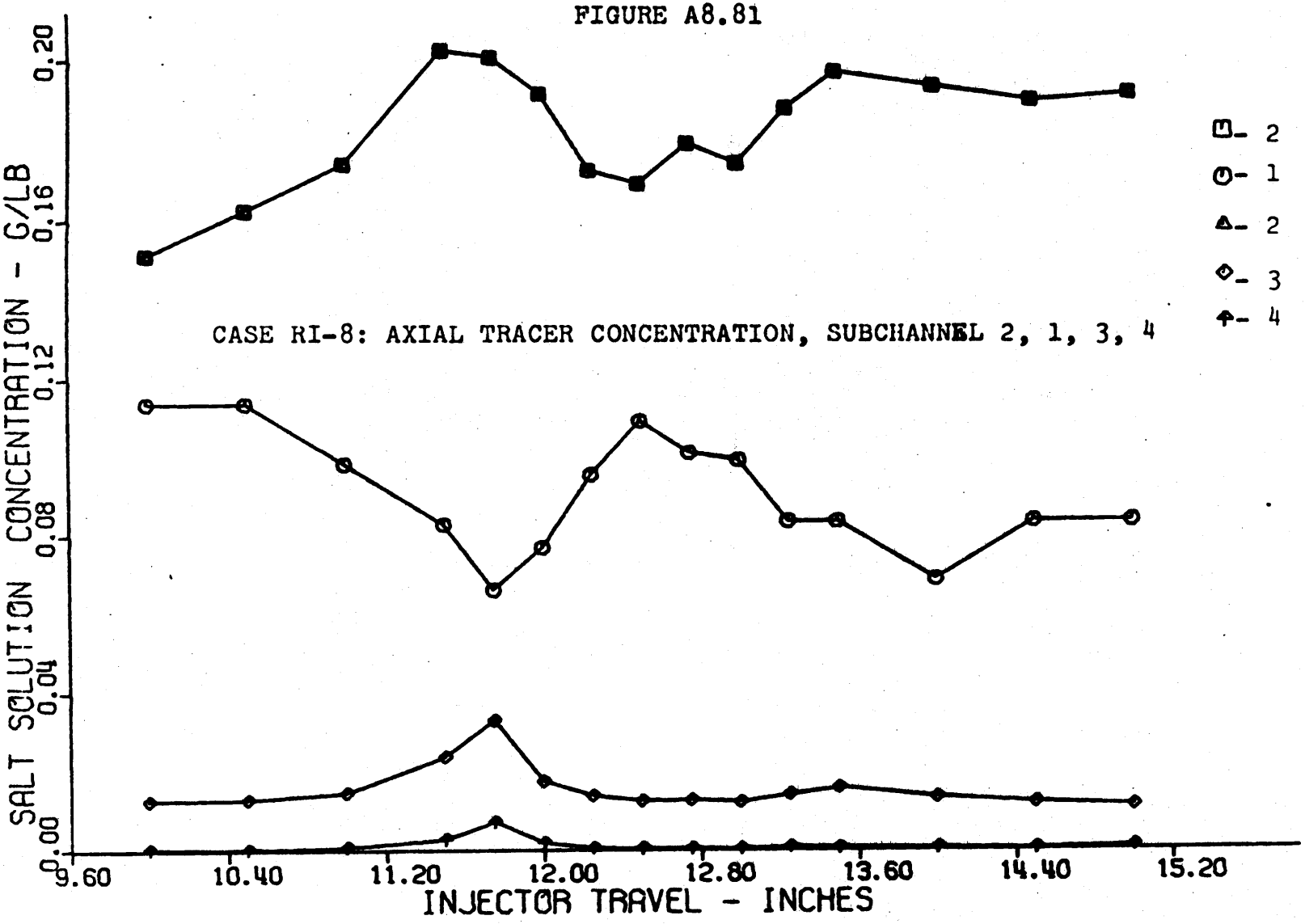
CASE RI-8: AXIAL TRACER CONCENTRATION, SUBCHANNEL 2, 1, 3, 4
SALT SOLUTION CONCENTRATION - G/LB
0.00
0.04
0.08
0.12
0.16
0.20
9.60
10.40
11.20
12.00
12.80
13.60
14.40
15.20
INJECTOR TRAVEL - INCHES
2
1
2
3
4

FIGURE A8.82

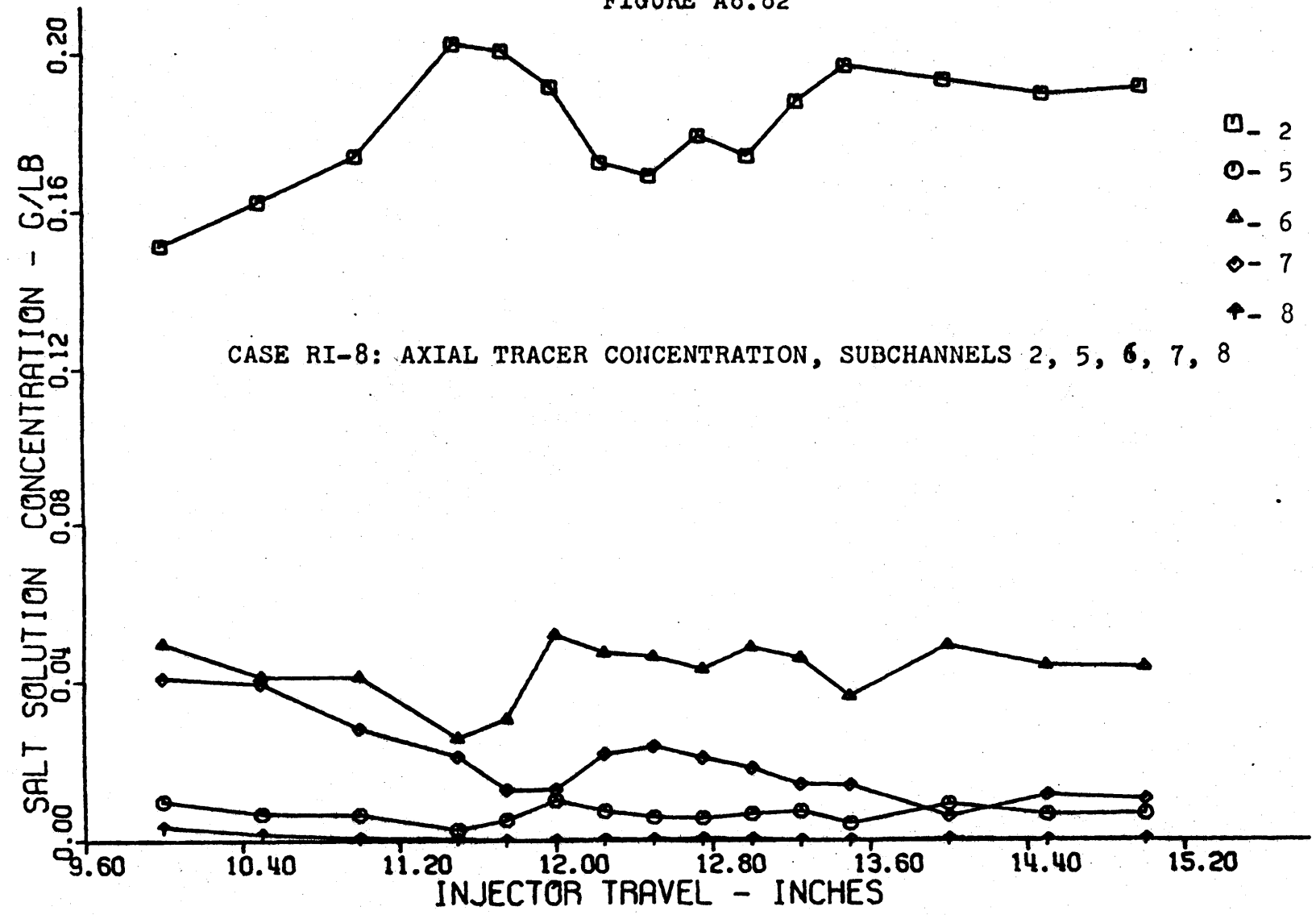

CASE RI-8: AXIAL TRACER CONCENTRATION, SUBCHANNELS 2, 5, 6, 7, 8

FIGURE A8.83

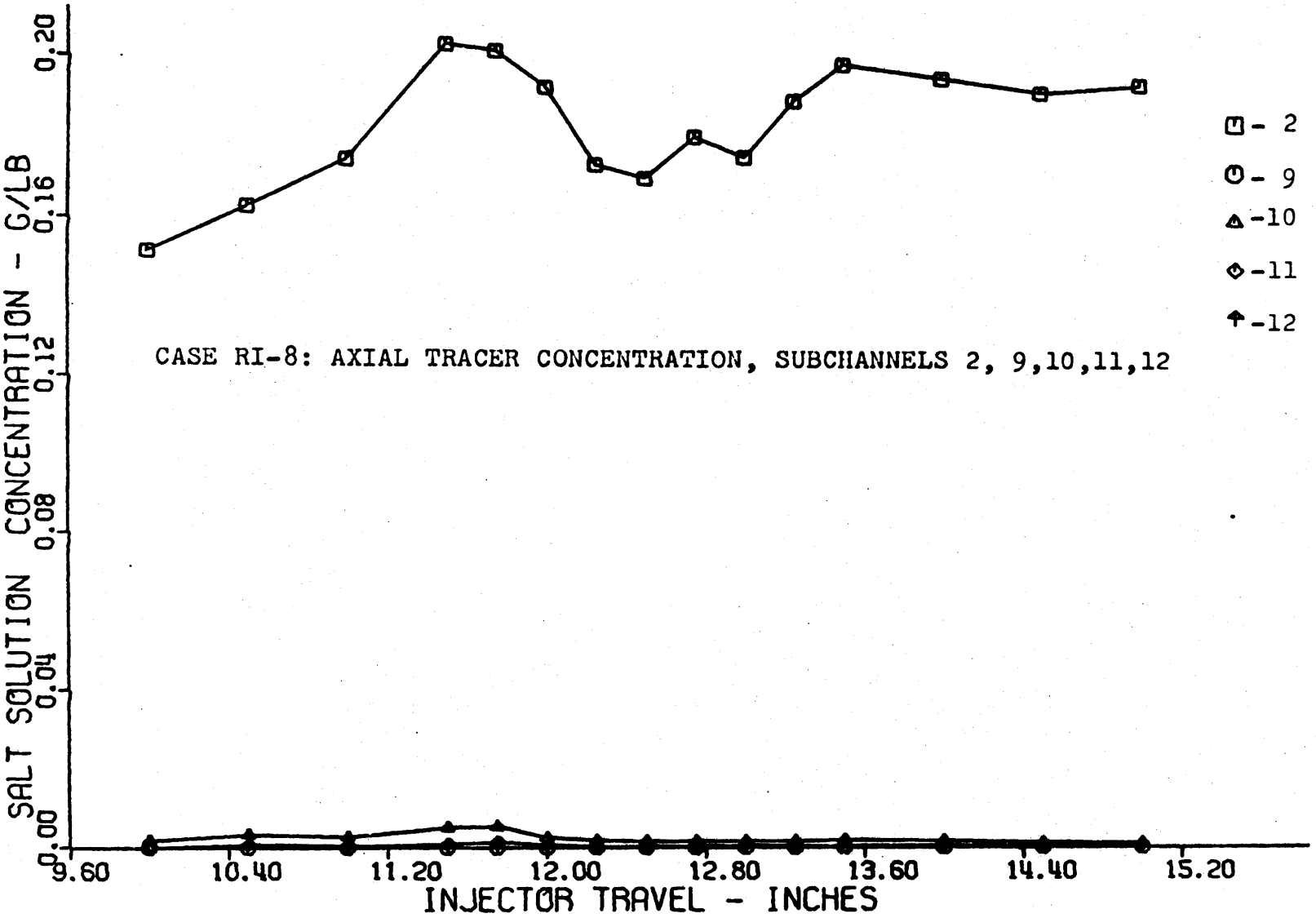

CASE RI-8: AXIAL TRACER CONCENTRATION, SUBCHANNELS 2, 9,10,11,12

FIGURE A8.84

CASE RI-9: MASS BALANCE VERSUS INJECTOR TRAVEL

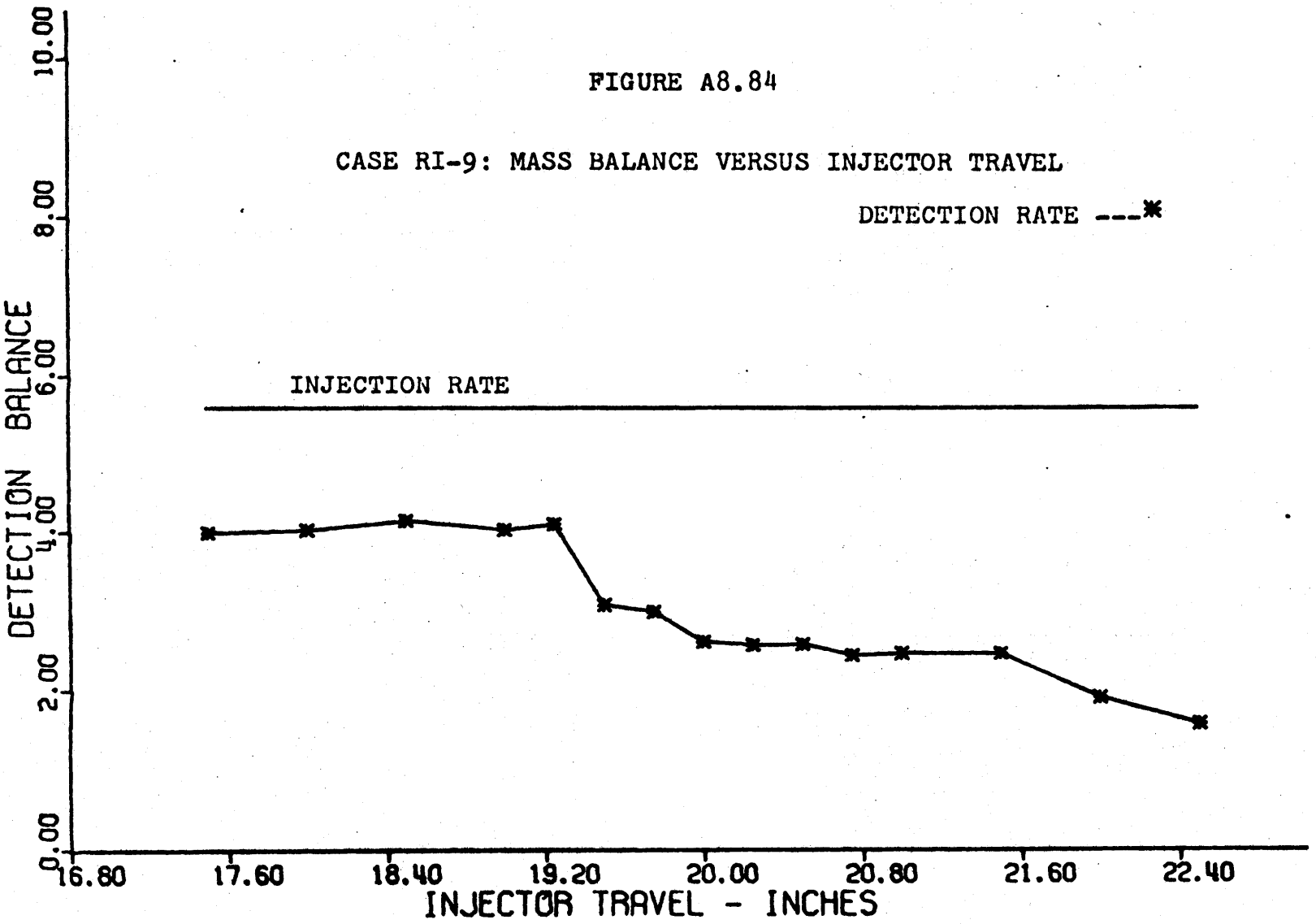

FIGURE A8.85

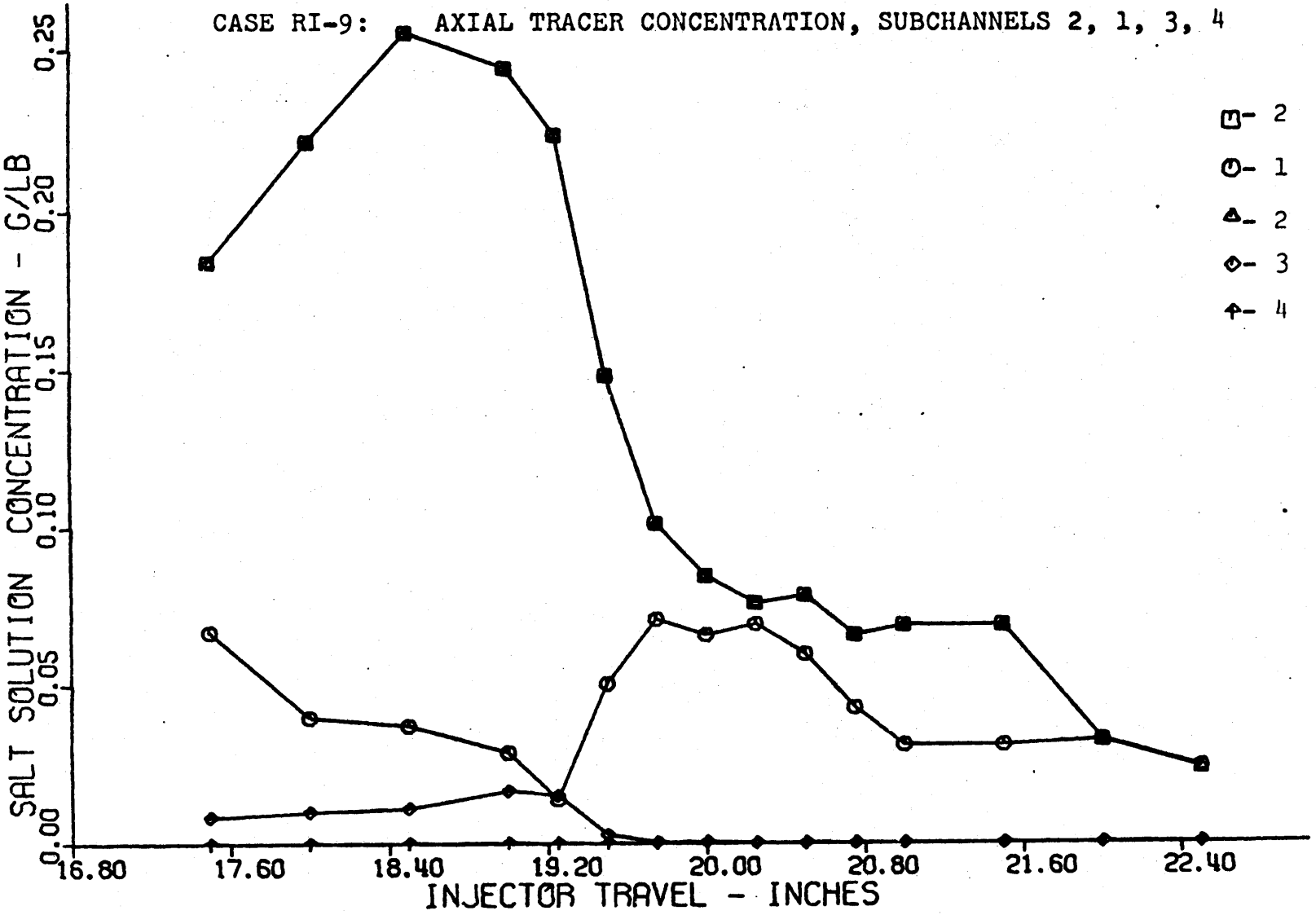
CASE RI-9: AXIAL TRACER CONCENTRATION, SUBCHANNELS 2, 1, 3, 4
SALT SOLUTION CONCENTRATION - G/LB
0.00
0.05
0.10
0.15
0.20
0.25
16.80
17.60
18.40
19.20
20.00
20.80
21.60
22.40
INJECTOR TRAVEL - INCHES
2
1
2
3
4

FIGURE A8.86

CASE RI-9: AXIAL TRACER CONCENTRATION, SUBCHANNELS 2, 5,6,7,8

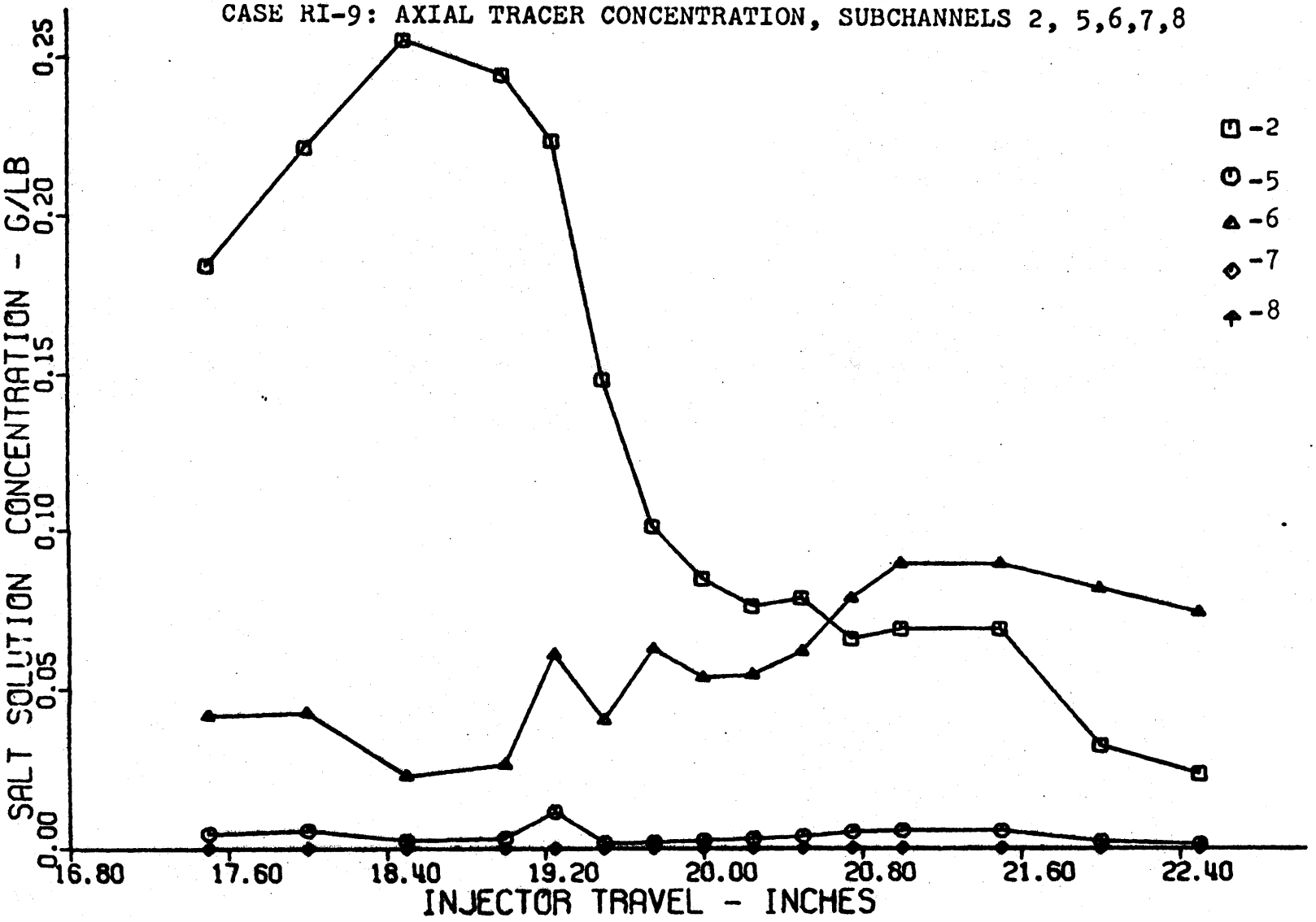

FIGURE A8.87

CASE RI-10: MASS BALANCE VERSUS INJECTOR TRAVEL

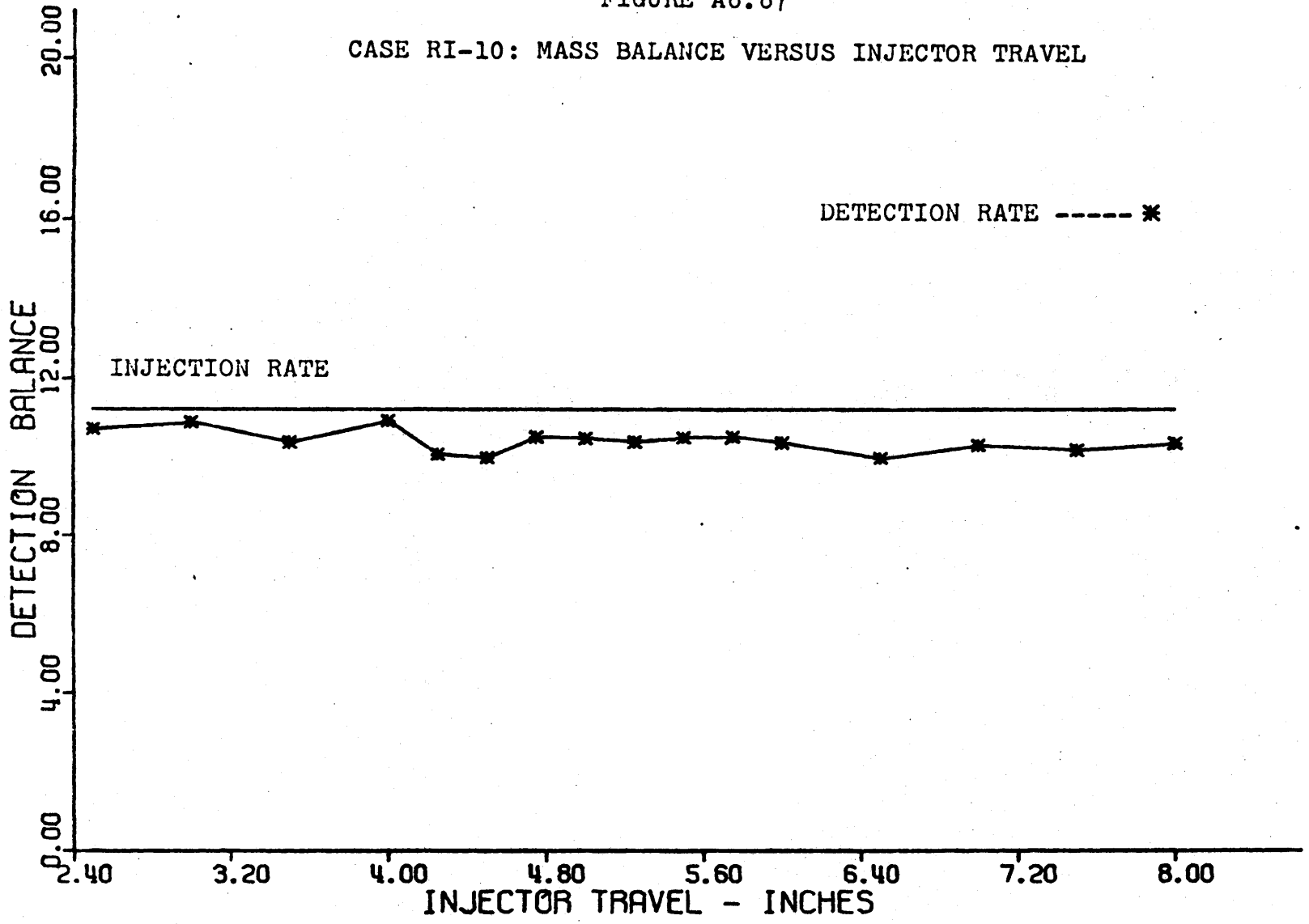

FIGURE A8.88

CASE RI-10: AXIAL TRACER CONCENTRATION, SUBCHANNELS 2, 1, 3, 4

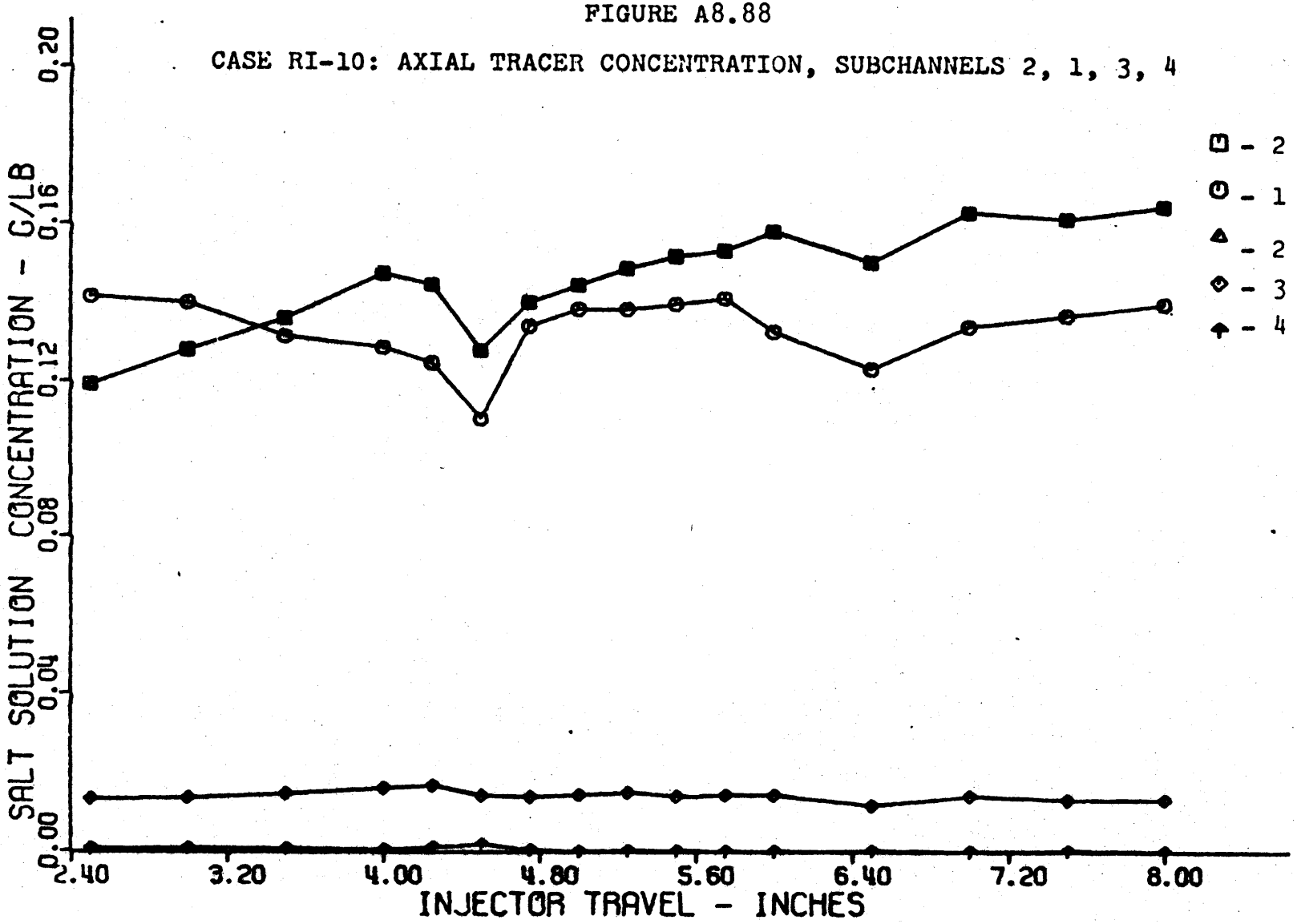

FIGURE A8.89

CASE RI-10: AXIAL TRACER CONCNETRATION, SUBCHANNELS 2, 5, 6, 7, 8

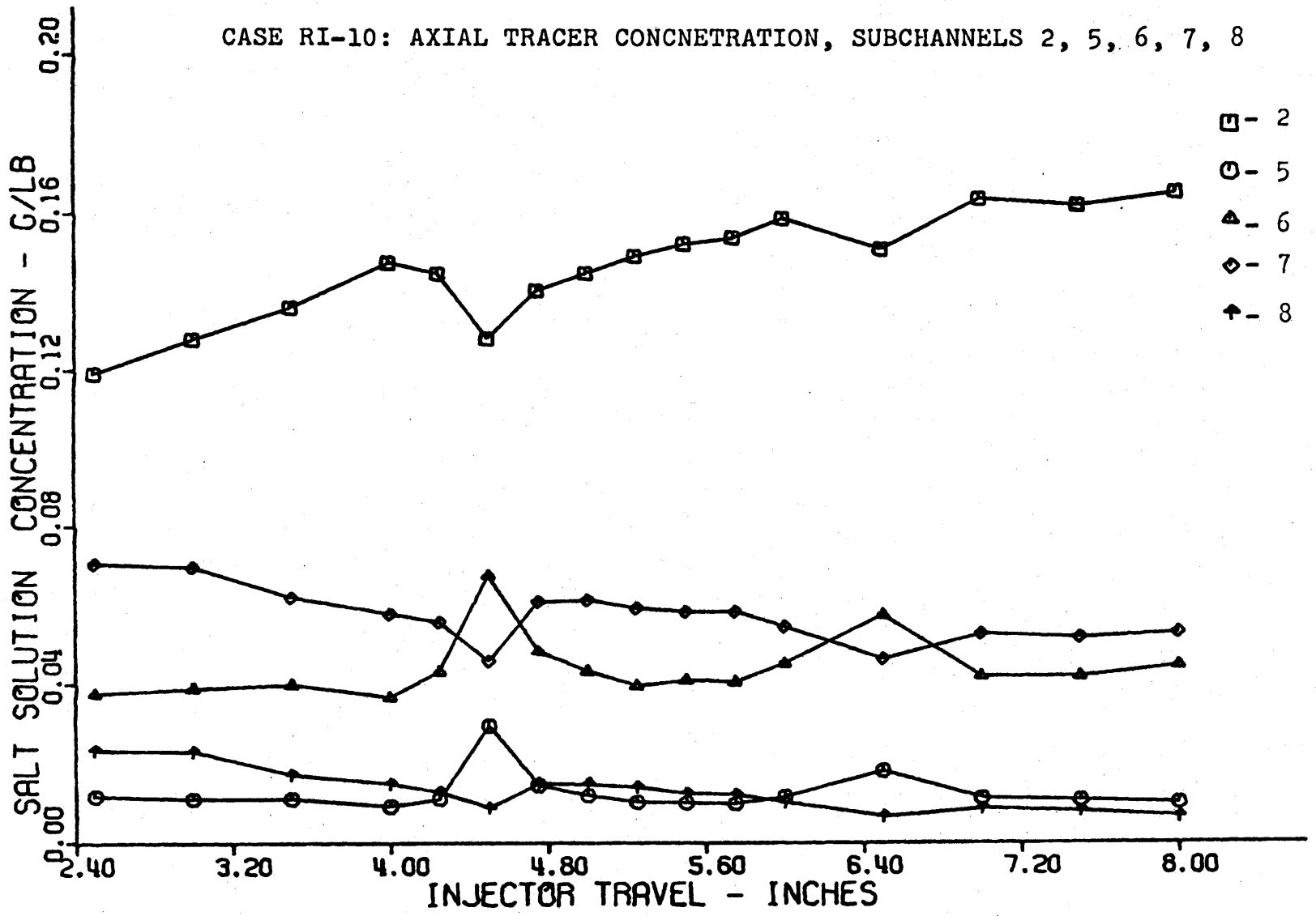

FIGURE A8.90

CASE RI-10: AXIAL TRACER CONCENTRATION, SUBCHANNELS 2, 9,10,11,12

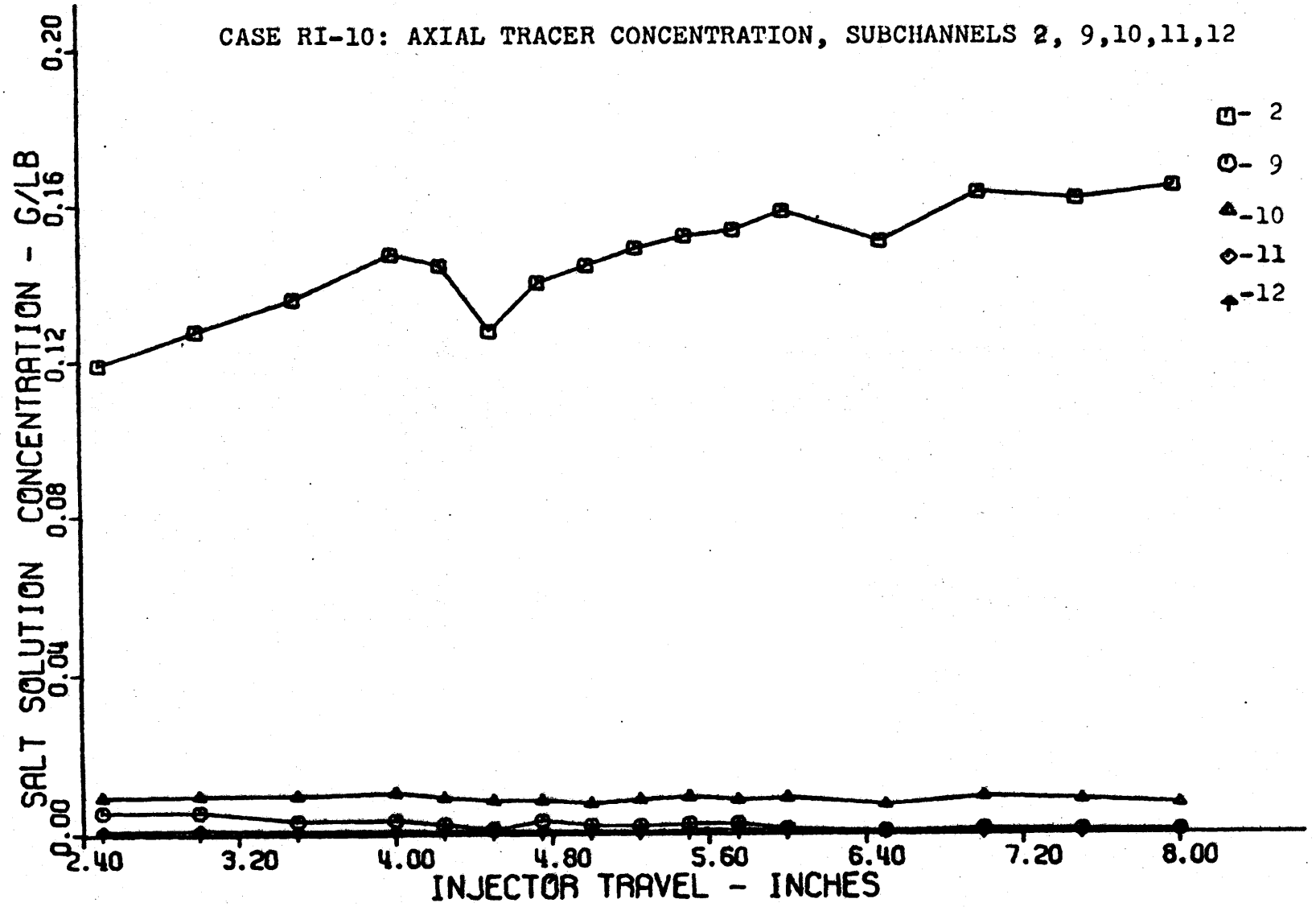

FIGURE A8.91

CASE RI-10: AXIAL TRACER CONCENTRATION, SUBCHANNELS 2,21,22,23,24

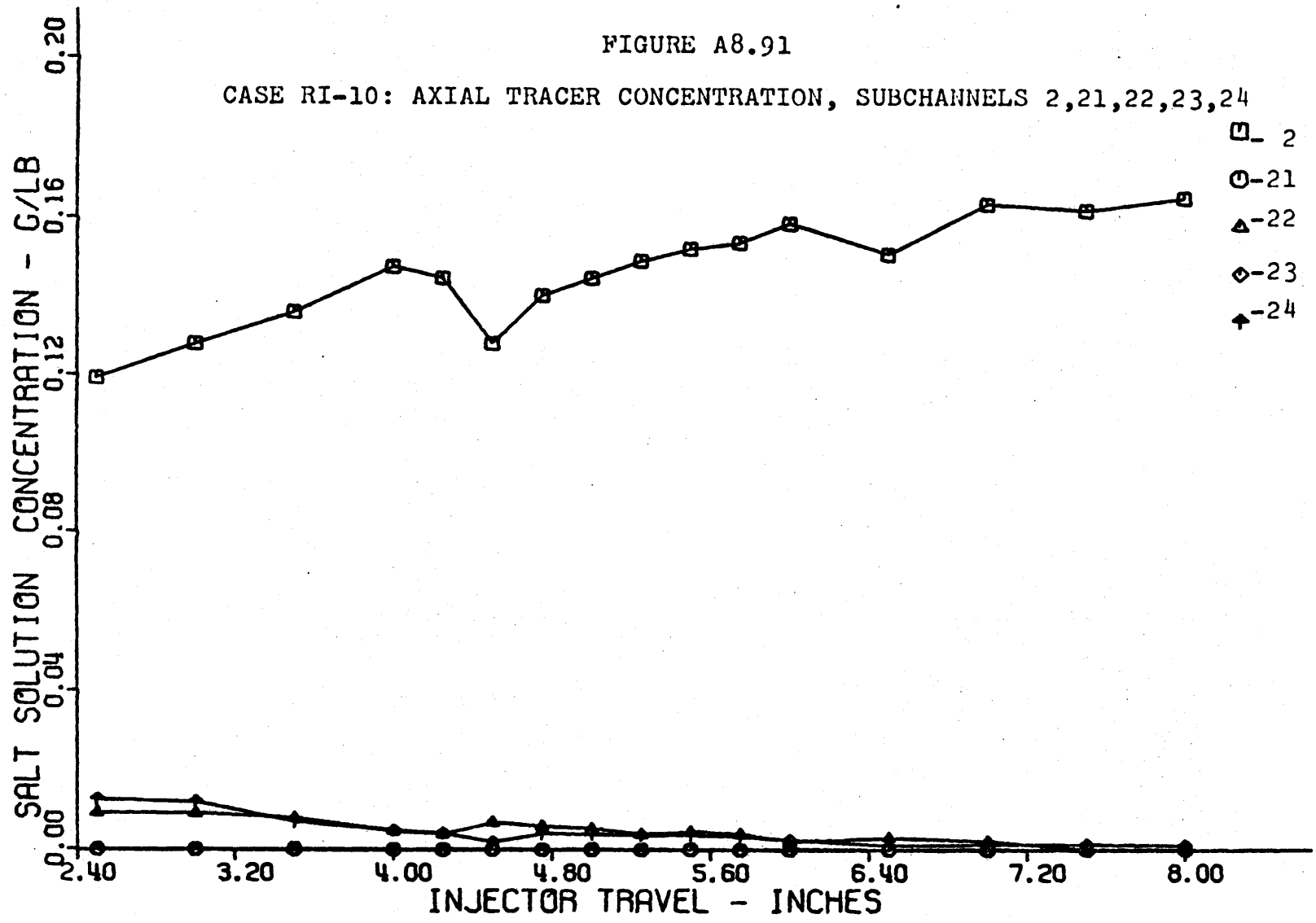

FIGURE A8.92

CASE RI-11: MASS BALANCE VERSUS INJECTOR TRAVEL

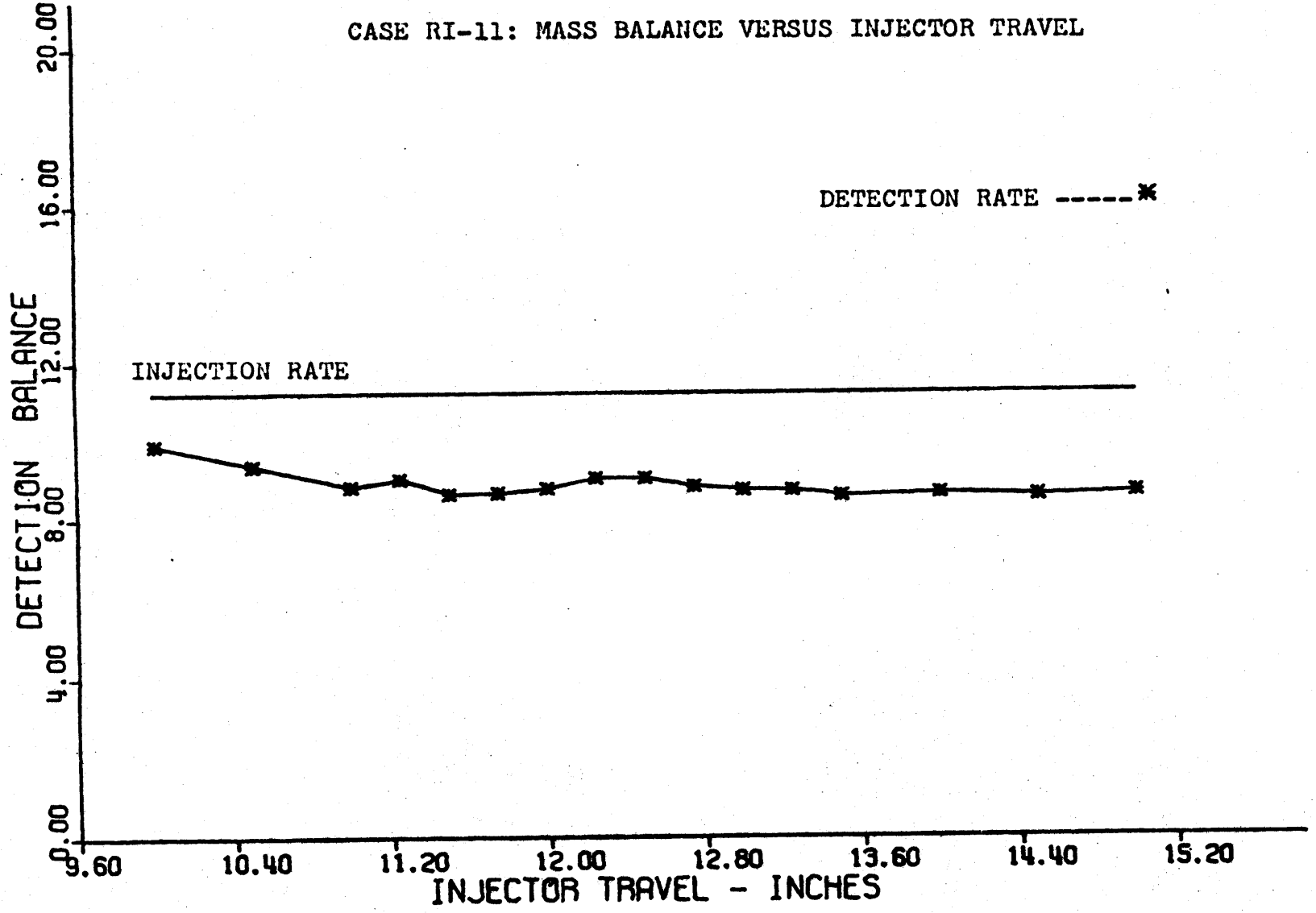

FIGURE A8.93

CASE RI-11: AXIAL TRACER CONCENTRATION, SUBCHANNELS 2, 1, 3, 4

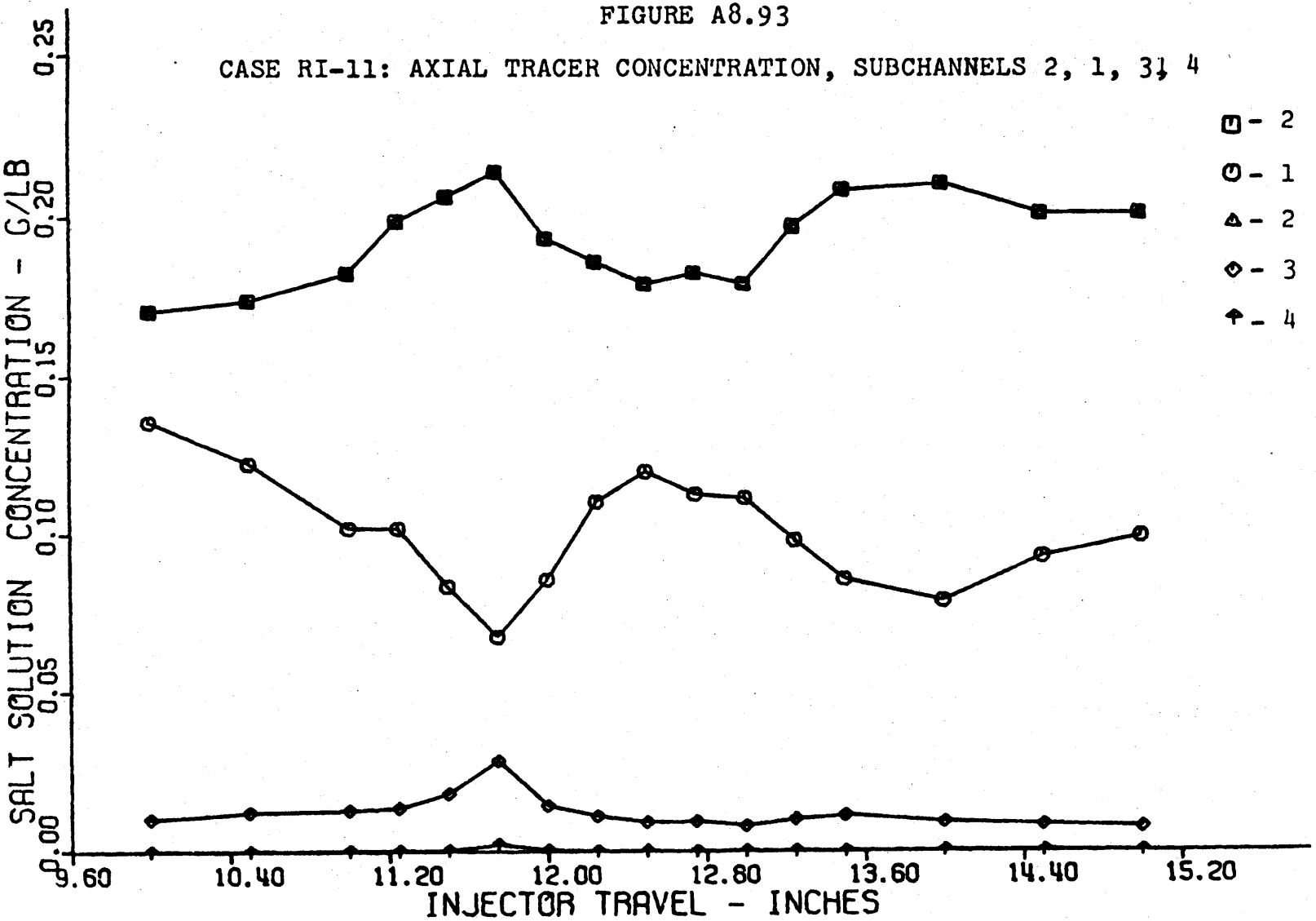

FIGURE A8.94

CASE RI-11: AXIAL TRACER CONCENTRATION, SUBCHANNELS 2, 5, 6, 7, 8

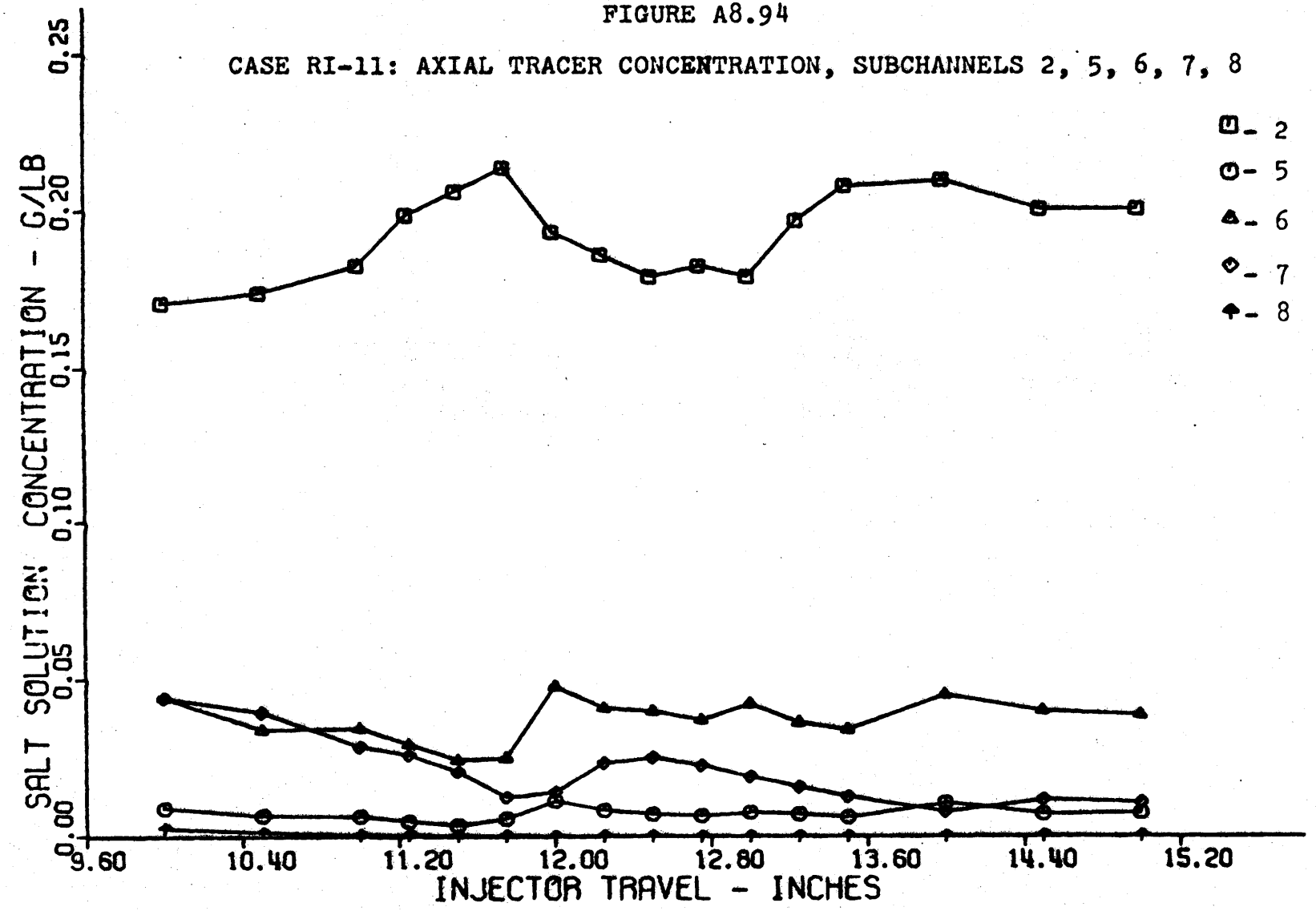

FIGURE A8.95

CASE RI-11: AXIAL TRACER CONCENTRATION, SUBCHANNELS 2, 9,10,11,12

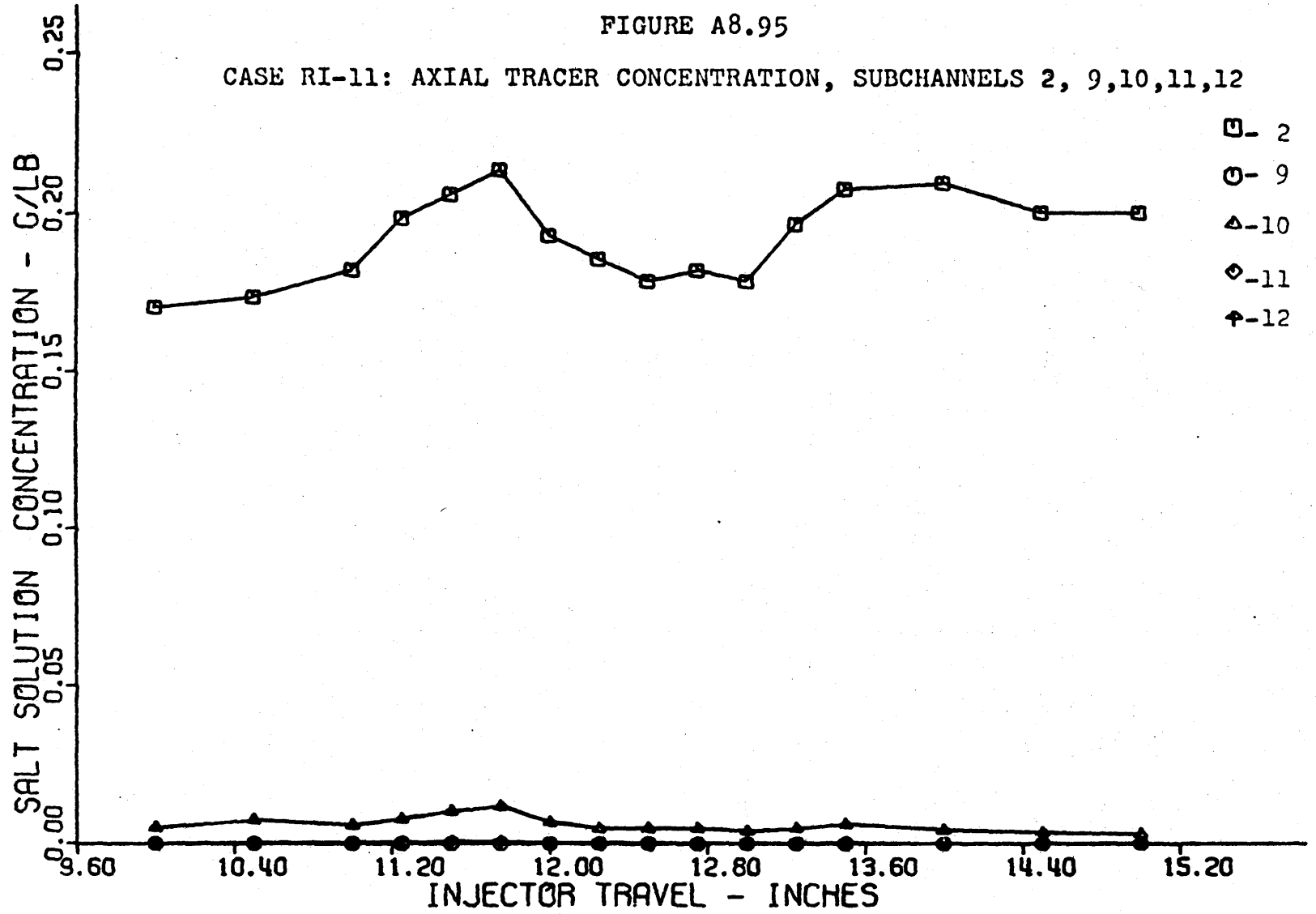

FIGURE A8.96

CASE RI-12: MASS BALANCE VERSUS INJECTOR TRAVEL

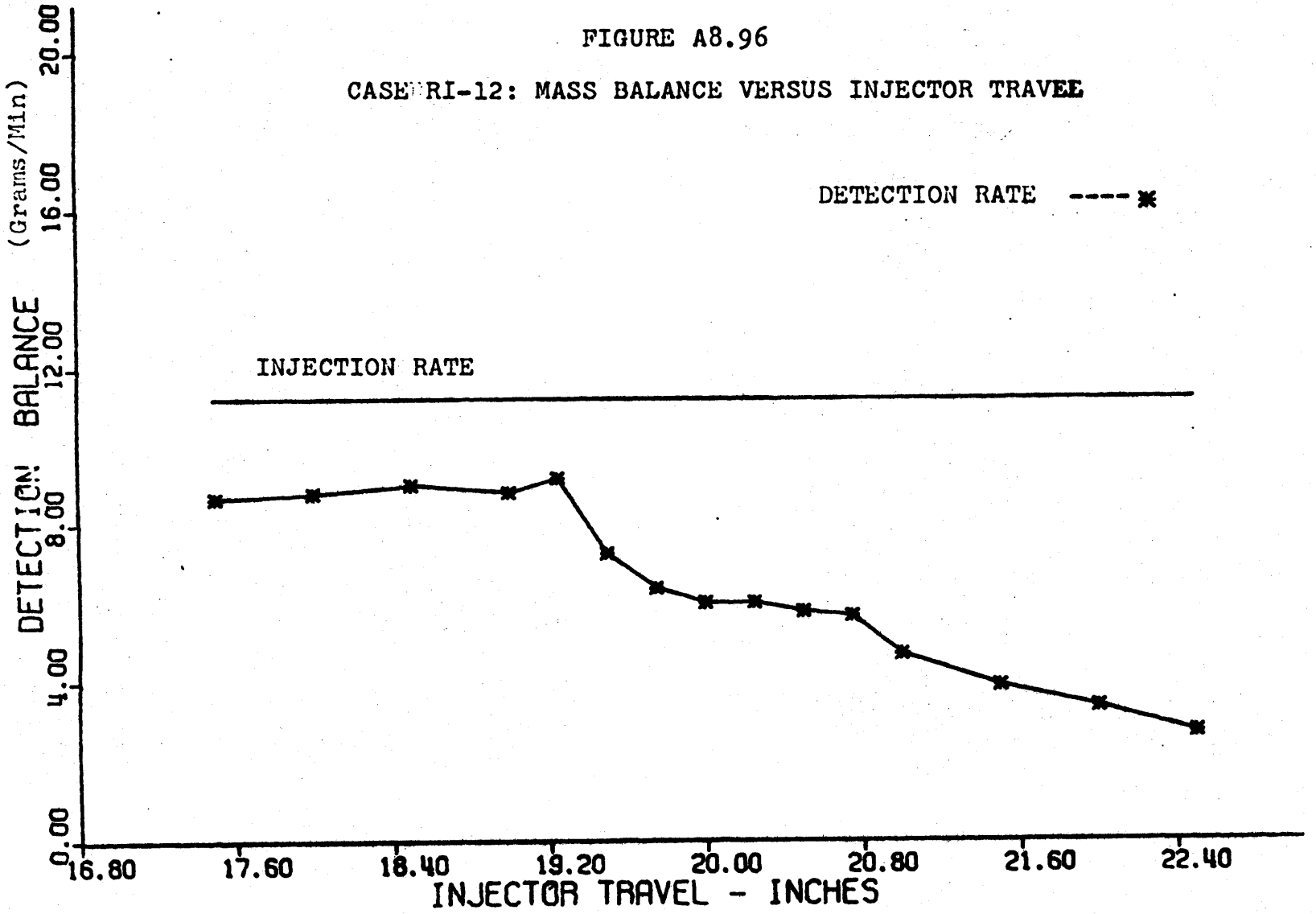

FIGURE A8.97

CASE RI-12: AXIAL TRACER CONCENTRATION, SUBCHANNELS 2, 1, 3, 4

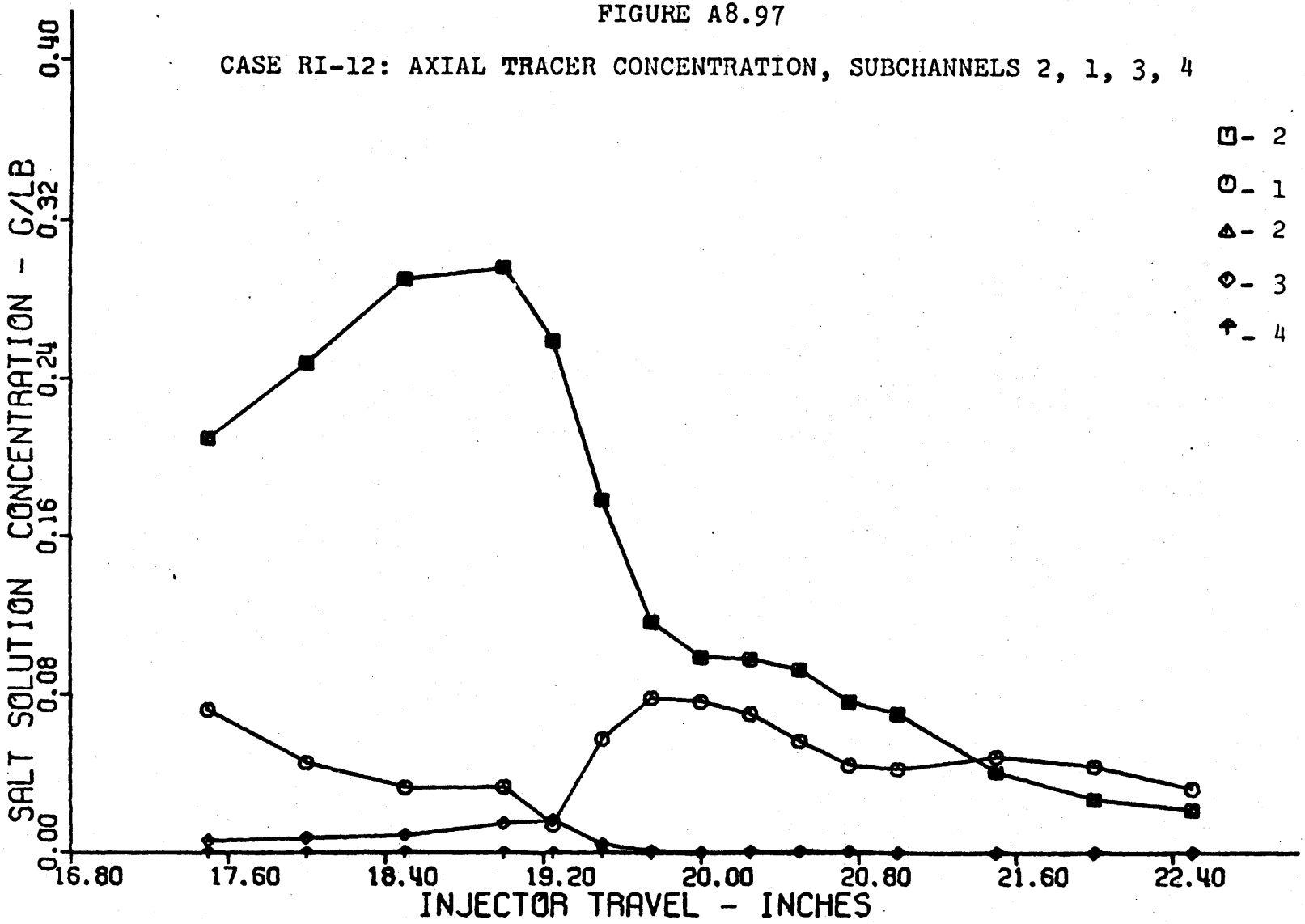

FIGURE A8.98

CASE RI-12: AXIAL TRACER CONCENTRATION, SUBCHANNELS 2, 5, 6, 7, 8

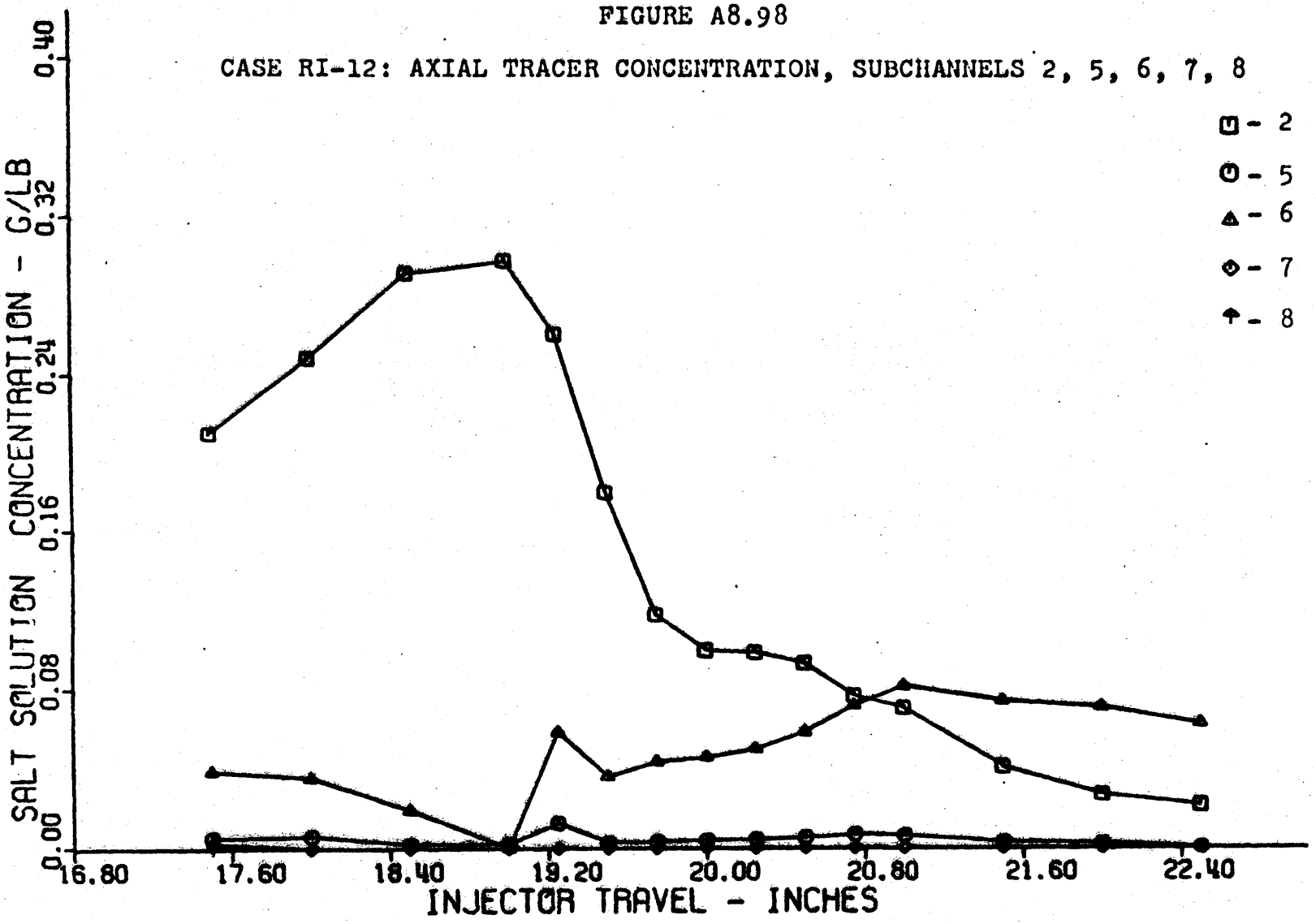

FIGURE A8.99

CASE RP-1: MASS BALANCE VERSUS INJECTOR TRAVEL

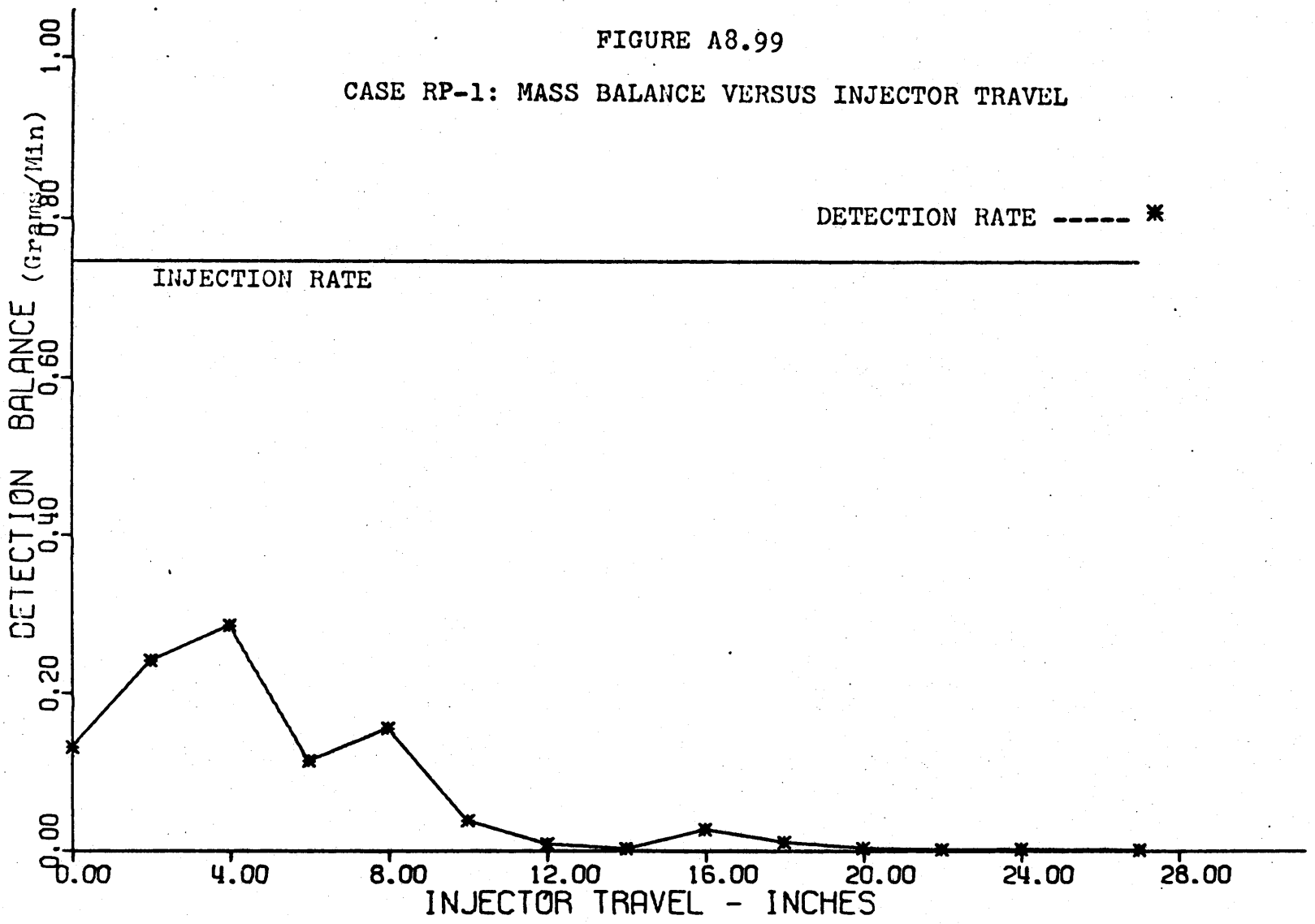

FIGURE A8.100

CASE RP-1: AXIAL TRACER CONCENTRATION, SUBCHANNELS 48,29,30,31, and 32

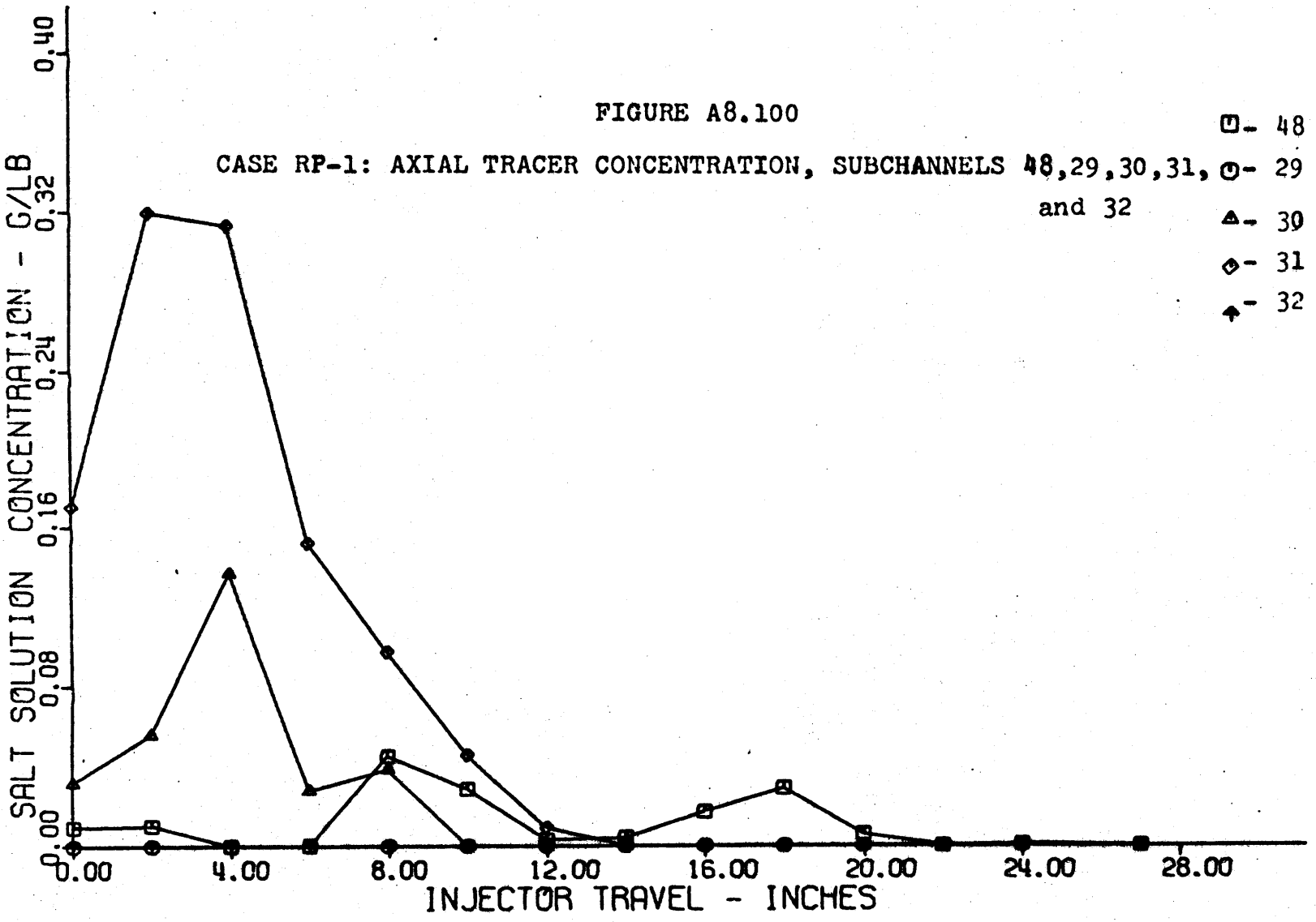

FIGURE A8.101

CASE RP-2: MASS BALANCE VERSUS INJECTOR TRAVEL

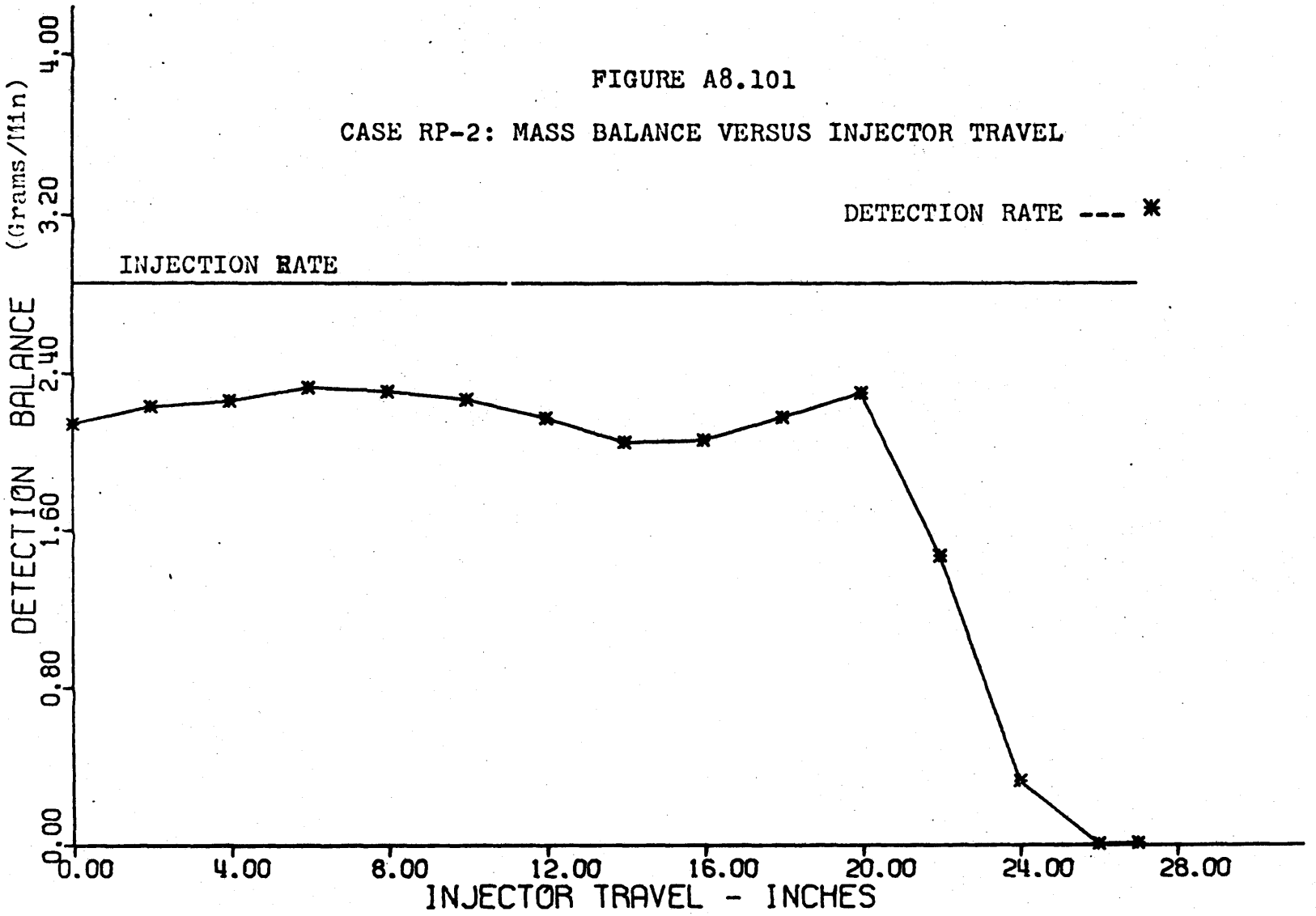

FIGURE A8.102

CASE RP-2: AXIAL TRACER CONCENTRATION, SUBCHANNELS 48,29,30,31,32

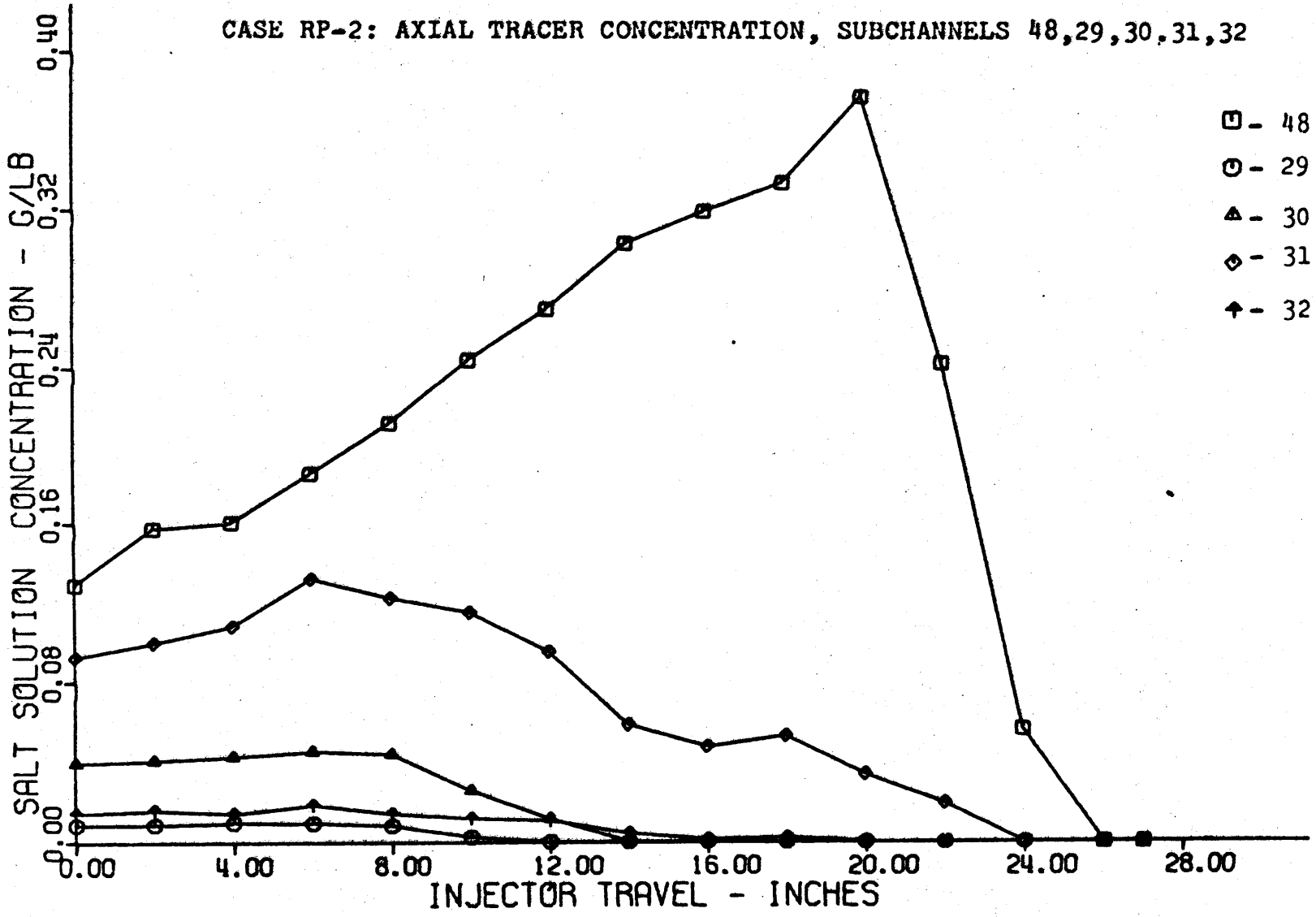

FIGURE A8.103

CASE RP-2: AXIAL TRACER CONCENTRATION, SUBCHANNELS 48,33,34,35,36

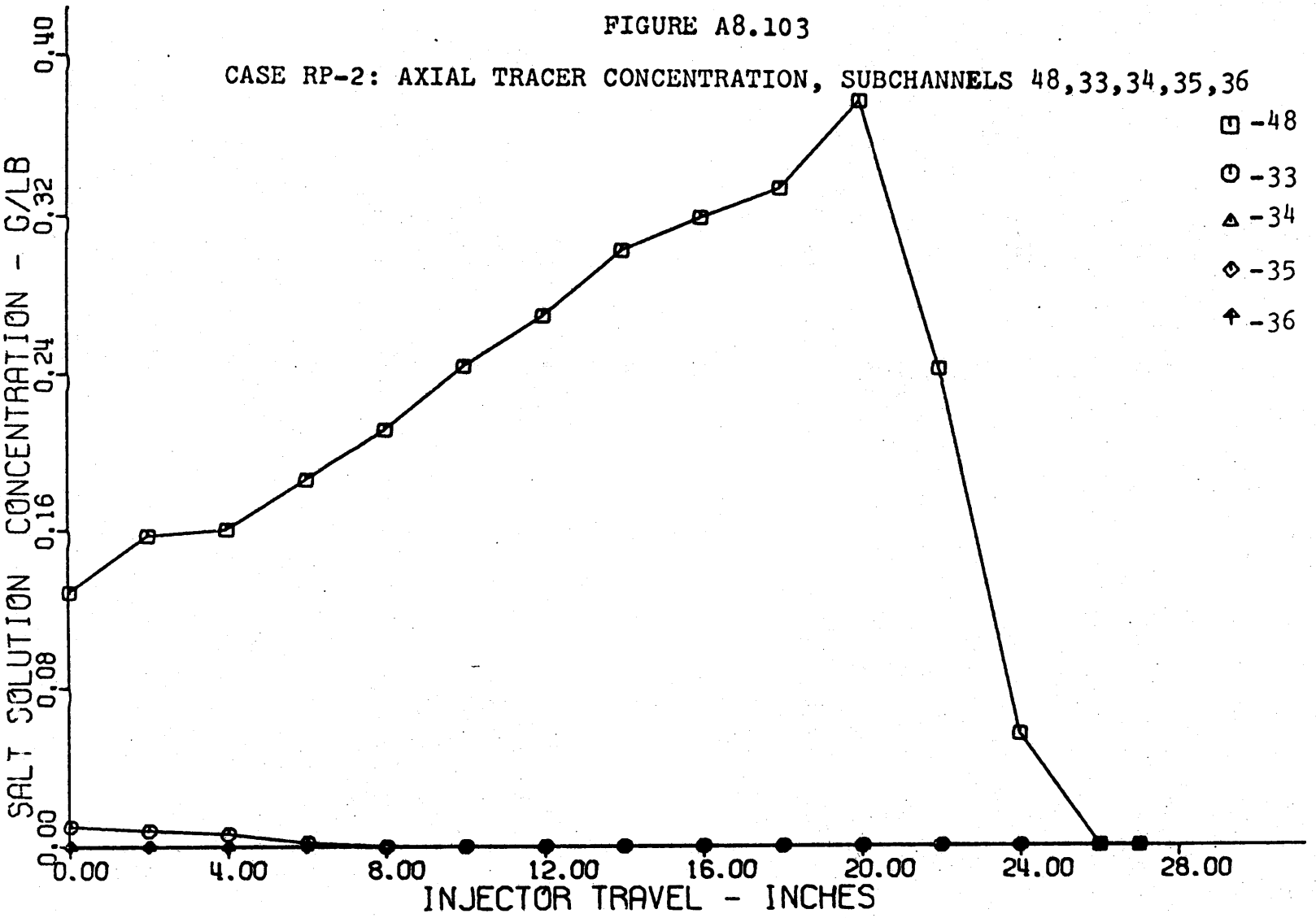

FIGURE A8.104

CASE RP-2: AXIAL TRACER CONCENTRATION, SUBCHANNELS 48,49, 50,51,52

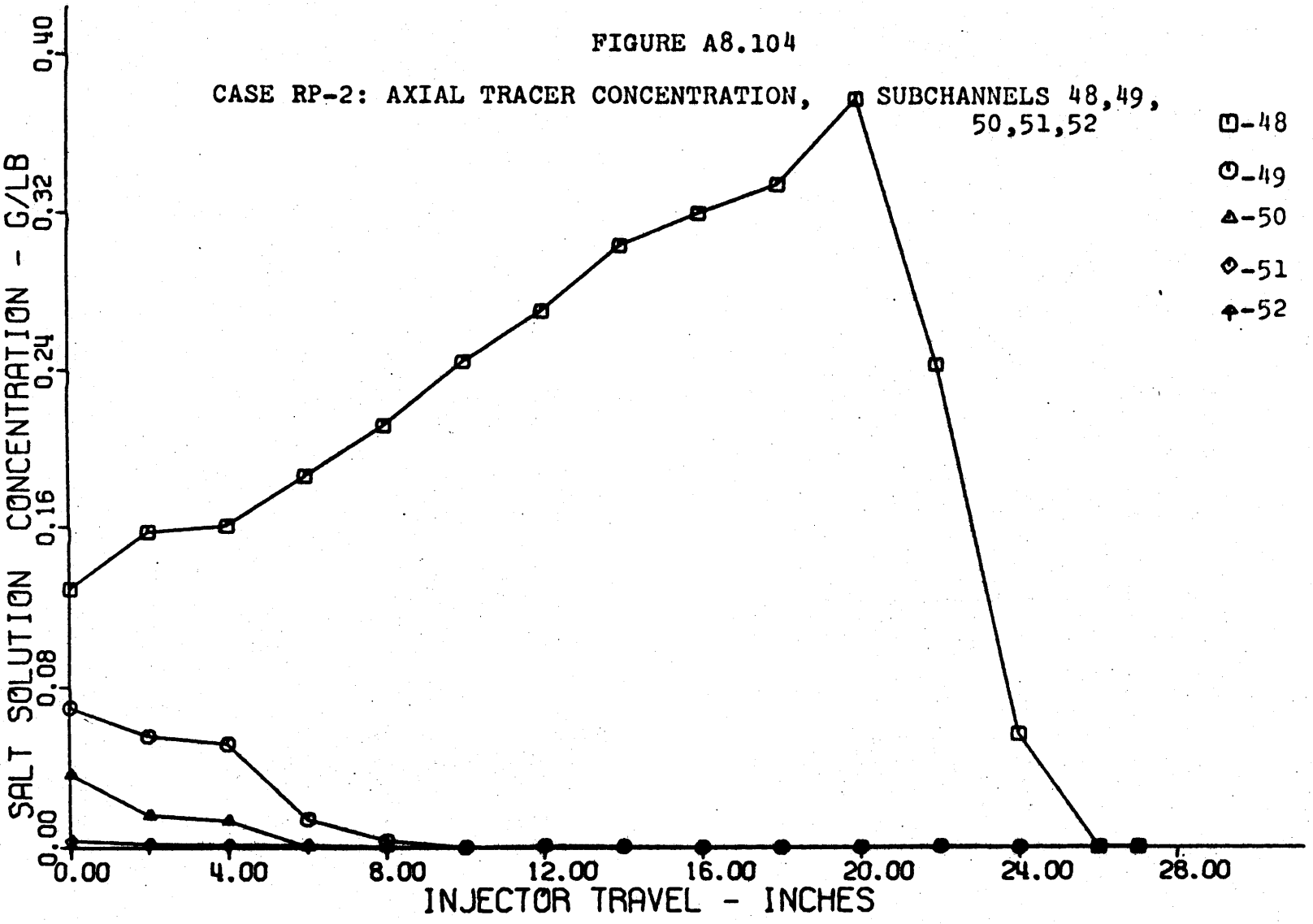

FIGURE A8.105

CASE RP-3: MASS BALANCE VERSUS INJECTOR TRAVEL

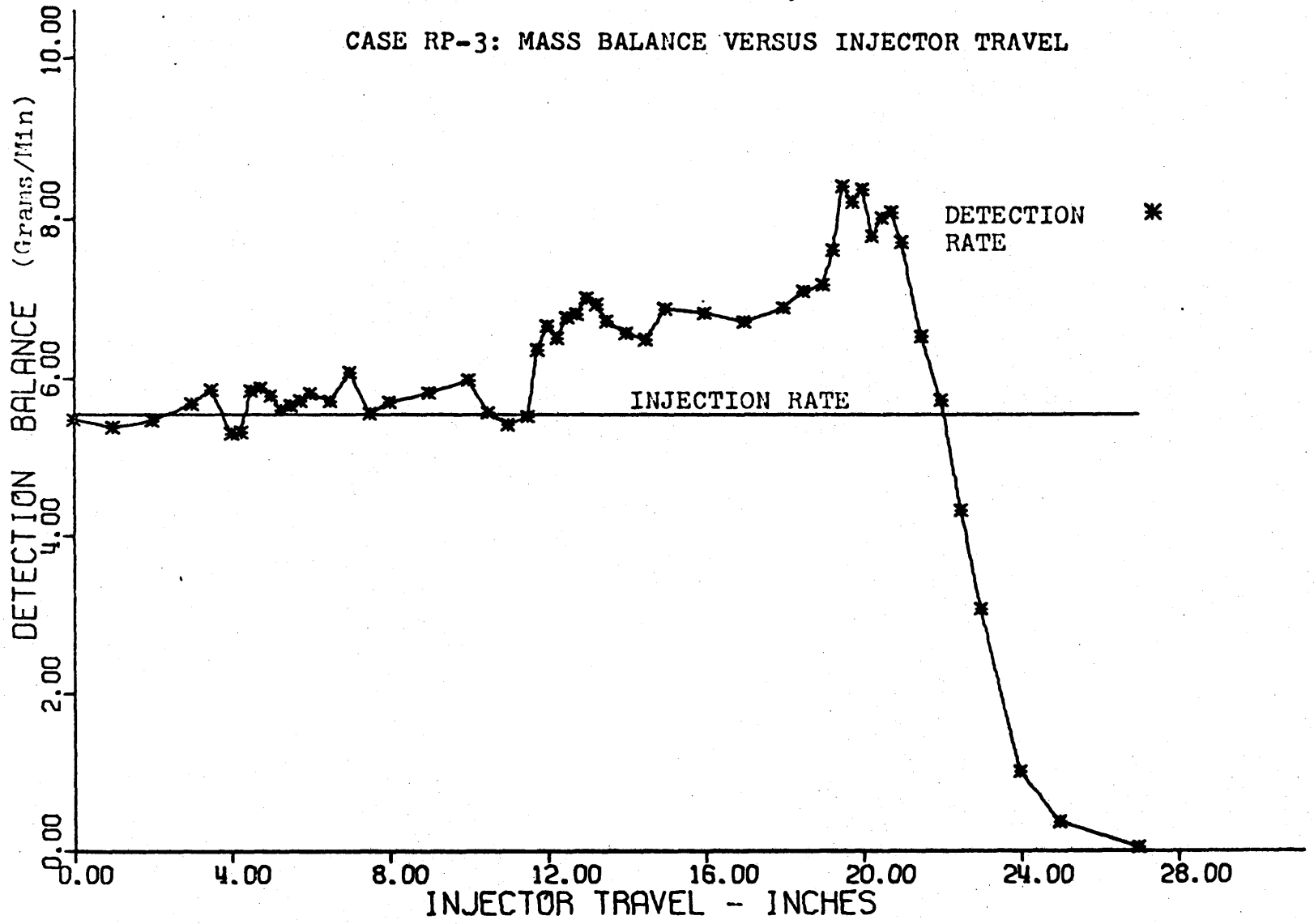

FIGURE A8.106

CASE RP-3: AXIAL TRACER CONCENTRATION, SUBCHANNELS 48,29,30, 31,32

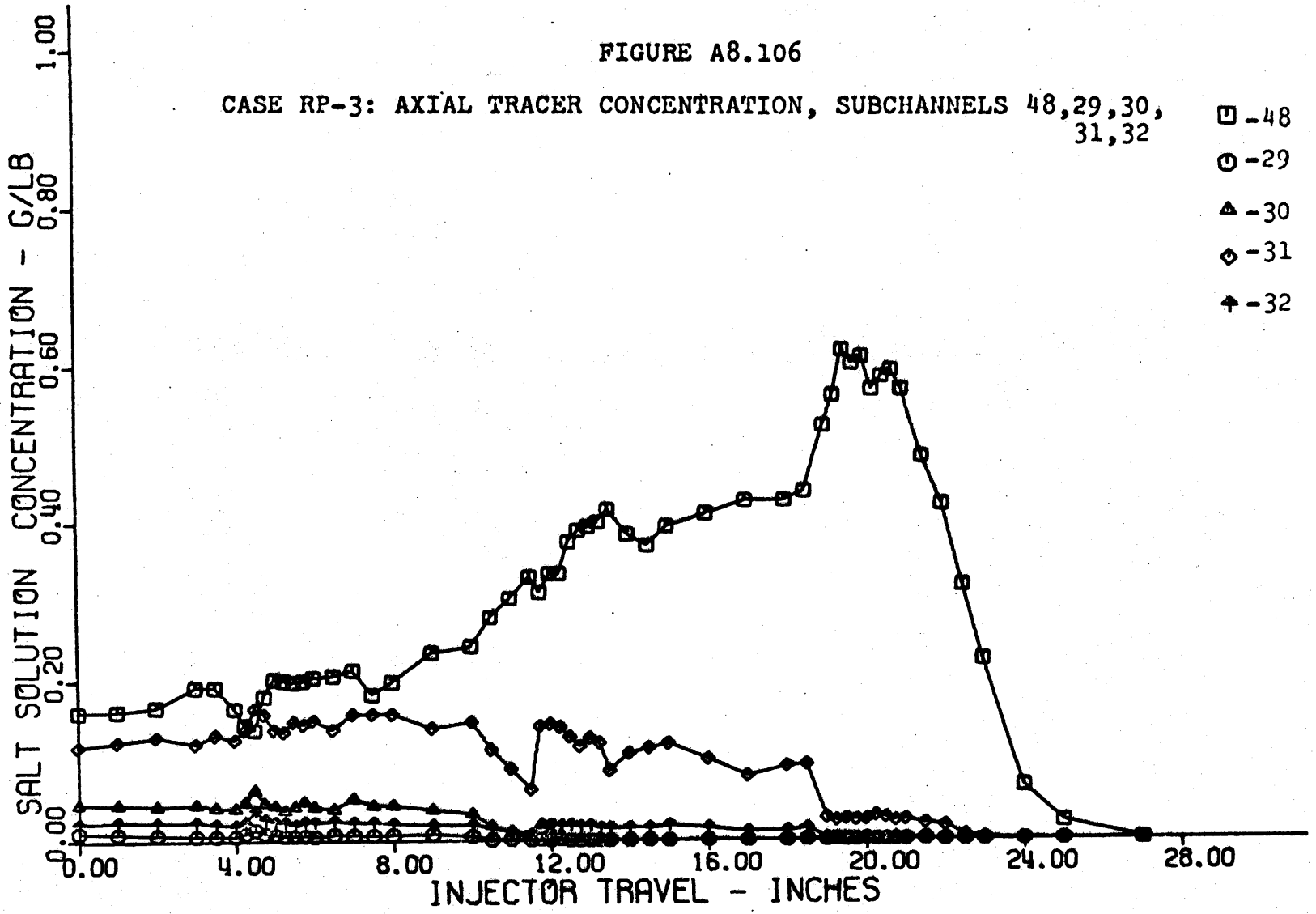

FIGURE A8.107

CASE RP-3: AXIAL TRACER CONCENTRATION, SUBCHANNELS 48,49,50,51,52

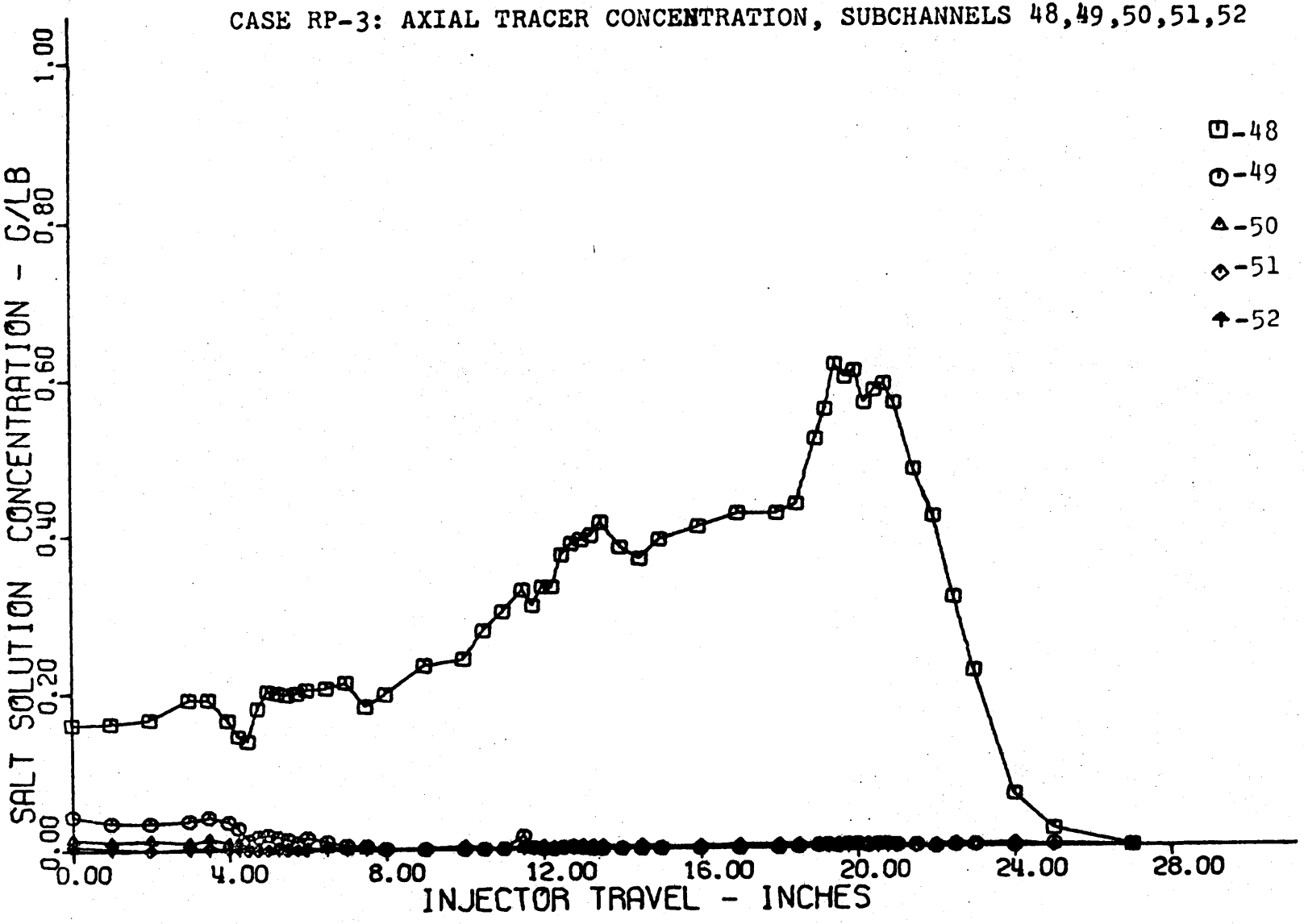

FIGURE A8.108

CASE RP-5: MASS BALANCE VERSUS INJECTOR TRAVEL (Experimental)

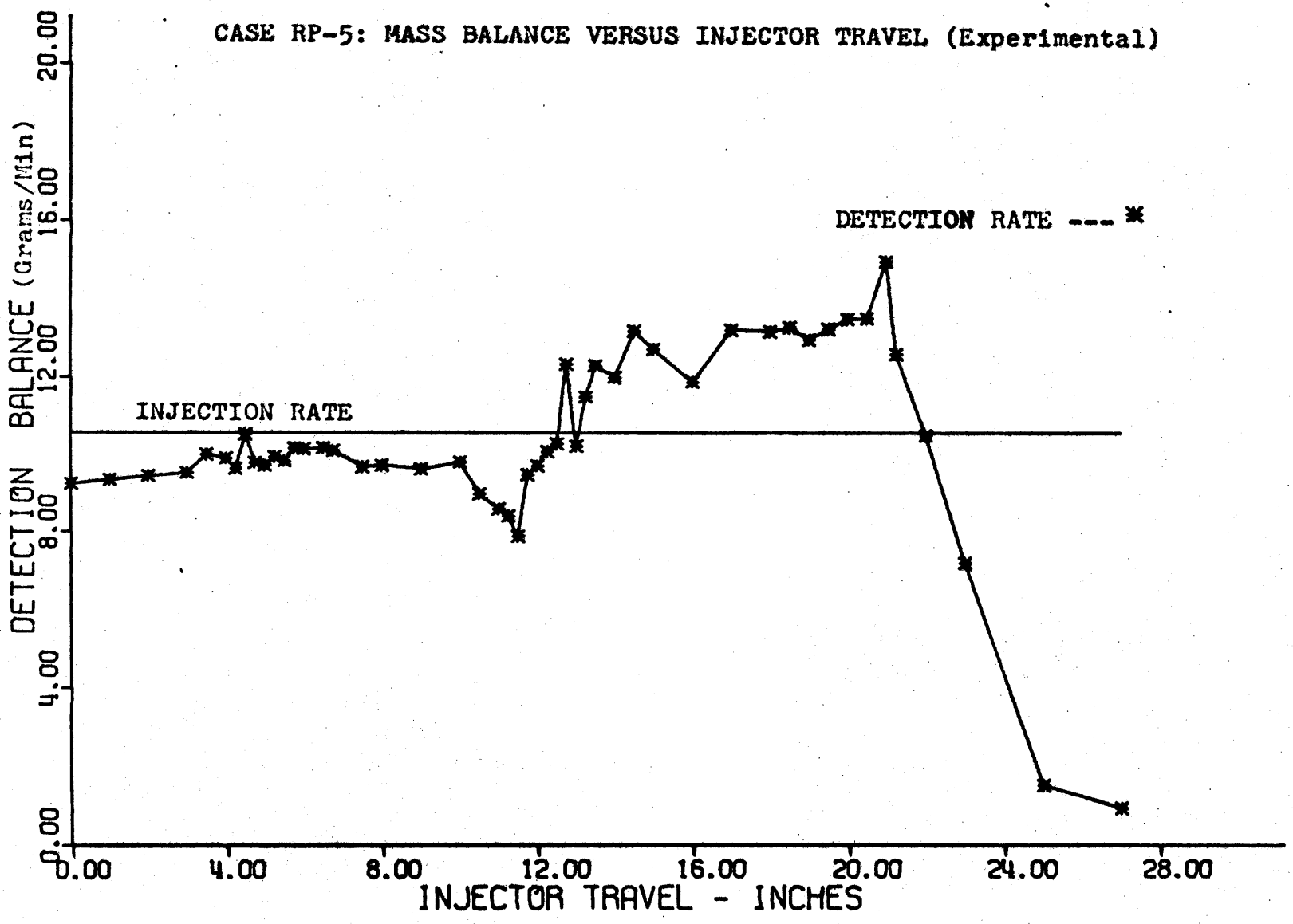

FIGURE A8.109

CASE RP-5: MASS BALANCE VERSUS INJECTOR TRAVEL (Analytical)

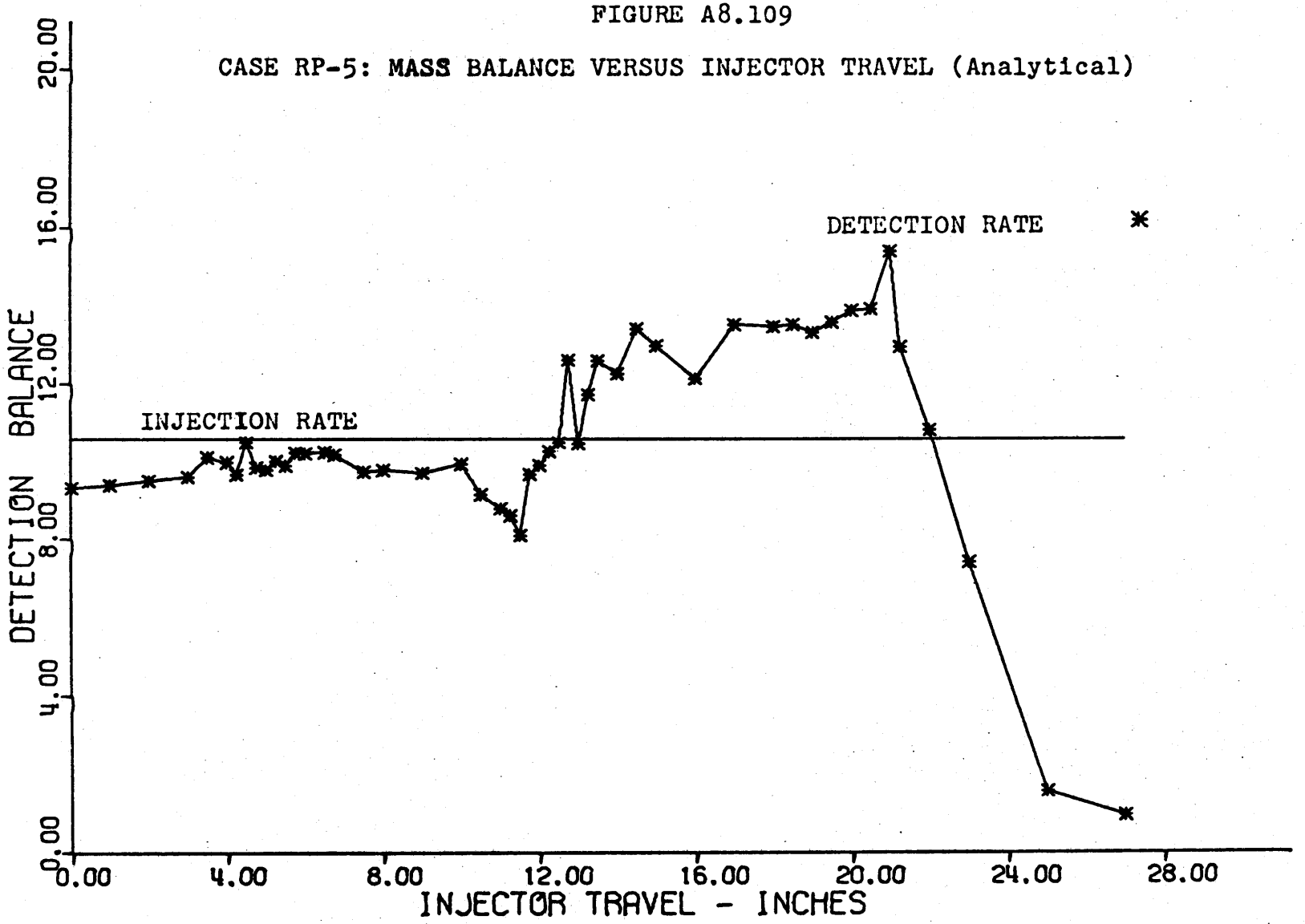

FIGURE A8.110

CASE RP-5: AXIAL TRACER CONCENTRATION, SUBCHANNELS 48,29,30,31,32

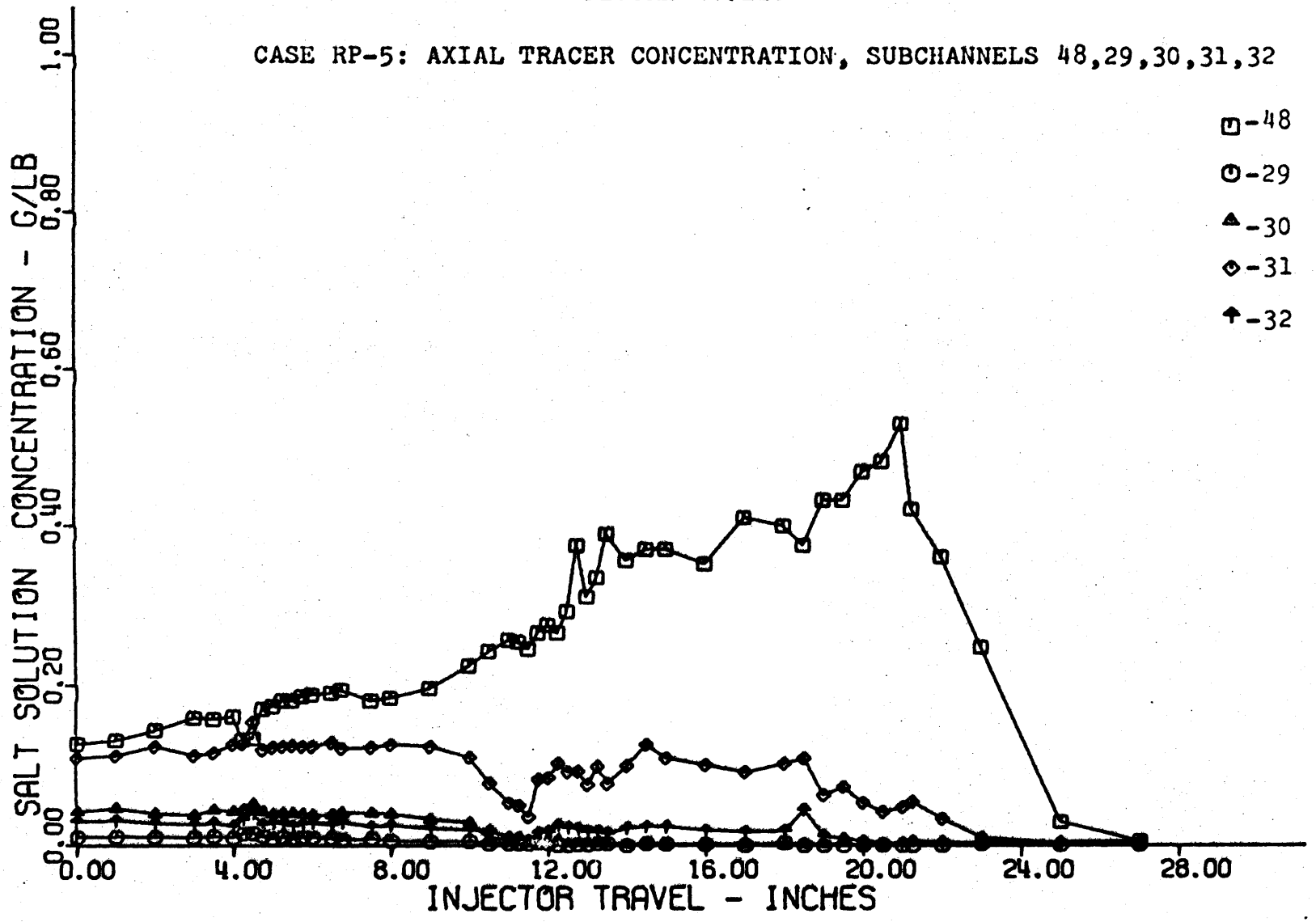

FIGURE A8.111

CASE RP-5: AXIAL TRACER CONCENTRATION, SUBCHANNELS 48,49,50,51,52

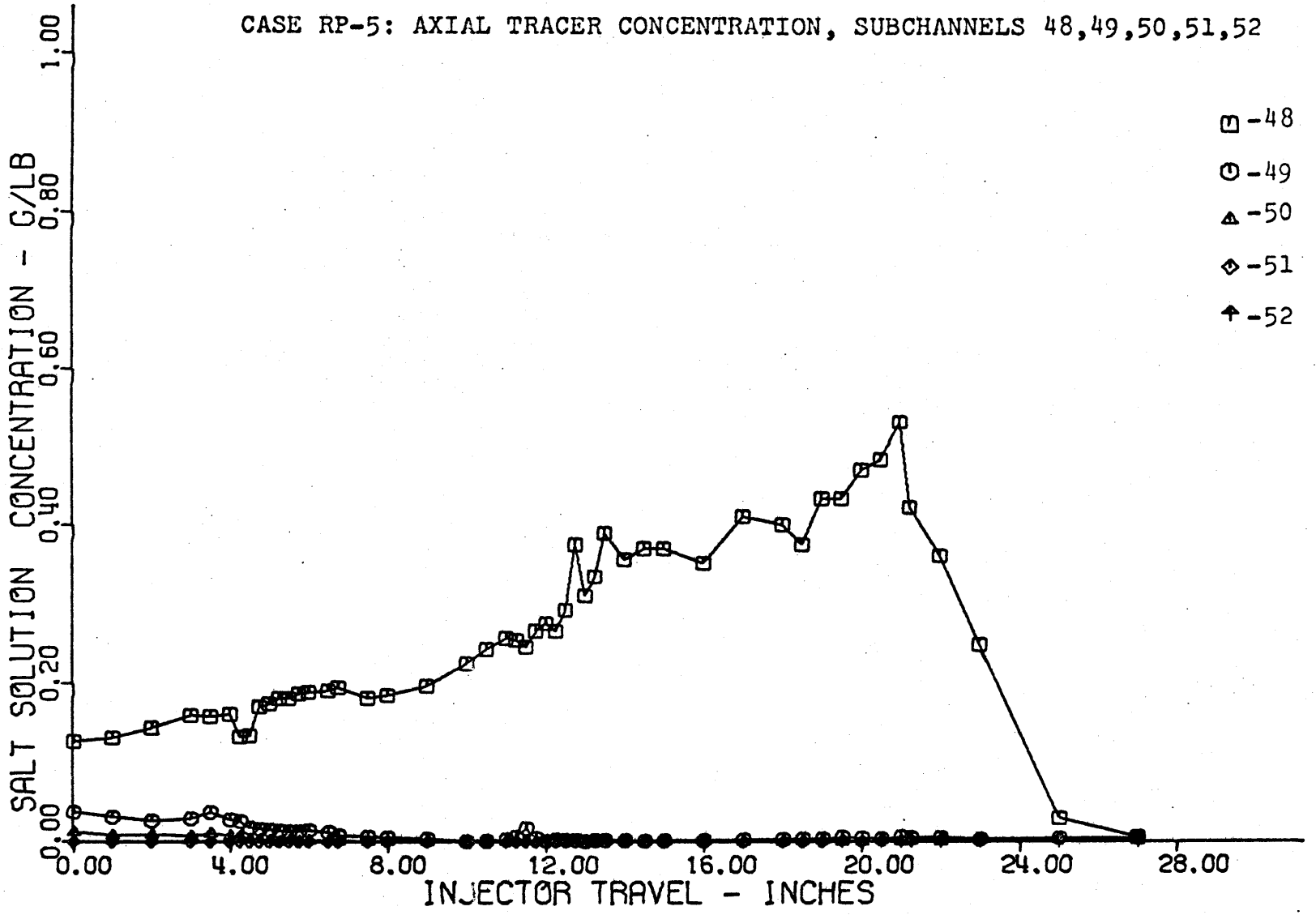

FIGURE A8.112

CASE RP-6: MASS BALANCE VERSUS INJECTOR TRAVEL

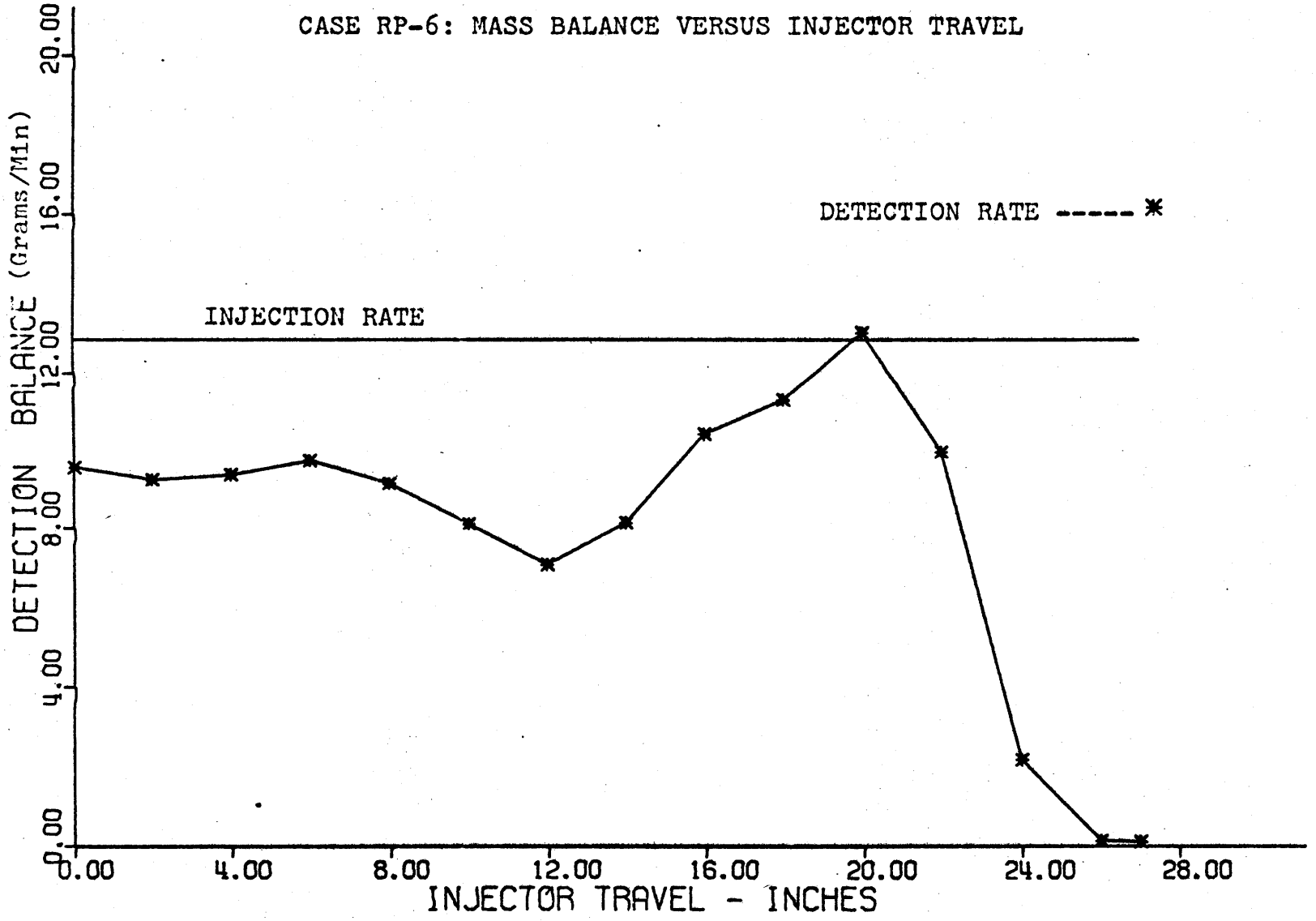

FIGURE A8.113

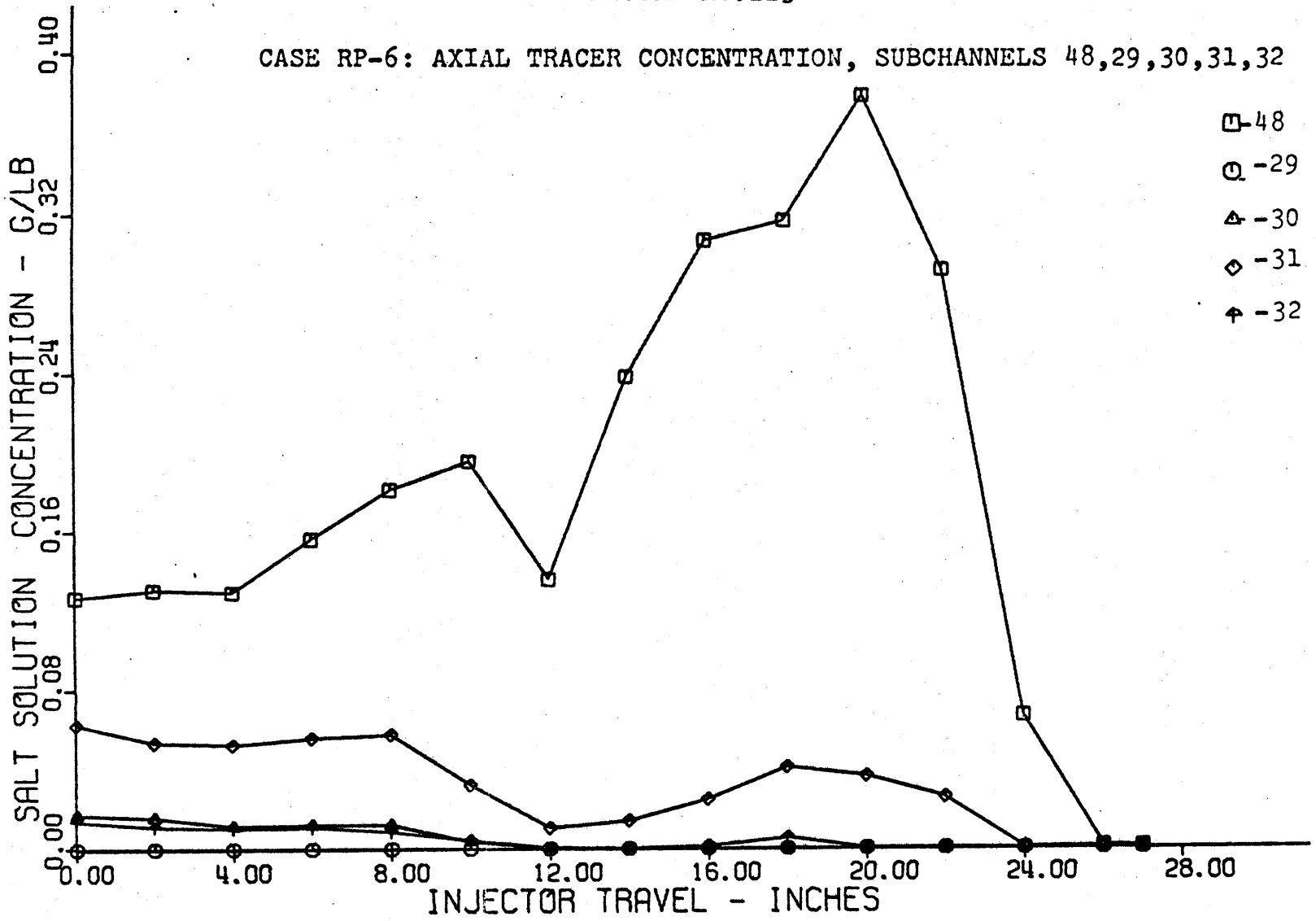

FIGURE A8.114

CASE RP-6: AXIAL TRACER CONCENTRATION, SUBCHANNELS 48,33,34,35,36

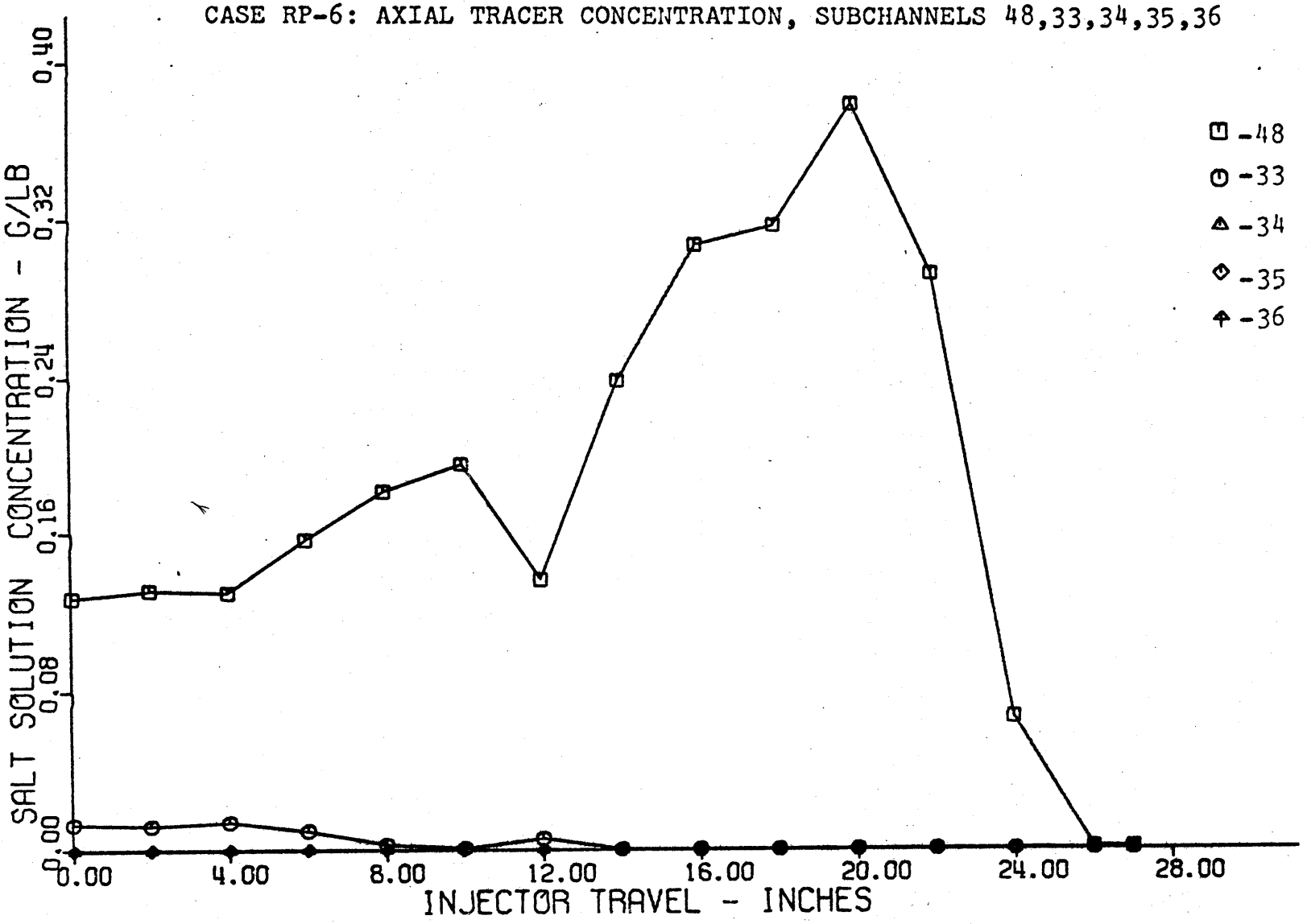

FIGURE A8.115

CASE RP-6: AXIAL TRACER CONCENTRATION, SUBCHANNELS 48,49,50,51,52

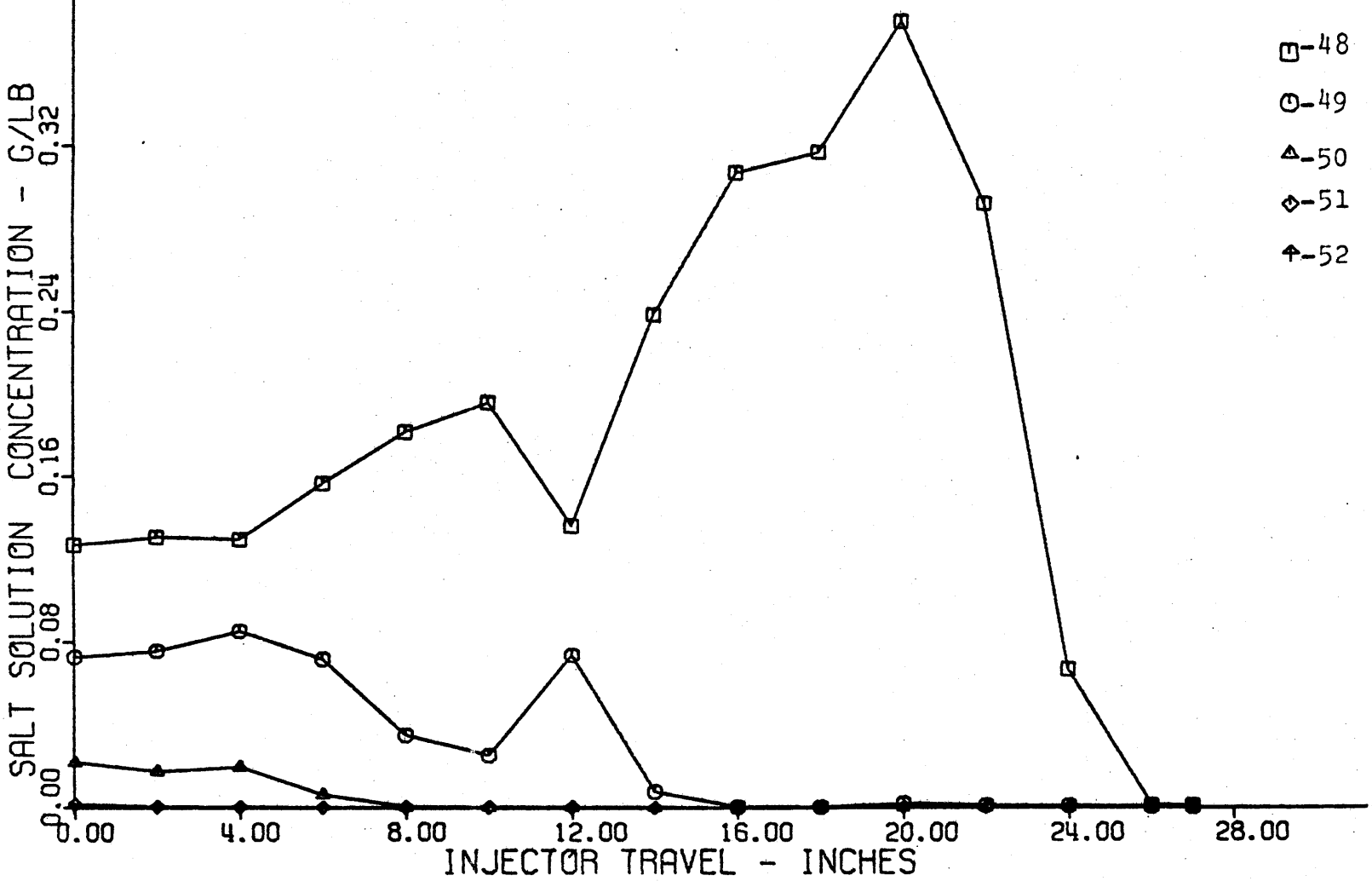

FIGURE A8.116

CASE RP-7: MASS BALANCE VERSUS INJECTOR TRAVEL

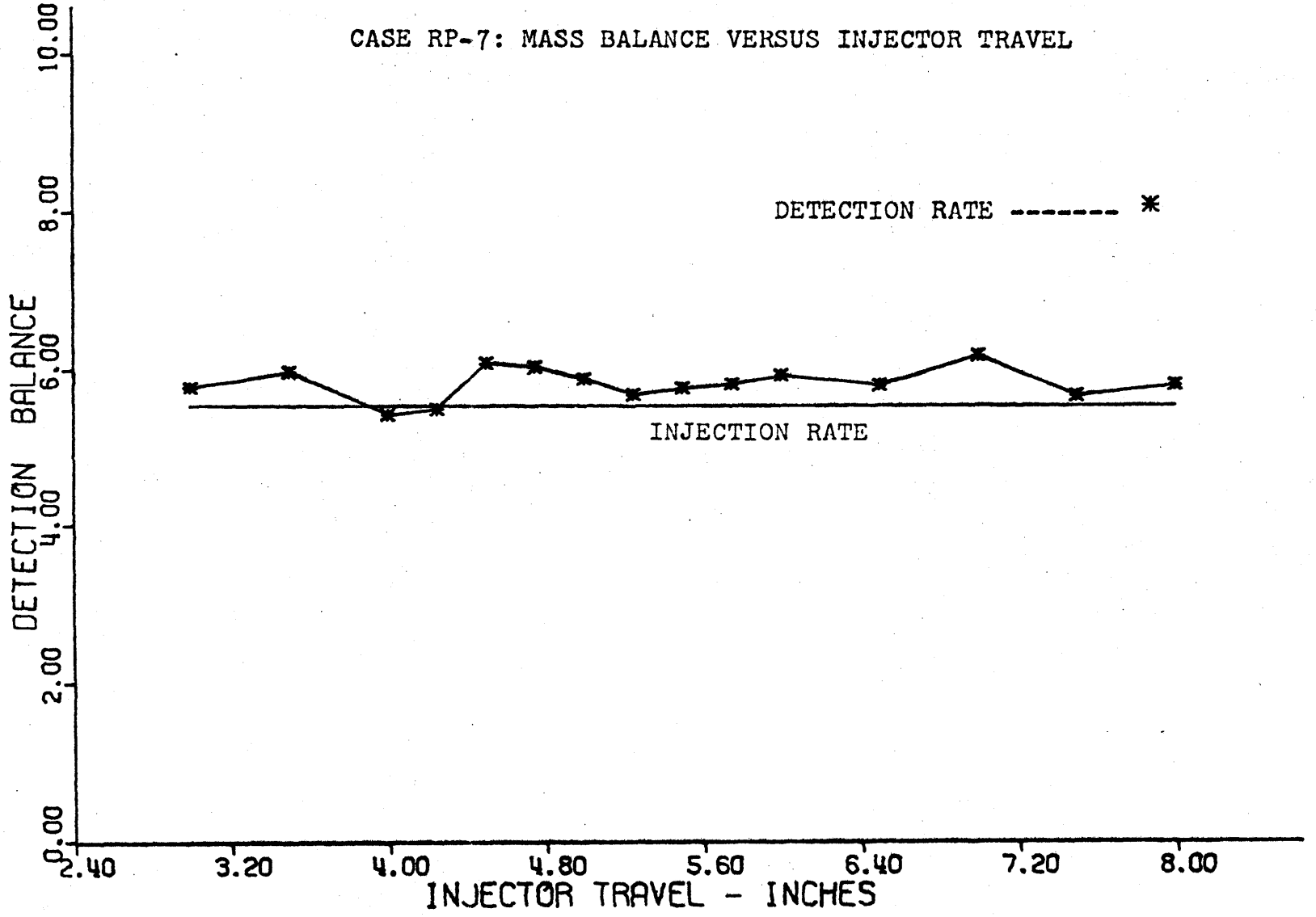

FIGURE A8.117

CASE RP-7: AXIAL TRACER CONCENTRATION, SUBCHANNELS 48,29,30,31,32

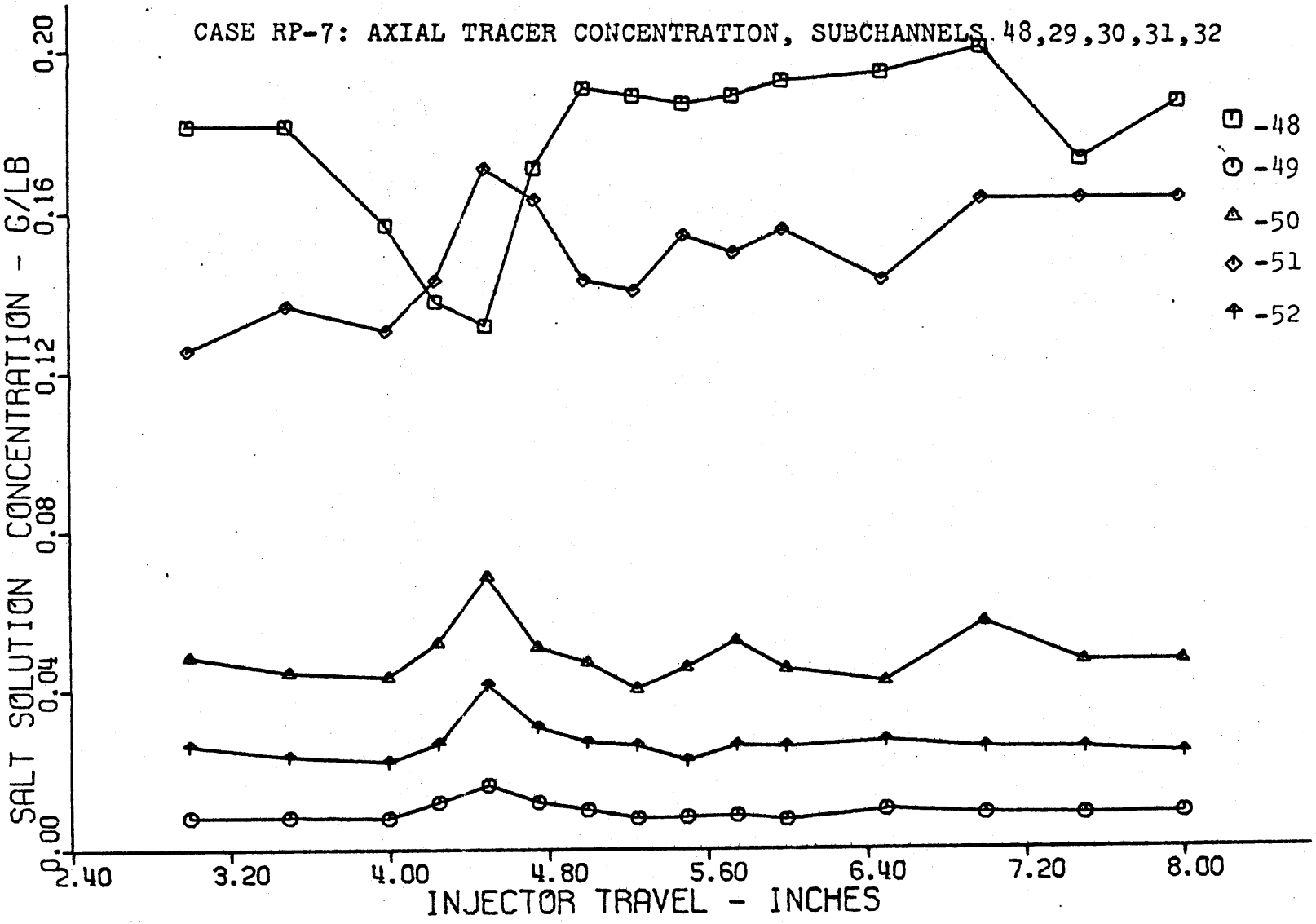

FIGURE A8.118

CASE RP-7: AXIAL TRACER CONCENTRATION, SUBCHANNELS 48,33,34,35,36

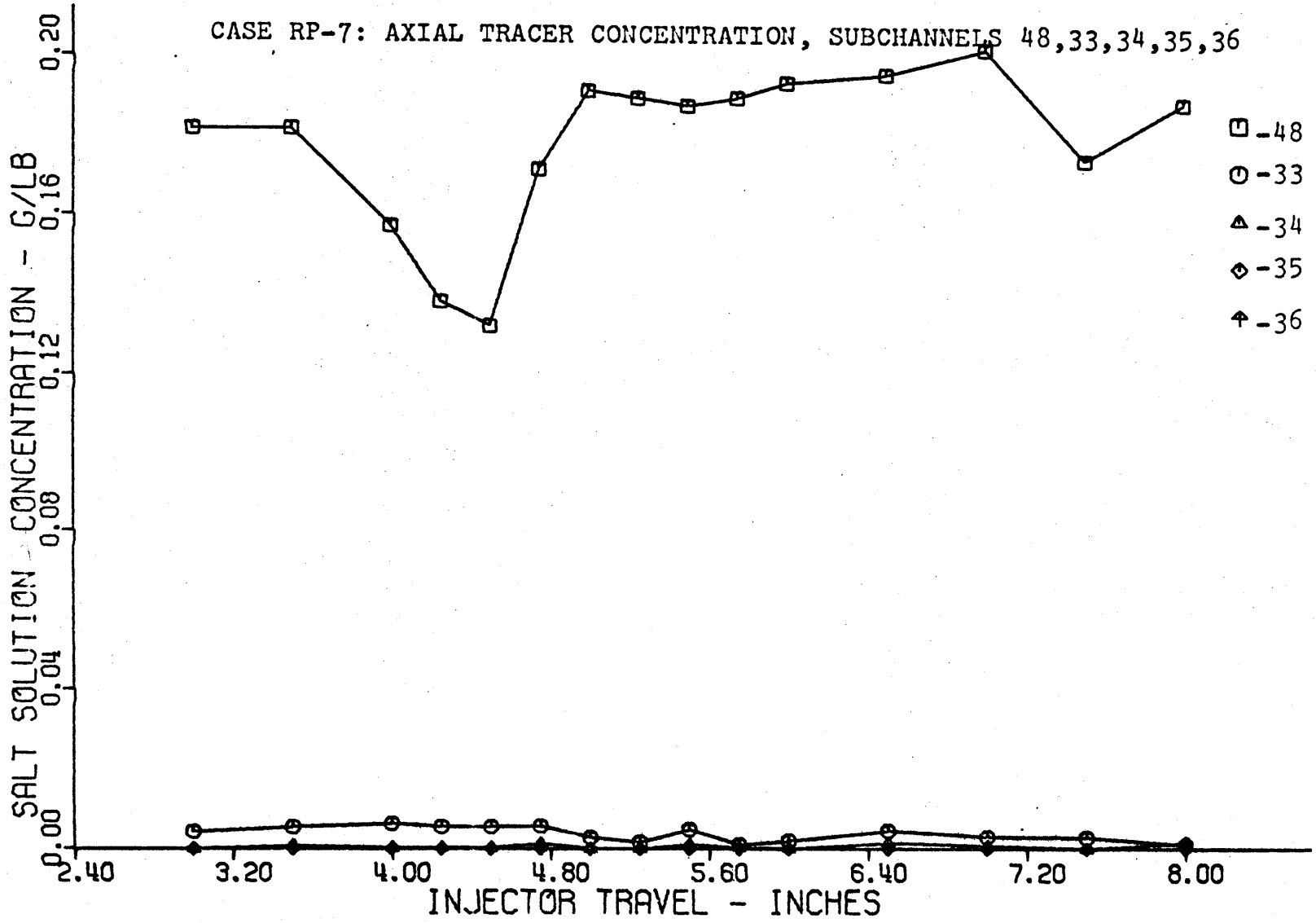

FIGURE A8.119

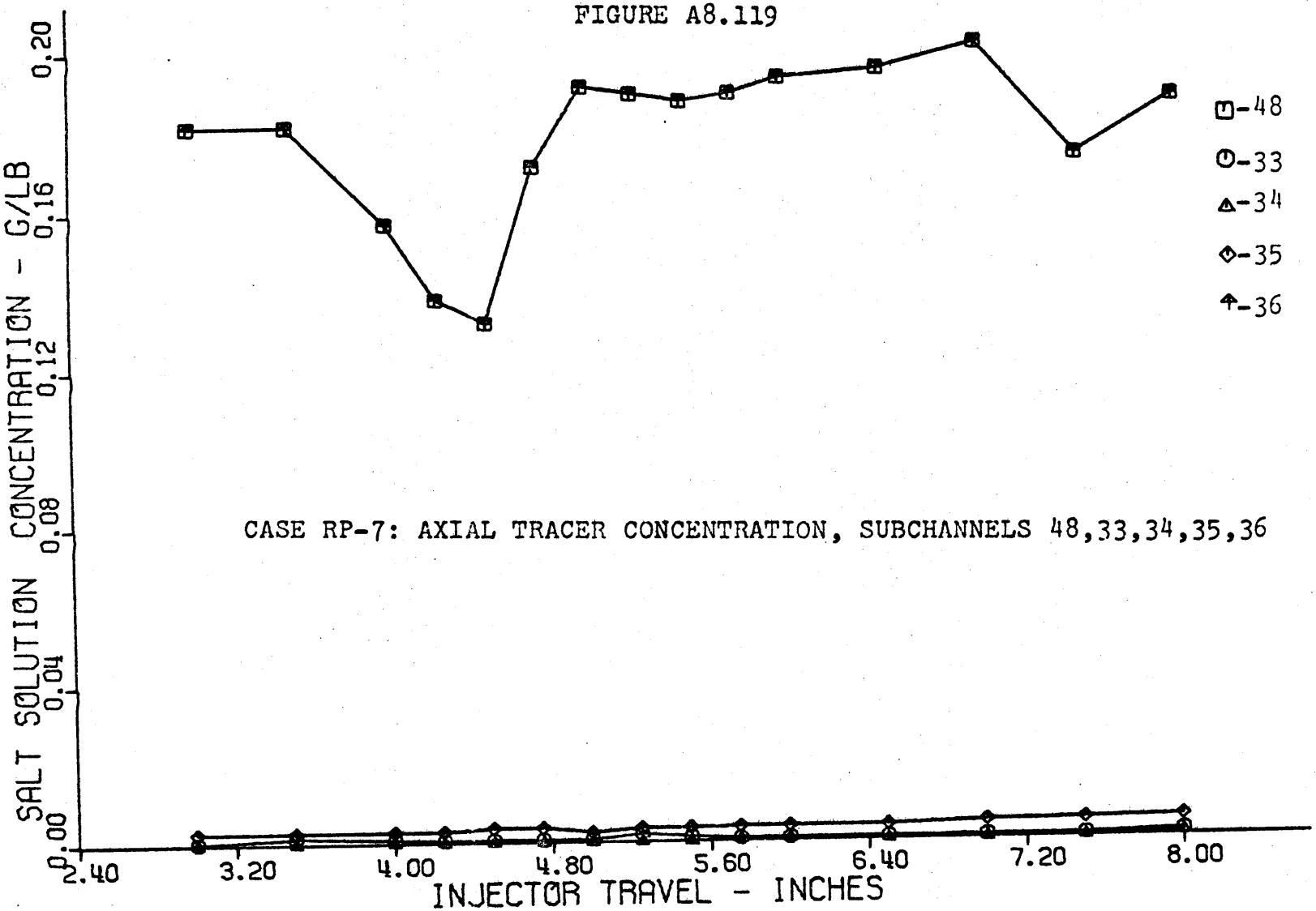

CASE RP-7: AXIAL TRACER CONCENTRATION, SUBCHANNELS 48,33,34,35,36

FIGURE A8.120

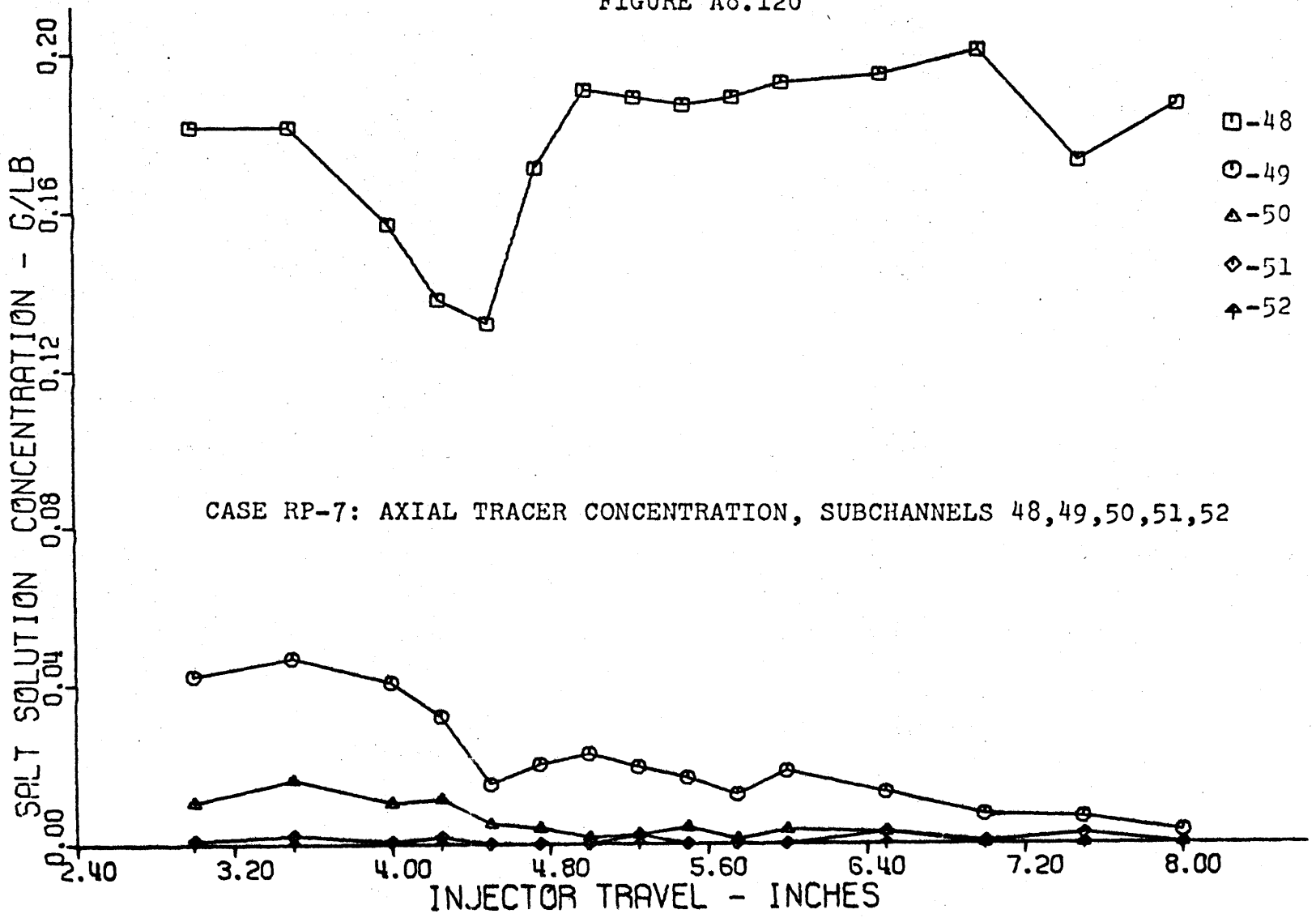

CASE RP-7: AXIAL TRACER CONCENTRATION, SUBCHANNELS 48,49,50,51,52

FIGURE A8.121

CASE RP-8: MASS BALANCE VERSUS INJECTOR TRAVEL

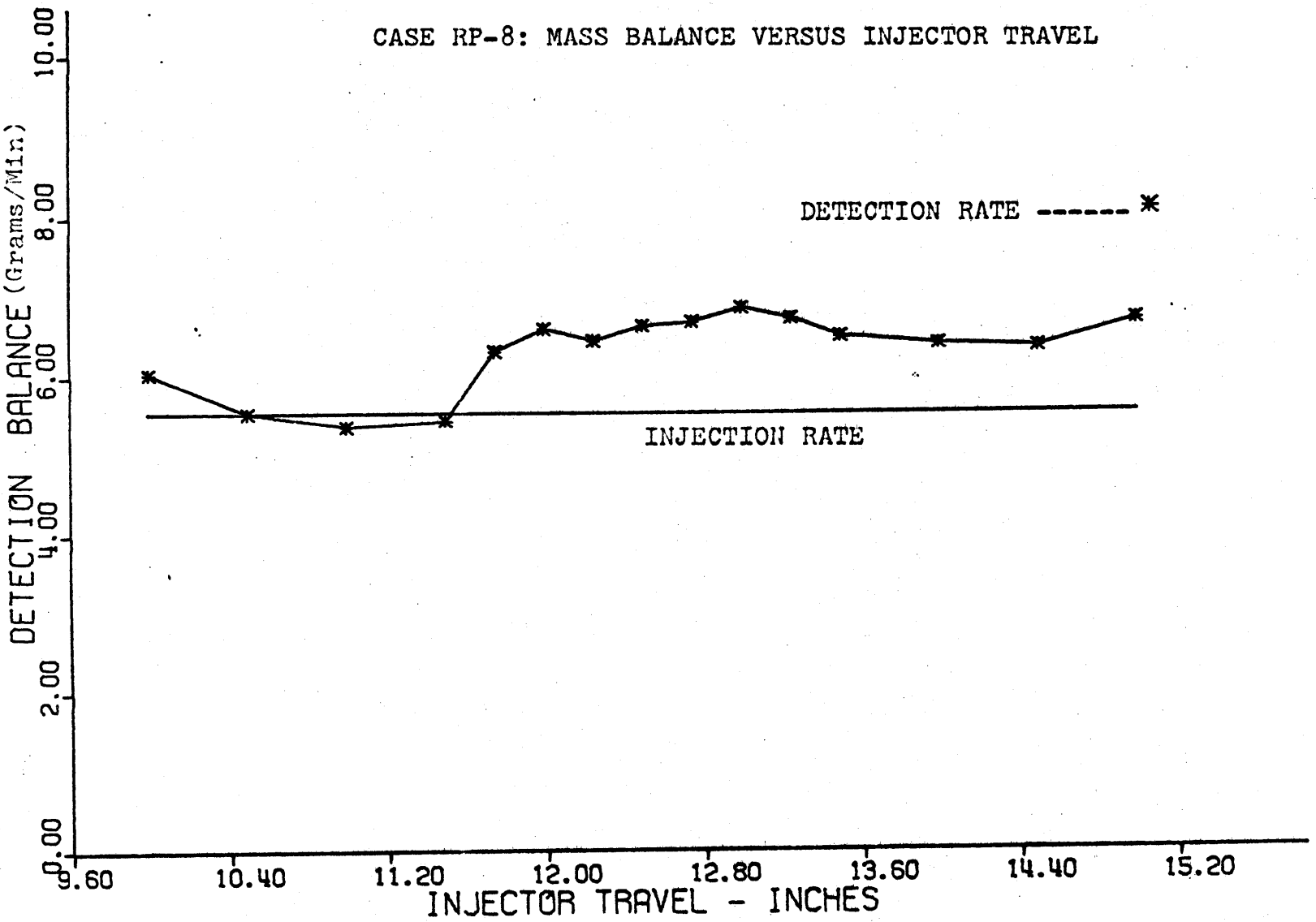

FIGURE A8.122

CASE RP-8: AXIAL TRACER CONCENTRATION, SUBCHANNELS 48,29,30,31,32

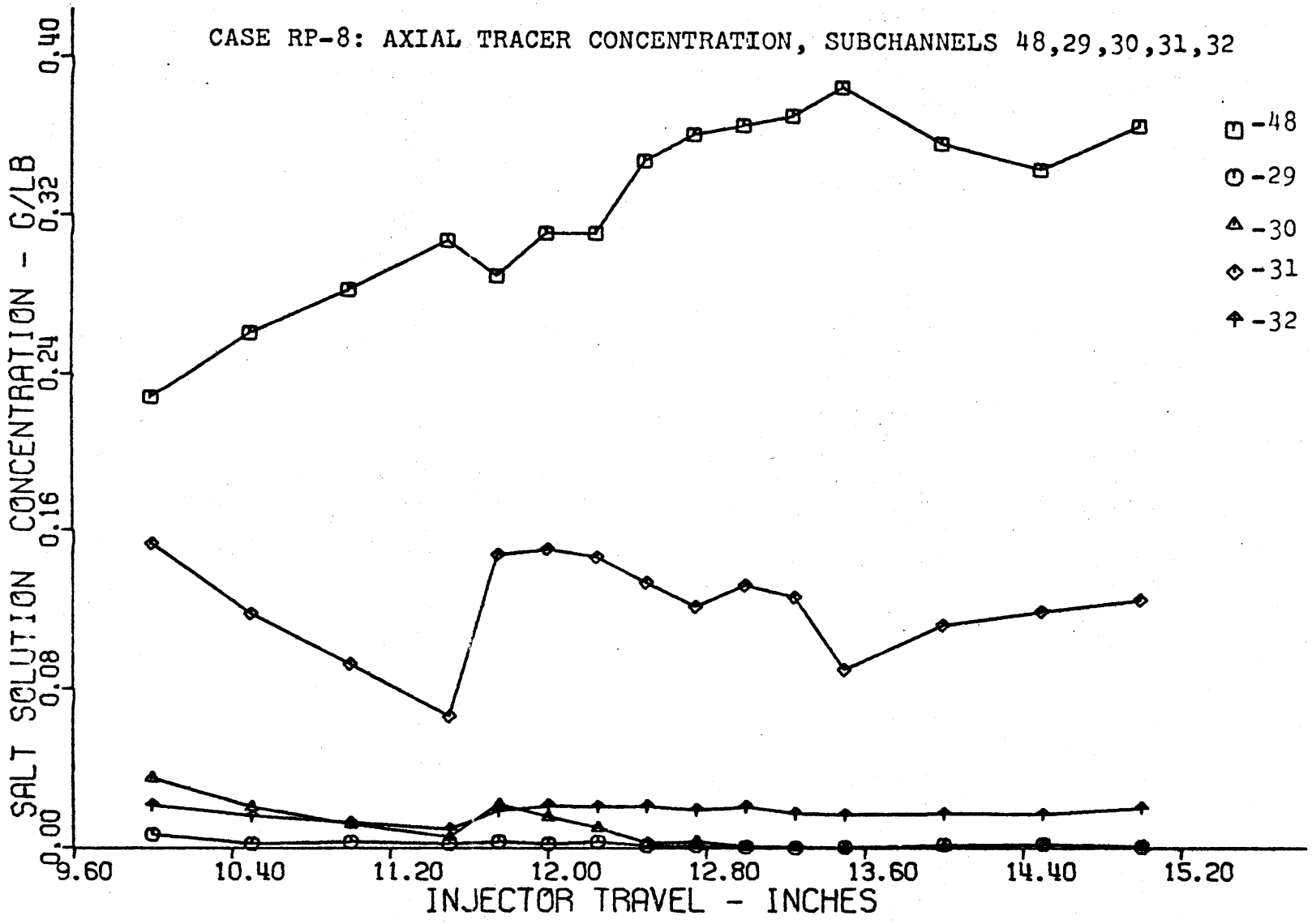

FIGURE A8.123

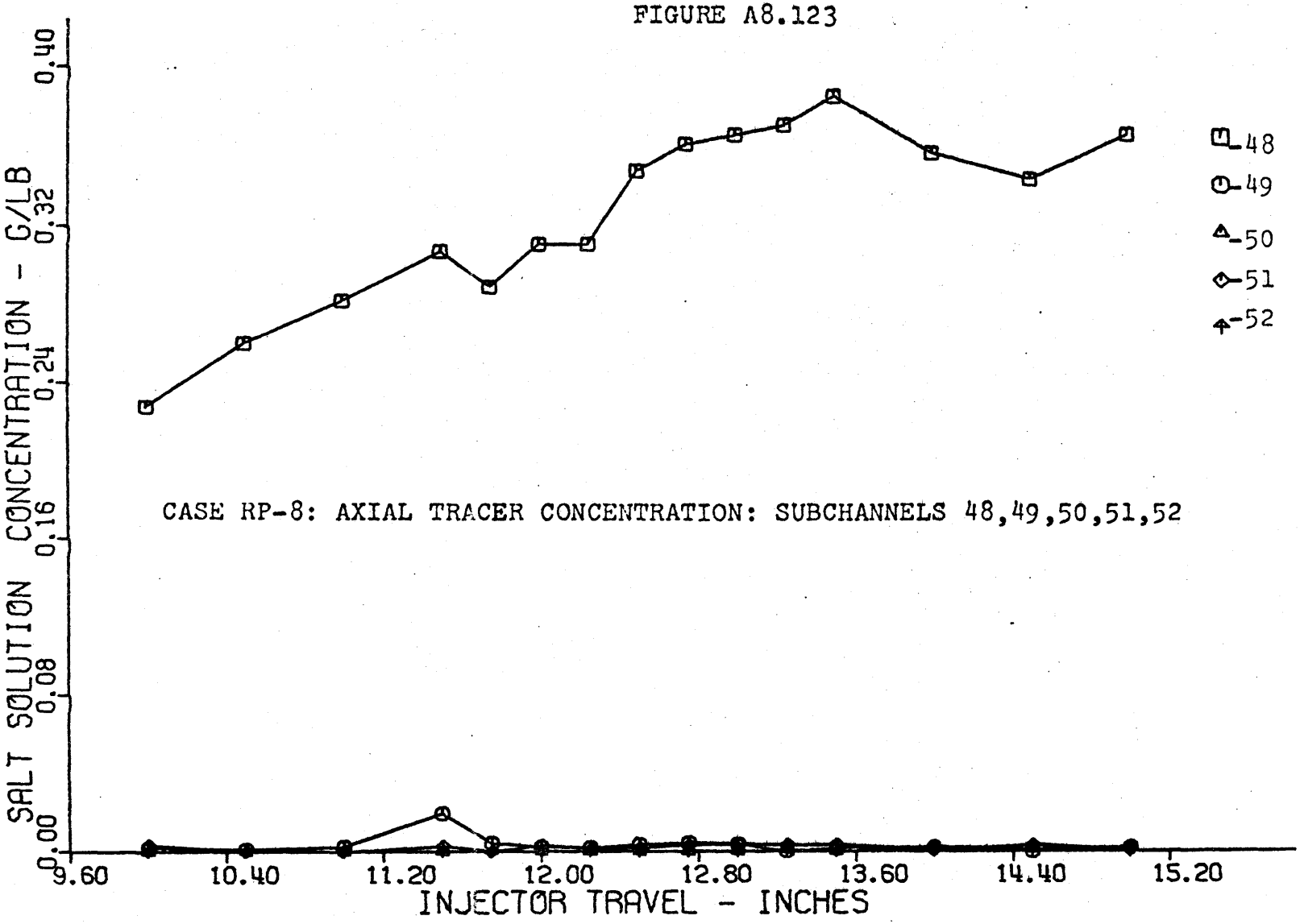

CASE RP-8: AXIAL TRACER CONCENTRATION: SUBCHANNELS 48,49,50,51,52

FIGURE A8.124

CASE RP-9: MASS BALANCE VERSUS INJECTOR TRAVEL

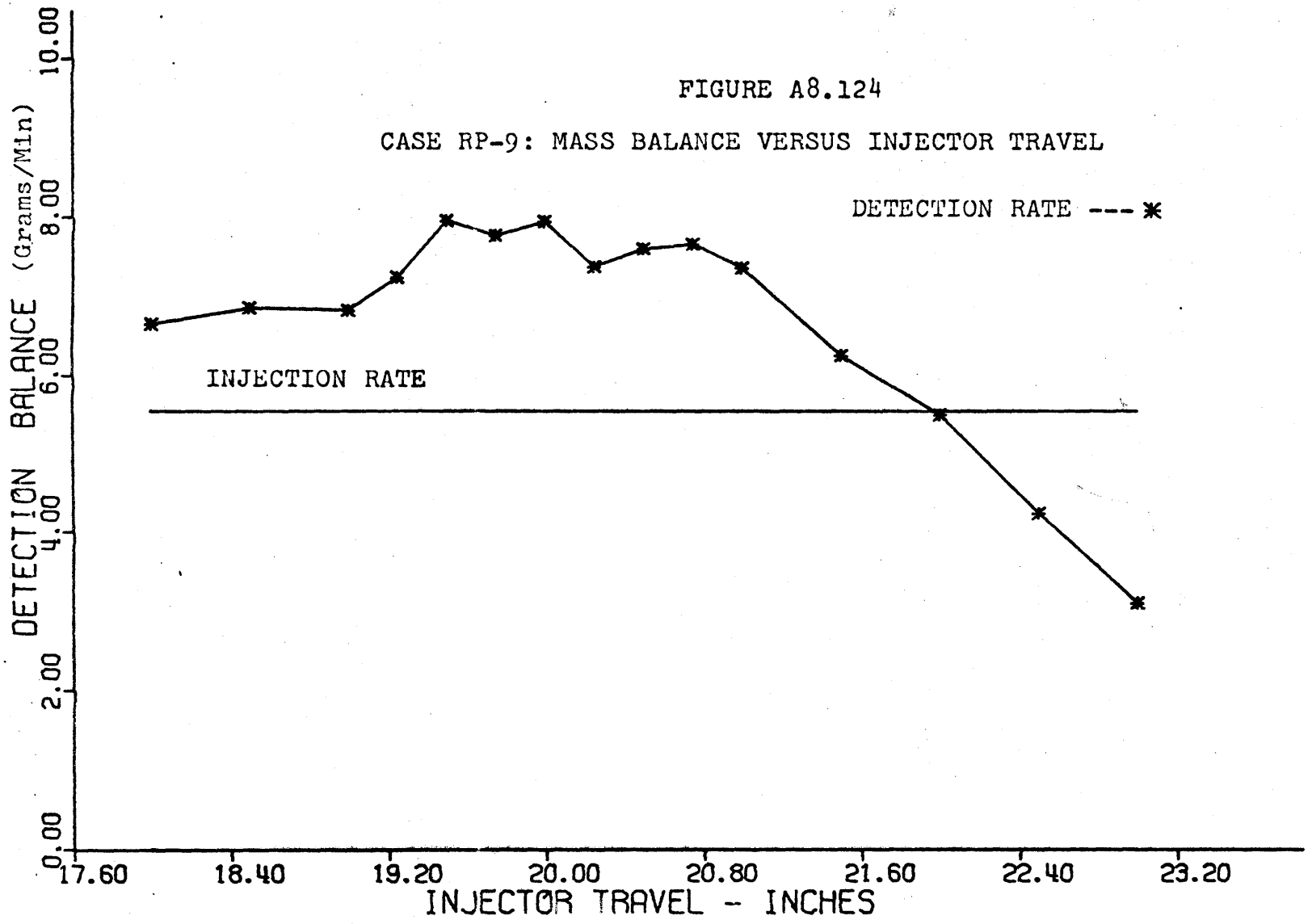

FIGURE A8.125

AXIAL TRACER CONCENTRATION, SUBCHANNELS 48,29,30,31,32

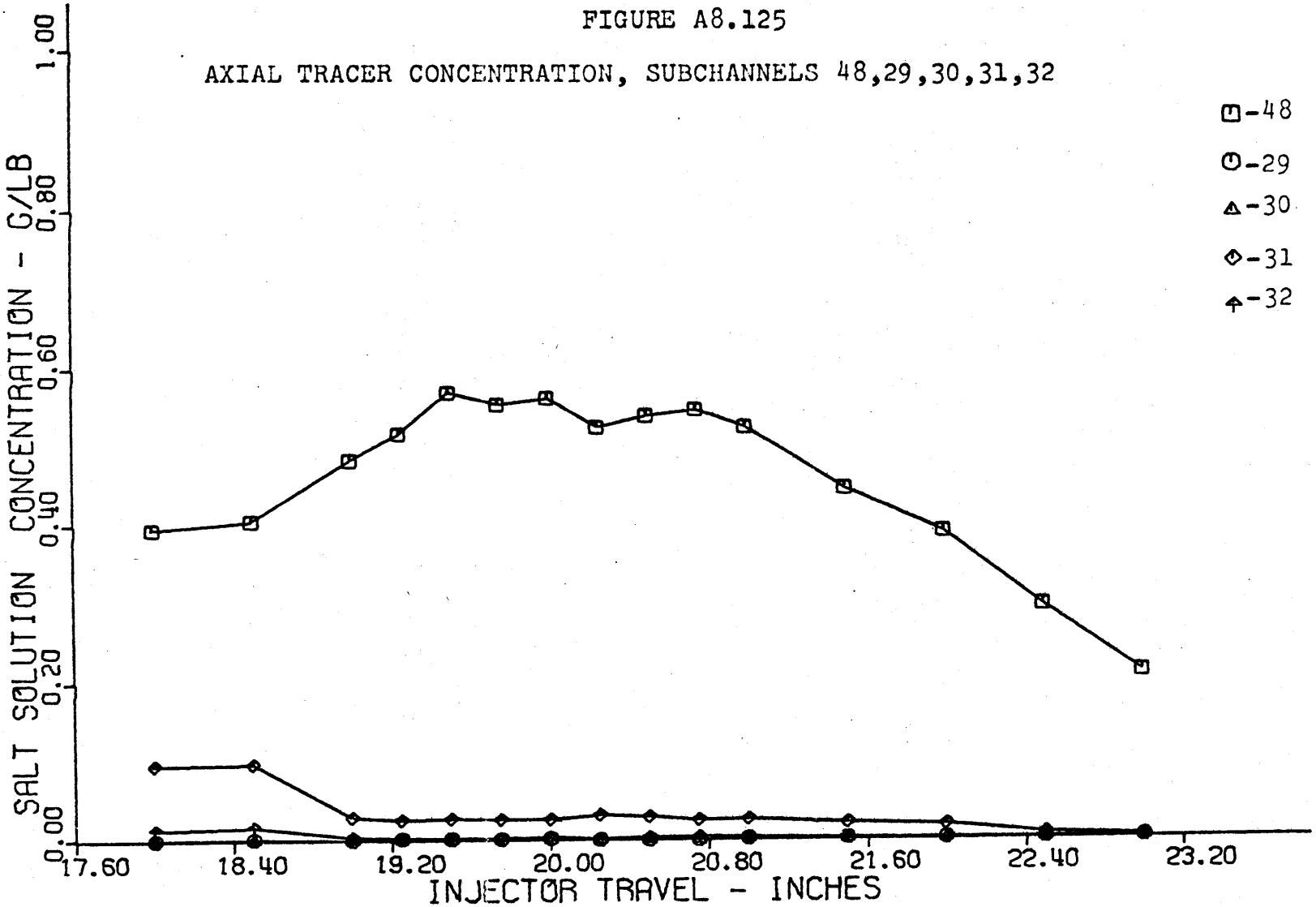

FIGURE A8.126

CASE RP-9: AXIAL TRACER CONCENTRATION, SUBCHANNELS 48,49,50,51,52

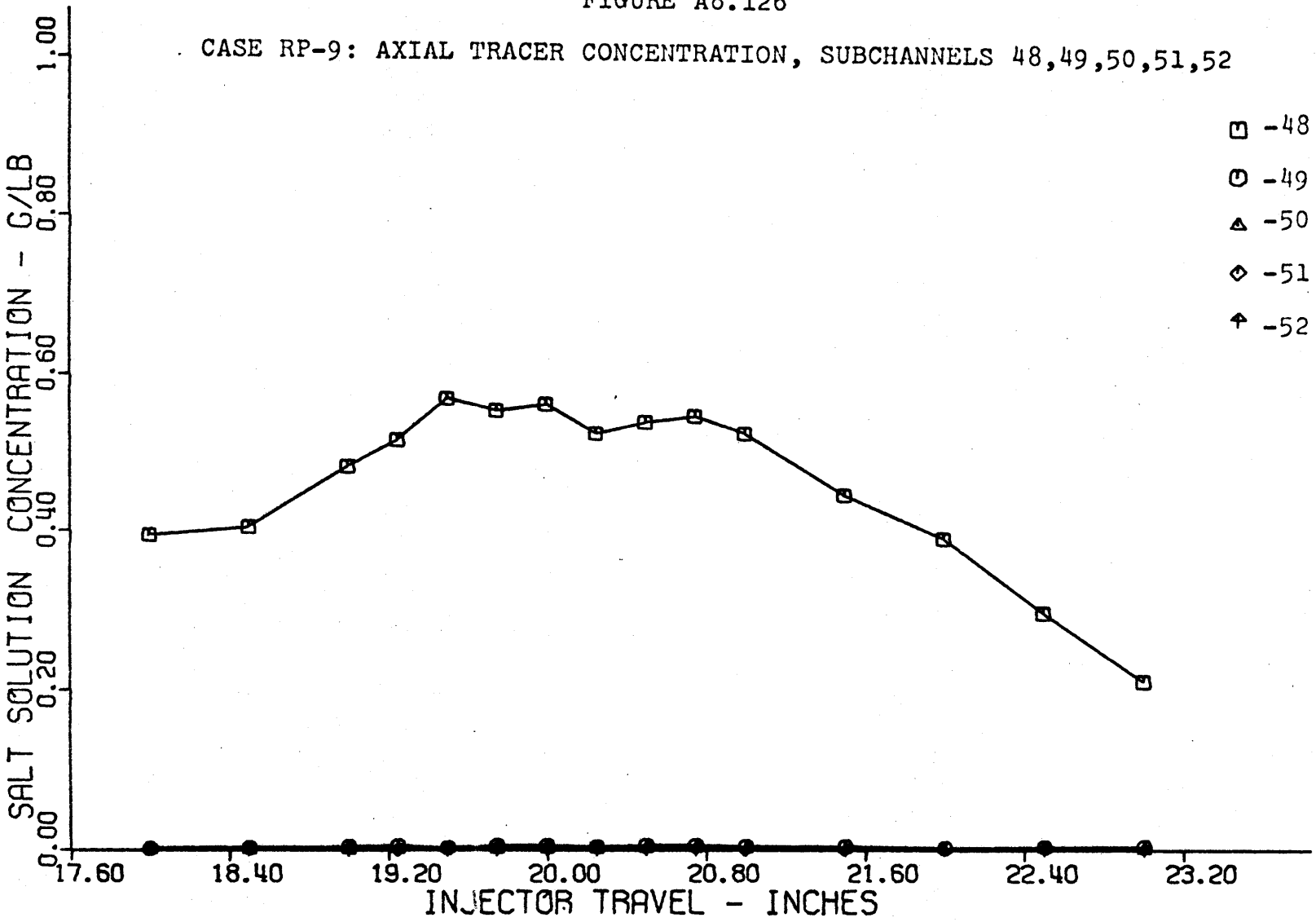

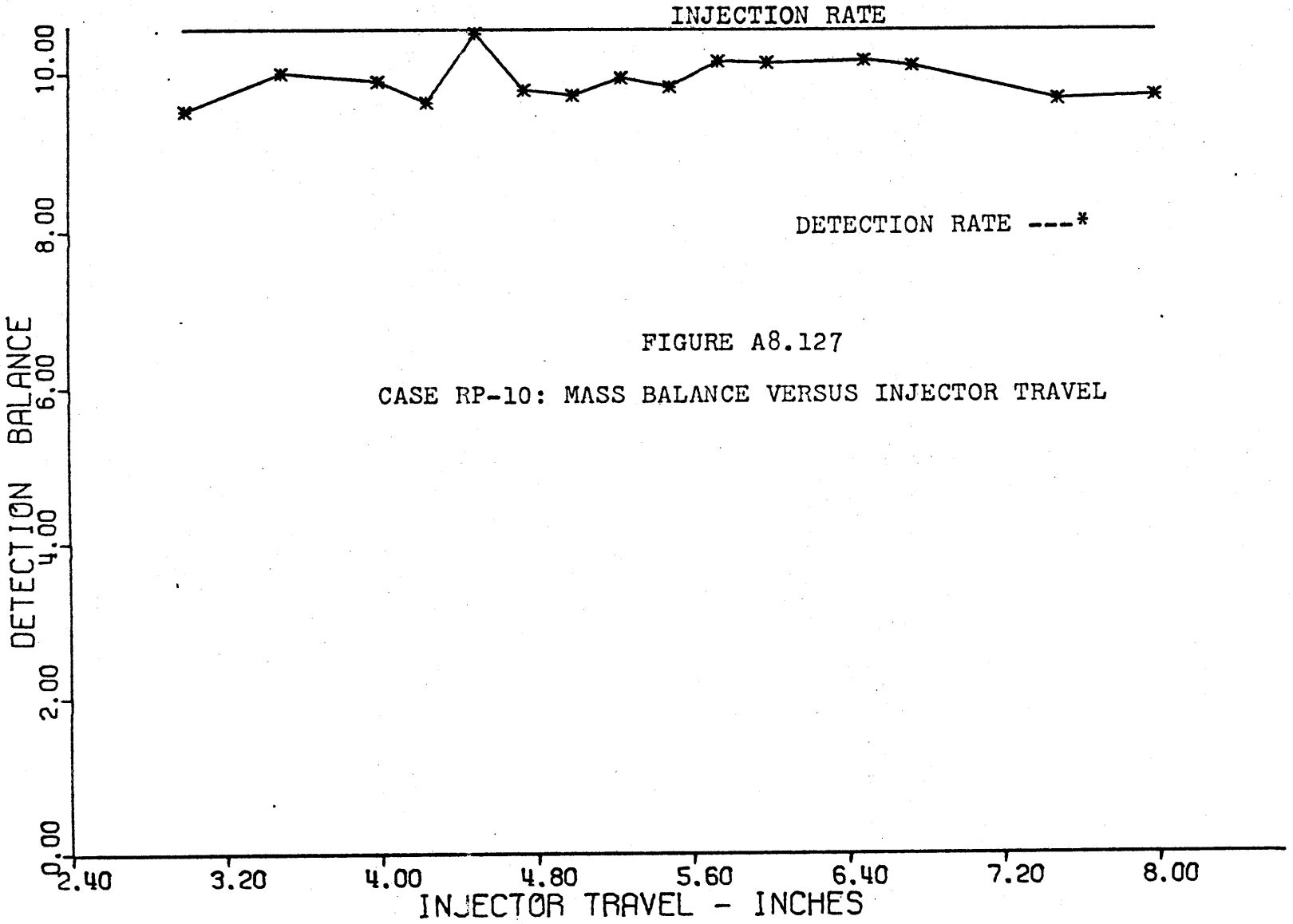

FIGURE A8.127

CASE RP-10: MASS BALANCE VERSUS INJECTOR TRAVEL

FIGURE A8.128

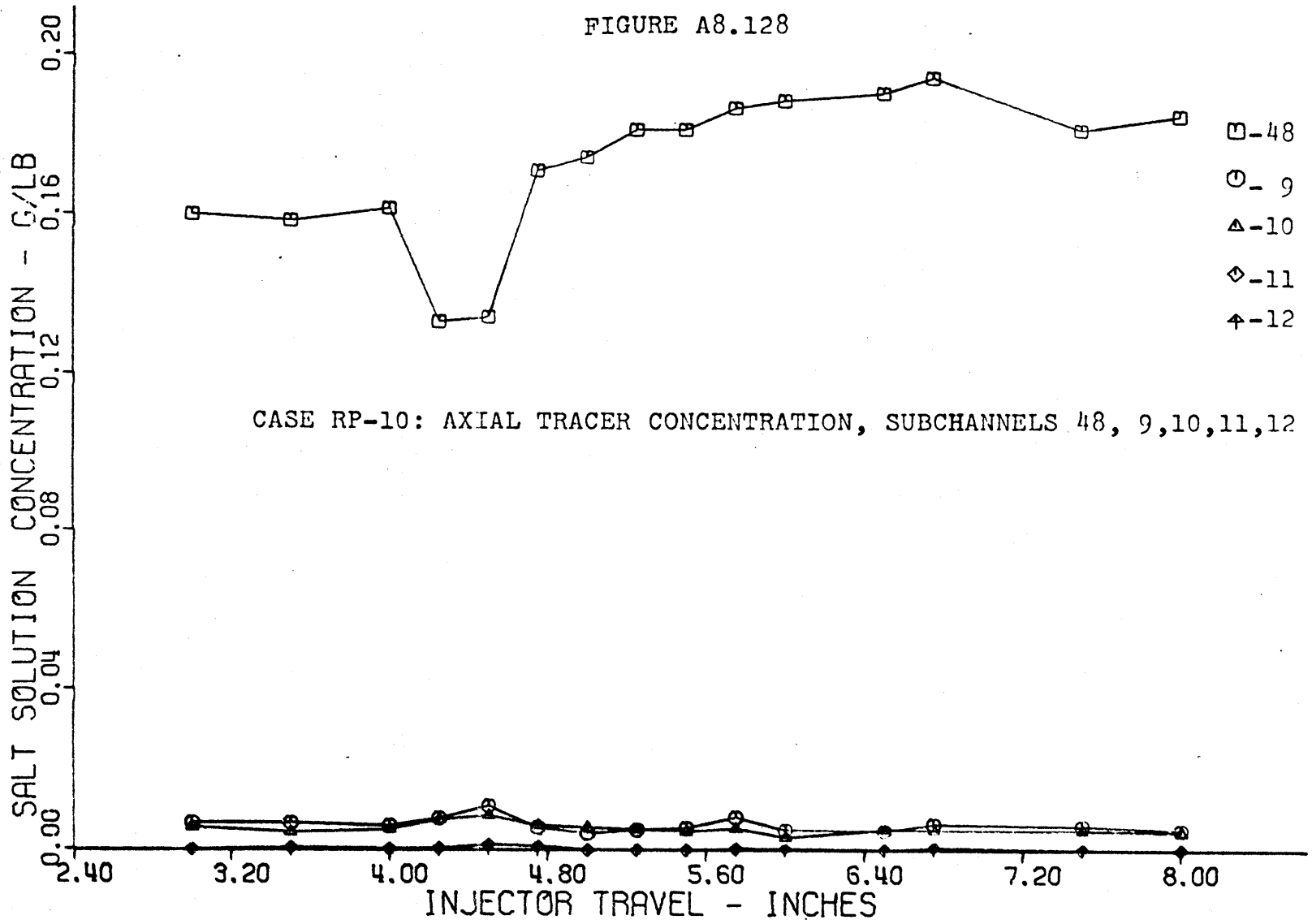

CASE RP-10: AXIAL TRACER CONCENTRATION, SUBCHANNELS 48, 9,10,11,12

FIGURE A8.129

CASE RP-10: AXIAL TRACER CONCENTRATION, SUBCHANNELS 48,29,30,31,32

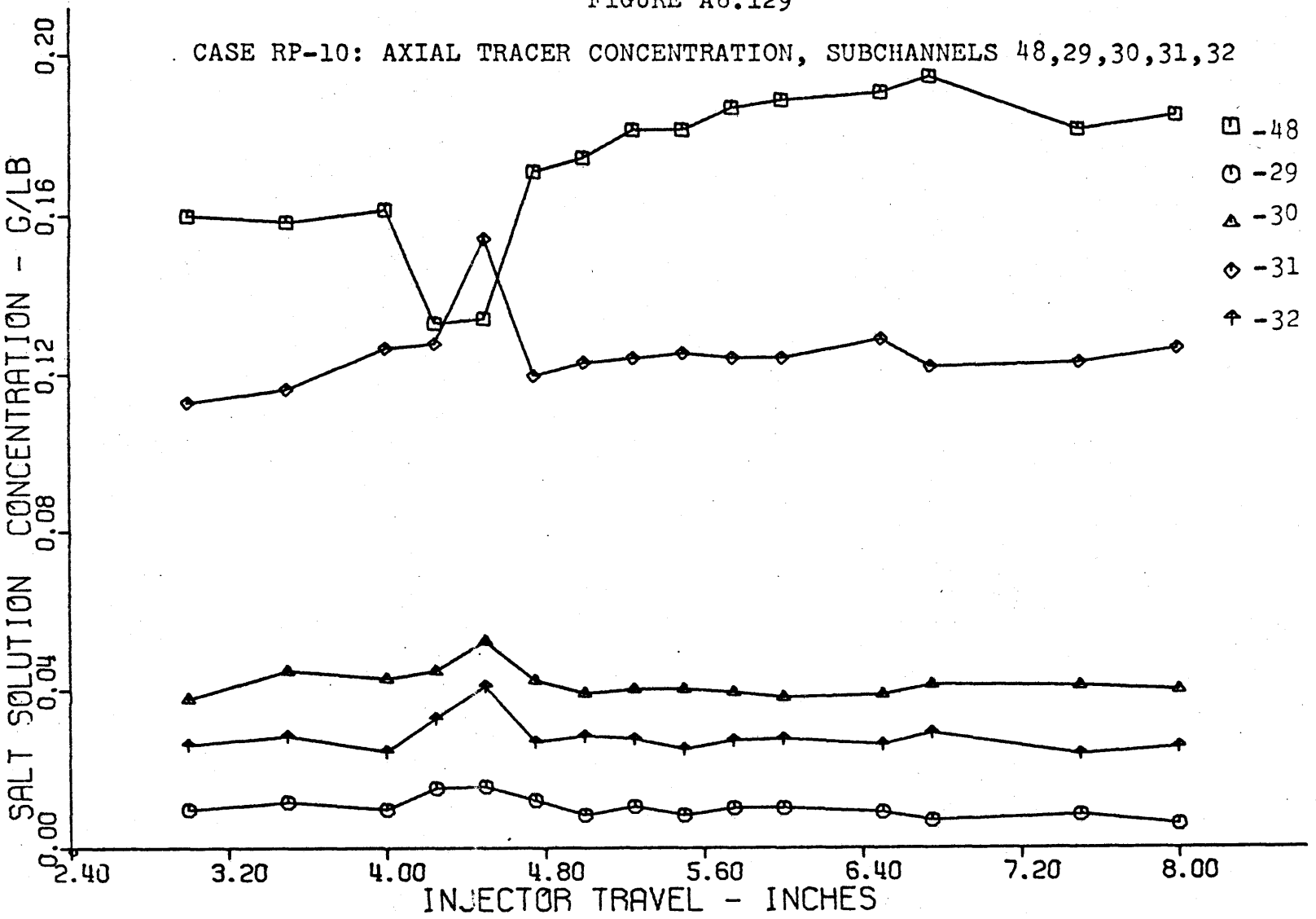

FIGURE A8.130

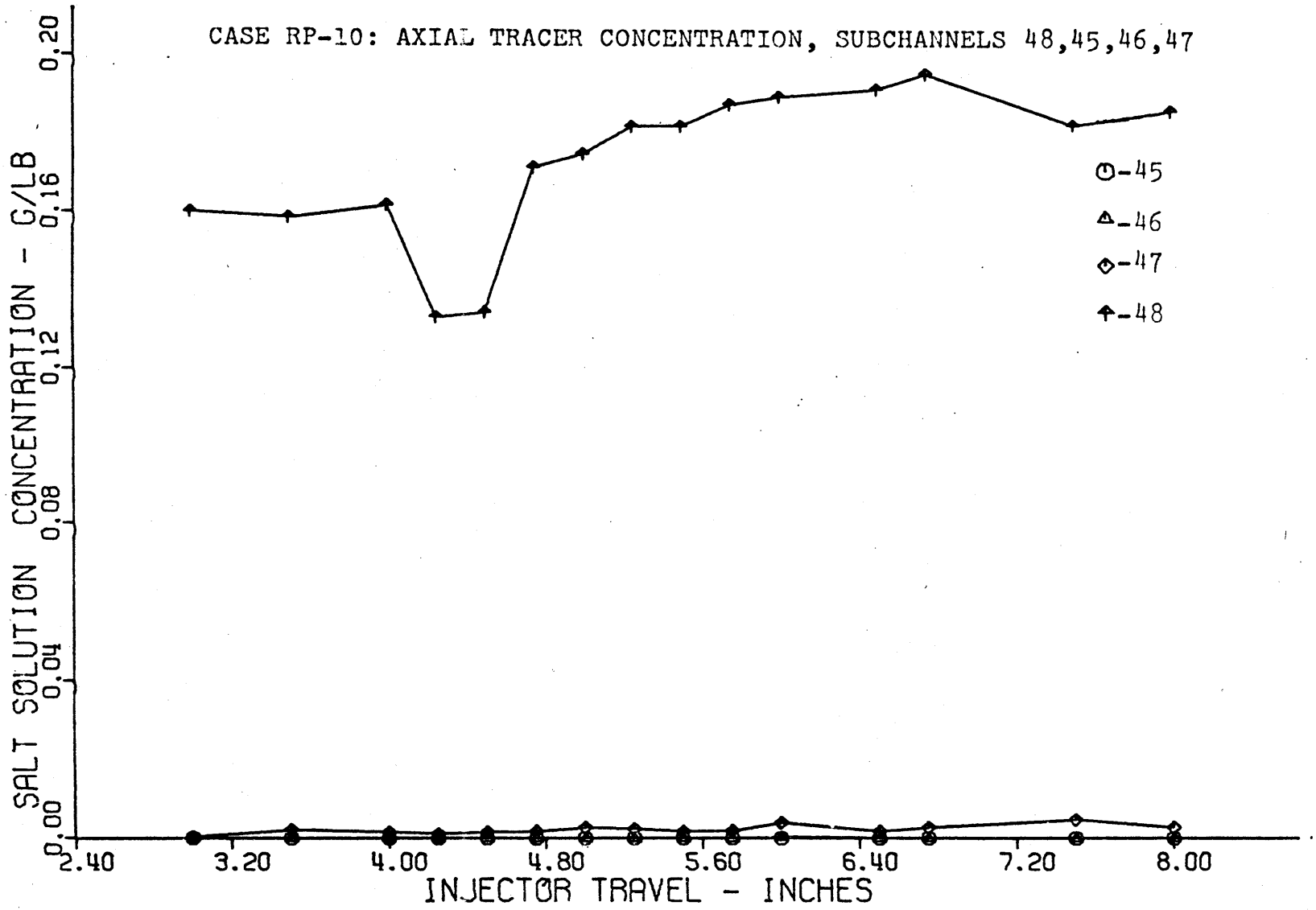

FIGURE A8.131

CASE RP-10: AXIAL TRACER CONCENTRATION, SUBCHANNELS 48,49,50,51,52

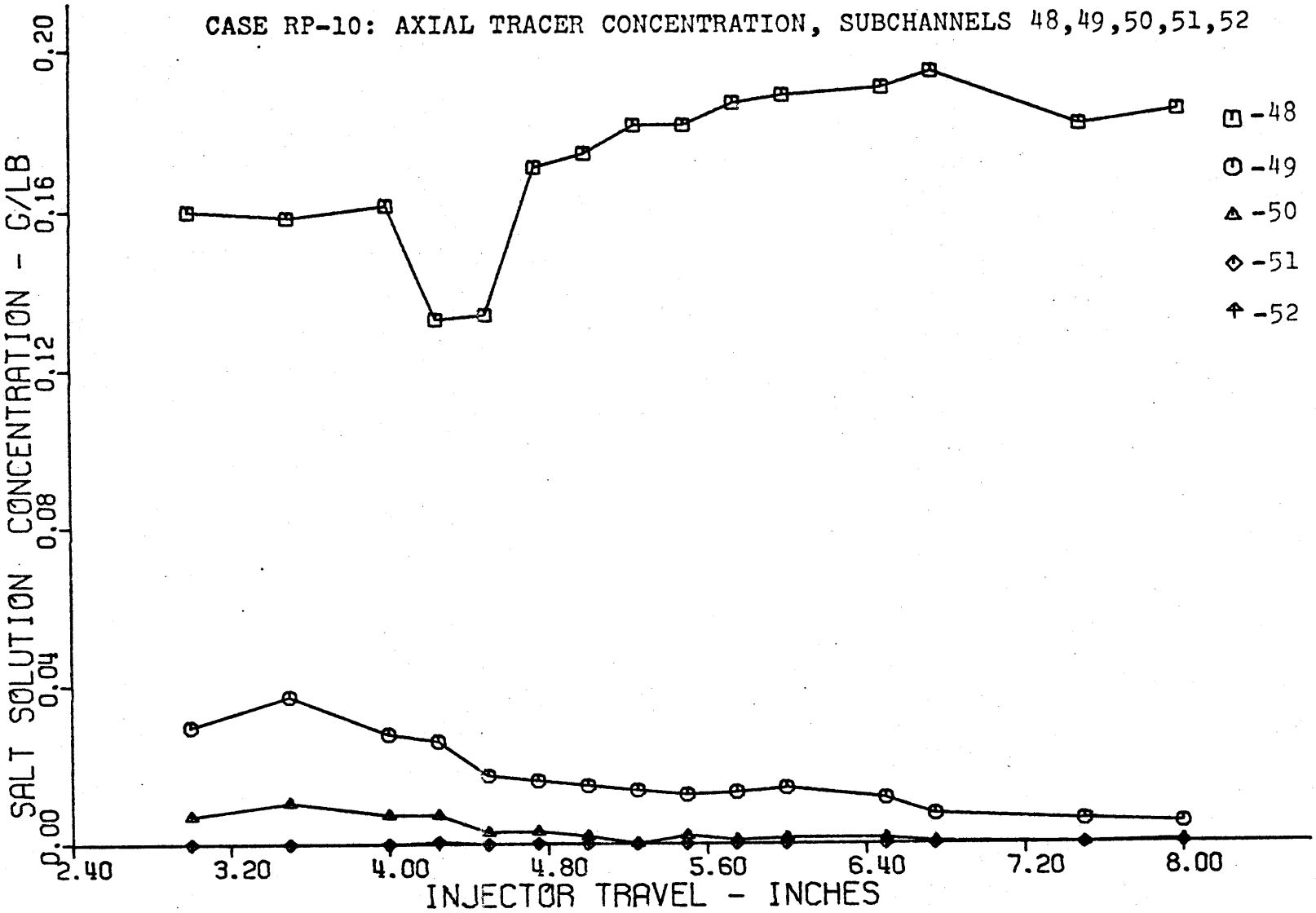

FIGURE A8.132

CASE RP-11: MASS BALANCE VERSUS INJECTOR TRAVEL

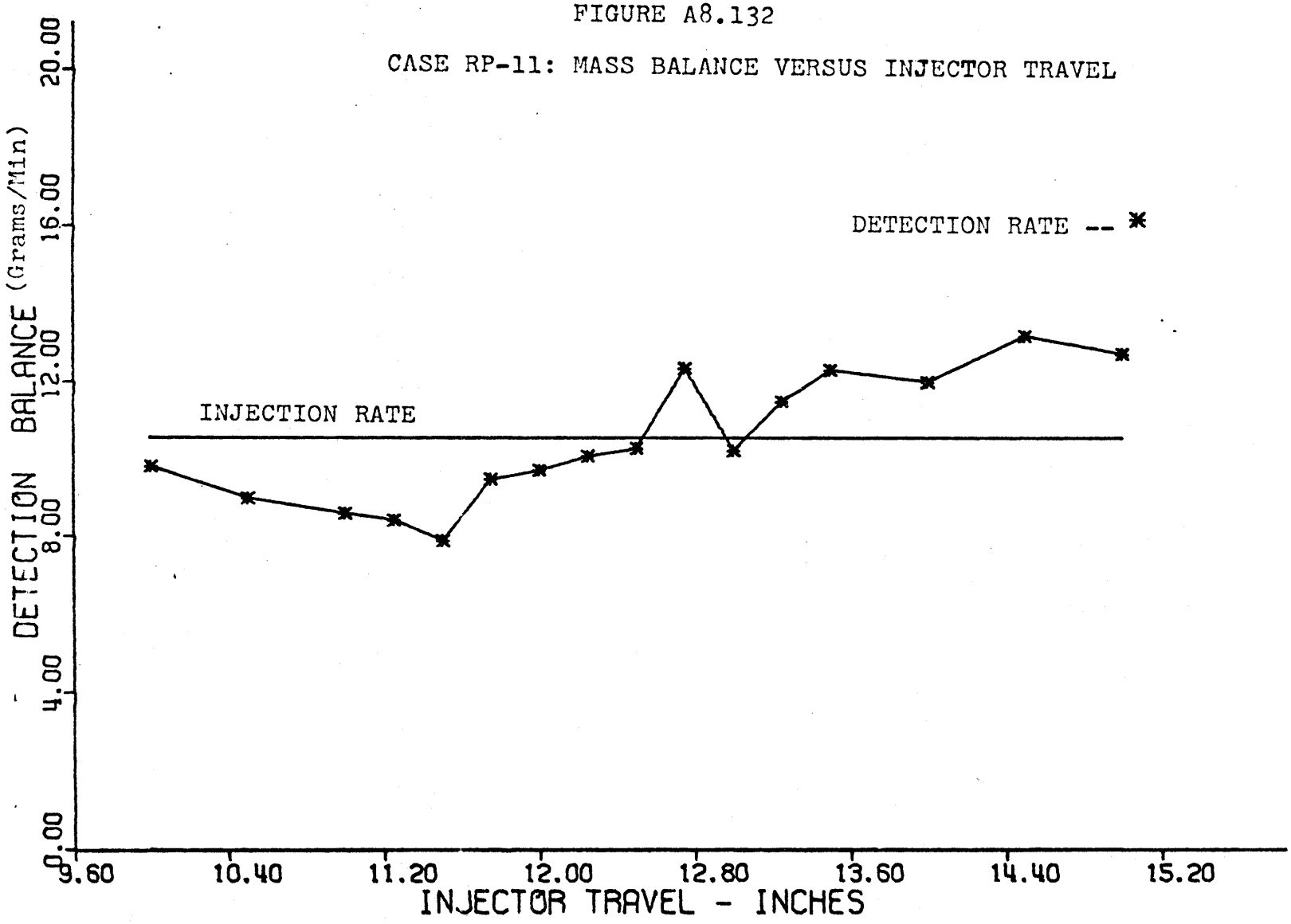

FIGURE A8.133

CASE RP-11: AXIAL TRACER CONCENTRATION, SUBCHANNELS 48,29,30,31,32

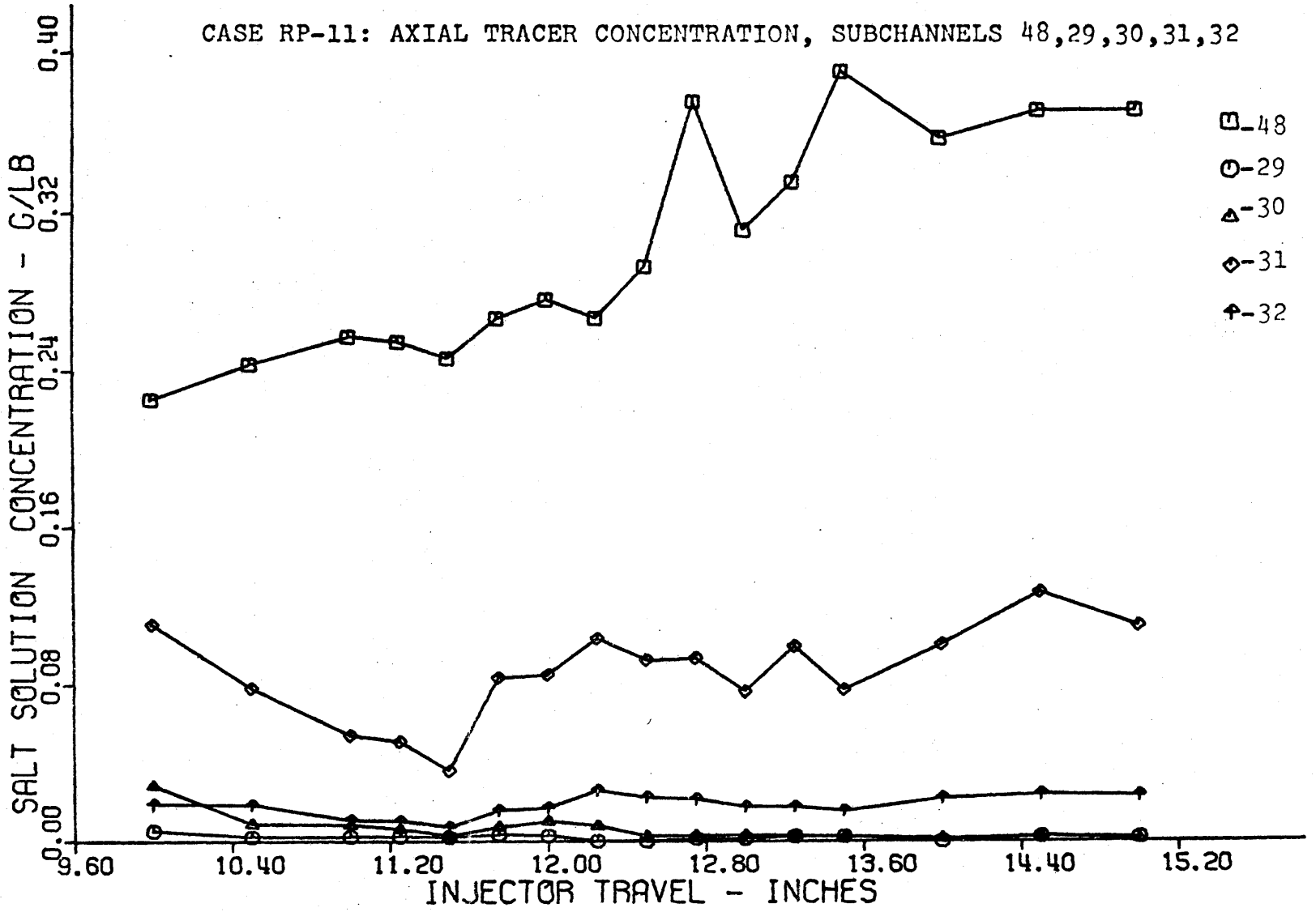

FIGURE A8.134

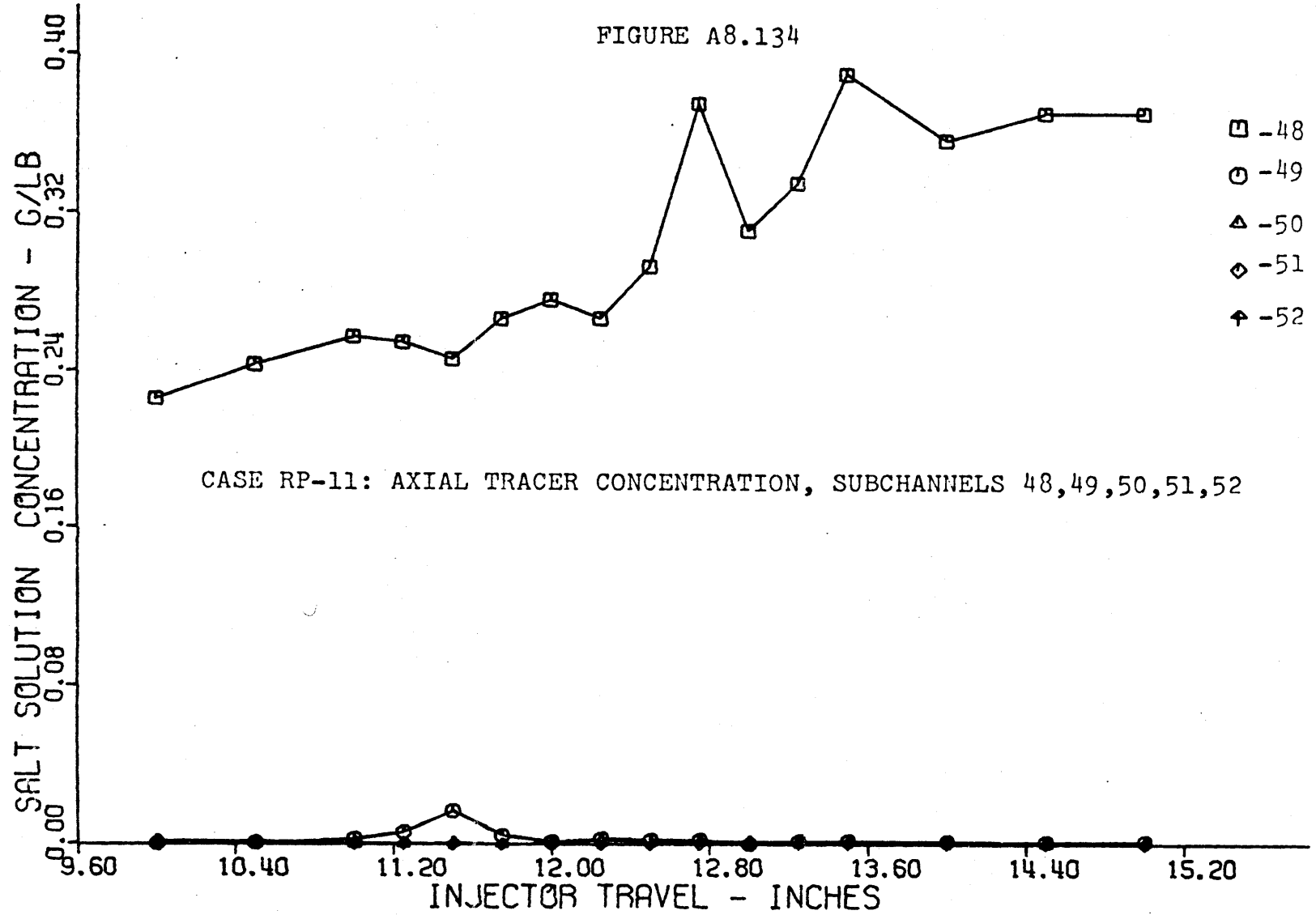

CASE RP-11: AXIAL TRACER CONCENTRATION, SUBCHANNELS 48,49,50,51,52

FIGURE A8.135

CASE RP-12: MASS BALANCE VERSUS INJECTOR TRAVEL

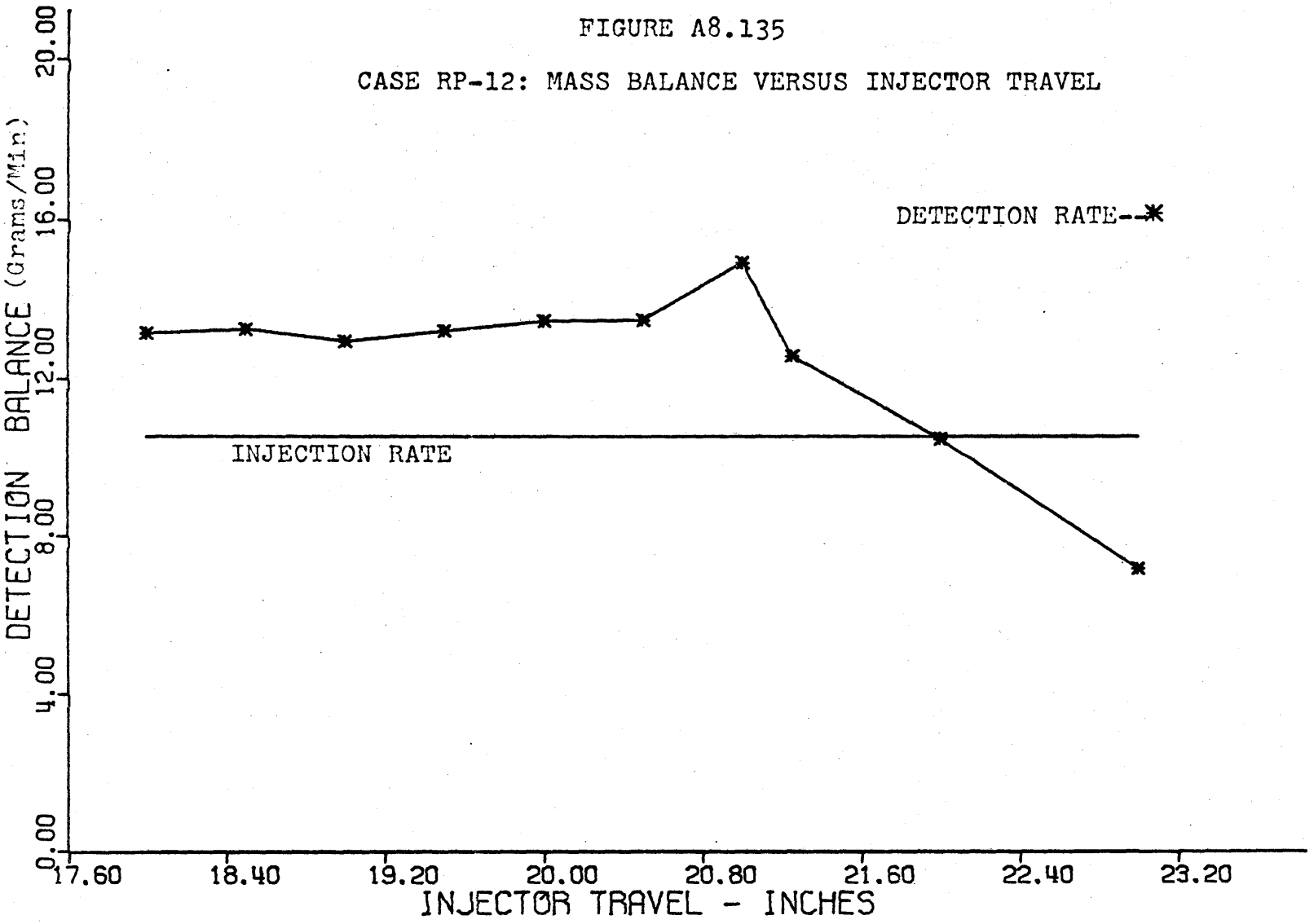

FIGURE A8.136

CASE RP-12: AXIAL TRACER CONCENTRATION, SUBCHANNELS 48,29,30,31,32

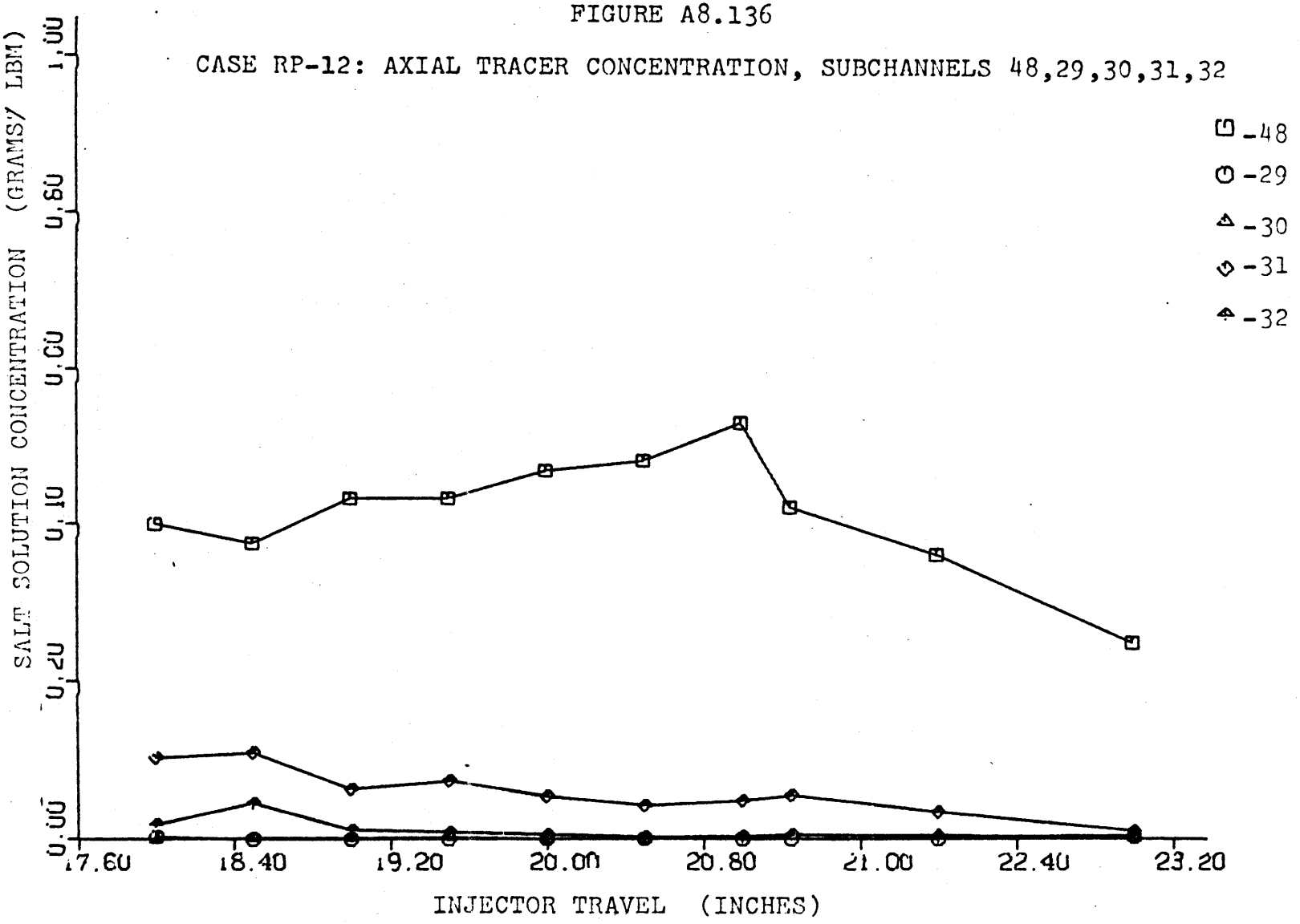

BIOGRAPHICAL NOTE

The author, Thomas Eldon Eaton, was born in Ironton, Missouri on 27 November 1948. He was educated in the public schools of Iron County, Missouri and graduated salutorian from Arcadia Valley High School in 1966.

The author attended the University of Missouri-Rolla, formerly known as the University of Missouri School of Mines and Metallurgy, during the period 1966 through 1970. He received a Bachelor of Science in Mechanical Engineering degree in January 1970 (minor in Nuclear Engineering). During the Spring and Summer, 1970 he was a Trainee of the National Science Foundation. He received a Master of Science in Mechanical Engineering in September 1970; the thesis performed for this degree was entitled: "Magnetohydrodynamic Stability of Developing Flow in the Entrance Region of a Parallel-Plate Channel."

The author attended the Massachusetts Institute of Technology from 1970 through 1975. He was a Fellow of the United States Atomic Energy Commission from 1970 through 1973, and was supported by the General Atomic Company from 1973 through 1974. In June, 1974, he received the degrees of Master of Science in Nuclear Engineering and Nuclear Engineer. The thesis work completed for these

degrees was entitled: "Instrumentation Methods for Inter-channel Coolant Mixing Experiments in Wire-Wrap Spaced Nuclear Fuel Assemblies."

The author is an elected member of the following honor societies: Tau Beta Pi, Pi Tau Sigma, Sigma Xi, Phi Kappa Phi, Sigma Pi Sigma, and the Nuclear Science and Engineering Honor Society (UMR). Also, he is a member of the following professional societies: American Society of Mechanical Engineers, Society of Mining Engineers, British Tunnelling Society and the American Nuclear Society. He is a Registered Professional Engineer in the Commonwealth of Virginia.